

A Local Flow Angle Approach to Centrifugal Compressor Vaneless Diffuser Stability

By

Christopher Clarke

A DISSERTATION

Submitted to
Michigan State University
in partial fulfillment of the requirements
for the degree of

MECHANICAL ENGINEERING – DOCTOR OF PHILOSOPHY

2016

ABSTRACT

A LOCAL FLOW ANGLE APPROACH TO CENTRIFUGAL COMPRESSOR VANELESS DIFFUSER STABILITY

By

Christopher Clarke

The vaneless diffuser is found in many applications of centrifugal compressors. Therefore, it has been the subject of numerous scientific investigations over the last several decades. While this has produced many results the issue of vaneless diffuser rotating stall still exists. This is because rotating stall is a dynamic instability tied directly to the compressor stage geometry. Most previous investigation have focused on determining the physical triggers that lead to rotating stall onset. This investigation is not meant to do that.

Previous investigations of centrifugal compressor stability have been focused on the time-dependent (transient) nature of the phenomenon. This investigation focuses on predicting the onset of rotating stall. In the preceding decades vaneless diffuser stability has been based upon the determining of a critical flow angle at the diffuser inlet based on the predictive Senoo – Kobayashi equation. However, it has been found that this one-dimensional method of predicting the critical flow angle is insufficient to properly determine the critical conditions for all diffuser models.

Using a steady state simulation the flow characteristics of fourteen unique geometries have been simulated at shaft speeds of 13100 RPM, 19240 RPM, and 21870 RPM. The local flow angle profile at the diffuser inlet as a function of span was determined and compared against the critical flow angle predicted by the Senoo – Kobayashi equation and the experimentally determined flow angle profiles provided by Solar Turbines Inc. This gave several interesting results.

It was found that the width ratio of the vaneless diffuser is the dominant parameter in predicting vaneless diffuser stability. For width ratios of 0.067 and above the local flow angle

profile breached the line determined by the Senoo – Kobayashi equation (henceforth Senoo line) at the point of rotating stall onset. For cases where the width ratio was 0.045 and smaller the local flow angle did not breach the Senoo line. For stages with width ratios between 0.045 and 0.067 the results showed that secondary influences help to determine whether or not the local profile is capable of breaching the Senoo line. It was discovered that it is possible to capture localized velocity reversal at the diffuser inlet for cases where the diffuser width ratio is 0.078 and greater.

Secondarily, it was found that the local flow angle approach was capable of capturing localized flow reversal inside of the diffuser. Through the use of a geometric parameter, b_4/d_{pitch} , it was determined that for geometries with values of 0.177 and above that localized flow reversal could be captured inside of the vaneless diffuser. However, for parameter values of 0.152 and below it was not possible to capture localized flow reversal in the diffuser. Nothing could be said about the region with parameter values between 0.152 and 0.177. This result leads to two very interesting conclusions. First, the results showed that there are two regions of flow breakdown. In the case where the parameter is above 0.177 the flow will breakdown in the span-wise direction allowing the steady state simulation to capture the localized flow reversal. In the region where the parameter is less than 0.152 the flow breaks down in the circumferential direction. This type of breakdown is washed out by the mass flow averaging process of the steady state simulation and does not allow for the detection of localized flow reversal inside of the diffuser.

Second, it has been taught that localized flow reversal is the trigger for rotating stall onset. However, it was determined that this is not the case. By use of the results showing localized flow reversal it was found that localized flow reversal preceded the onset of rotating stall and was not the trigger. Thus, it was determined that localized flow reversal is necessary for rotating stall onset, but not sufficient to be the primary trigger.

Copyright by
CHRISTOPHER CLARKE
2016

ACKNOWLEDGEMENTS

There are several people that I need to acknowledge without whom this work would not have been possible. First, my Lord and Savior Jesus Christ without whom I would be a lost sinner on my way to a devil's Hell instead of a child of God. Second, my beautiful wife, Tiffany, and our wonderful daughter, Adah, who have so graciously allowed their husband and daddy to work tirelessly on this project all while being drug from here to there and everywhere else. Third, my adviser Dr. Abraham Engeda who saw the potential in me and gave me a chance to do this work even when I did not. Thank you Professor for trusting me. Fourth, my friend and colleague Russ Marechale who provided much needed guidance and assistance with many of the simulations and with data interpretation. And for just helping me to know that I was on the right track. Fifth, Mike Cave of Solar Turbines for allowing me to use their geometries and experimental data for this project, without which there would be no project. Sixth, my committee for patiently waiting for me to finish and for allowing me to undertake this project even when nothing had been done beyond a lengthy literature review. Seventh, my parents who always encouraged me to keep at it and reminded me that even in the turmoil the Lord was in control and just to trust Him. Eighth, my colleague Dr. Tamara Reid-Bush for providing encouragement with the papers and the submission. Lastly, my friends and church family who provided much needed listening ears and prayer support when things did not go well. This is for all of you.

Table of Contents

LIST OF TABLES	x
LIST OF FIGURES	xii
KEY TO SYMBOLS	xxiv
CHAPTER 1: INTRODUCTION AND COMPRESSOR BASICS	31
1.1 The Centrifugal Compressor	2
1.1.1 The Compression Process	2
1.1.2 Differences between Centrifugal Compressors and Axial Compressors	3
1.1.3 Reasons for Frequent Use of Centrifugal Compressors vs. Axial Compressors	5
1.1.4 Applications of Centrifugal Compressors	8
1.1.5 Requirements of Centrifugal Compressors	8
1.2 The Vaneless Diffuser	10
1.2.1 Differences between Diffuser Types	11
1.2.2 Reasons behind the Frequent Use of Vaneless Diffusers and its Applications	11
CHAPTER 2: ROTATING STALL IN VANELESS DIFFUSERS OF CENTRIFUGAL COMPRESSORS	14
2.1 Rotating Stall Basics	14
2.1.1 Characteristics of Rotating Stall	14
2.1.2 Problems Caused by Rotating Stall	16
2.2 Rotating Stall Causes	18
2.2.1 Boundary Layer Separation Theory	18
2.2.2 Core Flow Destabilization Theory	19
2.2.3 Rotating Stall Cause Summary	20
2.3 Rotating Stall Solutions	20
2.3.1 Passive Control Solutions	20
2.3.2 Active Control Solutions	22
CHAPTER 3: THE LOCAL FLOW ANGLE APPROACH	24
3.1 Motivation for the Project	24
3.1.1 Need for an a Priori Prediction Method	24
3.1.2 Failure of the Senoo-Kobayashi Equation	25
3.2 Local Flow Angle Introduction	28
3.2.1 Genesis of the Approach	28
3.2.2 Application of the Approach	29
3.2.3 What is the Local Flow Angle Approach?	30
3.3 Goals of the Project	31
CHAPTER 4: LOCAL FLOW ANGLE APPROACH	32
4.1 Theoretical and Numerical Tools	32
4.1.1 Senoo – Kobayashi Equation	32
4.1.2 Use of ANSYS – CFX	33
4.1.3 Five Critical Parameters	33
4.2 Experimental Procedure for Performance Measurements	36
4.3 Experimental Procedure to Determine Diffuser Inlet Flow Angle	36

4.4 Experimental Procedure to Determine Rotating Stall Onset.....	37
CHAPTER 5: NUMERICAL PRECURSORS	41
5.1 How the Local Flow Angle Approach Works	41
5.2 Verifying the Validity of the Results	44
5.3 The Grid Sensitivity Study.....	45
5.3.1 What is a Grid Sensitivity Study and Why is it Important?	45
5.3.2 Results of the Grid Sensitivity Study	45
5.4 The Next Phase	51
CHAPTER 6: LOCAL FLOW ANGLE APPROACH RESULTS.....	52
6.1 Background on Experimental Geometries	52
6.2 Comparison of Average Flow Angles to the Five Critical Parameters	52
6.2.1 Width Ratio Comparison	53
6.2.2 Radius Ratio Comparison	56
6.2.3 Mach Number Comparison.....	58
6.2.4 Reynolds Number Comparison.....	60
6.2.5 Inlet Velocity Distortion Comparison.....	62
6.2.5.1 Meridional Velocity Comparison.....	63
6.2.5.2 Tangential Velocity Distortion.....	68
6.2.5.3 Failure of Senoo’s Distortion Correlation.....	73
6.2.6 Overall Trends Developed From Comparisons.....	74
6.3 Local Flow Angle Results.....	75
6.3.1 Compressor 1 Profiles.....	76
6.3.1.1 Compressor 1 13100 RPM Results	76
6.3.1.2 Compressor 1 19240 RPM Results	78
6.3.1.3 Compressor 1 21870 RPM Results	80
6.3.2 Compressor 2 Profiles.....	82
6.3.2.1 Compressor 2 13100 RPM Results	82
6.3.2.2 Compressor 2 19240 RPM Results	84
6.3.2.3 Compressor 2 21870 RPM Results	86
6.3.3 Compressor 3 Profiles.....	88
6.3.3.1 Compressor 3 13100 RPM Results	88
6.3.3.2 Compressor 3 19240 RPM Results	90
6.3.3.3 Compressor 3 21870 RPM Results	92
6.3.4 Compressor 4 Profiles.....	94
6.3.4.1 Compressor 4 13100 RPM Results	94
6.3.4.2 Compressor 4 19240 RPM Results	96
6.3.4.3 Compressor 4 21870 RPM Results	98
6.3.5 Compressor 5 Profiles.....	100
6.3.5.1 Compressor 5 13100 RPM Results	100
6.3.5.2 Compressor 5 19240 RPM Results	102
6.3.5.3 Compressor 5 21870 RPM Results	104
6.3.6 Compressor 6 Profiles.....	106
6.3.6.1 Compressor 6 13100 RPM Results	106
6.3.6.2 Compressor 6 19240 RPM Results	109
6.3.6.3 Compressor 6 21870 RPM Results	111
6.3.7 Compressor 7 Profiles.....	113
6.3.7.1 Compressor 7 13100 RPM Results	113
6.3.7.2 Compressor 7 19240 RPM Results	115
6.3.7.3 Compressor 7 21870 RPM Results	117

6.3.8 Compressor 8 Profiles	119
6.3.8.1 Compressor 8 13100 RPM Results	119
6.3.8.2 Compressor 8 19240 RPM Results	121
6.3.8.3 Compressor 8 21870 RPM Results	123
6.3.9 Compressor 9 Profiles	125
6.3.9.1 Compressor 9 13100 RPM Results	125
6.3.9.2 Compressor 9 19240 RPM Results	127
6.3.9.3 Compressor 9 21870 RPM Results	129
6.3.10 Compressor 10 Profiles	131
6.3.10.1 Compressor 10 13100 RPM Results	131
6.3.10.2 Compressor 10 19240 RPM Results	133
6.3.10.3 Compressor 10 21870 RPM Results	135
6.3.11 Compressor 11 Profiles	137
6.3.11.1 Compressor 11 13100 RPM Results	137
6.3.11.2 Compressor 11 19240 RPM Results	139
6.3.11.3 Compressor 11 21870 RPM Results	141
6.3.12 Compressor 12 Profiles	143
6.3.12.1 Compressor 12 13100 RPM Results	143
6.3.12.2 Compressor 12 19240 RPM Results	145
6.3.12.3 Compressor 12 21870 RPM Results	147
6.3.13 Compressor 13 Profiles	149
6.3.13.1 Compressor 13 13100 RPM Results	149
6.3.13.2 Compressor 13 19240 RPM Results	151
6.3.13.3 Compressor 13 21870 RPM Results	153
6.3.14 Compressor 14 Profiles	155
6.3.14.1 Compressor 14 13100 RPM Results	155
6.3.14.2 Compressor 14 19240 RPM Results	157
6.3.14.3 Compressor 14 21870 RPM Results	159
6.3.15 Overall Results found from Profile Comparisons	161
CHAPTER 7: OTHER INTERESTING RESULTS	168
7.1 Flow Reversal at the Diffuser Inlet	168
7.1.1 General Results	170
7.1.2 Geometric Consideration	174
7.1.3 Local Flow Velocity Reversal and Rotating Stall Onset	180
7.2 Digitized Senoo Curve Investigation	192
7.2.1 Process of Digitization	192
7.2.2 Digitization Results	196
7.2.3 Conclusions and Recommendations from Digitization Investigation	207
7.3 Distortion Correlation Investigation	208
7.4 Blade Number Investigation	210
7.4.1 Blade Number Comparison Investigation Background	210
7.4.2 Blade Number Comparison Results	210
CHAPTER 8: CONCLUSIONS	214
8.1 General Conclusions	214
8.1.1 Conclusions from Average Flow Angle Results	214
8.1.2 Conclusions from Local Flow Angle Results	214
8.1.3 Conclusions from Diffuser Inlet Flow Reversal Results	215
8.1.4 Conclusions from Digitized Senoo Curve Investigation	216
8.1.5 Conclusions from Distortion Correlation Results	216

8.1.6 Conclusions from Blade Number Investigation	217
8.2 Next Step of the Project	217
8.2.1 Different Turbulence Model Investigation.....	218
8.2.2 Transient Simulation Investigation for Comparison against Steady State Results	218
8.2.2.1 Single Passage Transient Simulation	219
8.2.2.2 Full 360 Degree Transient Simulation	219
8.2.3 Experimental Investigation of Prototype Compressor	220
APPENDICES	221
APPENDIX A: OPERATING ENVELOPE PLOTS	222
APPENDIX B: TEMPERATURE COMPARISONS.....	244
APPENDIX C: STEADY STATE SIMULATION AND SST INFORMATION.....	266
REFERENCES	273

LIST OF TABLES

Table 1: Pressure Ratio Comparison adapted and reproduced from [11]	5
Table 2: Compressor Geometries and Flow Details	46
Table 3: Width Ratio Comparison at 13100 RPM	54
Table 4: Width Ratio Comparison at 19240 RPM	54
Table 5: Width Ratio Comparison at 21870 RPM	55
Table 6: Radius Ratio Comparison at 13100 RPM	56
Table 7: Radius Ratio Comparison at 19240 RPM	57
Table 8: Radius Ratio Comparison at 21870 RPM	57
Table 9: Mach Number Comparison at 13100 RPM	58
Table 10: Mach Number Comparison at 19240 RPM	59
Table 11: Mach Number Comparison at 21870 RPM	59
Table 12: Reynolds Number Comparison at 13100 RPM	61
Table 13: Reynolds Number Comparison at 19240 RPM	61
Table 14: Reynolds Number Comparison at 21870 RPM	62
Table 15: Meridional Distortion Comparison at 0% and 100% at 13100 RPM	63
Table 16: Meridional Distortion Comparison at 0% and 100% at 19240 RPM	64
Table 17: Meridional Distortion Comparison at 0% and 100% at 21870 RPM	64
Table 18: Meridional Distortion Comparison at 5% and 95% at 13100 RPM	65
Table 19: Meridional Distortion Comparison at 5% and 95% at 19240 RPM	66
Table 20: Meridional Distortion Comparison at 5% and 95% at 21870 RPM	66
Table 21: New Meridional Distortion Comparison at 13100 RPM	67
Table 22: New Meridional Distortion Comparison at 19240 RPM	67

Table 23: New Meridional Distortion Comparison at 21870 RPM	68
Table 24: Tangential Distortion Comparison at 0% and 100% at 13100 RPM	69
Table 25: Tangential Distortion Comparison at 0% and 100% at 19240 RPM	69
Table 26: Tangential Distortion Comparison at 0% and 100% at 21870 RPM	70
Table 27: Tangential Distortion Comparison at 5% and 95% at 13100 RPM	70
Table 28: Tangential Distortion Comparison at 5% and 95% at 19240 RPM	71
Table 29: Tangential Distortion Comparison at 5% and 95% at 21870 RPM	71
Table 30: New Tangential Distortion Comparison at 13100 RPM.....	72
Table 31: New Tangential Distortion Comparison at 19240 RPM.....	72
Table 32: New Tangential Distortion Comparison at 21870 RPM.....	73
Table 33: Critical Values at 13100 RPM.....	162
Table 34: Critical Values at 19240 RPM.....	162
Table 35: Critical Values at 21870 RPM.....	163
Table 36: Localized Flow Reversal Results at 13100 RPM	171
Table 37: Localized Flow Reversal Results at 19240 RPM	172
Table 38: Localized Flow Reversal Results at 21870 RPM	172
Table 39: Localized Flow Reversal Results at 13100 RPM	175
Table 40: Localized Flow Reversal Results at 19240 RPM	175
Table 41: Localized Flow Reversal Results at 21870 RPM	176

LIST OF FIGURES

Figure 1: Axial Compressor Examples adapted and reproduced from [12].....	4
Figure 2: Centrifugal Compressor Example adapted and reproduced from [12].....	5
Figure 3: Axial Compressor adapted and reproduced from [11]	6
Figure 4: Centrifugal Compressor adapted and reproduced from [11].....	6
Figure 5: Example Compressor Map adapted and reproduced from [39].....	9
Figure 6: Centrifugal Compressor with Volute adapted and reproduced from [11]	10
Figure 7: Sketch of Spike Inception adapted and reproduced from [44]	14
Figure 8: Sketch of Modal-Wave Inception adapted and reproduced from [44]	15
Figure 9: Senoo – Kobayashi plot adapted and reproduced from [41]	27
Figure 10: Example of a Spectrum Plot provided by [27]	38
Figure 11: Example of a Coherence Plot adapted and reproduced from [38].....	38
Figure 12: Hanover Plot for Forward Direction Stall Cell Rotation provided by [27].	39
Figure 13: Hanover Plot for Reverse Direction Stall Cell Rotation provided by [27].....	40
Figure 14: Example Geometry	41
Figure 15: Performance Envelope Comparison	47
Figure 16: Stagnation Temperature Comparison	48
Figure 17: Meridional Velocity Comparison at Diffuser Inlet.....	48
Figure 18: Tangential Velocity Comparison at Diffuser Inlet	49
Figure 19: Meridional Velocity Comparison at Diffuser Inlet.....	49
Figure 20: Tangential Velocity Comparison at Diffuser Inlet	50
Figure 21: C_{m4} Comparison for Compressor 1 at 13100 RPM Stall Point.....	77
Figure 22: C_{t4} Comparison for Compressor 1 at 13100 RPM Stall Point.....	77

Figure 23: Stall Analysis for Compressor 1 at 13100 RPM Stall Point.....	78
Figure 24: C_{m4} Comparison for Compressor 1 at 19240 RPM Stall Point.....	79
Figure 25: C_{t4} Comparison for Compressor 1 at 19240 RPM Stall Point.....	79
Figure 26: Stall Analysis for Compressor 1 at 19240 RPM Stall Point.....	80
Figure 27: C_{m4} Comparison for Compressor 1 at 21870 RPM Stall Point.....	81
Figure 28: C_{t4} Comparison for Compressor 1 at 21870 RPM Stall Point.....	81
Figure 29: Stall Analysis for Compressor 1 at 21870 RPM Stall Point.....	82
Figure 30: C_{m4} Comparison for Compressor 2 at 13100 RPM Stall Point.....	83
Figure 31: C_{t4} Comparison for Compressor 2 at 13100 RPM Stall Point.....	83
Figure 32: Stall Analysis for Compressor 2 at 13100 RPM Stall Point.....	84
Figure 33: C_{m4} Comparison for Compressor 2 at 19240 RPM Stall Point.....	85
Figure 34: C_{t4} Comparison for Compressor 2 at 19240 RPM Stall Point.....	85
Figure 35: Stall Analysis for Compressor 2 at 19240 RPM Stall Point.....	86
Figure 36: C_{m4} Comparison for Compressor 2 at 21870 RPM Stall Point.....	87
Figure 37: C_{t4} Comparison for Compressor 2 at 21870 RPM Stall Point.....	87
Figure 38: Stall Analysis for Compressor 2 at 21870 RPM Stall Point.....	88
Figure 39: C_{m4} Comparison for Compressor 3 at 13100 RPM Stall Point.....	89
Figure 40: C_{t4} Comparison for Compressor 3 at 13100 RPM Stall Point.....	89
Figure 41: Stall Analysis for Compressor 3 at 13100 RPM Stall Point.....	90
Figure 42: C_{m4} Comparison for Compressor 3 at 19240 RPM Stall Point.....	91
Figure 43: C_{t4} Comparison for Compressor 3 at 19240 RPM Stall Point.....	91
Figure 44: Stall Analysis for Compressor 3 at 19240 RPM Stall Point.....	92
Figure 45: C_{m4} Comparison for Compressor 3 at 21870 RPM Stall Point.....	93
Figure 46: C_{t4} Comparison for Compressor 3 at 21870 RPM Stall Point.....	93

Figure 47: Stall Analysis for Compressor 3 at 21870 RPM Stall Point.....	94
Figure 48: C_{m4} Comparison for Compressor 4 at 13100 RPM Stall Point.....	95
Figure 49: C_{t4} Comparison for Compressor 4 at 13100 RPM Stall Point.....	95
Figure 50: Stall Analysis for Compressor 4 at 13100 RPM Stall Point.....	96
Figure 51: C_{m4} Comparison for Compressor 4 at 19240 RPM Stall Point.....	97
Figure 52: C_{t4} Comparison for Compressor 4 at 19240 RPM Stall Point.....	97
Figure 53: Stall Analysis for Compressor 4 at 19240 RPM Stall Point.....	98
Figure 54: C_{m4} Comparison for Compressor 4 at 21870 RPM Stall Point.....	99
Figure 55: C_{t4} Comparison for Compressor 4 at 21870 RPM Stall Point.....	99
Figure 56: Stall Analysis for Compressor 4 at 21870 RPM Stall Point.....	100
Figure 57: C_{m4} Comparison for Compressor 5 at 13100 RPM Stall Point.....	101
Figure 58: C_{t4} Comparison for Compressor 5 at 13100 RPM Stall Point.....	101
Figure 59: Stall Analysis for Compressor 5 at 13100 RPM Stall Point.....	102
Figure 60: C_{m4} Comparison for Compressor 5 at 19240 RPM Stall Point.....	103
Figure 61: C_{t4} Comparison for Compressor 5 at 19240 RPM Stall Point.....	103
Figure 62: Stall Analysis for Compressor 5 at 19240 RPM Stall Point.....	104
Figure 63: C_{m4} Comparison for Compressor 5 at 21870 RPM Stall Point.....	105
Figure 64: C_{t4} Comparison for Compressor 5 at 21870 RPM Stall Point.....	105
Figure 65: Stall Analysis for Compressor 5 at 21870 RPM Stall Point.....	106
Figure 66: C_{m4} Comparison for Compressor 6 at 13100 Last Stable Flow Point.....	107
Figure 67: C_{t4} Comparison for Compressor 6 at 13100 RPM Last Stable Flow Point.....	108
Figure 68: Stall Analysis for Compressor 6 at 13100 RPM Last Stable Flow Point.....	108
Figure 69: C_{m4} Comparison for Compressor 6 at 19240 RPM Last Stable Flow Point.....	109
Figure 70: C_{t4} Comparison for Compressor 6 at 19240 RPM Last Stable Flow Point.....	110

Figure 71: Stall Analysis for Compressor 6 at 19240 RPM Last Stable Flow Point	110
Figure 72: C_{m4} Comparison for Compressor 6 at 21870 RPM Last Stable Flow Point	111
Figure 73: C_{t4} Comparison for Compressor 6 at 21870 RPM Last Stable Flow Point	112
Figure 74: Stall Analysis for Compressor 6 at 21870 RPM Last Stable Flow Point	112
Figure 75: C_{m4} Comparison for Compressor 7 at 13100 RPM Stall Point.....	113
Figure 76: C_{t4} Comparison for Compressor 7 at 13100 RPM Stall Point.....	114
Figure 77: Stall Analysis for Compressor 7 at 13100 RPM Stall Point.....	114
Figure 78: C_{m4} Comparison for Compressor 7 at 19240 RPM Stall Point.....	115
Figure 79: C_{t4} Comparison for Compressor 7 at 19240 RPM Stall Point.....	116
Figure 80: Stall Analysis for Compressor 7 at 19240 RPM Stall Point.....	116
Figure 81: C_{m4} Comparison for Compressor 7 at 21870 RPM Stall Point.....	117
Figure 82: C_{t4} Comparison for Compressor 7 at 21870 RPM Stall Point.....	118
Figure 83: Stall Analysis for Compressor 7 at 21870 RPM Stall Point.....	118
Figure 84: C_{m4} Comparison for Compressor 8 at 13100 RPM Stall Point.....	119
Figure 85: C_{t4} Comparison for Compressor 8 at 13100 RPM Stall Point.....	120
Figure 86: Stall Analysis for Compressor 8 at 13100 RPM Stall Point.....	120
Figure 87: C_{m4} Comparison for Compressor 8 at 19240 RPM Stall Point.....	121
Figure 88: C_{t4} Comparison for Compressor 8 at 19240 RPM Stall Point.....	122
Figure 89: Stall Analysis for Compressor 8 at 19240 RPM Stall Point.....	122
Figure 90: C_{m4} Comparison for Compressor 8 at 21870 RPM Stall Point.....	123
Figure 91: C_{t4} Comparison for Compressor 8 at 21870 RPM Stall Point.....	124
Figure 92: Stall Analysis for Compressor 8 at 21870 RPM Stall Point.....	124
Figure 93: C_{m4} Comparison for Compressor 9 at 13100 RPM Stall Point.....	125
Figure 94: C_{t4} Comparison for Compressor 9 at 13100 RPM Stall Point.....	126

Figure 95: Stall Analysis for Compressor 9 at 13100 RPM Stall Point.....	126
Figure 96: C_{m4} Comparison for Compressor 9 at 19240 RPM Stall Point.....	127
Figure 97: C_{t4} Comparison for Compressor 9 at 19240 RPM Stall Point.....	128
Figure 98: Stall Analysis for Compressor 9 at 19240 RPM Stall Point.....	128
Figure 99: C_{m4} Comparison for Compressor 9 at 21870 RPM Last Stable Flow Point.....	129
Figure 100: C_{t4} Comparison for Compressor 9 at 21870 RPM Last Stable Flow Point.....	130
Figure 101: Stall Analysis for Compressor 9 at 21870 RPM Last Stable Flow Point.....	130
Figure 102: C_{m4} Comparison for Compressor 10 at 13100 RPM Last Stable Flow Point.....	131
Figure 103: C_{t4} Comparison for Compressor 10 at 13100 RPM Last Stable Flow Point.....	132
Figure 104: Stall Analysis for Compressor 10 at 13100 RPM Last Stable Flow Point.....	132
Figure 105: C_{m4} Comparison for Compressor 10 at 19240 RPM Last Stable Flow Point.....	133
Figure 106: C_{t4} Comparison for Compressor 10 at 19240 RPM Last Stable Flow Point.....	134
Figure 107: Stall Analysis for Compressor 10 at 19240 RPM Last Stable Flow Point.....	134
Figure 108: C_{m4} Comparison for Compressor 10 at 21870 RPM Last Stable Flow Point.....	135
Figure 109: C_{t4} Comparison for Compressor 10 at 21870 RPM Last Stable Flow Point.....	136
Figure 110: Stall Analysis for Compressor 10 at 21870 RPM Last Stable Flow Point.....	136
Figure 111: C_{m4} Comparison for Compressor 11 at 13100 RPM Stall Point.....	137
Figure 112: C_{t4} Comparison for Compressor 11 at 13100 RPM Stall Point.....	138
Figure 113: Stall Analysis for Compressor 11 at 13100 RPM Stall Point.....	138
Figure 114: C_{m4} Comparison for Compressor 11 at 19240 RPM Stall Point.....	140
Figure 115: C_{t4} Comparison for Compressor 11 at 19240 RPM Stall Point.....	140
Figure 116: Stall Analysis for Compressor 11 at 19240 RPM Stall Point.....	141
Figure 117: C_{m4} Comparison for Compressor 11 at 21870 RPM Last Stable Flow Point.....	142
Figure 118: C_{t4} Comparison for Compressor 11 at 21870 RPM Last Stable Flow Point.....	142

Figure 119: Stall Analysis for Compressor 11 at 21870 RPM Last Stable Flow Point	143
Figure 120: C_{m4} Comparison for Compressor 12 at 13100 RPM Stall Point.....	144
Figure 121: C_{t4} Comparison for Compressor 12 at 13100 RPM Stall Point.....	144
Figure 122: Stall Analysis for Compressor 12 at 13100 RPM Stall Point.....	145
Figure 123: C_{m4} Comparison for Compressor 12 at 19240 RPM Stall Point.....	146
Figure 124: C_{t4} Comparison for Compressor 12 at 19240 RPM Stall Point	146
Figure 125: Stall Analysis for Compressor 12 at 19240 RPM Stall Point.....	147
Figure 126: C_{m4} Comparison for Compressor 12 at 21870 RPM Stall Point.....	148
Figure 127: C_{t4} Comparison for Compressor 12 at 21870 RPM Stall Point.....	148
Figure 128: Stall Analysis for Compressor 12 at 21870 RPM Stall Point.....	149
Figure 129: C_{m4} Comparison for Compressor 13 at 13100 RPM Stall Point.....	150
Figure 130: C_{t4} Comparison for Compressor 13 at 13100 RPM Stall Point.....	150
Figure 131: Stall Analysis for Compressor 13 at 13100 RPM Stall Point.....	151
Figure 132: C_{m4} Comparison for Compressor 13 at 19240 RPM Stall Point.....	152
Figure 133: C_{t4} Comparison for Compressor 13 at 19240 RPM Stall Point.....	152
Figure 134: Stall Analysis for Compressor 13 at 19240 RPM Stall Point.....	153
Figure 135: C_{m4} Comparison for Compressor 13 at 21870 RPM Stall Point.....	154
Figure 136: C_{t4} Comparison for Compressor 13 at 21870 RPM Stall Point.....	154
Figure 137: Stall Analysis for Compressor 13 at 21870 RPM Stall Point.....	155
Figure 138: C_{m4} Comparison for Compressor 14 at 13100 RPM Stall Point.....	156
Figure 139: C_{t4} Comparison for Compressor 14 at 13100 RPM Stall Point.....	156
Figure 140: Stall Analysis for Compressor 14 at 13100 RPM Stall Point.....	157
Figure 141: C_{m4} Comparison for Compressor 14 at 19240 RPM Stall Point.....	158
Figure 142: C_{t4} Comparison for Compressor 14 at 19240 RPM Stall Point.....	158

Figure 143: Stall Analysis for Compressor 14 at 19240 RPM Stall Point.....	159
Figure 144: C_{m4} Comparison for Compressor 14 at 21870 RPM Stall Point.....	160
Figure 145: C_{t4} Comparison for Compressor 14 at 21870 RPM Stall Point.....	160
Figure 146: Stall Analysis for Compressor 14 at 21870 RPM Stall Point.....	161
Figure 147: Compressor 2, Full View.....	169
Figure 148: Compressor 2, Close Up.....	169
Figure 149: Compressor 13, Full View.....	170
Figure 150: Compressor 13, Close Up.....	170
Figure 151: Compressor 12, Full View, 19240 RPM	173
Figure 152: Compressor 12, Close Up, 19240 RPM	173
Figure 153: Compressor 10, 13100 RPM, Last Stable Flow Point.....	177
Figure 154: Compressor 10, 19240 RPM, Last Stable Flow Point.....	177
Figure 155: Compressor 10, 21870 RPM, Last Stable Flow Point.....	178
Figure 156: Compressor 6, 13100 RPM, Last Stable Flow Point.....	179
Figure 157: Compressor 6, 19240 RPM, Last Stable Flow Point.....	179
Figure 158: Compressor 6, 21870 RPM, Last Stable Flow Point.....	180
Figure 159: Compressor 2, $\phi = 0.026027$	181
Figure 160: Compressor 2, $\phi = 0.022083$	181
Figure 161: Compressor 2, $\phi = \phi_{RS} = 0.019$	182
Figure 162: Compressor 2, $\phi = 0.018883$	182
Figure 163: Compressor 5, $\phi = 0.0385$	183
Figure 164: Compressor 5, $\phi = 0.0336$	183
Figure 165: Compressor 5, $\phi = \phi_{RS} = 0.0299$	184
Figure 166: Compressor 5, $\phi = 0.0295$	184

Figure 167: Compressor 7, $\phi = 0.0066$	185
Figure 168: Compressor 7, $\phi = 0.005$	185
Figure 169: Compressor 7, $\phi = \phi_{RS} = 0.00498$	186
Figure 170: Compressor 7, $\phi = 0.004017$	186
Figure 171: Compressor 9, $\phi = 0.040208$	187
Figure 172: Compressor 9, $\phi = 0.033401$	187
Figure 173: Compressor 9, $\phi = \phi_{RS} = 0.03324$	188
Figure 174: Compressor 9, $\phi = 0.028244$	188
Figure 175: Compressor 13, $\phi = 0.064257$	189
Figure 176: Compressor 13, $\phi = 0.055032$	189
Figure 177: Compressor 13, $\phi = \phi_{RS} = 0.046943$	190
Figure 178: Compressor 13, $\phi = 0.045548$	190
Figure 179: Compressor 14, $\phi = 0.08472$	191
Figure 180: Compressor 14, $\phi = 0.077772$	191
Figure 181: Compressor 14, $\phi = \phi_{RS} = 0.07766$	191
Figure 182: Compressor 14, $\phi = 0.064187$	192
Figure 183: Tangential Distortion Example Adapted and Reproduced from [32]	193
Figure 184: Radius Ratio Plot Adapted and Reproduced from [26]	194
Figure 185: Digitized Tangential Distortion Example of Plot from [32]	194
Figure 186: Digitized Radius Ratio Example of Plot from [32]	195
Figure 187: Compressor 1 Angle Comparison Using Meridional Distortion at Stall Point	197
Figure 188: Compressor 1 Angle Comparison Using Mach Number at Stall Point	198
Figure 189: Compressor 1 Angle Comparison Using Radius Ratio at Stall Point	198
Figure 190: Compressor 1 Angle Comparison Using Tangential Distortion at Stall Point	199

Figure 191: Compressor 5 Angle Comparison Using Meridional Distortion at Stall Point	200
Figure 192: Compressor 5 Angle Comparison Using Mach Number at Stall Point	200
Figure 193: Compressor 5 Angle Comparison Using Radius Ratio at Stall Point.....	201
Figure 194: Compressor 5 Angle Comparison Using Tangential Distortion at Stall Point	201
Figure 195: Compressor 7 Angle Comparison Using Meridional Distortion at Stall Point	202
Figure 196: Compressor 7 Angle Comparison Using Mach Number at Stall Point	203
Figure 197: Compressor 7 Angle Comparison Using Radius Ratio at Stall Point.....	203
Figure 198: Compressor 7 Angle Comparison Using Tangential Distortion at Stall Point	204
Figure 199: Compressor 13 Angle Comparison Using Meridional Distortion at Stall Point	205
Figure 200: Compressor 13 Angle Comparison Using Mach Number at Stall Point	205
Figure 201: Compressor 13 Angle Comparison Using Radius Ratio at Stall Point.....	206
Figure 202: Compressor 13 Angle Comparison Using Tangential Distortion at Stall Point	206
Figure 203: Comparison between Critical Flow Angle and Meridional Distortion ($0 \leq b_4/R_4 \leq 0.056$) ..	208
Figure 204: Comparison between Critical Flow Angle and Meridional Distortion ($0.057 \leq b_4/R_4 \leq 0.134$)	209
Figure 205: Compressor 5 Local Flow Angle at 13100 RPM Stall Point, 13 Blade Comparison	212
Figure 206: Compressor 5 Local Flow Angle at 19240 RPM Stall Point, 13 Blade Comparison	212
Figure 207: Compressor 5 Local Flow Angle at 21870 RPM Stall Point, 13 Blade Comparison	213
Figure 208: Compressor 1 13100 RPM Operation Envelope	223
Figure 209: Compressor 1 19240 RPM Operation Envelope	223
Figure 210: Compressor 1 21870 RPM Operation Envelope	224
Figure 211: Compressor 2 13100 RPM Operation Envelope	224
Figure 212: Compressor 2 19240 RPM Operation Envelope	225
Figure 213: Compressor 2 21870 RPM Operation Envelope	225

Figure 214: Compressor 3 13100 RPM Operation Envelope	226
Figure 215: Compressor 3 19240 RPM Operation Envelope	226
Figure 216: Compressor 3 21870 RPM Operation Envelope	227
Figure 217: Compressor 4 13100 RPM Operation Envelope	227
Figure 218: Compressor 4 19240 RPM Operation Envelope	228
Figure 219: Compressor 4 21870 RPM Operation Envelope	228
Figure 220: Compressor 5 13100 RPM Operation Envelope	229
Figure 221: Compressor 5 19240 RPM Operation Envelope	229
Figure 222: Compressor 5 21870 RPM Operation Envelope	230
Figure 223: Compressor 6 13100 RPM Operation Envelope	230
Figure 224: Compressor 6 19240 RPM Operation Envelope	231
Figure 225: Compressor 6 21870 RPM Operation Envelope	231
Figure 226: Compressor 7 13100 RPM Operation Envelope	232
Figure 227: Compressor 7 19240 RPM Operation Envelope	232
Figure 228: Compressor 7 21870 RPM Operation Envelope	233
Figure 229: Compressor 8 13100 RPM Operation Envelope	233
Figure 230: Compressor 8 19240 RPM Operation Envelope	234
Figure 231: Compressor 8 21870 RPM Operation Envelope	234
Figure 232: Compressor 9 13100 RPM Operation Envelope	235
Figure 233: Compressor 9 19240 RPM Operation Envelope	235
Figure 234: Compressor 9 21870 RPM Operation Envelope	236
Figure 235: Compressor 10 13100 RPM Operation Envelope	236
Figure 236: Compressor 10 19240 RPM Operation Envelope	237
Figure 237: Compressor 10 21870 RPM Operation Envelope	237

Figure 238: Compressor 11 13100 RPM Operation Envelope	238
Figure 239: Compressor 11 19240 RPM Operation Envelope	238
Figure 240: Compressor 11 21870 RPM Operation Envelope	239
Figure 241: Compressor 12 13100 RPM Operation Envelope	239
Figure 242: Compressor 12 19240 RPM Operation Envelope	240
Figure 243: Compressor 12 21870 RPM Operation Envelope	240
Figure 244: Compressor 13 13100 RPM Operation Envelope	241
Figure 245: Compressor 13 19240 RPM Operation Envelope	241
Figure 246: Compressor 13 21870 RPM Operation Envelope	242
Figure 247: Compressor 14 13100 RPM Operation Envelope	242
Figure 248: Compressor 14 19240 RPM Operation Envelope	243
Figure 249: Compressor 14 21870 RPM Operation Envelope	243
Figure 250: Compressor 1 13100 RPM Temperature Comparison	245
Figure 251: Compressor 1 19240 RPM Temperature Comparison	245
Figure 252: Compressor 1 21870 RPM Temperature Comparison	246
Figure 253: Compressor 2 13100 RPM Temperature Comparison	246
Figure 254: Compressor 2 19240 RPM Temperature Comparison	247
Figure 255: Compressor 2 21870 RPM Temperature Comparison	247
Figure 256: Compressor 3 13100 RPM Temperature Comparison	248
Figure 257: Compressor 3 19240 RPM Temperature Comparison	248
Figure 258: Compressor 3 21870 RPM Temperature Comparison	249
Figure 259: Compressor 4 13100 RPM Temperature Comparison	249
Figure 260: Compressor 4 19240 RPM Temperature Comparison	250
Figure 261: Compressor 4 21870 RPM Temperature Comparison	250

Figure 262: Compressor 5 13100 RPM Temperature Comparison	251
Figure 263: Compressor 5 19240 RPM Temperature Comparison	251
Figure 264: Compressor 5 21870 RPM Temperature Comparison	252
Figure 265: Compressor 6 13100 RPM Temperature Comparison	252
Figure 266: Compressor 6 19240 RPM Temperature Comparison	253
Figure 267: Compressor 6 21870 RPM Temperature Comparison	253
Figure 268: Compressor 7 13100 RPM Temperature Comparison	254
Figure 269: Compressor 7 19240 RPM Temperature Comparison	254
Figure 270: Compressor 7 21870 RPM Temperature Comparison	255
Figure 271: Compressor 8 13100 RPM Temperature Comparison	255
Figure 272: Compressor 8 19240 RPM Temperature Comparison	256
Figure 273: Compressor 8 21870 RPM Temperature Comparison	256
Figure 274: Compressor 9 13100 RPM Temperature Comparison	257
Figure 275: Compressor 9 19240 RPM Temperature Comparison	257
Figure 276: Compressor 9 21870 RPM Temperature Comparison	258
Figure 277: Compressor 10 13100 RPM Temperature Comparison	258
Figure 278: Compressor 10 19240 RPM Temperature Comparison	259
Figure 279: Compressor 10 21870 RPM Temperature Comparison	259
Figure 280: Compressor 11 13100 RPM Temperature Comparison	260
Figure 281: Compressor 11 19240 RPM Temperature Comparison	260
Figure 282: Compressor 11 21870 RPM Temperature Comparison	261
Figure 283: Compressor 12 13100 RPM Temperature Comparison	261
Figure 284: Compressor 12 19240 RPM Temperature Comparison	262
Figure 285: Compressor 12 21870 RPM Temperature Comparison	262

Figure 286: Compressor 13 13100 RPM Temperature Comparison 263

Figure 287: Compressor 13 19240 RPM Temperature Comparison 263

Figure 288: Compressor 13 21870 RPM Temperature Comparison 264

Figure 289: Compressor 14 13100 RPM Temperature Comparison 264

Figure 290: Compressor 14 19240 RPM Temperature Comparison 265

Figure 291: Compressor 14 21870 RPM Temperature Comparison 265

KEY TO SYMBOLS

Lower Case Roman Letters

a_1 = A constant used in the SST model

b_2/R_2 and b_4/R_4 = Diffuser width ratio

b_4 = Diffuser width at station 4

b_4/d_{pitch} = Parameter comparing diffuser width to impeller blade pitch distance

d_{pitch} = Circumferential (pitch) distance between impeller blades

e_x = Unit vector in x direction

e_y = Unit vector in y direction

e_z = Unit vector in z direction

\vec{g} = External body force vector

g = Gravitational constant near Earth's surface with a value of 9.81 m/s^2

k = Turbulent kinetic energy

\dot{m} = Mass flow rate

p = pressure

t = Time

u = Velocity fluctuation in x direction

$\bar{u}(x,t)$ = Fluctuation term

$\overline{\bar{u}(x,t)}$ = Time averaged fluctuation term

$\overline{\bar{u}_i * \bar{u}_j}$ = Time average of the product of velocity fluctuation vectors

u^* = friction velocity

v = Velocity fluctuation in y direction

w = Velocity fluctuation in z direction

$x_i = x_j$ = spacial coordinates in index notation

y = Distance to the nearest wall

y^+ = Dimensionless wall distance

Upper Case Roman Letters

A_c = Cross sectional area

C = Total velocity

C_i = Total velocity at station i

C_m = Meridional velocity

$C_{m,i}$ = Mass flow averaged meridional velocity at station i

$C_{t,i}$ = Mass flow averaged tangential velocity at station i

$C_{m4,average}$ = Mass flow averaged meridional velocity at station 4

$C_{m4,k}$ = Meridional velocity at span value k for station 4

$C_{m4,max}$ = Maximum meridional velocity at station 4

$C_{m4,min}$ = Minimum meridional velocity at station 4

$C_{m4,average}$ = Mass flow averaged meridional velocity at station 4

C_r = Radial flow velocity

$C_{t4,average}$ = Mass flow averaged tangential velocity at station 4

$C_{t4,k}$ = Tangential velocity at span value k for station 4

$C_{t4,max}$ = Maximum tangential velocity at station 4

$C_{t4,min}$ = Minimum tangential velocity at station 4

$CDk\omega$ = A function used in the SST model

F_1 = Blending function 1

F_2 = Blending function 2

H_{BEP} = Head at best efficiency point

M_4 = Mach number at station 4

N = Compressor running speed in revolutions per minute (RPM)

$N_{s,avg}$ = Average specific speed

\bar{P} = Time averaged pressure

P_k = Reynolds stress term

\tilde{P}_k = Turbulence production limiter

P_s = Static pressure

P_{s80} = Mass flow averaged static pressure at station 8

P_0 = Total pressure

P_{02} = Total pressure at stage outlet

P_{01} = Total pressure at stage inlet

Q_{BEP} = Volumetric flow rate at best efficiency point

Re_4 = Reynolds number at station 4

R_{tip} = Radius at impeller tip

RTV = Return Guide Vane

R_4 = Diffuser radius at station 4

R_5 = Diffuser radius at station 5

R_5/R_4 = Diffuser radius ratio

S = Invariant measure of the strain rate

T_0 = Mass flow averaged total temperature

\vec{U} = Velocity vector

$U(x,t)$ = Quantity to be time averaged

$\bar{U}(x)$ = Time average term

U_i = Rotational speed at station i

$U_i = U_j$ = Velocity vector in index notation (only in Appendix C)

$\bar{U}_i = \bar{U}_j$ = Time averaged velocity vector in index notation

U_{tip} = Rotational velocity at impeller tip

W_i = Relative velocity at station i

Z_{imp} = Number of impeller blades

Greek Letters

α = A constant used in the SST model

$\alpha_c = \alpha_{critical}$ = Alpha 4 Critical = Critical Flow Angle at station 4

$\alpha_{C,j}$ = Critical flow angle determined at width ratio j

α_4 = Mass Flow Averaged Flow Angle at Station 4

α_4 = Local flow angle at station 4 in Chapter 7 for Figures 187 – 202

α_5 = Mass Flow Averaged Flow Angle at Station 5

$\alpha_{local,max}$ = Local maximum flow angle

$\alpha_{C,Senoo} = \alpha_{Senoo} = \alpha_{4,Senoo} = \alpha_s$ = Critical flow angle calculated from Senoo – Kobayashi Equation

$\alpha_{C,num}$ = Numerically determined critical flow angle

$\alpha_{4,critical,avg.,exp.} = \alpha_e$ = Mass flow averaged experimentally determined critical flow angle

$\alpha_{4,critical,avg.,num.} = \alpha_n$ = Mass flow averaged numerically determined critical flow angle

$\alpha_{4,13\text{ Blades}}$ = Local flow angle determined with 13 impeller blades for Compressor 5 instead of 15 impeller blades

β = A constant used in the SST model

β^* = A constant used in the SST model

γ = Ratio of Specific Heats

$\Delta\alpha$ = Difference between local maximum flow angle and Critical Flow Angle from Senoo – Kobayashi Equation

$\Delta C_{m,4}$ = Meridional Velocity Distortion at Station 4

$\Delta C_{m4,0,100}$ = Meridional velocity distortion at station 4 calculated from span values at 0% and 100%

$\Delta C_{m4,5,95}$ = Meridional velocity distortion at station 4 calculated from span values at 5% and 95%

$\Delta C_{m4,min,max}$ = Meridional velocity distortion at station 4 calculated from minimum and maximum meridional velocity values at station 4

$\Delta C_{t,4}$ = Tangential Velocity Distortion at Station 4

$\Delta C_{t4,0,100}$ = Tangential velocity distortion at station 4 calculated from span values at 0% and 100%

$\Delta C_{t4,5,95}$ = Tangential velocity distortion at station 4 calculated from span values at 5% and 95%

$\Delta C_{t4,min,max}$ = Tangential velocity distortion at station 4 calculated from minimum and maximum tangential velocity values at station 4

$\Delta h_{\text{internal losses}}$ = Change in Enthalpy Due to Internal Losses

$\Delta h_{0,12}$ = Change in Total Enthalpy between State Inlet and Stage Outlet

Δt = Time step over which time averaging is done

μ = Viscosity

μ_t = Turbulent eddy viscosity

ν = Kinematic viscosity

ν_t = Turbulent kinematic eddy viscosity

$\Phi = \phi$ = Flow Coefficient

$\phi_{R.S.}$ = Flow coefficient at rotating stall onset

$\phi_{\text{exp, stall}}$ = Experimentally determined local value at stall onset point

$\phi_{\text{exp, quasi-stall}}$ = Experimentally determined local value at flow point directly preceding the stall onset point

$\phi_{\text{num, stall}}$ = Numerically determined local value at stall onset point

ϕ_{exp} = Value determined at experimental flow point usually the last stable flow point

ϕ_{num} = Value determined at numerical flow point usually the last stable flow point

ρ = Fluid density

σ_k = A constant used in the SST model

σ_ω = A constant used in the SST model

$\sigma_{\omega 2}$ = A constant used in the SST model

τ = Viscous shear stress tensor

$\overline{\tau_{ij}}$ = Time averaged viscous shear stress tensor in index notation

ω = Rotational speed in rad/s

ω = Dissipation of the turbulent kinetic energy into heat energy (only in Appendix C)

Subscripts and Symbols

BEP = Best Efficiency Point

i = Specific station location

imp = Impeller

j = Specific width ratio of stage geometry

k = Specific span value (only allowed values 0%, 5%, 95%, 100%)

Tip = Value at impeller tip

0 = Total Value

1 = Stage Inlet

2 = Impeller Inlet

3 = Impeller Outlet

4 = Diffuser Inlet

5 = Diffuser Outlet

6 = RTV Inlet

8 = RTV Outlet

∇ = Del operator

CHAPTER 1: INTRODUCTION AND COMPRESSOR BASICS

Compressor stability has been a field of interest for the industrial and academic communities for over sixty years. The development of the jet engine spawned the need for higher and higher compression ratios. These compression ratios are needed to provide the required gas density for the combustion process to function. Thus, there has been a push for better, more efficient, more powerful compression systems [31]. However, with that push there has come to light a fatal flaw in all compression systems. That flaw being that all compression systems are inherently unsteady machines that potentially experience unstable operating conditions [8]. This dissertation is about one of the possible unstable states for modern compression systems: rotating stall. Contained within is the numerical and experimental data used to develop and test a new method for determining compressor stability.

1.1 The Centrifugal Compressor

1.1.1 The Compression Process

The compressor works by the method of energy conservation and transfer. This method of energy conservation may be written as:

$$P_0 = P_s + \frac{1}{2} * \rho * C^2 \quad (1.1)$$

where the stagnation pressure, P_0 , is equal to the sum of the static pressure, P_s , and the dynamic pressure, $\frac{1}{2} * \rho * C^2$ with C being the total velocity and ρ being the fluid density. Equation 1.1 is similar to the form of Bernoulli's equation that is seen in undergraduate fluid mechanics courses. However, equation 1.1 is only valid for flows having a Mach number, M , less than or equal to 0.3 [27], but it is still reasonably accurate for flows with $0.3 < M < 0.6$ [27]. Once the flow increases to $M > 0.6$ compressibility effects begin to play a role and must be accounted for [27]. However, equation 1.1 serves as a way to understand the basics behind the compression process.

The compression process is best described as follows: first the flow is accelerated by a rotating element in the compressor stage increasing the stagnation pressure. Then the flow is decelerated in the stationary part of the compressor stage decreasing the dynamic pressure. Due to energy conservation¹ the static pressure must increase in direct proportion to the decrease in dynamic pressure to preserve the stagnation pressure. This leads to the pressure rise in a compressor stage. Afterwards, the flow is able to experience this same process again in the next stage and so on until reaching its maximum pressure rise at the outlet of the final compressor stage.

1.1.2 Differences between Centrifugal Compressors and Axial Compressors

There are two types of compressors: the centrifugal compressor and the axial compressor [11]. There are several differences between the two types of compressors. The most notable differences are: efficiency, pressure ratio, size/number of stages required, and direction of main flow through the compressor. Figures 1 and 2 show an example of each compressor type. For an axial compressor, see Figure 1, the main flow enters along the compressor rotation axis and proceeds through each compressor stage in the same direction.

¹ There are losses in the compression cycle [11]. These losses cannot be ignored for an effective analysis. However, the analysis presented is meant only to serve as a basic overview of the compression process and not an exhaustive investigation of the process itself.

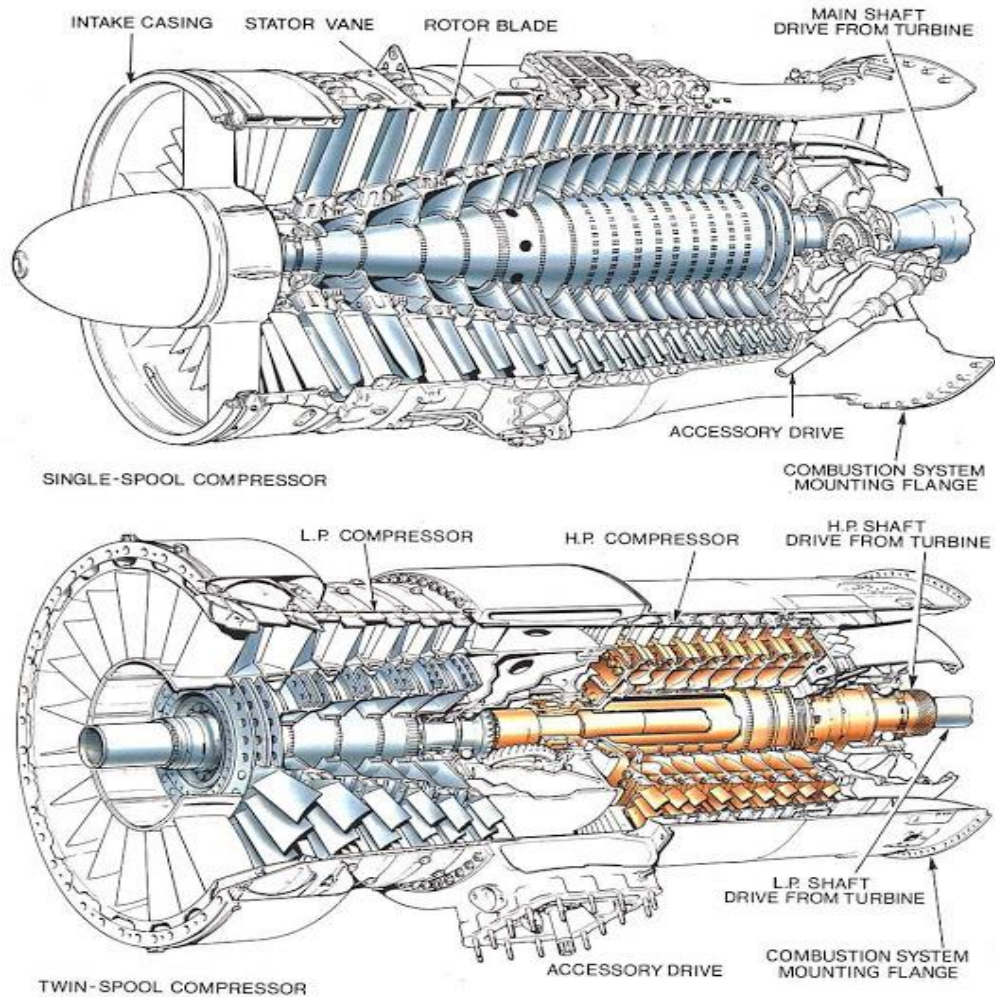


Figure 1: Axial Compressor Examples adapted and reproduced from [12]

Figure 2, shows an example of a centrifugal compressor. Like the axial compressor the centrifugal compressor draws air into each stage along the rotation axis. However, unlike the axial compressor the flow direction changes by 90 degrees as the flow moves through the impeller (i.e. rotating component), see Figure 2. In this case the flow is expelled from the impeller in a radial direction from the compressor centerline. From there the flow will be expanded in the diffuser region and rerouted through the “U-Bend” and return guide vane regions (RTV) before entering the next stage along the rotation axis.

Vertically-split compressors

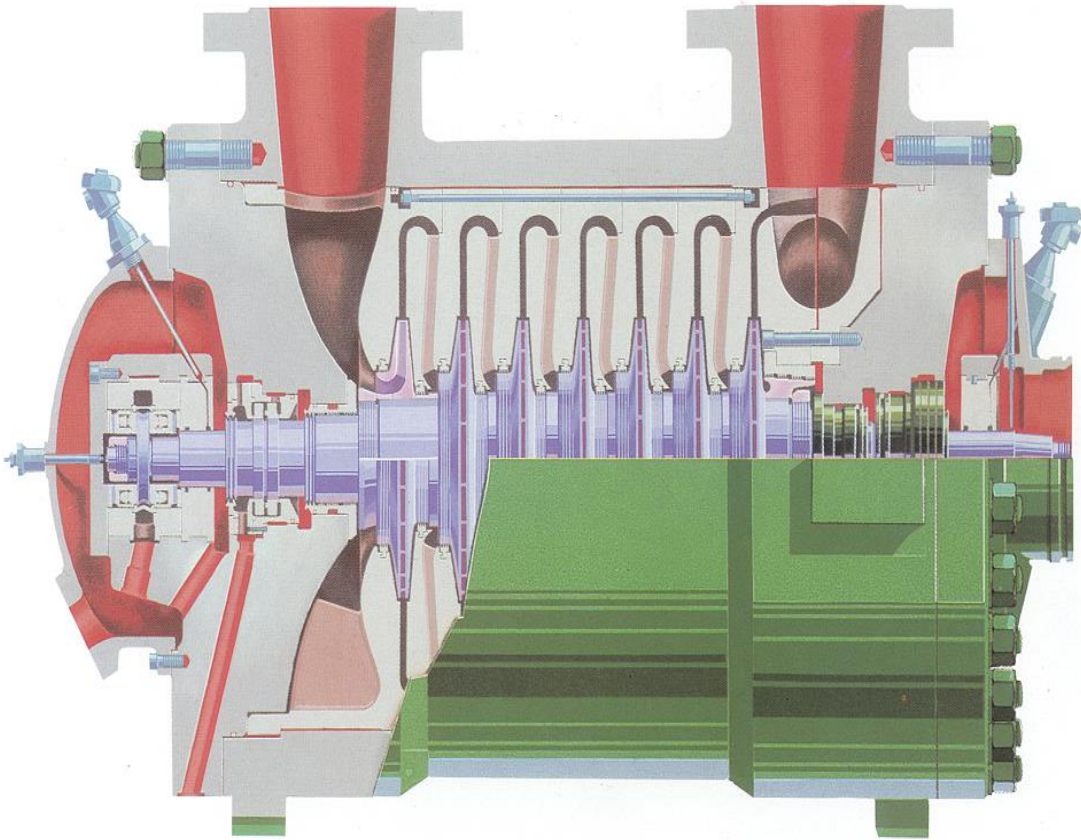


Figure 2: Centrifugal Compressor Example adapted and reproduced from [12].

1.1.3 Reasons for Frequent Use of Centrifugal Compressors vs. Axial Compressors

The main reason that a centrifugal compressor is preferred to an axial compressor is that the centrifugal compressor is able to attain a much greater pressure rise than the axial compressor, see Table 1.

Type	Industrial	Aerospace	Research	Efficiency
Axial	1.05 – 1.3	1.1 – 1.5	2.5	80-93%
Centrifugal	1.2 – 1.9	2 – 9	13	75-90%

Table 1: Pressure Ratio Comparison adapted and reproduced from [11]

According to Table 1 the axial compressor is slightly more efficient than the centrifugal compressor. However, in all cases the centrifugal compressor is able to produce a much greater

pressure rise than the axial compressor. This is due to the design of the centrifugal compressor. Figure 3 shows that each rotor blade is flat in an axial compressor. Thus, as the flow passes over the axial rotor blade it does not change height. However, Figure 4 shows that the flow is forced to change height as it passes through the impeller region of the centrifugal compressor. It is this design difference that causes the vast difference in stage pressure rise.

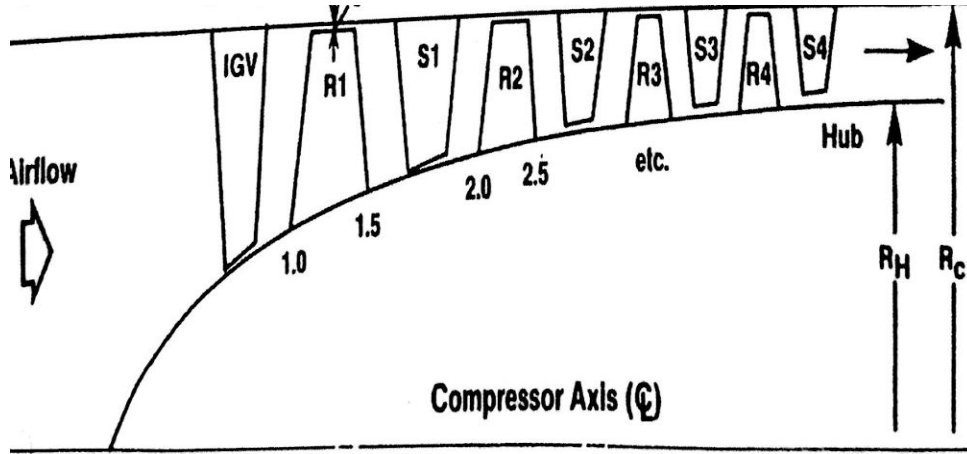


Figure 3: Axial Compressor adapted and reproduced from [11]

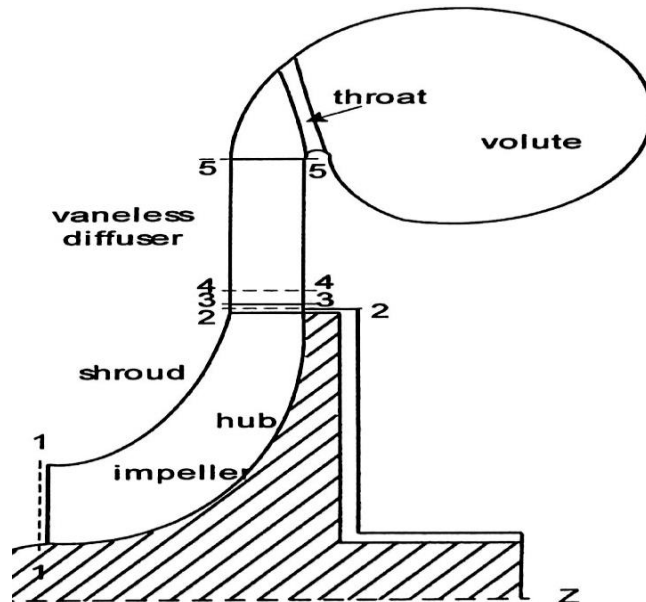


Figure 4: Centrifugal Compressor adapted and reproduced from [11].

The stage pressure rise is given as follows:

$$\frac{P_{02}}{P_{01}} = \left\{ \frac{\Delta h_{0,12} - \sum \Delta h_{\text{internal losses}}}{C_p * T_{01}} \right\}^{\frac{\gamma}{\gamma-1}} \quad (1.2)$$

where P_{02} is the outlet stagnation pressure, P_{01} is the inlet stagnation pressure, C_p is the gas specific heat at constant pressure, T_{01} is the inlet stagnation temperature, γ is the ratio of specific heats, $\Delta h_{0,12}$ is the stagnation enthalpy rise, and $\Delta h_{\text{internal losses}}$ represents the losses due to internal resistance. Equation 1.2 holds true for both axial and centrifugal compressor stages [11]. However, by expanding out the change in stagnation enthalpy, $\Delta h_{0,12}$, one will arrive at:

$$\Delta h_{0,12} = \frac{1}{2} * [(U_2^2 - U_1^2) + (C_2^2 - C_1^2) + (W_2^2 - W_1^2)] \quad (1.3)$$

where C is the total velocity, W is the relative velocity, and U is the rotational velocity, location 1 is the stage inlet, and location 2 is the impeller tip location [11]. Investigating, equation 1.3 one finds that both the axial and centrifugal stages will experience a change in their absolute velocities, C , and their relative velocities, W . However, because the flow does not change height in the axial compressor there is no change in the rotation velocity of the flow, U , in the axial compressor. This is not the case for the centrifugal compressor. Therefore, it is the change in flow direction facilitated by the impeller blade design that gives rise to the change in rotational velocity, U , inside of the centrifugal compressor. This is the reason the centrifugal compressor is capable of attaining much higher pressure ratios than the axial compressor.

The other issue that leads to the frequent use of centrifugal compressors over axial compressors is tied to the difference in pressure rise offered by each design. Since the centrifugal compressor is capable of attaining much higher pressure rises in each stage it will require fewer stages to reach the desired pressure rise. This leads to a decrease in the size of the overall compressor package. Furthermore, due to the more compact size of the centrifugal compressor design versus that of the axial compressor a centrifugal compressor can be used in more confined

spaces than the axial compressor. This combined with the increased pressure ratio and the comparable efficiency make the centrifugal compressor a more frequent choice than the axial compressor.

1.1.4 Applications of Centrifugal Compressors

There are several different areas of application for centrifugal compressors. Centrifugal compressors are often used in chemical plants for the purpose of performing chemical reactions at very high pressure [17]. Centrifugal compressors are also used in the oil industry when reinjecting high pressure gas into oil wells [17]. Centrifugal compressors are used in mines for ventilation [21] as well as in train cooling systems [43] and Heating-Ventilating-Air Conditioning (HVAC) systems [43]. Centrifugal compressors are used in pneumatic conveyors and refrigerators [21]. They have even been used in armored cars and small aircraft engines [21]. As the authors of [43] have stated, a centrifugal compressor is used whenever a large pressure rise is required with limited space. The point of describing all of these possible applications is because the centrifugal compressor is very widely used. Thus, anything that has a negative or positive effect on the design of a centrifugal compressor will have far reaching implications for the entire centrifugal compressor industry.

1.1.5 Requirements of Centrifugal Compressors

Centrifugal compressors are desirable in situations where space is limited. Due to their ability to produce much higher pressure ratios per stage a centrifugal compressor will need fewer stages and therefore less space to produce the required pressure ratio. This means that there will be less power required in the operation of fewer stages due to smaller overall losses and the driving of fewer stages. According to [11] centrifugal compressors tend to have a larger operating range

from choke to surge than axial compressors, see Figure 5. Due to this larger operating range centrifugal compressors can be used in situations where off-design operations are likely.

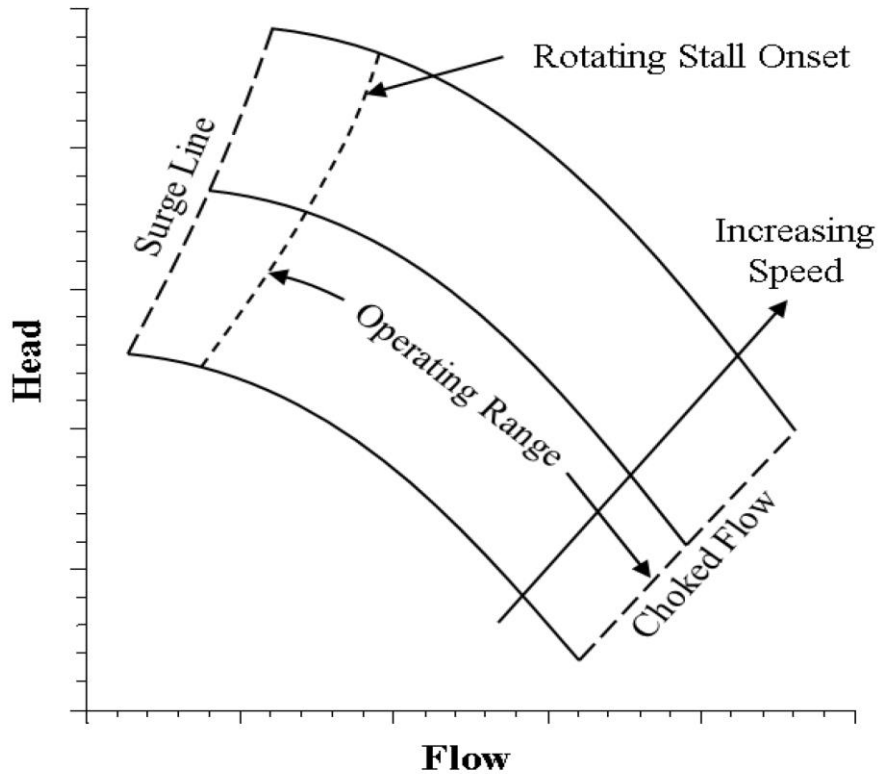


Figure 5: Example Compressor Map adapted and reproduced from [39]

As a summary comparison the requirements of axial compressors and centrifugal compressors are quite different. Where the axial compressor requires more stages to reach a desired pressure ratio the centrifugal compressor can reach that same pressure ratio with fewer stages. This means that the centrifugal compressor will require less space than an axial compressor. However, depending on the application, the centrifugal compressor will require more material to construct because of its need for a gas collection area. This collection area, see Figure 6, often referred to as a volute, is more difficult to design than the exit region of an axial compressor requiring greater care and diligence in development [27].

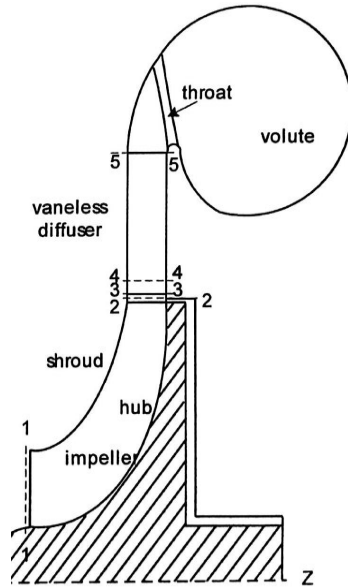


Figure 6: Centrifugal Compressor with Volute adapted and reproduced from [11]

Given the higher pressure ratios and speeds involved in the use of a centrifugal compressor more can go wrong in its operation [10, 28]. The centrifugal compressor requires more care in development due to the high degree of turning experienced by the flow [11]. Also, with higher pressure ratios come much higher temperature ratios than in the axial compressor. Therefore, the centrifugal compressor will require different materials that can withstand the combination of higher pressures and temperatures as well as the myriad of aerodynamic forces impacting the rotating blades of the compressor. These requirements lead to many design issues that impact the flow through the centrifugal compressor and the need to better understand the potential instabilities of the flow.

1.2 The Vaneless Diffuser

To facilitate compressor pressure recovery each stage is fitted with a diffuser. The diffuser expands the flow increasing the static pressure, see section 1.1.1 for more information on the basics of the compression process. For this work only the vaneless diffuser is considered, however a brief overview of diffusers is in order.

1.2.1 Differences between Diffuser Types

There are three basic types of diffusers: the vaneless diffuser, the low solidity vaneless diffuser, and the vaned diffuser. The vaneless diffuser is characterized as a passage that has parallel or diverging walls, but no solid material inside the passage. The vaned diffuser has expansion vanes in the passage that seek to control the expansion of the flow and thereby increase the pressure recovery. The low solidity vaneless diffuser possesses vanes in the passage, but there are significantly fewer vanes in the low solidity vaneless diffuser than in the vaned diffuser. Each type of diffuser has its advantages and disadvantages. Thus, the main difference between diffuser types is the amount of material inside of the diffuser and the pressure recovery that can be achieved. Vaned diffusers tend to have greater pressure recovery [4, 11]. However, they also tend to have greater issues with stability [4, 15] which makes them more difficult to design.

1.2.2 Reasons behind the Frequent Use of Vaneless Diffusers and its Applications

Though there are three basic types of diffusers the vaneless diffuser is the most often used diffuser type. There are a few reasons for this. First, the vaneless diffuser is cheaper and easier to manufacture [4, 11]. Since a vaneless diffuser is basically two parallel walls that form a passage it is objectively simpler to construct. The greatest difficulty in vaneless diffuser manufacturing is the usual need for a pinch at the diffuser entrance². However, care must be taken with the initial design of the vaneless diffuser to avoid rotating stall. According to Aungier this is something that can be avoided if proper design techniques are employed [5].

Second, there is the issue of vibrations. Rotating stall at its core is a rotating non-uniform pressure disturbance [28]. Therefore, it has the potential to induce vibrations in the components

² This pinch is added to improve the vaneless diffuser's stability [27].

of a compressor [4, 12, 27 & 28]. According to Marshall and Sorokes these vibrations can have an unbalancing effect on the compressor drive shaft [28], which would be a significant issue. Over time these vibrations will cause chronic material fatigue [35]. This fatigue leads to early replacement of parts and sometimes catastrophic failure of parts causing damage to the entire machine [35]. Also, a vaned diffuser will have issues with fouling and erosion caused by particles in the flow [4]; these issues can be avoided or minimized by using a vaneless diffuser [4].

The issue of material fatigue can be reduced by implementing a vaneless diffuser due to the lack of material. But, there is still the issue of noise created by interaction of the rotating stall cell with the structure itself. This will still exist even in a vaneless diffuser, but should be reduced due to the lack of material in a vaneless diffuser.

These vibrations also tend to generate a noticeable tone or range of tones [43]. These tones tend to have a range of frequencies, but are generally unpleasant to human hearing [28, 43]. All of these problems are possible for vaned and low solidity vaneless diffusers due to the fact that they possess material in the diffuser.

Third, there is the issue of the compressor operating range. Figure 5 showed a sample operating range for a centrifugal compressor. A vaneless diffuser offers the designer a wider operating range than a vaned diffuser [4, 12]. But a vaneless diffuser must be longer in extent to achieve a satisfactory pressure rise [4, 12]. According to Anish and Sitaram a low solidity vaneless diffuser is an attempt to gain the higher pressure rise of a vaned diffuser and the operating range of a vaneless diffuser [4]. It was found that a low solidity vaneless diffuser can provide a good tradeoff between operating range and pressure recovery [4]. However, care must still be taken in the diffuser design [5].

Overall the reasons for diffuser choice can be summarized as follows. A vaneless diffuser offers a larger operating range than the vaned diffuser, but it does not have the pressure rise capability of the vaned diffuser requiring much longer diffusers to achieve a satisfactory pressure rise [4, 12]. A low solidity vaneless diffuser tends to reach a happy medium between pressure rise and operating range.

The issue of mechanical vibrations exists for all diffuser types. However, with less material than vaned or low solidity vaneless diffusers the vaneless diffuser is much less susceptible to these vibrations and their effects. Thus, the material fatigue caused by rotating stall induced vibrations will have less of an effect in the vaneless diffuser.

Lastly, vaneless diffusers are cheaper to manufacture. They require less material to construct, they do not possess vanes in the flow path, and they require less time to design. Therefore, the overall research and development as well as manufacturing cost is lower. However, the design must be accurate and precise if stability issues are to be avoided [5]. However, one nice benefit of diffuser vanes is that they can have a stabilizing effect if impeller rotating stall exists [28]. Thus, there are many considerations when choosing a diffuser. But for most applications the wide operating range, lack of mechanical vibrations, smaller financial and time costs, and possibility for satisfactory pressure recovery allow for a vaneless diffuser to be chosen over its counterparts.

CHAPTER 2: ROTATING STALL IN VANELESS DIFFUSERS OF CENTRIFUGAL COMPRESSORS

2.1 Rotating Stall Basics

There is a phenomenon that occurs at low mass flows in the centrifugal compressor. This phenomenon is known as rotating stall. Rotating stall is best described as a non-uniform circumferential pressure field that rotates at a speed other than that of the compressor shaft [28]. This phenomenon is different than surge which is a full flow reversal of the flow inside of the compressor that returns out the stage entrance [28]. However, for cases of rotating stall the mass flow rate through the compressor stage remains unchanged [39]. It is rotating stall that is the focus of this investigation therefore surge will only be mentioned in passing, if at all, from here on out.

2.1.1 Characteristics of Rotating Stall

There are three main features that characterize rotating stall: the type of stall inception, the number of stall cells, and the rotation speed of the stall cells. There are two different types of stall inception: spike inception (see Figure 7) and modal wave inception (see Figure 8) [7].

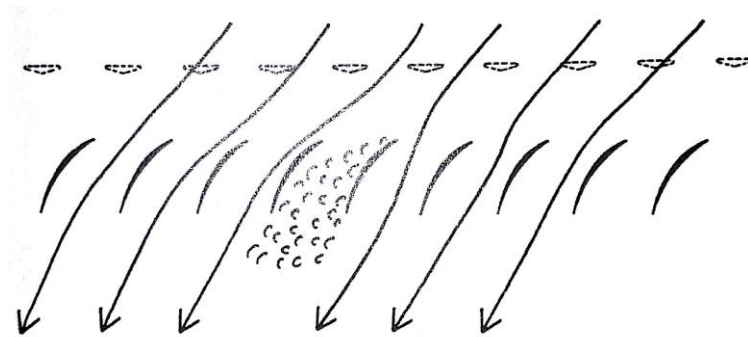


Figure 7: Sketch of Spike Inception adapted and reproduced from [44]

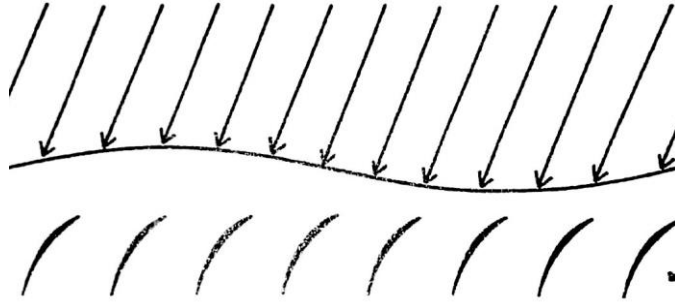


Figure 8: Sketch of Modal-Wave Inception adapted and reproduced from [44]

Spike inception is best described as a small wavelength inception that has a geometric cause while modal-wave inception grows out of a fluid instability [1, 15]. The type of inception will tell a design engineer where to look for the root cause of the rotating stall issue allowing for possible solutions. The type of stall inception can be determined based upon the rotating speed of the stall cell [28].

Often rotating stall is quantified by the number of stall cells that form. Jansen found that the number of stall cells that occurred could range from one to three with two being the most likely number [15]. Ljevar et al. found that the number of stall cells was influenced by all of the critical factors that Senoo et al. found were important to the critical flow angle [23, 32]. Abdelhamid found three to four rotating stall cells [2]. Spakovszky found four stall cells [36].

Knowing how many stall cells can be important. According to Emmons et al. it was one of the most important problems associated with rotating stall [45]. The number of stall cells is driven by the mass flow rate [45]. The greater the decrease in the mass flow rate the larger the number of stall cells will grow until the maximum number of stall cells is attained [45]. Afterwards, as the mass flow rate decreases the number of stall cells decreases [45], which means that the stall cells are beginning to coalesce for the onset of surge.

The final characterizing factor of rotating stall is the speed of rotation of the stall cell(s). Rotation speed is used to quantify the location of the stall inception as well as the type of inception [28]. According to Marshall and Sorokes if rotating stall is initiated in the diffuser it will rotate between 6% and 33% of the compressor running speed [28]. However, if rotating stall is initiated in the impeller it will rotate at 50% to 80% of the compressor rotating speed [28]. It has been found that diffuser rotating stall also rotates at a slower speed than impeller rotating stall with a speed no greater than 20% of the shaft speed [13]. However, impeller rotating stall rotates at no less than 20% of the shaft speed [13]. The stall cells can rotate in either the same direction as the stage rotor or opposite to it [36, 39]. The speed of stall cell propagation was used as a factor for determining how diffuser stability is effected by the diffuser's geometry [23 – 25].

2.1.2 Problems Caused by Rotating Stall

As an unstable flow phenomenon rotating stall tends to cause several problems for a centrifugal compressor stage. However, there are two specific problems that are most important. First, one must consider the loss of pressure rise caused by rotating stall. When rotating stall onsets the mass flow through the compressor stage will remain the same [39], but there is a significant decrease in the pressure rise across the stage [10]. This is a significant problem for a device that is supposed to create pressure rise. This loss in pressure is due to the fact that the stall cell represents an area of stopped (i.e. stalled) fluid [20]. Since the streaks of stall discussed by Kline and Runstadler in [19], as well as Kline in [20], have coalesced into an actual stall cell the cell will impact the moving fluid. Thus, the dynamic fluid is forced to reenergize the stalled fluid expending energy and decreasing the pressure rise [20]. However, one cannot simply increase the mass flow through the compressor stage to “wash out” the stall cells [10, 28]. Instead there is a hysteresis zone that must be overcome before normal operation can continue [28]. This loss of pressure rise

leads to an overall shrinking of the operating range of the compressor stage [1]. This decrease the overall usefulness of the compressor stage itself.

The second main issue that arises with rotating stall is that of mechanical vibrations. Since rotating stall is a rotating pressure field [28] it has the potential to interact with the mechanical parts of a compressor in the form of mechanical vibrations [40]. This is best detailed in [31, 35] where the authors detail how these vibrations effect the long term structural stability of rotating blades by promoting mechanical fatigue. It was found that the vibrations induced by rotating stall significantly decreased the life span of the centrifugal fan components [35]. It was also found that it is possible for these vibrations, if large enough, to lead to immediate catastrophic failure of mechanical parts [35]. This dissertation is on vaneless diffusers which possess no solid material inside of the diffuser region itself. However, the vibrations induced by rotating stall have the ability to effect the compressor drive shaft [27]. This will lead to a diminished life for the seals and bearings in the overall compressor package³ [27]. This requires a shutting down of the compressor to change the seals and bearings which can be a time consuming process leading to lost operating time. Furthermore, these types of vibrations can lead to issues with rotordynamic stability in the compressor package. This means that these vibrations have the ability to cause the compressor to shut down to prevent contact between the drive shaft and the shaft casing. This is a major issue that must be prevented to allow for safe compressor operation.

A final issue caused by these vibrations is that of audible tones. This was discussed at some length in [43]. These tones develop from interactions between the rotating stall cell(s) and the mechanical parts of the compressor [43]. These tones are most often generated in the impeller region of the compressor stage [43]. Thus, they are not something to be as concerned with in a

³ A compressor package is the entire structure that houses all of the compressor stages as well as the bearings, seals, etc.

vaneless diffuser, due to the reduced amount of material, but the tones are unpleasant to human hearing [25] which makes them a problem. So, the ability to predict and prevent rotating stall will help those working around compressors from having to experience this unpleasant and harmful phenomenon.

2.2 Rotating Stall Causes

There are two main theories to what causes rotating stall. They are the boundary separation theory and the core flow destabilization theory. To this point no one has been able to absolutely confirm which theory is correct. However, it is possible that both theories have validity to them and a comprehensive approach to the cause of rotating stall is most applicable. In both theories it is clear that there is a critical flow angle where the diffuser will stall [23 – 26, 32 – 34, & 41].

2.2.1 Boundary Layer Separation Theory

In [1, 6, 15, 22, 26, 32 – 34, & 41] the cause of rotating stall is determined to be some form of boundary layer separation. In these cases the main flow angle drops below a specific value such that the flow at the wall stops [26, 32]. At this point the flow is considered to be stalled [26]. This stopping will add to the buildup of stalled fluid at the wall [15, 20]. With the fluid flow stopped the “bubble” of stalled fluid will grow [15, 20]. This stall “bubble” is unstable and easily disturbed [15, 34]. Once, it is disturbed a stall cell will arise which will grow and shrink in such a way as to rotate around the vaneless diffuser. It is of note that these stalled cells are legitimate solutions to the physical equations defining flow through the vaneless diffuser [15]. However, despite representing real, physical solutions they are not solutions that produce high efficiency and pressure rise.

It has been found that the critical flow angle for this to occur at is dependent upon the width ratio (b_4/R_4), radius ratio (R_5/R_4), diffuser inlet Reynolds Number (Re_4), diffuser inlet Mach

number (M_4), and diffuser inlet velocity distortion [26, 32 – 34, & 41]. These parameters can be used to determine the critical flow angle at which point rotating stall will onset [32, 34, & 41]. However, these parameters tend to be more useful in determining whether or not the rotating stall onset is caused by a geometric issue or a flow issue. But they are certainly of use in the design of a compressor and its modelling.

2.2.2 Core Flow Destabilization Theory

As with the boundary layer separation theory the core flow destabilization theory takes place as the mass flow rate through the compressor is decreased [23]. This theory has been put forth in [23 – 25, & 40]. Ljevar et al. investigated rotating stall in “wide” vaneless diffusers ($b_4/R_4 \geq 0.1$) [23 – 25]. The study suggests that it is the core flow through the diffuser that is inherently unstable [23, 40]. And as the boundary layer grows it will not separate so much as provoke the core flow to destabilize [40]. Most diffusers have a width ratio that is much less than 0.1 which allows the boundary layers to have a significant effect on the core flow provoking the instability [23]. So, to avoid the influence of the boundary layers a wide diffuser was employed to allow for the core flow to dominate the flow through the vaneless diffuser [23]. However, it is possible for the viscous effects of the boundary layer to still trigger the core flow destabilization [40]. So, it appears that while the core flow is considered to be unstable here the boundary layer still triggers the instability similar to a small pebble causing a boulder to roll down a mountain side.

The work of Ljevar et al. in [23 – 25] showed that the stability of a “wide” vaneless diffuser was dependent on the radius ratio, the number of blades, and the jet to wake ratio (the jet is the main flow and the wake is the secondary flow influenced by the boundary layer). These results are in agreement with [1, 9, 26, 32 – 34, & 41]. This agreement is in spite of the fact that the previously cited studies are based upon a boundary layer destabilization method.

2.2.3 Rotating Stall Cause Summary

The overall conclusion from the two theories is that both causes of rotating stall are accurate. However, the width of the diffuser turns out to be the driving factor. In cases where the diffuser is narrow the walls bound the compressor flow forcing the flow breakdown to be caused by the boundary layer, which would include breakdown in the circumferential direction. However, when the diffuser is much wider the boundary layer is unable to significantly affect the flow stability. This means that it is the core flow that must destabilize for rotating stall to occur. This would force the flow to destabilize in more of a span-wise direction. So, overall the geometry of the system will determine which method of rotating stall onset is applicable. More importantly these theories reveal that rotating stall is a dynamic system phenomenon that cannot be avoided without changing the geometry, in agreement with Jansen's work in [15].

2.3 Rotating Stall Solutions

If a compressor stage experiences rotating stall there are two ways to counteract the phenomenon: passive control [35] or active control [7, 10]. These are the only two methods available outside of a complete redesign of the compressor stage itself [5]. But a complete redesign is a very time consuming and expensive operation.

2.3.1 Passive Control Solutions

The best way to describe a passive control device is one where there are no moving parts. The device itself functions to help stabilize the flow either by increasing the mass flow rate or allowing the streaks of stall [19, 20] to be realigned and wash out [28] of the compressor. There are three common forms of passive control. First, there is the stabilization ring. A good example of the stabilization ring is found in [35]. This ring works to realign the swirling vortices created at the blade tips with the main flow preventing the buildup of low energy fluid [35]. A similar

solution was employed by Tamaki [37]. Though a very useful control solution it is not an effective solution for a vaneless diffuser.

The second method of passive control is the pinch. The pinch is a physical decrease in the vaneless diffuser width that helps to work to increase the radial or through-flow velocity component through the diffuser allowing for operation at a reduced mass flow rate [27]. The pinch is routinely used because it is a quick and effective solution even in cases where the vaneless diffuser is an older model [27]. However, the pinch can affect the critical flow angle of the diffuser itself [26]. The issue of the critical flow angle will be discussed later on, but suffice it to say that any change in the critical flow angle of the diffuser could make the situation worse [15].

Lastly, there is the bleed slot [7]. This slot works to artificially increase the mass flow rate through the compressor stage by venting high pressure fluid from the stage as the mass flow rate is decreased [7]. It effectively increases the through flow velocity by removing some of the mass flow forcing the velocity to increase to maintain the stage total mass flow rate thus helping to prevent the buildup of stall precursors [20]. While this method does allow the compressor to operate at a lower flow rate than previously possible it also leads to a loss of high pressure fluid which in turn leads to a drop in attainable pressure rise at the new mass flow rate [7]. And since the pressure rise increases as the mass flow rate decreases [11] this means that the compressor is only able to produce the pressure rise of a higher mass flow rate. So, the operating mass flow rate range is increased, but this does not really add any new pressure generation capacity to the compressor stage [7].

As a side note Jansen discussed that the only way to completely avoid rotating stall in a vaneless diffuser was to remove the diffuser region itself and dump the flow into a collector [15].

However, this leads to a considerable loss in pressure rise and efficiency [15]. That is not a useful solution, but it bears repeating for the sake of depth.

2.3.2 Active Control Solutions

Active control is best described as a system where the flow instabilities are stabilized by the use of devices effecting the flow itself [10]. These devices are controlled by a “controller” and a computer that takes sensor data and tunes the devices to properly suppress the stall precursors [10]. This method of control is much more in depth than that employed by the passive control methods, but should be capable of effecting much greater change to the compressor stability and allow for increased pressure rise. A few examples of active stall control as supplied below.

Chen et al. discussed using a high pressure fluid injection system to energize regions of low speed flow [6]. Their research was on impeller stall onset, but it was discovered that using this injection method they were able to increase the centrifugal compressor’s stability [6]. A similar method was used by Day in [7] for axial compressors, Sankar et al. in [31] for centrifugal compressors, and by de Jager in [10] for his profound overview paper on stall and stall control. However, Day found that there would come a point of no return where the fluid injection method could no longer prevent the buildup of low momentum fluid and the system would either experience rotating stall or surge [7]. Day’s results are in agreement with the unsteady nature of the flow in a compressor as detailed by Dean [8] and Kline [19, 20].

However, none of the previous examples help prevent rotating stall in a vaneless diffuser which is an already unstable compressor component [13]. There is one paper by Abdelhamid that offers a potential solution for rotating stall in a vaneless diffuser [3]. It was suggested that using a movable ring that would close off the diffuser exit area forcing the through flow velocity to increase to keep the mass flow rate constant [3]. It was found that whether the flow was constricted

by going from hub to shroud, shroud to hub, or with two plates meeting in the middle that the compressor stability was improved [3].

Overall, there are many methods that can be employed to help control compressor stability. But few of these solutions would be applicable to a diffuser. And while it is possible to see how the fluid injection solution method could be implemented in a vaned diffuser where the region of stall cell formation is possible to discover [6], what happens inside of a vaneless diffuser where the stall cell has the potential to form anywhere from the entrance to the outlet [28, 32 – 34]. And though the solution offered by Abdelhamid in [3] was effective and easily implemented it is not necessarily effective when it comes to a compressor package with more than one stage and limited space. Therefore, the ability to predict rotating stall in the design phase of the compressor should serve as a way to prevent the need for stall control solutions by providing a better compressor design before the prototype is constructed.

CHAPTER 3: THE LOCAL FLOW ANGLE APPROACH

3.1 Motivation for the Project

As has been discussed in the previous chapter compressor stability is a difficult, but important topic. Since compressors will continue to be used and greater pressure rises will be called for the importance of a better understanding of compressor stability cannot be overstated. Contained within this section is the motivation for this entire work: “The Local Flow Angle Approach”. This approach is a new endeavor to be able to determine compressor stability from a simulation perspective instead of an analytic perspective. There are two main reasons that this project is important: the need for an a priori prediction method and the failure of the Senoo-Kobayashi equation.

3.1.1 Need for an a Priori Prediction Method

A great need in the compressor industry is that of an effective method of determining compressor stability a priori. The main problem with rotating stall is that it is a dynamic effect that is based on the geometry and flow characteristics of the system [32, 34]. Thus, a compression system can seem perfectly reasonable in its initial design, but have serious stability issues once in operation. And due to the coupling between the compressor and diffuser [1, 32 – 34, & 41] a stable diffuser can be easily influenced by an unstable impeller and vice versa. So, a compressor stage must be treated as a whole element and not broken into its specific parts.

This is where the local flow angle approach comes into play. Currently, the most accurate way to detect rotating stall is to build a prototype and run experimental tests on the compressor checking for rotating stall. However, this is time consuming and if rotating stall is detected it will force a redesign of the prototype. But this will not solve the problem because the new design may still experience rotating stall. Therefore, being able to quickly point to possible design flaws and

then implement design changes all while being able to determine if those changes are effective before building a prototype is helpful. The local flow angle approach will help with this method. Employing the Senoo – Kobayashi equation and the results of the local flow angle approach one can model the diffuser inlet flow and check against the predictive Senoo – Kobayashi equation to see if rotating stall is a possibility for the compressor stage in question. If rotating stall is possible then a redesign of the geometry can be performed and the new geometry tested to see if it has had any effect. If rotating stall is not detected, initially or in subsequent testing, then either the stage has been rendered “stable” or the compressor characteristics make it such that the local flow angle approach is not capable of determining the stability of the stage.

3.1.2 Failure of the Senoo-Kobayashi Equation

The Senoo – Kobayashi equation is shown below:

$$\alpha_c = 90 - \left(4.09685 + \left(93.2669 * \frac{b_2}{r_2} \right) - \left(229.774 * \left(\frac{b_2}{r_2} \right)^2 \right) + \left(4953.57 * \left(\frac{b_2}{r_2} \right)^3 \right) - \left(51284.8 * \left(\frac{b_2}{r_2} \right)^4 \right) + \left(136173 * \left(\frac{b_2}{r_2} \right)^5 \right) \right) \quad (3.1)$$

where α_c is the critical flow angle and b_2/R_2 is the diffuser width ratio (this will be written as b_4/R_4 for the remainder of the dissertation). It is based on the work of Senoo and his colleagues in [32 – 34], but it comes from a curve fit of Figure 35 in [41]. There is one obvious problem with this equation. It is a function of only one variable, the width ratio (given as b_2/r_2 in equation 3.1). This is a problem for several reasons. First, rotating stall is itself a multi-parameter problem. According to [1, 9, 17, 23 – 25, 32 – 34, & 41] there are seven different parameters that have an effect on the critical flow angle of the vaneless diffuser. They are: impeller blade number (Z_{imp}), jet – wake ratio, b_4/R_4 , R_5/R_4 , Re_4 , M_4 , and diffuser inlet velocity distortion. Thus, the width ratio is not the only important parameter. Second, this equation does not account for the unsteadiness of the

compressor flow [8] or that the flow is multi-dimensional [15]. Third, this equation does not account for impeller – diffuser coupling which was found in [1, 16, 32, & 40] to have a significant impact on vaneless diffuser stability. Fourth, this approach relies on what could be considered a one dimensional analysis. A one dimensional approach is often used in the early stages of compressor design [11]. And it might work for an impeller since the impeller is a naturally stable compressor component [13]. However, the diffuser is not a stable component [13]. Furthermore, according to Aungier the design of a vaneless diffuser is based on a number of different radii [5]. Changing just one can have consequences for the compressor design [5] unless the design is overly conservative [1]. And any of these could have consequences for the compressor stability [1, 15, 23 – 25, 32 – 34, 40, & 41] that would not be detected by equation 3.1. However, a conservative design will be hard pressed to meet the pressure rise required in modern centrifugal compressor applications. Therefore, this type of one dimensional analysis is inadequate in properly resolving vaneless diffuser stability in centrifugal compressors. Fifth, there is a limited range of applicability for this equation. Equation 3.1 is plotted in Figure 9.

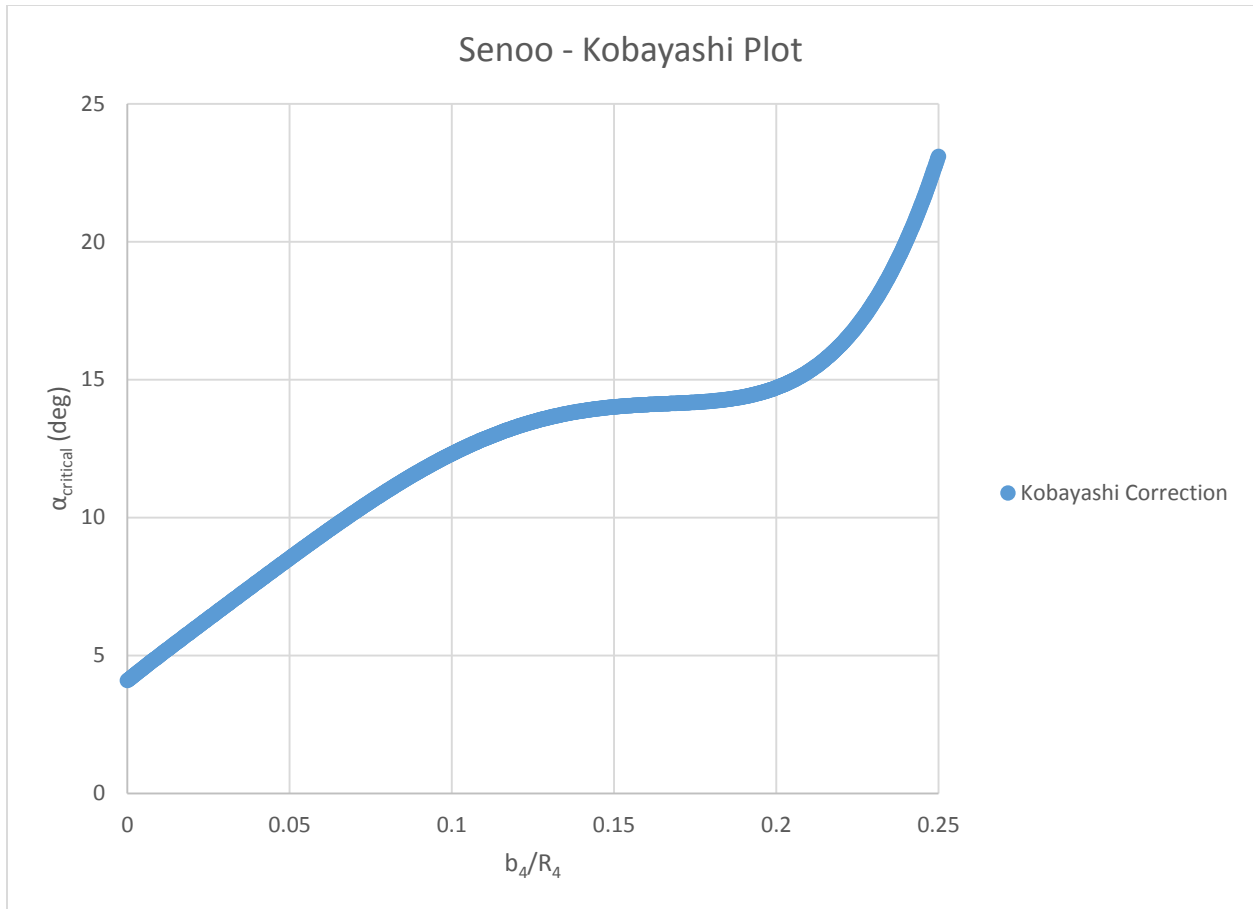


Figure 9: Senoo – Kobayashi plot adapted and reproduced from [41]

A brief look at Figure 9 shows that for width ratios (defined here as b_4/r_4) between 0 and 0.2 equation 3.1 is effective. However, once the width ratio reaches 0.25 it is clear that the plot is beginning to diverge and this divergence grows worse as the diffuser width increases. Thus, if the width ratio increases beyond 0.2 this equation is no longer trustworthy. And while a wide diffuser is defined as one with a width ratio greater than 0.05 [34] or 0.1 [23, 24] there are cases where the width ratio can reach 0.4, or at least these cases are expected [32]. Thus, equation 3.1 has a large, but still limited range of applicability. All of these reasons combine to show that relying solely on one equation to determine the stability for all compressor stages is not a reasonable approach. Therefore, the local flow angle approach came into being as a way to offset the issues inherent in equation 3.1.

3.2 Local Flow Angle Introduction

3.2.1 Genesis of the Approach

This approach came out of a conversation between the author and [27]. It centered on the observation that the Senoo-Kobayshi equation, equation 3.1, could not be trusted to properly predict the critical flow angle at the vaneless diffuser inlet for all cases. In fact this angle and the mass flow averaged flow angle at the diffuser inlet were often several degrees off [27]. One investigation found that there was a difference of 4 degrees or more [27] (a detailed discussion of the significance of the magnitude of the angular difference can be found in Chapter 6). A look at how mass flow rate and flow angle relate shows that:

$$\dot{m} = \rho * A_c * C_m = \rho * A_c * C * \cos \alpha \quad (3.2)$$

where \dot{m} is the mass flow rate, A_c is the cross sectional area, ρ is the fluid density, C_m is the meridional velocity, C is the total velocity, and α is the flow angle. Equation 3.2 shows how the mass flow rate varies with angle (Note: the angle is measured from the vertical). Thus, as the angle increases the mass flow will decrease and vice versa. Therefore, at large angles of attack, say where the compressor will be reaching its peak pressure rise, a difference between the mass flow rate and the critical mass flow rate for that compressor can vanish with just a small change in flow angle. Differences in either direction will make it difficult for a customer to run the compressor and the operation engineer to know how much leeway he will have between stability and instability when running the compressor. Also, the customer needs to trust that the compressor can do what a company says it will do. Therefore, there is great incentive in being able to properly determine the critical flow angle at the compressor

So, it was suggested that an investigation be made that would look into the actual flow profile at the diffuser inlet [27]. This set of simulations would look to see whether or not the local

profile combined with the Senoo-Kobayashi equation was a better predictor of compressor stability. This was the genesis of the local flow angle approach.

3.2.2 Application of the Approach

This approach to compressor stability has a wide range of applications. The approach uses a steady state simulation procedure to model the flow inside of a compressor stage from inlet to the outlet of the return guide vane (RTV). This allows for an engineer to model the flow in a short amount of time when compared to the hours often required for transient solutions [6] or the massive computational resources required to shorten the time to run a transient simulation [39]. This approach can be employed on a powerful desktop computer (it needs 18-20 core processors) or using onsite servers. It was found that the approach can run a data point in approximately four hours. To properly run a full speed line between 8 – 12 data points are required and there are between 3 – 5 speed lines per compressor stage. So, accounting for all the numbers a full speed line can be run in about 40 hours (assuming 10 data points and that data points can be run overnight) on a personal computer it would take about 3 days to run a full speed line and analyze the data. Thus, there is the ability to run five speed lines in three weeks. Therefore, the stability and performance characteristics of a compressor stage could be mapped out in less than one month. If the engineer had access to multiple servers this time can be shortened to less than one week per compressor stage. And with so few computational recourses being required this approach will not tie up more pressing simulations or server time.

The small amount of simulation time required and the need for fewer computational resources allows for the local flow angle approach to be employed in almost any situation where a compressor stage needs to be analyzed for stability. The only requirement is that the geometry be provided. Without that no modelling can take place. Thus, the local flow angle approach is

best suited for older compressor models that are used as templates for newer models. It would have trouble if the geometry was not as well defined. Because as was found in [1, 17, 23 – 25, 32 – 34, 40, & 41] the geometry matters a great deal. Incidentally, this was one of the conclusions reached in this work, see Chapter 8 for details. So, this approach would work, but it is not good for an abstract simulation procedure.

The downside to the local flow angle approach is that while it works well at helping to determine the compressors stability it cannot resolve what is going on with the stall cell. The local flow angle approach can help determine if rotating stall or localized flow reversal are possibilities for the compressor stage in question. However, it cannot determine the number of stall cells, the rotation speed of the stall cell(s), or the type of stall inception. All three of these features are considered to be very important [2, 13, 15, 22 – 25, 28, & 44] to the overall understanding of the phenomenon of rotating stall. However, none of these features are of concern to a company that produces compressors. Their interest is in whether or not rotating stall can be predicted in a compressor design and how quickly that prediction can be attained.

Overall the local flow angle approach is useful when a simulation is required using a small amount of time and few computational resources. It is applicable for a concretely designed compressor, but not good for abstract simulation. It would be good in quickly testing new prototypes and design revisions. It is not really applicable when trying to determine the characteristics of rotating stall (i.e. cell propagation speed, cell number, and type of inception). Thus, it is ideally suited for an industrial environment with some research application.

3.2.3 What is the Local Flow Angle Approach?

To this point the motivation, genesis, and applications of the local flow angle approach has been discussed. However, one important point is lacking. What exactly is the local flow angle

approach to compressor stability? The local flow angle approach is a modelling procedure that uses a steady state simulation method to model the flow inside of a single compressor passage. The flow profile at the diffuser inlet is measured and plotted as a function of the span (dimensionless compressor width) which means it is “local” to the diffuser inlet. From here the investigator will be able to make possible conclusions on the stability of the compressor stage in question.

3.3 Goals of the Project

First, it needs to be determined whether or not the local flow angle approach actually works. Given that there is solid experimental data to compare against a solid conclusion can be made on whether or not the local flow angle approach is any better at determining compressor stability than the currently employed (at least by Solar Turbines Inc.) Senoo – Kobayashi equation. Second, one needs to see how much detail can be gained from the local flow angle approach. Will it only be able to determine the stability of the stage or is there more that can be determined? It is good to know if this is a method that has only one output or if it will allow for more to be learned about the compressor stage as a whole. Third, all stability approaches have their limits when it comes to applications. This method is no different, so the range of applicability is required. This way in the future when someone is employing this approach they will have an idea on whether or not it will be useful. Fourth, can the local flow angle approach be made predictive? To this point the local flow angle approach has been considered in a validating fashion. The Senoo – Kobayashi equation is used to predict the critical flow angle and then the local flow angle is used to validate this prediction. However, is it possible to use this method to predict whether or not the compressor will experience rotating stall without having some other method of prediction already in existence? These are the main goals of this project.

CHAPTER 4: LOCAL FLOW ANGLE APPROACH

The local flow angle analysis is a numerical approach to a real world problem. This puts it somewhere between the realm of experimental and theoretical applications. It is a hybrid of the two that should help to bridge the gap between vaneless diffuser stability theory and the real world practice of vaneless diffuser stability that is associated with vaneless diffuser design. The work in this dissertation is based on a number of different parameters that are tied to numerical and experimental results. This chapter outlines the theoretical or predictive tools, the numerical tools and their application, and the experimental methods through which the experimental compressor results were obtained.

4.1 Theoretical and Numerical Tools

There are three areas that the numerical and theoretical tools are discussed. First, there is the Senoo – Kobayashi equation that was shown as equation 3.1 which serves as a method of predicting the critical flow angle. Second, is ANSYS – CFX, a canned modelling software used to test the many different compressor geometries used in this project. Lastly, there are the five critical parameters that are said to influence the diffuser inlet critical flow angle. Each of these is expected to have somewhat of an influence on the critical flow angle of the diffuser.

4.1.1 Senoo – Kobayashi Equation

As was already discussed in chapter 3 the main method of diffuser stability prediction is the Senoo – Kobayashi equation (see equation 3.1 in 3.1.2). As was already discussed in chapter 3 equation 3.1 comes from a curve fit of Figure 35 in [41]. It is often employed in the determination of diffuser critical flow angle in the compressor design phase [27]. However, as was pointed out in section 3.1.2 the Senoo – Kobayashi equation is not a fully reliable measure of diffuser stability. The Senoo – Kobayashi equation is used in this work as a means of testing the local flow angle

approach against the many different compressor geometries employed. Before one questions this it is known that equation 3.1 does work in many cases, it is just not accurate 100% of the time. A secondary goal of this work is to determine the applicable range of the Senoo – Kobayashi equation. Therefore, there is no need to toss aside a predictive method that is simple and generally effective. It will be used as a means to compare the numerical flow angles and experimental flow angles against the predicted critical flow angle. This way a range of applicability can be developed for the Senoo – Kobayashi equation itself.

4.1.2 Use of ANSYS – CFX

To perform the numerical investigation a modelling software was chosen. This investigation was meant to focus more on speed and adaptability than being able to model the structure of the flow breakdown. Essentially this tool is meant to be able to determine whether or not rotating stall occurs, not the characteristics of its inception or propagation. Therefore, the readily available ANSYS – CFX software was chosen to model each geometry. The software allows for the creation of templates that streamline the simulation procedure allowing for more time to be spent running simulations than setting up the runs. This software also tends to be more stable than user developed in house codes that have bugs to work around and may not be easily adaptable to wide differences in compressor geometries, like those experimented on here.

4.1.3 Five Critical Parameters

Senoo and Kinoshita detail five separate parameters that have an influence on the critical flow angle at the diffuser inlet [32]. Those five parameters are: the width ratio (b_4/R_4), the radius ratio (R_5/R_4), the inlet Mach number (M_4), the inlet Reynolds number (Re_4), and the inlet velocity distortion ($\Delta C_{m,4}$ and $\Delta C_{t,4}$) [32]. Each of these five parameters will have an influence on the critical flow angle, with some influences being greater or smaller than others [32].

There are several other works that back up the influence of these parameters. It was determined that rotating stall could onset from what is called a longitudinal wave method [15, 44]. This is essentially a periodic wave that rotates around the compressor face with areas of greater and lesser velocity [44]. This is best classified as a jet – wake velocity profile. In [1, 4, 9, 14, 16, 24, 26, 30, & 41] it was determined that these jet – wake profiles rotate around the compressor face [9] and that they have an influence on the stability of the vaneless diffuser through what is known as coupling [1]. This is akin to the velocity distortion that was found by Senoo and Kinoshita to have an influence on the critical flow angle [32].

In [2, 15, 17, 23 – 25, 33, & 41] it was shown that R_5/R_4 has an impact on the critical flow angle of the diffuser. However, it was found by Van Den Braembussche in [41] that the impact was less than expected by Jansen in [15]. Thus, R_5/R_4 may be more of a secondary factor than a primary factor. Also, Van Den Braembussche found that b_4/R_4 had an immediate impact on the critical flow angle for the diffuser [41]. The work of Ludtke in [26] and Senoo and Kinoshita in [32] show that M_4 effects the critical flow angle. However there is a shrinking of the compressor operating envelope that accompanies an increase in the running speed on the compressor [10, 11]. By default the running speed of the compressor will allow for larger flow rates and higher flow speed through the compressor stage leading to an increase in the Mach number at the diffuser inlet, M_4 . Therefore, while no direct correlation to stability outside of [26, 32] was found for M_4 , there is evidence provided in [10, 11] that shows that the Mach number does have an impact on the stability of the diffuser. Furthermore, according to Kline and Runstadler in [19, 20] there is a buildup of stalled fluid that occurs in the flow as the flow velocity decreases ultimately leading to stall, this was also validated in [15]. The point is that an increase in M_4 , will lead to a decrease in the boundary layer thickness, but it can make the boundary layer easier to disturb due to the large

shear stresses which exist in the boundary layer. Thus, a poorly planned diffuser as defined by Aungier in [5] could provide the impetus for spike inception inside of the vaneless diffuser. So, overall given the chaotic nature of the flow inside of a compressor [8] it is reasonable to expect that as speeds increase there will be a decrease in stability.

It was found that Re_4 had some effect on the critical flow angle [23, 41]. However, one must be careful with Reynolds number effects because it was found by Wiesner that as the Reynolds number increases there is an effect associated with it [42]. Also, according Wiesner that effect will dissipate at high enough values of Re [42]. These values are on the order of $10^6 - 10^7$ [42], which are values not often reached at the diffuser inlet, but it is a terminating place to look for Reynolds number effects in vaneless diffuser stability.

As a note, in the work of Ljevar et al. [23 – 25], which focused on wide diffusers (a wide diffuser has $b_4/R_4 > 0.1$ [24]), it was determined that the number of impeller blades, Z_{imp} , had an effect on compressor stability, with the stability growing worse for 10 – 13 blades and then decreasing until being fully diminished by 16 – 18 blades. This dependence was confirmed by [27] because one of the compressors tested for this work exhibited rotating stall with only 13 blades, but when that was increased to 15 – 18 blades the stall cells no longer formed.

One of the goals of this work is to try to find out how much of an influence each of these parameters have on the critical flow angle. It may be that for the cases tested here one of these parameters dominates all of the others, this is the premise behind the Senoo – Kobayashi equation and its dependence on only width ratio. Or it is possible that none of the parameters is dominant and diffuser stability is determined by more random factors like those that lead to spike inception [44]. The point is that one needs to know how these factors influence the trends seen in the critical flow angle which tell a designer whether or not it is safe to use a geometrically or dynamically

similar design for their next compressor prototype. The expectation is that one parameter holds greater sway than the others, but all things being equal or similar, the other parameters will push the compressor toward being more or less stable.

4.2 Experimental Procedure for Performance Measurements

The experimental performance measurements were taken at the Solar Turbines Aero Test Facility in San Diego, CA [46]. The test gas used was air. The facility performs the tests in a closed loop environment with the loop being inside and the piping system being properly insulated [46]. The system is controlled by an Allen-Bradley PLC-5 control system [46]. The temperature readings are found using thermocouples inserted directly into the flow. The pressure measurements are taken from pressure taps attached directly to the test rig. The Allen-Bradley converts the pressure and temperature measurements into values for work, efficiency, head, mass flow rate, etc. [46]. The mass flow rate is controlled via two valves that are adjusted by the test engineer [46]. For an insulated test the flow is allowed to stabilize for 5-10 minutes before data is taken [46]. This allows fluctuations in the system to damp out. These fluctuations are caused by a change in flow point, as well as differences in cooling water due to the use of shared plant cooling water resources [46]. The cooling water is used to cool the discharge gas via an external heat exchanger [46]. For the performance values the compressor stage is tested from the choke point to surge via manual control of the mass flow rate [46]. The number of data points changes based upon the type of compressor stage, but usually 8 – 11 data points are taken.

4.3 Experimental Procedure to Determine Diffuser Inlet Flow Angle

The diffuser inlet flow angle is determined by a traverse test [46]. The traverse test uses a stepper motor that controls a three element cobra probe to measure the flow angle and pressure at different locations in the compressor stage [46]. When setting the initial angle a machine protractor

is used [46]. The cobra probe begins at the shroud side of the compressor stage and moves in increments of 5 – 10% until the cobra probe reaches the hub side. The cobra probe is able to measure the local flow angle and pressure for span values from 10% - 90% (in increments of 10% span), however that can change based on the geometry. For low specific speed impellers the traverse test may only include points at span values of 25%, 50%, and 75% respectively. But, for a mixed flow impeller the traverse test may run from 3% - 97% span. The average flow angle is an average of the local values from hub to shroud. The traverse test is run at the diffuser inlet (station 4), the diffuser outlet (station 5), and the RTV inlet (station 6). The test is normally run for three separate speed lines of 13100 RPM, 19240 RPM, and 21870 RPM, representing low, medium, and high running speeds.

4.4 Experimental Procedure to Determine Rotating Stall Onset

To experimentally determine rotating stall onset and the flow angle associated with it a simple procedure is used. The flow angle is found using the traverse procedure discussed above and found in [46]. During the test run the control room monitors two separate plots: the Magnitude Spectrum Plot and the Coherence Plot. See Figures 10 and 11 below for examples.

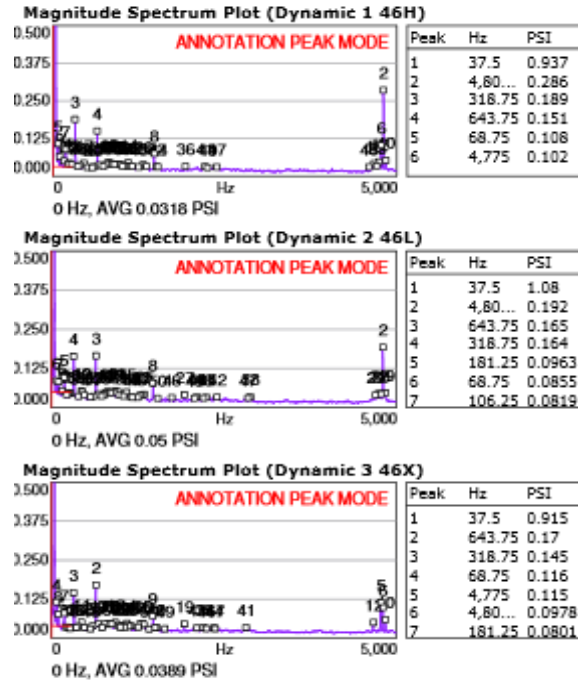


Figure 10: Example of a Spectrum Plot provided by [27]

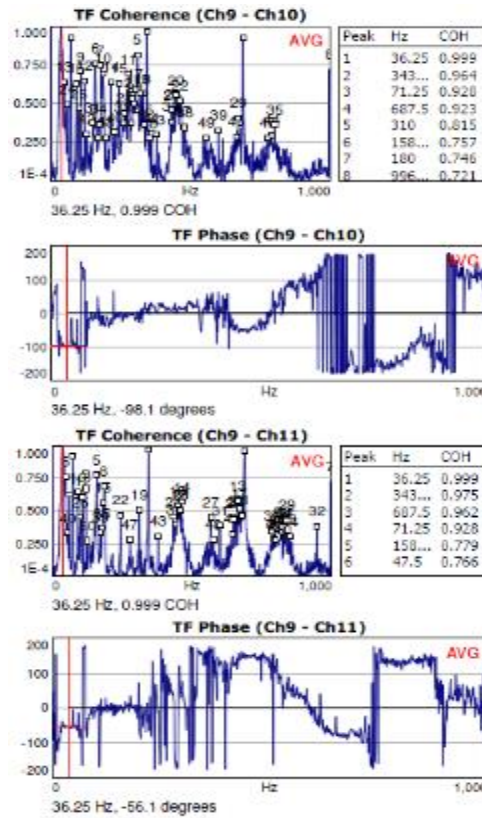


Figure 11: Example of a Coherence Plot adapted and reproduced from [38].

Using the magnitude spectrum plot the frequencies that occur are compared to frequencies that correspond to the running speed (called 1x) and twice that of the running speed (called 2x) [27]. These vibration frequencies are almost always seen [27]. When an unusual frequency appears it is compared to the 1x and 2x values. If it reaches the magnitude of the 1x and 2x values then it is taken seriously and the coherence plot is employed [27]. There the phase shift of the anomalous frequency is compared between the three cobra probes giving two phase shifts (one is between probes 1 and 2 and the other is between probes 2 and 3) [27]. Once the phase shift has been calculate the Hanover plot is employed, see Figures 12 and 13.

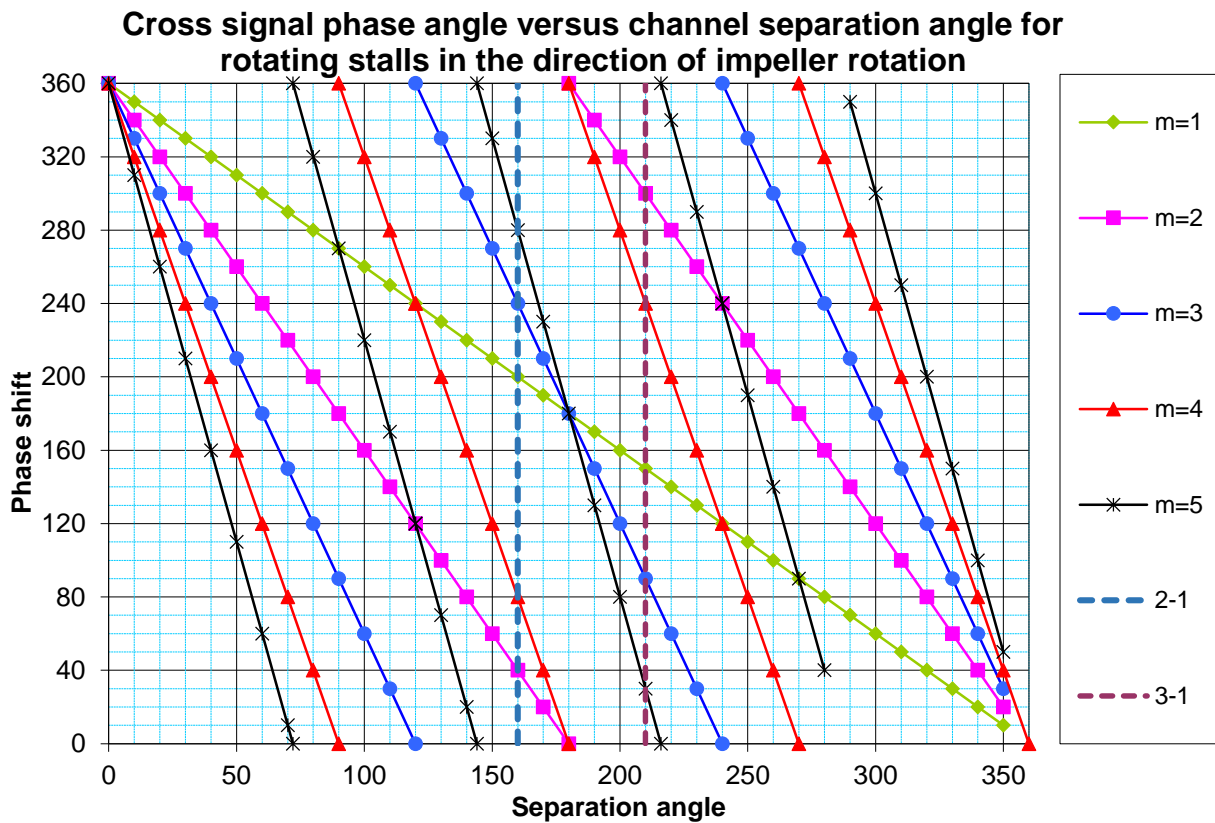


Figure 12: Hanover Plot for Forward Direction Stall Cell Rotation provided by [27].

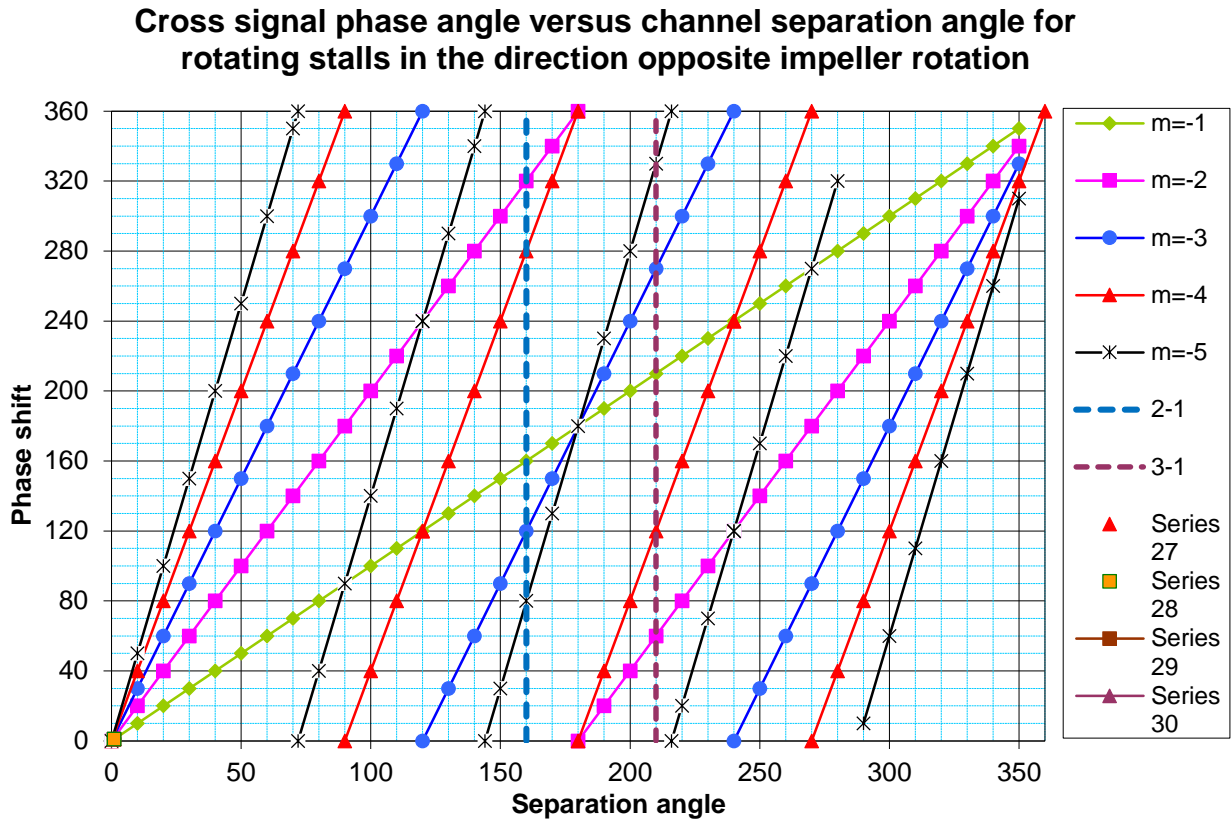


Figure 13: Hanover Plot for Reverse Direction Stall Cell Rotation provided by [27]

To use the Hanover Plot one looks to see if the phase angle intersects with a line on the plot at the corresponding separation angle (i.e. at the point where the phase angle and separation angle have the same value). If the phase angle is found to match for both phases within 5 degrees then rotating stall is considered to be occurring at the frequency of interest [27]. Note as well that if the phases correspond to a different number of stall cells this may not be considered a match because only one stall pattern is expected to occur at a time [15]. However, if no match has been found then the frequency is considered to be a non-rotating unsteady flow that is less of a threat to the stability of the rotor [27]. Since the test engineer knows what flow rate the rotating stall occurred, from the traverse test the flow angle at that flow rate can be found as well as the velocity profile [27] (if needed linear interpolation between data points was found to be useful as well).

CHAPTER 5: NUMERICAL PRECURSORS

5.1 How the Local Flow Angle Approach Works

The local flow angle approach is a numerical modelling procedure that simulates the flow through a centrifugal compressor stage. Figure 14 shows a sample geometry.

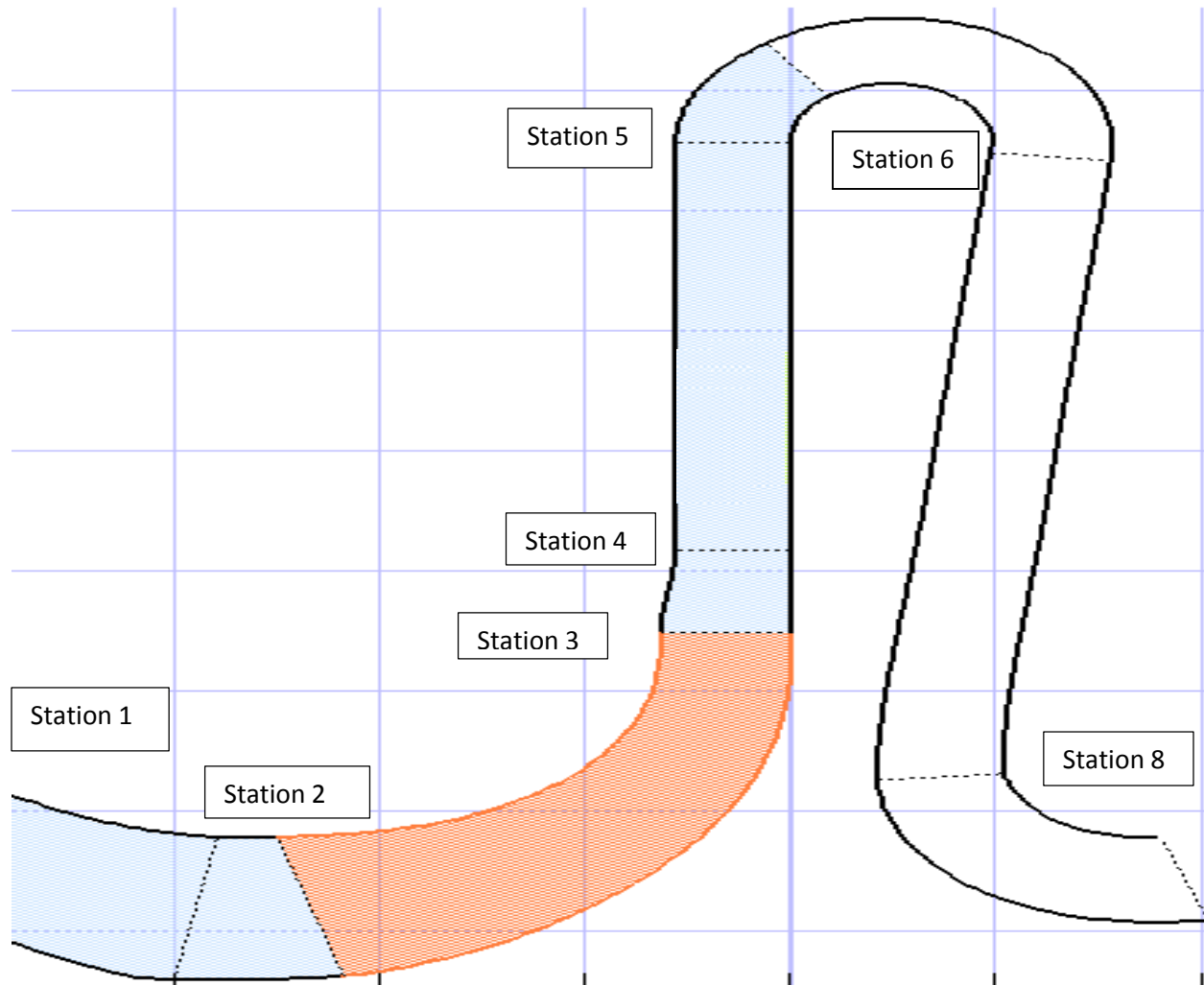


Figure 14: Example Geometry

In Figure 14 several station locations are shown. Station 1 is the stage inlet, station 2 is the impeller inlet, station 3 is the impeller exit, station 4 is the vaneless diffuser inlet, station 5 is the vaneless diffuser outlet, station 6 is the RTV inlet, and station 8 is the RTV outlet. The actual

stage outlet is at station 9, not shown. Station 9's geometry was not given and was not needed for simulation purposes [27]. The blue regions represent the flow path and the red regions represent bladed sections.

The local flow angle approach uses a steady state simulation (see Appendix C for details on how a steady state simulation works) to investigate the local profiles at the inlet to the vaneless diffuser, station 4. Each of the fourteen geometries provided by Solar Turbines were simulated from choke to surge along the operating line for three speed lines (13100 RPM, 19240 RPM, and 21870 RPM). The stage geometries were provide by Solar Turbines Inc. in the form of machine lines that were imported into the simulation software. The simulation includes two geometric domains: the first is a single blade passage for the impeller region, while the second is a single blade passage for the RTV region. By use of an in-house excel macro the stage geometry is split apart in the diffuser region allowing for only two geometric domains to be employed. The regions are brought together via a stage interface using a stage average velocity boundary condition. The inlet boundaries were the total pressure and total temperature. The outlet boundary used the mass flow rate⁴. The time scale used was the physical time scale with a value of 0.0001s⁵. Each of the domains was meshed separately and then brought together for the full simulation. The turbulence model used was the Shear Stress Transport (SST) model (see Appendix C for the equations relating to SST).

There are a few points that need to be cleaned up. First, there is the issue of the flow inside of a compressor being unsteady [8]. This, is true, however as a compressor runs at a specific flow point it reaches what is known as dynamic stability. So, the flow at this point is essentially steady

⁴ There were instances where the mass flow rate boundary caused divergence. In these cases a static pressure boundary was used.

⁵ Compressor 6 could not be simulated using the physical time scale. In this case auto-time scale was used.

and can therefore be modelled using a steady state approach [27]. Furthermore, since rotating stall is a dynamic instability the flow will remain more or less stable (i.e. un-stalled) until the point of rotating stall onset [27]. It is at this point that the dynamic stability breaks down and the steady state simulation may or may not be trustworthy, that will depend on how the performance parameters listed below (see section 5.2) compare with the experimental data. That said the flow is steady until rotating stall onsets, which is all that is needed to get the flow profile at the critical flow rate. From here a design engineer can analyze the flow profile and compare against the Senoo – Kobayashi equation, or some other predictor of flow stability, for instability issues.

The other point is why a steady state run versus a transient run. A transient simulation is used when the characteristics of the rotating stall pattern are desired. And since all flows have some amount of unsteadiness in them [20], a transient study must be run to get these results. However, this study is based upon the need to determine whether or not rotating stall is occurring, its details are less significant and cannot be determined through a steady state approach [15, 39].

A transient run also requires many more computational resources or a significantly longer running time [6, 39]. Vagani explained that a minimum of 75000 grid nodes must be run per computer processing unit (CPU) when solving a simulation using parallel processing [39]. This is to avoid numerical error associated with parallel processing [39]. Thus, as the number of nodes increases so does the length of simulation time. Furthermore, a transient simulation usually requires a full 360 degree geometry to properly resolve the stall structure, although Anish and Sitaram found some success using a single blade passage transient simulation [4]. For the simulations considered here that would mean approximately 15 – 20 million grid nodes would be needed for a full 360 degree study per geometry and around 1.5 million nodes for a single passage study, which is significantly more than used by Hildebrandt and Genrup [14], but similar to the

number used by Wolfram and Carolus [43]. This calculates to between 200 – 250 core processors to minimize the running time. Even if available this is a large number of resources that are better spent elsewhere. And if not available then the time required to run a single data point can be as long as 24 – 48 hours [6, 39] which is not acceptable in a competitive market like centrifugal compressor engineering. Thus, the allure of the steady state simulation which can be run using a single blade passage for the impeller region and the RTV region respectively.

5.2 Verifying the Validity of the Results

With all compressor stability studies one must be able to determine whether or not the results can be trusted. For this project the fourteen tested geometries have all been tested at three different speed lines (13100 RPM, 19240 RPM, and 21870 RPM) experimentally by Solar Turbines. Thus, the experimental results will be compared to the numerically simulated results provided by the local flow angle approach. For validation purposes the local flow angle approach results will be compared to the experimental results for the following parameters: P_{s80} , C_{m4} , C_{t4} , C_{m5} , C_{t5} , T_0 , ϕ , α_4 , and α_5 ⁶. All of these parameters are mass flow average values. Along with these values the local variation of C_{m4} , C_{t4} , and α_4 are calculated and compared as well. The local value consists of data taken on an analysis line across the span. The data is taken at 40 separate span locations and mass flow averaged around the circumference. If a good comparison is achieved then the results can be trusted. It must be noted that results beyond the experimentally determined stall point are included, but it is not expected that they will compare well with the experimental data. Another note, the local flow profiles are not required to agree quantitatively with the experimental results for this study. This is because a breach of the Senoo angle is what

⁶ Please note that the pressure rise (P_{s80}/P_{01}) and temperature rise (T_{08}/T_{01}) plots can be found in Appendices A and B. The other plots have not been included to conserve space.

is being sought. If the profiles just show qualitative agreement it will be enough to confirm validity.

5.3 The Grid Sensitivity Study

5.3.1 What is a Grid Sensitivity Study and Why is it Important?

A grid sensitivity analysis is an investigation that is done to see if the density of grid nodes influences the numerical results. Since the amount of time required to run the simulation is directly proportional to the number of grid nodes used the more grid nodes required the longer the simulation time and vice versa. Thus, a grid study is performed to make sure that the number of nodes being used gives stable results that do not change with the addition of significant numbers of additional nodes (this would be on the order of 50% – 100% more nodes to the overall geometry). The desire is to find a grid number that is sufficiently large to properly resolve the results, small enough to allow for feasible running time, and large enough to allow for changes in geometry across different compressor geometries. This way testing templates can be made and easily applied to many different classes of centrifugal compressor stages.

5.3.2 Results of the Grid Sensitivity Study

For the grid sensitivity study Compressor 1 was chosen as a middle ground in terms of flow capacity and size. The geometric details of all compressor geometries can be found in Table 2 below.

Number	b_4/R_4	R_5/R_4	Z_{imp}	$N_{s,avg.}$
1	0.067	1.343	16	0.62
2	0.038	1.712	13	0.49
3	0.055	1.886	13	0.48
4	0.045	1.714	15	0.48
5	0.056	1.714	15	0.48
6	0.021	1.557	19	0.35
7	0.016	1.557	15	0.29
8	0.013	1.512	15	0.28
9	0.065	1.580	15	0.57
10	0.062	1.343	19	0.58
11	0.078	1.623	13	0.63
12	0.078	1.623	13	0.69
13	0.112	1.692	11	0.80
14	0.134	1.178	13	1.10

Table 2: Compressor Geometries and Flow Details

Table 2 contains the width ratio, b_4/R_4 , the radius ratio, R_5/R_4 , the number of impeller blades, Z_{imp} , and the average specific speed, $N_{s,avg.}$. The average specific speed is the arithmetic average of the specific speed at each of the three speed lines. The specific speed is given as:

$$N_s = \frac{\omega \cdot \sqrt{Q_{BEP}}}{(g \cdot H_{BEP})^{3/4}} \quad (5.1)$$

where g is the gravitational constant near Earth's surface in m/s^2 , H_{BEP} is the head rise at the best efficiency point in meters, Q_{BEP} is the volume flow rate at the best efficiency point in m^3/s , and ω is the running speed in rad/second. The 13100 RPM speed line was chosen to differentiate between different grid sizes. The three grid sizes represent coarse (569000 nodes), medium (1164000 nodes), and fine (2276000 nodes) meshes. The results of the grid study are found in Figures 15 – 20. Also, each parameter in Figures 15 – 20 are compared against the flow coefficient, Φ or ϕ . Note, all results have been non-dimensionalized based on the following procedure: all pressure have been divided by the inlet stagnation pressure, P_{01} , for each specific stage and speed line, all temperatures have been divided by the inlet stagnation temperature, T_{01} , for each specific stage

and speed line, and all velocities have been divided by the impeller tip velocity, U_{tip} , for each specific stage and speed line.

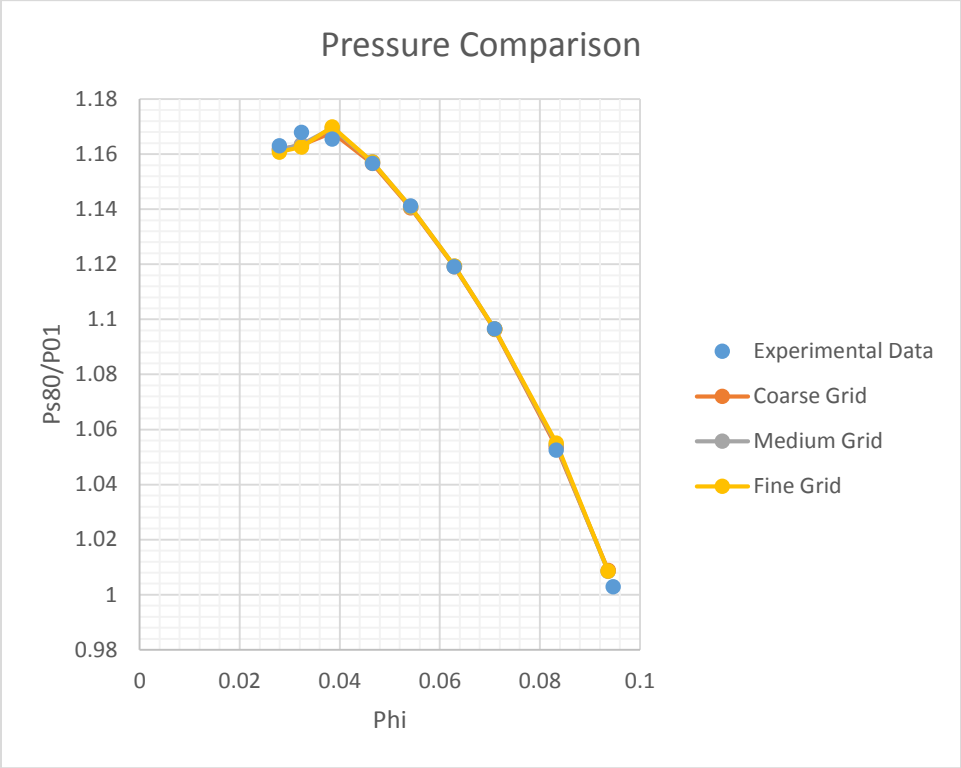


Figure 15: Performance Envelope Comparison

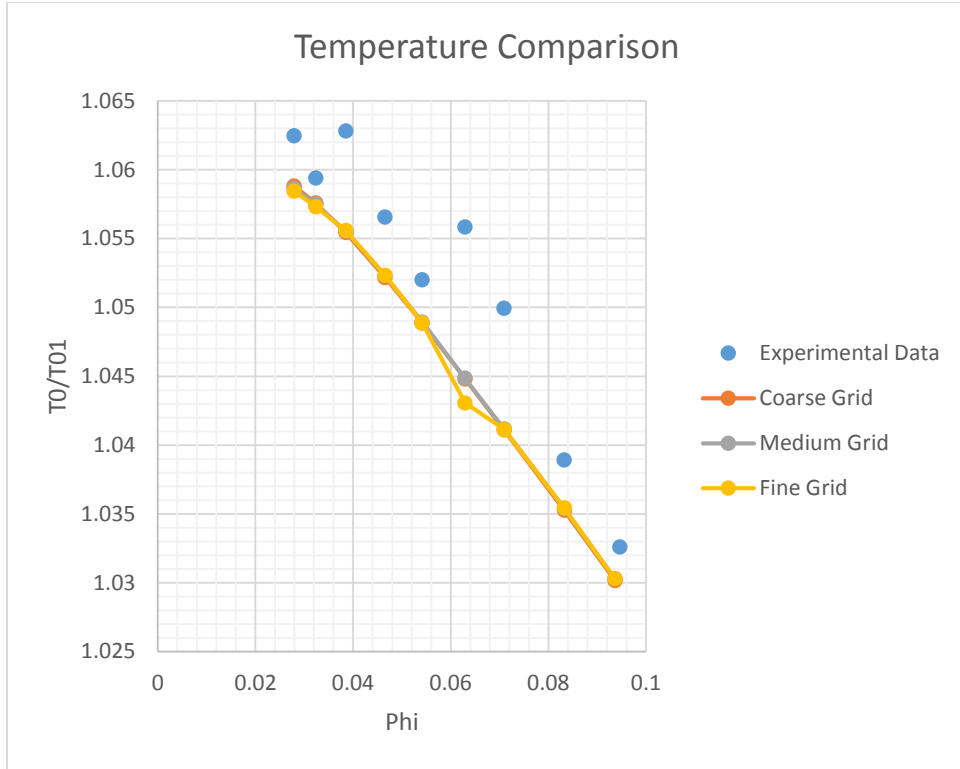


Figure 16: Stagnation Temperature Comparison

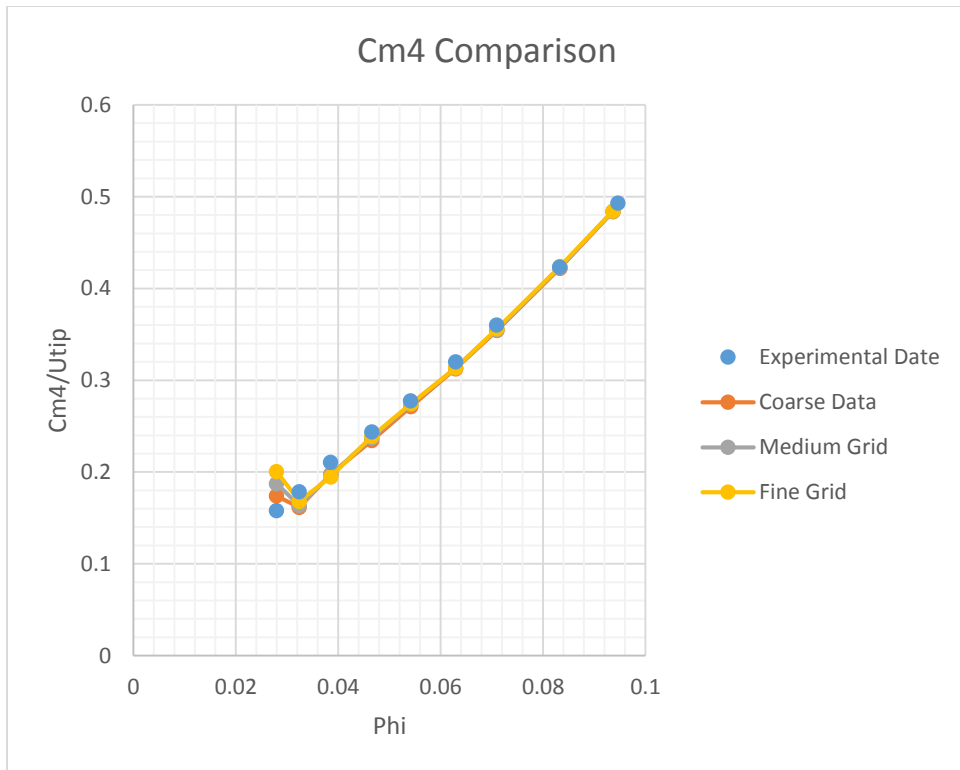


Figure 17: Meridional Velocity Comparison at Diffuser Inlet

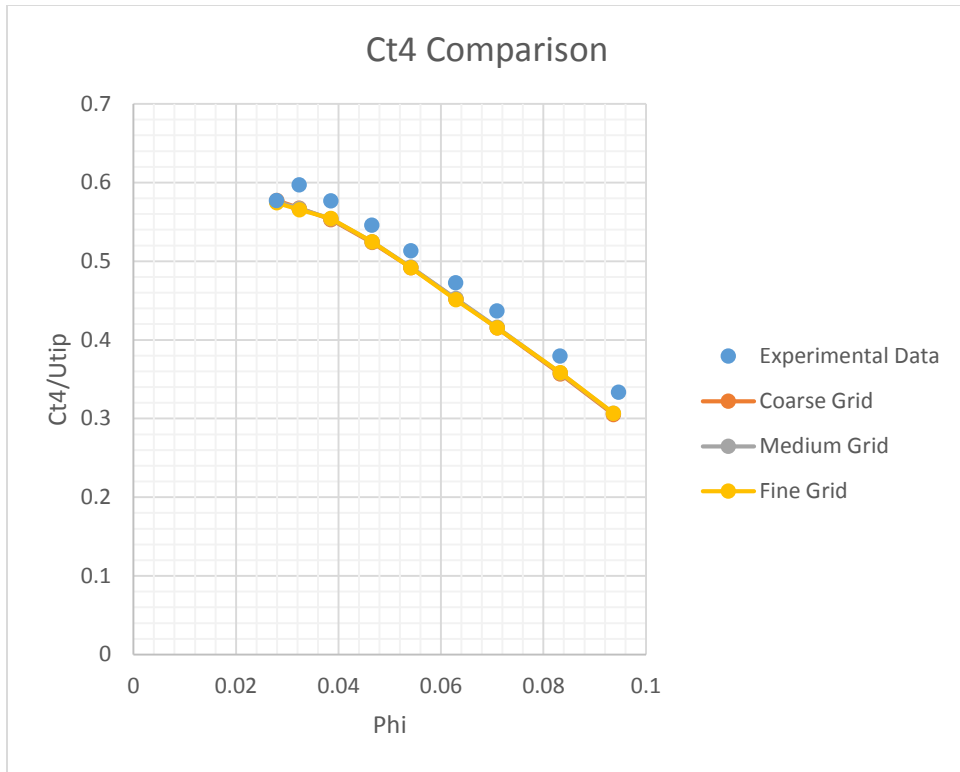


Figure 18: Tangential Velocity Comparison at Diffuser Inlet

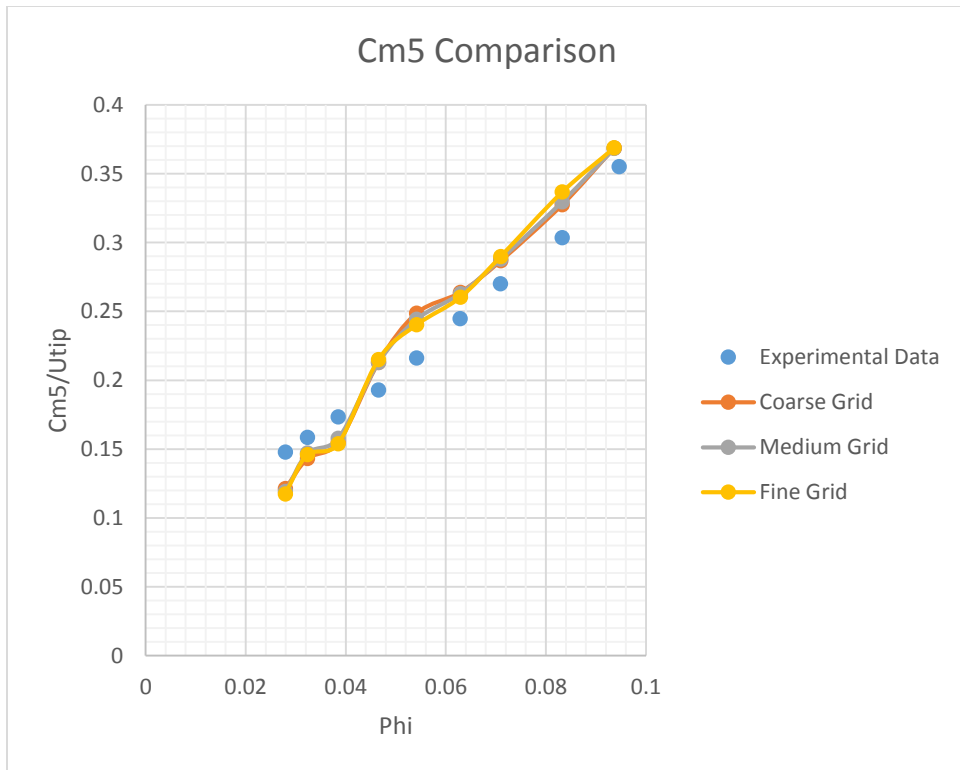


Figure 19: Meridional Velocity Comparison at Diffuser Inlet

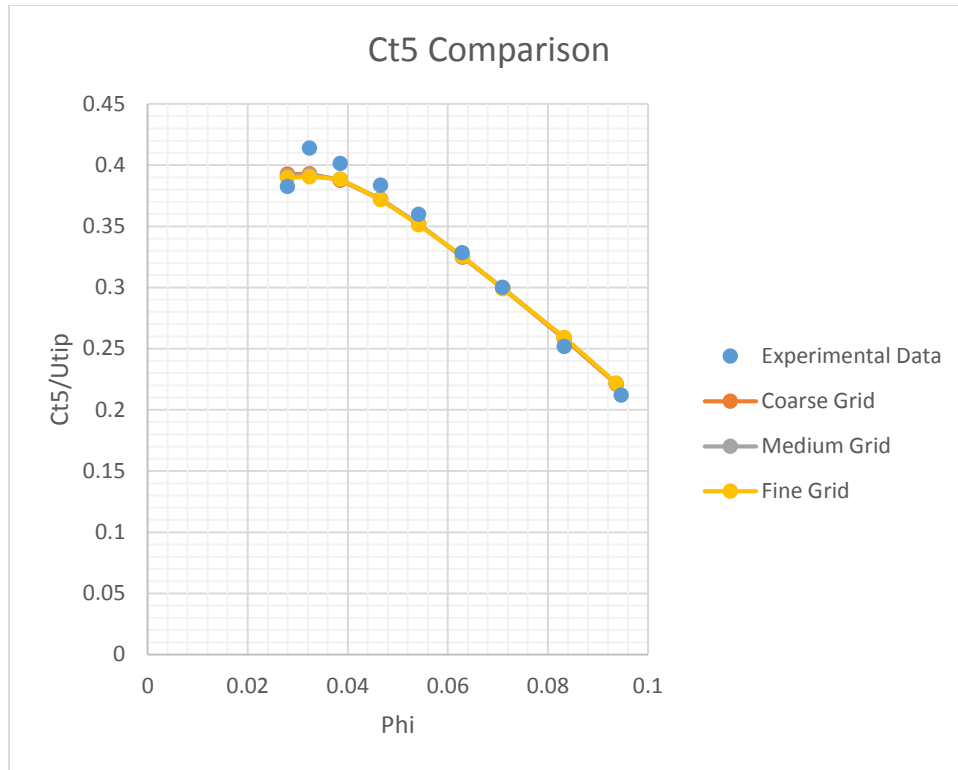


Figure 20: Tangential Velocity Comparison at Diffuser Inlet

As can be seen in Figures 15 – 20 there is little deviation between the different grids. Furthermore, all of the grid sizes match well with the experimental data. The exception to this can be found in Figure 19. Figure 19 compares the meridional velocity at station 5 for the grids to the experimental results. The difference between experimental and numerical results is between 3% – 10%. This difference is measurable. However, since the profile matches well at the diffuser inlet the study is still viable, since the diffuser inlet is the more important location as far as the local flow angle approach is concerned. Also, at station 5 the flow has slowed by roughly 1/3 for the choke condition and 2/3 by surge when compared to the diffuser inlet. Thus, at this point small changes in velocity can make large changes in percentage difference between experiment and simulation. All of this is mentioned so that it can be said that the grid the results of the local flow angle approach can be trusted. From the results since there is no real variation between the grids

the medium grid will be used for further simulations. This grid has about 1.2 million nodes and offers both detail and adaptability between mesh sizes.

5.4 The Next Phase

The grid study was able to show viability in the local flow angle approach. It was also able to provide a mesh template to streamline the creation of the simulation. From there all fourteen geometries were simulated along the three previously mentioned speed lines from choke to surge. If a stall point existed for a geometry it was simulated as well. All of the results can be found in Chapter 6.

CHAPTER 6: LOCAL FLOW ANGLE APPROACH RESULTS

6.1 Background on Experimental Geometries

For this investigation 14 unique geometries were simulated at three separate speed lines. The geometric details are listed in Table 2, see section 5.3.2. As can be seen from Table 2 there is a wide range of diffuser widths and lengths as well as a number of different specific speeds. These fourteen geometries serve to represent a spectrum of results that will provide a good overall understanding of whether or not the local flow angle approach is a good measure of centrifugal compressor vaneless diffuser stability.

6.2 Comparison of Average Flow Angles to the Five Critical Parameters

From the work of Senoo and Kinoshita it was determined that there are five critical flow parameters that determine vaneless diffuser stability [32]. Part of this investigation was to see whether or not these parameters actually had an effect on the stability of the vaneless diffuser. To that end several tables have been provided to compare a specific critical parameter against the numerically determined rotating stall onset angle and the critical angle calculated from the Senoo – Kobayashi equation. Results have been provided at all three speed lines to better facilitate understanding in whether or not a change in speed line or critical parameter has led to a gain or loss of stability. There are two issues of note. One, each table contains a parameter named $\Delta\alpha$. This parameter is defined as:

$$\Delta\alpha = \alpha_{\text{local,max}} - \alpha_{\text{c,Senoo}} \quad (6.1)$$

where $\alpha_{\text{local,max}}$ is the maximum flow angle along the span profile and $\alpha_{\text{c,Senoo}}$ is the critical flow angle determined by the Senoo – Kobayashi equation (see equation 3.1). This parameter compares the local flow angle maximum⁷ from each simulation to the critical angle from the Senoo –

⁷ Please note that these values have been mass flow averaged around the circumference of the geometry.

Kobayashi equation. If the $\Delta\alpha$ parameter is less than zero then the Senoo line was not breached and if $\Delta\alpha$ is positive then the Senoo line was breached. This serves to show whether or not the Senoo line accurately predicted rotating stall onset. Two, if a geometry did not experience rotating stall then it is placed in the table, but no data, other than geometric data, has been provided due to the lack of rotating stall. However, they have been included because their lack of rotating stall onset still gives valuable information about the overall physical factors influencing the critical parameters of vaneless diffusers.

6.2.1 Width Ratio Comparison

Tables 3 – 5 compare the mass flow averaged critical flow angle for each geometry against the critical flow angle predicted by the Senoo – Kobayashi equation as the width ratio changes. Since the flow angle is measured from the vertical as the flow angle increases towards 90 degrees the compressor is considered to be more likely to experience rotating stall. What is shown in these tables is that as the width ratio changes the average flow angle changes too. For this case as the width ratio changes it can be seen that the critical flow angle decreases as the diffuser widens. This is expected from the results of Senoo and Kinoshita [32] and Van Den Braembussche [41].

Number	$\phi_{R.S.}$	b_4/R_4	α_{Senoo} (deg)	$\alpha_{C,num}$ (deg)	$\Delta\alpha$ (deg)
1	0.03270	0.067	80.03	73.92	2.71
2	0.01700	0.038	82.47	73.05	-5.27
3	0.01700	0.055	81.07	75.26	6.53
4	0.02316	0.045	81.93	71.19	-8.13
5	0.02588	0.056	80.93	72.20	-7.17
6	N/A	0.021	83.99	N/A	N/A
7	0.00532	0.016	84.46	76.38	-5.96
8	0.00511	0.013	84.68	74.55	-7.68
9	0.03025	0.065	80.17	73.53	-0.27
10	N/A	0.062	80.48	N/A	N/A
11	0.03620	0.078	79.17	74.31	0.23
12	0.04220	0.078	79.17	71.20	-5.97
13	0.04616	0.112	77.05	73.89	3.75
14	0.07376	0.134	76.26	70.74	23.25

Table 3: Width Ratio Comparison at 13100 RPM

Number	$\phi_{R.S.}$	b_4/R_4	α_{Senoo} (deg)	$\alpha_{C,num}$ (deg)	$\Delta\alpha$ (deg)
1	0.04147	0.067	80.03	71.13	1.70
2	0.01900	0.038	82.47	72.74	-6.27
3	0.01800	0.055	81.07	75.77	7.23
4	0.02545	0.045	81.93	71.25	-8.23
5	0.02990	0.056	80.93	70.97	-8.53
6	N/A	0.021	83.99	N/A	N/A
7	0.00498	0.016	84.46	78.58	-3.16
8	0.00669	0.013	84.68	70.92	-11.74
9	0.03324	0.065	80.17	73.88	-0.37
10	N/A	0.062	80.48	N/A	N/A
11	0.03230	0.078	79.17	78.02	19.12
12	0.04720	0.078	79.17	70.85	-7.17
13	0.04694	0.112	77.05	75.55	18.25
14	0.07766	0.134	76.26	70.74	23.21

Table 4: Width Ratio Comparison at 19240 RPM

Number	$\phi_{R.S.}$	b_4/R_4	α_{Senoo} (deg)	$\alpha_{C,num}$ (deg)	$\Delta\alpha$ (deg)
1	0.04350	0.067	80.03	71.23	0.17
2	0.02100	0.038	82.47	71.67	-7.67
3	0.02370	0.055	81.07	72.63	-2.27
4	0.02525	0.045	81.93	72.46	-6.13
5	0.03113	0.056	80.93	71.10	-8.43
6	N/A	0.021	83.99	N/A	N/A
7	0.00500	0.016	84.46	79.09	-2.52
8	0.00726	0.013	84.68	70.00	-12.69
9	N/A	0.065	80.17	N/A	N/A
10	N/A	0.062	80.48	N/A	N/A
11	N/A	0.078	79.17	N/A	N/A
12	0.05070	0.078	79.17	70.22	-7.87
13	0.04845	0.112	77.05	75.86	21.18
14	0.08910	0.134	76.26	67.20	9.26

Table 5: Width Ratio Comparison at 21870 RPM

The idea is that as the average flow angle increases towards 90 degrees the local flow angles as a whole must approach larger and larger values leading to localized flow reversal, which is considered to be a prime cause of rotating stall onset [41].

However, looking one dimensionally at an average flow angle is not an accurate way to determine vaneless diffuser stability. At no point in Tables 3 – 5 does the average critical flow angle cross the Senoo line. This means that just looking at the average flow angle will find one still falling short of the critical flow angle as predicted by the Senoo – Kobayashi equation. The closest that any of the average angles approach is one degree. This one degree translates into about a 10% difference in mass flow rate between the predicted critical mass flow rate and the actual critical mass flow rate⁸, see note 8. Looking through Tables 3 – 5 one can see that the difference

⁸ Begin with the definition of mass flow rate for two separate flow angles, θ .

$$\dot{m}_1 = \rho * A_c * C_{m,1} = \rho * A_c * C * \cos(\theta_1) \quad \dot{m}_2 = \rho * A_c * C_{m,2} = \rho * A_c * C * \cos(\theta_2)$$

Assume that $\theta_1 - \theta_2 = \Delta\theta$ and substitute.

$$\dot{m}_2 = \rho * A_c * C * \cos(\theta_2) = \rho * A_c * C * \cos(\theta_1 - \Delta\theta) = \rho * A_c * C * (\cos \theta_1 * \cos \Delta\theta + \sin \theta_1 * \sin \Delta\theta)$$

Now take the difference between the mass flow rates and collect like terms to find:

between the numerical critical flow angle and the Senoo critical flow angle is often greater than five degrees. Thus, the difference between predicted and critical mass flow rate is often greater than 50%, see note 8, which is too large of a gap to be considered accurate.

6.2.2 Radius Ratio Comparison

Tables 6 – 8 compare the radius ratio to the average critical flow angles.

Number	$\phi_{R.S.}$	R_5/R_4	α_{Senoo} (deg)	$\alpha_{C,num}$ (deg)	$\Delta\alpha$ (deg)
1	0.03270	1.343	80.03	73.92	2.71
2	0.01700	1.712	82.47	73.05	-5.27
3	0.01700	1.886	81.07	75.26	6.53
4	0.02316	1.714	81.93	71.19	-8.13
5	0.02588	1.714	80.93	72.20	-7.17
6	N/A	1.557	83.99	N/A	N/A
7	0.00532	1.557	84.46	76.38	-5.96
8	0.00511	1.512	84.68	74.55	-7.68
9	0.03025	1.580	80.17	73.53	-0.27
10	N/A	1.343	80.48	N/A	N/A
11	0.03620	1.623	79.17	74.31	0.23
12	0.04220	1.623	79.17	71.20	-5.97
13	0.04616	1.692	77.05	73.89	3.75
14	0.07376	1.178	76.26	70.74	23.25

Table 6: Radius Ratio Comparison at 13100 RPM

$$\frac{\dot{m}_2 - \dot{m}_1}{\dot{m}_1} = \cos \Delta\theta + \tan \theta_1 * \sin \Delta\theta - 1$$

This is a comparison equation between the mass flow rates at different flow angles. Now assume that $\theta_1 = 80$ degrees. Which is a reasonable critical flow angle according to [15]. Now assume that $\Delta\theta = 5$ degrees. Plugging in these numbers yields:

$$\frac{\dot{m}_2 - \dot{m}_1}{\dot{m}_1} = 0.4905$$

This means that the actual critical mass flow is ~49% greater than the expected Senoo mass flow rate. This will lead to a loss in both efficiency and pressure rise in a real test.

Number	$\phi_{R.S.}$	R_5/R_4	α_{Senoo} (deg)	$\alpha_{C,num}$ (deg)	$\Delta\alpha$ (deg)
1	0.04147	1.343	80.03	71.13	1.70
2	0.01900	1.712	82.47	72.74	-6.27
3	0.01800	1.886	81.07	75.77	7.23
4	0.02545	1.714	81.93	71.25	-8.23
5	0.02990	1.714	80.93	70.97	-8.53
6	N/A	1.557	83.99	N/A	N/A
7	0.00498	1.557	84.46	78.58	-3.16
8	0.00669	1.512	84.68	70.92	-11.74
9	0.03324	1.580	80.17	73.88	-0.37
10	N/A	1.343	80.48	N/A	N/A
11	0.03230	1.623	79.17	78.02	19.12
12	0.04720	1.623	79.17	70.85	-7.17
13	0.04694	1.692	77.05	75.55	18.25
14	0.07766	1.178	76.26	70.74	23.21

Table 7: Radius Ratio Comparison at 19240 RPM

Number	$\phi_{R.S.}$	R_5/R_4	α_{Senoo} (deg)	$\alpha_{C,num}$ (deg)	$\Delta\alpha$ (deg)
1	0.04350	1.343	80.03	71.23	0.17
2	0.02100	1.712	82.47	71.67	-7.67
3	0.02370	1.886	81.07	72.63	-2.27
4	0.02525	1.714	81.93	72.46	-6.13
5	0.03113	1.714	80.93	71.10	-8.43
6	N/A	1.557	83.99	N/A	N/A
7	0.00500	1.557	84.46	79.09	-2.52
8	0.00726	1.512	84.68	70.00	-12.69
9	N/A	1.580	80.17	N/A	N/A
10	N/A	1.343	80.48	N/A	N/A
11	N/A	1.623	79.17	N/A	N/A
12	0.05070	1.623	79.17	70.22	-7.87
13	0.04845	1.692	77.05	75.86	21.18
14	0.08910	1.178	76.26	67.20	9.26

Table 8: Radius Ratio Comparison at 21870 RPM

From [23 – 26, 32 – 34, & 41] it is expected that as the radius ratio increases the critical flow angle will decrease allowing for a less stable vaneless diffuser. This is not the conclusion that can be found from the data presented in Tables 6 – 8. Tables 6 – 8 point to an average critical flow angle that grows larger as the radius ratio increases. It is of note that for the results of Ljevar et al found in [23 – 25] the compressors simulated had width ratios greater than 0.1. For this study

Compressors 13 and 14 match that criteria. But as can be seen Compressor 13 which is longer than Compressor 14 is considerably more stable. Thus, something else must be at play here. Senoo and Kinoshita found that the critical flow angle was actually a function of the width ratio and radius ratio combined [32]. Thus, the width ratio has a greater influence than the radius ratio on compressor stability. Also Senoo et al. found that it is possible for the vaneless diffuser to have regions of rotating stall combined with regions of un-stalled flow inside of the same diffuser at the same operating point [32, 33]. So, a diffuser inlet could be un-stalled and operating normally, while just downstream the diffuser may experience rotating stall [32, 33]. Therefore, the radius ratio has a secondary effect when compared to the width ratio on vaneless diffuser stability. However, this effect is likely hidden from this data set because it only compares the average flow angle and the Senoo angle at the diffuser inlet and not the local downstream velocity profiles.

6.2.3 Mach Number Comparison

Tables 9 – 11 show the comparison between the critical flow angle and the Mach number.

Number	$\phi_{R.S.}$	M_4	α_{Senoo} (deg)	$\alpha_{C,num}$ (deg)	$\Delta\alpha$ (deg)
1	0.03270	0.259	80.03	73.92	2.71
2	0.01700	0.255	82.47	73.05	-5.27
3	0.01700	0.233	81.07	75.26	6.53
4	0.02316	0.260	81.93	71.19	-8.13
5	0.02588	0.251	80.93	72.20	-7.17
6	N/A	N/A	83.99	N/A	N/A
7	0.00532	0.262	84.46	76.38	-5.96
8	0.00511	0.252	84.68	74.55	-7.68
9	0.03025	0.280	80.17	73.53	-0.27
10	N/A	N/A	80.48	N/A	N/A
11	0.03620	0.264	79.17	74.31	0.23
12	0.04220	0.254	79.17	71.20	-5.97
13	0.04616	0.248	77.05	73.89	3.75
14	0.07376	0.210	76.26	70.74	23.25

Table 9: Mach Number Comparison at 13100 RPM

Number	$\phi_{R.S.}$	M_4	α_{Senoo} (deg)	$\alpha_{C,num}$ (deg)	$\Delta\alpha$ (deg)
1	0.04147	0.371	80.03	71.13	1.70
2	0.01900	0.364	82.47	72.74	-6.27
3	0.01800	0.336	81.07	75.77	7.23
4	0.02545	0.374	81.93	71.25	-8.23
5	0.02990	0.356	80.93	70.97	-8.53
6	N/A	N/A	83.99	N/A	N/A
7	0.00498	0.385	84.46	78.58	-3.16
8	0.00669	0.353	84.68	70.92	-11.74
9	0.03324	0.401	80.17	73.88	-0.37
10	N/A	N/A	80.48	N/A	N/A
11	0.03230	0.390	79.17	78.02	19.12
12	0.04720	0.364	79.17	70.85	-7.17
13	0.04694	0.361	77.05	75.55	18.25
14	0.07766	0.299	76.26	70.74	23.21

Table 10: Mach Number Comparison at 19240 RPM

Number	$\phi_{R.S.}$	M_4	α_{Senoo} (deg)	$\alpha_{C,num}$ (deg)	$\Delta\alpha$ (deg)
1	0.04350	0.417	80.03	71.23	0.17
2	0.02100	0.405	82.47	71.67	-7.67
3	0.02370	0.359	81.07	72.63	-2.27
4	0.02525	0.424	81.93	72.46	-6.13
5	0.03113	0.400	80.93	71.10	-8.43
6	N/A	N/A	83.99	N/A	N/A
7	0.00500	0.433	84.46	79.09	-2.52
8	0.00726	0.394	84.68	70.00	-12.69
9	N/A	N/A	80.17	N/A	N/A
10	N/A	N/A	80.48	N/A	N/A
11	N/A	N/A	79.17	N/A	N/A
12	0.05070	0.406	79.17	70.22	-7.87
13	0.04845	0.310	77.05	75.86	21.18
14	0.08910	0.335	76.26	67.20	9.26

Table 11: Mach Number Comparison at 21870 RPM

It is expected from [26, 27, 32 – 34] that as the inlet Mach number increases the critical flow angle will decrease leading to earlier onset of rotating stall. Overall it can be seen that there is some degree of correlation between an increase in the Mach number and a decrease in the average critical flow angle. Compressors 1, 2, 3, 8, and 14 appear to show that as the Mach number increased the critical flow angle decreased. However, the remaining compressors show either contradictory

results (see Compressors 7, 11, and 13) or no real influence (see Compressors 4 – 6, 9, 10, and 12). The point is that once again other factors seem to be playing a role that is preventing the Mach number from consistently having a direct effect on the critical flow angle. It is likely that the bounding geometry of the width and radius ratios are still exerting significant influence on the critical flow angle. This is in agreement with the results of Ludtke [26] and Senoo and Kinoshita [32].

6.2.4 Reynolds Number Comparison

Tables 12 – 14 compare the critical flow angle to changes in the inlet Reynolds number. Overall, it is difficult to see any correlation between the changes in Reynolds number and its effect on the critical flow angle. Senoo and Kinoshita found that for diffusers with width ratios at or below 0.05 the Reynolds number would not affect the critical flow angle [32]. For wider diffusers there were varying degrees of effect imposed on the critical flow angle caused by changes in the Reynolds number [32]. This effect was magnified as the width ratio increased [32]. The compressors that have width ratios at or below 0.05 are 2, 4, and 6 – 8. Compressors 13 and 14 have width ratios above 0.1 and the remaining compressor fall between 0.05 and 0.1. But looking at Tables 12 – 14 shows contradictory results at best. Furthermore, Ljevar et al. found that for Reynolds numbers between 10^4 and 10^5 the stability would decrease as the Reynolds number increased, but at Reynolds numbers of 10^5 the effect levelled off [23]. This is in conflict with the work of Senoo and Kinoshita [32]. However, Wiesner found in [42] that many parameters are affected by changes in the Reynolds number. Wiesner's work showed that the Reynolds number effects started to level off as the Reynolds number approached 10^5 and by 10^6 most Reynolds number effects had completely disappeared [42]. Thus, Senoo and Kinoshita [32], Wiesner [42], and Ljevar et al [23] it appears that Reynolds number effects are secondary when determining

vaneless diffuser stability. This is something seen in Tables 12 – 14 by the often contradictory nature of the results. These results again demonstrate that more analysis dimensions are required when determining compressor stability.

Number	$\phi_{R.S.}$	$Re_4 * 10^5$	α_{Senoo} (deg)	$\alpha_{C,num}$ (deg)	$\Delta\alpha$ (deg)
1	0.03270	2.972	80.03	73.92	2.71
2	0.01700	2.127	82.47	73.05	-5.27
3	0.01700	2.305	81.07	75.26	6.53
4	0.02316	2.258	81.93	71.19	-8.13
5	0.02588	2.729	80.93	72.20	-7.17
6	N/A	N/A	83.99	N/A	N/A
7	0.00532	0.774	84.46	76.38	-5.96
8	0.00511	0.640	84.68	74.55	-7.68
9	0.03025	4.747	80.17	73.53	-0.27
10	N/A	N/A	80.48	N/A	N/A
11	0.03620	3.459	79.17	74.31	0.23
12	0.04220	3.324	79.17	71.20	-5.97
13	0.04616	5.033	77.05	73.89	3.75
14	0.07376	4.976	76.26	70.74	23.25

Table 12: Reynolds Number Comparison at 13100 RPM

Number	$\phi_{R.S.}$	$Re_4 * 10^5$	α_{Senoo} (deg)	$\alpha_{C,num}$ (deg)	$\Delta\alpha$ (deg)
1	0.04147	3.536	80.03	71.13	1.70
2	0.01900	3.074	82.47	72.74	-6.27
3	0.01800	3.755	81.07	75.77	7.23
4	0.02545	3.037	81.93	71.25	-8.23
5	0.02990	3.608	80.93	70.97	-8.53
6	N/A	N/A	83.99	N/A	N/A
7	0.00498	1.285	84.46	78.58	-3.16
8	0.00669	0.994	84.68	70.92	-11.74
9	0.03324	3.794	80.17	73.88	-0.37
10	N/A	N/A	80.48	N/A	N/A
11	0.03230	3.406	79.17	78.02	19.12
12	0.04720	3.191	79.17	70.85	-7.17
13	0.04694	5.240	77.05	75.55	18.25
14	0.07766	4.513	76.26	70.74	23.21

Table 13: Reynolds Number Comparison at 19240 RPM

Number	$\phi_{R.S.}$	$Re_4 * 10^5$	α_{Senoo} (deg)	$\alpha_{C,num}$ (deg)	$\Delta\alpha$ (deg)
1	0.04350	2.683	80.03	71.23	0.17
2	0.02100	2.418	82.47	71.67	-7.67
3	0.02370	2.817	81.07	72.63	-2.27
4	0.02525	2.690	81.93	72.46	-6.13
5	0.03113	3.144	80.93	71.10	-8.43
6	N/A	N/A	83.99	N/A	N/A
7	0.00500	1.197	84.46	79.09	-2.52
8	0.00726	0.907	84.68	70.00	-12.69
9	N/A	N/A	80.17	N/A	N/A
10	N/A	N/A	80.48	N/A	N/A
11	N/A	N/A	79.17	N/A	N/A
12	0.05070	2.923	79.17	70.22	-7.87
13	0.04845	3.949	77.05	75.86	21.18
14	0.08910	2.633	76.26	67.20	9.26

Table 14: Reynolds Number Comparison at 21870 RPM

6.2.5 Inlet Velocity Distortion Comparison

Senoo and Kinoshita found that the inlet velocity distortion had a significant effect on vaneless diffuser stability [32]. This was confirmed by Abdelhamid in [1]. The velocity distortion can be broken into two components: meridional velocity distortion and tangential velocity distortion. For this analysis three different span-wise locations have been used to calculate the velocity distortion. The velocity distortion was calculated using the velocities at 0% and 100% span (this would be at the walls), at 5% and 95% span (slightly in from the walls), and using the minimum and maximum velocities across the span. The meridional velocity distortion and the tangential velocity distortion:

$$\Delta C_{m_{4,0,100}} = \frac{C_{m_{4,100}} - C_{m_{4,0}}}{C_{m_{4,average}}}; \quad \Delta C_{m_{4,5,95}} = \frac{C_{m_{4,95}} - C_{m_{4,5}}}{C_{m_{4,average}}}; \quad \Delta C_{m_{4,min,max}} = \frac{C_{m_{4,max}} - C_{m_{4,min}}}{C_{m_{4,average}}} \quad (6.2)$$

$$\Delta C_{t_{4,0,100}} = \frac{C_{t_{4,100}} - C_{t_{4,0}}}{C_{t_{4,average}}}; \quad \Delta C_{t_{4,5,95}} = \frac{C_{t_{4,95}} - C_{t_{4,5}}}{C_{t_{4,average}}}; \quad \Delta C_{t_{4,min,max}} = \frac{C_{t_{4,max}} - C_{t_{4,min}}}{C_{t_{4,average}}} \quad (6.3)$$

where $C_{m_{4,100}}$ is the meridional velocity at 100% span at station 4, $C_{m_{4,95}}$ is the meridional velocity at 95% span at station 4, $C_{m_{4,max}}$ is the maximum local meridional velocity at station 4, $C_{m_{4,5}}$ is the meridional velocity at 5% span at station 4, $C_{m_{4,0}}$ is the meridional velocity at 0% span at

station 4, $C_{m4,min}$ is the minimum meridional velocity at station 4, $C_{m4,average}$ is the average meridional velocity at station 4, $C_{t4,100}$ is the tangential velocity at 100% span at station 4, $C_{t4,95}$ is the tangential velocity at 95% span at station 4, $C_{t4,max}$ is the maximum local tangential velocity at station 4, $C_{t4,5}$ is the tangential velocity at 5% span at station 4, $C_{t4,0}$ is the tangential velocity at 0% span at station 4, $C_{t4,min}$ is the minimum tangential velocity at station 4, and $C_{t4,average}$ is the average tangential velocity at station 4.

6.2.5.1 Meridional Velocity Comparison

Tables 15 – 17 compare the critical flow angle to the meridional distortion⁹ measured at the walls. The prevailing wisdom is that as the distortion increases the critical flow angle will decrease.

Number	$\phi_{R.S.}$	$\Delta C_{m4,0,100}$	α_{Senoo} (deg)	$\alpha_{C,num}$ (deg)	$\Delta\alpha$ (deg)
1	0.03270	0.280	80.03	73.92	2.71
2	0.01700	0.108	82.47	73.05	-5.27
3	0.01700	0.382	81.07	75.26	6.53
4	0.02316	-0.024	81.93	71.19	-8.13
5	0.02588	0.018	80.93	72.20	-7.17
6	N/A	N/A	83.99	N/A	N/A
7	0.00532	0.005	84.46	76.38	-5.96
8	0.00511	-0.020	84.68	74.55	-7.68
9	0.03025	0.128	80.17	73.53	-0.27
10	N/A	N/A	80.48	N/A	N/A
11	0.03620	-0.138	79.17	74.31	0.23
12	0.04220	0.149	79.17	71.20	-5.97
13	0.04616	0.289	77.05	73.89	3.75
14	0.07376	-1.645	76.26	70.74	23.25

Table 15: Meridional Distortion Comparison at 0% and 100% at 13100 RPM

⁹ Please note that the sign of the distortion only points to which side had the velocity deficit. It is not really relevant in determining stability. Instead it is the magnitude of the distortion that is important.

Number	$\phi_{R.S.}$	$\Delta C_{m_{4,0,100}}$	α_{Senoo} (deg)	$\alpha_{C,num}$ (deg)	$\Delta\alpha$ (deg)
1	0.04147	0.225	80.03	71.13	1.70
2	0.01900	0.067	82.47	72.74	-6.27
3	0.01800	0.393	81.07	75.77	7.23
4	0.02545	-0.037	81.93	71.25	-8.23
5	0.02990	-0.041	80.93	70.97	-8.53
6	N/A	N/A	83.99	N/A	N/A
7	0.00498	0.007	84.46	78.58	-3.16
8	0.00669	-0.029	84.68	70.92	-11.74
9	0.03324	0.168	80.17	73.88	-0.37
10	N/A	N/A	80.48	N/A	N/A
11	0.03230	1.457	79.17	78.02	19.12
12	0.04720	0.077	79.17	70.85	-7.17
13	0.04694	1.106	77.05	75.55	18.25
14	0.07766	-1.619	76.26	70.74	23.21

Table 16: Meridional Distortion Comparison at 0% and 100% at 19240 RPM

Number	$\phi_{R.S.}$	$\Delta C_{m_{4,0,100}}$	α_{Senoo} (deg)	$\alpha_{C,num}$ (deg)	$\Delta\alpha$ (deg)
1	0.04350	0.010	80.03	71.23	0.17
2	0.02100	0.074	82.47	71.67	-7.67
3	0.02370	0.074	81.07	72.63	-2.27
4	0.02525	-0.051	81.93	72.46	-6.13
5	0.03113	-0.057	80.93	71.10	-8.43
6	N/A	N/A	83.99	N/A	N/A
7	0.00500	0.016	84.46	79.09	-2.52
8	0.00726	-0.034	84.68	70.00	-12.69
9	N/A	N/A	80.17	N/A	N/A
10	N/A	N/A	80.48	N/A	N/A
11	N/A	N/A	79.17	N/A	N/A
12	0.05070	0.044	79.17	70.22	-7.87
13	0.04845	1.306	77.05	75.86	21.18
14	0.08910	-0.922	76.26	67.20	9.26

Table 17: Meridional Distortion Comparison at 0% and 100% at 21870 RPM

Senoo and Kinoshita found a linear relationship¹⁰ between distortion and critical flow angle [32].

However, that is not what was discovered when looking at Tables 15 – 17. In fact there were many times when the critical flow angle increased even as the distortion increased. Clearly, this is an

¹⁰ As a note Senoo and Kinoshita only included distortion values that were less than or equal to 0.3 [32]. This is something to consider when looking at the results here. Especially the results for Compressor 14.

issue. However, measurements at the wall may not be trustworthy due to the chaotic nature of the flow at that location. So, what happens if one moves out from the walls to 5% and 95%?

Tables 18 – 20 show the results for the meridional distortion at 5% and 95% compared to the critical flow angle. As with the distortion results at 0% and 100% the results at 5% and 95% show no correlation between meridional distortion and the critical flow angle. This is in contradiction to the works of Abdelhamid [1], Ljevar et al. [24], and Senoo and Kinoshita [32]. See Compressor 7 for an example of these contradictory results. So, what would happen if the distortion was calculate using the minimum and maximum velocities across the span?

Number	$\phi_{R.S.}$	$\Delta C_{m_{4,5,95}}$	α_{Senoo} (deg)	$\alpha_{C,num}$ (deg)	$\Delta\alpha$ (deg)
1	0.03270	0.284	80.03	73.92	2.71
2	0.01700	0.131	82.47	73.05	-5.27
3	0.01700	0.425	81.07	75.26	6.53
4	0.02316	-0.003	81.93	71.19	-8.13
5	0.02588	0.010	80.93	72.20	-7.17
6	N/A	N/A	83.99	N/A	N/A
7	0.00532	0.009	84.46	76.38	-5.96
8	0.00511	-0.021	84.68	74.55	-7.68
9	0.03025	0.124	80.17	73.53	-0.27
10	N/A	N/A	80.48	N/A	N/A
11	0.03620	-0.126	79.17	74.31	0.23
12	0.04220	0.117	79.17	71.20	-5.97
13	0.04616	0.284	77.05	73.89	3.75
14	0.07376	-1.690	76.26	70.74	23.25

Table 18: Meridional Distortion Comparison at 5% and 95% at 13100 RPM

Number	$\phi_{R.S.}$	$\Delta C_{m_{4,5,95}}$	α_{Senoo} (deg)	$\alpha_{C,num}$ (deg)	$\Delta\alpha$ (deg)
1	0.04147	0.236	80.03	71.13	1.70
2	0.01900	0.088	82.47	72.74	-6.27
3	0.01800	0.443	81.07	75.77	7.23
4	0.02545	-0.016	81.93	71.25	-8.23
5	0.02990	-0.053	80.93	70.97	-8.53
6	N/A	N/A	83.99	N/A	N/A
7	0.00498	0.011	84.46	78.58	-3.16
8	0.00669	-0.030	84.68	70.92	-11.74
9	0.03324	0.166	80.17	73.88	-0.37
10	N/A	N/A	80.48	N/A	N/A
11	0.03230	1.582	79.17	78.02	19.12
12	0.04720	0.037	79.17	70.85	-7.17
13	0.04694	0.946	77.05	75.55	18.25
14	0.07766	-1.652	76.26	70.74	23.21

Table 19: Meridional Distortion Comparison at 5% and 95% at 19240 RPM

Number	$\phi_{R.S.}$	$\Delta C_{m_{4,5,95}}$	α_{Senoo} (deg)	$\alpha_{C,num}$ (deg)	$\Delta\alpha$ (deg)
1	0.04350	-0.004	80.03	71.23	0.17
2	0.02100	0.098	82.47	71.67	-7.67
3	0.02370	0.089	81.07	72.63	-2.27
4	0.02525	-0.036	81.93	72.46	-6.13
5	0.03113	-0.070	80.93	71.10	-8.43
6	N/A	N/A	83.99	N/A	N/A
7	0.00500	0.022	84.46	79.09	-2.52
8	0.00726	-0.036	84.68	70.00	-12.69
9	N/A	N/A	80.17	N/A	N/A
10	N/A	N/A	80.48	N/A	N/A
11	N/A	N/A	79.17	N/A	N/A
12	0.05070	0.000	79.17	70.22	-7.87
13	0.04845	1.398	77.05	75.86	21.18
14	0.08910	-0.829	76.26	67.20	9.26

Table 20: Meridional Distortion Comparison at 5% and 95% at 21870 RPM

Tables 21 – 23 contain the results for what is called the “new” meridional distortion calculation as detailed in equation 6.2. The first thing of note is that the distortion values rendered by this method are much higher than those calculated using Senoo’s method. However, as with the other results there is no correlation between meridional distortion and critical flow angle. See Compressor 3 for an example of this lack of correlation.

Number	$\phi_{R.S.}$	$\Delta C_{m4, \min, \max}$	α_{Senoo} (deg)	$\alpha_{C, \text{num}}$ (deg)	$\Delta\alpha$ (deg)
1	0.03270	0.811	80.03	73.92	2.71
2	0.01700	0.557	82.47	73.05	-5.27
3	0.01700	1.078	81.07	75.26	6.53
4	0.02316	0.431	81.93	71.19	-8.13
5	0.02588	0.360	80.93	72.20	-7.17
6	N/A	N/A	83.99	N/A	N/A
7	0.00532	0.527	84.46	76.38	-5.96
8	0.00511	0.545	84.68	74.55	-7.68
9	0.03025	0.661	80.17	73.53	-0.27
10	N/A	N/A	80.48	N/A	N/A
11	0.03620	0.625	79.17	74.31	0.23
12	0.04220	0.442	79.17	71.20	-5.97
13	0.04616	0.679	77.05	73.89	3.75
14	0.07376	1.835	76.26	70.74	23.25

Table 21: New Meridional Distortion Comparison at 13100 RPM

Number	$\phi_{R.S.}$	$\Delta C_{m4, \min, \max}$	α_{Senoo} (deg)	$\alpha_{C, \text{num}}$ (deg)	$\Delta\alpha$ (deg)
1	0.04147	0.839	80.03	71.13	1.70
2	0.01900	0.496	82.47	72.74	-6.27
3	0.01800	1.113	81.07	75.77	7.23
4	0.02545	0.414	81.93	71.25	-8.23
5	0.02990	0.313	80.93	70.97	-8.53
6	N/A	N/A	83.99	N/A	N/A
7	0.00498	0.614	84.46	78.58	-3.16
8	0.00669	0.455	84.68	70.92	-11.74
9	0.03324	0.665	80.17	73.88	-0.37
10	N/A	N/A	80.48	N/A	N/A
11	0.03230	1.859	79.17	78.02	19.12
12	0.04720	0.360	79.17	70.85	-7.17
13	0.04694	1.487	77.05	75.55	18.25
14	0.07766	1.798	76.26	70.74	23.21

Table 22: New Meridional Distortion Comparison at 19240 RPM

Number	$\phi_{R.S.}$	$\Delta C_{m_{4,min,max}}$	α_{Senoo} (deg)	$\alpha_{C,num}$ (deg)	$\Delta\alpha$ (deg)
1	0.04350	0.750	80.03	71.23	0.17
2	0.02100	0.462	82.47	71.67	-7.67
3	0.02370	0.654	81.07	72.63	-2.27
4	0.02525	0.473	81.93	72.46	-6.13
5	0.03113	0.332	80.93	71.10	-8.43
6	N/A	N/A	83.99	N/A	N/A
7	0.00500	0.640	84.46	79.09	-2.52
8	0.00726	0.443	84.68	70.00	-12.69
9	N/A	N/A	80.17	N/A	N/A
10	N/A	N/A	80.48	N/A	N/A
11	N/A	N/A	79.17	N/A	N/A
12	0.05070	0.311	79.17	70.22	-7.87
13	0.04845	1.731	77.05	75.86	21.18
14	0.08910	1.153	76.26	67.20	9.26

Table 23: New Meridional Distortion Comparison at 21870 RPM

So, overall using three different calculations of meridional distortion it was not possible to correlate meridional distortion to the critical flow angle. Yet, it has been asserted that the distortion does effect the critical flow angle [27, 32]. Furthermore, in light of the coupling that exists between impeller and diffuser [1, 5] as well as the fact that there are rotating wakes in the flow field [9] which can effect vaneless diffuser stability [24] it would make sense that any distortion of the flow would cause issues with the stability of the vaneless diffuser, especially when related to the modal wave version of rotating stall onset [44]. Thus, something else must be going on that is having a more dominant effect on the stability of the vaneless diffuser.

6.2.5.2 Tangential Velocity Distortion

Lastly, there is tangential velocity distortion to consider. As with meridional velocity distortion the tangential velocity distortion has been calculated at three separate span-wise locations. Tables 24 – 26 show how the tangential velocity at 0% and 100% correlate to the critical flow angle. As with the meridional velocity distortion results at these locations there was no correlation between the tangential velocity distortion and the critical flow angle.

Number	$\phi_{R.S.}$	$\Delta C_{t_{4,0,100}}$	α_{Senoo} (deg)	$\alpha_{C,num}$ (deg)	$\Delta\alpha$ (deg)
1	0.03270	0.091	80.03	73.92	2.71
2	0.01700	0.040	82.47	73.05	-5.27
3	0.01700	0.061	81.07	75.26	6.53
4	0.02316	-0.034	81.93	71.19	-8.13
5	0.02588	-0.018	80.93	72.20	-7.17
6	N/A	N/A	83.99	N/A	N/A
7	0.00532	0.003	84.46	76.38	-5.96
8	0.00511	-0.004	84.68	74.55	-7.68
9	0.03025	-0.028	80.17	73.53	-0.27
10	N/A	N/A	80.48	N/A	N/A
11	0.03620	0.048	79.17	74.31	0.23
12	0.04220	0.030	79.17	71.20	-5.97
13	0.04616	0.069	77.05	73.89	3.75
14	0.07376	-0.601	76.26	70.74	23.25

Table 24: Tangential Distortion Comparison at 0% and 100% at 13100 RPM

Number	$\phi_{R.S.}$	$\Delta C_{t_{4,0,100}}$	α_{Senoo} (deg)	$\alpha_{C,num}$ (deg)	$\Delta\alpha$ (deg)
1	0.04147	0.074	80.03	71.13	1.70
2	0.01900	0.024	82.47	72.74	-6.27
3	0.01800	0.054	81.07	75.77	7.23
4	0.02545	-0.034	81.93	71.25	-8.23
5	0.02990	-0.029	80.93	70.97	-8.53
6	N/A	N/A	83.99	N/A	N/A
7	0.00498	0.005	84.46	78.58	-3.16
8	0.00669	-0.005	84.68	70.92	-11.74
9	0.03324	0.012	80.17	73.88	-0.37
10	N/A	N/A	80.48	N/A	N/A
11	0.03230	0.242	79.17	78.02	19.12
12	0.04720	0.020	79.17	70.85	-7.17
13	0.04694	0.281	77.05	75.55	18.25
14	0.07766	-0.613	76.26	70.74	23.21

Table 25: Tangential Distortion Comparison at 0% and 100% at 19240 RPM

Number	$\phi_{R.S.}$	$\Delta C_{t_{4,0,100}}$	α_{Senoo} (deg)	$\alpha_{C,num}$ (deg)	$\Delta\alpha$ (deg)
1	0.04350	0.051	80.03	71.23	0.17
2	0.02100	0.016	82.47	71.67	-7.67
3	0.02370	0.024	81.07	72.63	-2.27
4	0.02525	-0.043	81.93	72.46	-6.13
5	0.03113	-0.035	80.93	71.10	-8.43
6	N/A	N/A	83.99	N/A	N/A
7	0.00500	0.008	84.46	79.09	-2.52
8	0.00726	-0.007	84.68	70.00	-12.69
9	N/A	N/A	80.17	N/A	N/A
10	N/A	N/A	80.48	N/A	N/A
11	N/A	N/A	79.17	N/A	N/A
12	0.05070	0.013	79.17	70.22	-7.87
13	0.04845	0.263	77.05	75.86	21.18
14	0.08910	-0.507	76.26	67.20	9.26

Table 26: Tangential Distortion Comparison at 0% and 100% at 21870 RPM

Tables 27 – 29 show how the critical flow angle correlates to the tangential velocity distortion at 5% and 95% span. However, no correlation could be found between the tangential velocity distortion and the critical flow angle for these span-wise locations either. So, what would happen if the “new” tangential velocity distortion method was used?

Number	$\phi_{R.S.}$	$\Delta C_{t_{4,5,95}}$	α_{Senoo} (deg)	$\alpha_{C,num}$ (deg)	$\Delta\alpha$ (deg)
1	0.03270	0.099	80.03	73.92	2.71
2	0.01700	0.046	82.47	73.05	-5.27
3	0.01700	0.077	81.07	75.26	6.53
4	0.02316	-0.029	81.93	71.19	-8.13
5	0.02588	-0.023	80.93	72.20	-7.17
6	N/A	N/A	83.99	N/A	N/A
7	0.00532	0.006	84.46	76.38	-5.96
8	0.00511	-0.005	84.68	74.55	-7.68
9	0.03025	-0.036	80.17	73.53	-0.27
10	N/A	N/A	80.48	N/A	N/A
11	0.03620	0.056	79.17	74.31	0.23
12	0.04220	0.015	79.17	71.20	-5.97
13	0.04616	0.055	77.05	73.89	3.75
14	0.07376	-0.623	76.26	70.74	23.25

Table 27: Tangential Distortion Comparison at 5% and 95% at 13100 RPM

Number	$\phi_{R,S}$	$\Delta Ct_{4,5,95}$	α_{Senoo} (deg)	$\alpha_{C,num}$ (deg)	$\Delta\alpha$ (deg)
1	0.04147	0.078	80.03	71.13	1.70
2	0.01900	0.029	82.47	72.74	-6.27
3	0.01800	0.074	81.07	75.77	7.23
4	0.02545	-0.030	81.93	71.25	-8.23
5	0.02990	-0.035	80.93	70.97	-8.53
6	N/A	N/A	83.99	N/A	N/A
7	0.00498	0.007	84.46	78.58	-3.16
8	0.00669	-0.005	84.68	70.92	-11.74
9	0.03324	0.005	80.17	73.88	-0.37
10	N/A	N/A	80.48	N/A	N/A
11	0.03230	0.272	79.17	78.02	19.12
12	0.04720	0.007	79.17	70.85	-7.17
13	0.04694	0.249	77.05	75.55	18.25
14	0.07766	-0.632	76.26	70.74	23.21

Table 28: Tangential Distortion Comparison at 5% and 95% at 19240 RPM

Number	$\phi_{R,S}$	$\Delta Ct_{4,5,95}$	α_{Senoo} (deg)	$\alpha_{C,num}$ (deg)	$\Delta\alpha$ (deg)
1	0.04350	0.050	80.03	71.23	0.17
2	0.02100	0.022	82.47	71.67	-7.67
3	0.02370	0.027	81.07	72.63	-2.27
4	0.02525	-0.040	81.93	72.46	-6.13
5	0.03113	-0.041	80.93	71.10	-8.43
6	N/A	N/A	83.99	N/A	N/A
7	0.00500	0.010	84.46	79.09	-2.52
8	0.00726	-0.007	84.68	70.00	-12.69
9	N/A	N/A	80.17	N/A	N/A
10	N/A	N/A	80.48	N/A	N/A
11	N/A	N/A	79.17	N/A	N/A
12	0.05070	0.001	79.17	70.22	-7.87
13	0.04845	0.269	77.05	75.86	21.18
14	0.08910	-0.489	76.26	67.20	9.26

Table 29: Tangential Distortion Comparison at 5% and 95% at 21870 RPM

Tables 30 – 32 show how the tangential velocity distortion calculated from the maximum and minimum velocities across the span correlates to the critical flow angle. However, no real correlation was found. Again the results contradict the work of Senoo and Kinoshita [32].

Number	$\phi_{R.S.}$	$\Delta Ct_{4,min,max}$	α_{Senoo} (deg)	$\alpha_{C,num}$ (deg)	$\Delta\alpha$ (deg)
1	0.03270	0.318	80.03	73.92	2.71
2	0.01700	0.312	82.47	73.05	-5.27
3	0.01700	0.350	81.07	75.26	6.53
4	0.02316	0.298	81.93	71.19	-8.13
5	0.02588	0.255	80.93	72.20	-7.17
6	N/A	N/A	83.99	N/A	N/A
7	0.00532	0.346	84.46	76.38	-5.96
8	0.00511	0.363	84.68	74.55	-7.68
9	0.03025	0.272	80.17	73.53	-0.27
10	N/A	N/A	80.48	N/A	N/A
11	0.03620	0.242	79.17	74.31	0.23
12	0.04220	0.235	79.17	71.20	-5.97
13	0.04616	0.230	77.05	73.89	3.75
14	0.07376	0.711	76.26	70.74	23.25

Table 30: New Tangential Distortion Comparison at 13100 RPM

Number	$\phi_{R.S.}$	$\Delta Ct_{4,min,max}$	α_{Senoo} (deg)	$\alpha_{C,num}$ (deg)	$\Delta\alpha$ (deg)
1	0.04147	0.330	80.03	71.13	1.70
2	0.01900	0.297	82.47	72.74	-6.27
3	0.01800	0.335	81.07	75.77	7.23
4	0.02545	0.288	81.93	71.25	-8.23
5	0.02990	0.241	80.93	70.97	-8.53
6	N/A	N/A	83.99	N/A	N/A
7	0.00498	0.340	84.46	78.58	-3.16
8	0.00669	0.337	84.68	70.92	-11.74
9	0.03324	0.279	80.17	73.88	-0.37
10	N/A	N/A	80.48	N/A	N/A
11	0.03230	0.437	79.17	78.02	19.12
12	0.04720	0.219	79.17	70.85	-7.17
13	0.04694	0.433	77.05	75.55	18.25
14	0.07766	0.720	76.26	70.74	23.21

Table 31: New Tangential Distortion Comparison at 19240 RPM

Number	$\phi_{R.S.}$	$\Delta Ct_{4,min,max}$	α_{Senoo} (deg)	$\alpha_{C,num}$ (deg)	$\Delta\alpha$ (deg)
1	0.04350	0.325	80.03	71.23	0.17
2	0.02100	0.298	82.47	71.67	-7.67
3	0.02370	0.329	81.07	72.63	-2.27
4	0.02525	0.306	81.93	72.46	-6.13
5	0.03113	0.248	80.93	71.10	-8.43
6	N/A	N/A	83.99	N/A	N/A
7	0.00500	0.339	84.46	79.09	-2.52
8	0.00726	0.334	84.68	70.00	-12.69
9	N/A	N/A	80.17	N/A	N/A
10	N/A	N/A	80.48	N/A	N/A
11	N/A	N/A	79.17	N/A	N/A
12	0.05070	0.209	79.17	70.22	-7.87
13	0.04845	0.420	77.05	75.86	21.18
14	0.08910	0.630	76.26	67.20	9.26

Table 32: New Tangential Distortion Comparison at 21870 RPM

Overall the tangential velocity distortion did not correlate with the average critical flow angle. This is in agreement with the results found for the meridional velocity distortion. However, this goes directly against what was expected from [27, 32]. These results appear to contradict the notion that the flow coming off of the impeller affects the stability of the vaneless diffuser as was found in [1]. But what could be going on that would cause this to happen?

6.2.5.3 Failure of Senoo's Distortion Correlation

What stands out most from the above meridional and tangential velocity distortion correlations is that they do not work. Senoo and Kinoshita found that there was a linear relationship between meridional velocity distortion and critical flow angle [32]. Senoo and Kinoshita also found that the relationship between tangential velocity distortion and critical flow angle was second to third order and less dominant than effects caused by the meridional velocity distortion [32]. However, the results found in Section 6.2.5 show otherwise. In fact no real correlation could be made. This suggests that what correlation there is between distortion and critical flow angle is either much more complicated than a simple linear model, is influenced by other factors, or there is no correlation. Senoo and Kinoshita found that the width and radius ratios

had a profound effect on the size of the effect the distortion had on the critical flow angle, but not on the distortion trend (i.e. the size may have changed, but the meridional distortion still had a linear effect on the critical flow angle) [32]. Thus, the results found in section 6.2.5 serve to contradict what has been a widely held belief in the compressor community, that velocity distortion directly effects the critical flow angle.

6.2.6 Overall Trends Developed From Comparisons

First, the width ratio appears to be the dominant factor in determining vaneless diffuser stability. Logically, this makes sense because the more space there is the more havoc fluctuations in the flow can wreak. Second, the radius ratio, Mach number, and Reynolds number have only secondary or tertiary effects on the compressor stability. This would make sense since the Mach number and Reynolds number plots in [32] were always compared at specific width and radius ratios. Third, the distortion whether meridional or tangential did not correlate with the average critical flow angle. This is in direct contrast to [27 & 32] and goes against [1, 9, 24, & 44]. It could be that the simulations were not detailed enough to properly resolve all of the values and thus the distortion correlation would work better using a transient simulation. However, it is more likely that the effect of the velocity distortion is bounded by the geometry of the compressor. And since rotating stall is a dynamic system phenomenon [15] it would make sense that the geometry would be the dominant factor.

There are a couple of point to add. First, does the number of impeller blades effect compressor stability? Ljevar et al. found that the number of compressor blades does have an effect on stability [24]. Also, it should be noted that in Table 2 the only two geometries (compressors 6 and 10) that do not experience rotating stall at all are the ones with the largest number of impeller blades (19). This is in agreement with Marechale who confirmed that Compressor 2 was tested

with an impeller with 17 blades as opposed to the normal 13 blades which led to a stabilizing of the flow [27]. Second, Compressors 9 and 11 do not experience rotating stall at 21870 RPM. It is possible that due to the shrinking of the compressor operating envelope as rotating speed increases [10] that the point of rotating stall onset now occurs outside of the operating envelope at a mass flow rate that is only reached after the onset of system surge. These are just a couple of points to keep in mind overall.

6.3 Local Flow Angle Results

Contained below are the local results for all fourteen geometries. Each section contains the results for all three speed lines. For each speed line there are three plots. The plots show the normalized meridional and tangential velocity profiles at the stall point as well as a comparison between all of the critical angles and the local flow angle profile at the stall point. All values were taken at station 4, the diffuser inlet. For each plot the experimental data at that point has been provided as well. In some cases the experimental data is listed as being at a quasi-stall point. The experimental data was linearly interpolated from the provided experimental data. In cases where rotating stall occurred at the last stable flow point (i.e. the point before surge onsets) the data cannot be linearly interpolated. Thus, the data from the point directly before the stall point is provided. Also, compressors 6 and 10 do not exhibit rotating stall and compressors 9 and 11 do not exhibit rotating stall at 21870 RPM. These plots have still been provided, but at the last stable flow point. According to Marechale until the flow becomes unstable the simulation should accurately predict the flow profiles therefore using this point one can expect that they are at the critical point for the flow [27]. The reason these points were not included in Section 6.2 is because that discussion was based solely on whether or not rotating stall occurred and how its occurrence correlated to the five critical parameters discussed in [32]. However, here the results for

Compressors 6, 9, 10, and 11 still provide vital information about the nature of vaneless diffuser stability and the factors influencing it.

Please note that in each flow plot provided the flow coefficient that the point was modelled at is listed. If interested one can go to Appendix A to find the pressure rise profiles and find the location of the stall onset point, or last stable flow point. Also, if interested in the temperature rise profile one can visit Appendix B. Both Appendix A and Appendix B contain plots for all fourteen compressor geometries at all three speed lines.

6.3.1 Compressor 1 Profiles

6.3.1.1 Compressor 1 13100 RPM Results

Figures 21 – 23 show the results for Compressor 1 at the 13100 RPM stall point. In Figure 21 the numerical and experimental profiles agree for the meridional velocity in the span regions from 0 – 20% and 80 – 100%, so in the wall regions. However, in the main flow region the profiles differ. Figure 22 shows that the experimental and numerical tangential velocity profiles are in rough agreement. Figure 23 compares the angular profiles against the average critical flow angles. Figure 23 shows that both the experimental and numerical profiles cross the Senoo line at the stall onset point. However, the average critical flow angles are several degrees from the Senoo line thus showing that a one dimensional approach is insufficient to determine compressor stability (see section 3.1 and chapter 4 for more details), but the local approach combined with the Senoo – Kobayashi equation is a better measure of stability.

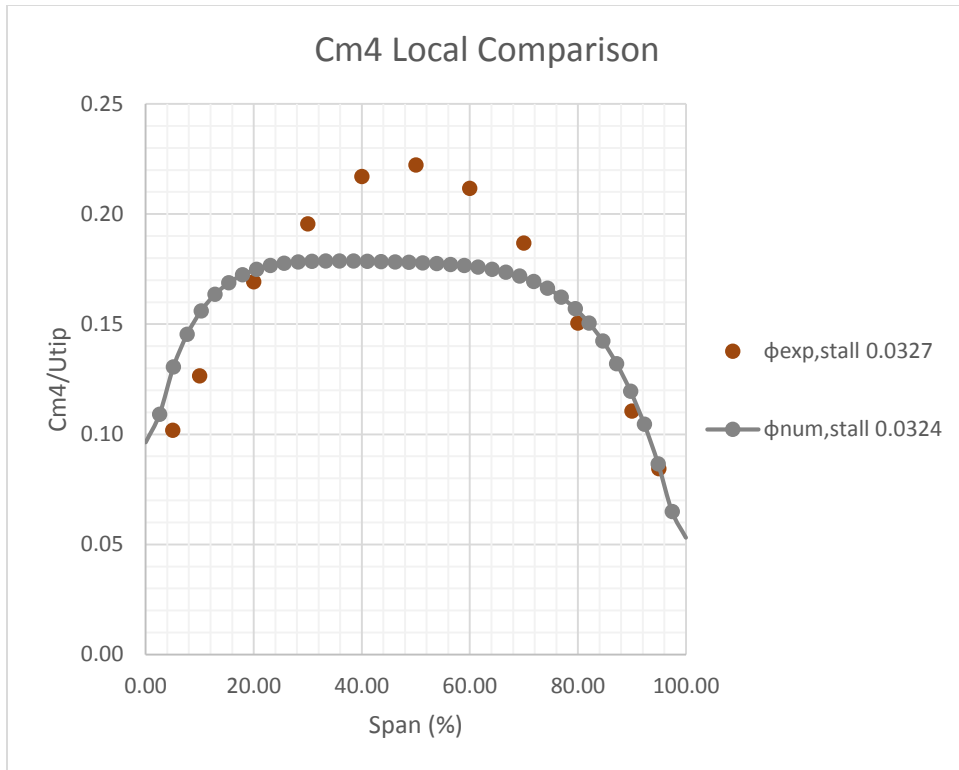


Figure 21: C_{m4} Comparison for Compressor 1 at 13100 RPM Stall Point

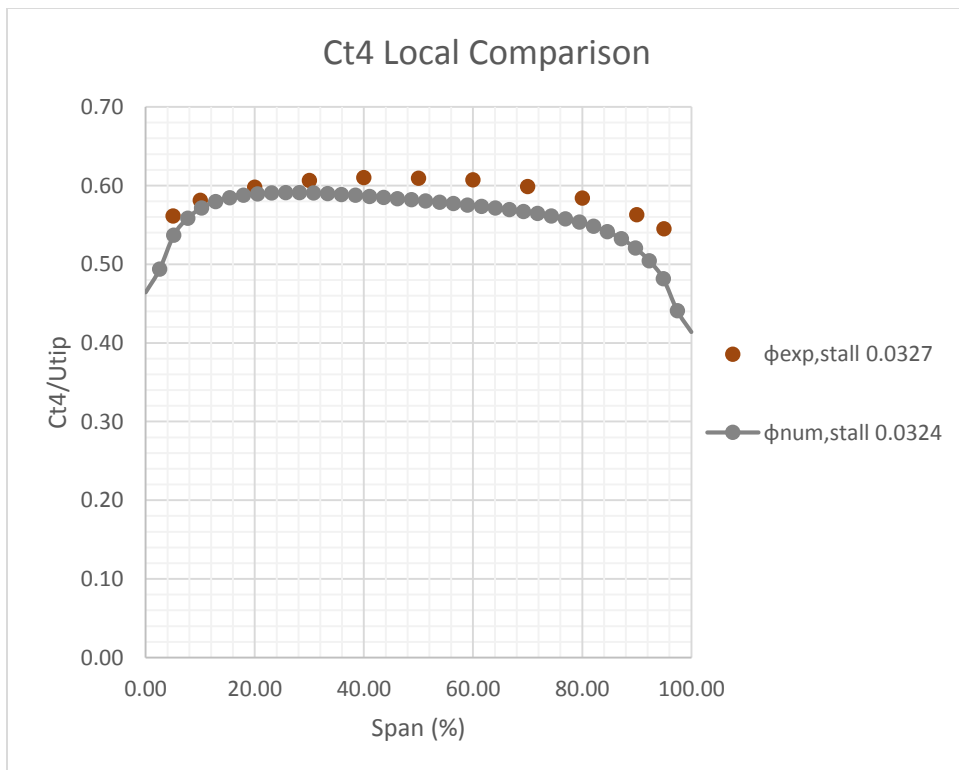


Figure 22: C_{t4} Comparison for Compressor 1 at 13100 RPM Stall Point

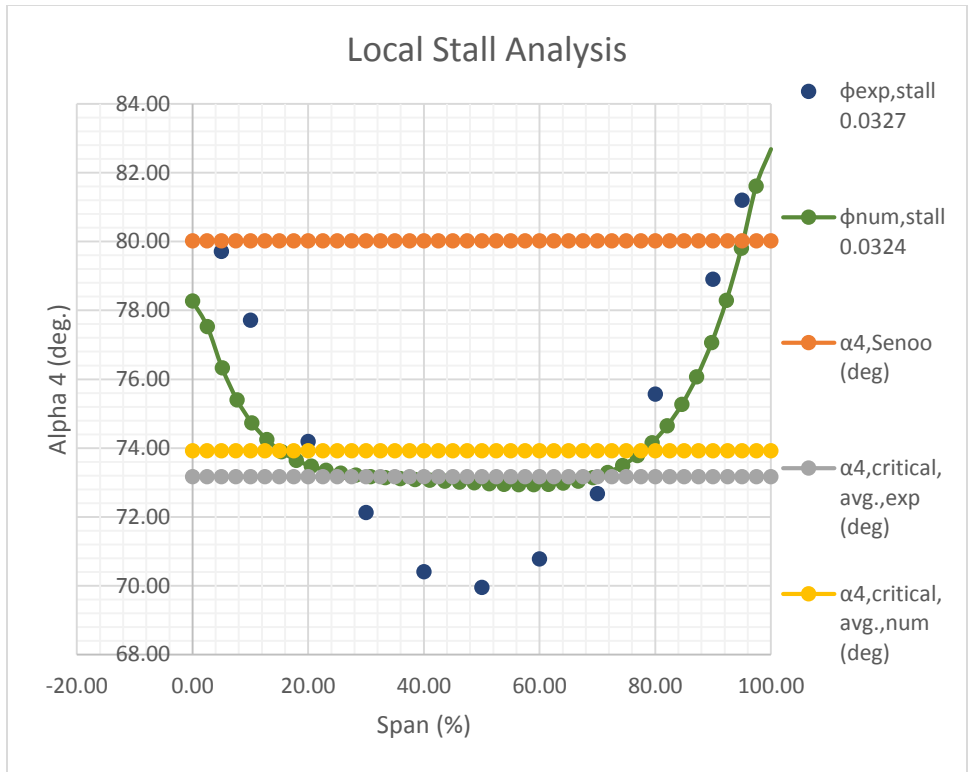


Figure 23: Stall Analysis for Compressor 1 at 13100 RPM Stall Point

6.3.1.2 Compressor 1 19240 RPM Results

Figures 24 – 26 show the results for Compressor 1 at the 19240 RPM stall point. Figure 24, shows that there is some agreement near the walls for the meridional velocity profiles. But that agreement does not extend beyond the near wall regions (span values that are roughly 0 – 10% and 90 – 100%). Also, there is poor agreement in the center of the flow profile in Figure 24. In Figure 25 the tangential velocity profiles agree well. A look at Figure 26 shows that the local experimental and numerical profiles cross the Senoo line, and the average critical flow angles are several degrees from reaching the Senoo line.

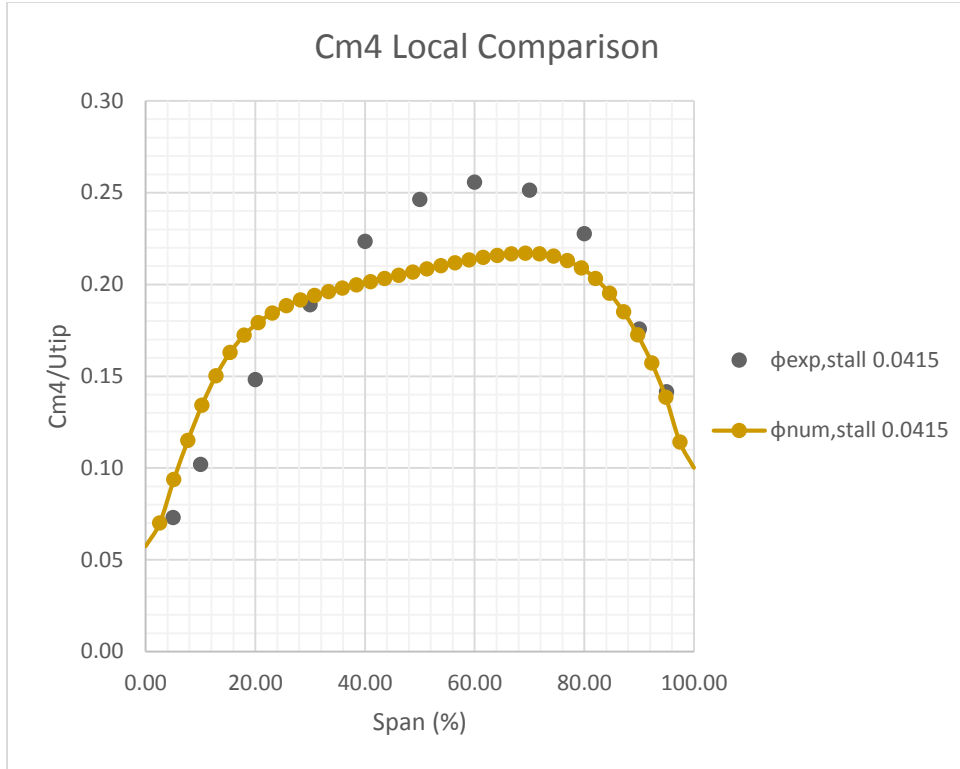


Figure 24: C_{m4} Comparison for Compressor 1 at 19240 RPM Stall Point

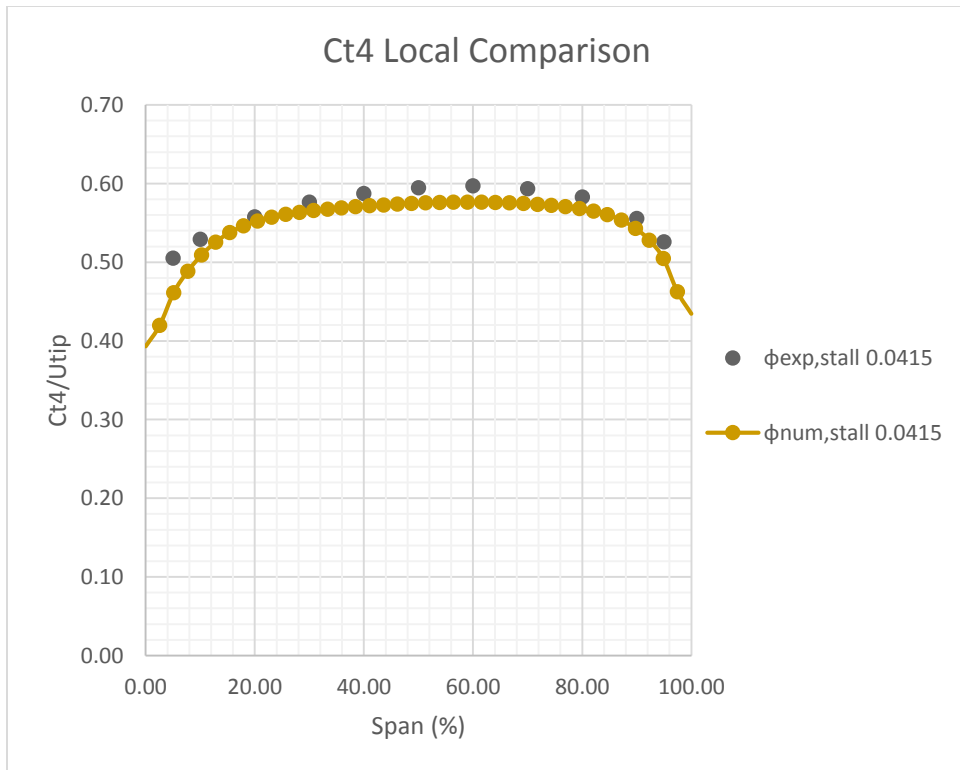


Figure 25: C_{t4} Comparison for Compressor 1 at 19240 RPM Stall Point

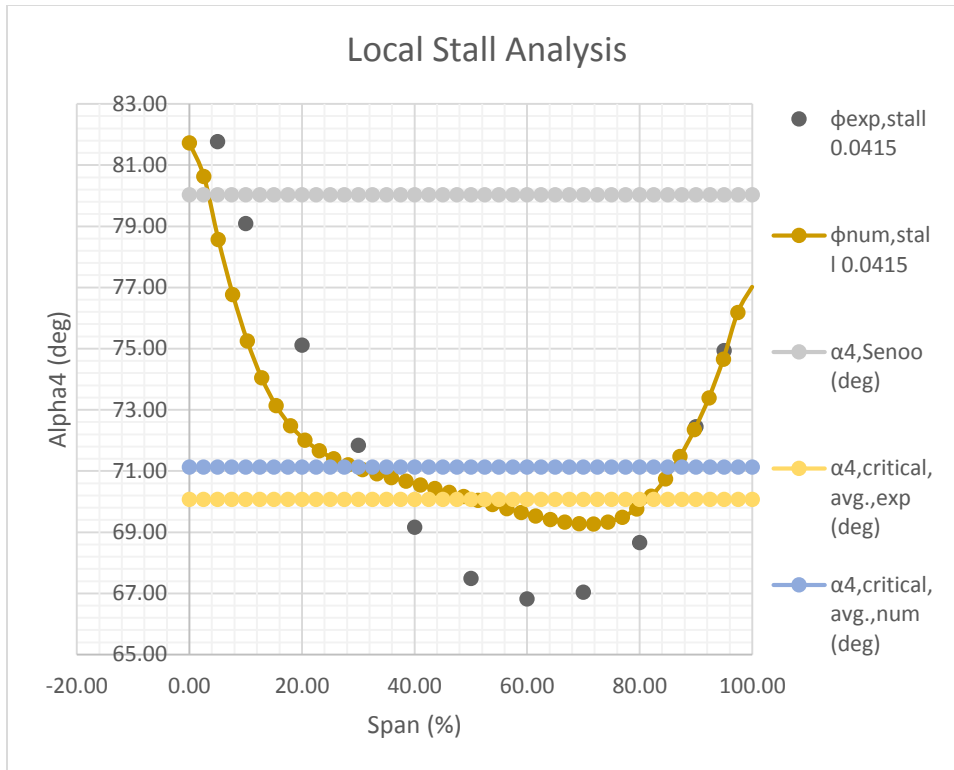


Figure 26: Stall Analysis for Compressor 1 at 19240 RPM Stall Point

6.3.1.3 Compressor 1 21870 RPM Results

Figures 27 – 29 show the results for Compressor 1 at the 21870 RPM stall point. Figure 27 shows that there is a certain agreement between the experimental and numerical meridional velocities, however that agreement is only qualitative. However, both experimental and numerical profiles predict that the flow is distorted toward the shroud side of the vaneless diffuser (the region between 50 – 100% span) based on the higher velocity bump at 60% span. In Figure 28 there is agreement between the numerical and experimental tangential velocity profiles. Figure 29 shows that both local angle profiles breach the Senoo line (see Table 5 above for confirmation of the numerical profile’s breach of the Senoo line). And while there is a difference in the shape of the angle profiles, due to differences in the velocity profiles shapes, the main observation is that the local profile and experimental profile breach the Senoo line.

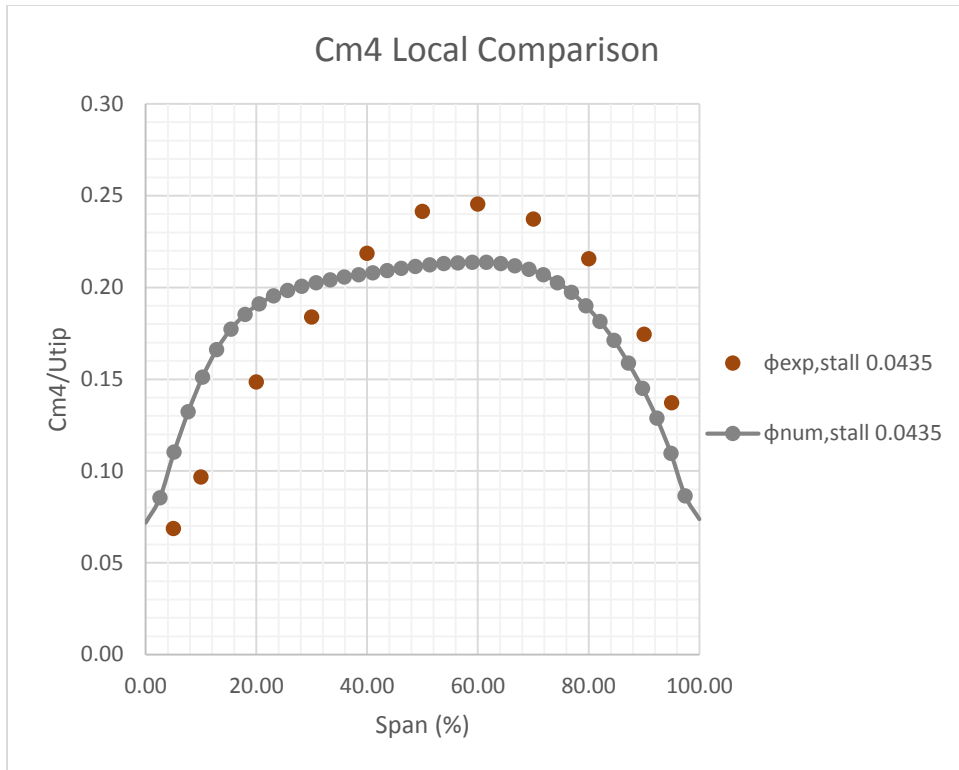


Figure 27: C_{m4} Comparison for Compressor 1 at 21870 RPM Stall Point

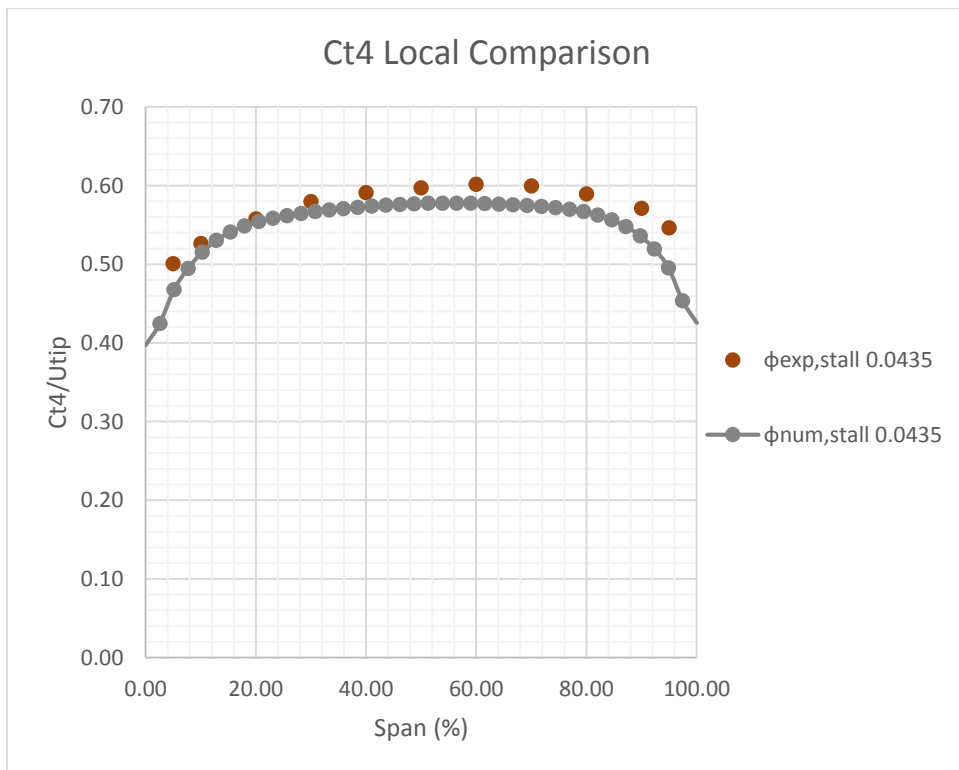


Figure 28: C_{t4} Comparison for Compressor 1 at 21870 RPM Stall Point

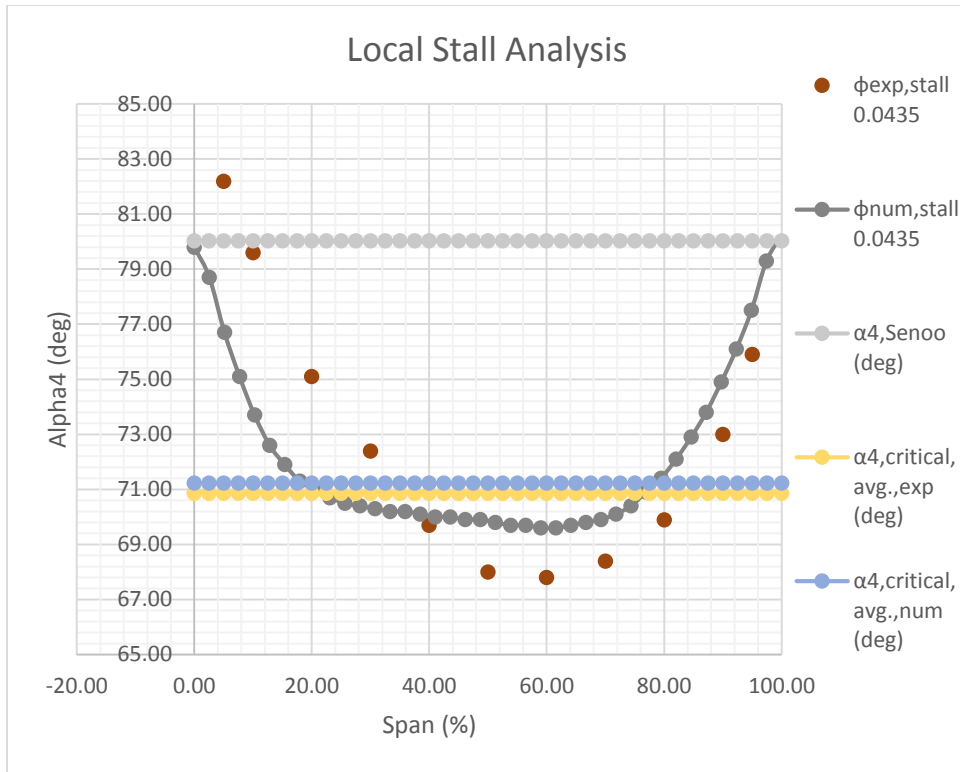


Figure 29: Stall Analysis for Compressor 1 at 21870 RPM Stall Point

6.3.2 Compressor 2 Profiles

6.3.2.1 Compressor 2 13100 RPM Results

Figures 30 – 32 show the results for Compressor 2 at the 13100 RPM stall point. Figure 30 shows how the meridional velocity profiles compare. In Figure 30 there is solid agreement between the experimental and numerical velocity profiles from 0% – 70% span. However, from there the experimental profile experiences a sharp decline and the numerical profile gradually decreases. This is likely due to the averaging procedure used in the steady state simulation to generate the numerical profile. Figure 31 shows that there is a strong agreement between the numerical and experimental tangential velocity profiles. Figure 32 shows that neither of the local flow profiles nor the average critical flow angles reach the Senoo line. The difference between the numerical maximum and the Senoo line is ~5 degrees. This is a large difference and serves to show that the Senoo line is not an omnipotent measure of vaneless diffuser stability.

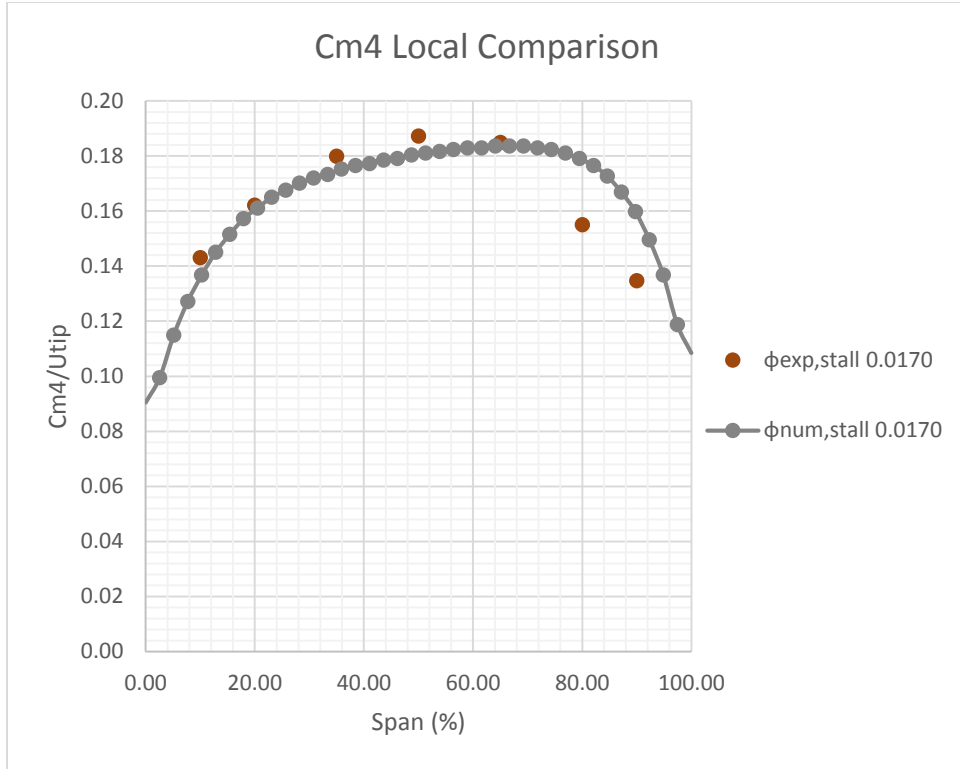


Figure 30: C_{m4} Comparison for Compressor 2 at 13100 RPM Stall Point

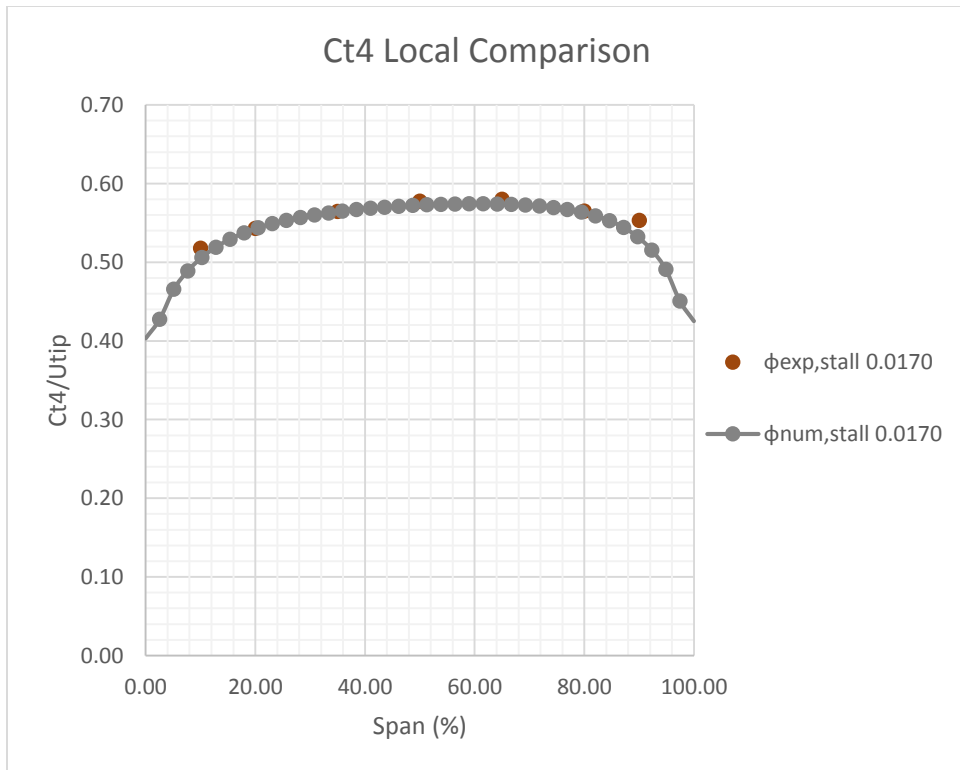


Figure 31: C_{t4} Comparison for Compressor 2 at 13100 RPM Stall Point

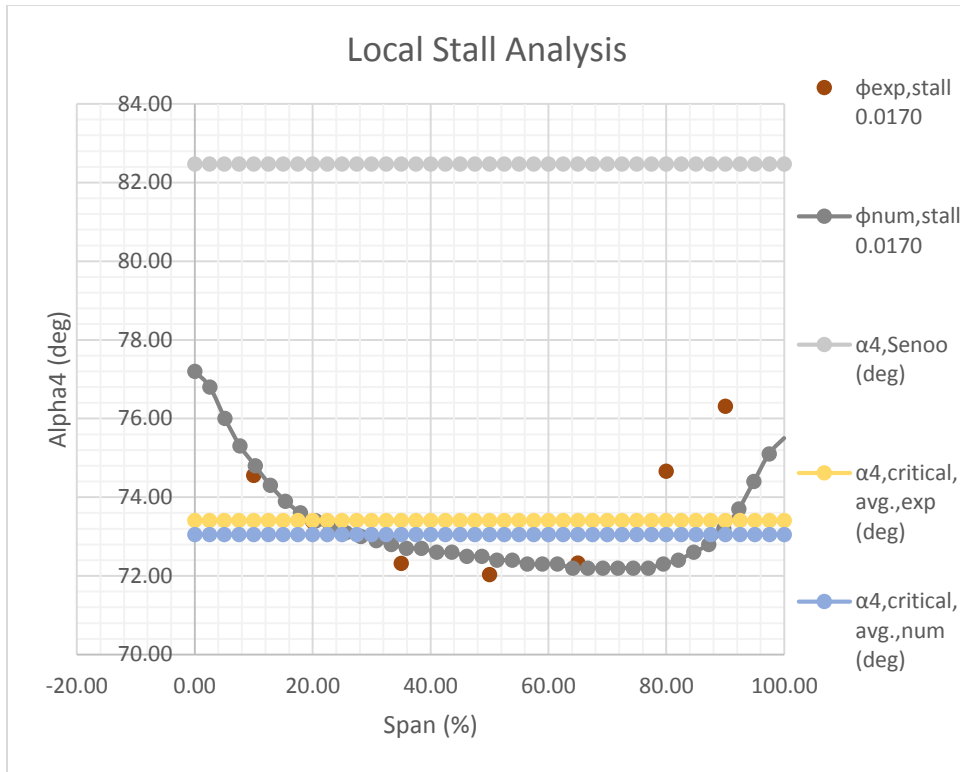


Figure 32: Stall Analysis for Compressor 2 at 13100 RPM Stall Point

6.3.2.2 Compressor 2 19240 RPM Results

Figures 33 – 35 show the results for Compressor 2 at the 19240 RPM stall point. As with the 13100 RPM results the numerical and experimental meridional velocity profiles agree for ~70% of the span. However, something is happening that the numerical method cannot pick up. Figure 34 shows strong agreement between the experimental and numerical data for the tangential velocity profiles. Figure 35 shows the same large gap between the Senoo line and the maxima of the experimental and numerical profiles (the gap is ~ 6 degrees). This result begins to suggest that there is something at play that is suppressing the local profile and causing the onset of rotating stall, but at much lower flow angles than expected.

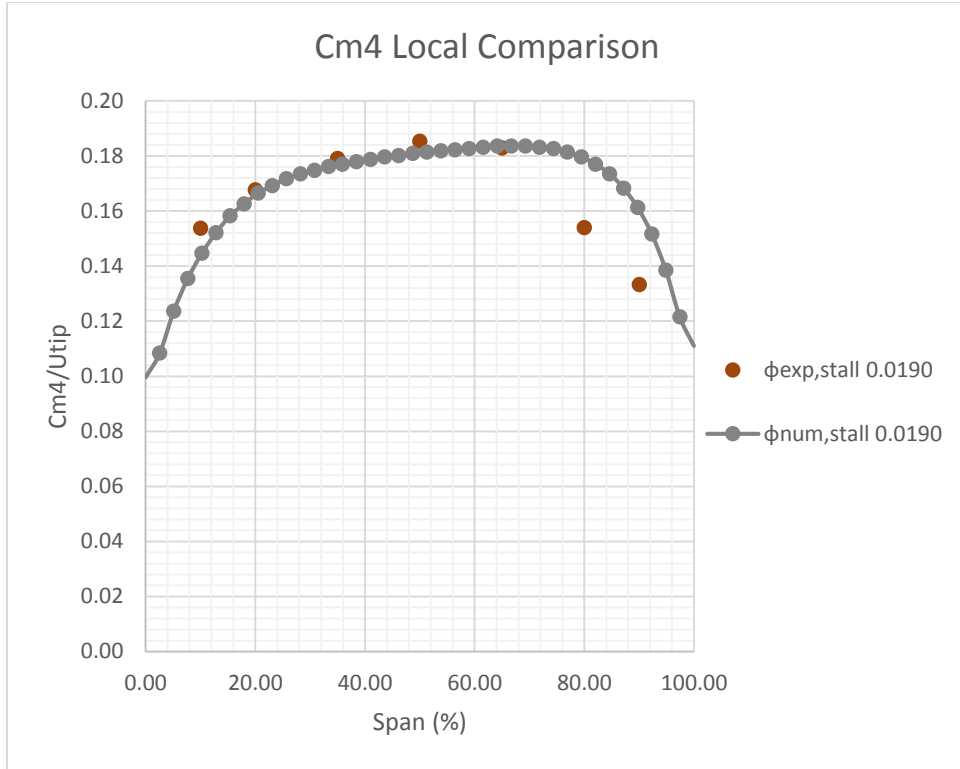


Figure 33: C_{m4} Comparison for Compressor 2 at 19240 RPM Stall Point

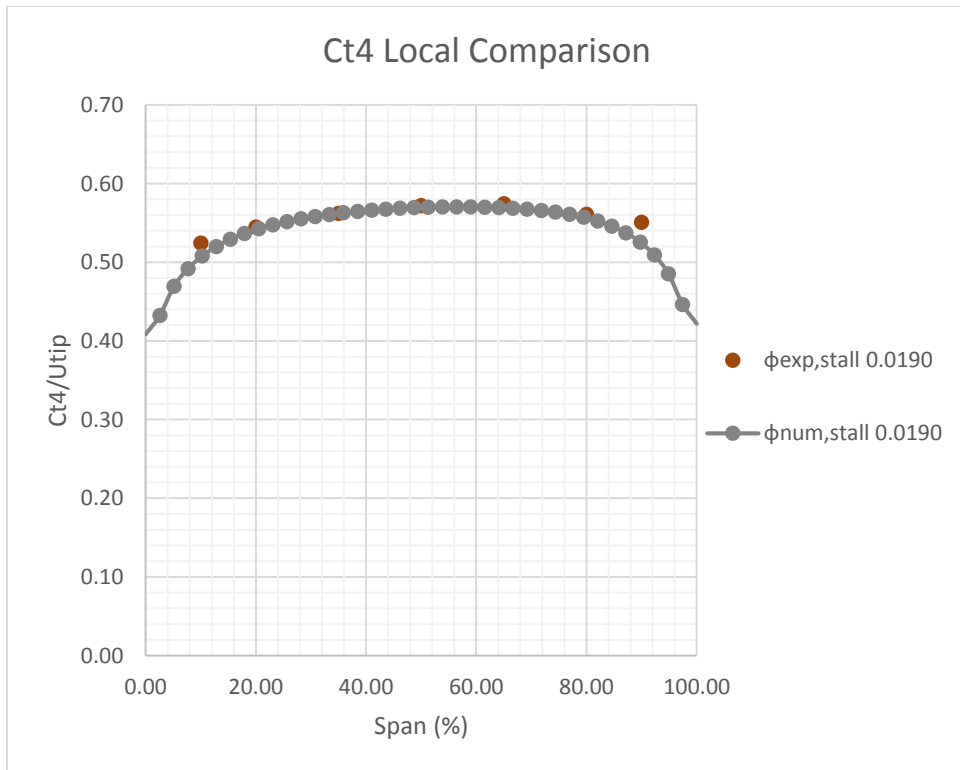


Figure 34: C_{t4} Comparison for Compressor 2 at 19240 RPM Stall Point

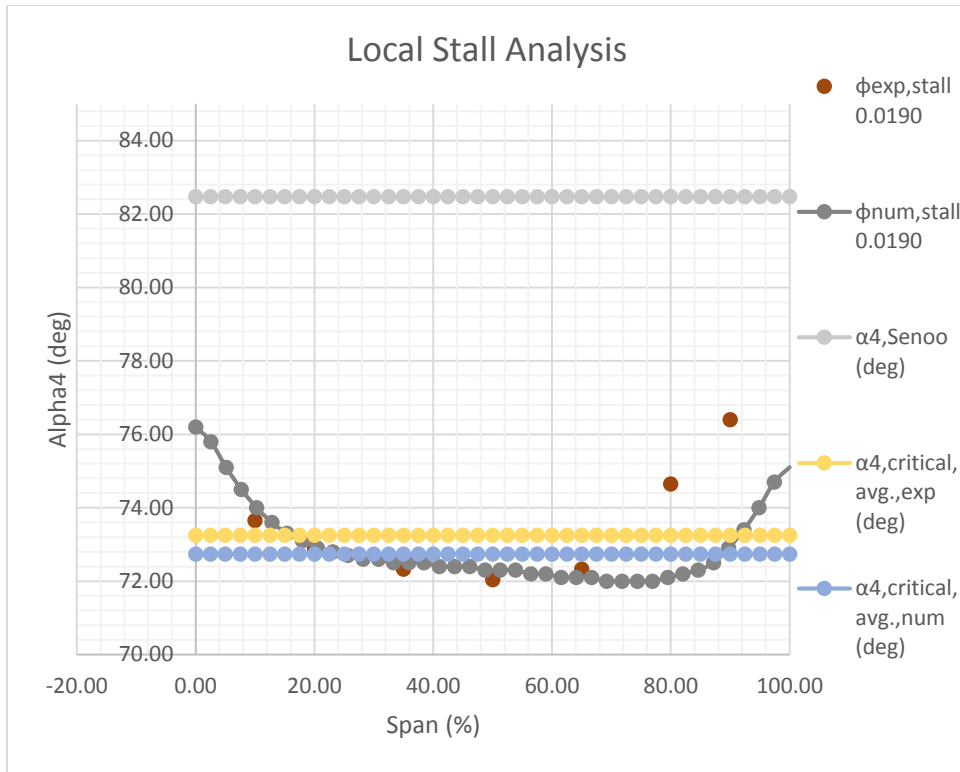


Figure 35: Stall Analysis for Compressor 2 at 19240 RPM Stall Point

6.3.2.3 Compressor 2 21870 RPM Results

Figures 36 – 38 show the results for Compressor 2 at the 21870 RPM stall point. Figure 36 shows the same drop in experimental meridional velocity at 70% span that was seen in Figures 30 and 33. Figure 37 shows strong agreement between the experimental and numerical tangential velocity profiles. Figure 38 shows that neither the experimental nor numerical local profiles breached the Senoo line. So, for Compressor 2 no breach of the Senoo line was found at the stall point for each of the three speed lines. Thus, there is something significantly different between Compressors 1 and 2 that is causing this behavior. However, as will be shown with the remaining twelve geometries, this is not an isolated case.

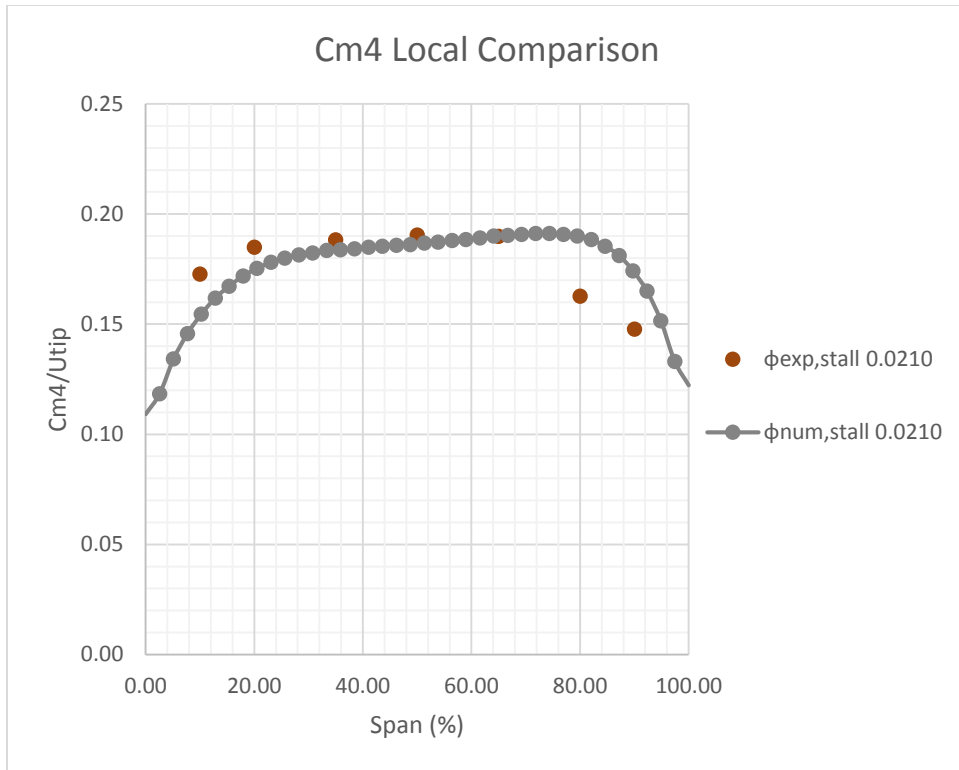


Figure 36: C_{m4} Comparison for Compressor 2 at 21870 RPM Stall Point

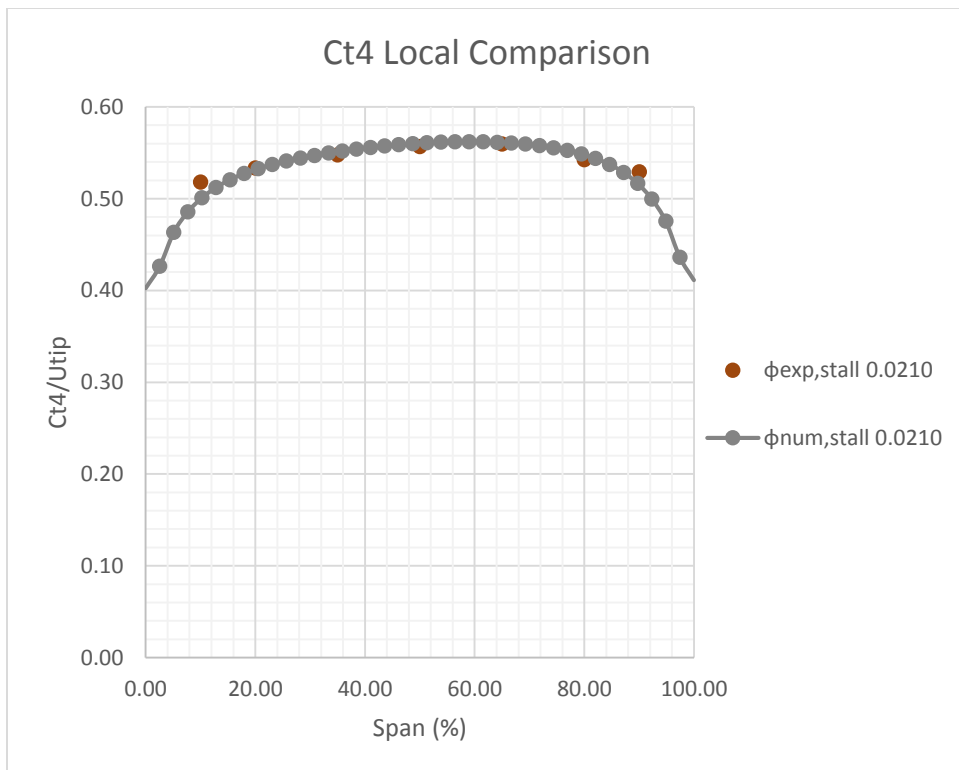


Figure 37: C_{t4} Comparison for Compressor 2 at 21870 RPM Stall Point

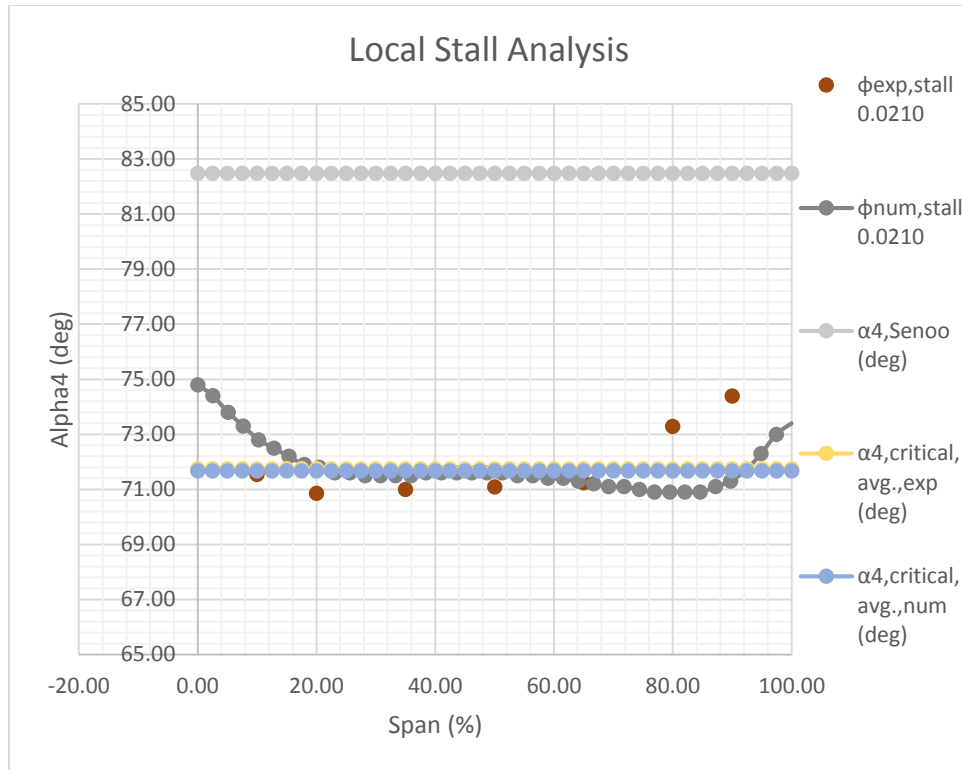


Figure 38: Stall Analysis for Compressor 2 at 21870 RPM Stall Point

6.3.3 Compressor 3 Profiles

6.3.3.1 Compressor 3 13100 RPM Results

Figures 39 – 41 show the results for Compressor 3 at the 13100 RPM stall point. In Figure 39 one sees that the numerical and experimental profiles match qualitatively, but they do not fall on top of each other. Figure 40 shows good agreement between the numerical and experimental tangential velocity profiles. Figure 41 shows that both the numerical and experimental profiles cross the Senoo line. As a note the local numerical profile shown in Figure 41 reaches ~88 degrees which is close to showing localized velocity flow reversal. This maximum angle is also larger than expected by Jansen in [15] for the onset of rotating stall. However, the average numerical flow angle of ~75 degrees is in agreement with Jansen’s work [15]. But these results appear to be in conflict with Senoo’s expectation of localized flow reversal where flow reversal needed to cover about 3.5% of the span for rotating stall to onset [34].

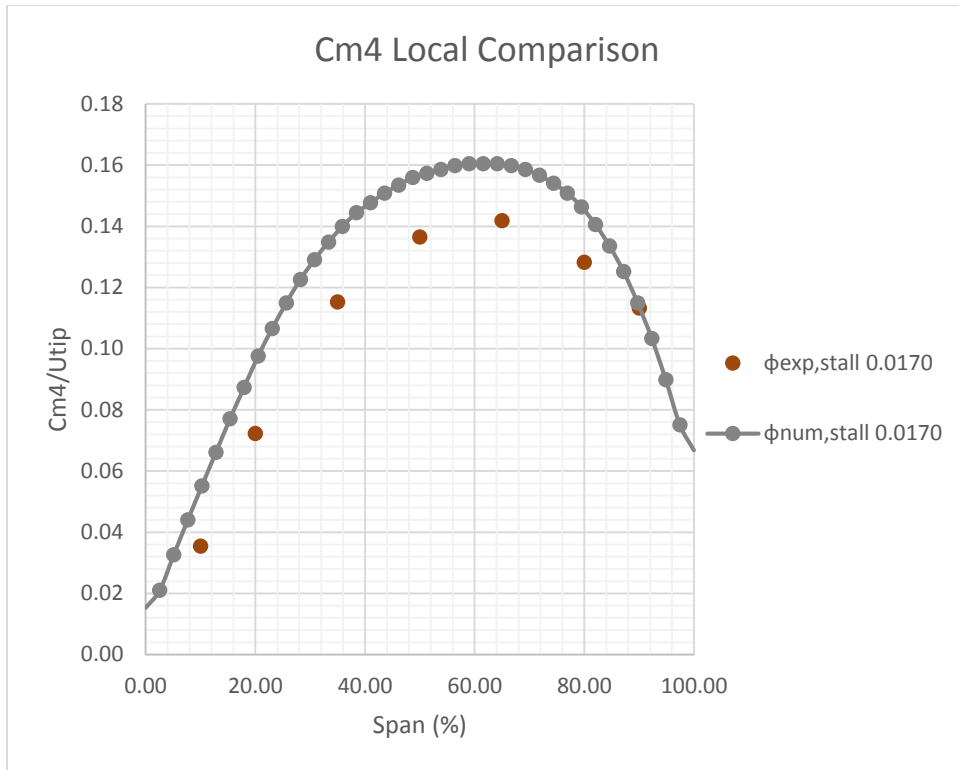


Figure 39: C_{m4} Comparison for Compressor 3 at 13100 RPM Stall Point

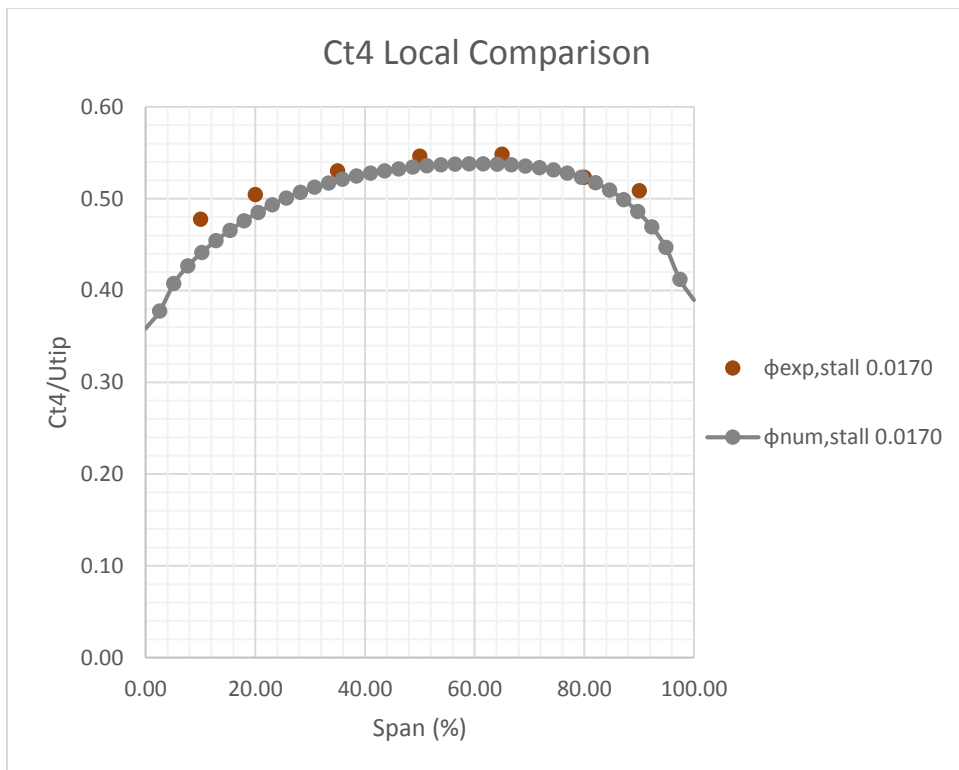


Figure 40: C_{t4} Comparison for Compressor 3 at 13100 RPM Stall Point

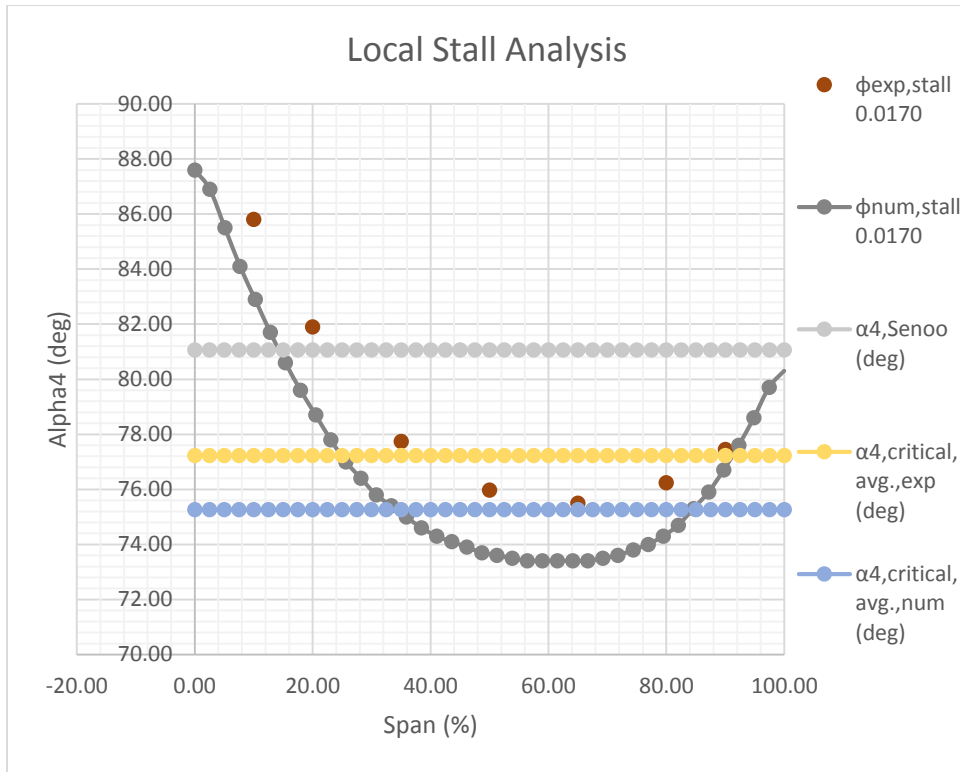


Figure 41: Stall Analysis for Compressor 3 at 13100 RPM Stall Point

6.3.3.2 Compressor 3 19240 RPM Results

Figures 42 – 44 give the results for Compressor 3 at the 19240 RPM stall point. In Figure 42 there is agreement between the numerical and experimental results on the hub side near the 25 – 30% span marker. Otherwise, there is an agreement between the trends of the meridional velocities, but no strong agreement in the magnitude of the profiles. Figure 43 shows pretty good agreement between the profiles except in the 0 – 20% span range. Figure 44 again sees a breach of the Senoo line by both the experimental and numerical angular profiles. It should be noted that the experimental data was not available due to the stall point occurring at the surge line. However, data was available at a point ($\phi = 0.0186$) that was very close to the stall point ($\phi = 0.0179$). These points are considered close enough to compare because the pressure profile is nearly flat at this point allowing for a satisfactory comparison (See Appendix A, Figure 215).

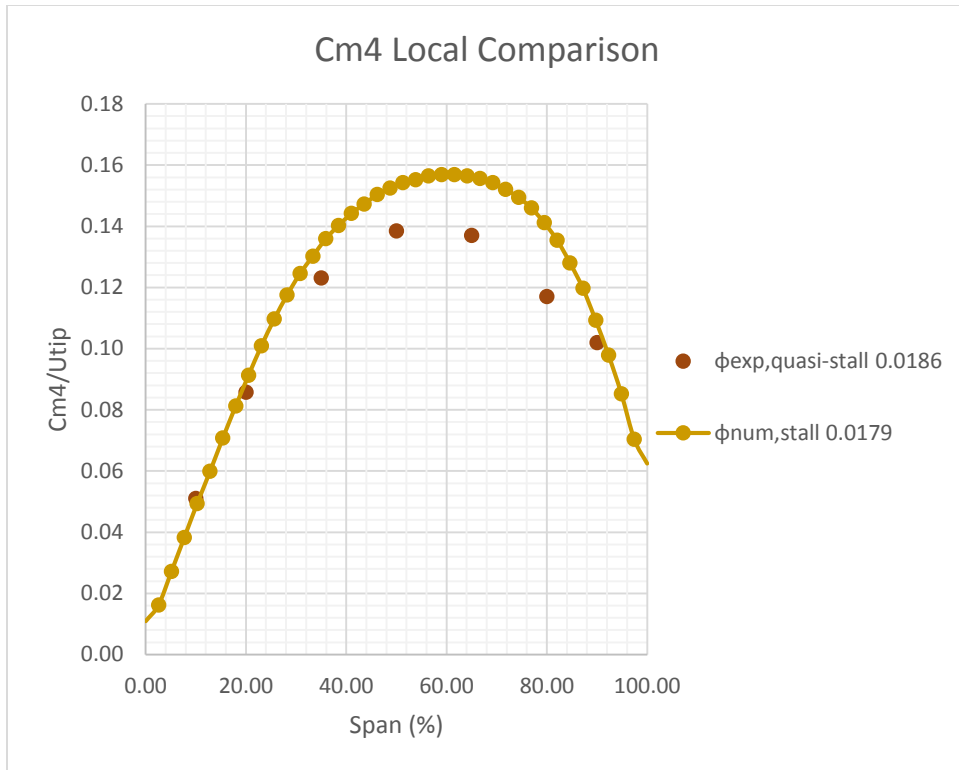


Figure 42: C_{m4} Comparison for Compressor 3 at 19240 RPM Stall Point

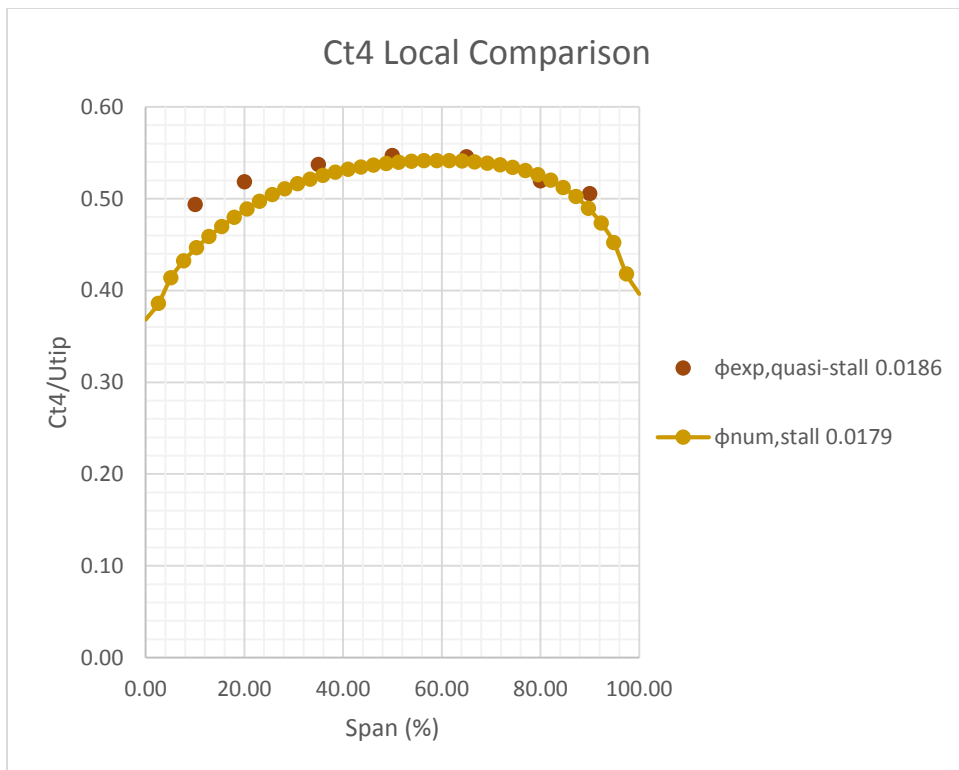


Figure 43: C_{t4} Comparison for Compressor 3 at 19240 RPM Stall Point

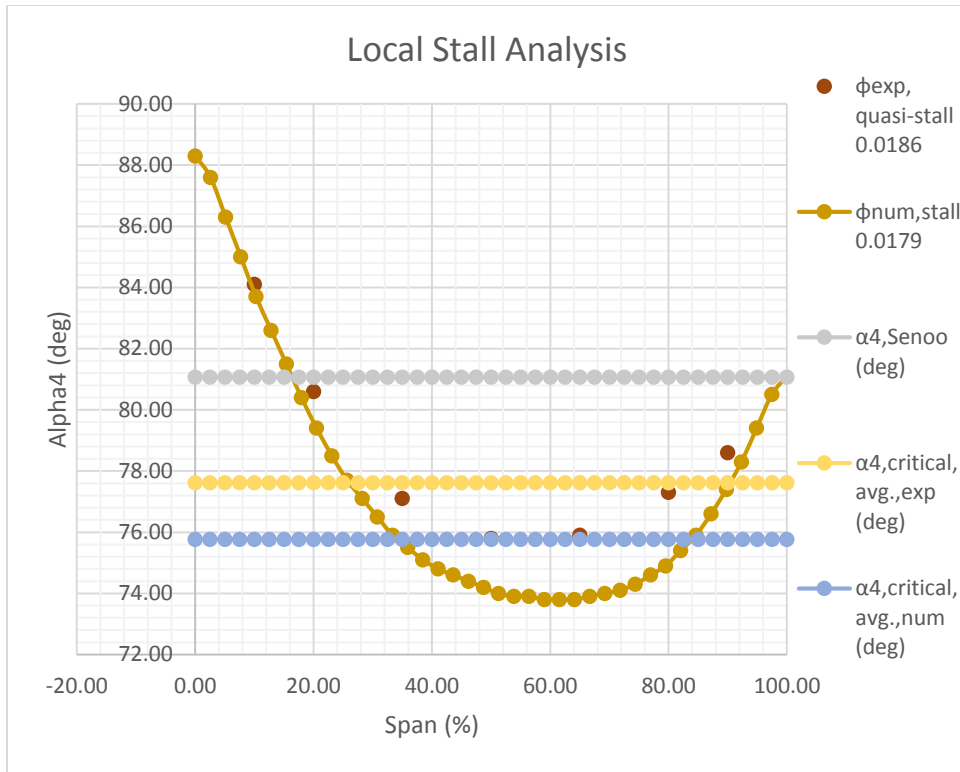


Figure 44: Stall Analysis for Compressor 3 at 19240 RPM Stall Point

6.3.3.3 Compressor 3 21870 RPM Results

Figures 45 – 47 show the results for Compressor 3 at the 21870 RPM stall point. In Figure 45 there is only small agreement between the numerical and experimental profiles (this was found in the 10% of the span closest to the walls). Although, both the numerical and experimental profiles experienced a wavelike characteristic though out of phase with each other. Figure 46 shows some agreement between the numerical and experimental profiles, but there is a divergence of the numerical and experimental profiles in the 0 – 30% span region. And in an interesting twist neither local angle profile breaches the Senoo line. This is contrary to what was seen with Compressor 1 and the 13100 RPM and 19240 RPM speed lines for Compressor 3. Causes for this issue will be discussed in section 6.3.15.

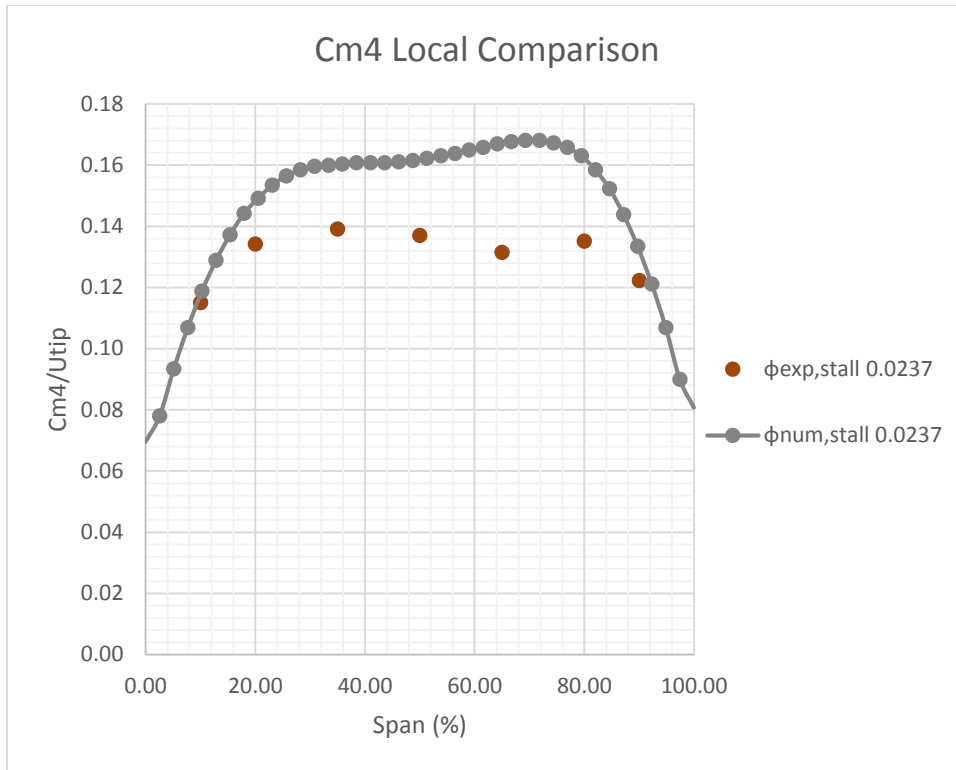


Figure 45: C_{m4} Comparison for Compressor 3 at 21870 RPM Stall Point

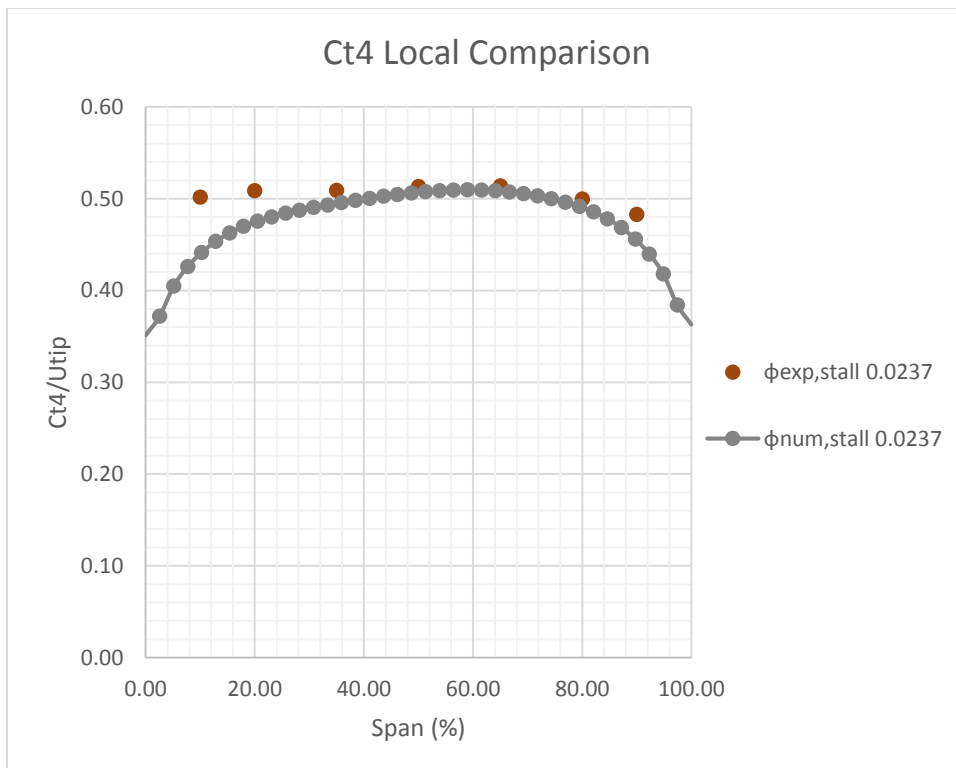


Figure 46: C_{t4} Comparison for Compressor 3 at 21870 RPM Stall Point

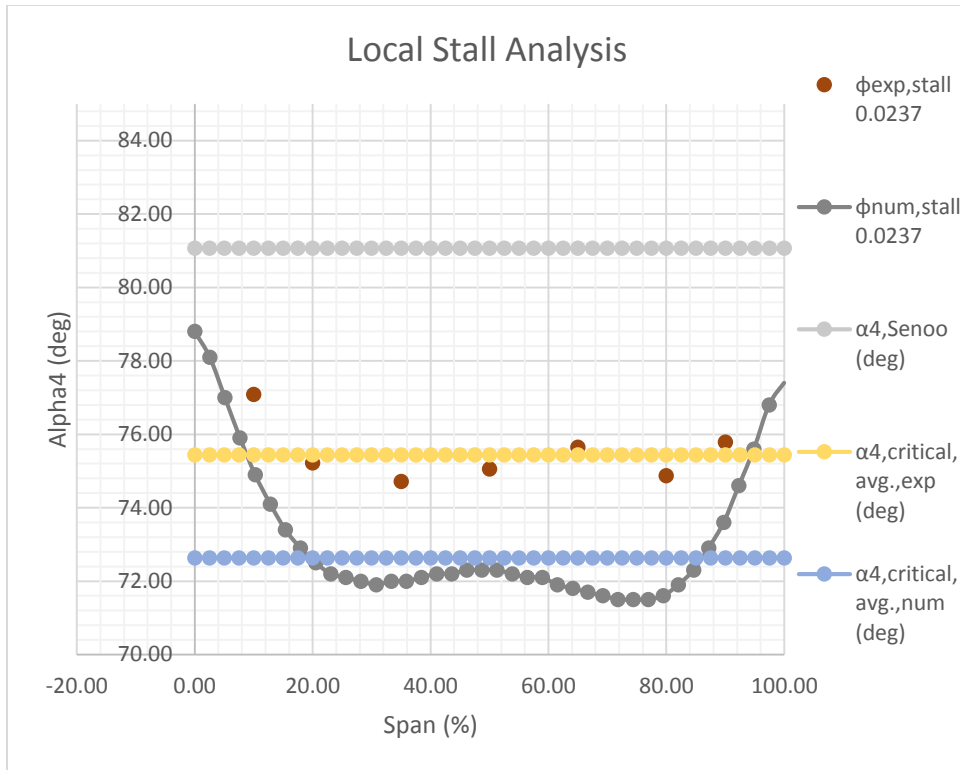


Figure 47: Stall Analysis for Compressor 3 at 21870 RPM Stall Point

6.3.4 Compressor 4 Profiles

6.3.4.1 Compressor 4 13100 RPM Results

Figures 48 – 50 show the results for Compressor 4 at the 13100 RPM stall point. Looking at Figures 48 and 49 one finds that the experimental and numerical profiles for both tangential and meridional velocity have strong agreement. In Figure 50 one finds that the local angle profiles do not reach or cross the Senoo line. In fact the profiles come no closer than 8 degrees. This is a large gap that adds more evidence to the unreliability of just using the Senoo – Kobayashi equation.

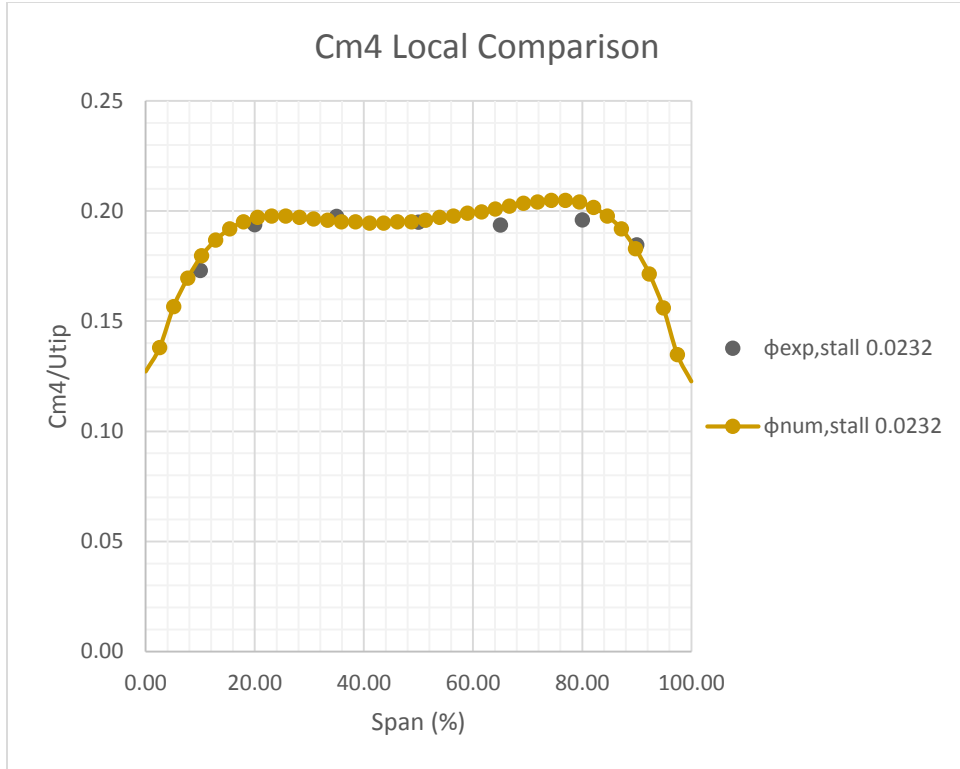


Figure 48: C_{m4} Comparison for Compressor 4 at 13100 RPM Stall Point

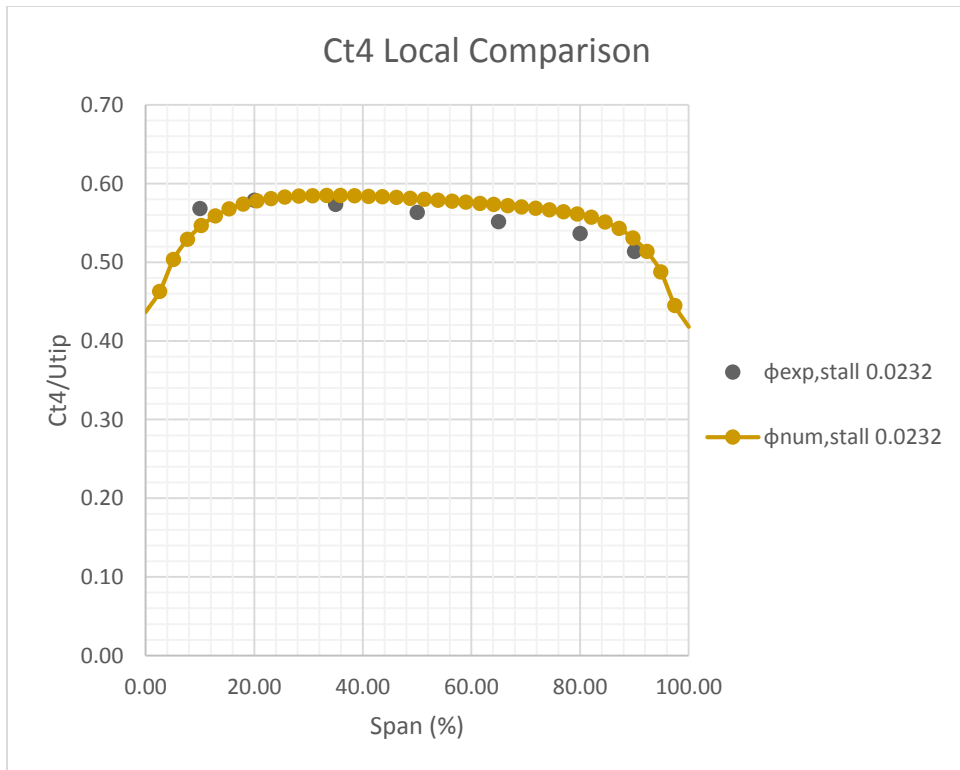


Figure 49: C_{t4} Comparison for Compressor 4 at 13100 RPM Stall Point

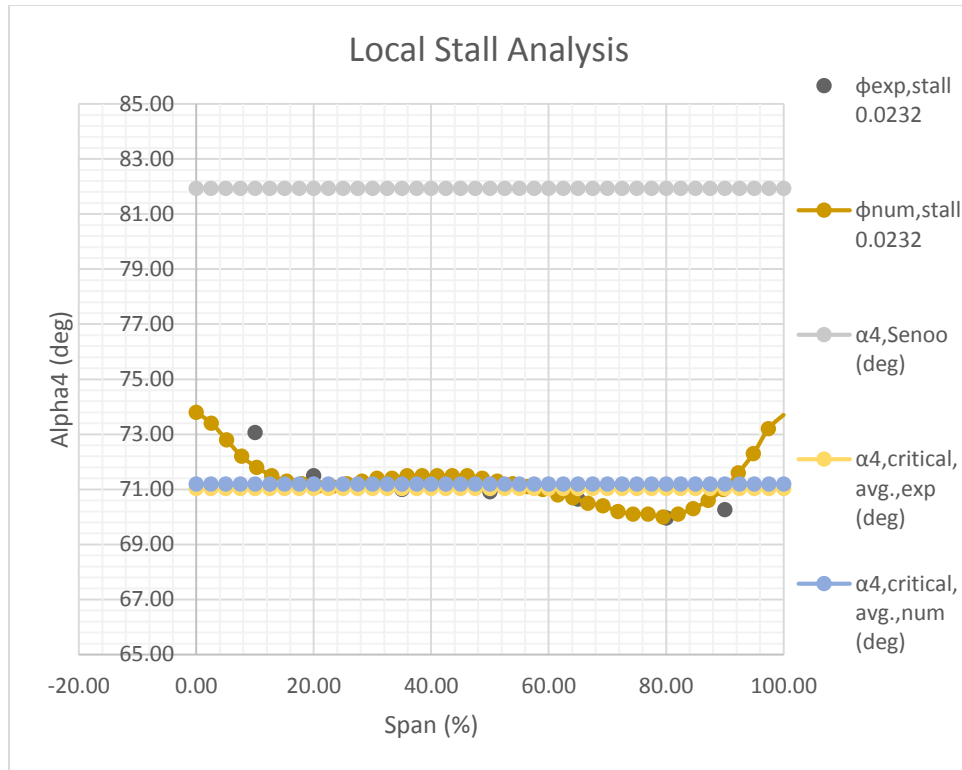


Figure 50: Stall Analysis for Compressor 4 at 13100 RPM Stall Point

6.3.4.2 Compressor 4 19240 RPM Results

Figures 51 – 53 show the results for Compressor 4 at the 19240 RPM stall point. In Figure 51 it is clear that there is little agreement between the numerical and experimental profiles for the meridional velocity. This is somewhat surprising given the agreement seen at 13100 RPM. However, in Figure 52 one finds that even the tangential profiles are not in agreement. In Figure 53 it is clear that neither the experimental nor the numerical angle profiles reach the Senoo line. So, even with the differences in velocity profiles at the stall point the Senoo angle did not accurately predict when rotating stall would occur. Furthermore, it is not expected that the profiles will match precisely due to the fact that the flow stability is breaking and a steady state simulation will smooth out the flow anomalies.

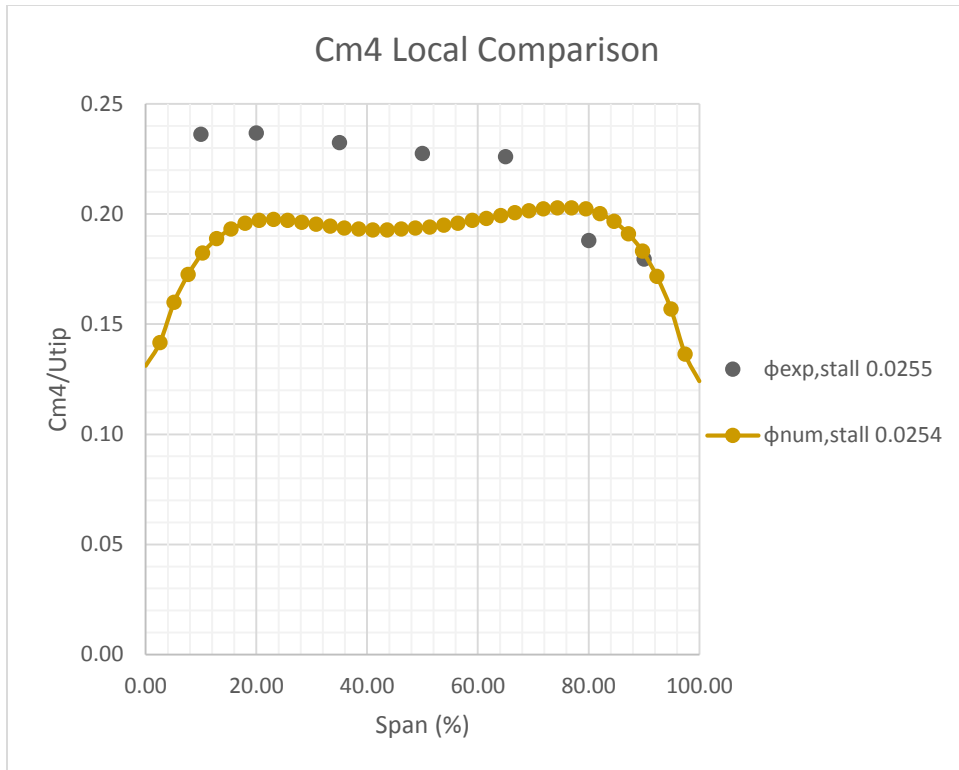


Figure 51: C_{m4} Comparison for Compressor 4 at 19240 RPM Stall Point

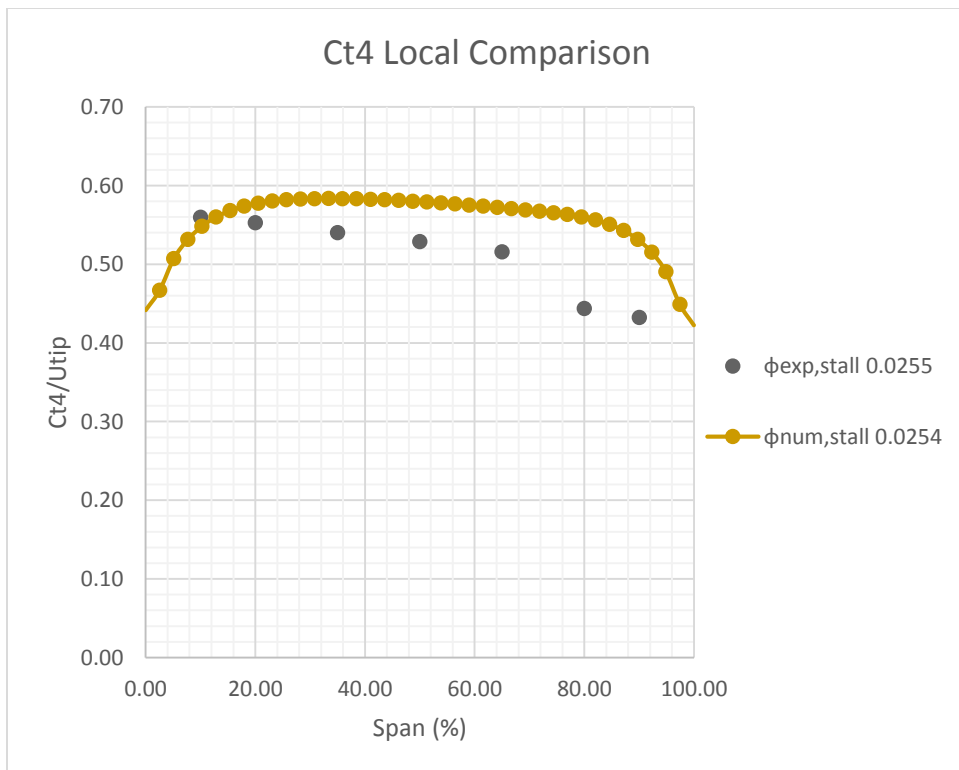


Figure 52: C_{t4} Comparison for Compressor 4 at 19240 RPM Stall Point

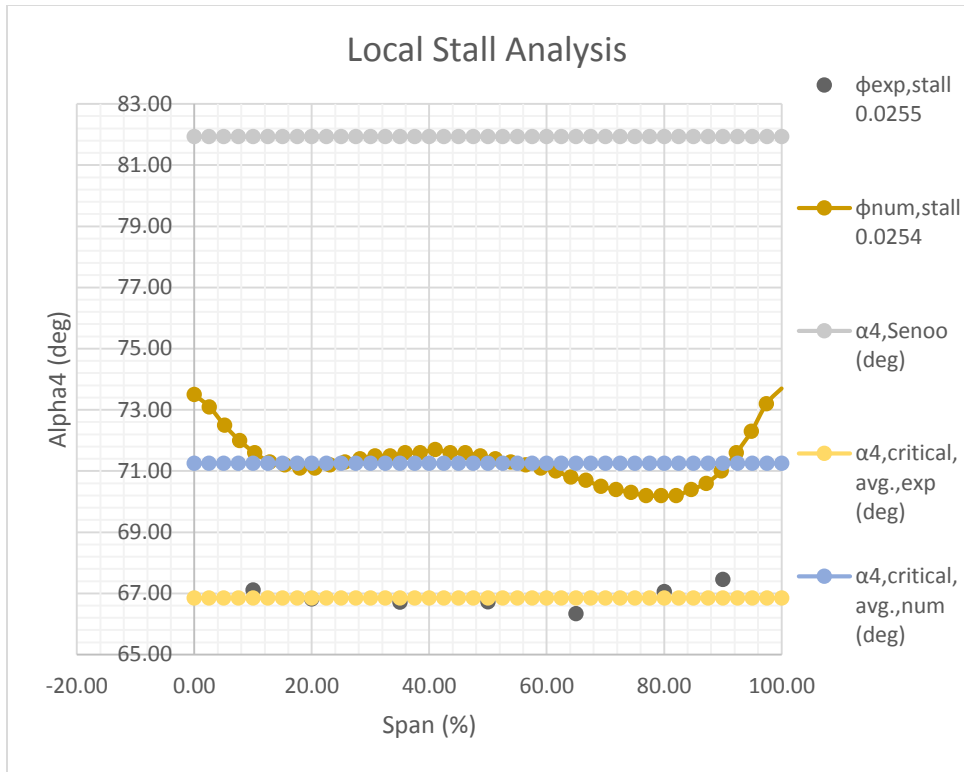


Figure 53: Stall Analysis for Compressor 4 at 19240 RPM Stall Point

6.3.4.3 Compressor 4 21870 RPM Results

Figures 54 – 56 show the results for Compressor 4 at the 21870 RPM stall point. As with the results at the 19240 RPM stall point the meridional and tangential velocity plots, Figures 54 and 55 respectively, show little agreement. This could be due to the averaging effect of the steady state simulation or to the fact that the stall point is not properly defined experimentally which would put the experimental profiles in the unstable region. Either way the important result is found in Figure 56. That result being that once again the local profiles do not reach the Senoo line. After four geometries a pattern of success and failure is forming around whether or not the Senoo line is breached. This pattern will be discussed in section 6.3.15, but please note that it is there and it is important to the overall understanding of vaneless diffuser stability.

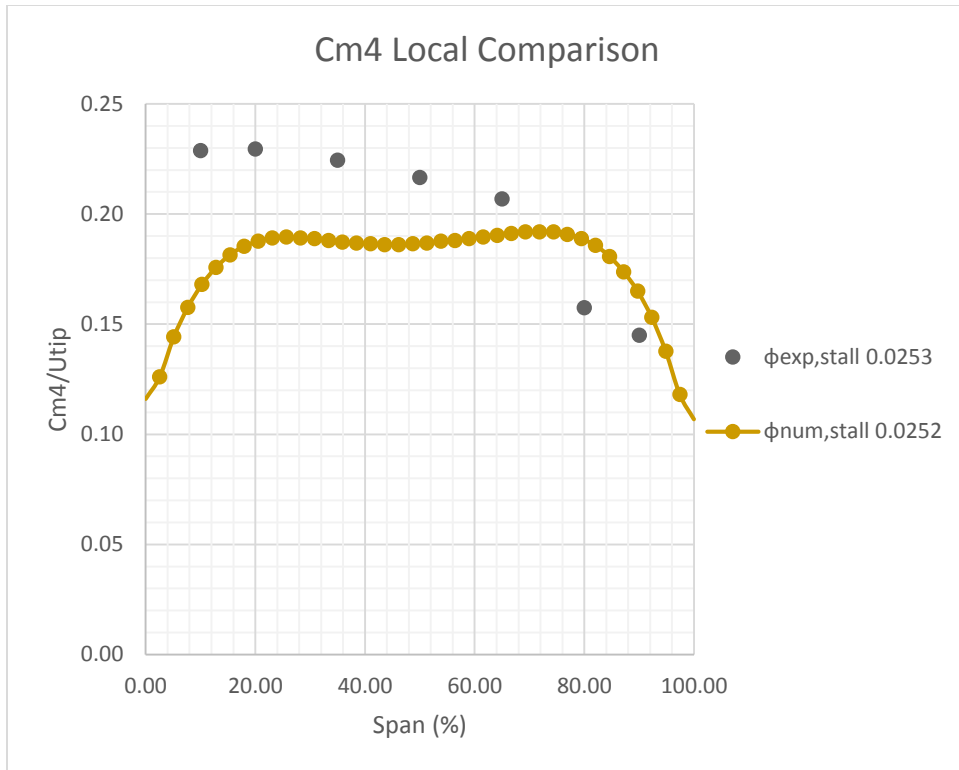


Figure 54: C_{m4} Comparison for Compressor 4 at 21870 RPM Stall Point

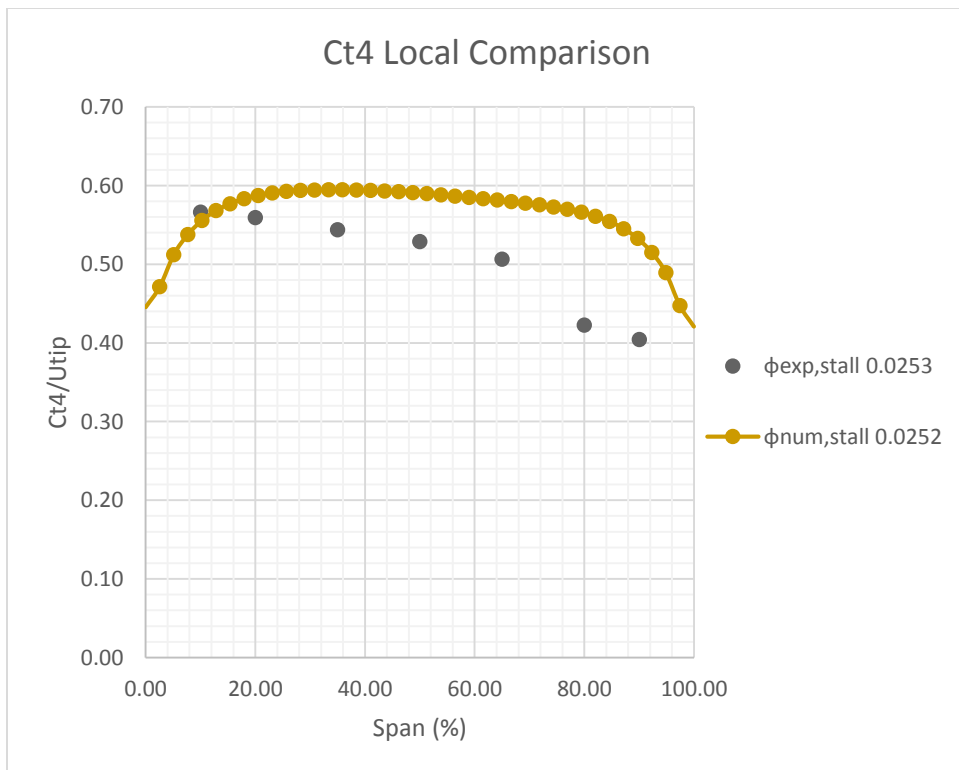


Figure 55: C_{t4} Comparison for Compressor 4 at 21870 RPM Stall Point

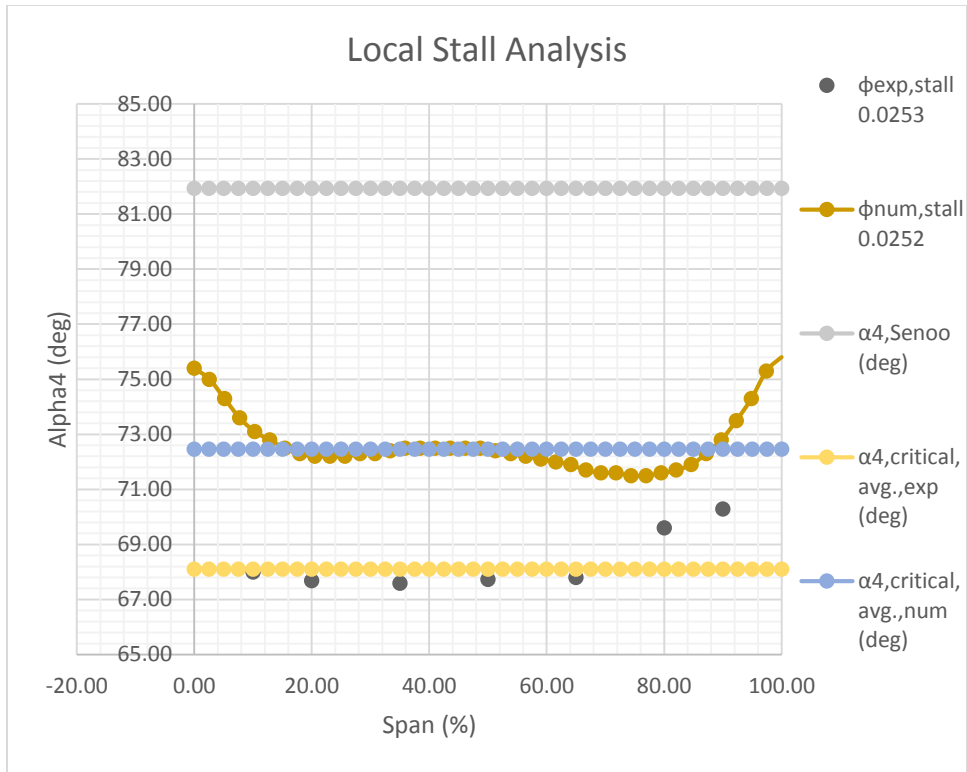


Figure 56: Stall Analysis for Compressor 4 at 21870 RPM Stall Point

6.3.5 Compressor 5 Profiles

6.3.5.1 Compressor 5 13100 RPM Results

Figures 57 – 59 show the results for Compressor 5 at the 13100 RPM stall point. In Figure 57 one can see that the numerical and experimental profiles appear to be out of phase with each other, but have roughly the same magnitude. In Figure 58 the tangential velocity profiles show good agreement. In Figure 59 it is clear that the Senoo line is not breached by either the experimental or numerical angle profiles.

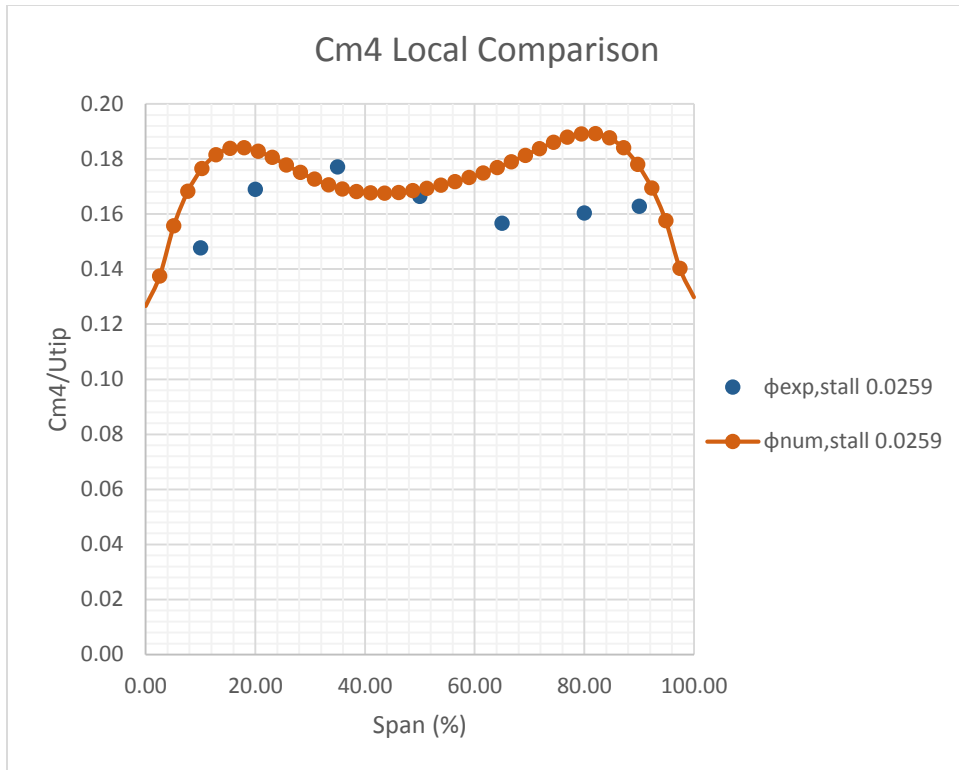


Figure 57: C_{m4} Comparison for Compressor 5 at 13100 RPM Stall Point

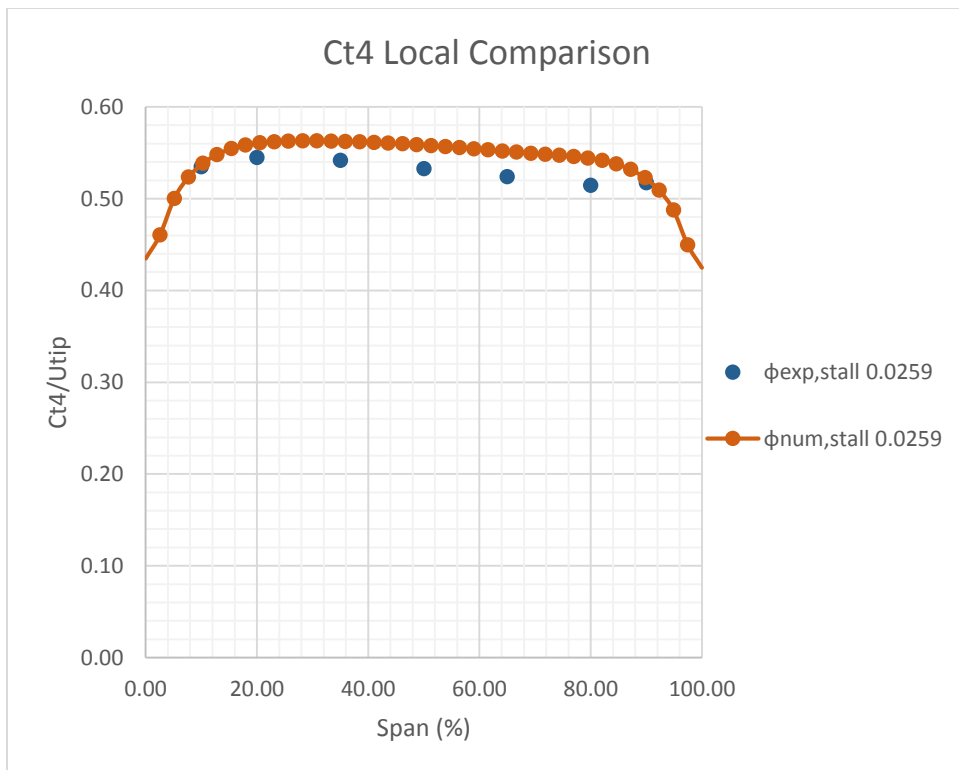


Figure 58: C_{t4} Comparison for Compressor 5 at 13100 RPM Stall Point

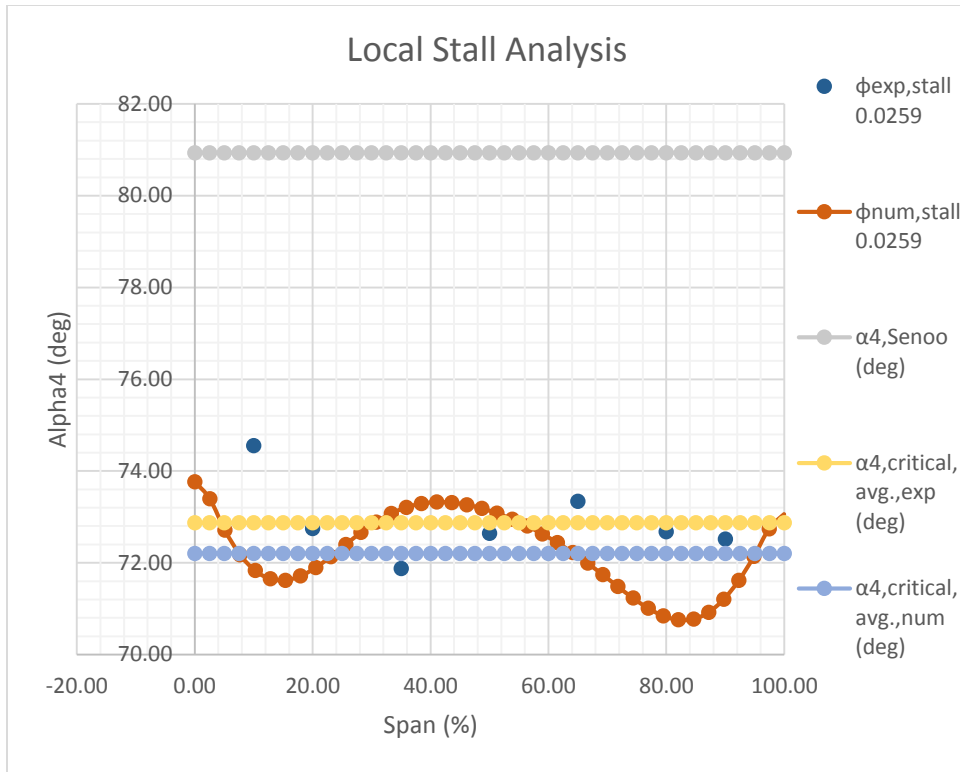


Figure 59: Stall Analysis for Compressor 5 at 13100 RPM Stall Point

6.3.5.2 Compressor 5 19240 RPM Results

In Figures 60 – 62 the results for Compressor 5 at 19240 RPM are shown. Figure 60 shows that the meridional velocity profiles are again out of phase between the numerical and experimental results. However, they share the same magnitude. In Figure 61 it is clear that the trends of the tangential velocity profiles agree between the numerical and experimental results. However, in this case their magnitudes do not match as well as those for the meridional velocity profiles. In Figure 62 it is clear that neither angular profile reaches the Senoo line.

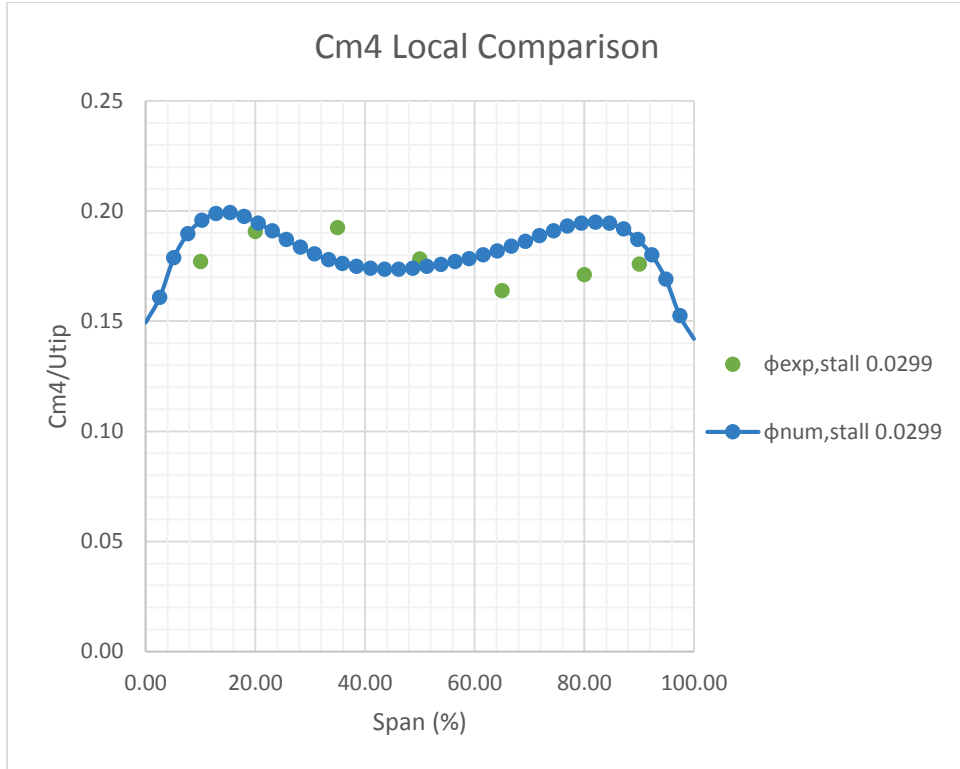


Figure 60: C_{m4} Comparison for Compressor 5 at 19240 RPM Stall Point

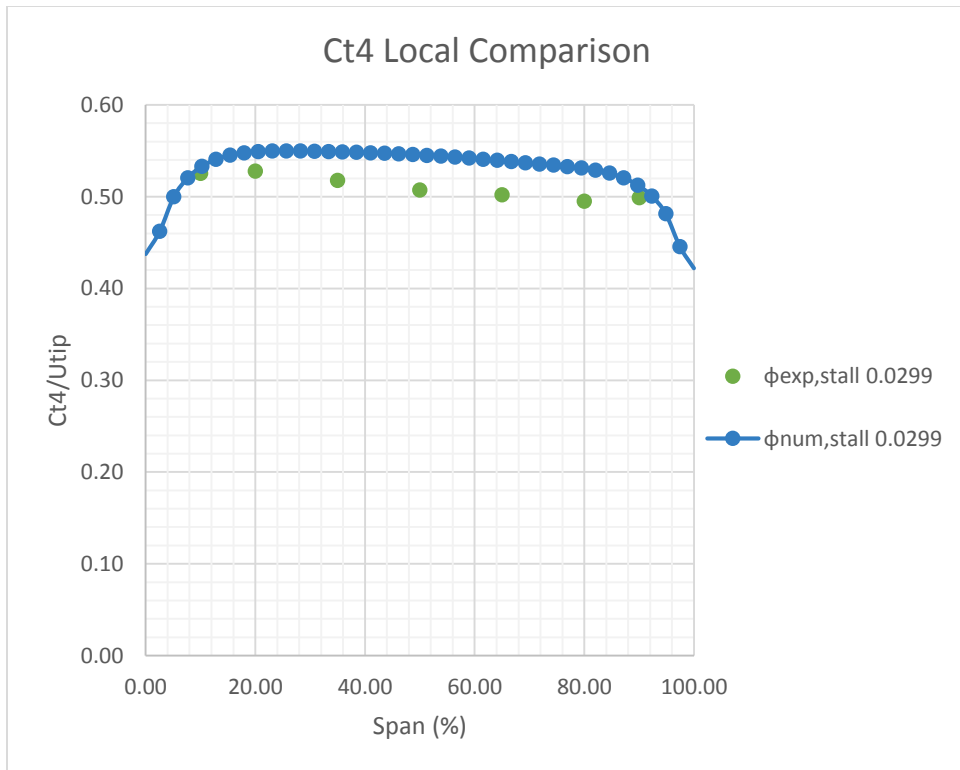


Figure 61: C_{t4} Comparison for Compressor 5 at 19240 RPM Stall Point

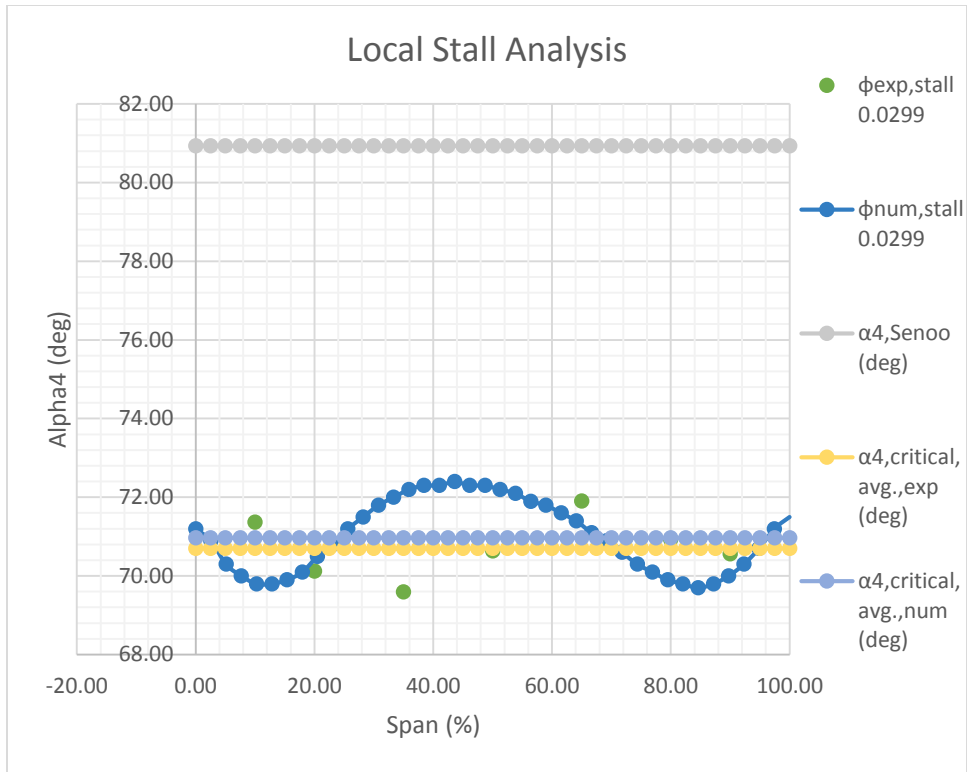


Figure 62: Stall Analysis for Compressor 5 at 19240 RPM Stall Point

6.3.5.3 Compressor 5 21870 RPM Results

Figures 63 – 65 show the results for Compressor 5 at the 21870 RPM stall point. The meridional velocity profiles shown in Figure 63 show less of their out of phase agreement, but the trend is still there. Also, the magnitudes of the meridional velocity profiles in Figure 63 are a good match. In Figure 64 the tangential profiles trends match, but not the magnitudes. This result was expected based on the 13100 RPM and 19240 RPM results. In Figure 65 the local profiles do not reach the Senoo line.

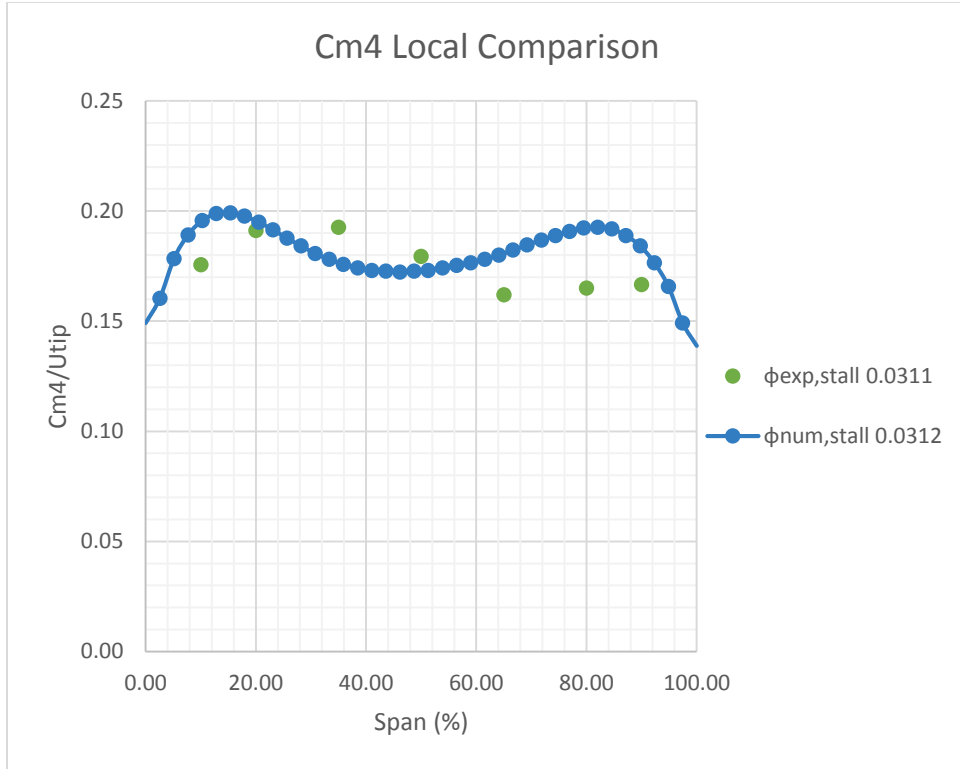


Figure 63: C_{m4} Comparison for Compressor 5 at 21870 RPM Stall Point

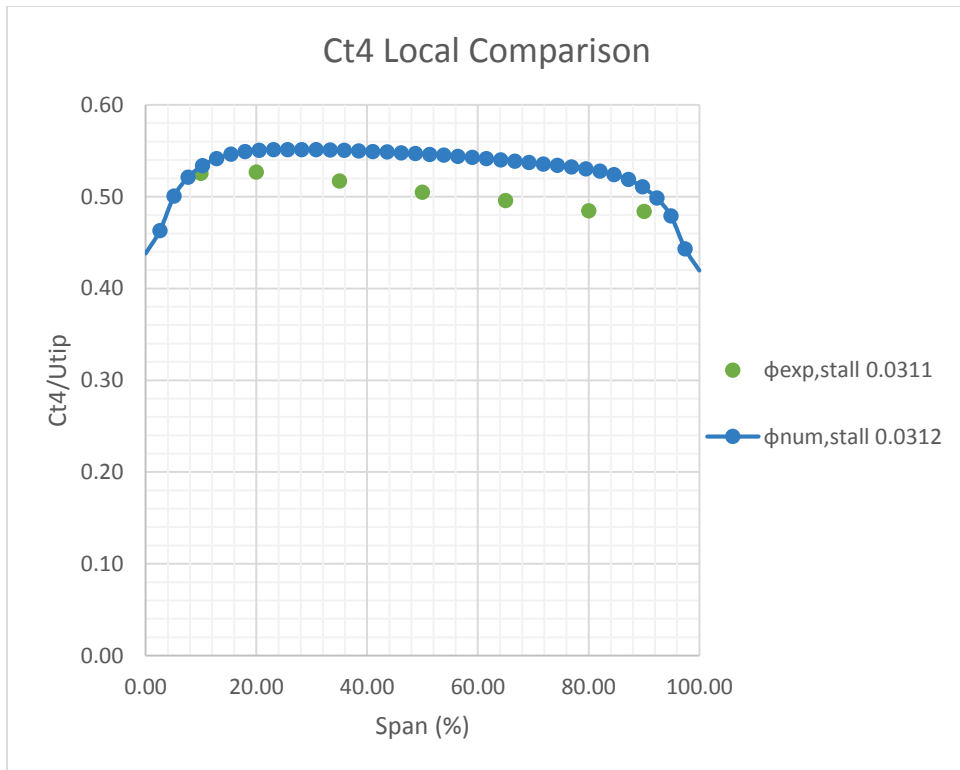


Figure 64: C_{t4} Comparison for Compressor 5 at 21870 RPM Stall Point

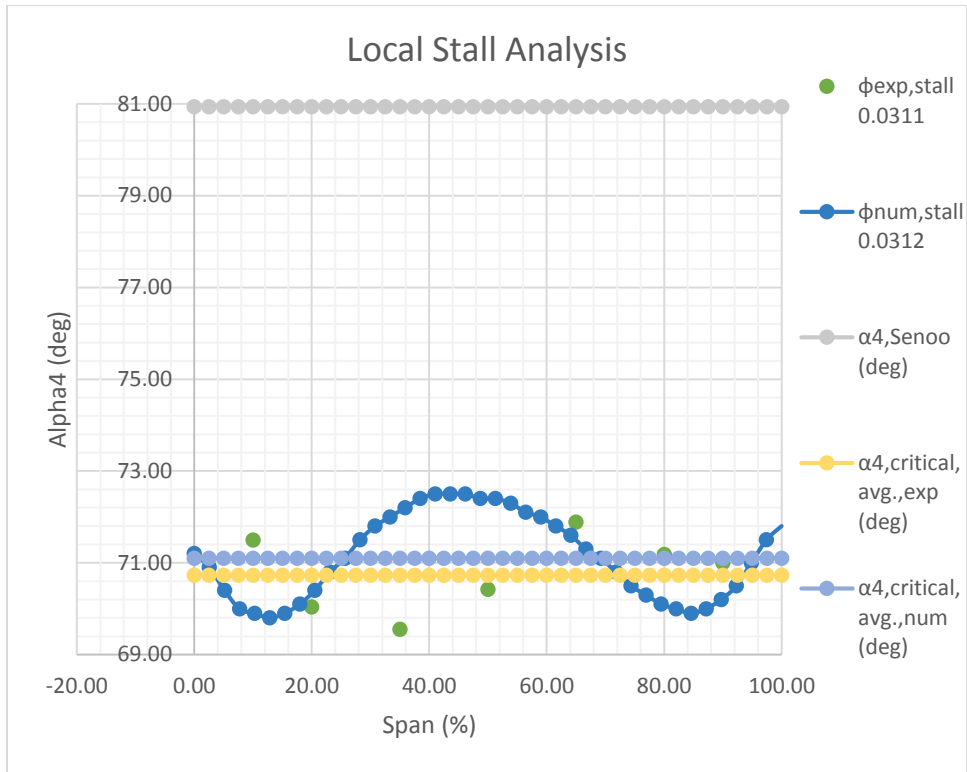


Figure 65: Stall Analysis for Compressor 5 at 21870 RPM Stall Point

6.3.6 Compressor 6 Profiles

Compressor 6 did not experience rotating stall. However, the results have been given at the last stable flow point. This is the operating point immediately preceding the onset of compressor surge. Though not a point of rotating stall onset it is a point of instability and will help to provide more detail to the overarching factors that influence vaneless diffuser stability.

6.3.6.1 Compressor 6 13100 RPM Results

Figures 66 – 68 provide the results for Compressor 6 at 13100 RPM for the last stable flow point. There is agreement between the meridional velocity profiles, which can be seen in Figure 66. In Figure 67 good agreement is seen between the tangential velocity profiles. And in Figure 68 neither the experiment nor the numerical angular profiles breach the Senoo line. Though close to surge it is somewhat unexpected to see the flow profiles still so far from localized flow reversal

at the diffuser inlet, although according to the results of [24 & 32] it is possible that the unstable region is developing further downstream of the diffuser inlet.

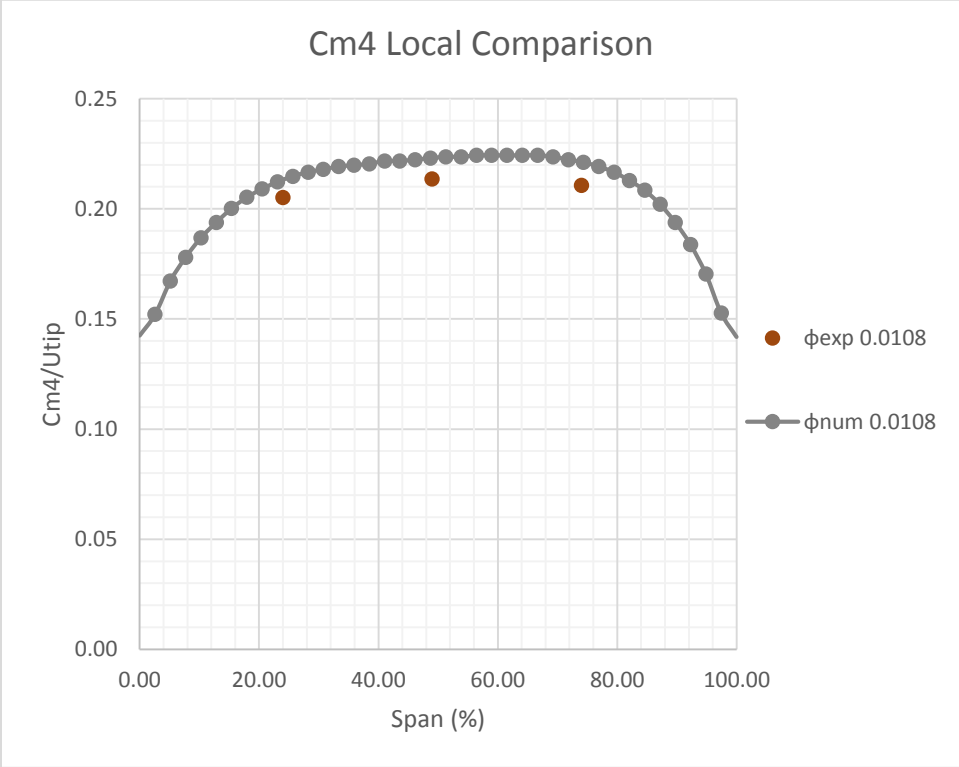


Figure 66: C_{m4} Comparison for Compressor 6 at 13100 Last Stable Flow Point

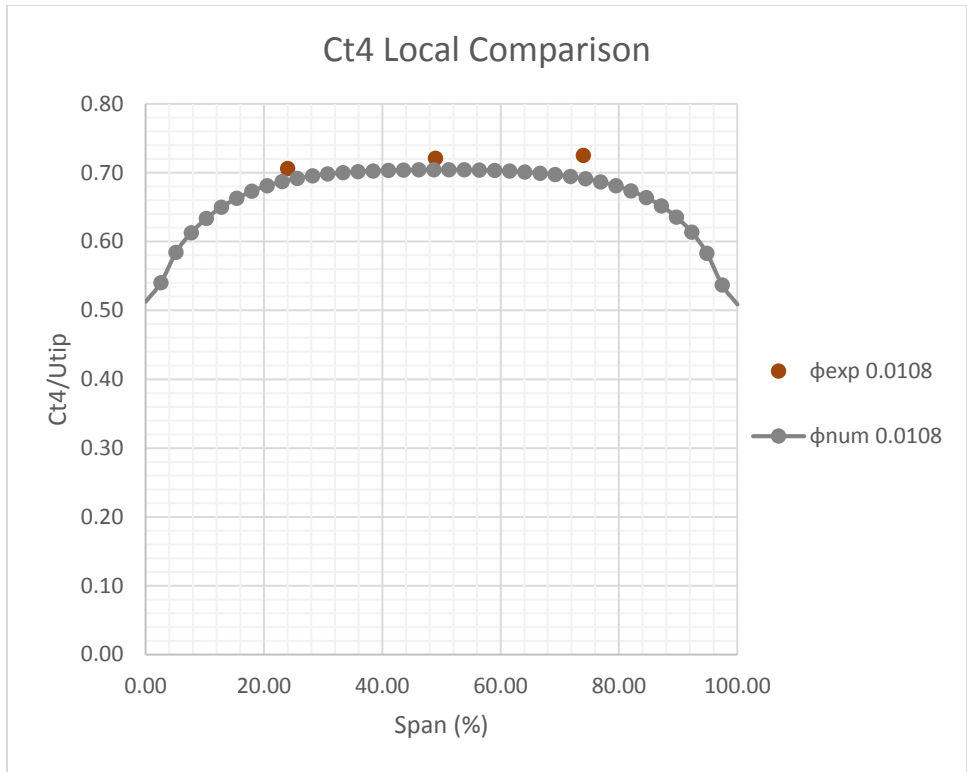


Figure 67: C_{t4} Comparison for Compressor 6 at 13100 RPM Last Stable Flow Point

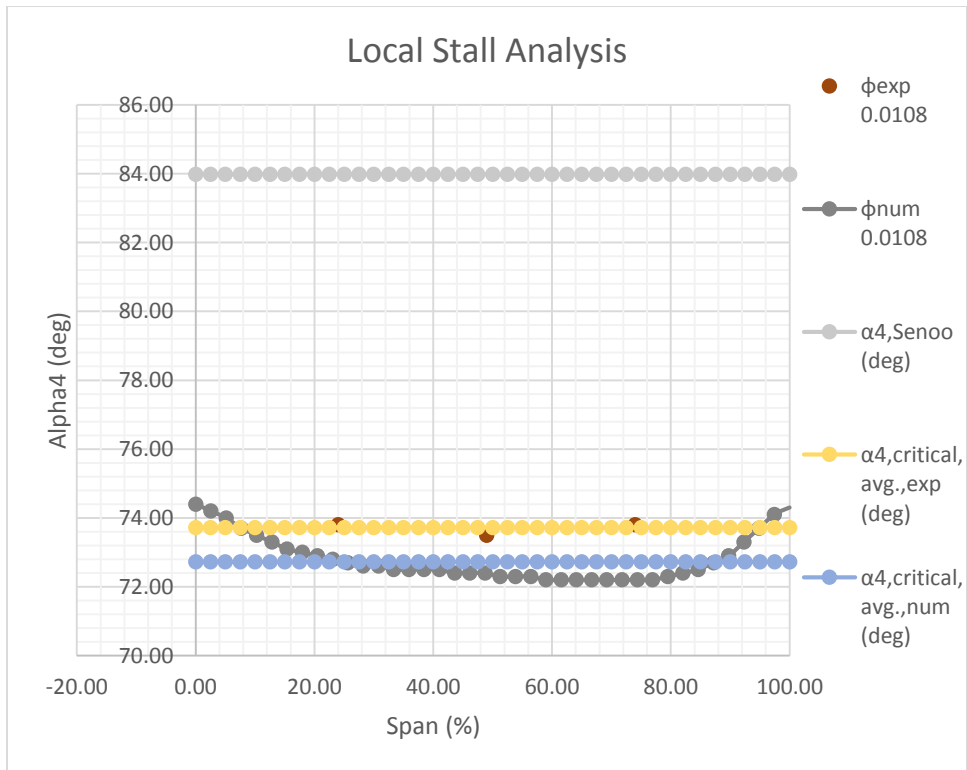


Figure 68: Stall Analysis for Compressor 6 at 13100 RPM Last Stable Flow Point

6.3.6.2 Compressor 6 19240 RPM Results

The results for Compressor 6 at the last stable point for the 19240 RPM speed line are shown in Figures 69 – 71. In Figure 69 one finds good agreement between the numerical and experimental meridional velocity profiles. In Figure 70 excellent agreement is found between the tangential velocity profiles. And in Figure 71 it is found that the Senoo line is not breached, as expected from the results at 13100 RPM.

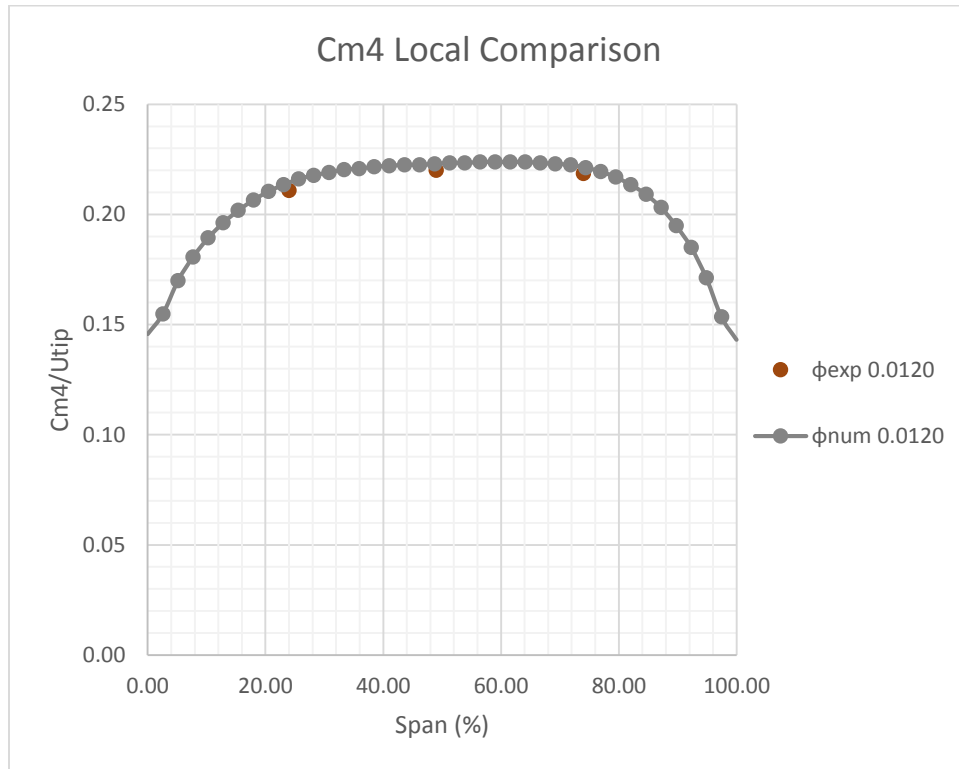


Figure 69: C_{m4} Comparison for Compressor 6 at 19240 RPM Last Stable Flow Point

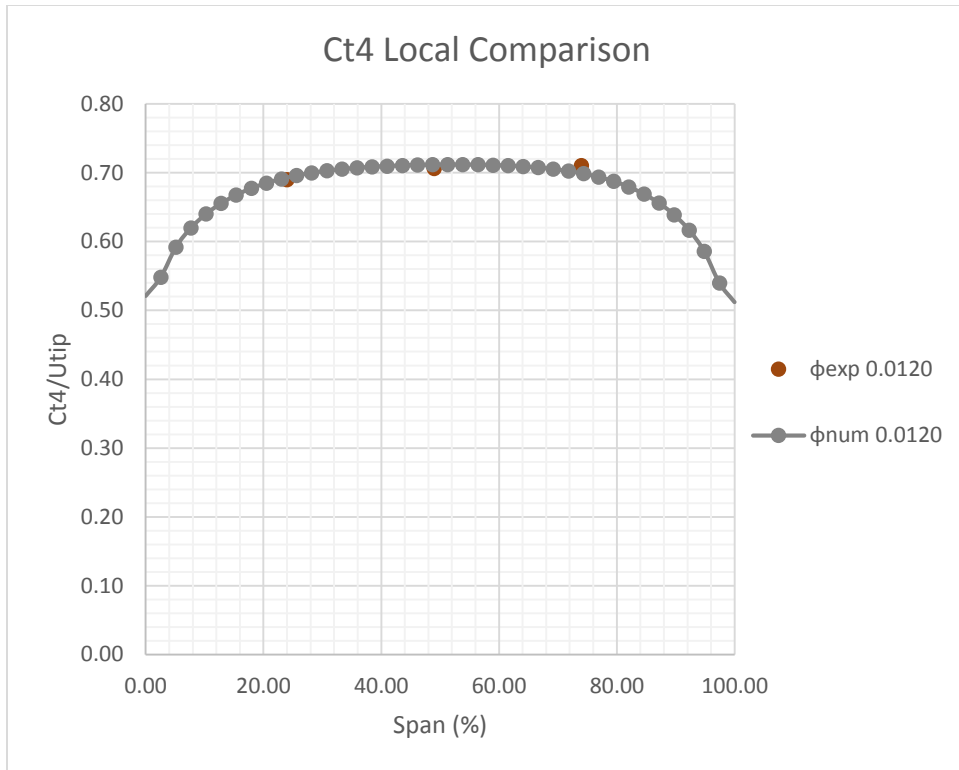


Figure 70: C_{t4} Comparison for Compressor 6 at 19240 RPM Last Stable Flow Point

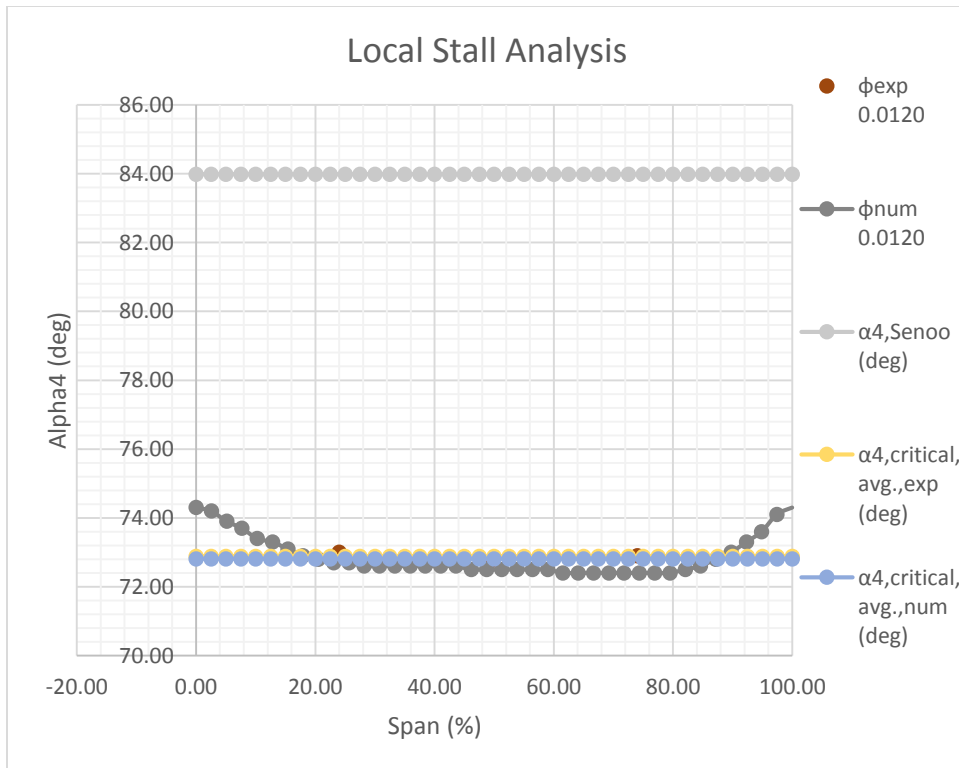


Figure 71: Stall Analysis for Compressor 6 at 19240 RPM Last Stable Flow Point

6.3.6.3 Compressor 6 21870 RPM Results

The results for Compressor 6 at the last stable point for the 21870 RPM speed line are shown in Figures 72 – 74. In Figure 72 one finds good agreement between the numerical and experimental meridional velocity profiles. In Figure 73 excellent agreement is found between the tangential velocity profiles for both the experimental and numerical results. In Figure 74 it is clear that the Senoo line is not breached.

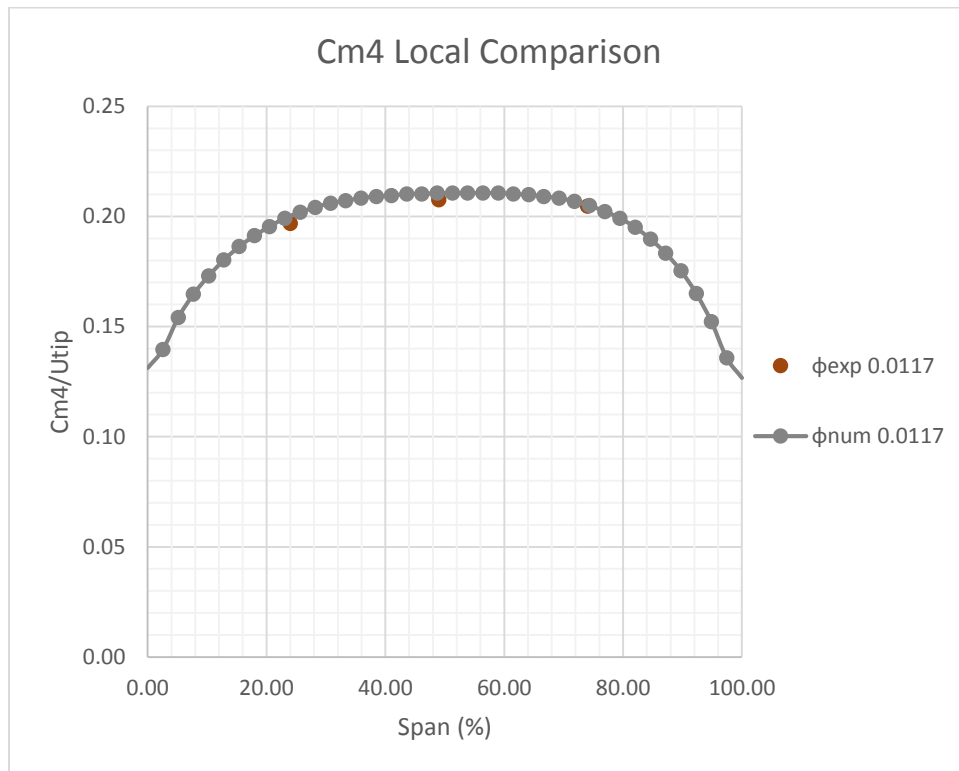


Figure 72: C_{m4} Comparison for Compressor 6 at 21870 RPM Last Stable Flow Point

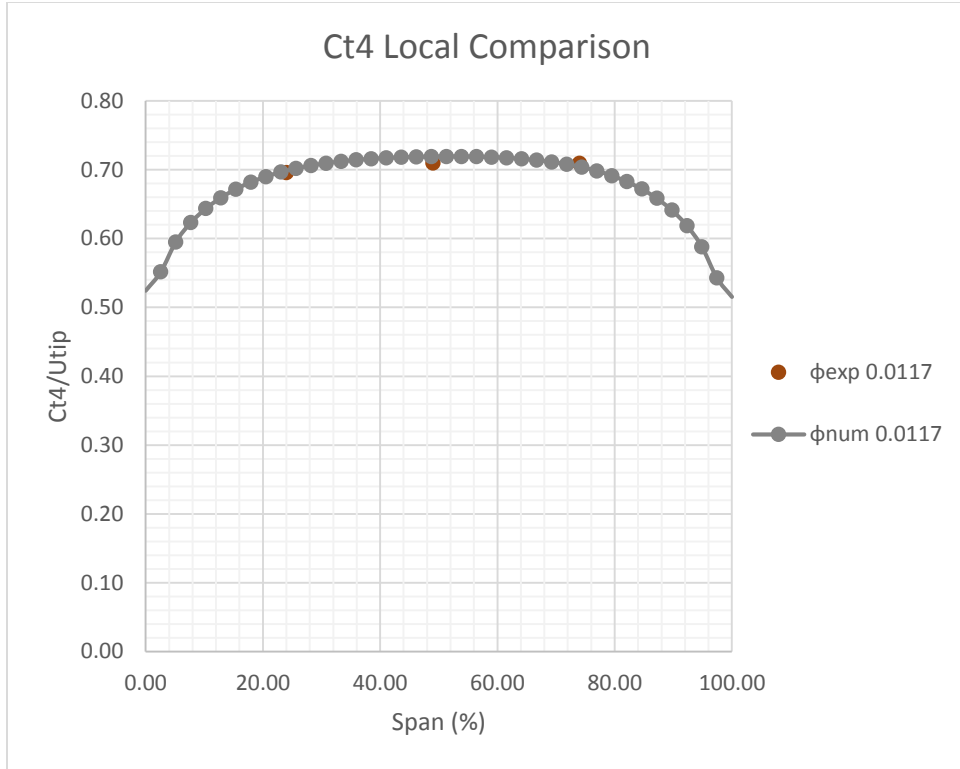


Figure 73: C_{t4} Comparison for Compressor 6 at 21870 RPM Last Stable Flow Point

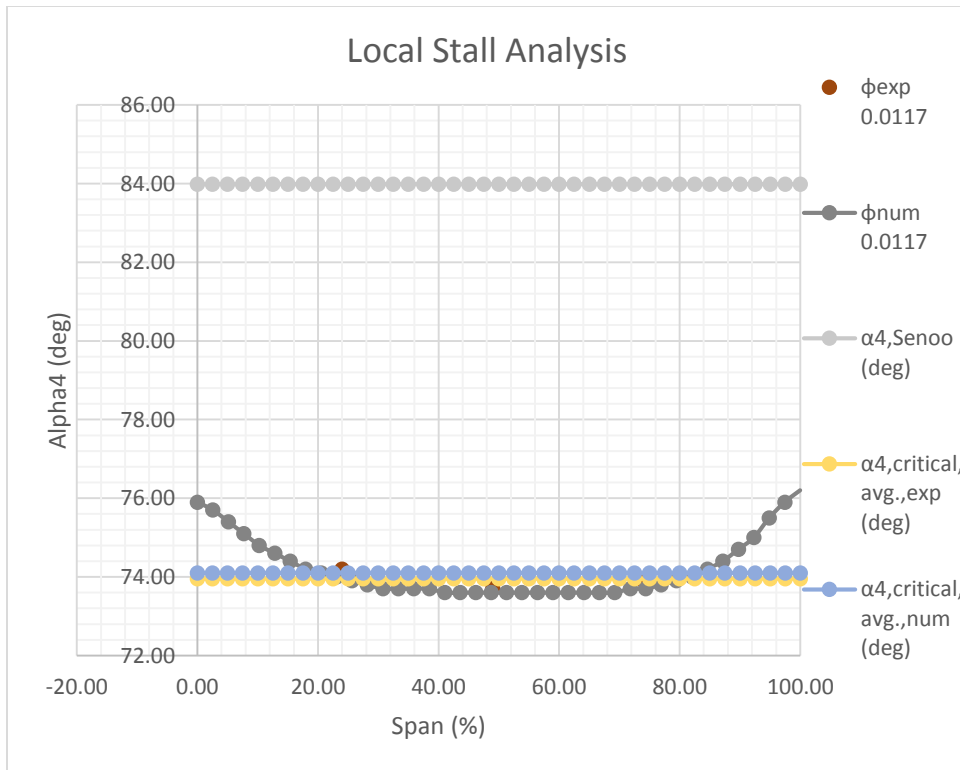


Figure 74: Stall Analysis for Compressor 6 at 21870 RPM Last Stable Flow Point

6.3.7 Compressor 7 Profiles

6.3.7.1 Compressor 7 13100 RPM Results

Figures 75 – 77 show the results for Compressor 7 at the 13100 RPM stall point. In Figure 75 there is some agreement between the numerical and experimental meridional velocity profiles. However, with only three experimental points (this is because this is a low N_s impeller [27]) it is hard to get an idea of the actual trends. In Figure 76 the trends are correct between the numerical and experimental tangential velocity profiles, but the magnitudes are not in agreement. In Figure 77 it is found that neither local profile reaches the Senoo line.

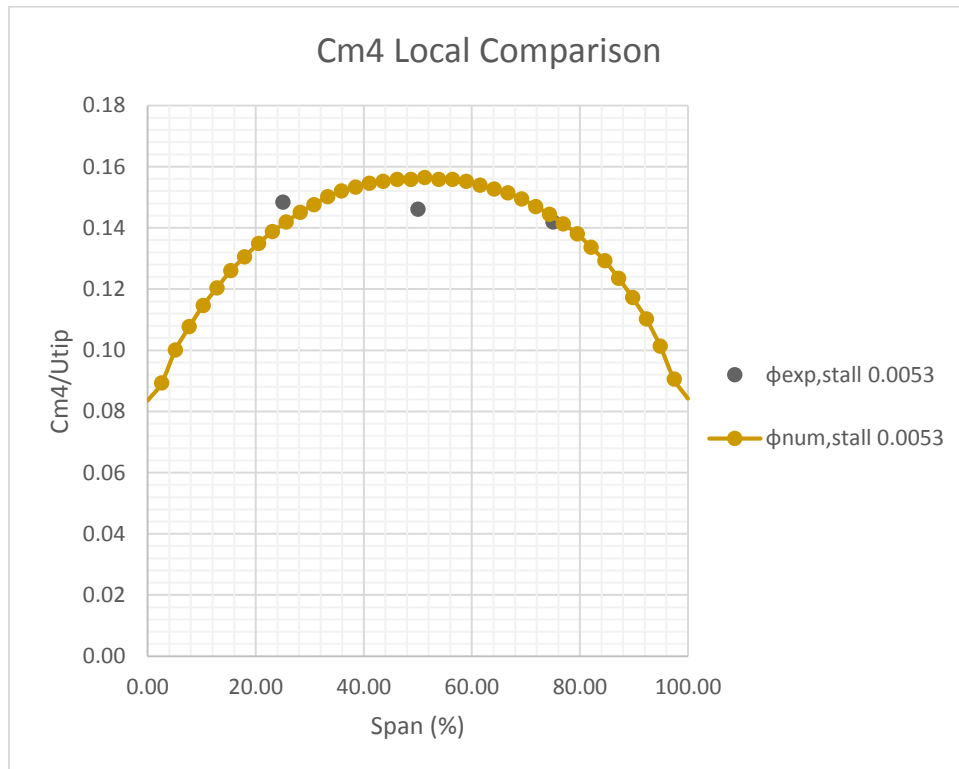


Figure 75: C_{m4} Comparison for Compressor 7 at 13100 RPM Stall Point

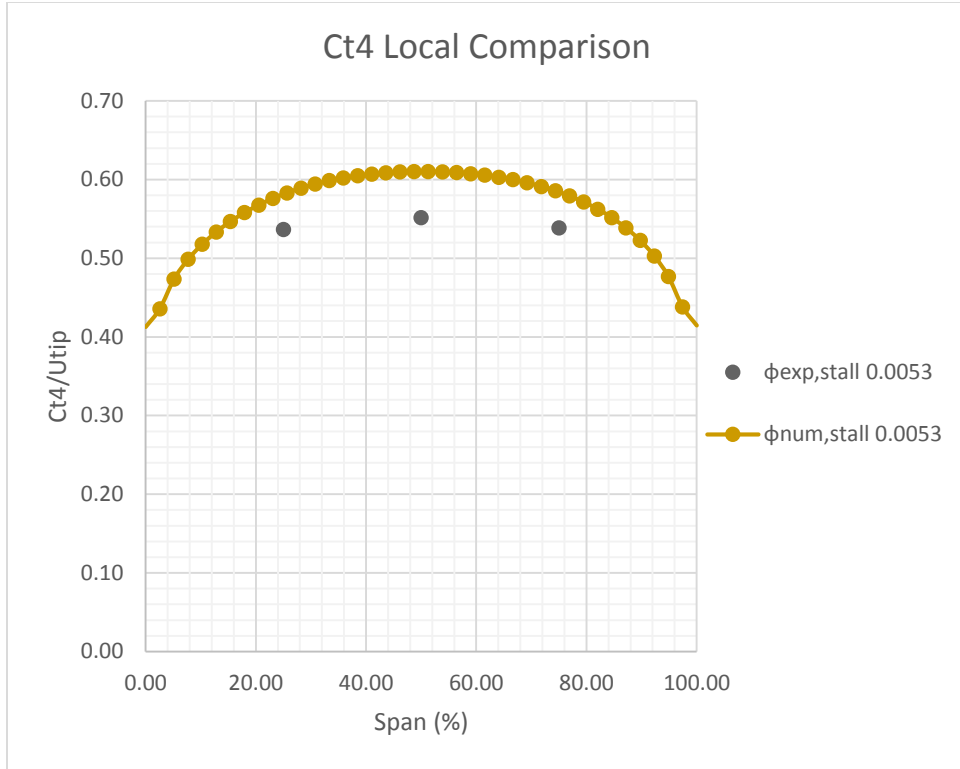


Figure 76: C₄ Comparison for Compressor 7 at 13100 RPM Stall Point

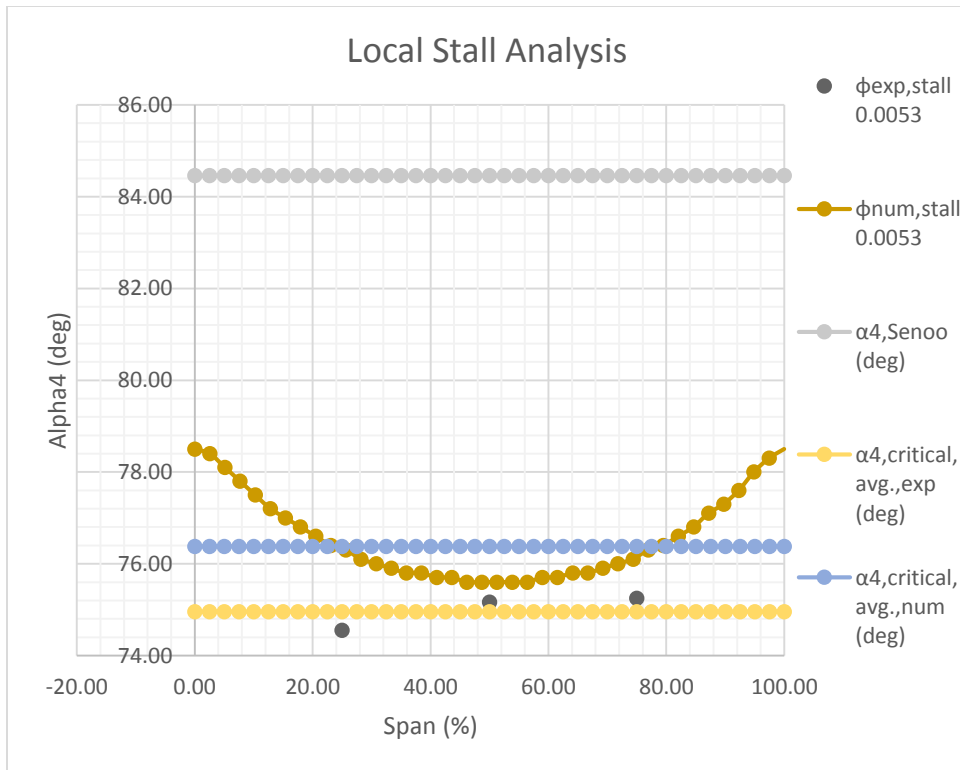


Figure 77: Stall Analysis for Compressor 7 at 13100 RPM Stall Point

6.3.7.2 Compressor 7 19240 RPM Results

Figure 78 – 80 provide the results for Compressor 7 at the 19240 RPM stall point. In Figure 78 it is found that the meridional velocity profiles show some agreement, but the degree of agreement is debatable. In Figure 79 one finds that the trends of the two tangential velocity profiles match, but the files do not have the same magnitude. In Figure 80 neither flow angle profile breaches the Senoo line.

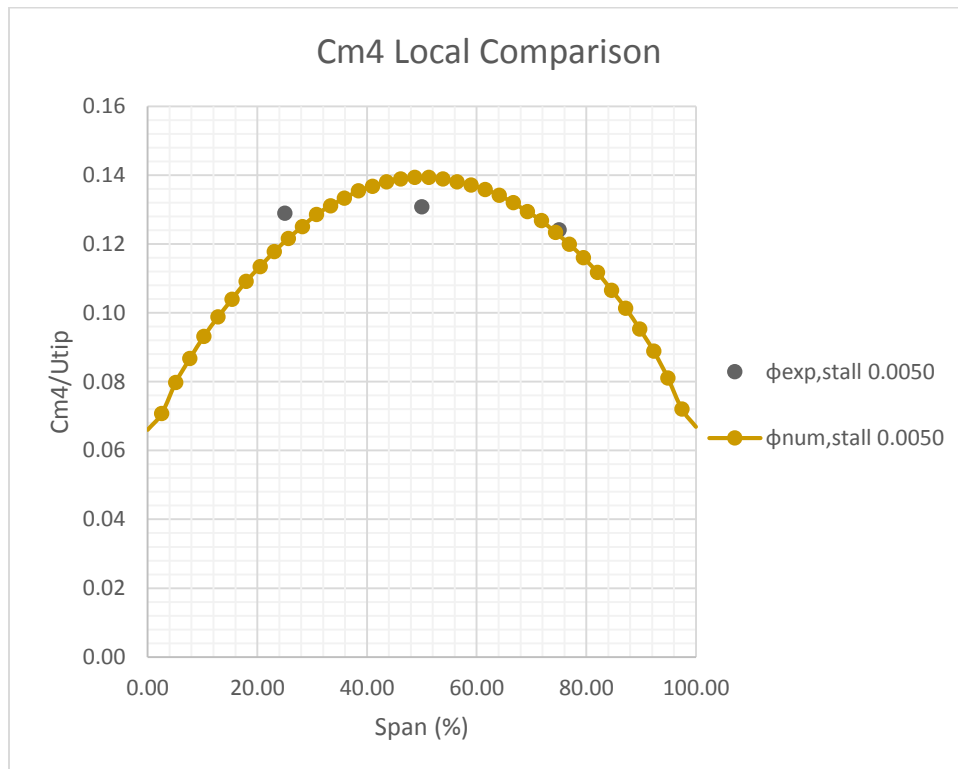


Figure 78: C_{m4} Comparison for Compressor 7 at 19240 RPM Stall Point

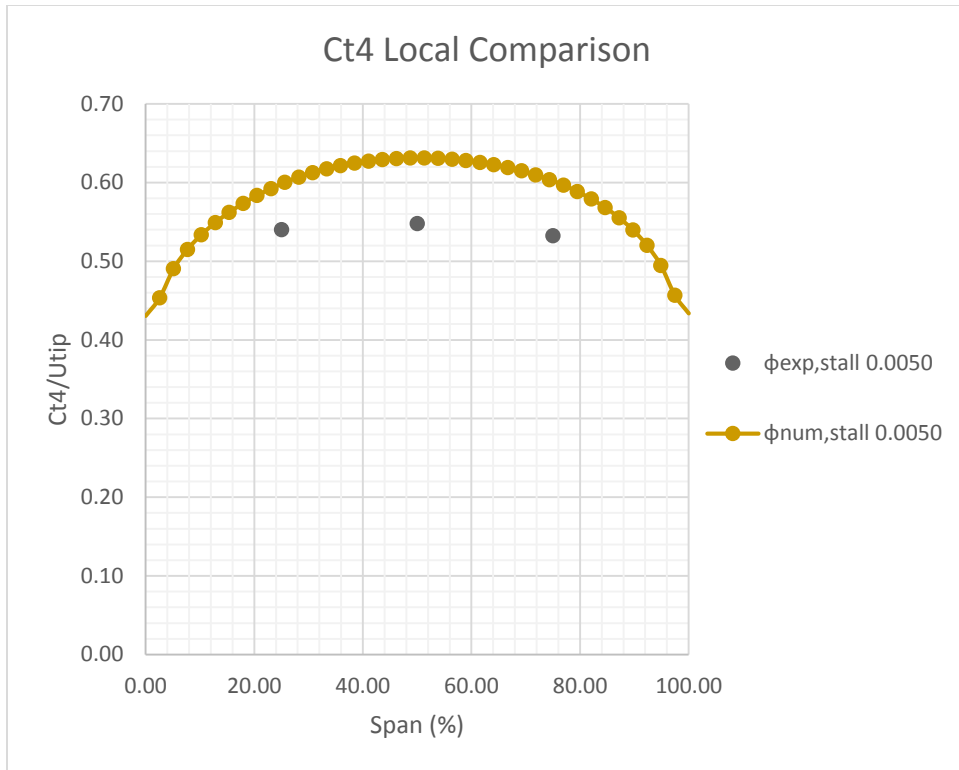


Figure 79: C_{t4} Comparison for Compressor 7 at 19240 RPM Stall Point

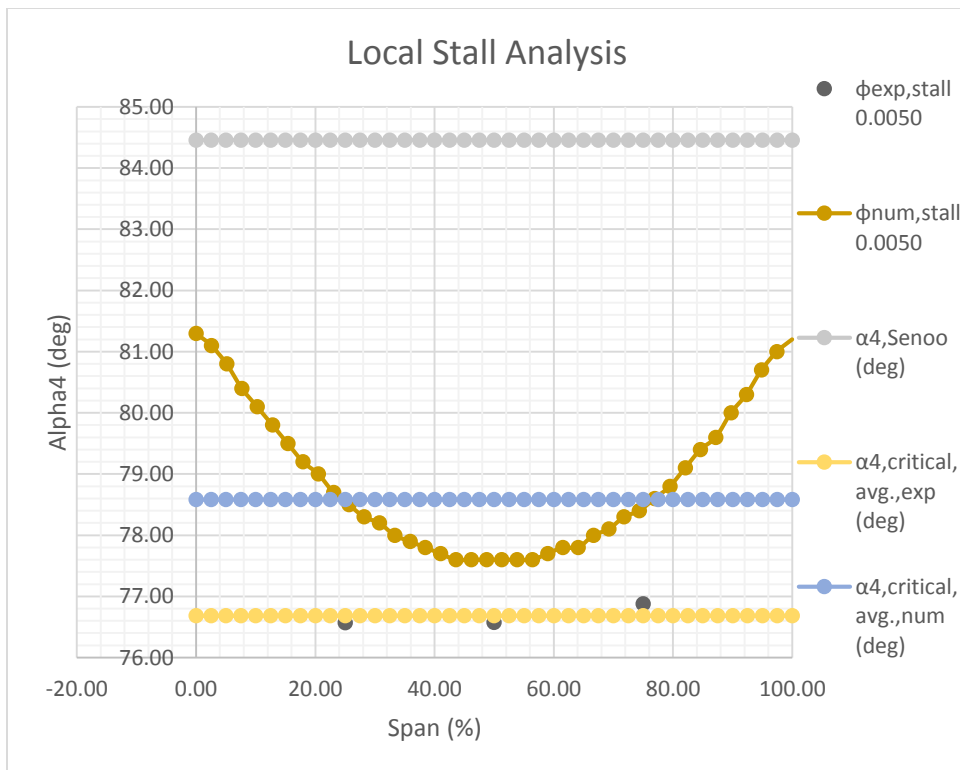


Figure 80: Stall Analysis for Compressor 7 at 19240 RPM Stall Point

6.3.7.3 Compressor 7 21870 RPM Results

In Figures 81 – 83 one finds that the results for Compressor 7 at the 21870 RPM stall point. Looking at Figure 81 shows that while the numerical meridional velocity profile is symmetric about the diffuser center the experimental profile is slightly distorted. The profiles do not really match in Figure 81 either. In Figure 82 one finds a symmetric numerical profile and distorted experimental profile, but the profiles are not in agreement. In Figure 83 it is found that the local flow angle profiles do not reach the Senoo line. If one looks at Figure 77, 80, and 83 one finds that the local maximum is at or above 78 degrees for each of the numerical plots. So, even though the Senoo line has not been breached the magnitudes of the angles are in agreement with Jansen's expectations for rotating stall onset in vaneless diffuser [15]. The experimental profiles confirm this by all being around 75 – 76 degrees which agrees with [15]. Even though the profiles don't reach the Senoo line rotating stall is still expected to onset, which the results support.

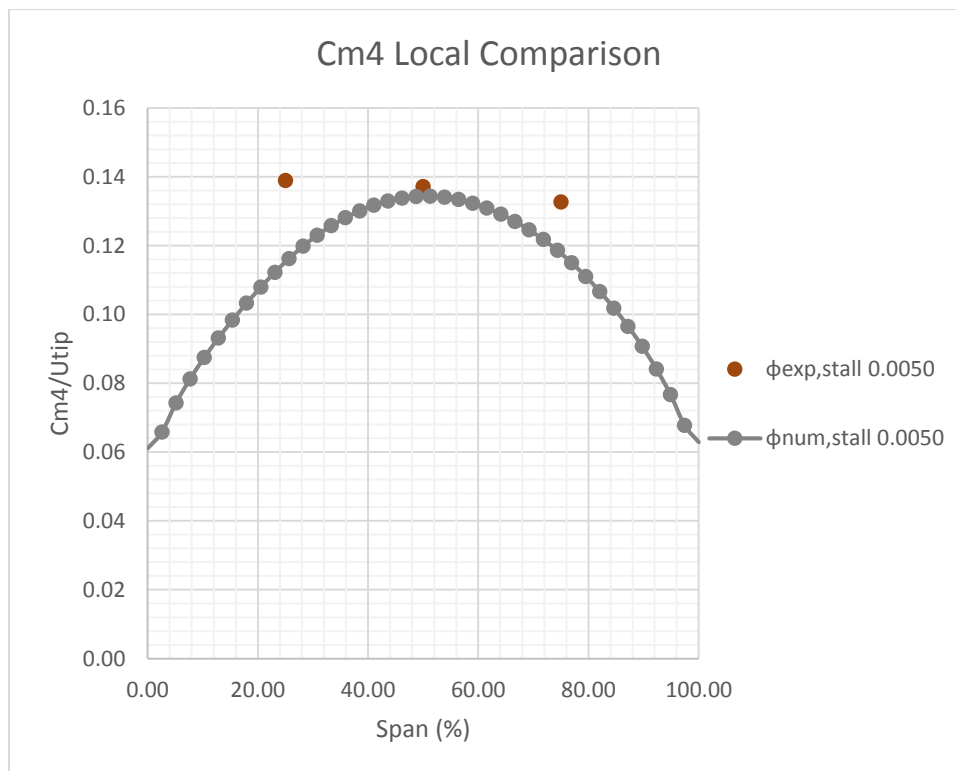


Figure 81: C_{m4} Comparison for Compressor 7 at 21870 RPM Stall Point

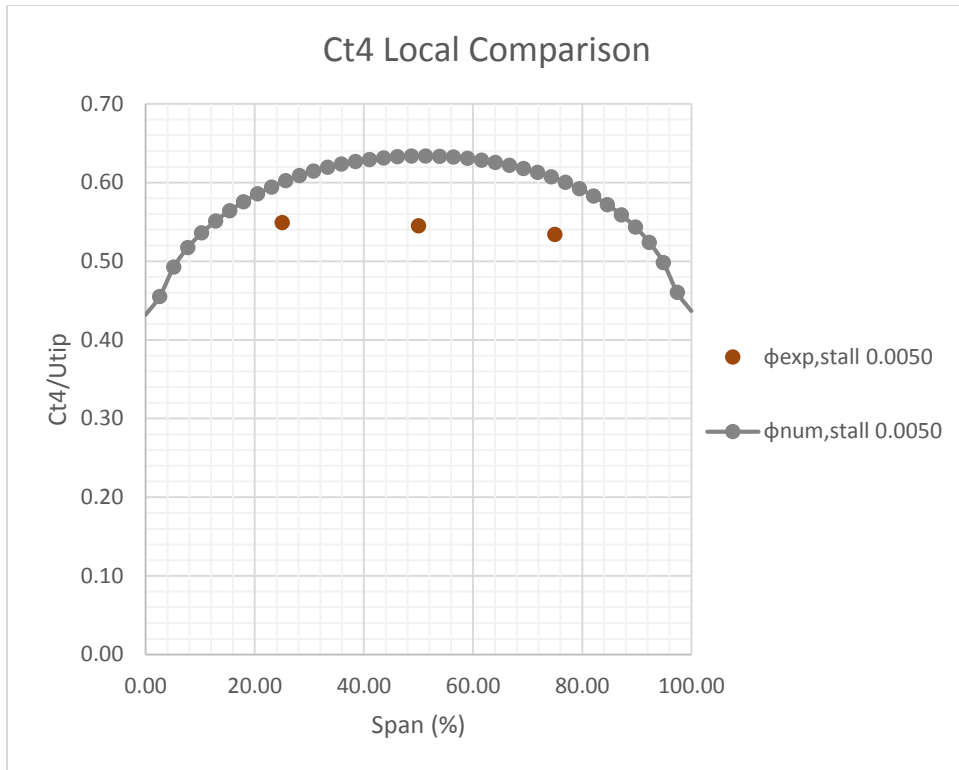


Figure 82: C₄ Comparison for Compressor 7 at 21870 RPM Stall Point

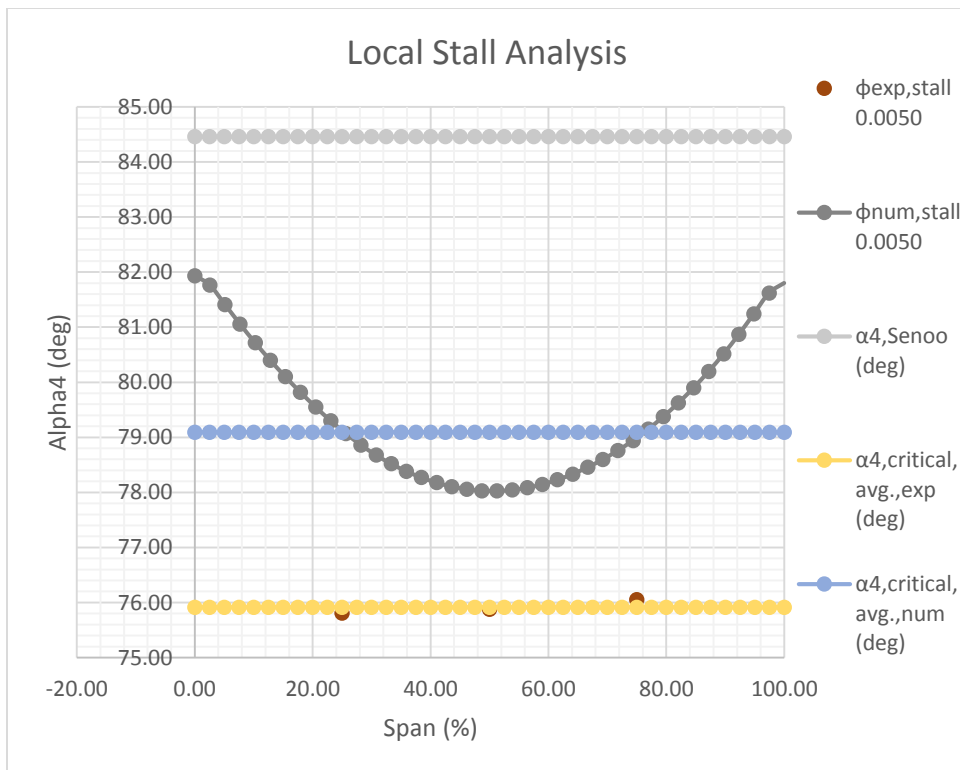


Figure 83: Stall Analysis for Compressor 7 at 21870 RPM Stall Point

6.3.8 Compressor 8 Profiles

6.3.8.1 Compressor 8 13100 RPM Results

Figures 84 – 86 show the results for Compressor 8 at the 13100 RPM stall point. In Figure 84 one finds a symmetric numerical profile and a distorted experimental profile that have a limited amount of agreement. In Figure 85 there is agreement in the trends of the tangential velocity plots, but not the magnitudes. In Figure 86 it is clear that neither of the local flow angle profiles breach the Senoo line.

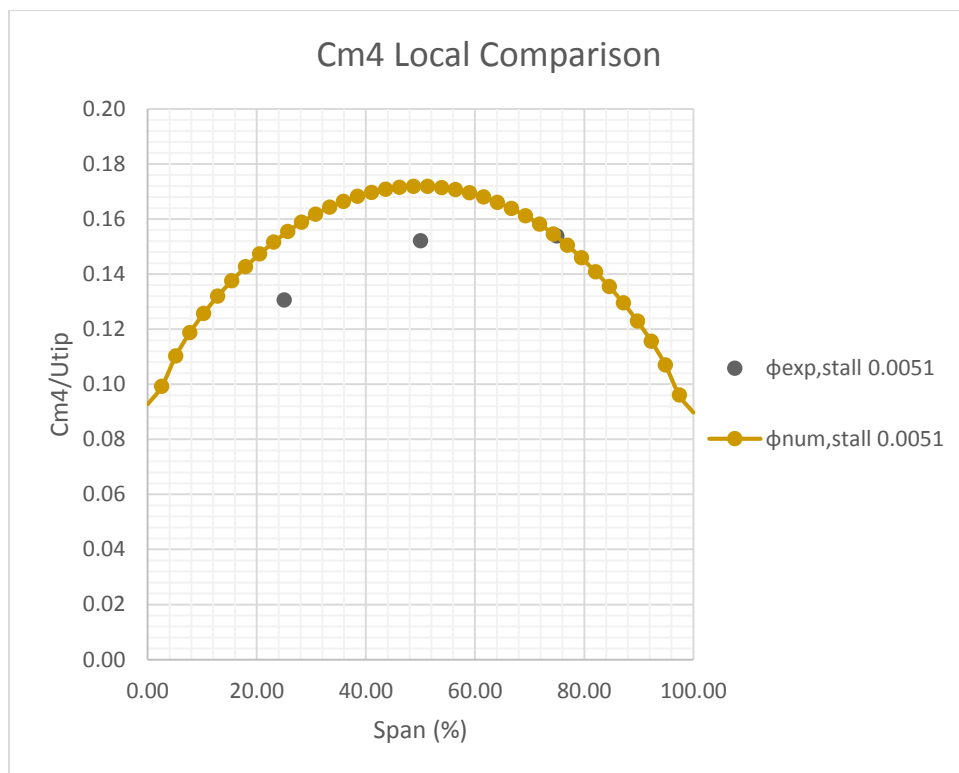


Figure 84: C_{m4} Comparison for Compressor 8 at 13100 RPM Stall Point

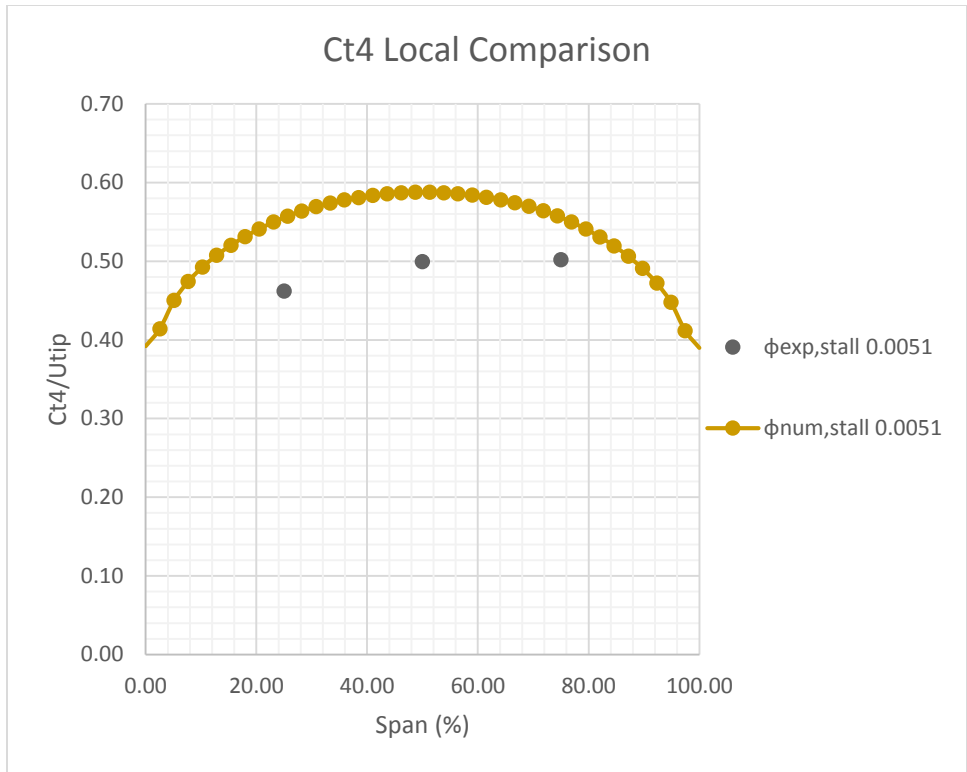


Figure 85: C_{t4} Comparison for Compressor 8 at 13100 RPM Stall Point

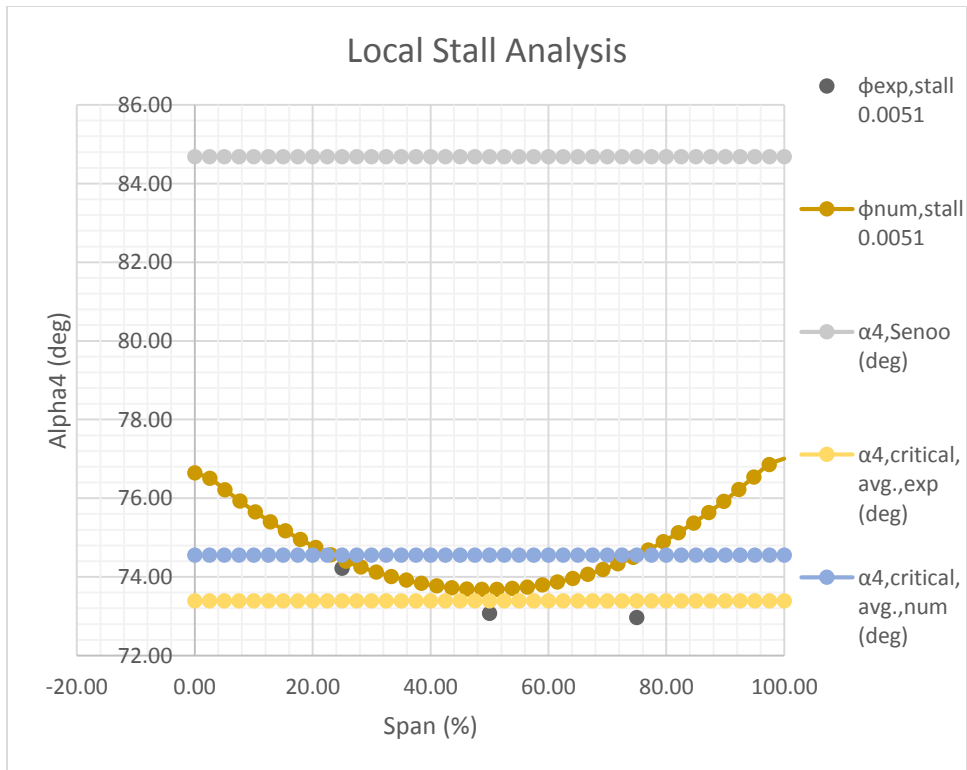


Figure 86: Stall Analysis for Compressor 8 at 13100 RPM Stall Point

6.3.8.2 Compressor 8 19240 RPM Results

Figures 87 – 89 provide the results for Compressor 8 at the 19240 RPM stall point. In Figure 87 the numerical profile is symmetric about the center of the diffuser, while the experimental profile is distorted. This is the same behavior as that seen in Figure 84 at 13100 RPM. In Figure 88 the tangential velocity plots are a closer match than those seen at 13100 RPM, but still do have the strong agreement that was seen for other compressors. In Figure 89 one finds that the flow angle profiles do not breach the Senoo line.

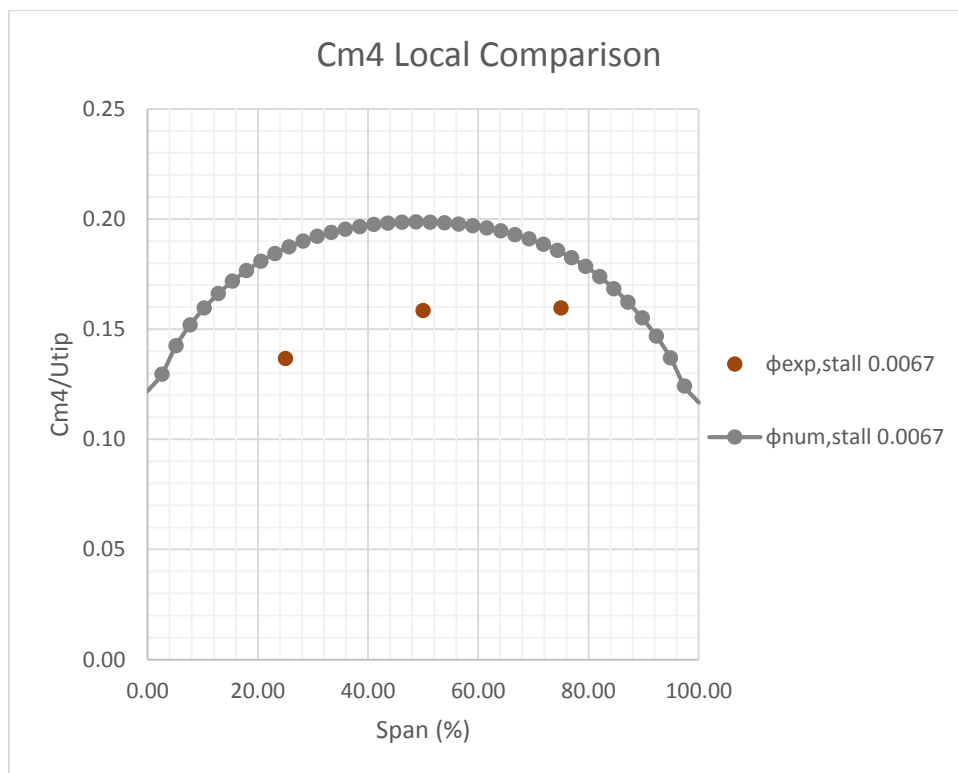


Figure 87: C_{m4} Comparison for Compressor 8 at 19240 RPM Stall Point

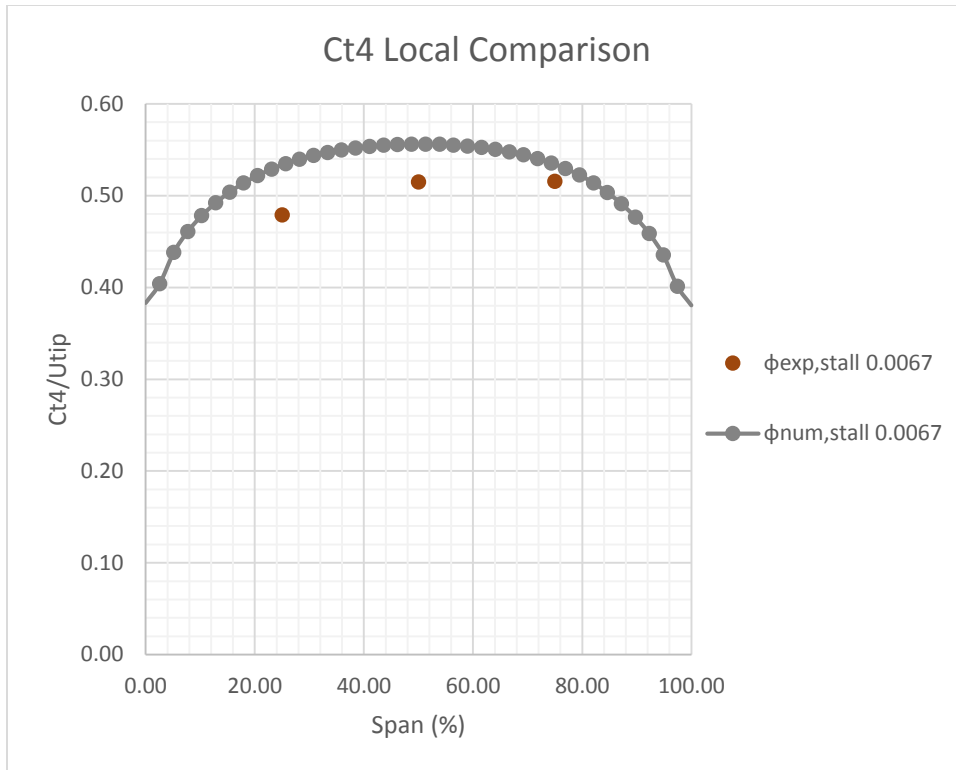


Figure 88: C_{t4} Comparison for Compressor 8 at 19240 RPM Stall Point

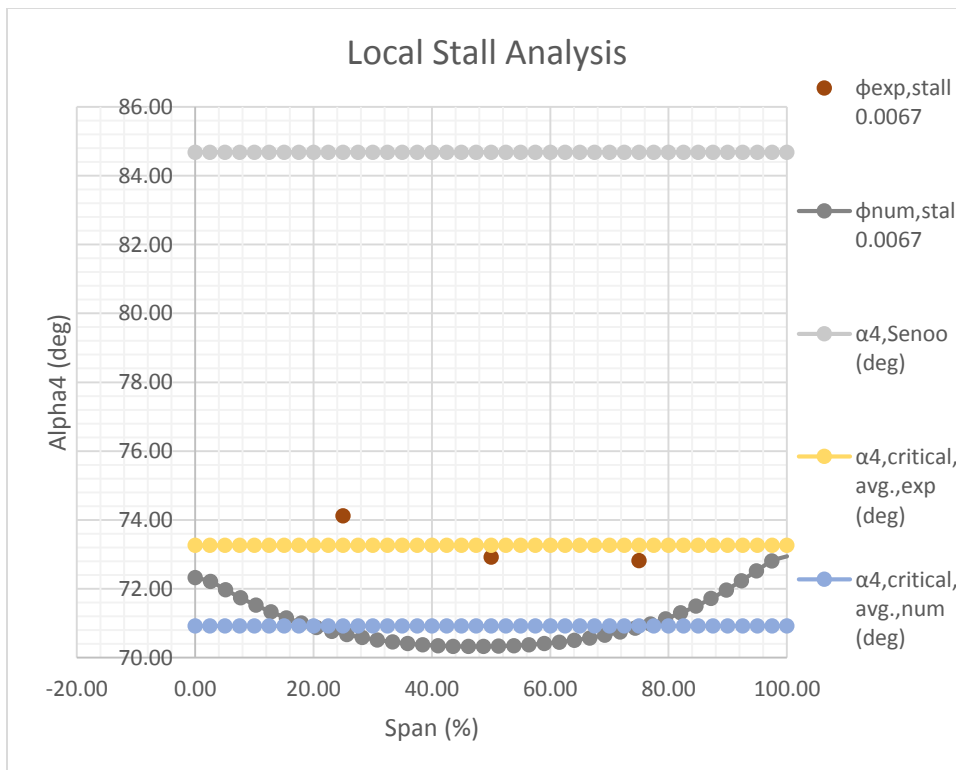


Figure 89: Stall Analysis for Compressor 8 at 19240 RPM Stall Point

6.3.8.3 Compressor 8 21870 RPM Results

Figures 90 – 92 provide the results for Compressor 8 at the 21870 RPM stall point. In Figure 90 the numerical profile is symmetric about the center of the diffuser, while the experimental profile is distorted. This is the same behavior as that seen in Figures 84 and 87. In Figure 91 the tangential velocity plots are a closer match than those seen in Figures 85 and 88, but still do have the strong agreement that was seen for other compressors. In Figure 92 one finds that the flow angle profiles do not breach the Senoo line.

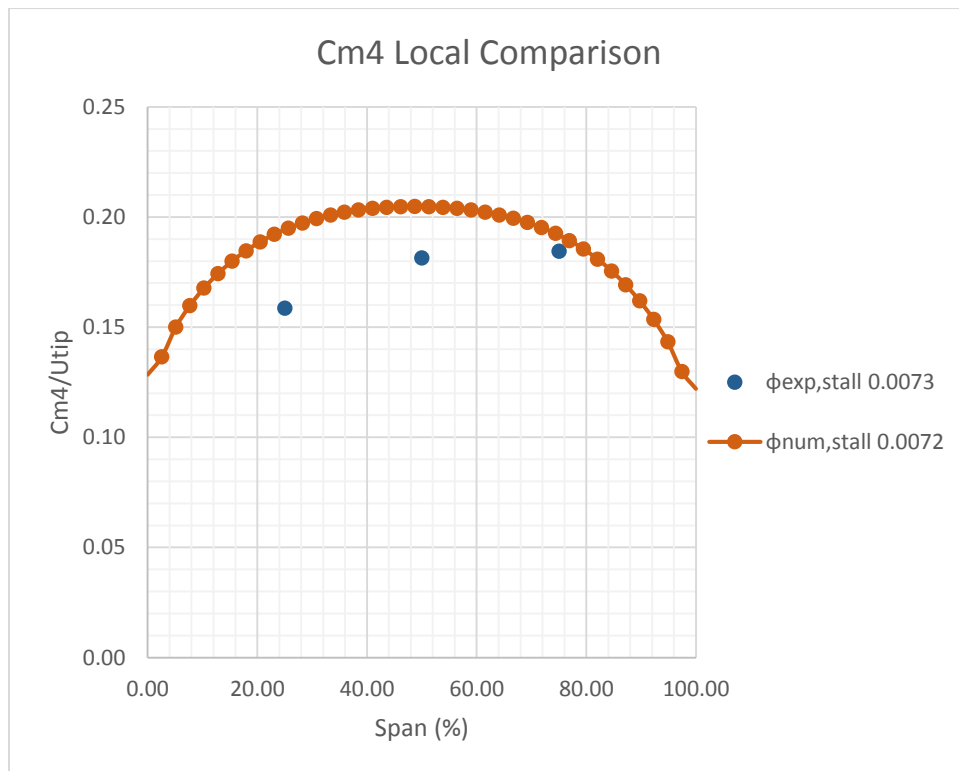


Figure 90: C_{m4} Comparison for Compressor 8 at 21870 RPM Stall Point

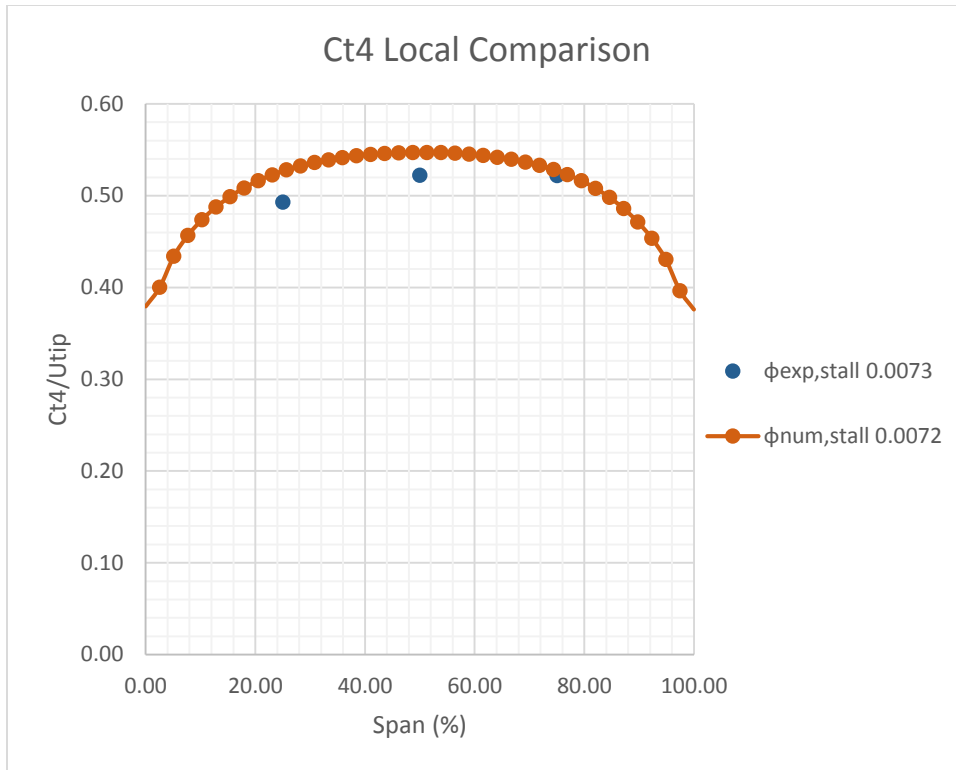


Figure 91: C_{t4} Comparison for Compressor 8 at 21870 RPM Stall Point

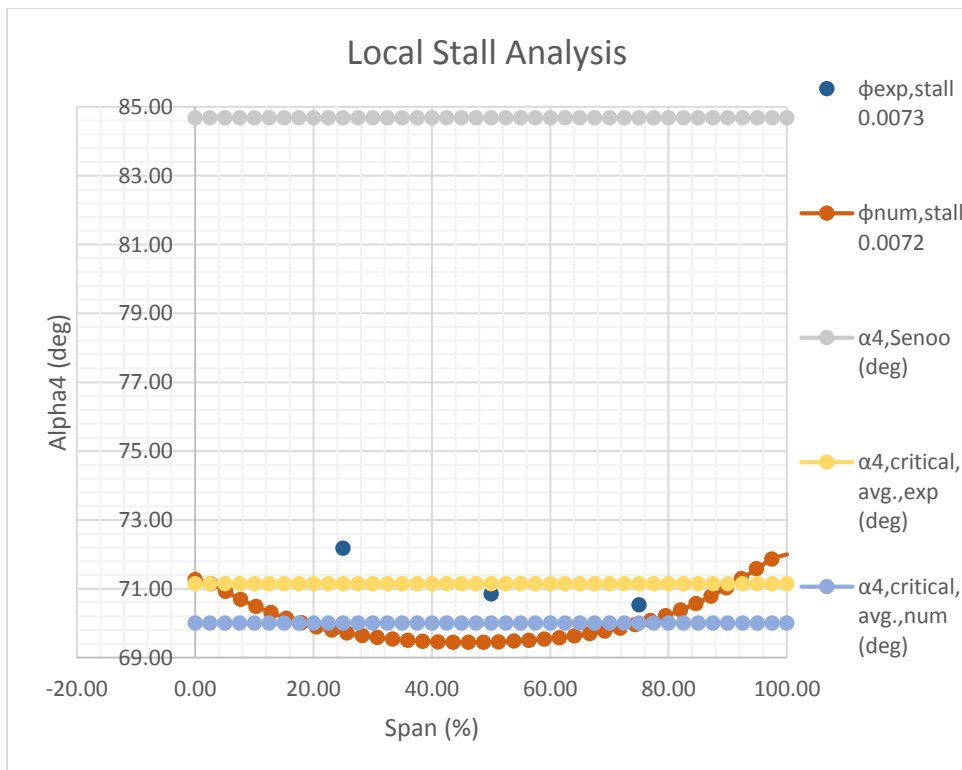


Figure 92: Stall Analysis for Compressor 8 at 21870 RPM Stall Point

6.3.9 Compressor 9 Profiles

6.3.9.1 Compressor 9 13100 RPM Results

Figures 93 – 95 show the results for Compressor 9 at the 13100 RPM stall point. In Figure 93 one finds that the experimental and numerical meridional velocity plots are ~180 degrees out of phase. However, the two plots do appear to have a similar magnitude and structure. In Figure 94 the tangential velocity plots appear to have some agreement, though not a perfect match. In Figure 95 it is found that the local flow angle is 0.27 degrees from the Senoo line. Based on the work in note 8 (pg. 52) it is an accurate assumption to claim this as a breach of the Senoo line. This is because 0.27 degrees represents an approximate mass flow difference of 3%, which is close enough in experimental circumstances to be considered a match.

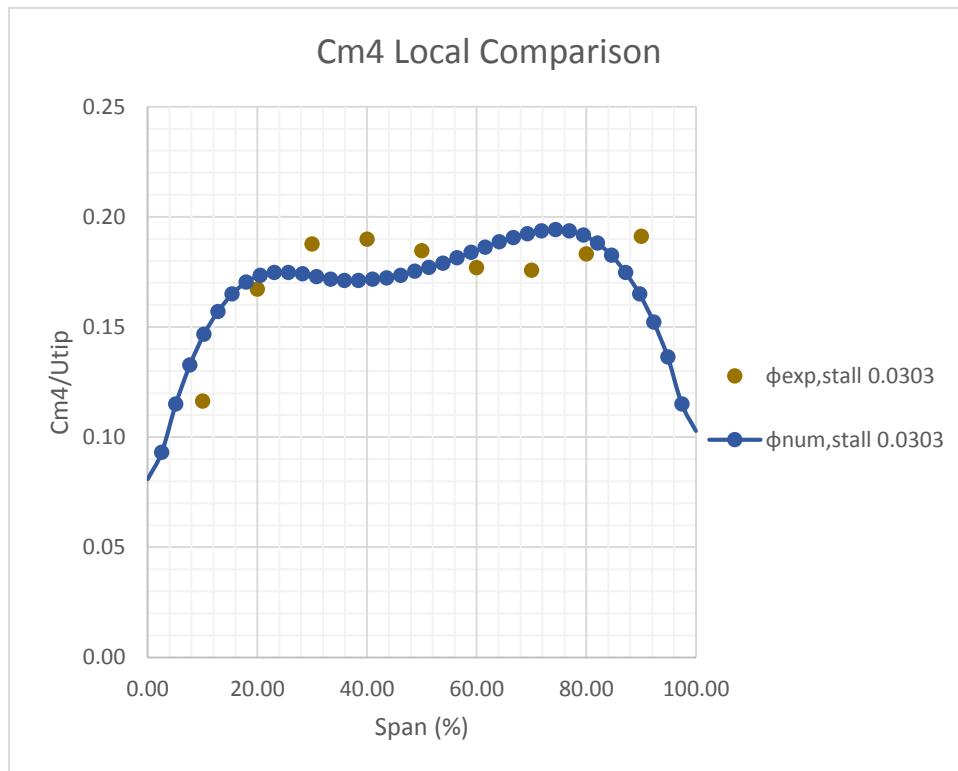


Figure 93: C_{m4} Comparison for Compressor 9 at 13100 RPM Stall Point

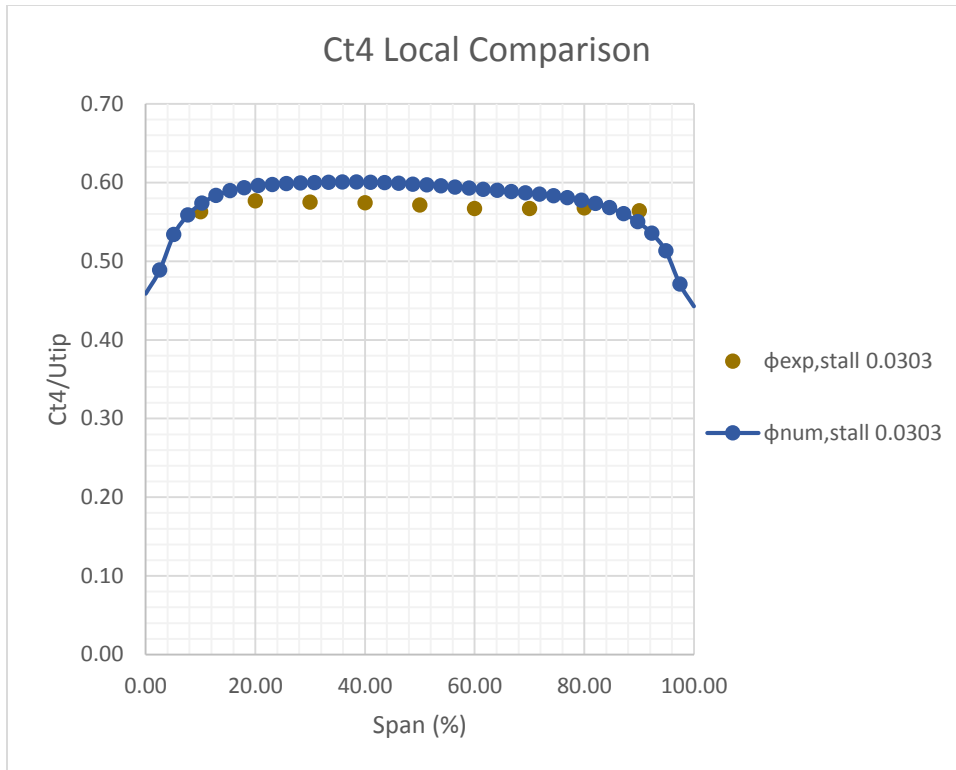


Figure 94: C₄ Comparison for Compressor 9 at 13100 RPM Stall Point

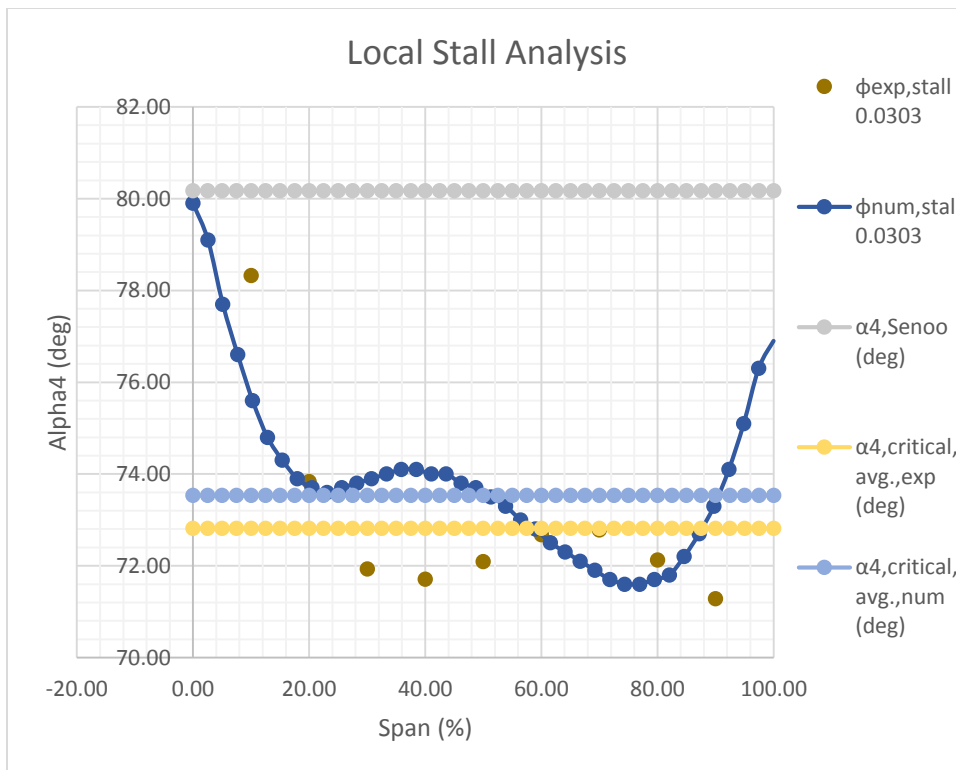


Figure 95: Stall Analysis for Compressor 9 at 13100 RPM Stall Point

6.3.9.2 Compressor 9 19240 RPM Results

Figures 96 – 98 provide the results for Compressor 9 at the 19240 RPM stall point. In Figure 96 the same out of phase behavior is seen in the meridional velocity plots as in Figure 93, however the structure and magnitude are similar. In Figure 97 one finds a qualitative agreement in the trends of the tangential velocity plots. However, the magnitudes do not match. In Figure 98 it is found that the numerical local flow angle plot is 0.37 degrees from the Senoo line. As was the case in Figure 95 this is considered to be close enough to consider a breach of the Senoo line.

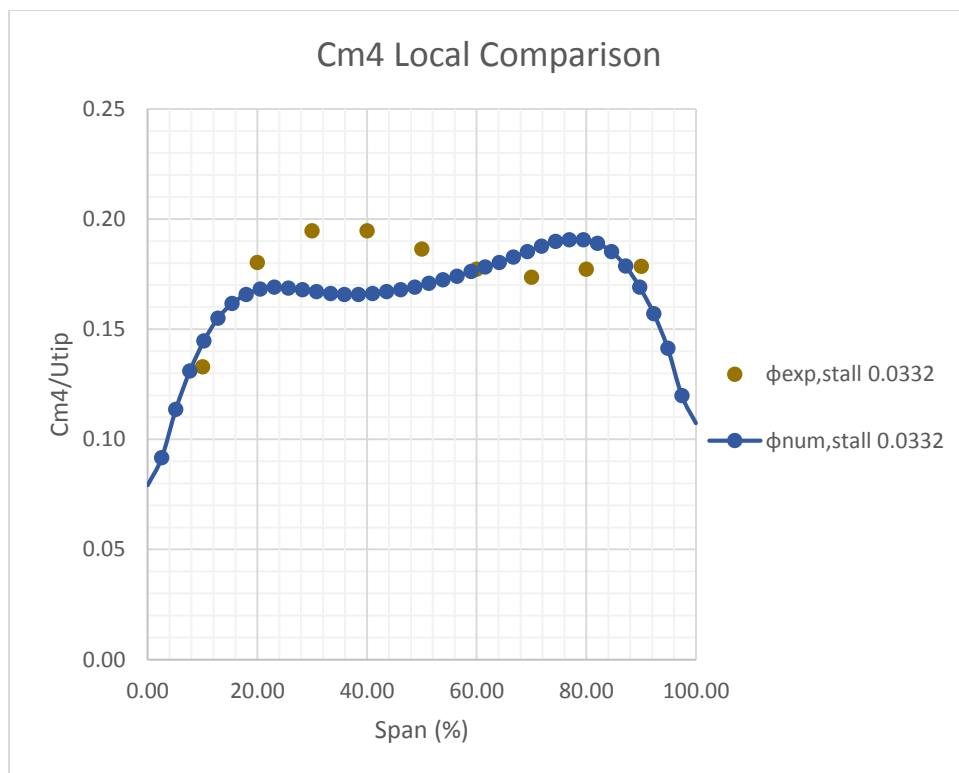


Figure 96: C_{m4} Comparison for Compressor 9 at 19240 RPM Stall Point

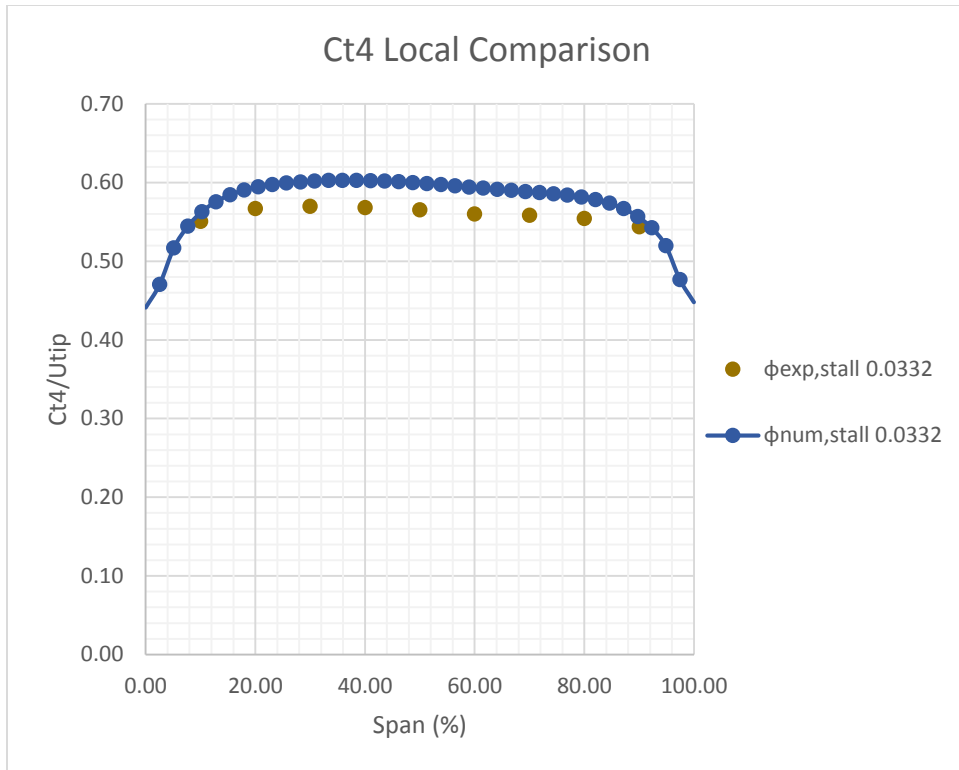


Figure 97: C₄ Comparison for Compressor 9 at 19240 RPM Stall Point

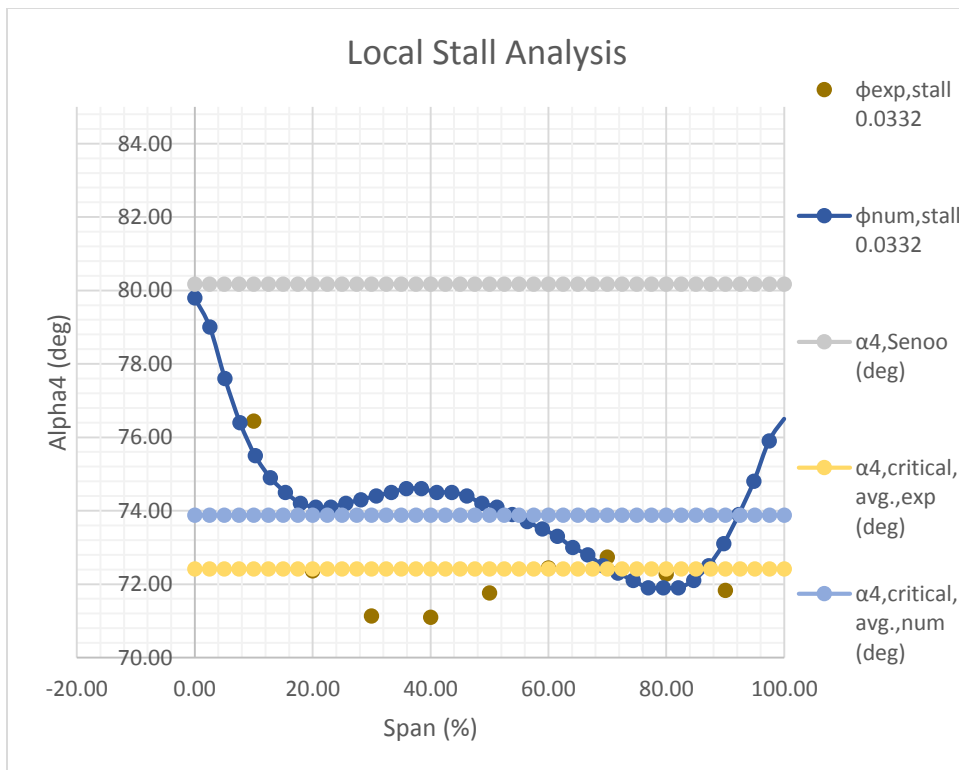


Figure 98: Stall Analysis for Compressor 9 at 19240 RPM Stall Point

6.3.9.3 Compressor 9 21870 RPM Results

Figures 99 – 101 provide the results for Compressor 9 at the last stable flow point at 21870 RPM. At 21870 RPM Compressor 9 did not experience rotating stall. However, in Figure 99 one finds that the numerical simulation was able to capture localized flow reversal. This is an important result because it shows that the assertion of Senoo and Kinoshita in [34] that localized flow reversal leads to rotating stall is not always accurate. Here no rotating stall onset is observed, but there is a flow instability forming because the compressor is about to experience surge. In Figure 100 one finds matching trends between the numerical and experimental tangential velocity plots, but a lack of agreement in magnitude. In Figure 101 both the experimental and numerical flow angle plots cross the Senoo line, but that would be expected seeing as how the stability of the vaneless diffuser flow is breaking down.

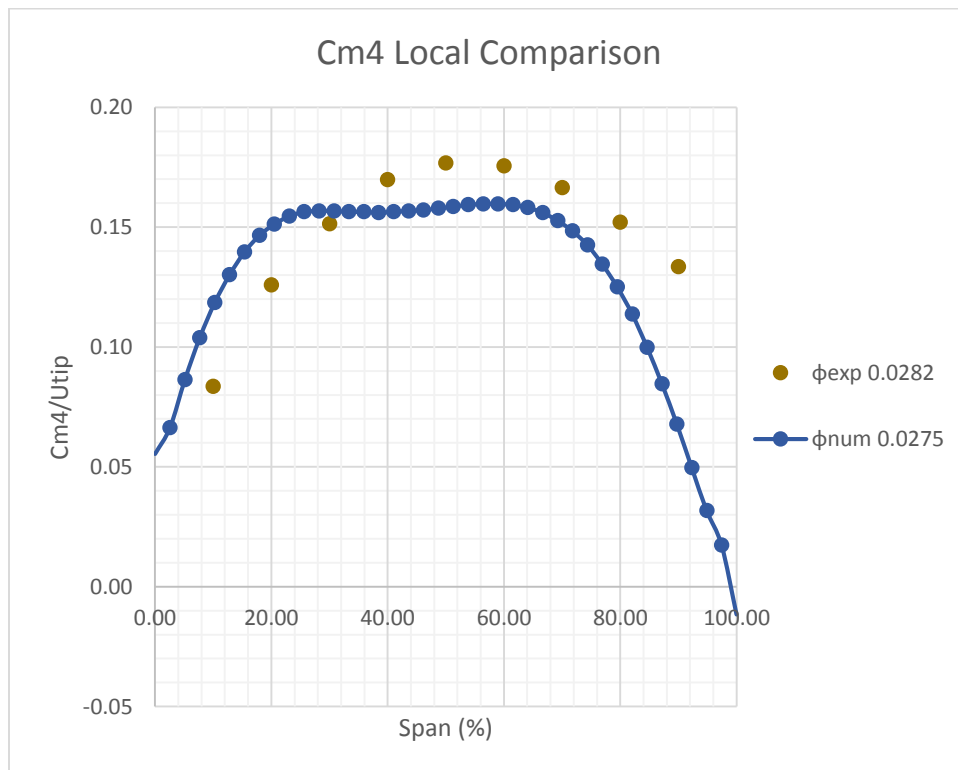


Figure 99: C_{m4} Comparison for Compressor 9 at 21870 RPM Last Stable Flow Point

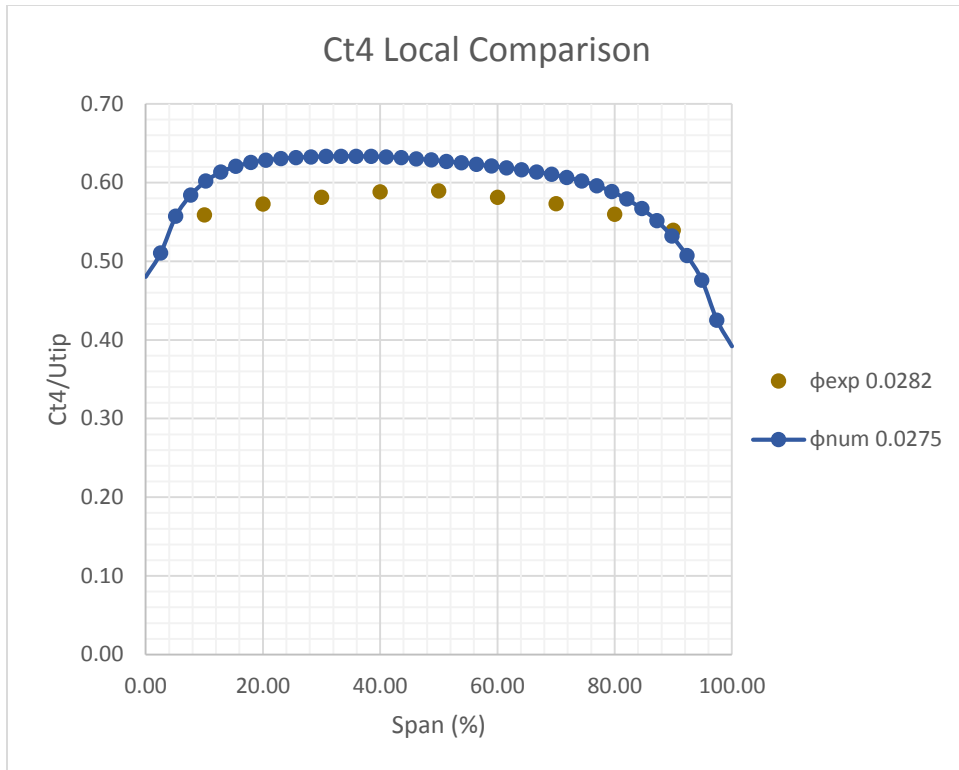


Figure 100: C_{t4} Comparison for Compressor 9 at 21870 RPM Last Stable Flow Point

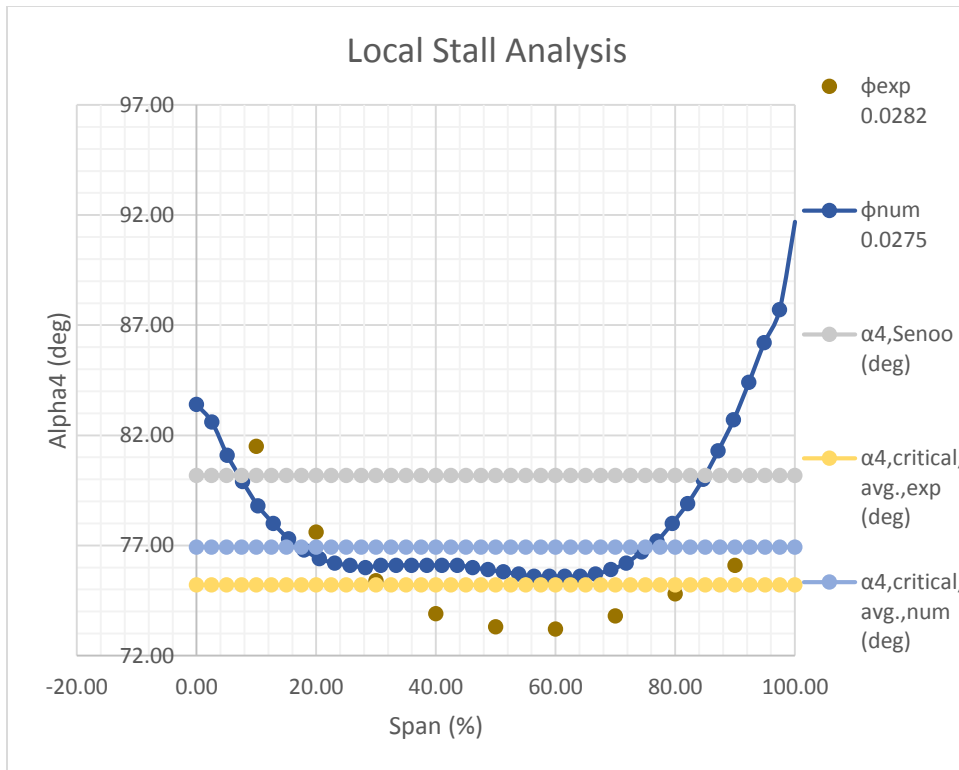


Figure 101: Stall Analysis for Compressor 9 at 21870 RPM Last Stable Flow Point

6.3.10 Compressor 10 Profiles

Compressor 10 did not experience rotating stall. As with Compressor 6 the values for Compressor 10 are presented at the last stable operating point on the compressor map. There is still information that can be gleaned from these cases.

6.3.10.1 Compressor 10 13100 RPM Results

Figures 102 – 104 provide the results for Compressor 10 at the last stable flow point for the 13100 RPM speed line. In Figure 102 there appears to be agreement between the meridional velocity plots, though the magnitude of the plots are not in perfect agreement. In Figure 103 there is a strong agreement between the tangential velocity plots. In Figure 104 one finds that the numerical local flow angle plot breaches the Senoo line.

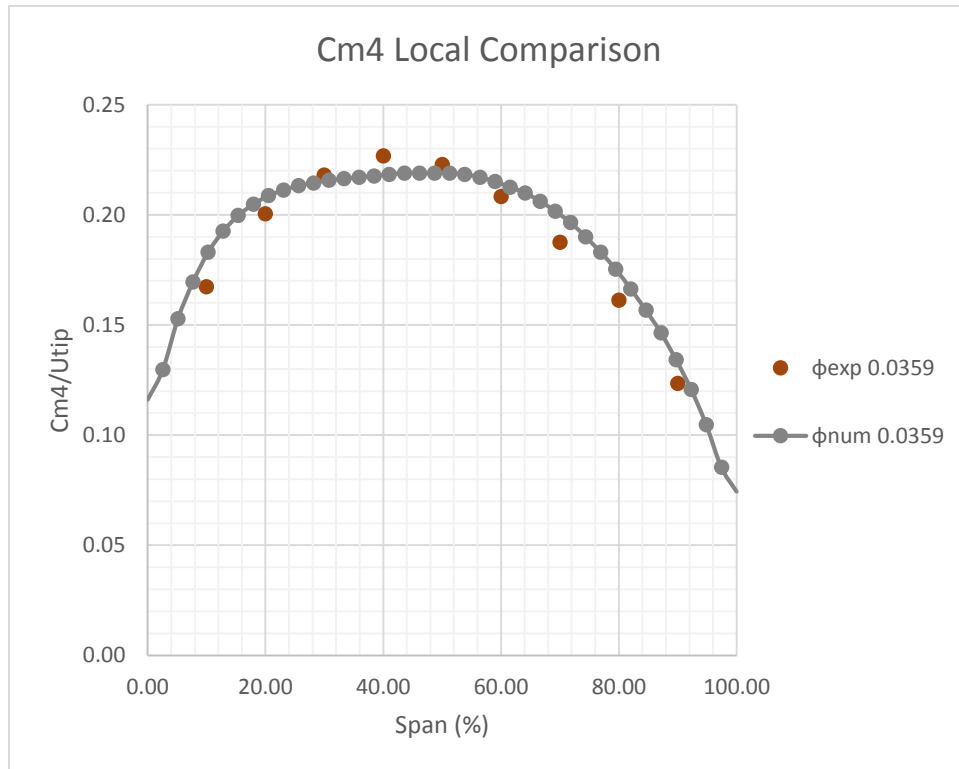


Figure 102: C_{m4} Comparison for Compressor 10 at 13100 RPM Last Stable Flow Point

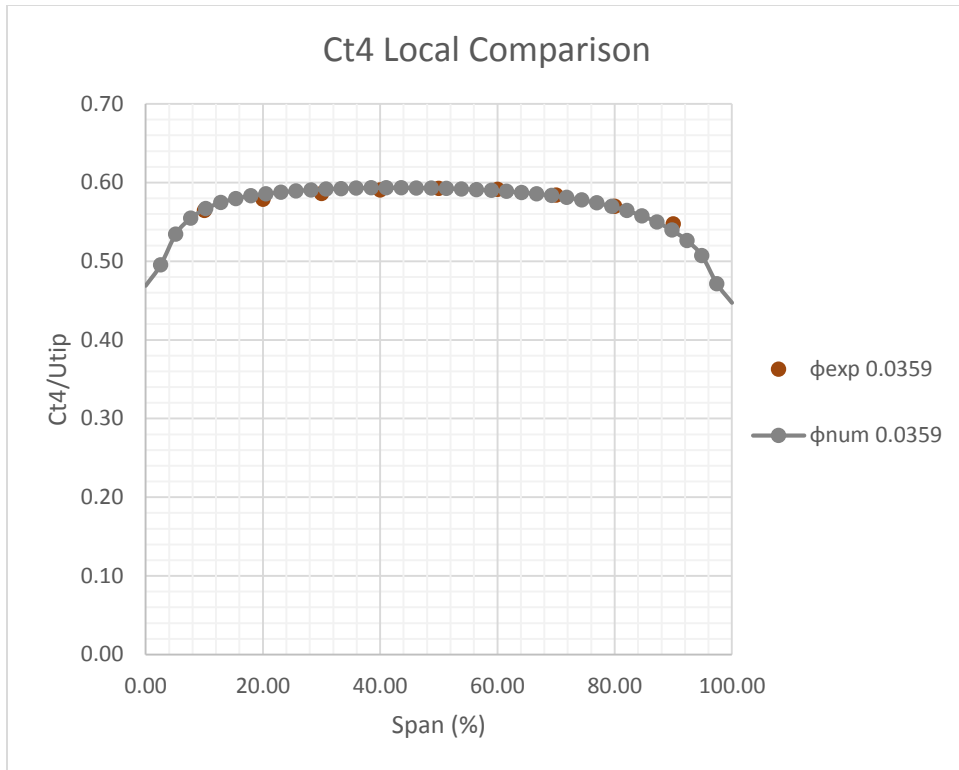


Figure 103: C_{t4} Comparison for Compressor 10 at 13100 RPM Last Stable Flow Point

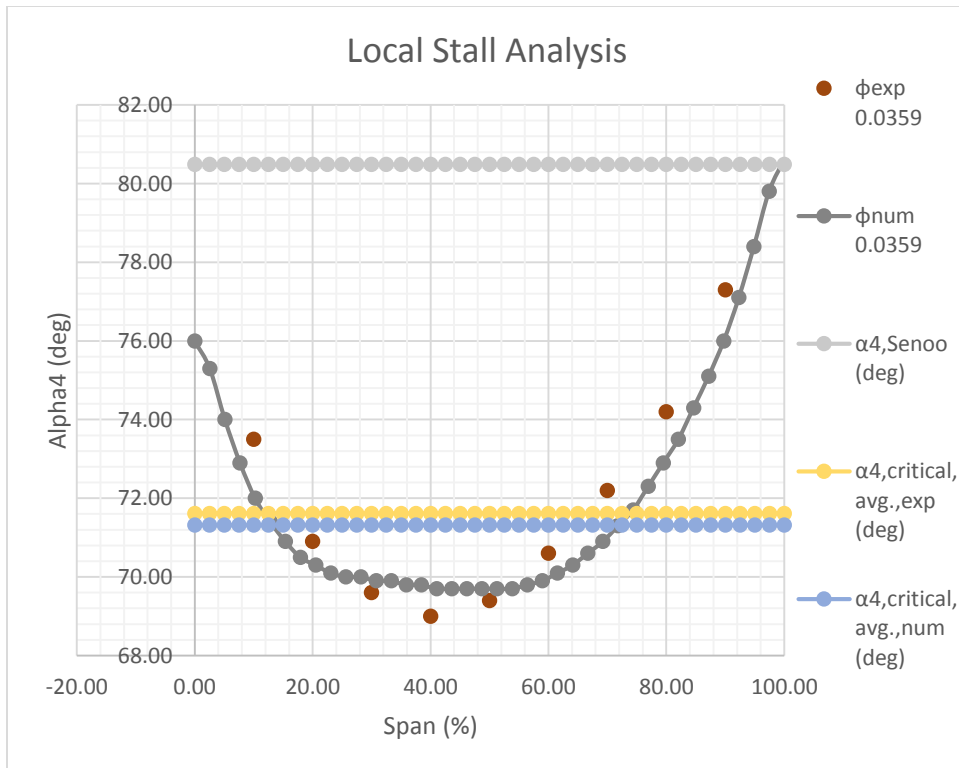


Figure 104: Stall Analysis for Compressor 10 at 13100 RPM Last Stable Flow Point

6.3.10.2 Compressor 10 19240 RPM Results

Figures 105 – 107 provide the results for Compressor 10 at the last stable flow point for the 19240 RPM speed line. In Figure 105 one finds limited agreement between the meridional velocity plots. Overall, the numerical profile is less distorted. In Figure 106 there is strong agreement between the numerical and experimental tangential velocity profiles. In Figure 107 neither the numerical profile nor the experimental profile breaches the Senoo line. This is a bit unexpected since a breach was seen at 13100 RPM, but not surprising due to the movement of the last stable point to a position of high flow coefficient, ϕ , as the running speed increases [10].

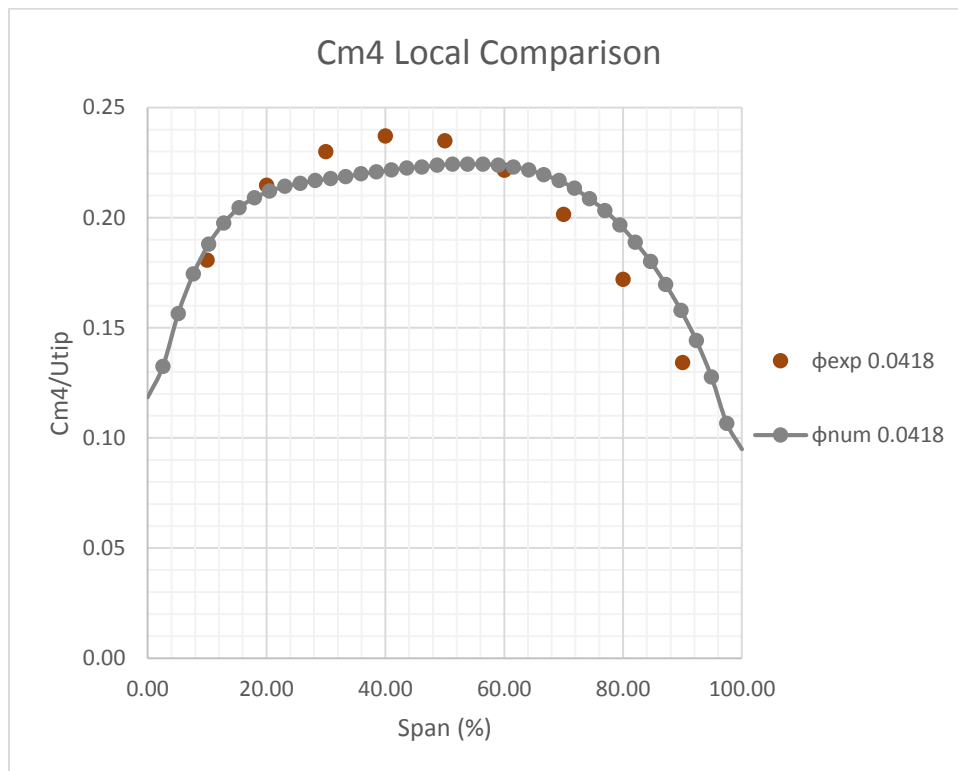


Figure 105: C_{m4} Comparison for Compressor 10 at 19240 RPM Last Stable Flow Point

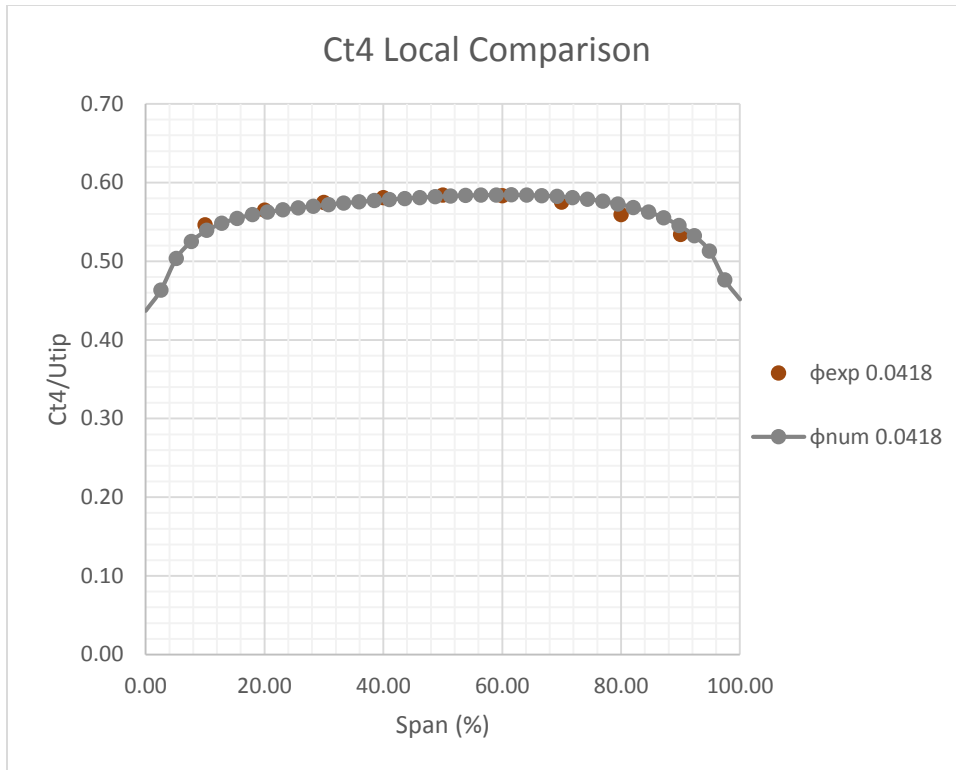


Figure 106: C_{t4} Comparison for Compressor 10 at 19240 RPM Last Stable Flow Point

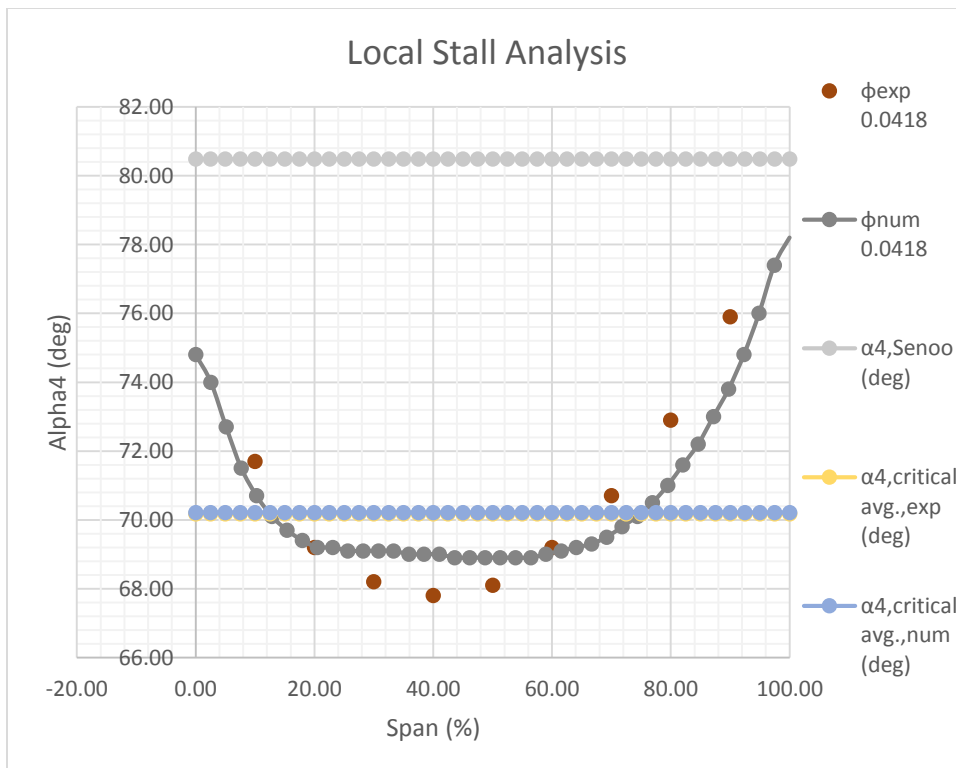


Figure 107: Stall Analysis for Compressor 10 at 19240 RPM Last Stable Flow Point

6.3.10.3 Compressor 10 21870 RPM Results

Figures 108 – 110 provide the results for Compressor 10 at the last stable flow point for the 21870 PRM speed line. In Figure 108 there is some agreement between the numerical and experimental meridional velocity profiles. However, that agreement is lacking for a span range of 10% - 25% on the hub side of the diffuser. In Figure 109 the overall trends of the tangential velocity profiles match, but the magnitudes are quite different. In Figure 110 neither of the flow angle profiles crosses the Senoo line. Again, this is likely because of the shrinking of the operating range caused by the increase in running speed [10]. However, the numerical plot was closer to breaching the Senoo line at 21870 RPM than at 19240 RPM.

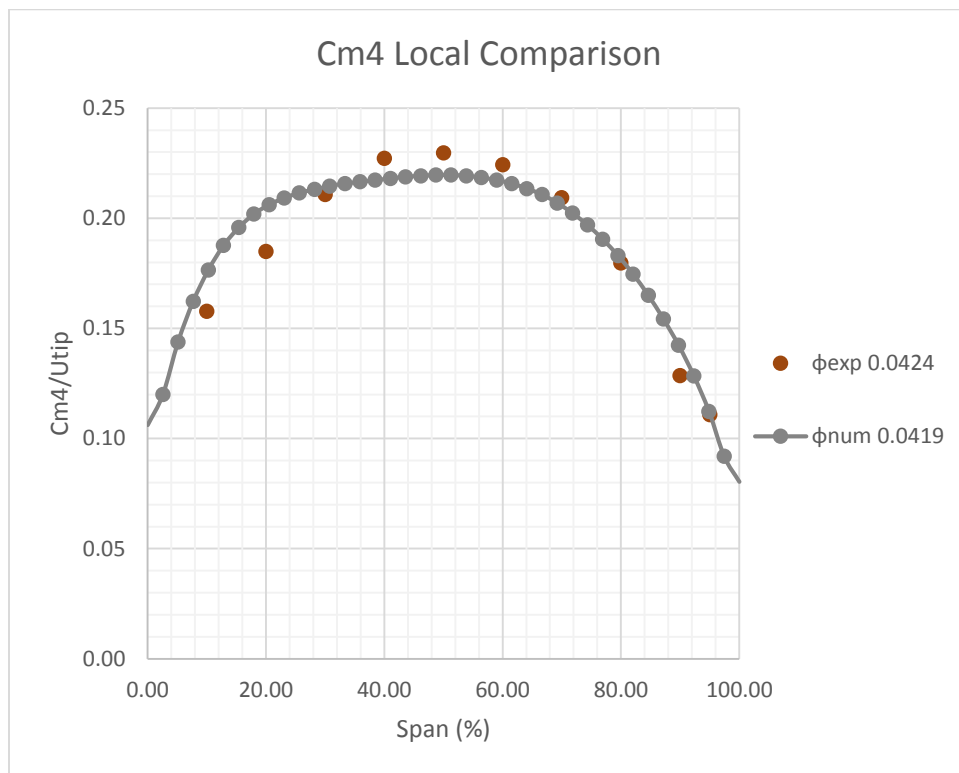


Figure 108: Cm4 Comparison for Compressor 10 at 21870 RPM Last Stable Flow Point

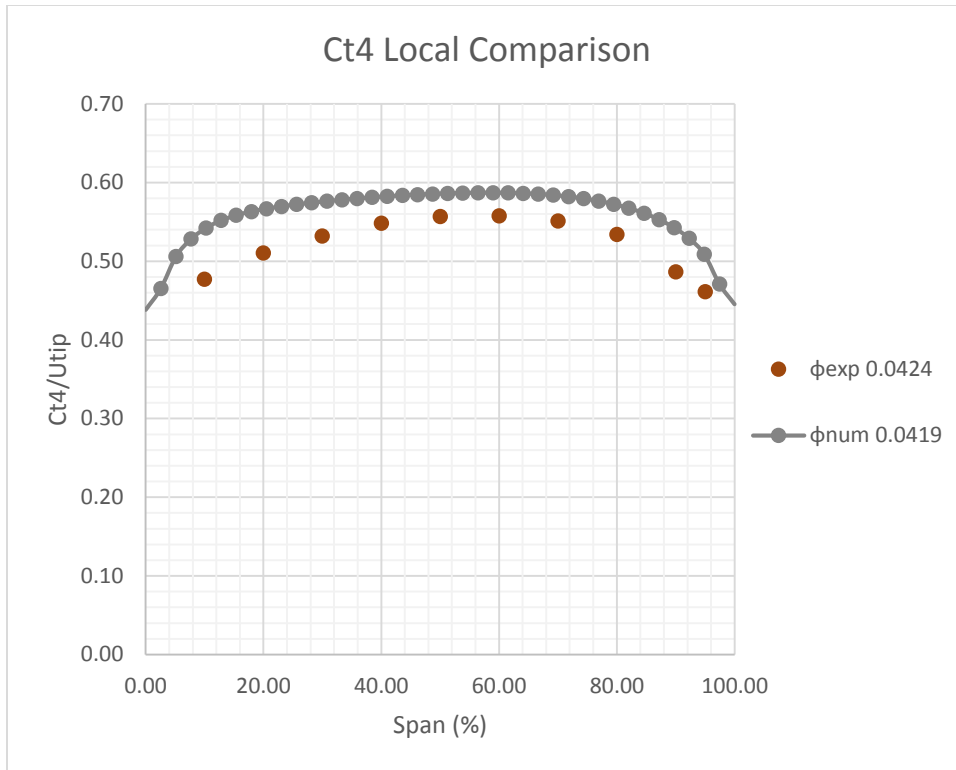


Figure 109: C_{t4} Comparison for Compressor 10 at 21870 RPM Last Stable Flow Point

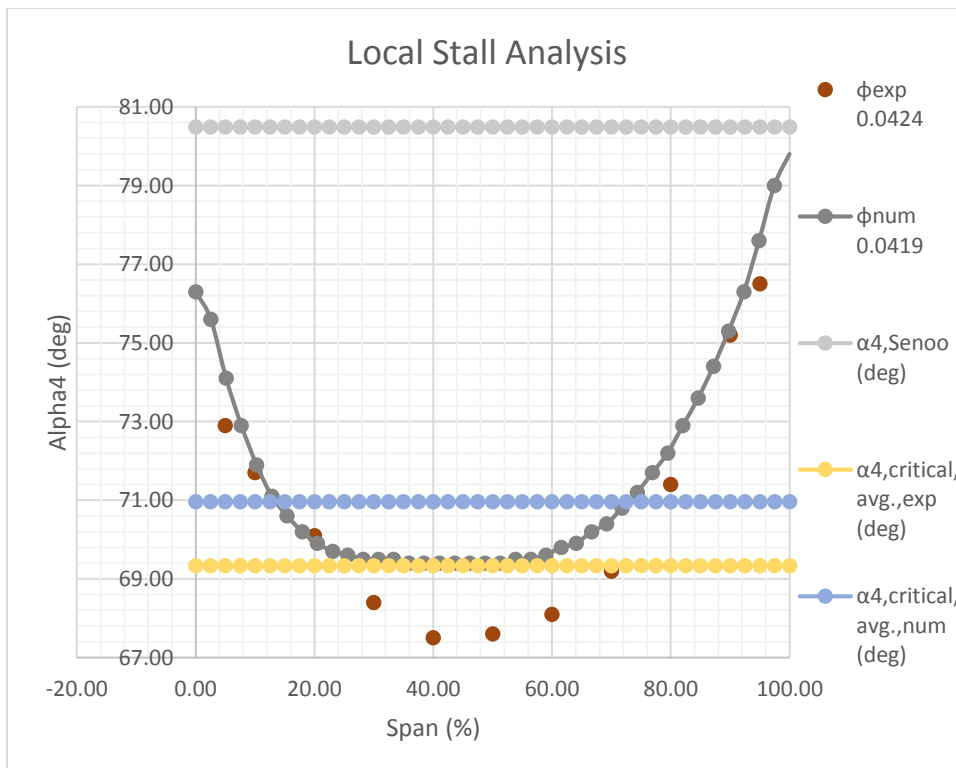


Figure 110: Stall Analysis for Compressor 10 at 21870 RPM Last Stable Flow Point

6.3.11 Compressor 11 Profiles

6.3.11.1 Compressor 11 13100 RPM Results

Figures 111 – 113 give the details for Compressor 11 at the 13100 RPM stall point. In Figure 111 the meridional velocity plots show little agreement. The two velocity profiles in Figure 111 are distorted, but in different ways. In Figure 112 one finds that the tangential velocity profiles match for a span range from 50% - 100%. But for the other range, there is a noticeable difference in the profiles. In Figure 113 both the experimental and numerical local flow angle plots breach the Senoo line.

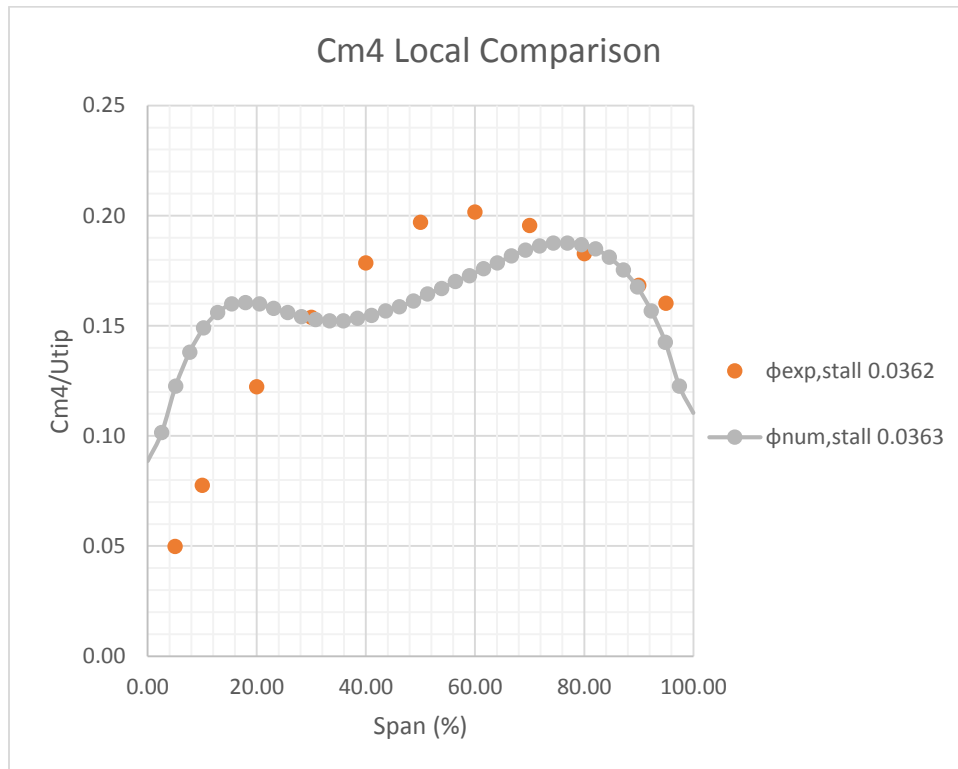


Figure 111: C_{m4} Comparison for Compressor 11 at 13100 RPM Stall Point

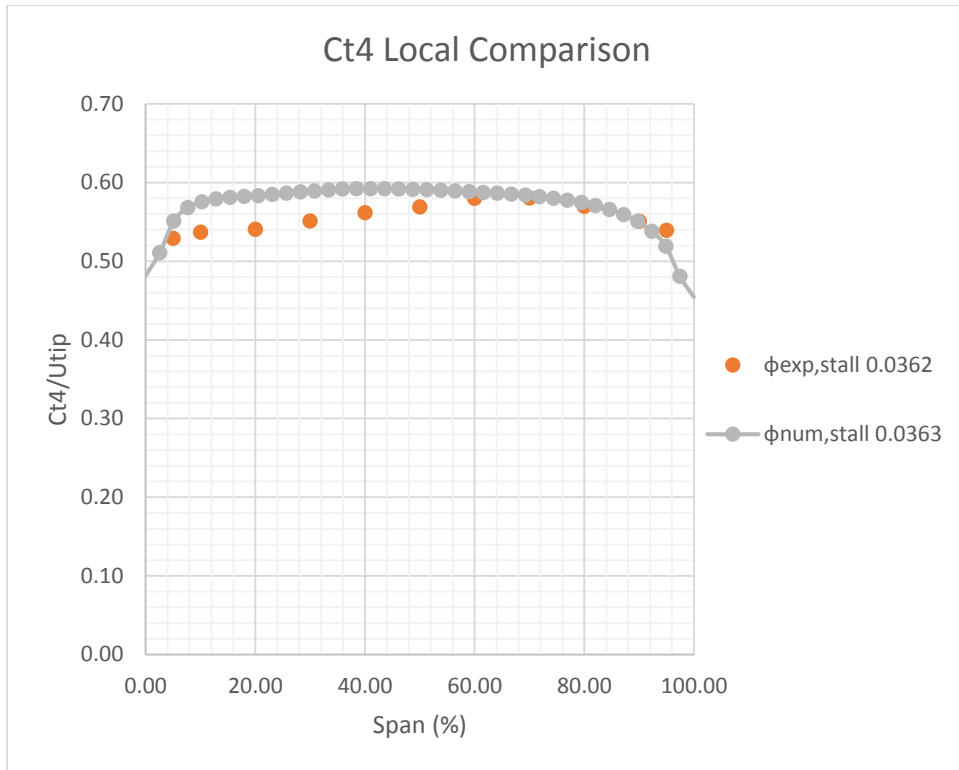


Figure 112: C_{t4} Comparison for Compressor 11 at 13100 RPM Stall Point

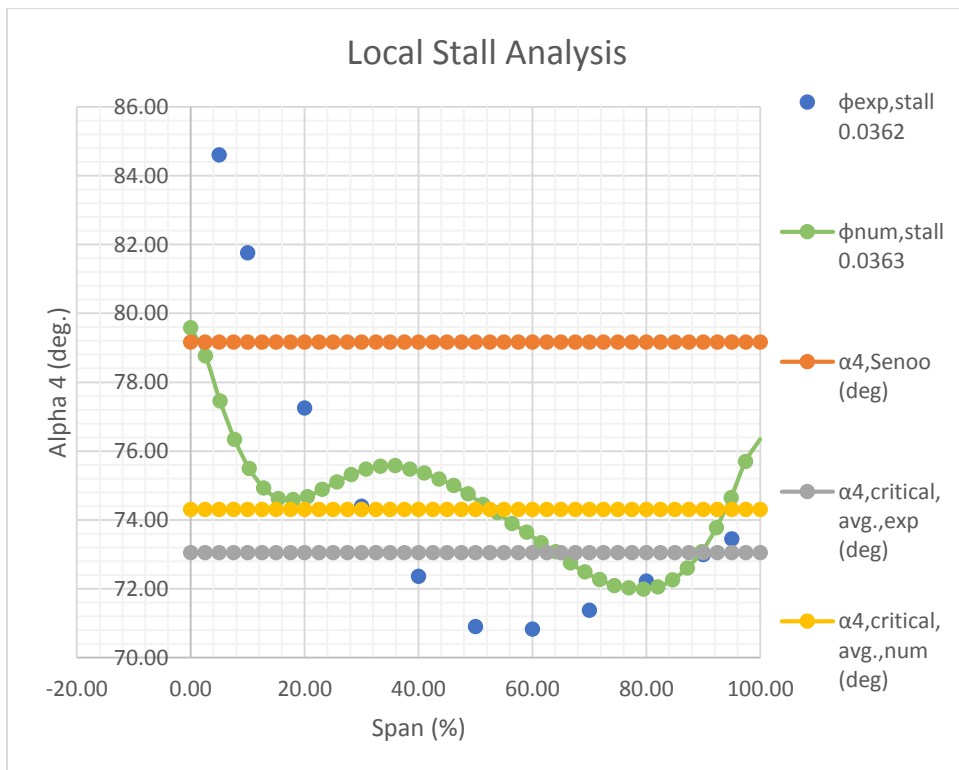


Figure 113: Stall Analysis for Compressor 11 at 13100 RPM Stall Point

6.3.11.2 Compressor 11 19240 RPM Results

Figures 114 – 116 show the results for Compressor 11 at the 19240 RPM stall point. For this flow point the rotating stall onset point occurred at the last stable flow point, so the experimental data at the last stable point was used for comparison purposes. In Figure 114 one finds that both meridional velocity profiles reach a velocity less than or equal to zero. Thus both sets of measurements are predicting localized flow reversal at the diffuser inlet. However, both meridional velocity plots reach zero on different sides of the diffuser. In Figure 115 one finds little agreement between the profiles. The experimental profile appears to reach zero, which would mean that about 5% of the span was totally blocked by the stalled fluid, or that something went wrong with the measurement. No such issue is shown by the numerical profile, but it should give one pause that the numerical profile can only be so accurate. In Figure 116 one finds that both profiles breach the Senoo line, but on opposite sides of the diffuser. For reasons that will become clear in section 6.3.15 it is the breaching of the Senoo line that is important, not the area of the diffuser breach.

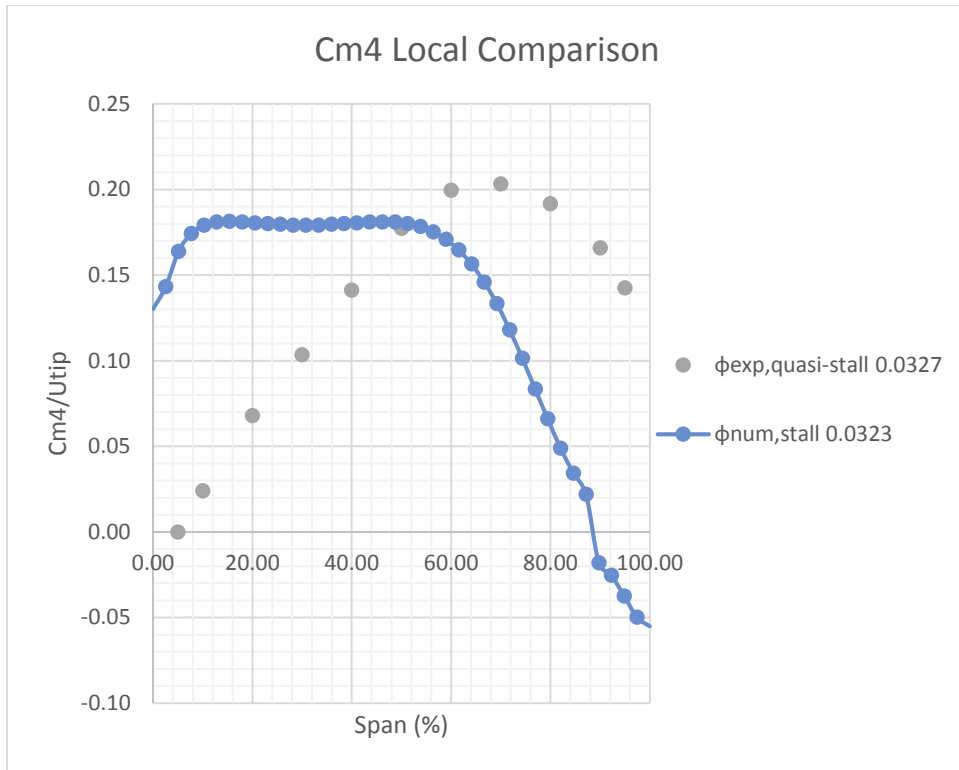


Figure 114: C_{m4} Comparison for Compressor 11 at 19240 RPM Stall Point

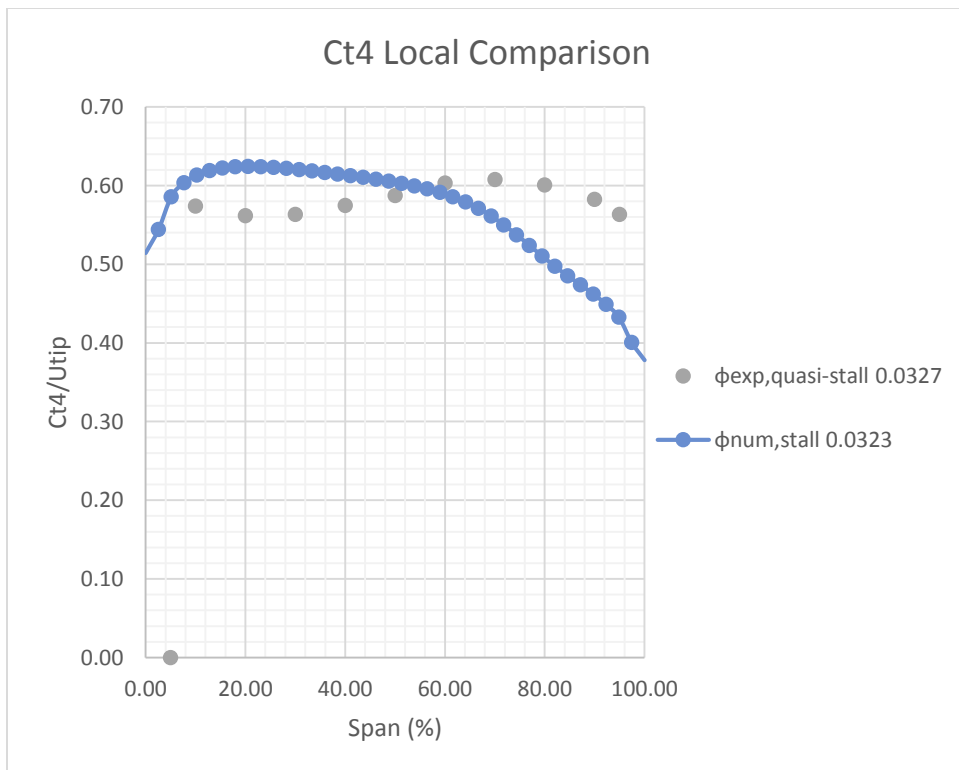


Figure 115: C_{t4} Comparison for Compressor 11 at 19240 RPM Stall Point

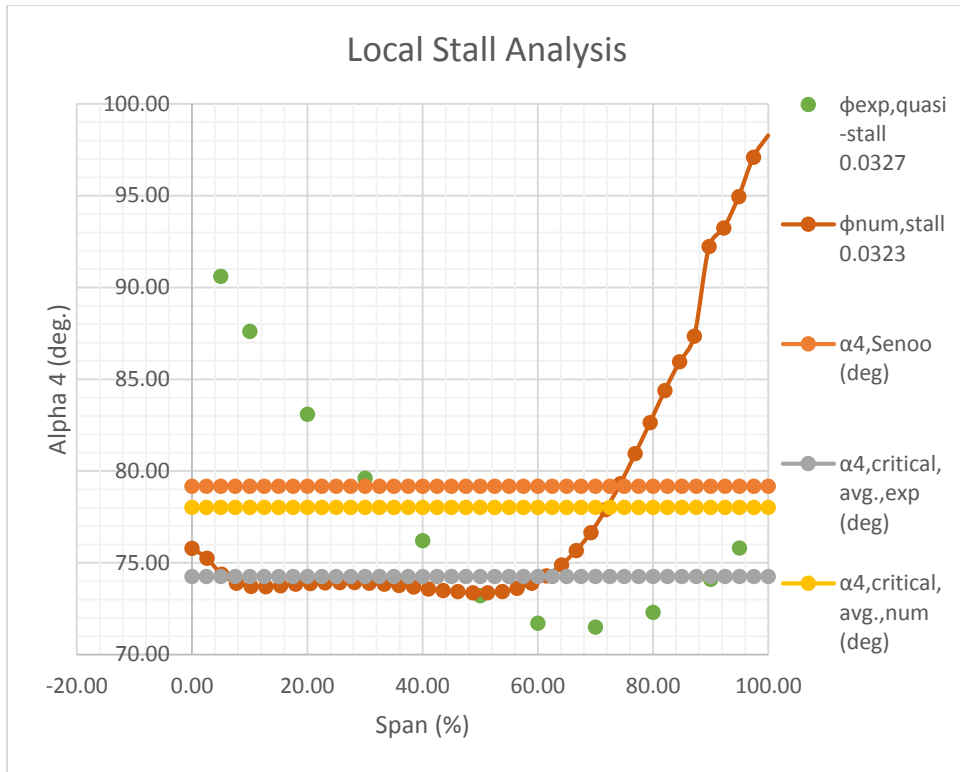


Figure 116: Stall Analysis for Compressor 11 at 19240 RPM Stall Point

6.3.11.3 Compressor 11 21870 RPM Results

Figures 117 – 119 provide the results for Compressor 11 at the last stable flow point on the 21870 RPM speed line. As with the preceding speed lines the results for the meridional velocity profile, Figure 117, show localized flow reversal at the diffuser inlet. Since this is the point directly preceding surge this is expected. In Figure 118 the experimental profile again reaches zero, but the numerical profile does not. However, by comparing Figure 118 to Figure 115 one finds that both experimental profiles and both numerical profiles match. This shows consistency between the model and the experiment at these respective speed lines, but also bolsters the case that the numerical simulation can only tell a person so much. In Figure 119 one finds a breach of the Senoo line, but this time the numerical profile breaches the Senoo line on both sides of the diffuser.

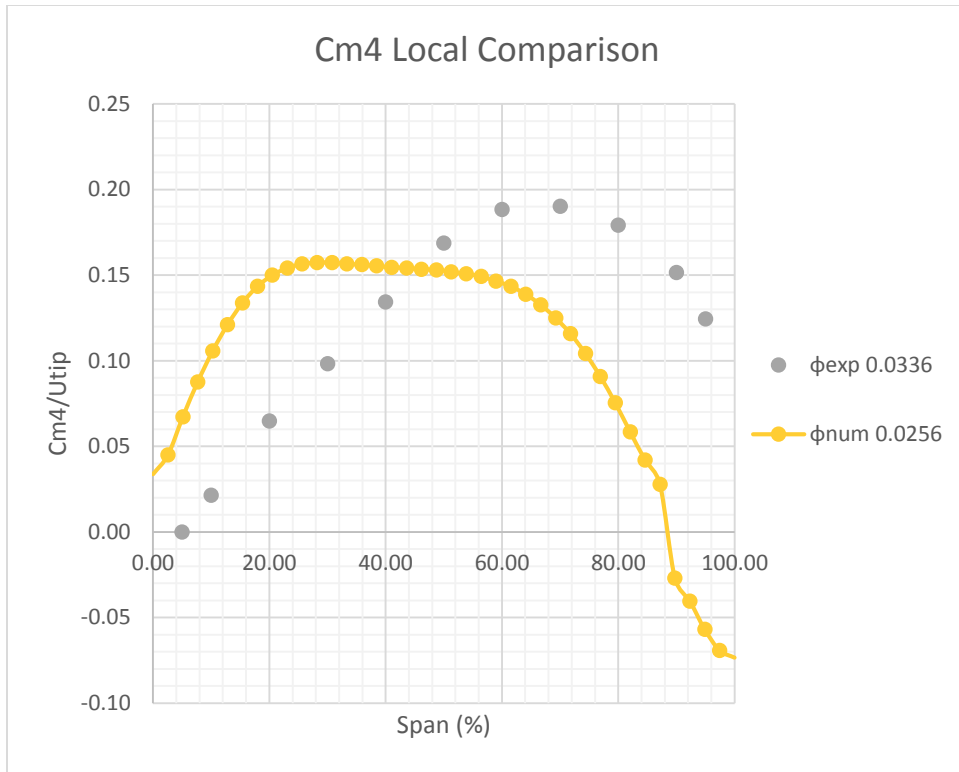


Figure 117: C_{m4} Comparison for Compressor 11 at 21870 RPM Last Stable Flow Point

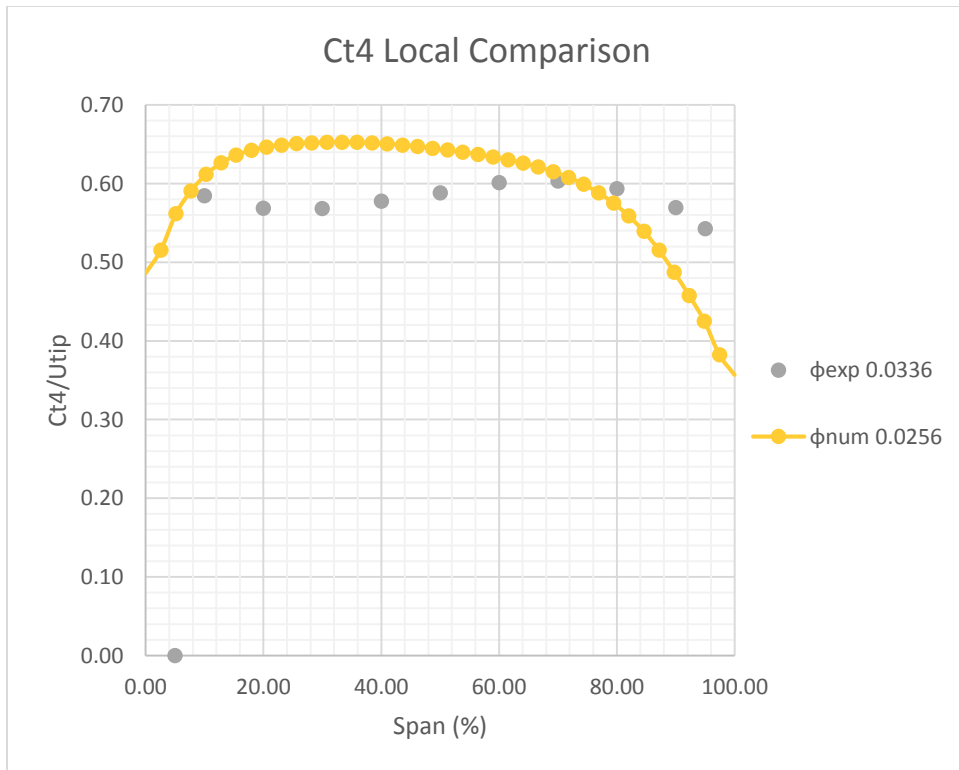


Figure 118: C_{t4} Comparison for Compressor 11 at 21870 RPM Last Stable Flow Point

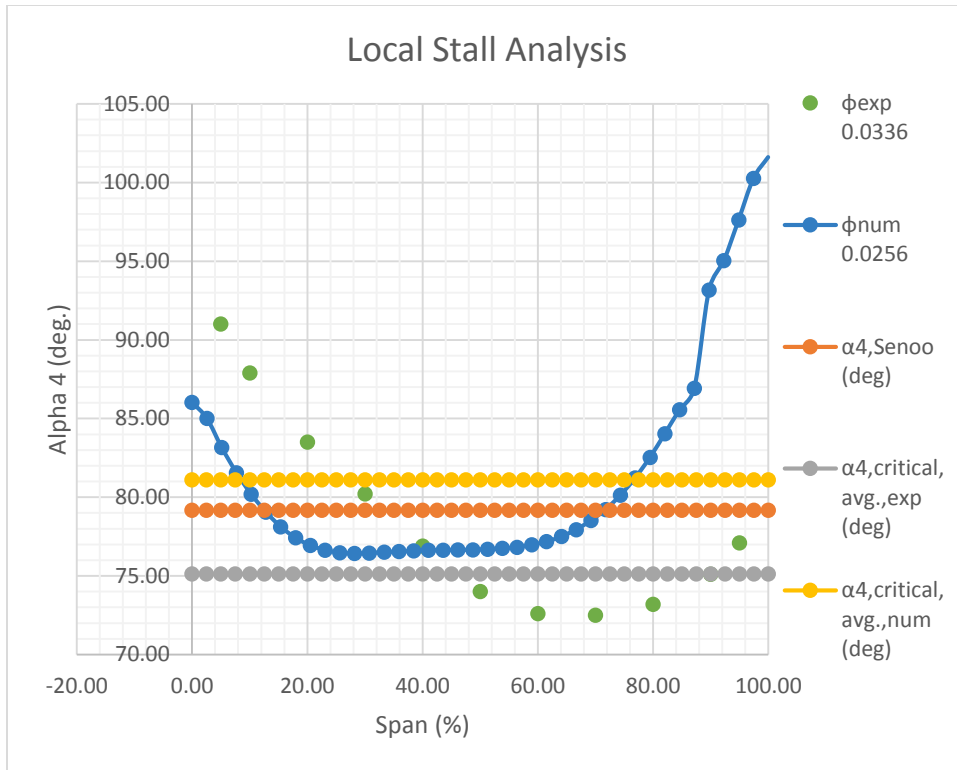


Figure 119: Stall Analysis for Compressor 11 at 21870 RPM Last Stable Flow Point

6.3.12 Compressor 12 Profiles

6.3.12.1 Compressor 12 13100 RPM Results

Figures 120 – 122 provide the results for Compressor 12 at the 13100 RPM stall point. In Figure 120 one finds that the experimental and numerical profiles do not match. In Figure 121 one finds that there is agreement between the tangential velocity profiles. Though the profiles differ in magnitude the trends of each line are the same. In Figure 122 one finds that the experimental profile crosses the Senoo line, but the numerical profile does not. This is an odd occurrence. It can be attributed to one of two things, either the stall cell develops outside of the diffuser in the “U-Bend” region, which can happen [27, 28], or the computational mesh is not accurate enough to properly resolve the flow field for this geometry [27]. This issue will be resolved in section 7.1.

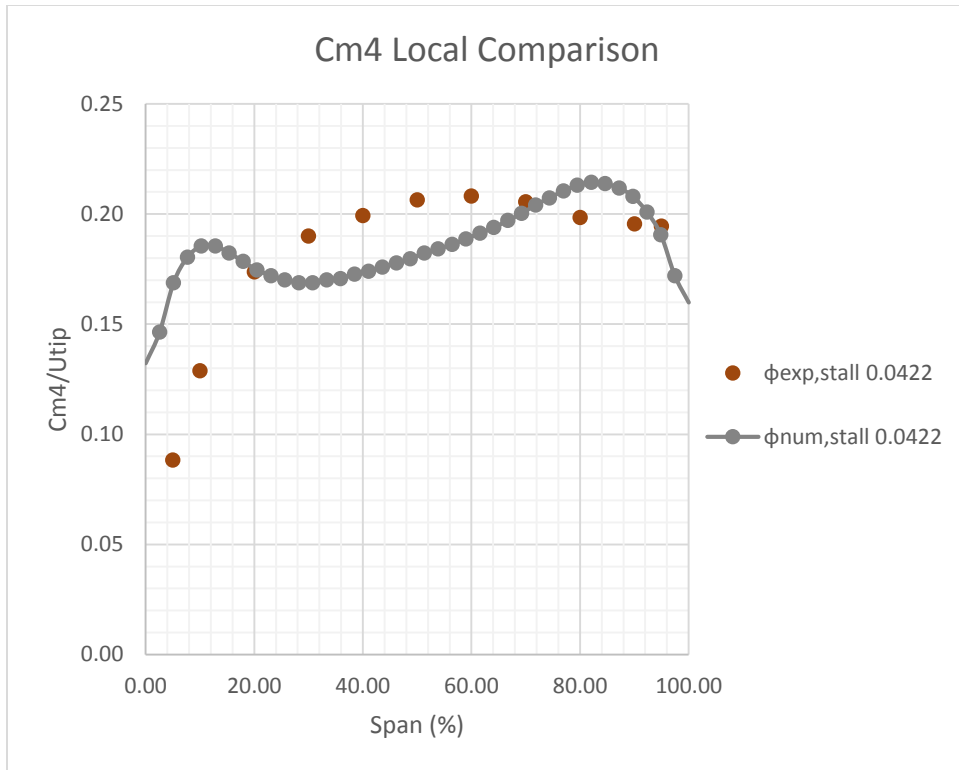


Figure 120: C_{m4} Comparison for Compressor 12 at 13100 RPM Stall Point

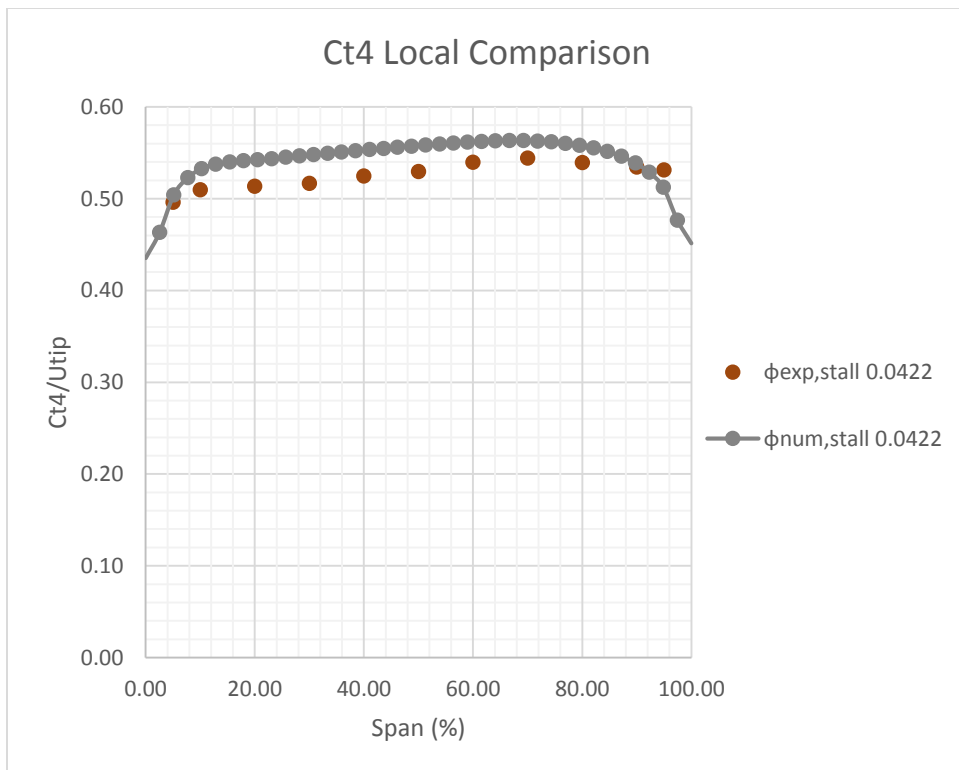


Figure 121: C_{t4} Comparison for Compressor 12 at 13100 RPM Stall Point

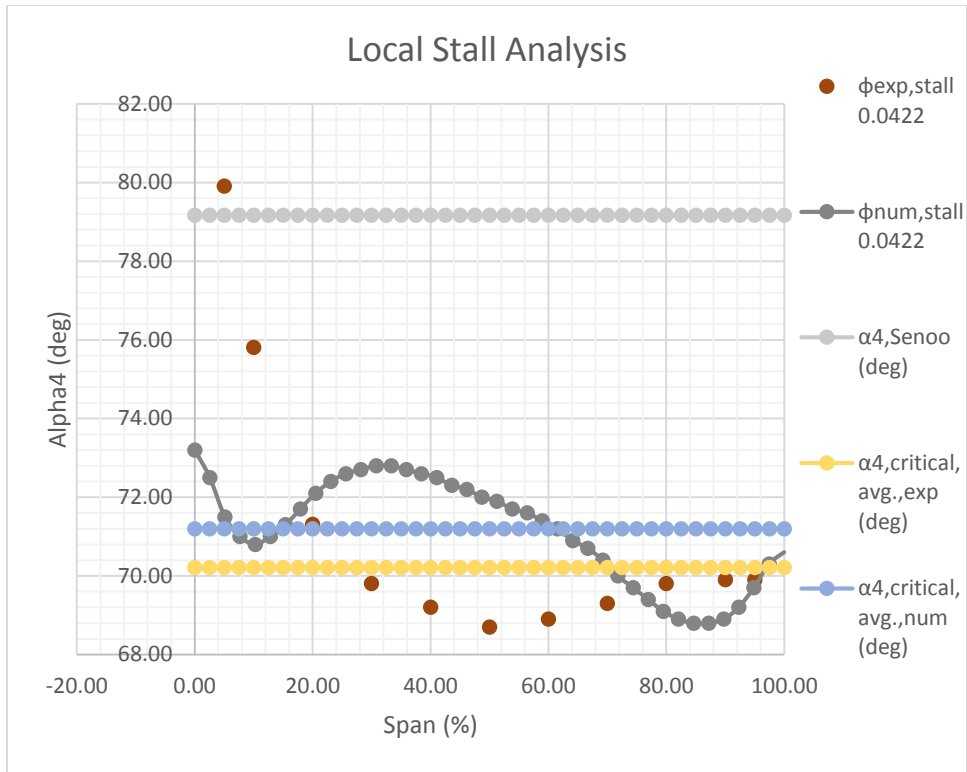


Figure 122: Stall Analysis for Compressor 12 at 13100 RPM Stall Point

6.3.12.2 Compressor 12 19240 RPM Results

Figures 123 – 125 provide the results for Compressor 12 at the 19240 RPM stall point. In Figure 123 one finds that the meridional velocity profiles do not match, just like at 13100 RPM. In Figure 124 one finds some agreement between the tangential velocity profiles. The structure of the tangential velocity profiles is a match, but they give different magnitudes. In Figure 125 one finds that the experimental profile crosses the Senoo line, but the numerical profile does not. This is the same results as at 19240 RPM. The possible reasons for this were discussed in section 6.3.12.1, and will be dealt with again in section 7.1.

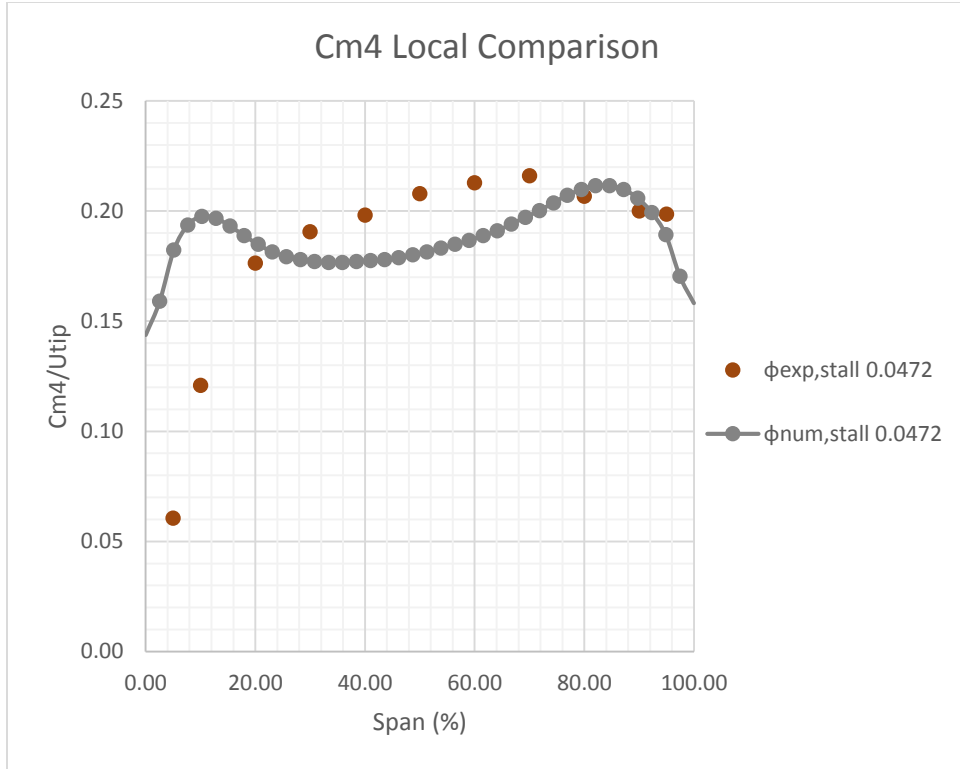


Figure 123: C_{m4} Comparison for Compressor 12 at 19240 RPM Stall Point

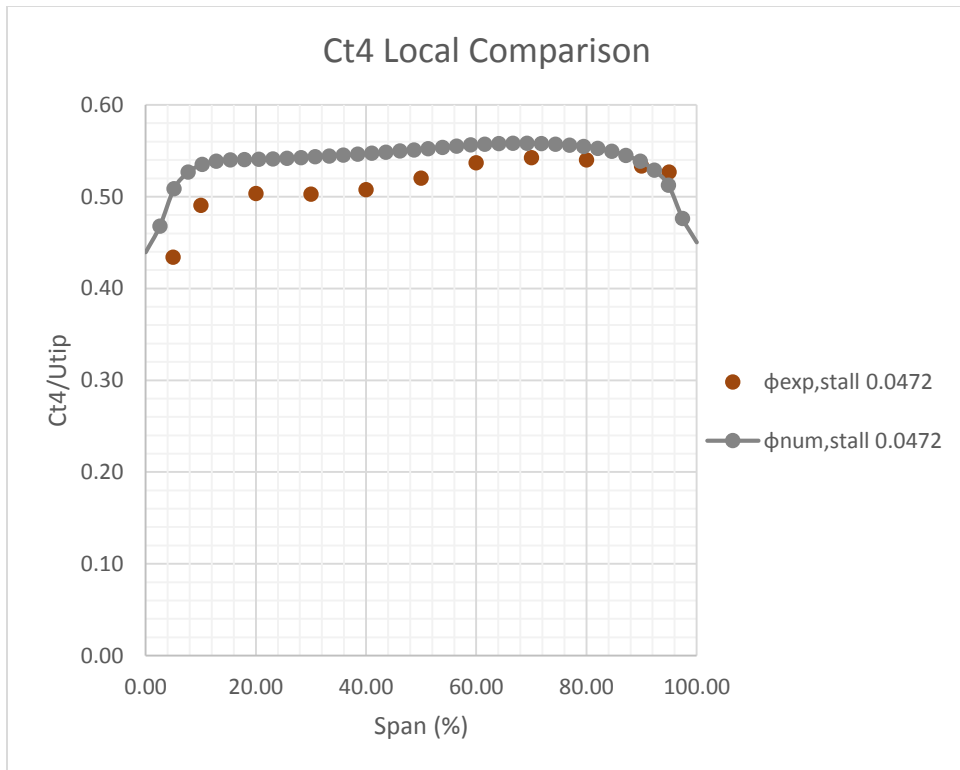


Figure 124: C_{t4} Comparison for Compressor 12 at 19240 RPM Stall Point

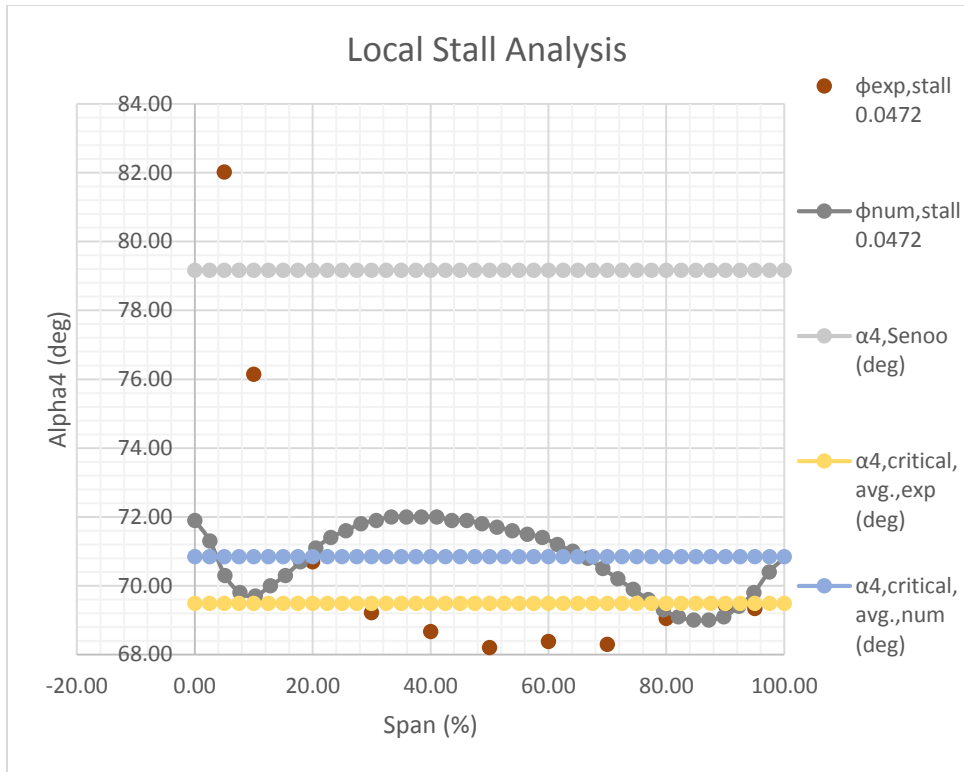


Figure 125: Stall Analysis for Compressor 12 at 19240 RPM Stall Point

6.3.12.3 Compressor 12 21870 RPM Results

Figures 126 – 128 provide the results for Compressor 12 at the 21870 RPM stall point. As with the 13100 RPM and 19240 RPM results one finds that the meridional velocity profiles again do not match (Figure 126), but the tangential profiles (Figure 127) match regarding their trend, but not magnitude. In Figure 128 one finds that neither the numerical profile nor the experimental profile cross the Senoo line. However, as with the 13100 RPM and 19240 RPM stall points the experimental profile is significantly closer to the Senoo line than the numerical profile.

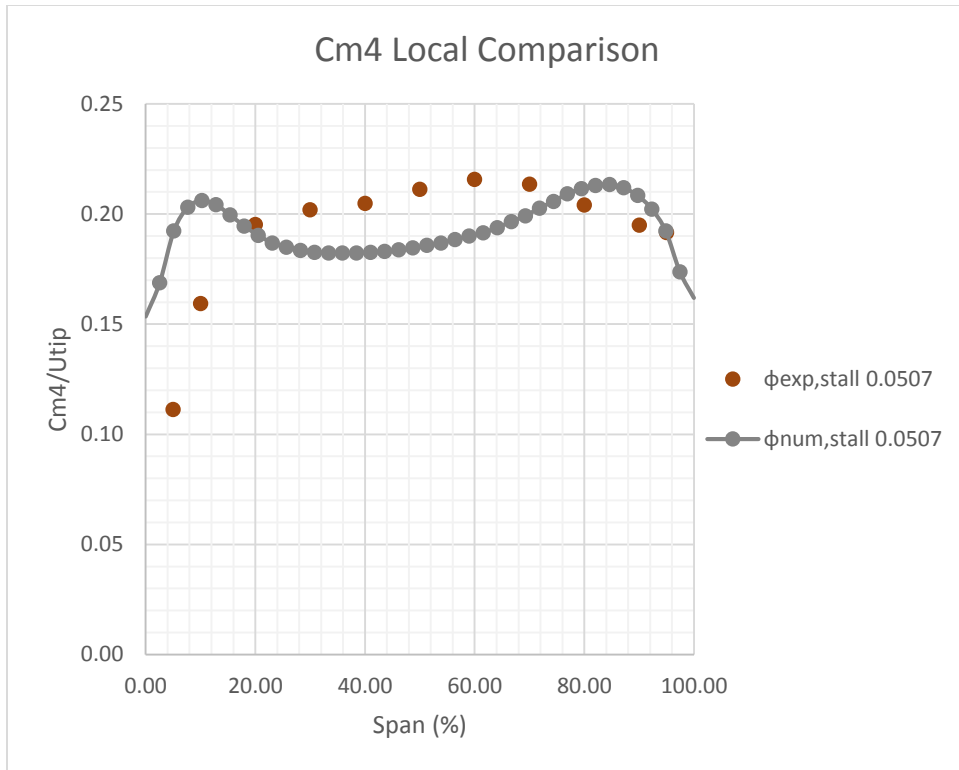


Figure 126: C_{m4} Comparison for Compressor 12 at 21870 RPM Stall Point

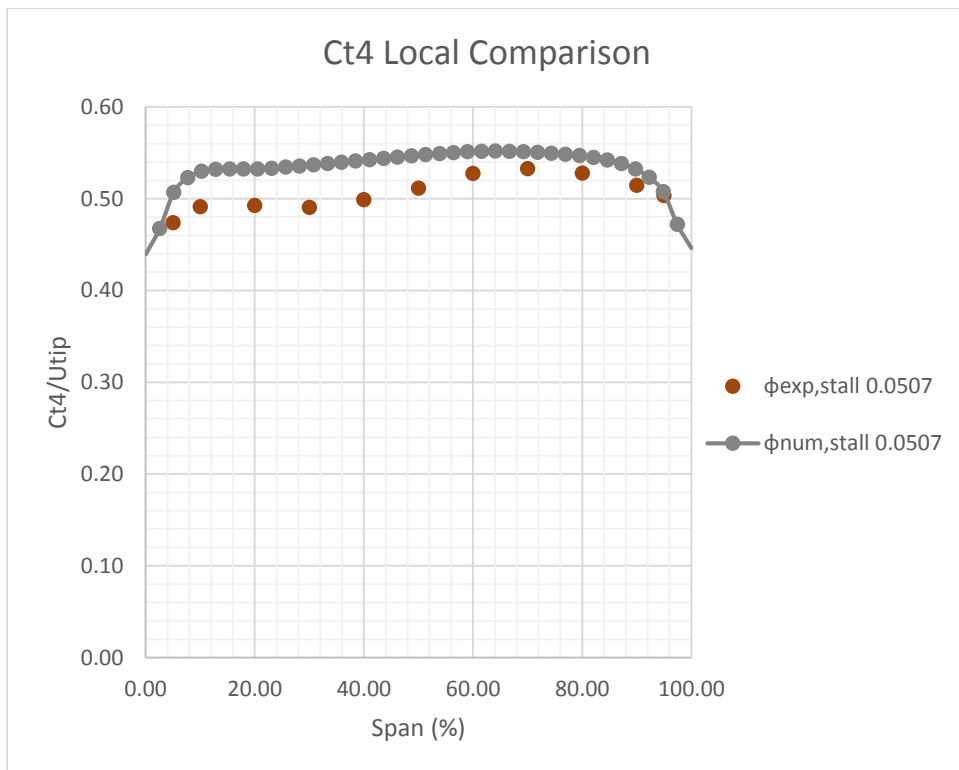


Figure 127: C_{t4} Comparison for Compressor 12 at 21870 RPM Stall Point

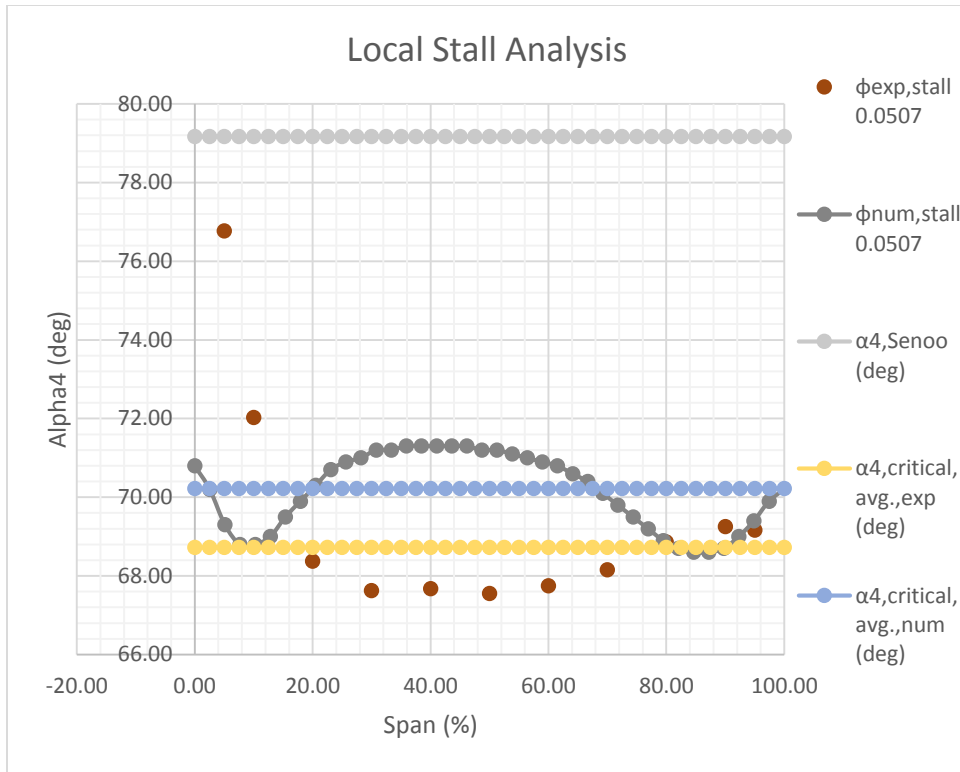


Figure 128: Stall Analysis for Compressor 12 at 21870 RPM Stall Point

6.3.13 Compressor 13 Profiles

6.3.13.1 Compressor 13 13100 RPM Results

Figures 129 – 131 provide the results for Compressor 13 at the 13100 RPM stall point. In Figure 129 one finds little agreement between the meridional velocity profiles. However, near the hub wall the profiles match, and near the shroud wall the trends of the profiles match. In Figure 130 one finds that the tangential profile have a comparable trend, but their magnitudes do not line up. In Figure 131 it is found that both numerical and experimental profiles cross the Senoo line.

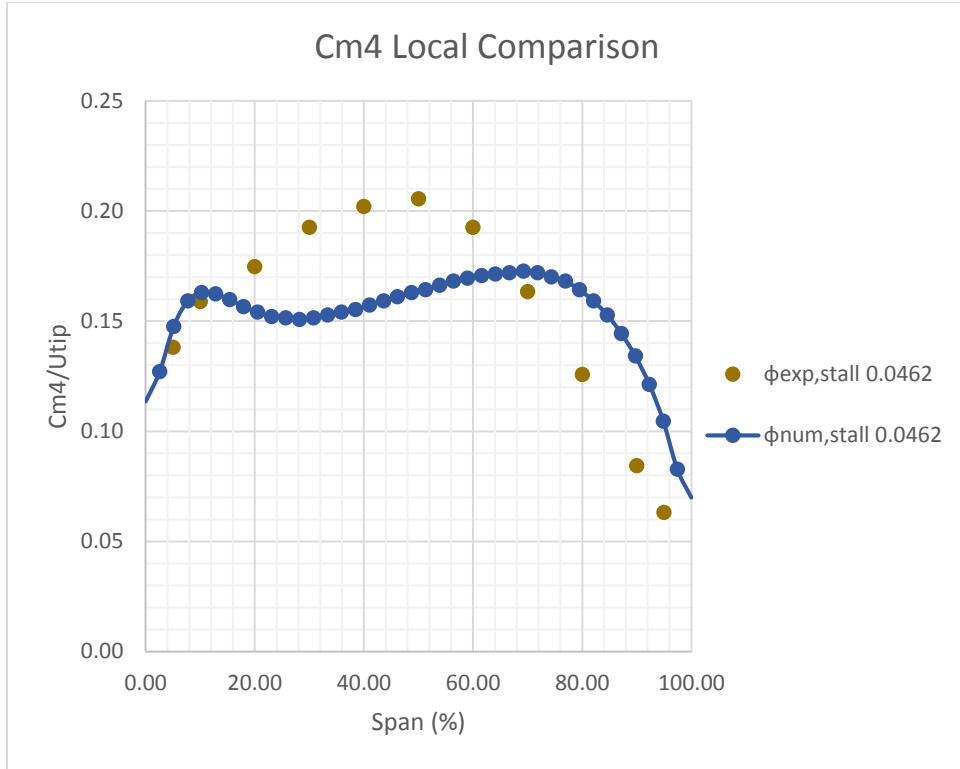


Figure 129: C_{m4} Comparison for Compressor 13 at 13100 RPM Stall Point

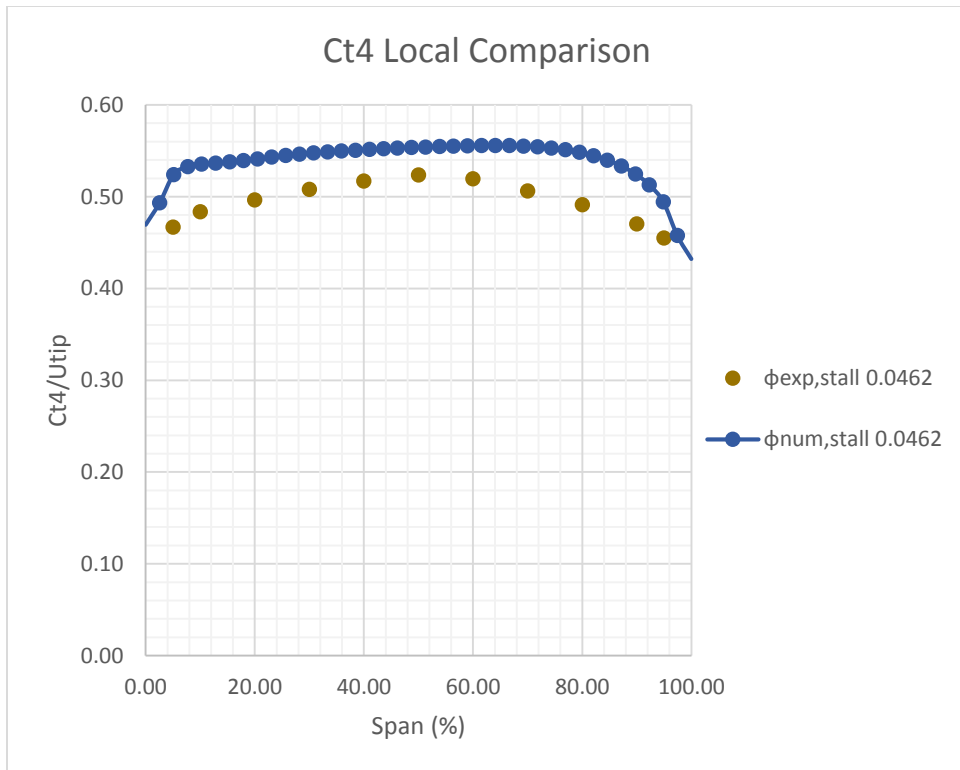


Figure 130: C_{t4} Comparison for Compressor 13 at 13100 RPM Stall Point

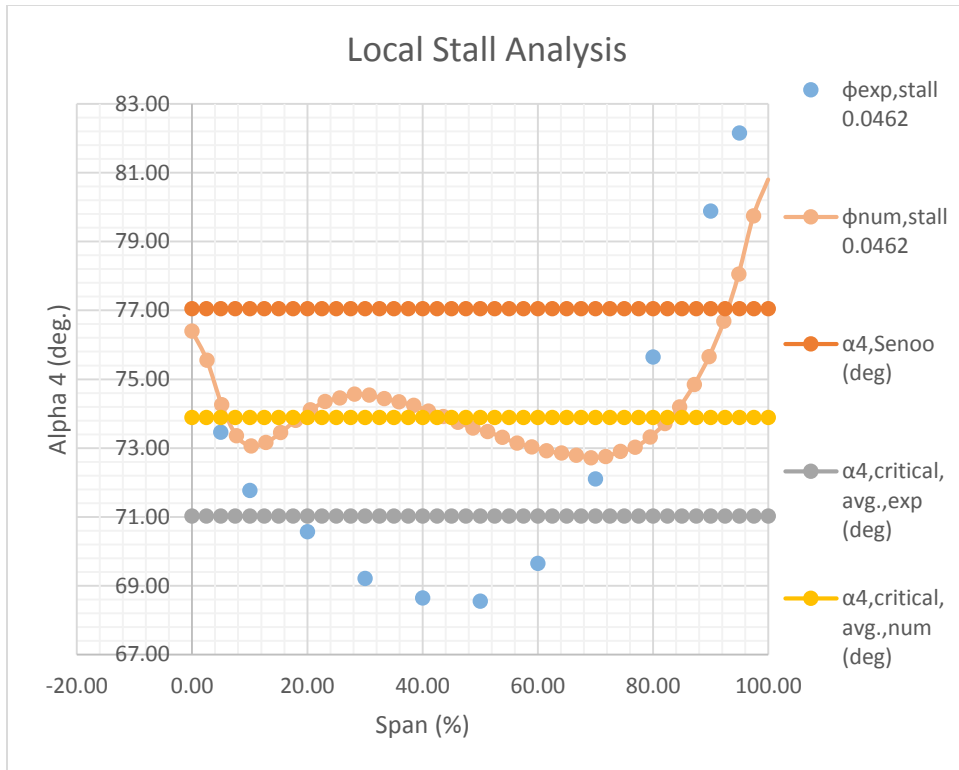


Figure 131: Stall Analysis for Compressor 13 at 13100 RPM Stall Point

6.3.13.2 Compressor 13 19240 RPM Results

In Figures 132 – 134 the results for Compressor 13 at the 19240 RPM stall point are given. In Figure 132 one finds that there is better agreement between the numerical and experimental meridional velocity plots. However, the interesting result is that the numerical profile shows localized flow reversal covering roughly 10% of the span near the shroud wall. This result is in line with those found in [34] for rotating stall onset. In Figure 133 some agreement is found in the trends of the tangential velocity profiles, but near the 80% span mark there is a marked difference in profile structure. In Figure 134 it was found that both numerical and experimental profiles exceed the Senoo line.

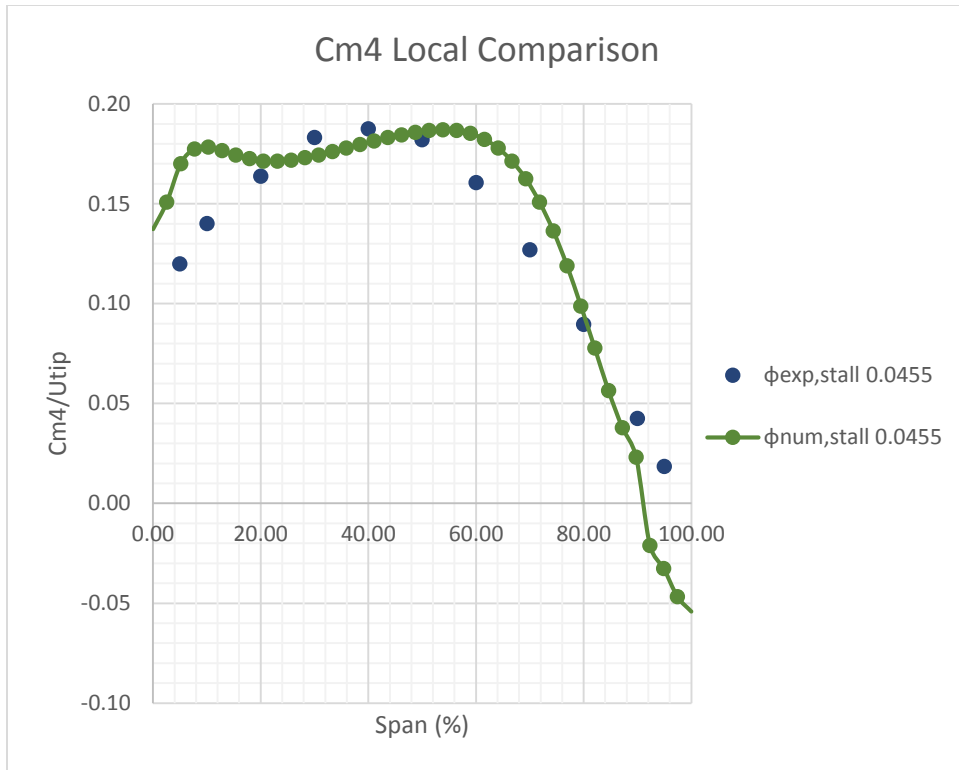


Figure 132: C_{m4} Comparison for Compressor 13 at 19240 RPM Stall Point

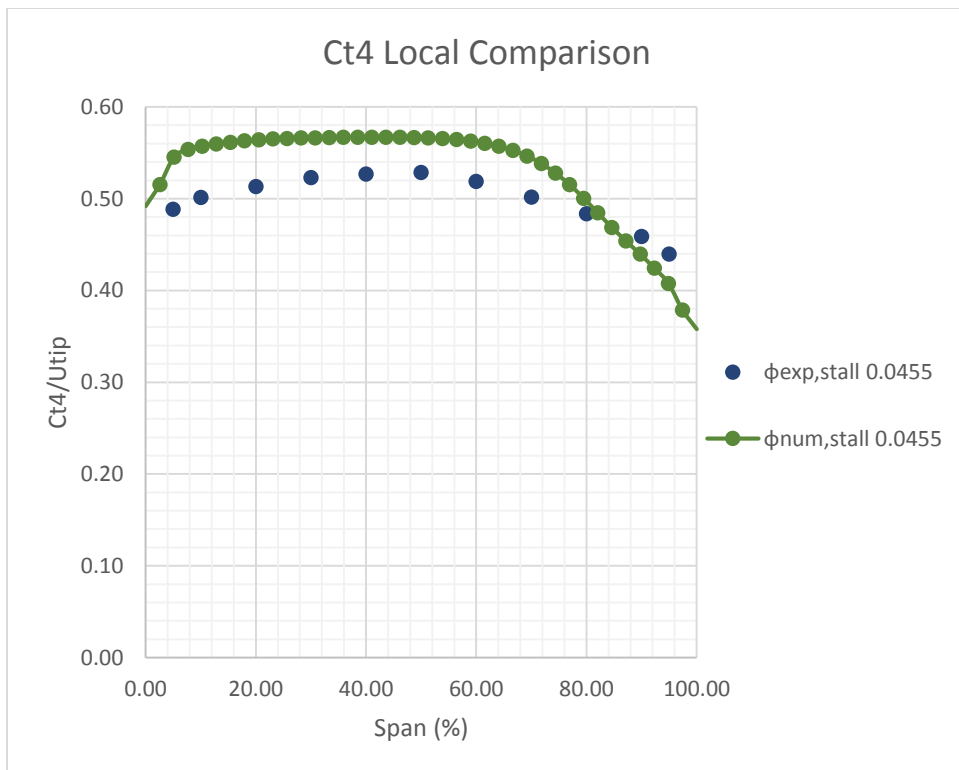


Figure 133: C_{t4} Comparison for Compressor 13 at 19240 RPM Stall Point

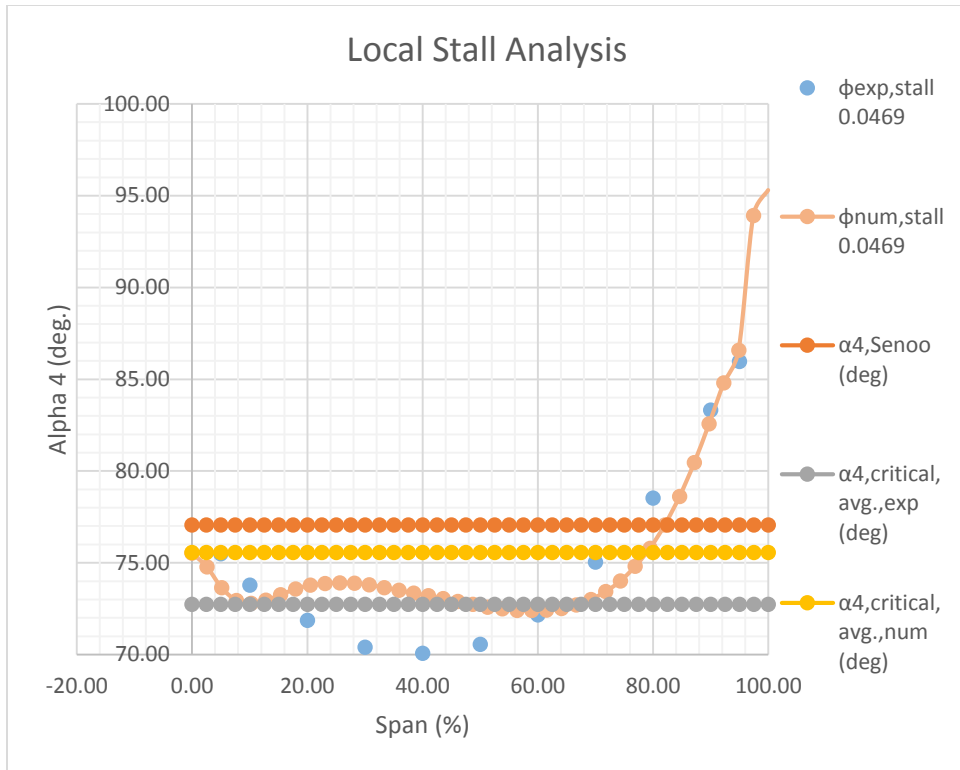


Figure 134: Stall Analysis for Compressor 13 at 19240 RPM Stall Point

6.3.13.3 Compressor 13 21870 RPM Results

The results for compressor 13 at the 21870 RPM stall point appear in Figures 135 – 137. In Figure 135 localized flow reversal is found for the numerical profile. Overall the two profiles have some agreement. In Figure 136 the same profile structure as seen at 19240 RPM (Figure 133) was found for the tangential profiles. In Figure 137 the profiles breach the Senoo line.

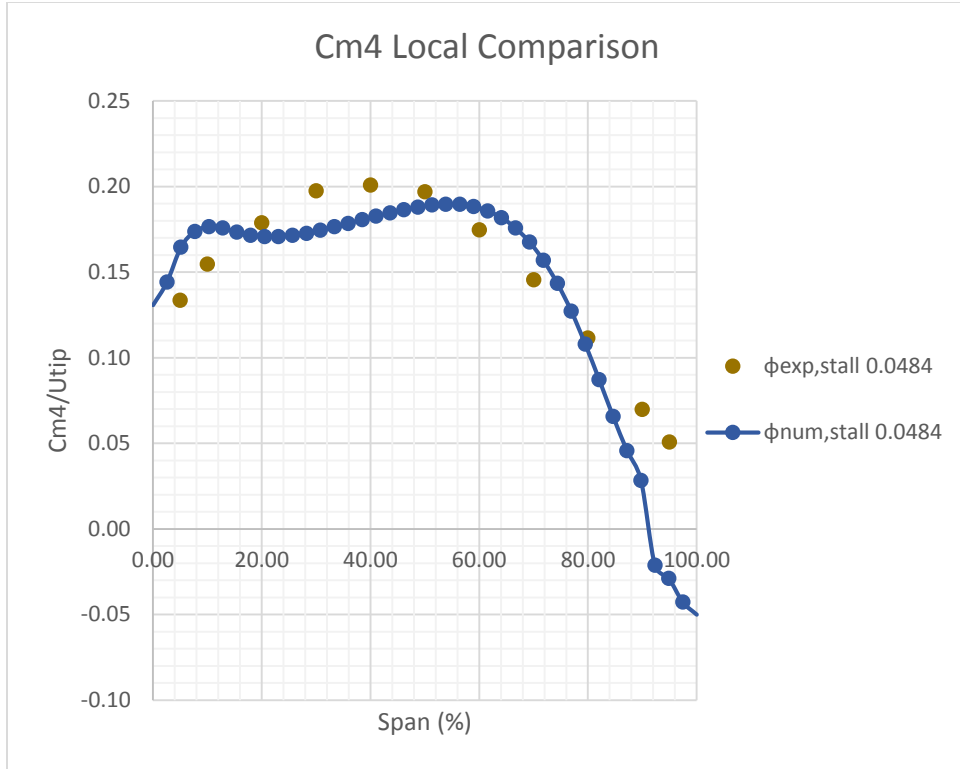


Figure 135: C_{m4} Comparison for Compressor 13 at 21870 RPM Stall Point

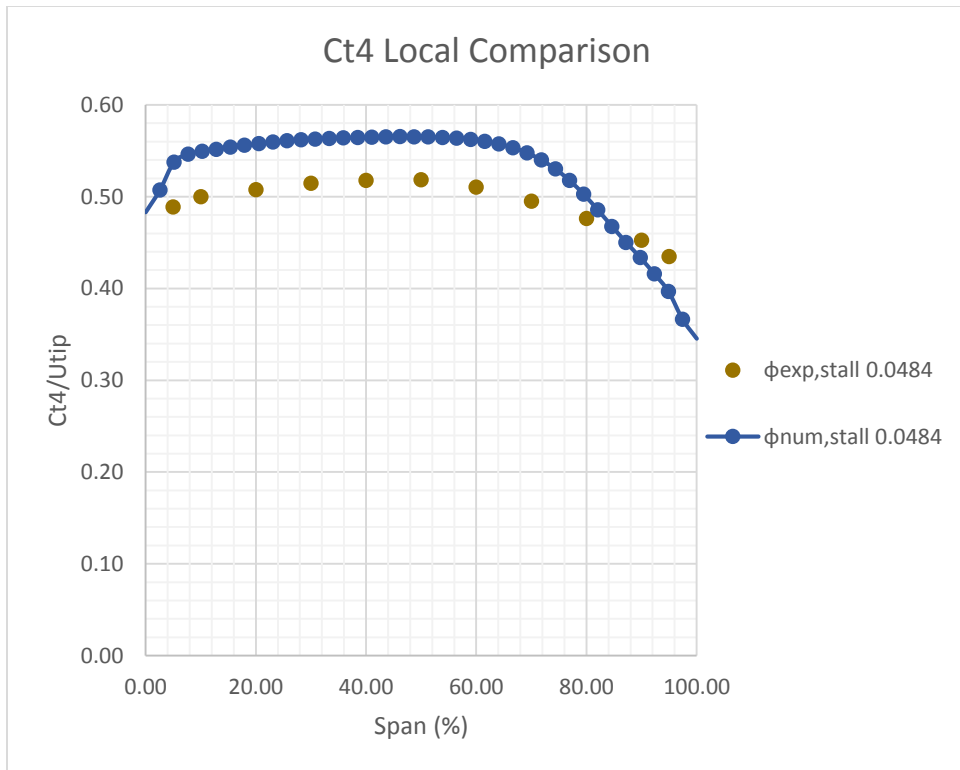


Figure 136: C_{t4} Comparison for Compressor 13 at 21870 RPM Stall Point

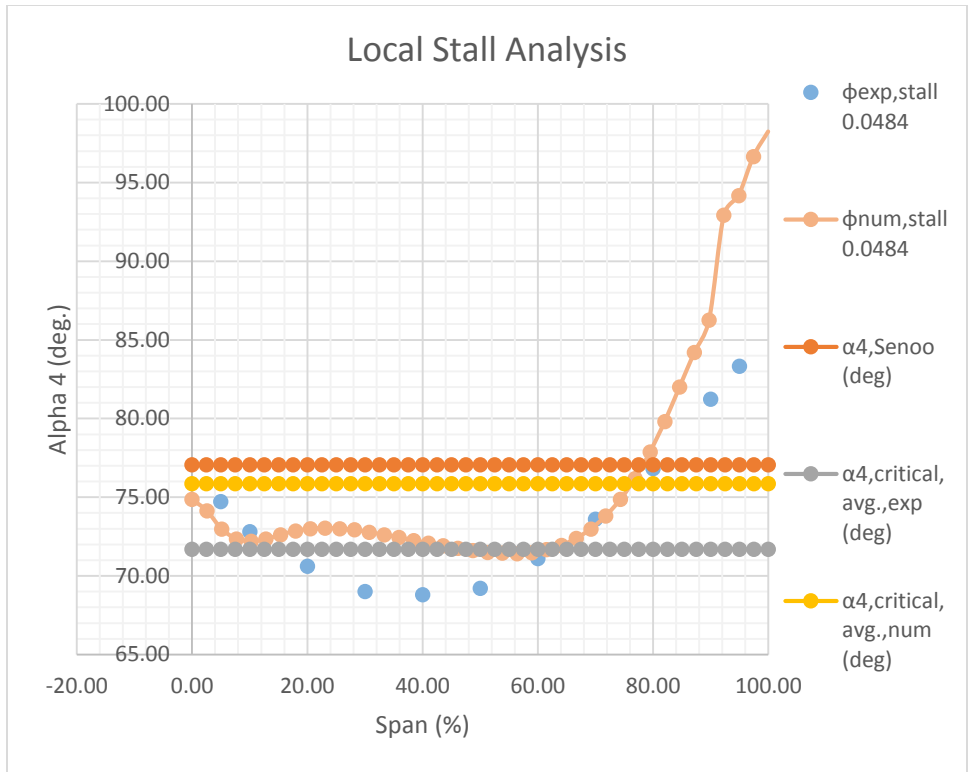


Figure 137: Stall Analysis for Compressor 13 at 21870 RPM Stall Point

6.3.14 Compressor 14 Profiles

6.3.14.1 Compressor 14 13100 RPM Results

The results for Compressor 14 at the 13100 RPM stall point are found in Figures 138 – 140. In Figure 138 the numerical profile shows localized flow reversal. For the span range of 0% - 40% the profiles share some agreement. In Figure 139 there is qualitative agreement between the tangential velocity profiles. In Figure 140 both profiles cross the Senoo line.

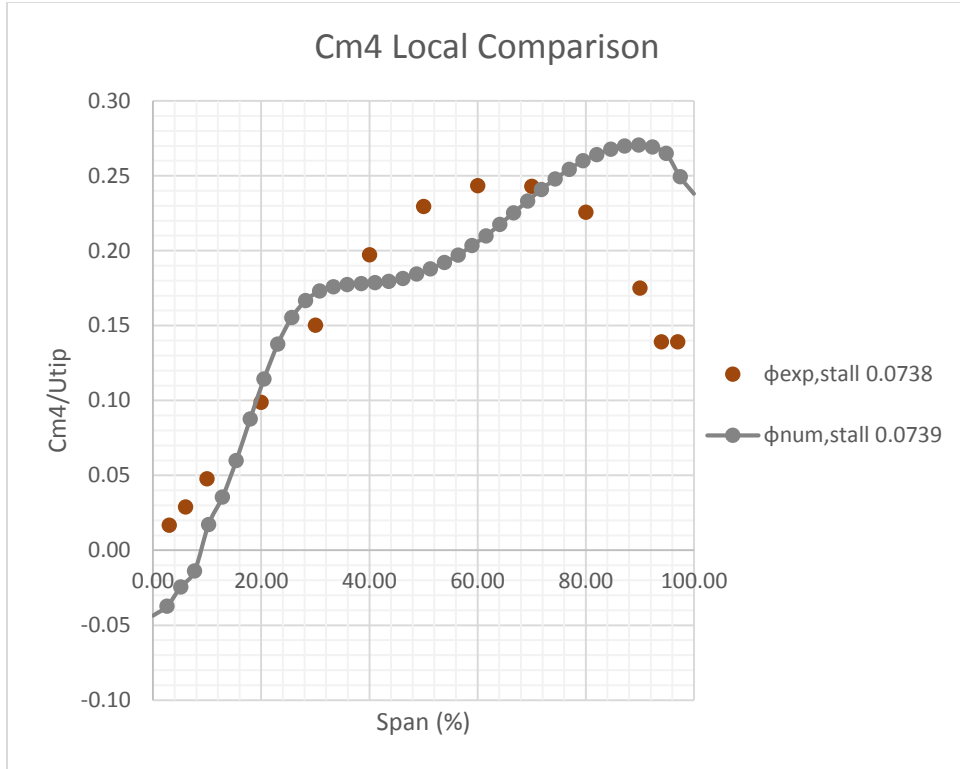


Figure 138: C_{m4} Comparison for Compressor 14 at 13100 RPM Stall Point

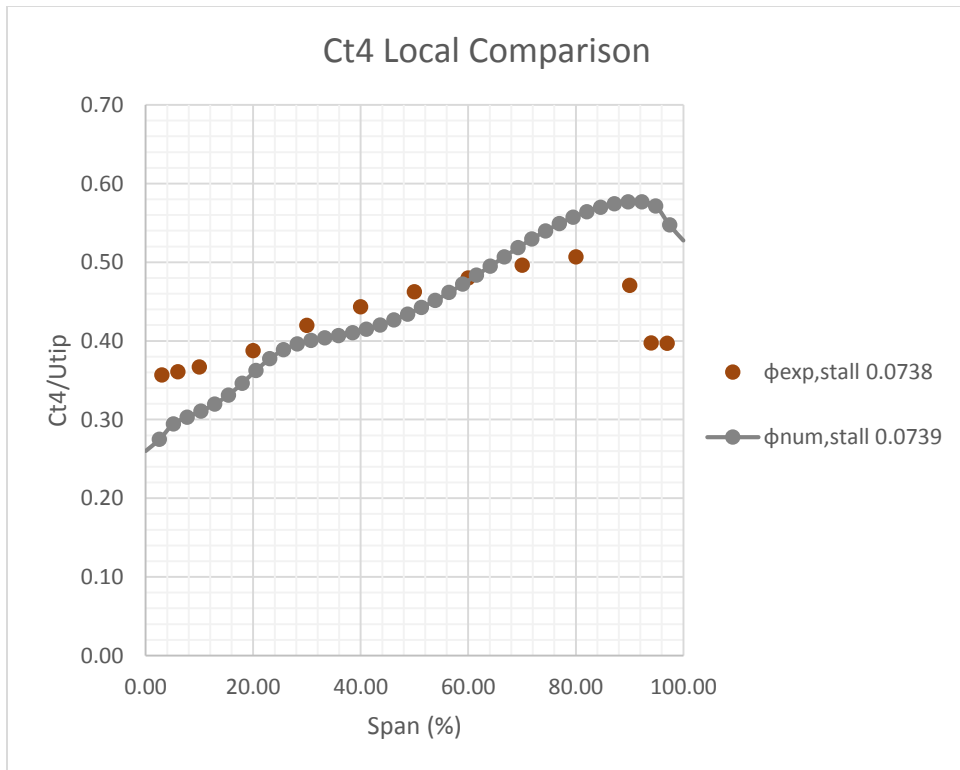


Figure 139: C_{t4} Comparison for Compressor 14 at 13100 RPM Stall Point

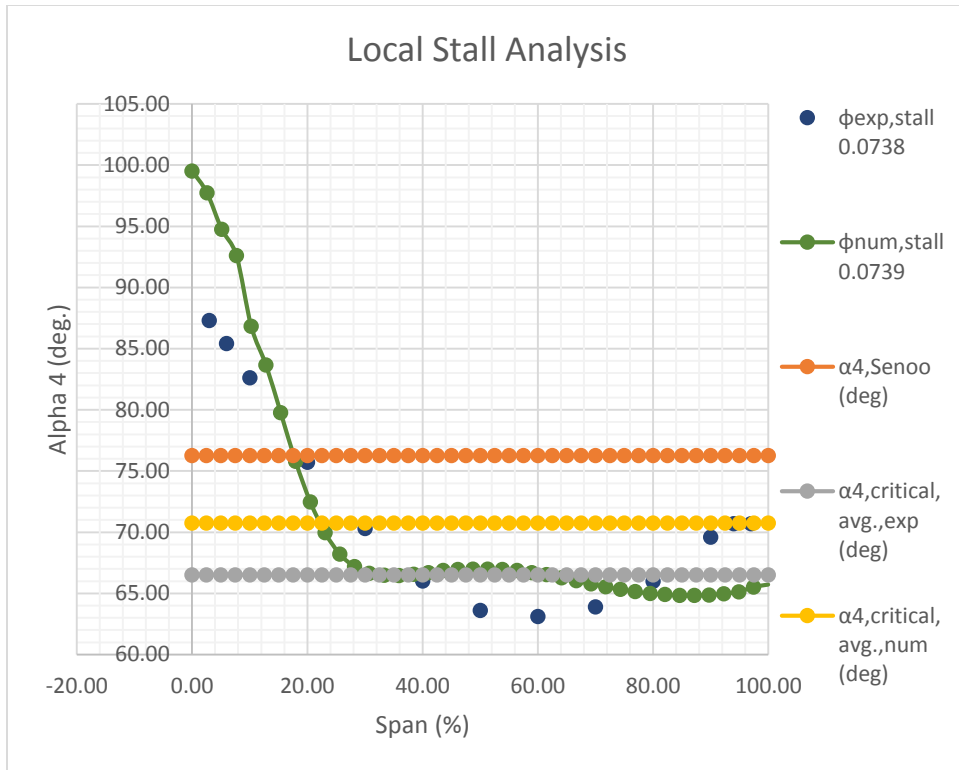


Figure 140: Stall Analysis for Compressor 14 at 13100 RPM Stall Point

6.3.14.2 Compressor 14 19240 RPM Results

Figures 141 – 143 provide the results for Compressor 14 at the 19240 RPM stall point. In Figure 141 the same profile structure as found at 19240 RPM was found here for both meridional velocity profiles. Also, Figure 141 shows localized flow reversal at the diffuser inlet. In Figure 142 it is found that for the span range of 20% - 60% the tangential profiles are in agreement. However, in Figure 142 one finds that the experimental tangential velocity drops to zero near the hub wall. In Figure 143 one finds that both profiles cross the Senoo line and show localized flow reversal at the diffuser inlet.

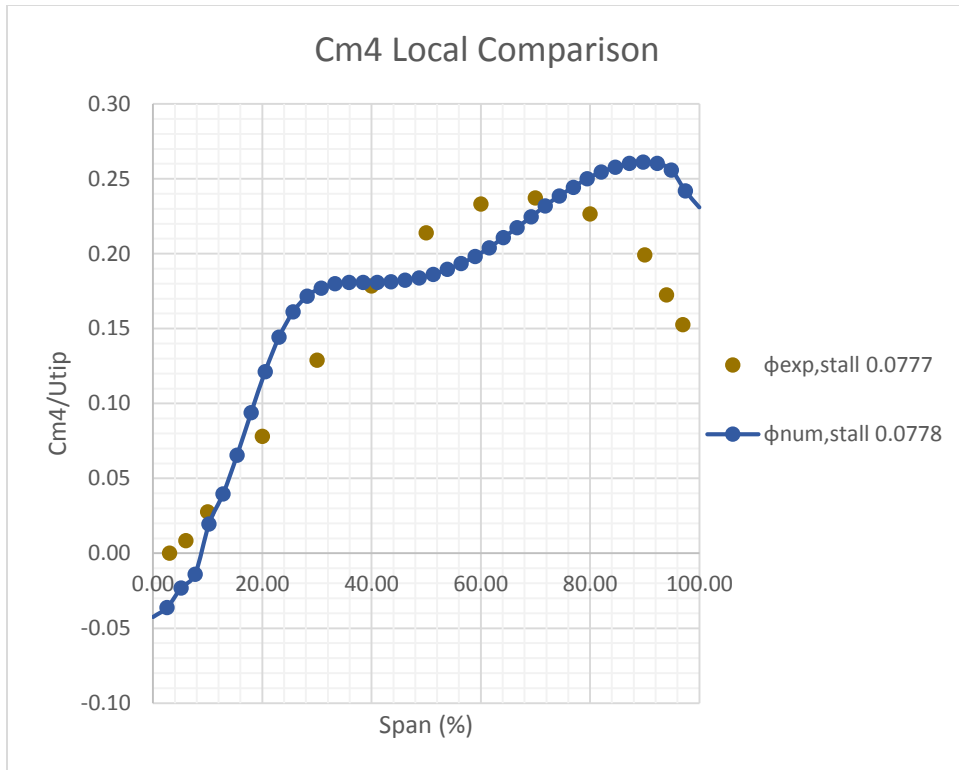


Figure 141: C_{m4} Comparison for Compressor 14 at 19240 RPM Stall Point

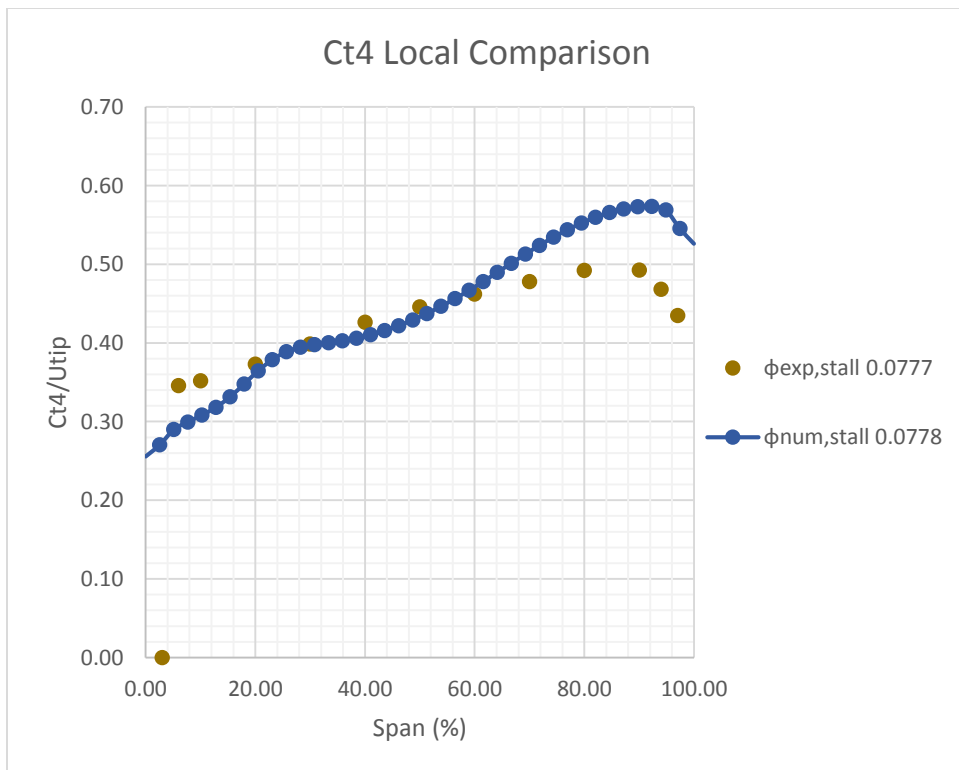


Figure 142: C_{t4} Comparison for Compressor 14 at 19240 RPM Stall Point

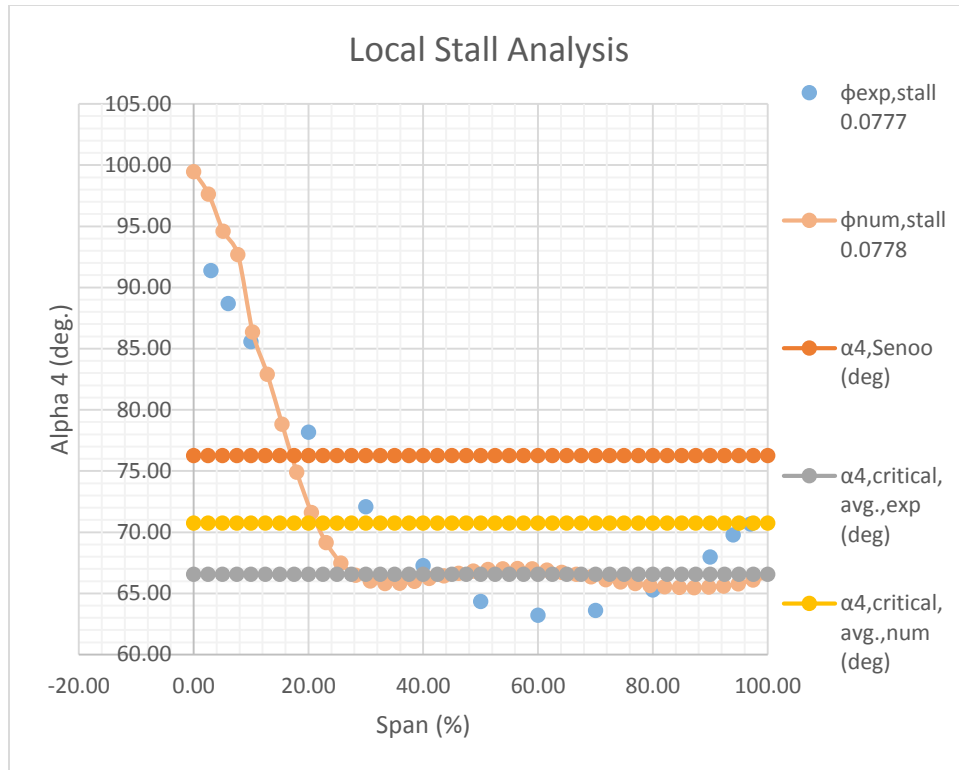


Figure 143: Stall Analysis for Compressor 14 at 19240 RPM Stall Point

6.3.14.3 Compressor 14 21870 RPM Results

In Figures 144 – 146 the results for Compressor 14 at the 21870 RPM stall point are given. In Figure 144 the two profiles agree for span values from 0% - 20%. However, for this speed line neither meridional velocity profile shows localized flow reversal. In Figure 145 one finds agreement between the tangential velocity profiles from 0% span to 50% span, afterwards the agreement is only qualitative. In Figure 146 both profiles are shown to cross the Senoo line. In fact at this flow point the experimental local flow angle profile crosses the Senoo line at both the hub and shroud walls.

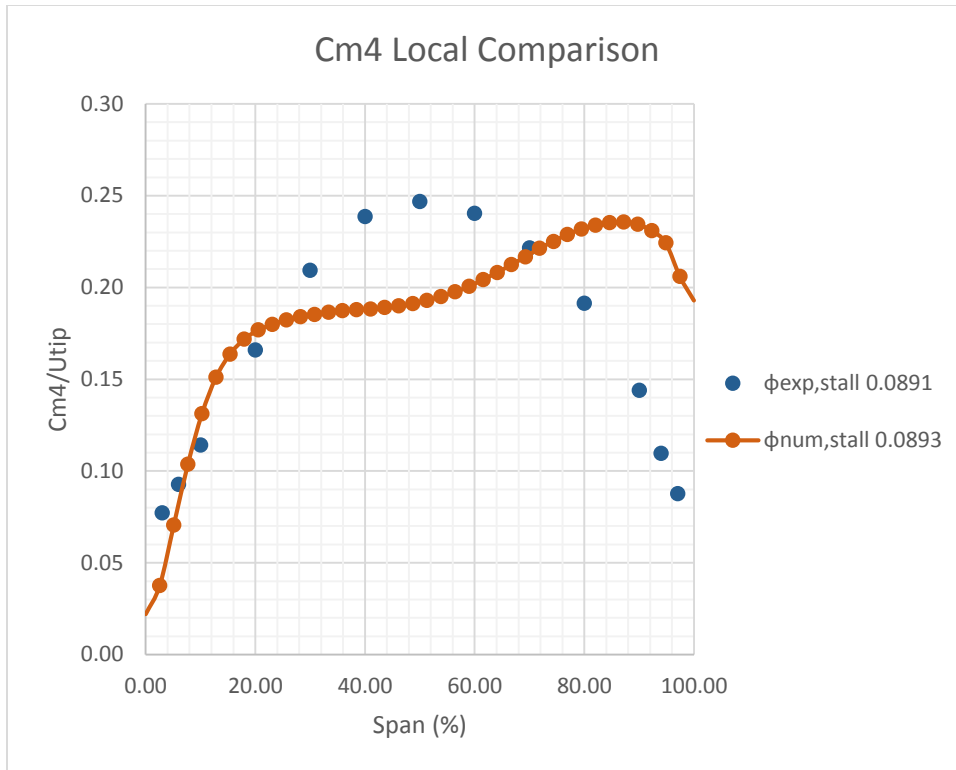


Figure 144: C_{m4} Comparison for Compressor 14 at 21870 RPM Stall Point

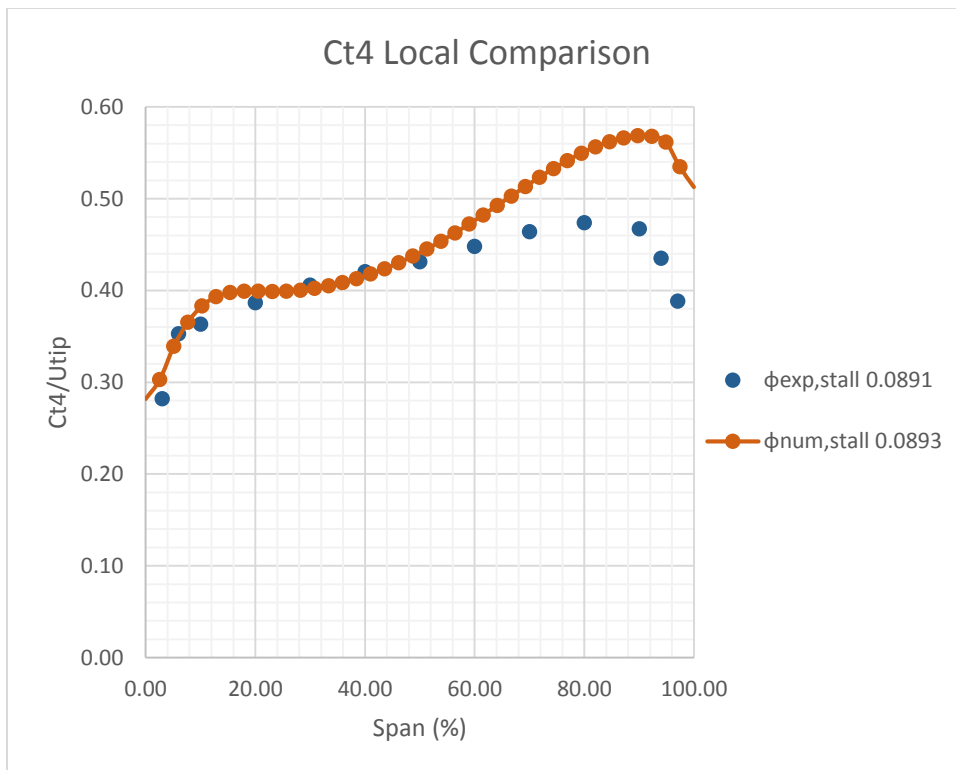


Figure 145: C_{t4} Comparison for Compressor 14 at 21870 RPM Stall Point

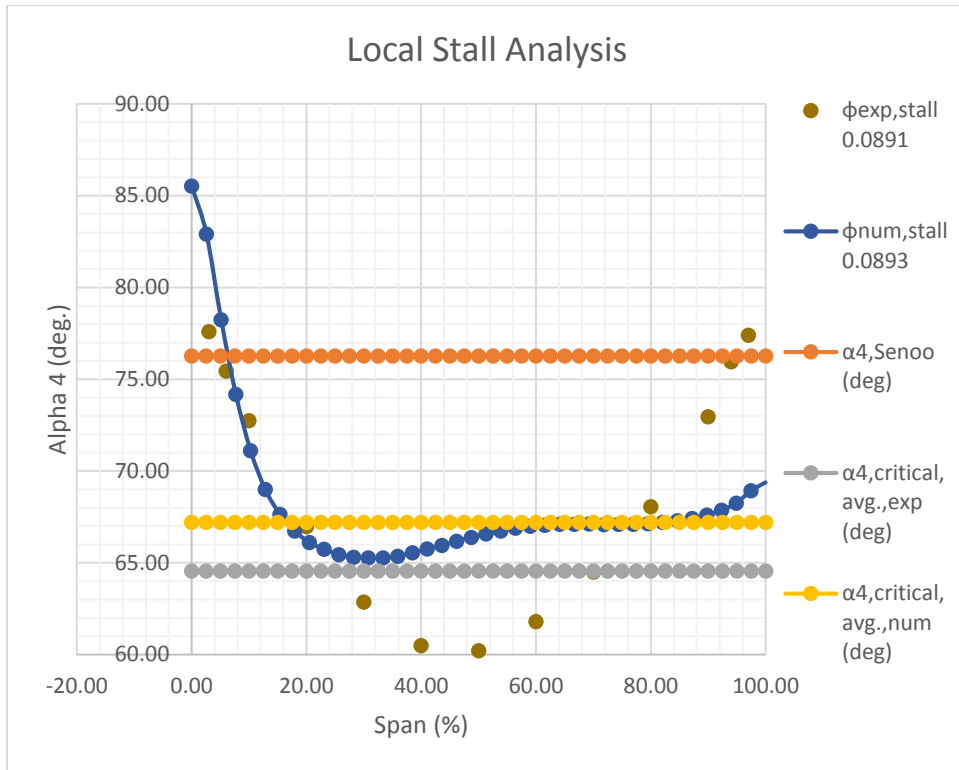


Figure 146: Stall Analysis for Compressor 14 at 21870 RPM Stall Point

6.3.15 Overall Results found from Profile Comparisons

In the previous several pages there have been many plots. Tables 33 – 35 are a way to distill the large amount of information down into something usable. Each table contains the width ratio, b_4/R_4 , the radius ratio, R_5/R_4 , the number of impeller blades, Z_{imp} , the critical flow angle, $\phi_{critical}$, and the difference in angle between the maximum of the local flow angle and the Senoo angle, $\Delta\alpha$ (see equation 6.1 above). For this discussion the critical values for Compressors 6 and 10, as well as those for Compressors 9 and 11 at 21870 RPM have been provided. This is because these values are given at the last stable flow point beyond which surge will onset. Therefore, they are considered critical points even though no rotating stall was found for Compressor 6, Compressor 10, and Compressor 9 and 11 at 21870 RPM. Also, if the $\Delta\alpha$ term is greater than zero then the numerical local flow angle profile breached the Senoo line. If the value is less than zero then the Senoo line was not breached. However, based on footnote 8 (pg. 54) if the $\Delta\alpha$ term is

negative, but has a value greater than -0.5 degrees then it is also considered to be a breach of the Senoo line.

Number	b_4/R_4	R_5/R_4	Z_{imp}	$\phi_{critical}$	$\Delta\alpha$ (deg)
1	0.067	1.343	16	0.03270	2.71
2	0.038	1.712	13	0.01700	-5.27
3	0.055	1.886	13	0.01700	6.53
4	0.045	1.714	15	0.02316	-8.13
5	0.056	1.714	15	0.02588	-7.17
6	0.021	1.557	19	0.01080	-9.60
7	0.016	1.557	15	0.00532	-5.96
8	0.013	1.512	15	0.00511	-7.68
9	0.065	1.580	15	0.03025	-0.27
10	0.062	1.343	19	0.03590	0.12
11	0.078	1.623	13	0.03620	0.23
12	0.078	1.623	13	0.04220	-5.97
13	0.112	1.692	11	0.04616	3.75
14	0.134	1.178	13	0.07376	23.25

Table 33: Critical Values at 13100 RPM

Number	b_4/R_4	R_5/R_4	Z_{imp}	$\phi_{Critical}$	$\Delta\alpha$ (deg)
1	0.067	1.343	16	0.04147	1.70
2	0.038	1.712	13	0.01900	-6.27
3	0.055	1.886	13	0.01800	7.23
4	0.045	1.714	15	0.02545	-8.23
5	0.056	1.714	15	0.02990	-8.53
6	0.021	1.557	19	0.01200	-9.70
7	0.016	1.557	15	0.00498	-3.16
8	0.013	1.512	15	0.00669	-11.74
9	0.065	1.580	15	0.03324	-0.37
10	0.062	1.343	19	0.04180	-2.28
11	0.078	1.623	13	0.03230	19.12
12	0.078	1.623	13	0.04720	-7.17
13	0.112	1.692	11	0.04694	18.25
14	0.134	1.178	13	0.07766	23.21

Table 34: Critical Values at 19240 RPM

Number	b_4/R_4	R_5/R_4	Z_{imp}	$\phi_{Critical}$	$\Delta\alpha$ (deg)
1	0.067	1.343	16	0.04350	0.17
2	0.038	1.712	13	0.02100	-7.67
3	0.055	1.886	13	0.02370	-2.27
4	0.045	1.714	15	0.02525	-6.13
5	0.056	1.714	15	0.03113	-8.43
6	0.021	1.557	19	0.01170	-8.10
7	0.016	1.557	15	0.00500	-2.52
8	0.013	1.512	15	0.00726	-12.69
9	0.065	1.580	15	0.02820	11.52
10	0.062	1.343	19	0.04190	-0.68
11	0.078	1.623	13	0.03360	22.45
12	0.078	1.623	13	0.05070	-7.87
13	0.112	1.692	11	0.04845	21.18
14	0.134	1.178	13	0.08910	9.26

Table 35: Critical Values at 21870 RPM

Observation one, the width ratio is the dominant factor in determining whether or not the Senoo line was breached. For width ratios greater than or equal to 0.065 the local flow angle profile almost always breached the Senoo line, this corresponds to Compressor 1, 9, 11, 12, 13, and 14. The notable exception to this rule is Compressor 12. For width ratios less than 0.045 no local profile crossed the Senoo line, this corresponds to Compressors 2, 4, 6, 7, and 8. Compressors 3, 5, and 10 fall in the range of $0.045 \leq b_4/R_4 \leq 0.065$. In this range Compressor 3 breached the Senoo line at 13100 RPM and 19240 RPM, but not at 21870 RPM. Compressor 5 never breached the Senoo line. Compressor 10 breached the Senoo line at 13100 RPM and was close at 21870 RPM (-0.68 degrees), but not at 19240 RPM. This means that there is a clear width ratio value (0.065) where the Senoo angle predicts rotating stall, but once beneath that value things are not so clear. Furthermore, the results show that there is a value for width ratio (0.045) beneath which the Senoo angle cannot be trusted to properly predict the critical flow angle. Lastly, there is a transition region where other factors have equal influence with the width ratio and therefore reflect a transition region in dominance of critical flow parameters.

One, final word on Compressor 12. Compressor 12 should have a local flow angle profile that crosses the Senoo line. This was unexpected because it is in the range where the local flow angle profile is supposed to cross the Senoo line based on the width ratio. In discussion with Marechale a couple of issues came up [27]. First, it is possible that the computational mesh is not accurate enough to properly resolve the flow field for Compressor 12 [27]. Second, it is possible that the rotating stall develops in the “U-Bend” region that connects the vaneless diffuser to the RTV, see Figure 14. Rotating stall has been found to occur in these regions [28]. Based on this [27] went back and ran the simulations independently of the author and found that a finer mesh did show rotating stall in the vaneless diffuser region. However, the author found, see section 7.1, that there was a region of localized flow reversal in the “U-Bend” region. Thus, it is possible that both solutions are valid.

In Compressor 3 and 5 there is an odd trend. Compressor 3 breaches the Senoo line at 13100 RPM and 19240 RPM, but not at 21870 RPM¹¹. Compressor 5 does not breach the Senoo line at all. However, Compressors 3 and 5 have nearly identical width ratios of 0.055 and 0.056, respectively. So, what could be the difference? Back in section 6.2.2 it was argued that the radius ratio had a secondary effect on the critical flow angle. This was based on conclusions in [23 – 26, 32, & 34] where it was found that the radius ratio does effect the critical flow angle. Compressors 3 and 5 have different radius ratios (1.886 and 1.714). Therefore, it highly possible that the radius ratio is causing Compressor 3 to be more unstable than Compressor 5.

¹¹ A note about the 21870 RPM rotating stall onset point for Compressor 3. It was found that the compressor operating range decreases as the operating speed increases [10]. So, it is possible that the rotating stall onset point occurs much earlier. This would be in line with the results in [26, 32] that discuss how the Mach number effects the critical flow angle. Though it was pointed out that the Mach number has a second order effect in section 6.2.3, the Mach number is still tied to the rotating speed of the impeller. This means that a faster rotating speed could destabilize the flow and create a greater buildup of stalled fluid in line with the observations in [19, 20]. This would also be in line with the effect distortion is claimed to have on the critical angle for rotating stall onset in [1, 24, & 32], but was not seen in sections 6.3.5.1 and 6.3.5.2.

Ljevar et al. found that the number of blade effects the critical flow angle as well [24]. Compressor 3 and Compressor 5 share different numbers of blades (13 and 15), so this too could be effecting the critical flow angle. In section 7.1 a simple geometric parameter will be discussed that is able to clearly outline where the local flow angle is capable of crossing the Senoo line and where it is not. But the point at hand is that for nearly identical width ratios the radius ratio and blade numbers are capable of determining whether or not the local flow angle crosses the Senoo line. This leads to the idea that the flow is not breaking down in the span-wise direction, which is dominated by diffuser width, but the circumferential direction where the constraints imposed on the flow by the diffuser walls have less influence. As a note, Senoo and Kinoshita found that if the boundary layers are able to fill up the diffuser flow passage then the flow cannot experience rotating stall [32]. It is logical then that for narrow diffusers the boundary layers are thick enough to prevent span-wise rotating stall which would be captured using the steady state model and instead leads to a circumferential flow breakdown, which is washed out by the circumferential averaging procedure employed to develop the span-wise curves.

While Compressor 6 and 10 do not exhibit rotating stall it was still found in Compressor 10 that breaches of the Senoo line were possible, see Tables 33 – 35. Compressor 6 is much narrower than Compressor 10 (width ratios of 0.021 and 0.062), but Compressor 10 is shorter (radius ratios of 1.343 and 1.557). Therefore, it is likely that the shorter radius ratio in Compressor 10 has prevented the local flow angle from breaching the Senoo line at all points, but a wider diffuser has allowed for a less stable span-wise flow which is why Compressor 10 still gets close to the Senoo line and Compressor 6 does not.

Compressors 6 and 10 have 19 blades. And neither experiences rotating stall. However, Compressors 6 and 7 have the same radius ratio (1.557) and Compressor 7 is narrower than

Compressor 6 (width ratios of 0.016 and 0.021), but Compressor 7 experiences rotating stall and Compressor 6 does not. However, Compressor 7 has only 15 blades while Compressor 6 has 19. So, the number of blades seems to effect overall diffuser stability even if the effect cannot be seen in a breach of the Senoo line. However, looking at the $\Delta\alpha$ terms for both compressors one finds that for all three speed lines Compressor 6 has $\Delta\alpha$ terms of -9.6, -9.7, and -8.1 degrees, but Compressor 7 has $\Delta\alpha$ terms of -6, -3.12, and -2.52 degrees. So, even though Compressor 7 did not breach the Senoo line, and is narrower, it was still significantly closer to the Senoo line than Compressor 7. This shows that the blade number is important to compressor stability confirming the analysis in [24].

Also, Compressors 9 and 10 can be looked at in a similar way. According to [23 – 26, & 32] a longer diffuser is less stable. Theoretically then Compressor 9 should be less stable than Compressor 10 because it is wider (width ratio of 0.065 compared to 0.062), longer (radius ratio of 1.580 compared to 1.343), and has fewer blades (15 versus 19). But Compressor 10 does not experience rotating stall at all. So, it appears that all three factors combined may have prevented a similarly designed compressor from experiencing rotating stall. It is also possible that since the critical flow coefficients, ϕ , are much larger for Compressor 10 than Compressor 9 that the onset point for rotating stall is similar for both Compressors 9 and 10, and is not reached before surge onsets in Compressor 10 because rotating stall like surge is a dynamic instability [26], intrinsically related to the design of the compressor itself [10] that can only occur if the right solution to the flow equations is obtained [15].

There is a final point to make, but it is something that requires looking back at a few figures. In Figures 101, 116, 119, 134, 137, 140, and 143 one finds localized flow reversal. The figures correspond to Compressors 9 at 21870 RPM, 11 at 19240 RPM and 21870 RPM, 13 at 19240 RPM

and 21870 RPM, and 14 at 13100 RPM and 19240 RPM. Looking at Table 35 one sees that the minimum width ratio required to capture localized flow reversal at the diffuser inlet was 0.065 for Compressor 9¹². However, this occurred at the last stable flow point at 21870 RPM as the compressor was heading into surge. For a rotating stall onset point Compressor 11 having a width ratio of 0.078 was the first case where localized flow reversal was captured at the diffuser inlet. So, to capture localized flow reversal at the rotating stall onset point a width ratio of at least 0.078 is required.

¹² As a note it was found that Compressor 1 having a width ratio of 0.067 also had localized flow reversal at the last stable flow point for the 13100 RPM speed line. This flow point has not been shown since Compressor 1 already experienced rotating stall onset before the last stable flow point and the local flow angle had already crossed the Senoo line. Thus, more flow points need not be shown to point out that rotating stall onset has already been confirmed numerically. But this note is just for reference sake and to show that Compressor 1 behaves in the same fashion as the geometrically similar Compressor 9.

CHAPTER 7: OTHER INTERESTING RESULTS

Along with the local flow investigation there were four additional investigations that were performed. Based on the results of Compressors 11, 13, and 14 which showed localized flow reversal at the inlet an idea was hatched to see if any other compressors showed localized flow reversal somewhere downstream of the diffuser inlet. Second, Senoo and Kinoshita provided several different curves to determine the critical flow angle based on the five critical parameters [32]. Using a public domain digitization software these curves were digitized and curve fit in Excel to determine if different classes of curves were better at determining the critical flow angle. Third, due to the odd distortion results (see section 6.2.5) an attempt was made to correlate distortion with critical flow angle. This investigation provided an interesting overall result. Fourth, Compressor 5 was retested using 13 blades instead of 15 to see if changing blade number brought the result in line with those for Compressor 3.

7.1 Flow Reversal at the Diffuser Inlet

Based on the results at the diffuser inlet for Compressors 11, 13, and 14 which showed localized flow reversal an investigation was started at the critical flow point for all compressors. To perform this analysis the simulation results were plotted on a meridional plot. This type of plot uses different colors to represent different numerical values of a chosen variable. In this case the radial velocity was chosen because if localized flow reversal occurred, then the radial velocity would become negative. Shown below in Figures 147 – 150 one will find two example plots. These plots were taken at the stall point for Compressors 2 and 13. What is found is that by clipping the radial velocity using a “user specified” value of -5 m/s to 0 m/s the areas of zero or greater flow appear in red, while all other areas appear in a different color allowing an investigator to distinguish between the regions of localized flow reversal and positive flow. This color scheme

works quite well. One point to make, the region that is in the box is that of the vaneless diffuser, so it should be red, while the blue region to the right in Figures 147 and 149 represents the RTV region, and the entirety of the region is expected to be blue.

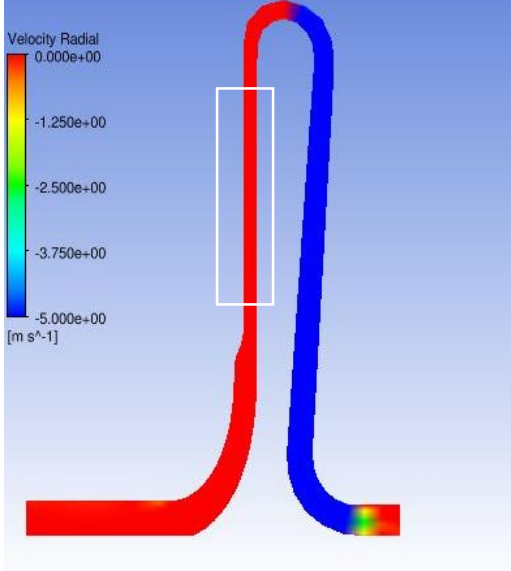


Figure 147: Compressor 2, Full View

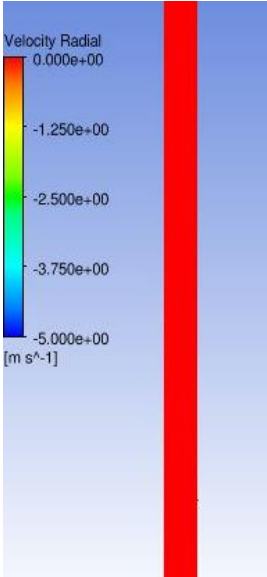


Figure 148: Compressor 2, Close Up

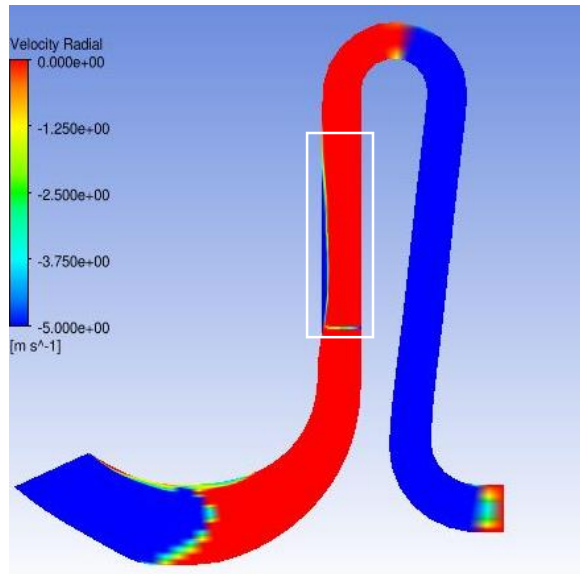


Figure 149: Compressor 13, Full View

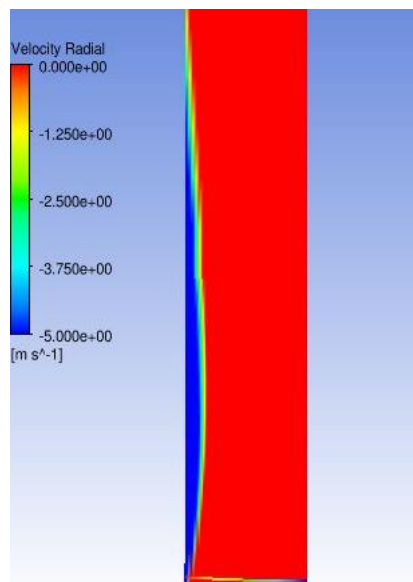


Figure 150: Compressor 13, Close Up

7.1.1 General Results

Tables 36 – 38 provide the results for the attempt to capture localized flow reversal in the vaneless diffuser. Looking at the tables one finds that for compressors with a width ratio of 0.065 or greater the steady state simulation procedure was capable of capturing localized flow reversal in the diffuser. This was the case for all compressors with a width ratio of 0.065 or greater so long

as the vaneless diffuser actually experienced rotating stall. In cases where rotating stall did not onset it was not possible to make conclusions. Although a secondary investigation was performed that found that at the last stable flow point no localized flow reversal was discovered for Compressors 6 and 10 for all three speed lines. However, for Compressors 9 and 11 localized flow reversal was found at the last stable flow point for both compressors at 21870 RPM. The only point that had a width ratio above 0.065 and did not show rotating stall was Compressor 1 at 21870 RPM. This was an odd result, but does not discount the established trend. Also, despite using the last stable flow point no localized flow reversal could be found in Compressors 6 and 10. This implies that each compressor is overall more stable than the others that experienced rotating stall.

Type	b_4/R_4	$N_{s,ave}$	$\phi_{R.S.}$	Captured $C_r < 0$
1	0.067	0.62	0.03270	Yes
2	0.038	0.49	0.01700	No
3	0.055	0.48	0.01700	No
4	0.045	0.48	0.02316	No
5	0.056	0.48	0.02588	No
6	0.021	0.35	N/A	N/A
7	0.016	0.29	0.00532	No
8	0.013	0.28	0.00511	No
9	0.065	0.57	0.03025	Yes
10	0.062	0.58	N/A	N/A
11	0.078	0.63	0.03620	Yes
12	0.078	0.69	0.04220	Yes
13	0.112	0.80	0.04616	Yes
14	0.134	1.10	0.07376	Yes

Table 36: Localized Flow Reversal Results at 13100 RPM

Type	b_4/R_4	$N_{s,ave}$	$\phi_{R.S.}$	Captured $C_r < 0$
1	0.067	0.62	0.04147	Yes
2	0.038	0.49	0.01900	No
3	0.055	0.48	0.01800	No
4	0.045	0.48	0.02545	No
5	0.056	0.48	0.02990	No
6	0.021	0.35	N/A	N/A
7	0.016	0.29	0.00498	No
8	0.013	0.28	0.00669	No
9	0.065	0.57	0.03324	Yes
10	0.062	0.58	N/A	N/A
11	0.078	0.63	0.03230	Yes
12	0.078	0.69	0.04720	Yes
13	0.112	0.80	0.04694	Yes
14	0.134	1.10	0.07766	Yes

Table 37: Localized Flow Reversal Results at 19240 RPM

Type	b_4/R_4	$N_{s,ave}$	$\phi_{R.S.}$	Captured $C_r < 0$
1	0.067	0.62	0.04350	No
2	0.038	0.49	0.02100	No
3	0.055	0.48	0.02370	No
4	0.045	0.48	0.02525	No
5	0.056	0.48	0.03113	No
6	0.021	0.35	N/A	N/A
7	0.016	0.29	0.00500	No
8	0.013	0.28	0.00726	No
9	0.065	0.57	N/A	N/A
10	0.062	0.58	N/A	N/A
11	0.078	0.63	N/A	N/A
12	0.078	0.69	0.05070	Yes
13	0.112	0.80	0.04845	Yes
14	0.134	1.10	0.08910	Yes

Table 38: Localized Flow Reversal Results at 21870 RPM

There is a point to make here. In section 6.3.12 it was discussed how the numerical profile did not breach the Senoo line, but that the experimental profile did. For this investigation it was found that localized flow reversal did occur in Compressor 12. However, it was found that the region of localized flow reversal occurred in the “U-Bend” region of the vaneless diffuser, see Figures 151 and 152.

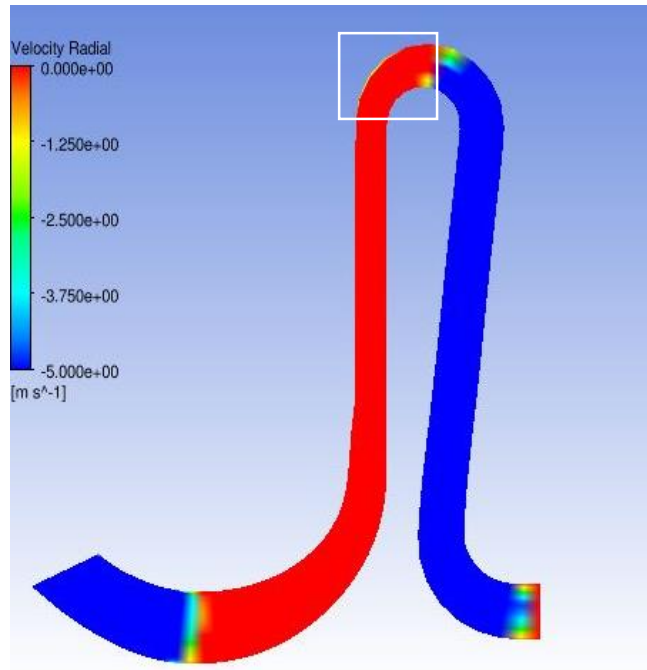


Figure 151: Compressor 12, Full View, 19240 RPM

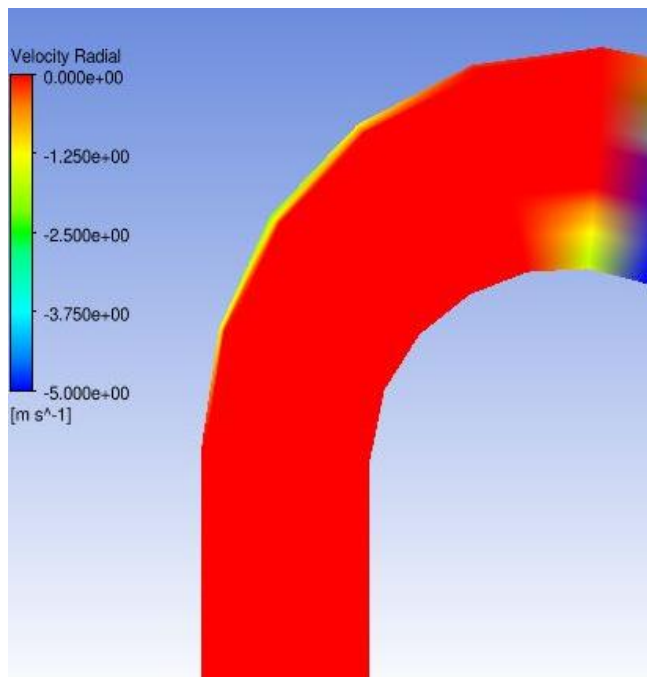


Figure 152: Compressor 12, Close Up, 19240 RPM

A look at Figures 151 and 152 shows that there is a region of localized flow reversal at the stall point inside of the vaneless diffuser “U-Bend” region. This result would make sense in light of the inability of the numerical profile to breach the Senoo line. Since the region of stall onset occurs

outside of the vaneless diffuser the diffuser inlet would likely not experience as great of an effect and therefore not breach the Senoo line. However, with the experimental profile breaching the Senoo line it is possible that the mesh was not fine enough to resolve the flow field in the diffuser. Although it is also possible that both interpretations are correct and there is a stalled region in both the vaneless diffuser and in the “U-Bend”. To determine which is outside the scope of this work.

7.1.2 Geometric Consideration

Based on the results shown in Tables 36 – 38 it was suggested that there is a geometric ratio that might be of use. So, after a discussion with [27] it was theorized that the flow might experience instability in the circumferential direction as opposed to the span-wise direction, and therefore the circumferential averaging of the flow profile would remove the regions of localized flow reversal. Thus, the b_4/d_{pitch} parameter was developed. The d_{pitch} and b_4/d_{pitch} terms are defined as:

$$d_{pitch} = \frac{2*\pi*R_{tip}}{Z_{imp}} \quad (7.1)$$

$$\frac{b_4}{d_{pitch}} = \frac{b_4*Z_{imp}}{2*\pi*R_{tip}} \quad (7.2)$$

where b_4 is the diffuser inlet width, R_{tip} is the impeller tip radius, and Z_{imp} is the number of impeller blades. This parameter is used as a measure of the width of the diffuser versus the distance between impeller blades. It is used to take the impeller – diffuser coupling [1] into account and determine whether the flow is more likely to breakdown in the span-wise direction between the diffuser walls or in the circumferential direction defined by the wavelength associated with the distance between impeller blade tips. The comparison of the b_4/d_{pitch} parameter to the localized flow reversal results can be found in Tables 39 – 41.

Type	b_4/R_4	$\phi_{R.S.}$	Captured $C_r < 0$	b_4/d_{pitch}
1	0.067	0.03270	Yes	0.20428
2	0.038	0.01700	No	0.09012
3	0.055	0.01700	No	0.11954
4	0.045	0.02316	No	0.12075
5	0.056	0.02588	No	0.15215
6	0.021	N/A	N/A	0.06896
7	0.016	0.00532	No	0.04083
8	0.013	0.00511	No	0.03507
9	0.065	0.03025	Yes	0.17704
10	0.062	N/A	N/A	0.22243
11	0.078	0.03620	Yes	0.19081
12	0.078	0.04220	Yes	0.19081
13	0.112	0.04616	Yes	0.22176
14	0.134	0.07376	Yes	0.34507

Table 39: Localized Flow Reversal Results at 13100 RPM

Type	b_4/R_4	$\phi_{R.S.}$	Captured $C_r < 0$	b_4/d_{pitch}
1	0.067	0.04147	Yes	0.20428
2	0.038	0.01900	No	0.09012
3	0.055	0.01800	No	0.11954
4	0.045	0.02545	No	0.12075
5	0.056	0.02990	No	0.15215
6	0.021	N/A	N/A	0.06896
7	0.016	0.00498	No	0.04083
8	0.013	0.00669	No	0.03507
9	0.065	0.03324	Yes	0.17704
10	0.062	N/A	N/A	0.22243
11	0.078	0.03230	Yes	0.19081
12	0.078	0.04720	Yes	0.19081
13	0.112	0.04694	Yes	0.22176
14	0.134	0.07766	Yes	0.34507

Table 40: Localized Flow Reversal Results at 19240 RPM

Type	b_4/R_4	$\phi_{R.S.}$	Captured $C_r < 0$	b_4/d_{pitch}
1	0.067	0.04350	No	0.20428
2	0.038	0.02100	No	0.09012
3	0.055	0.02370	No	0.11954
4	0.045	0.02525	No	0.12075
5	0.056	0.03113	No	0.15215
6	0.021	N/A	N/A	0.06896
7	0.016	0.00500	No	0.04083
8	0.013	0.00726	No	0.03507
9	0.065	N/A	N/A	0.17704
10	0.062	N/A	N/A	0.22243
11	0.078	N/A	N/A	0.19081
12	0.078	0.05070	Yes	0.19081
13	0.112	0.04845	Yes	0.22176
14	0.134	0.08910	Yes	0.34507

Table 41: Localized Flow Reversal Results at 21870 RPM

Looking at Tables 39 – 41 one finds that it was possible to capture localized flow reversal inside of the diffuser if b_4/d_{pitch} was equal to or greater than 0.177 (Compressor 9), but if b_4/d_{pitch} was less than 0.152 it was not possible (Compressor 5). These results provide a couple of points. First, for values of b_4/d_{pitch} between 0.152 and 0.177 there is nothing that can be said without actual data in this region. Second, the b_4/d_{pitch} parameter is very predictive of whether or not localized flow reversal can be captured using a steady state simulation. Third, these results point to the fact that if b_4/d_{pitch} is greater than or equal to 0.177 that the flow field will breakdown in the span-wise direction allowing for a breach of the Senoo line. However, if the b_4/d_{pitch} term is less than or equal to 0.152 then the flow field is breaking down in the circumferential direction. This is most likely caused by the boundary layers growing together in the span-wise direction and preventing the flow from breaking down [32]. But to solve the flow equations the flow must breakdown somewhere [15], so the circumferential direction becomes the direction of flow instability. Fourth, the region where b_4/d_{pitch} is between 0.152 and 0.177 is best seen as a transition region where the span-wise destabilization and circumferential destabilization effects fight for dominance. Fifth, Compressor

10 happens to be in the range of predictability for localized flow reversal since it has a b_4/d_{pitch} value of 0.222. This geometry was investigated at the last stable flow point, but localized flow reversal was not captured, see Figures 153 - 155.

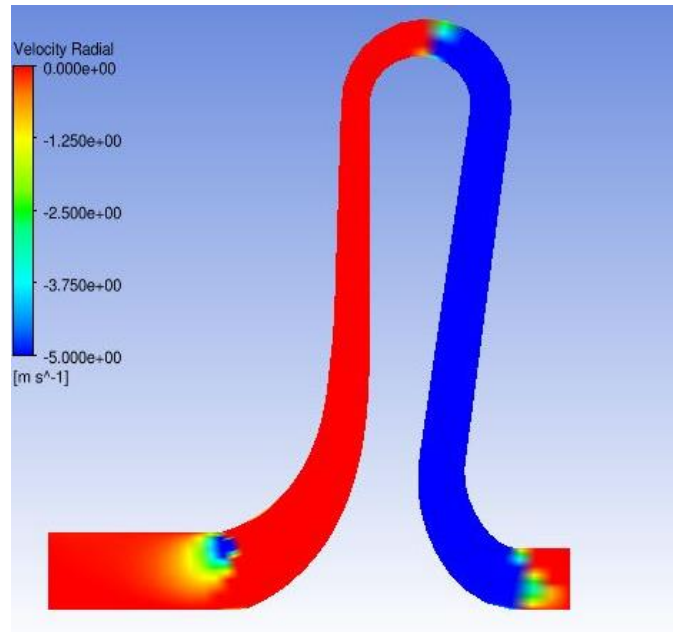


Figure 153: Compressor 10, 13100 RPM, Last Stable Flow Point

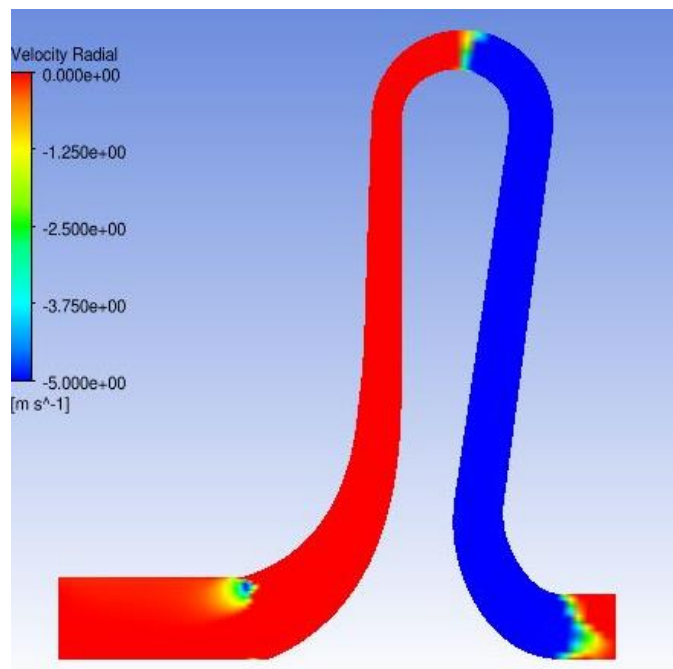


Figure 154: Compressor 10, 19240 RPM, Last Stable Flow Point

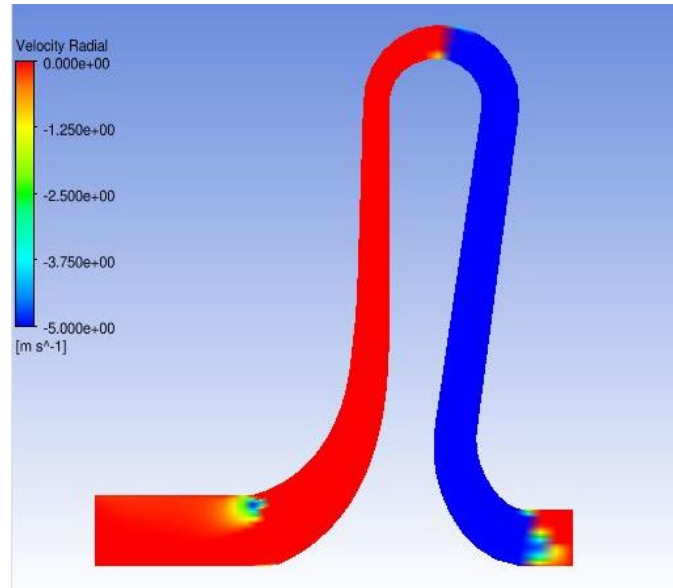


Figure 155: Compressor 10, 21870 RPM, Last Stable Flow Point

This was somewhat surprising, but there are two things of note. First, Compressor 10 was stable. Therefore, it is possible that there was no localized flow reversal to be found in the diffuser. Second, Compressor 10 has a width ratio of 0.062 it is possible that the narrower walls combined with a shorter diffuser (radius ratio 1.343) helped to cause the flow to breakdown in the circumferential direction. This would contradict the other results based upon the b_4/d_{pitch} parameter. Overall, since Compressor 10 did not experience rotating stall it is difficult to draw conclusions from the data, since it is compared against other compressors that did experience rotating stall. As a note Compressor 6 was also found to not experience localized flow reversal inside of the diffuser at the last stable flow point see Figures 156 - 158. However, with a b_4/d_{pitch} parameter of 0.069 this result is expected.

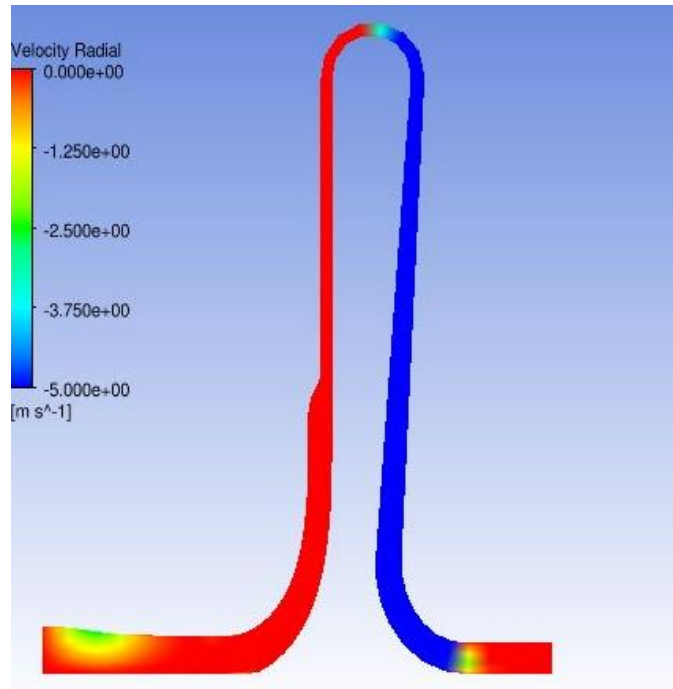


Figure 156: Compressor 6, 13100 RPM, Last Stable Flow Point

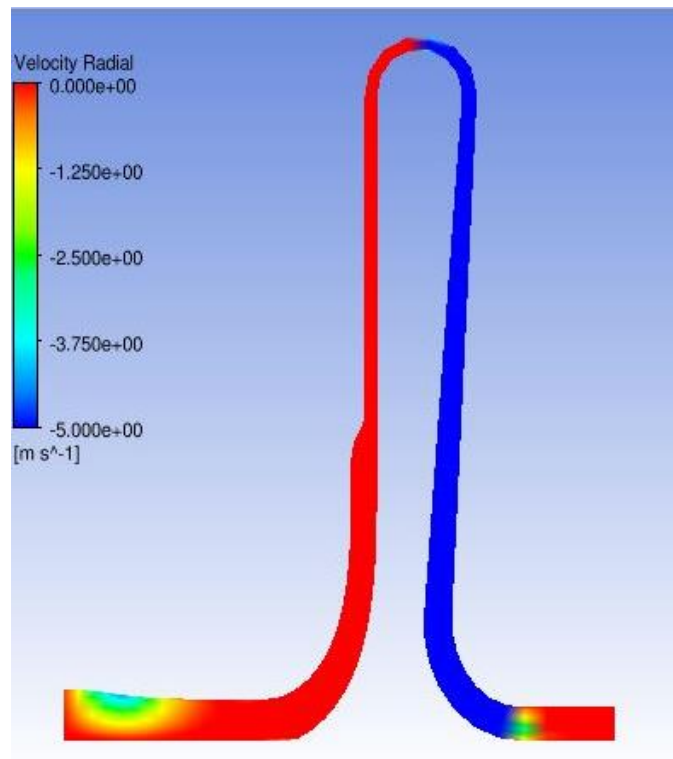


Figure 157: Compressor 6, 19240 RPM, Last Stable Flow Point

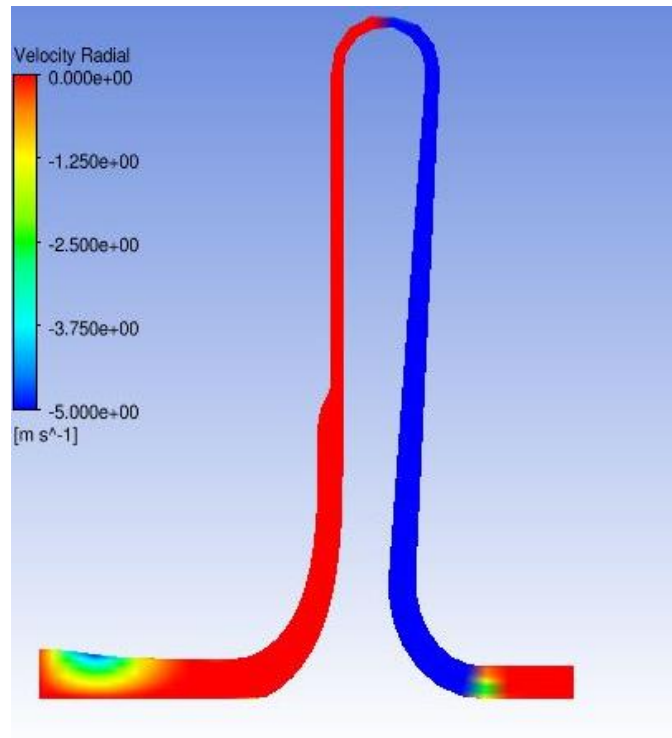


Figure 158: Compressor 6, 21870 RPM, Last Stable Flow Point

7.1.3 Local Flow Velocity Reversal and Rotating Stall Onset

In [26, 34, & 41] it was claimed that localized flow reversal was the trigger mechanism for rotating stall onset. So, using the ability to capture localized flow reversal using the meridional plots it was decided to check and see whether or not localized flow reversal really is the trigger for rotating stall. Shown below in Figures 159 – 182 are four figures for six specific compressors: Compressors 2, 5, 7, 9, 13, and 14. There are three compressors that should not show localized flow reversal: 2, 5, and 7, and there are three compressors that should show localized flow reversal: 9, 13, and 14. These figures were taken for each compressor at the 19240 speed line and contain four flow points: two points before the rotating stall onset point, the rotating stall onset point, and one point after the rotating stall onset point.

The results for Compressors 2, 5, and 7 (see Figures 159 – 170) show that no localized flow reversal was found for any of these three compressors. It goes on to show that the flow is not

breaking down in the span-wise direction, but in the circumferential direction. These results are expected based upon the b_4/d_{pitch} results given above in section 7.1.2.

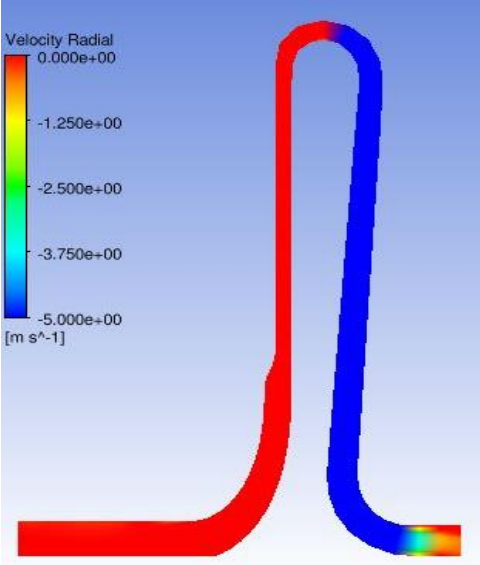


Figure 159: Compressor 2, $\phi = 0.026027$

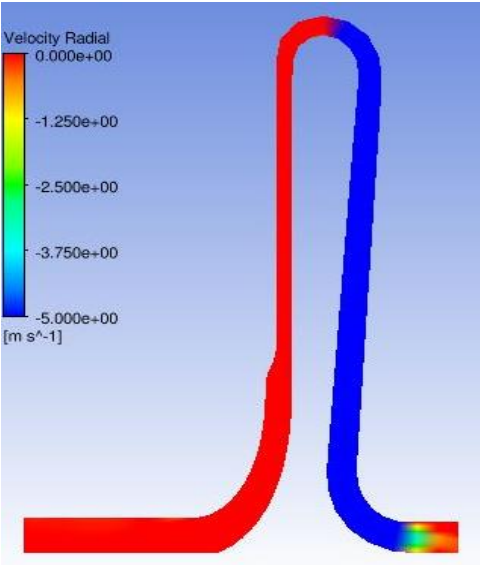


Figure 160: Compressor 2, $\phi = 0.022083$

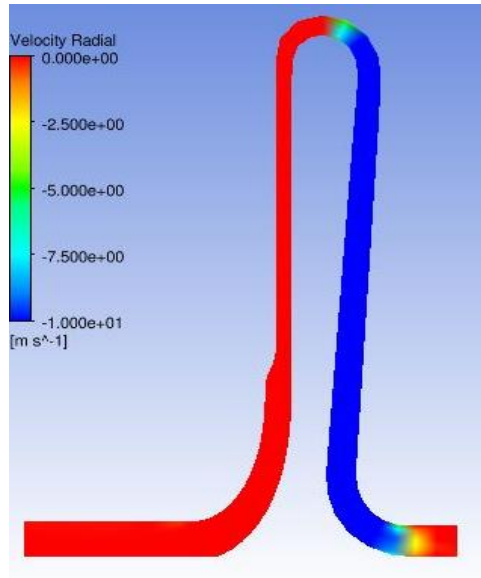


Figure 161: Compressor 2, $\phi = \phi_{RS} = 0.019$

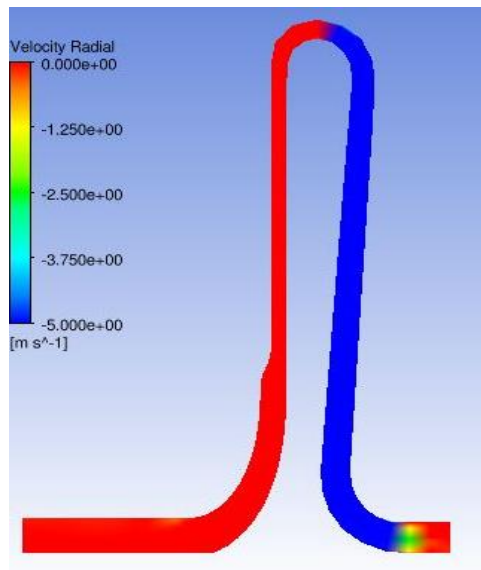


Figure 162: Compressor 2, $\phi = 0.018883$

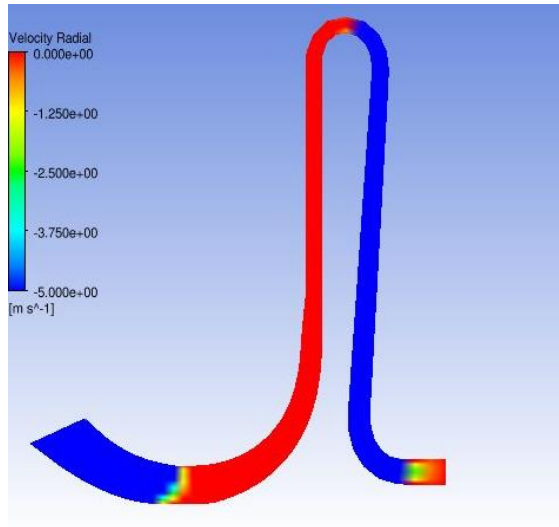


Figure 163: Compressor 5, $\phi = 0.0385$

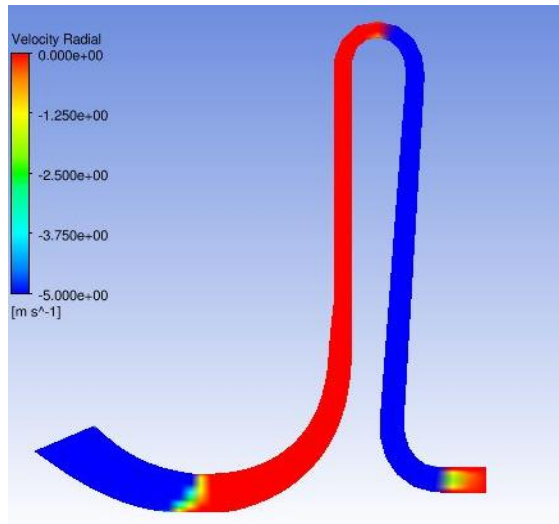


Figure 164: Compressor 5, $\phi = 0.0336$

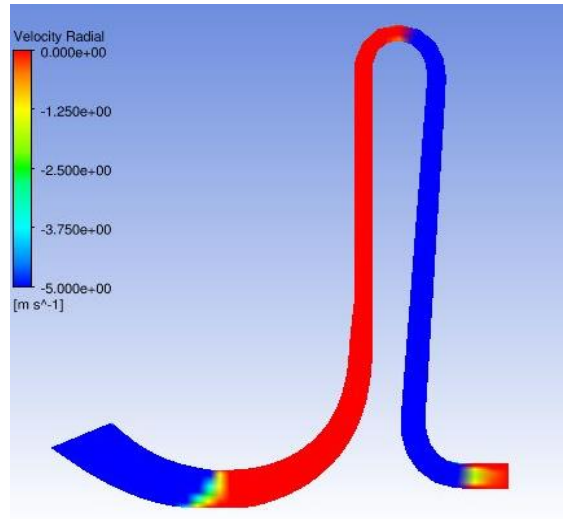


Figure 165: Compressor 5, $\phi = \phi_{RS} = 0.0299$

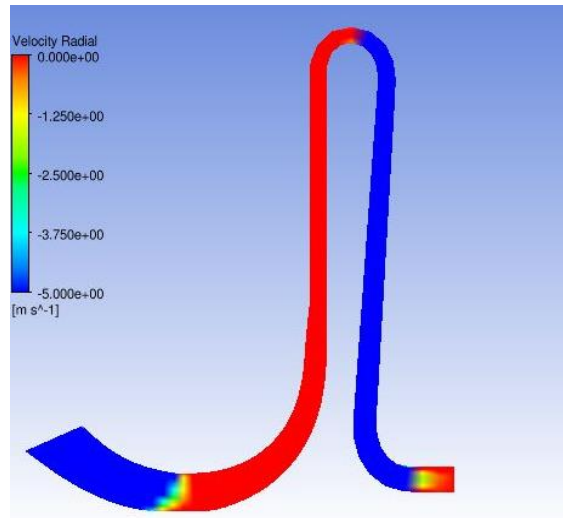


Figure 166: Compressor 5, $\phi = 0.0295$

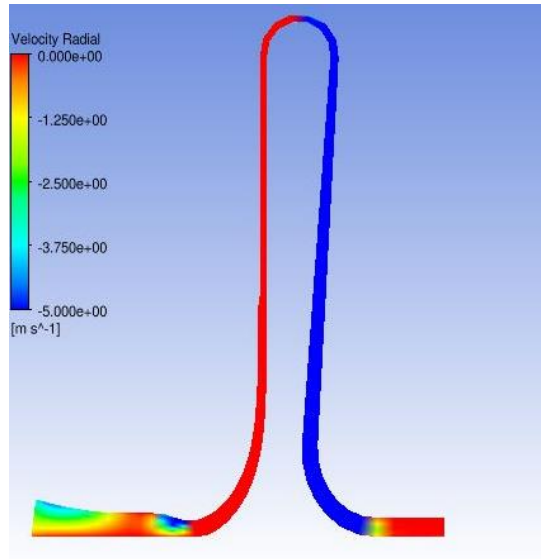


Figure 167: Compressor 7, $\phi = 0.0066$

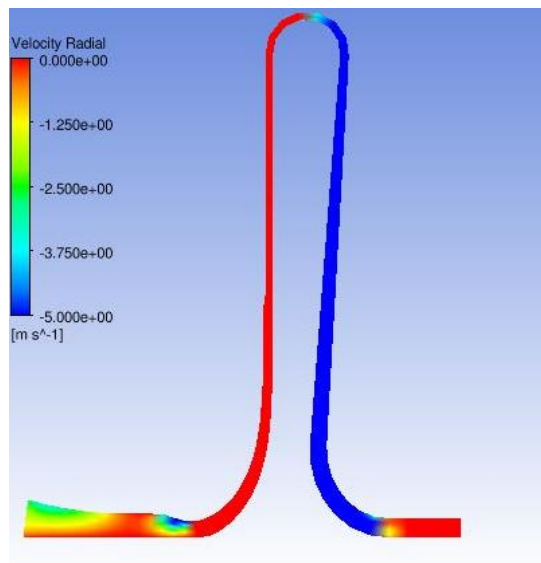


Figure 168: Compressor 7, $\phi = 0.005$

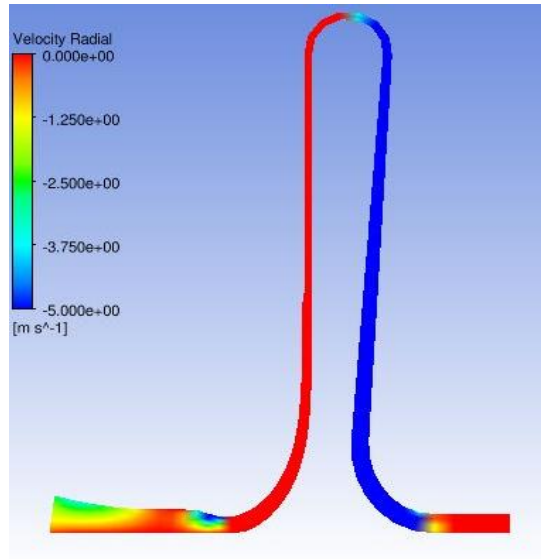


Figure 169: Compressor 7, $\phi = \phi_{RS} = 0.00498$

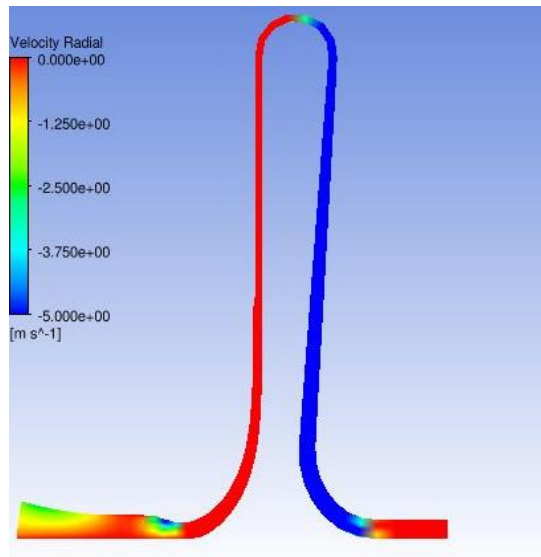


Figure 170: Compressor 7, $\phi = 0.004017$

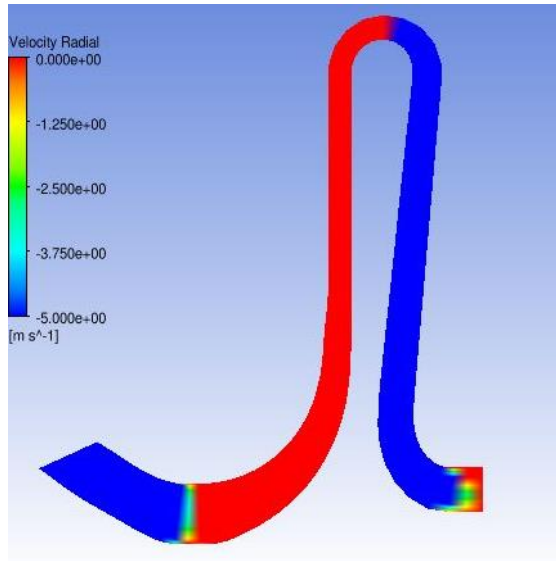


Figure 171: Compressor 9, $\phi = 0.040208$

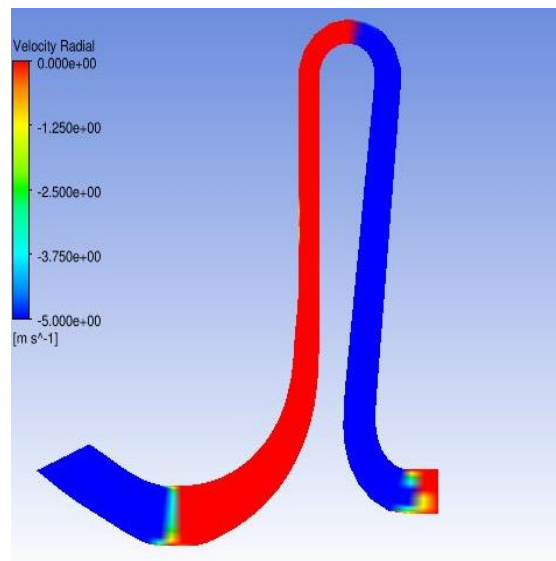


Figure 172: Compressor 9, $\phi = 0.033401$

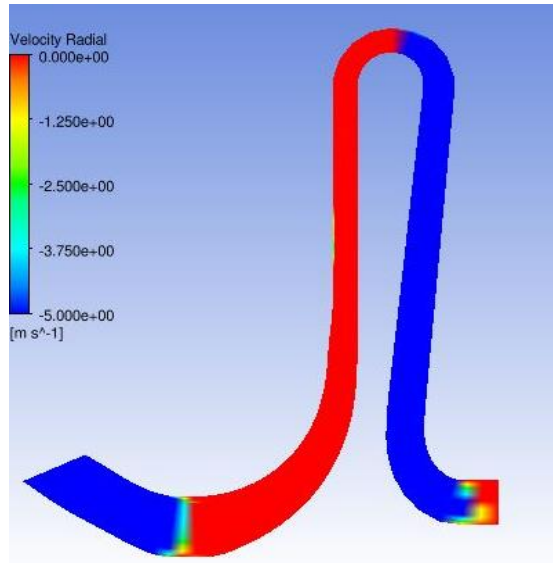


Figure 173: Compressor 9, $\phi = \phi_{RS} = 0.03324$

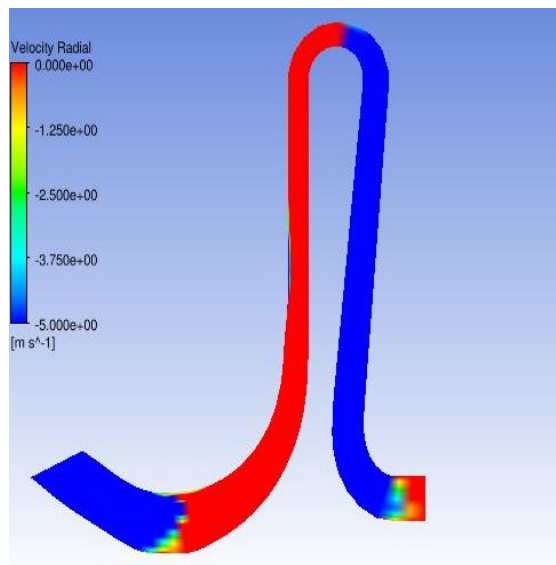


Figure 174: Compressor 9, $\phi = 0.028244$

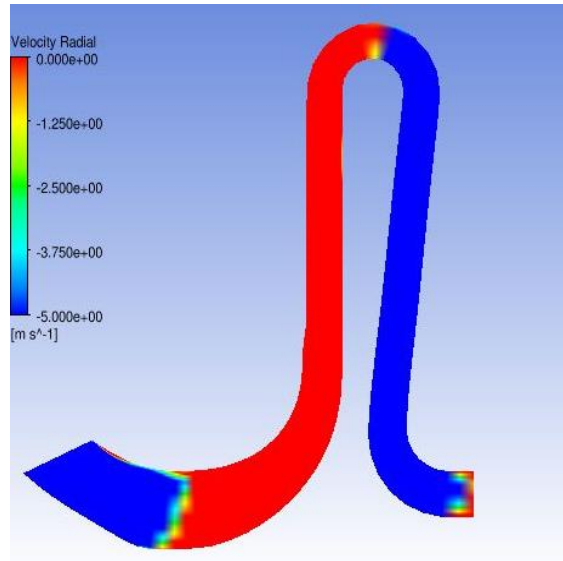


Figure 175: Compressor 13, $\phi = 0.064257$

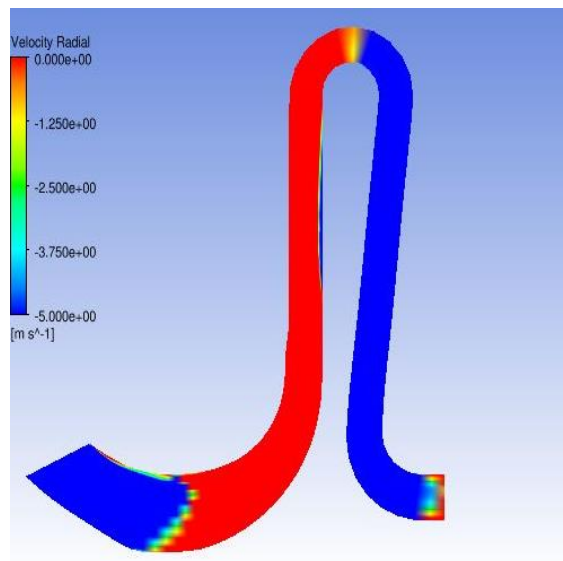


Figure 176: Compressor 13, $\phi = 0.055032$

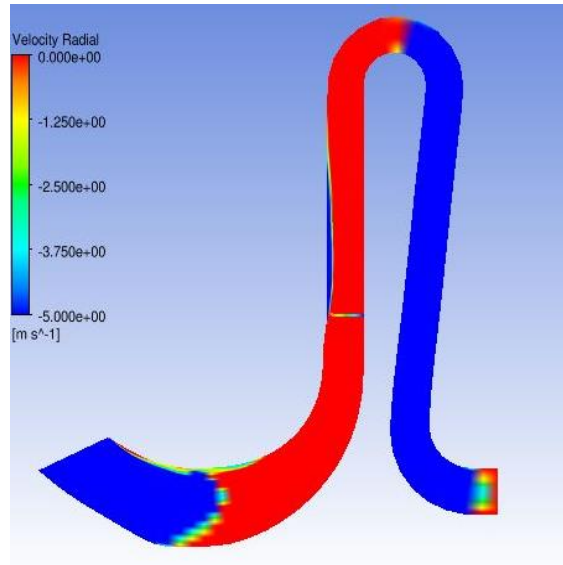


Figure 177: Compressor 13, $\phi = \phi_{RS} = 0.046943$

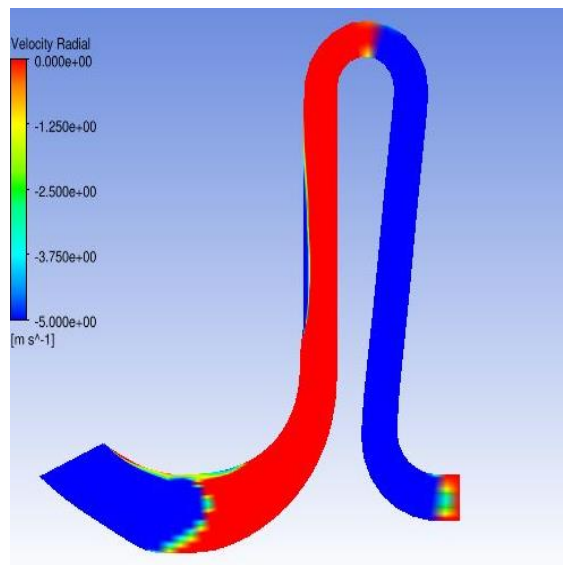


Figure 178: Compressor 13, $\phi = 0.045548$

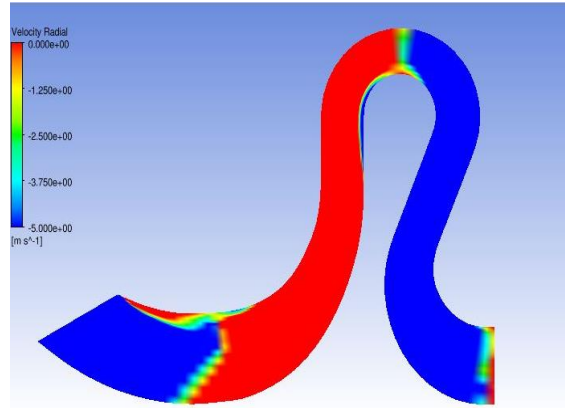


Figure 179: Compressor 14, $\phi = 0.08472$

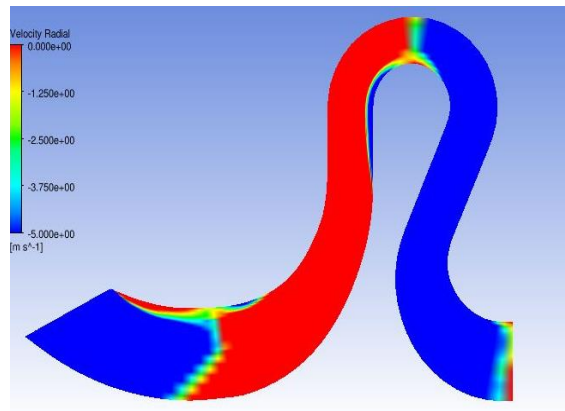


Figure 180: Compressor 14, $\phi = 0.077772$

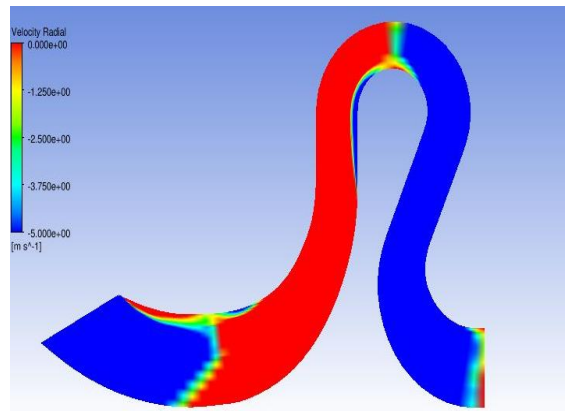


Figure 181: Compressor 14, $\phi = \phi_{RS} = 0.07766$

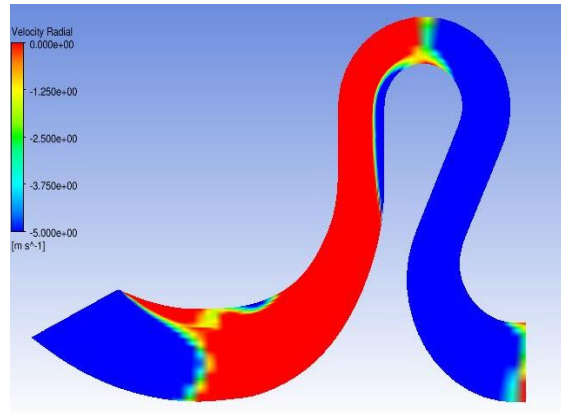


Figure 182: Compressor 14, $\phi = 0.064187$

Looking at the results for Compressors 9, 13, and 14 (see Figures 171 – 182) one finds that there is localized flow reversal for each compressor. This result is expected from the results given in section 7.1.2. However, what was not expected is that in each case (see Figures 172, 176, and 180) localized flow reversal developed before the onset point of rotating stall. And for Compressors 13 and 14 (Figures 176 and 180) the localized flow reversal developed a significant distance in flow coefficient from the rotating stall point. Therefore, from these results it can be concluded that localized flow reversal while necessary to the triggering of rotating stall was not sufficient to trigger rotating stall onset in contradiction of [26, 34, & 41].

7.2 Digitized Senoo Curve Investigation

While working on the local flow angle investigation it became clear that it would be best if the method could be made predictive. At this moment the method still requires comparison against a predicted critical flow angle (i.e. the Senoo – Kobayashi equation). Senoo and Kinoshita developed several different curves in [32] and it was thought that by digitizing those curves a predictive method could be developed.

7.2.1 Process of Digitization

Digitization is a process where a figure is taken and loaded into a software that breaks the curve into readable data points. These data points can then be loaded into a spreadsheet (in this

case Excel). From there a curve can be fit to the data allowing for the any missing data point to be found using the curve and the independent variables. Shown below in Figures 183 and 184 are samples curves taken from [32] and [26]. These curves show how the critical flow angle changes as a function of tangential distortion (Figure 183) and radius ratio (Figure 184). It is of note that Senoo and Kinoshita have curves that also depend on Mach number, Reynolds number, and Meridional Distortion [32]. As one can see each figure has multiple curves that are broken down based on width ratio and radius ratio. The change in width ratio seeks to change the shape of the curve, while changes in radius ratio will change the separation between the curves (see [32] for more examples).

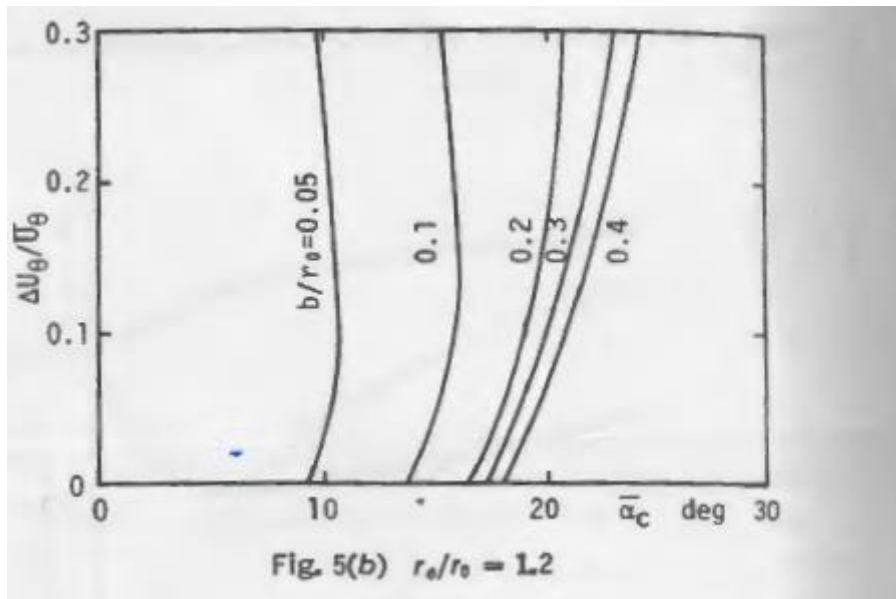


Figure 183: Tangential Distortion Example Adapted and Reproduced from [32]

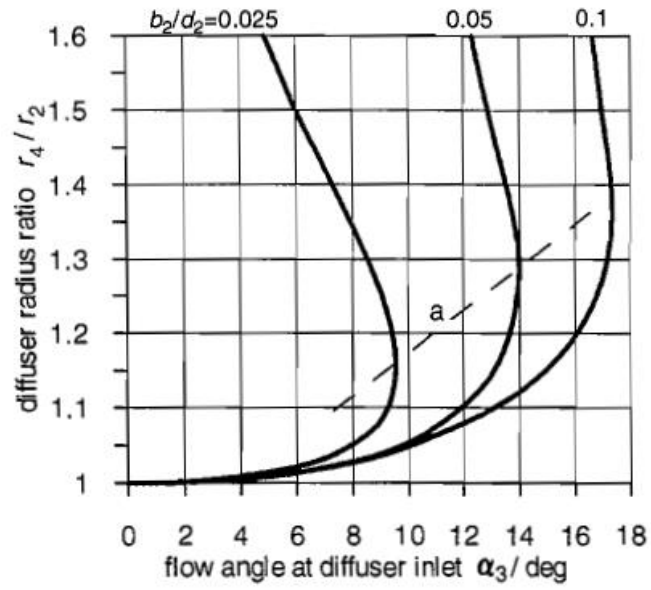


Figure 184: Radius Ratio Plot Adapted and Reproduced from [26]

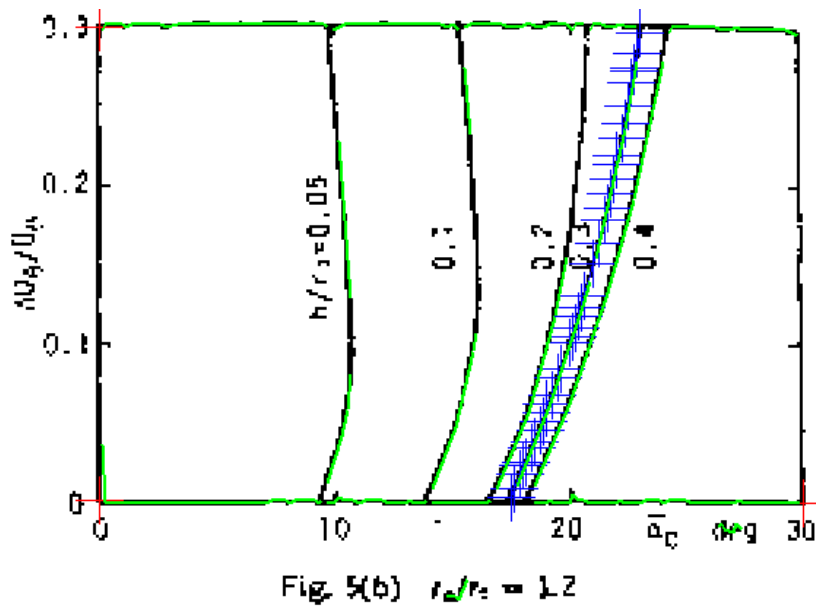


Figure 185: Digitized Tangential Distortion Example of Plot from [32]

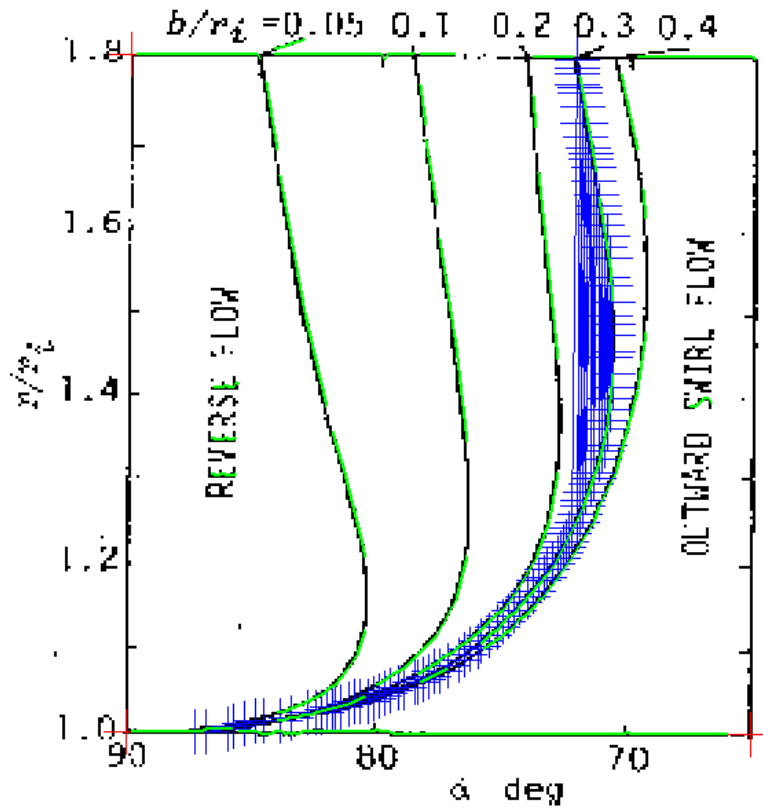


Figure 186: Digitized Radius Ratio Example of Plot from [32]

Once a screenshot of each curve has been taken the image is loaded into an open source digitizer found at <http://digitizer.sourceforge.net/>. There are two examples of this shown in Figures 185 and 186, above. At this point the x and y axes are determined by setting specific values represented by the red crosses in Figures 185 and 186. Then, a set of curve points is determined by clicking along the line that one wants to digitize, these points are represented by blue crosses above. From there the data is exported from the digitizer into an Excel file and the curve is plotted. A curve fit can be made to each plot and then using specific values one can determine the “appropriate” critical flow angle.

Once the curve fit was determined the curves were loaded into an Excel template based on the radius ratio of each geometry. From there the geometry of each compressor stage was used to determine which curve fit best represented the stage configuration. The now “predicted” critical

flow angle was plotted against the Senoo angle and local flow angles to see if it was possible to reach the Senoo line (or get within 0.5 degrees). This was done for four different variables: Mach number, tangential distortion, meridional distortion, and radius ratio. It was not possible to digitize the Reynolds number curves because of the need for linear scaling of the axes in digitization (the Reynolds number curves used log-linear scaling). Four specific geometries representing different stage width ratios are provided at the stall point at 19240 RPM. The 19240 RPM speed line is considered the design speed for the compressor, thus making it the most likely trouble spot for a compressor operator. See Table 2, in section 5.3.2, for the geometry of each stage. The stall point is shown because this is the operating speed where the critical values are determined. If the “predicted values” are close to the Senoo line then the method is a success, but if they are not or the local flow angle breaches the Senoo line then the method is no better than what has been discussed in Chapter 6.

7.2.2 Digitization Results

The results for the four specific geometries at the 19240 RPM speed line are shown below in Figures 187 – 202. As a note Compressor 1 has a critical flow angle determined using width ratios of 0.05 and 0.1 this is because the width ratio for Compressor 1 is 0.067 and falls in a grey area between two separate curves. Each figure has five or six lines. The lines show the Senoo angle (α_{4s}), the experimental critical flow angle (α_{4e}), the numerical critical flow angle (α_{4n}), the critical flow angle determined at the specific width ratio ($\alpha_{4C,0.05}$ for example), and the local flow angle (α_4).

Looking at Figures 187 – 190 for Compressor 1 it is found that the predictive method is really no better than the local flow angle approach. While this would serve as a good first approximation the distortion values (Figures 187 and 190) and the Mach number values (188)

require actual data to calculate, especially the distortion values. So, if one dimensional data is not available it could hamper the use of this method. The radius ratio value (Figure 189) has critical values that are mirrored around the Senoo angle showing that the Senoo angle falls between the two values. This means the Senoo angle serves as a happy medium between the two newly calculated critical flow angles. Overall, for Compressor 1 the digitized curves get closer to the Senoo angle, but are really no better than the Senoo angle.

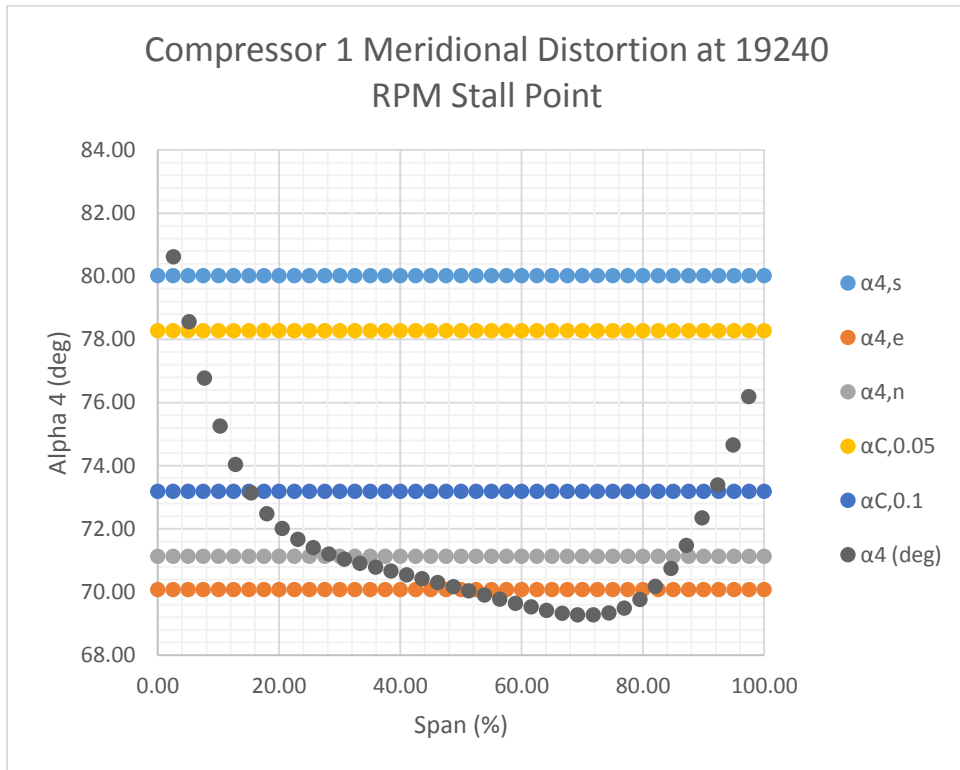


Figure 187: Compressor 1 Angle Comparison Using Meridional Distortion at Stall Point

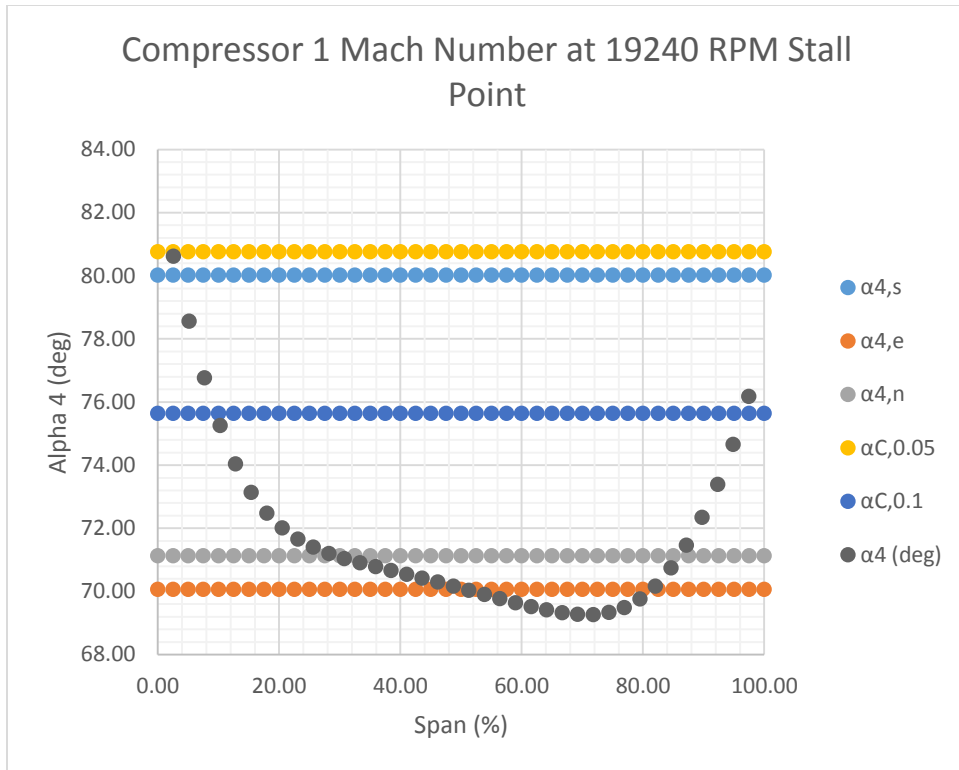


Figure 188: Compressor 1 Angle Comparison Using Mach Number at Stall Point

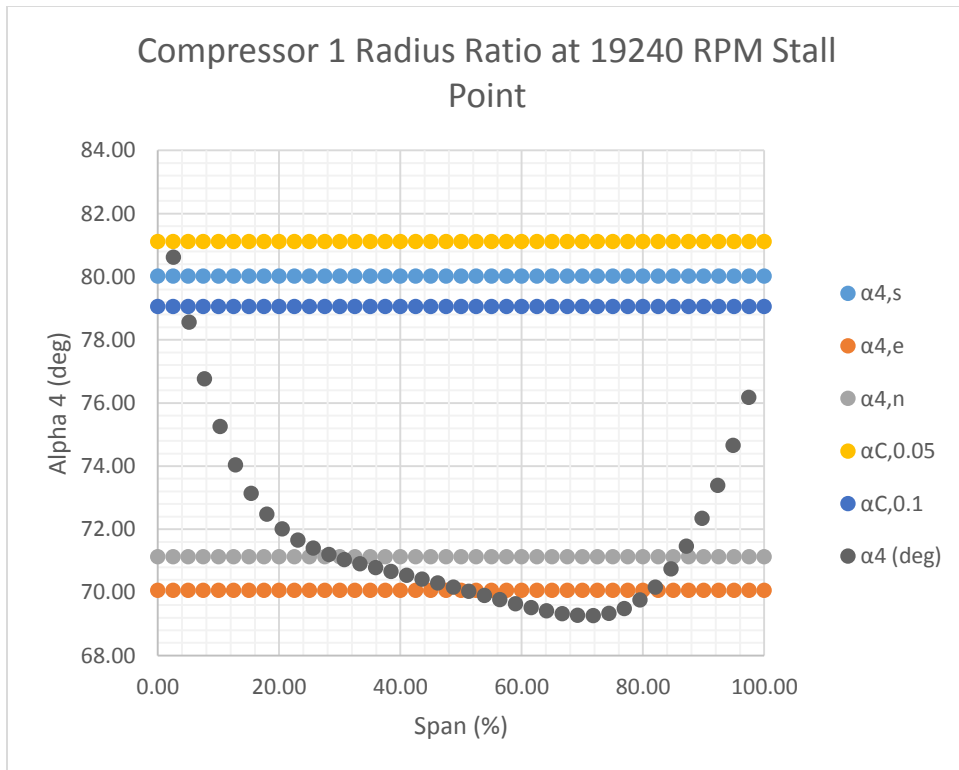


Figure 189: Compressor 1 Angle Comparison Using Radius Ratio at Stall Point

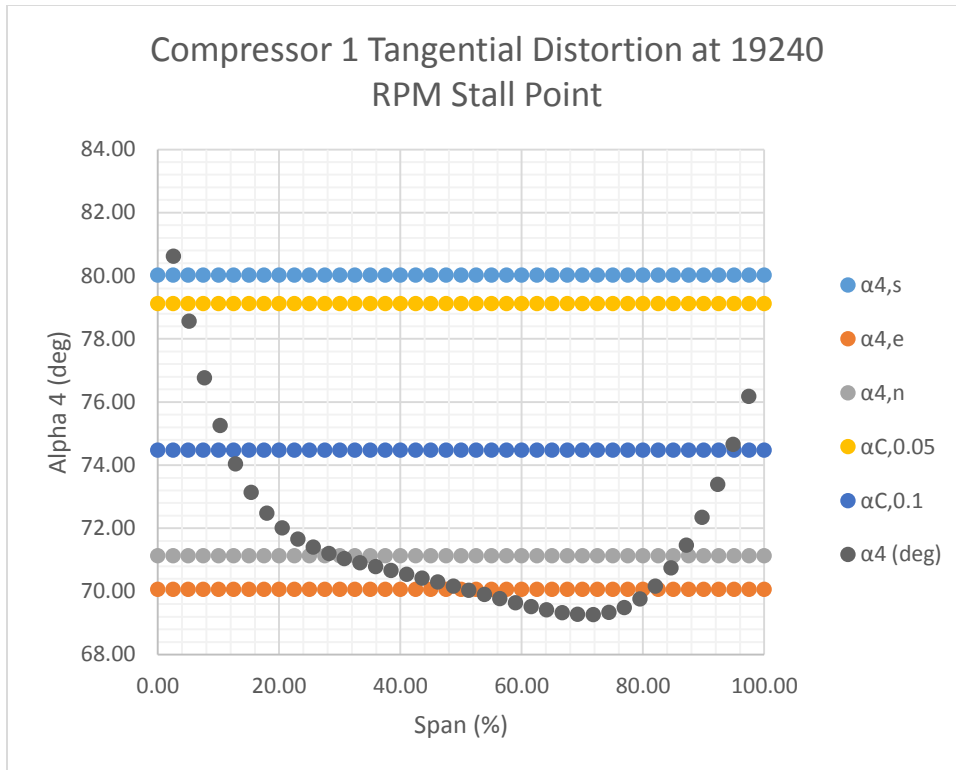


Figure 190: Compressor 1 Angle Comparison Using Tangential Distortion at Stall Point

The results for Compressor 5 (width ratio of 0.056) are found in Figures 191 – 194. In each case the predicted critical flow angle is much closer to the Senoo angle than the local flow angle. So, while the local flow angle shows that one is far from instability, the predictive angles show that one is much closer to an unstable situation.

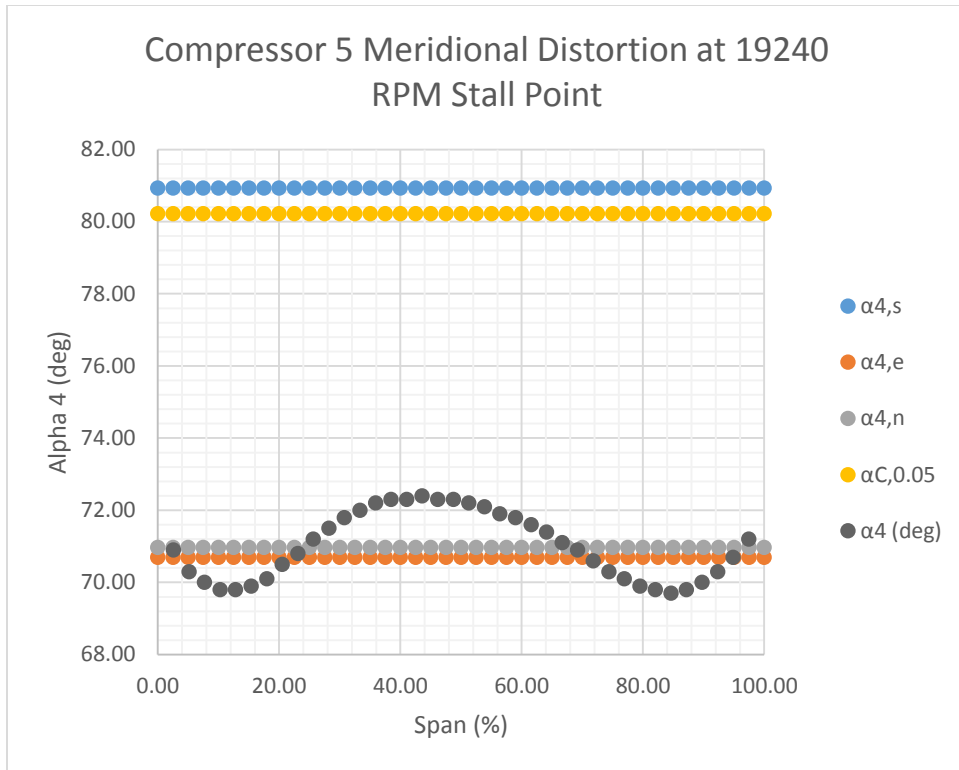


Figure 191: Compressor 5 Angle Comparison Using Meridional Distortion at Stall Point

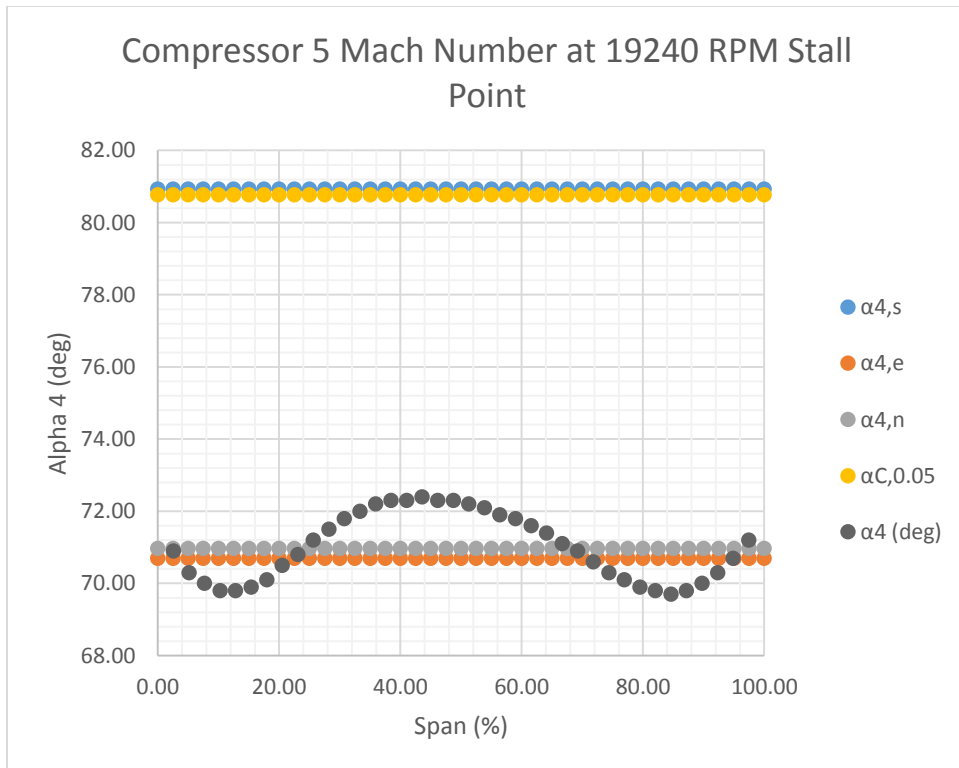


Figure 192: Compressor 5 Angle Comparison Using Mach Number at Stall Point

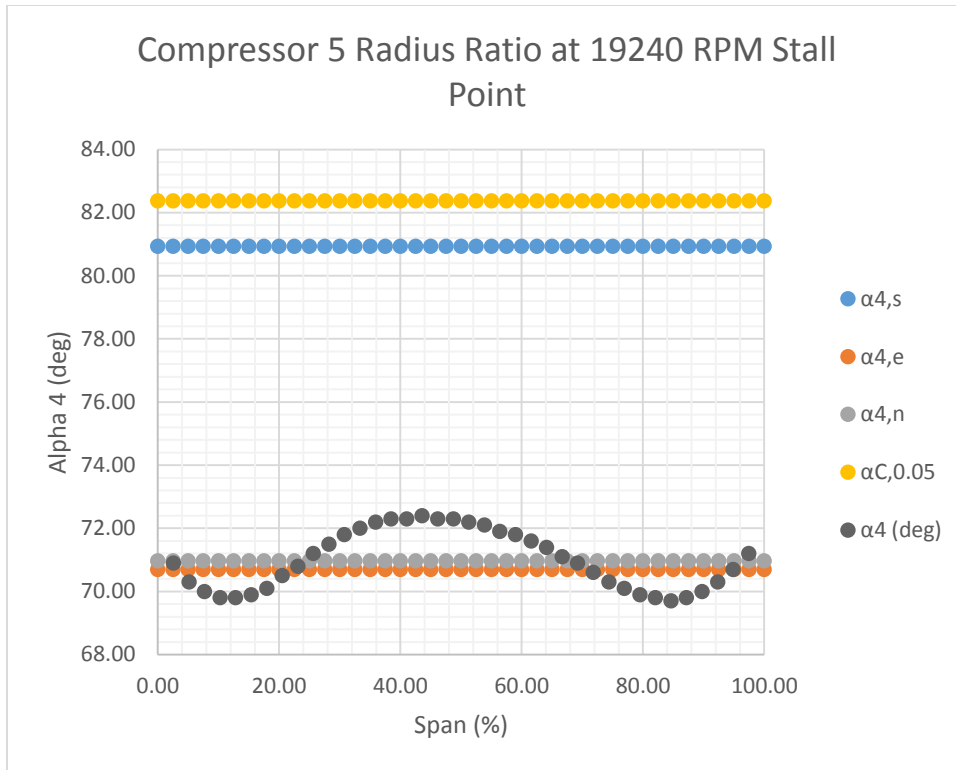


Figure 193: Compressor 5 Angle Comparison Using Radius Ratio at Stall Point

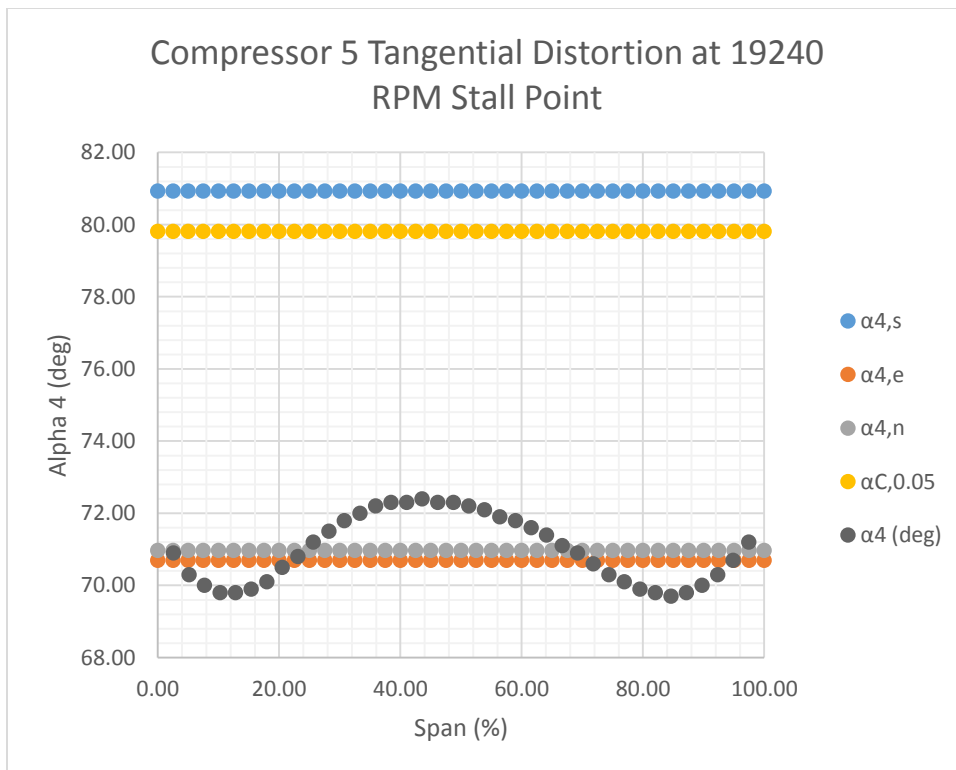


Figure 194: Compressor 5 Angle Comparison Using Tangential Distortion at Stall Point

The results for Compressor 7 (width ratio of 0.016) are found in Figures 195 – 198. For this geometry the predictive angles do not reach the Senoo line. However, for all cases except the radius ratio (Figure 197) the local flow angle crosses the predictive angle. This is an unexpected result. However, if it was consistent it would show that for this compressor stage using the predictive method would be better suited than the Senoo angle at determining stage stability.

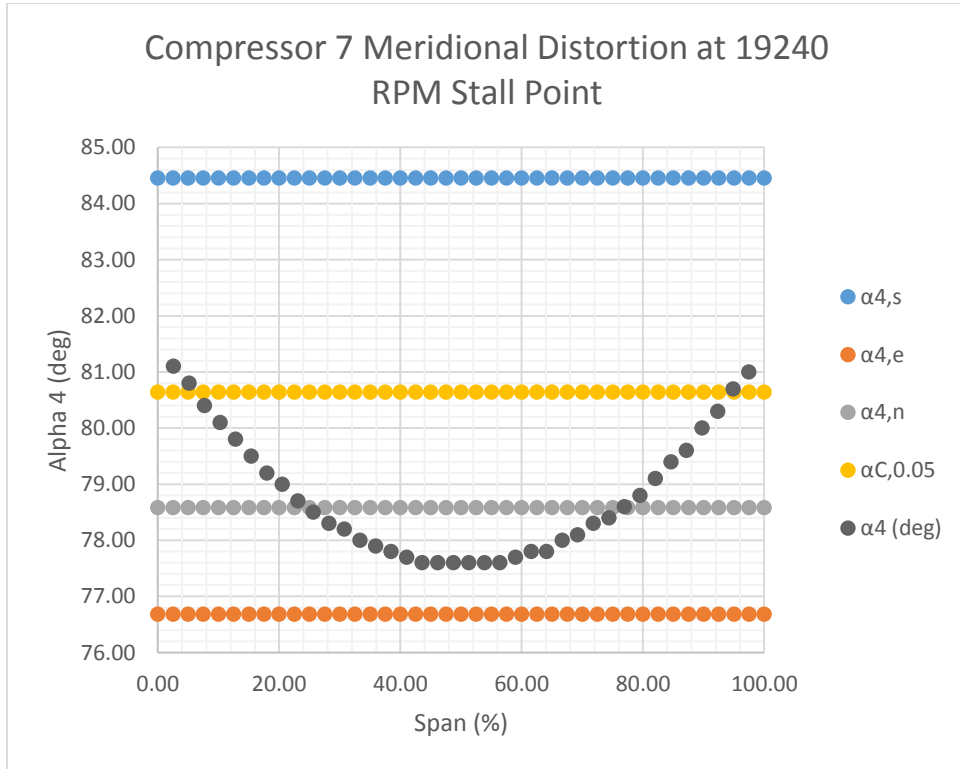


Figure 195: Compressor 7 Angle Comparison Using Meridional Distortion at Stall Point

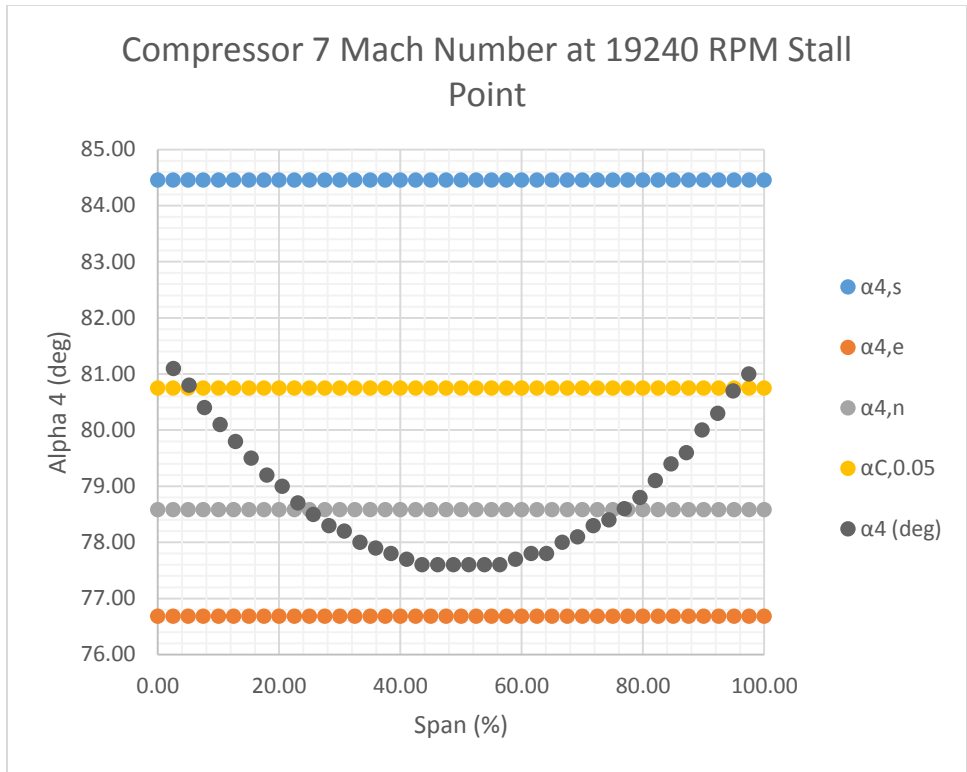


Figure 196: Compressor 7 Angle Comparison Using Mach Number at Stall Point

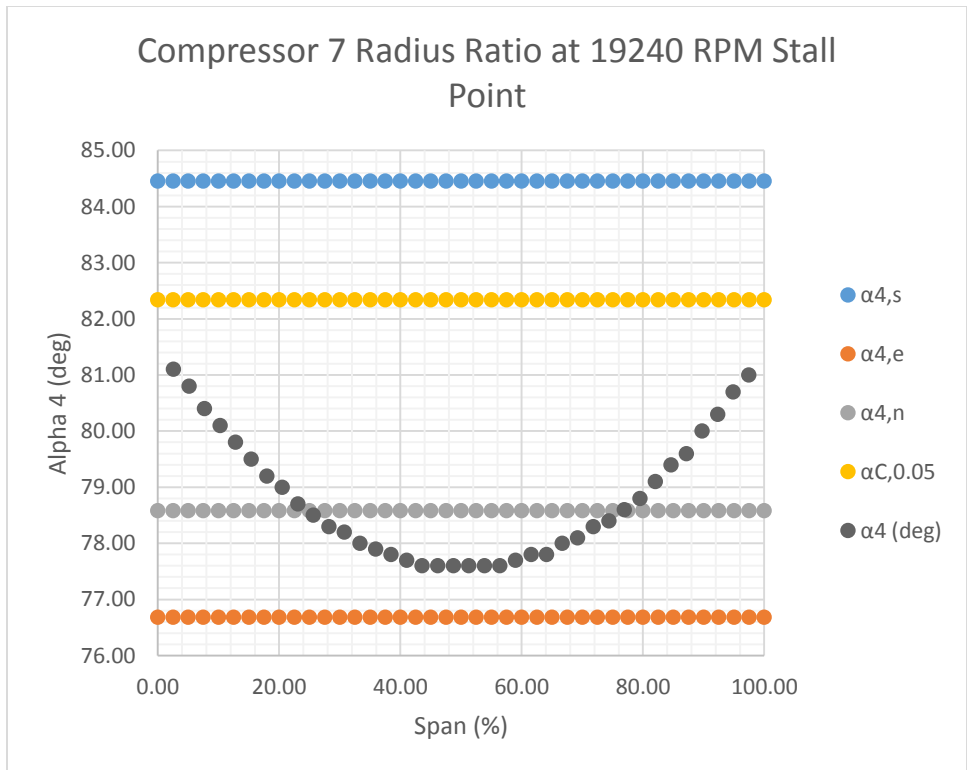


Figure 197: Compressor 7 Angle Comparison Using Radius Ratio at Stall Point

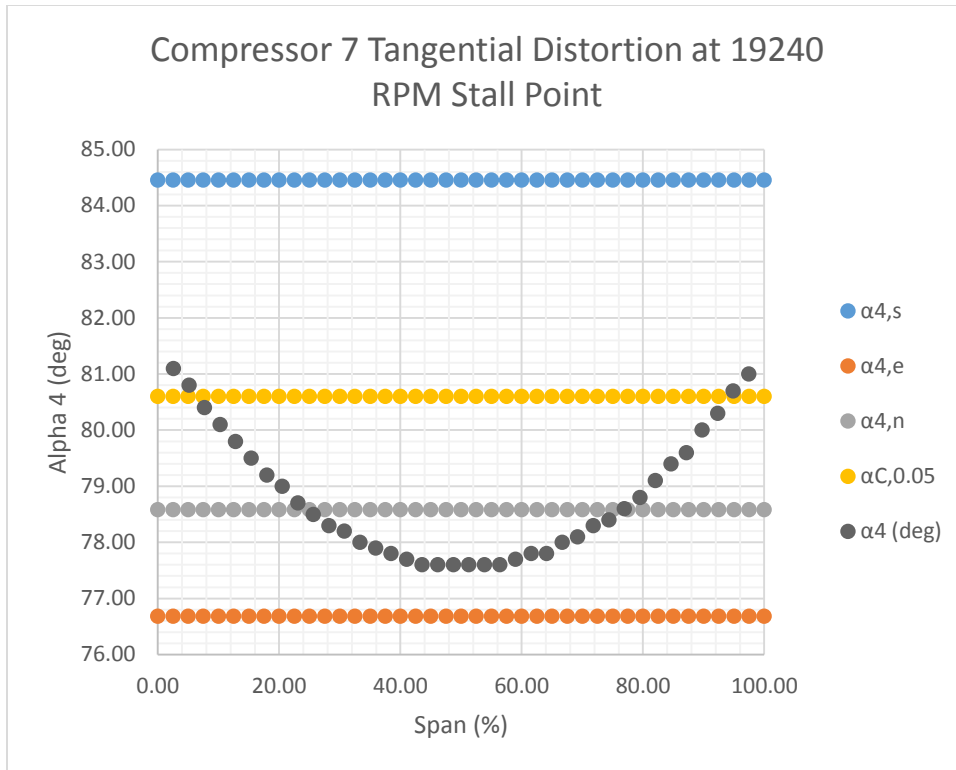


Figure 198: Compressor 7 Angle Comparison Using Tangential Distortion at Stall Point

The results for Compressor 13 (width ratio of 0.112) are found in Figures 199 – 202. For this geometry the local flow angle shows localized flow reversal. However, looking at Figures 200 – 202 one finds that the predictive angle is close to the Senoo angle. So, if one had nothing else available one might suspect that the limit of stability is being reached. Furthermore, in the radius ratio figure (Figure 201) one finds that the predicted angle is above the Senoo angle. So, a priori one might suspect that this stage geometry is unstable.

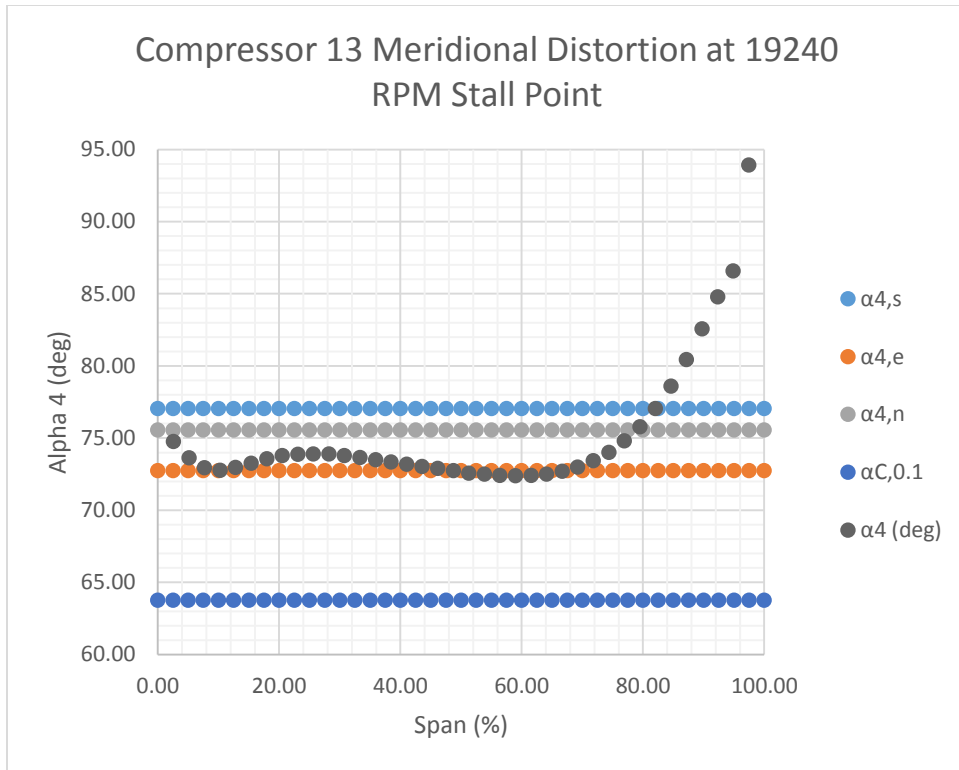


Figure 199: Compressor 13 Angle Comparison Using Meridional Distortion at Stall Point

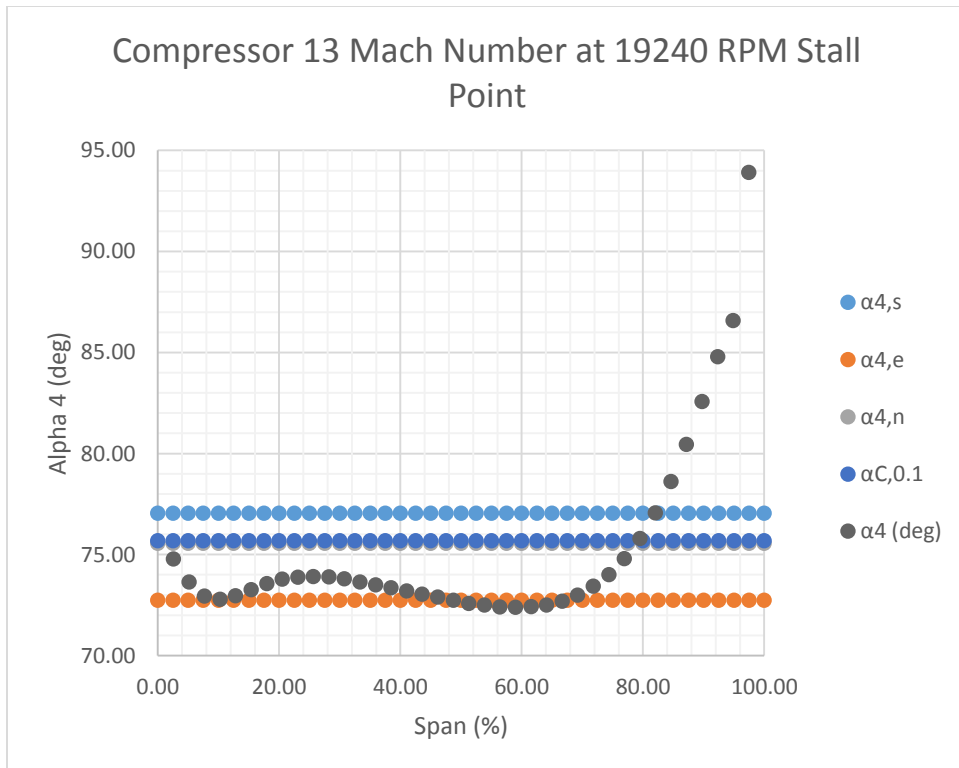


Figure 200: Compressor 13 Angle Comparison Using Mach Number at Stall Point

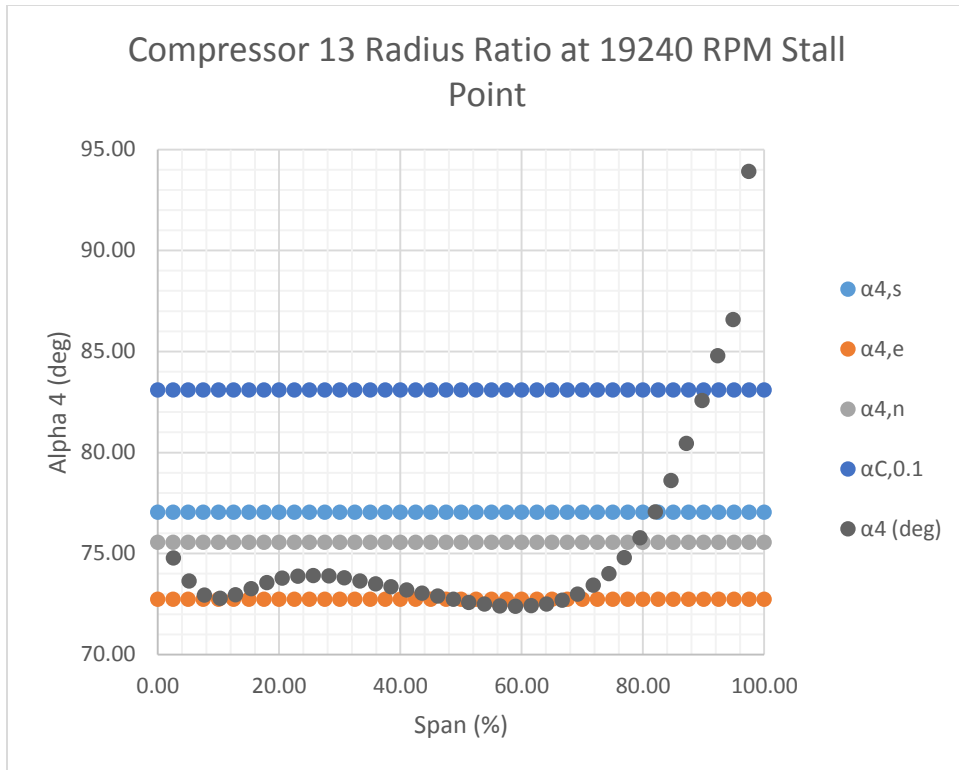


Figure 201: Compressor 13 Angle Comparison Using Radius Ratio at Stall Point

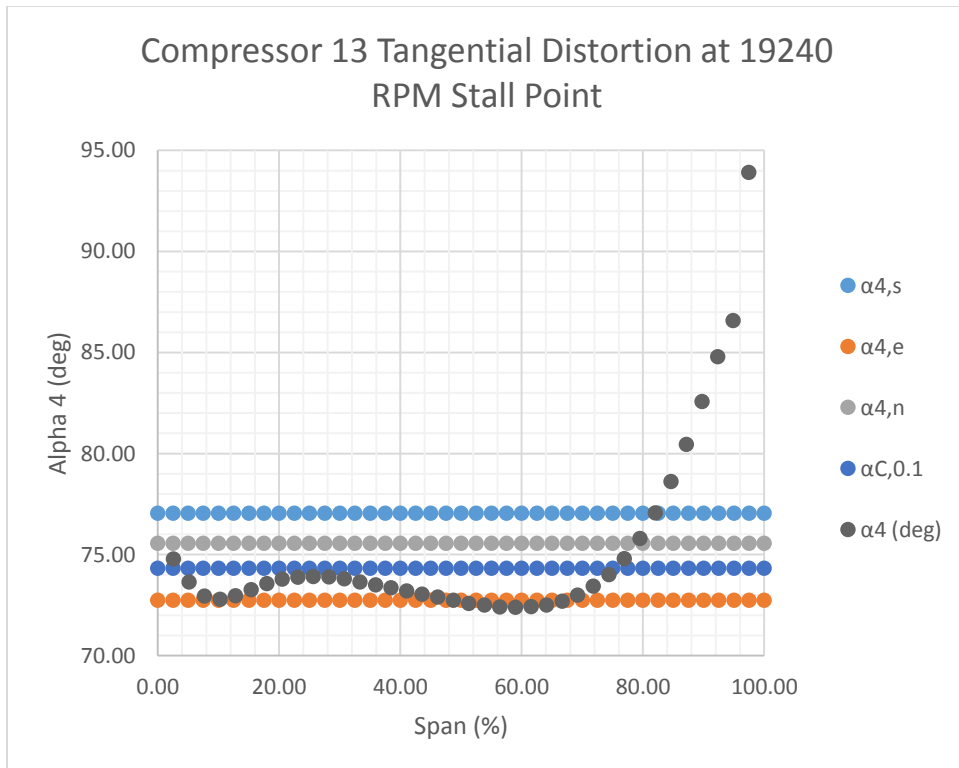


Figure 202: Compressor 13 Angle Comparison Using Tangential Distortion at Stall Point

7.2.3 Conclusions and Recommendations from Digitization Investigation

One, looking at Figures 189, 193, 197, and 201 one finds that the radius ratio tends to get closest to the Senoo angle. However, the radius ratio is a geometric parameter. This means that while it can help to predict whether or not a compressor stage will become unstable it does not take into account the dynamic nature of rotating stall onset [26]. Two, for compressors that have width ratios of 0.067 and above (Compressors 1 and 13) the digitized angle was unimportant because the local flow angle breached both it and the Senoo line meaning it was no better of a predictor of stall onset than the Senoo angle. Three, for a width ratio of 0.056 (Compressor 5) the digitized angle was much closer to the Senoo line than the local flow angle. So, in this case the digitized angle would show that one is approaching the stability limits of the compressor. Four, for a width ratio of 0.016 (Compressor 7) the digitized angle was reached by the local flow angle, but it was still several degrees from the Senoo angle. Therefore, for very narrow diffusers the digitized angle seems to be better at predicting stability when combined with the local flow angle approach.

The main recommendation from this analysis is that it can be useful. However, the results were too inconsistent across geometries to render it an effective method at predicting the critical flow angle. In fact without something to compare against, say either the Senoo angle or local flow angle, this analysis at best offers a shot at determining where the critical flow angle is. And be that as it may it is not a truly predictive analysis without either numerical or experimental data to compare against. Furthermore, most one dimensional analyses cannot be used to account for distortion without guessing a diffuser inlet profile making it difficult to use the digitized curves because they will be based on the input values. Therefore, this analysis is recommended as an

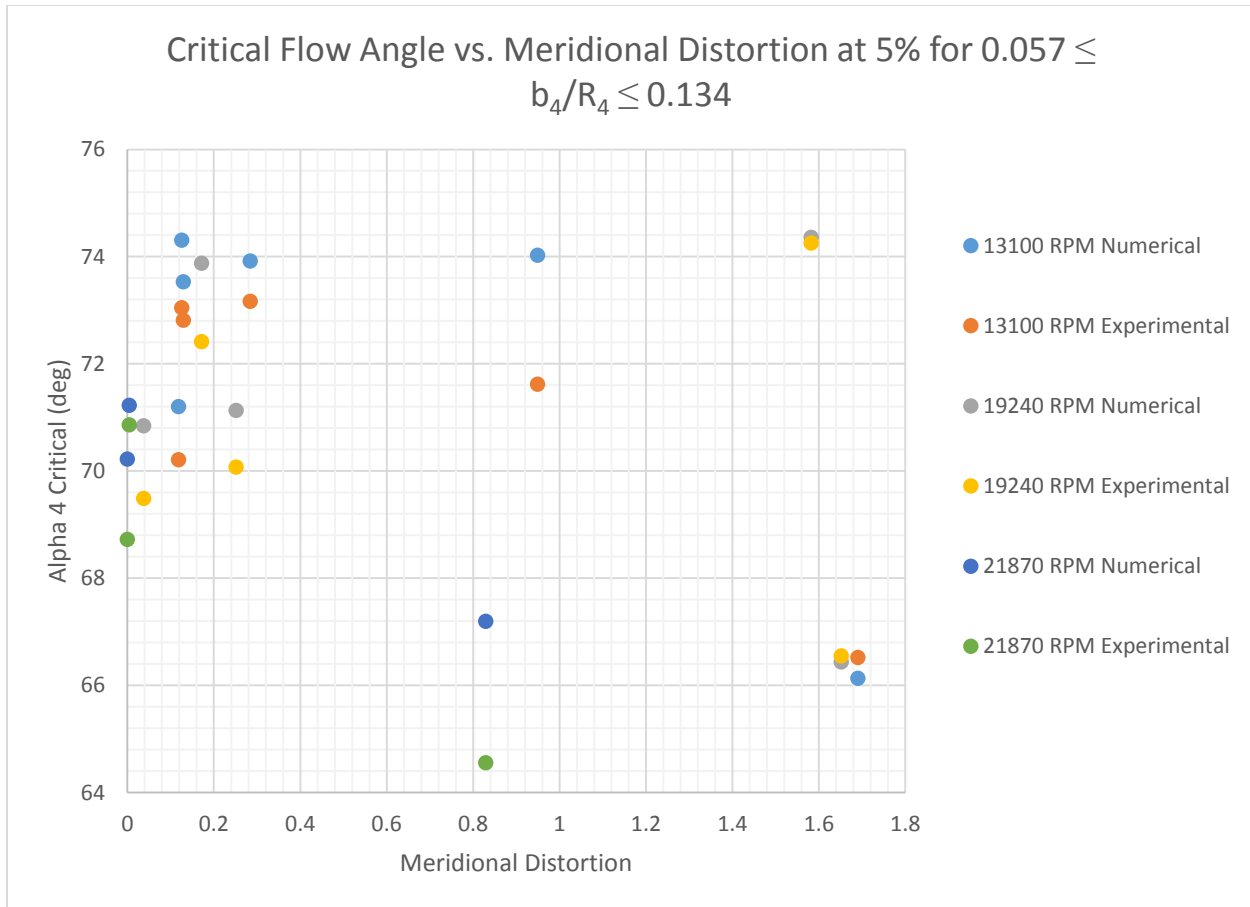


Figure 204: Comparison between Critical Flow Angle and Meridional Distortion ($0.057 \leq b_4/R_4 \leq 0.134$)

Figures 203 and 204 compare the numerical and experimental critical flow angle at all three speed lines against the meridional velocity distortion measured using the meridional velocity at span values of 5% (hub side) and 95% (shroud side). Only the numerically determined velocities were used to calculate meridional distortion. This is because not all experimental values had velocity data at 5% and 95%. This was the easiest way to correlate the data and see if a pattern arises. Also, only data at stall onset points is present. In some cases (Compressors 9 and 11 at 21870 RPM for example) rotating stall does not onset, these points were not included because it is only the rotating stall onset points that are of interest. Also, each figure is separated by width ratio. The geometries with width ratios between 0 and 0.056 are in Figure 203 and those with width ratios between 0.057 and 0.134 are found in Figure 204.

What is found in Figures 203 and 204 is that there is no correlation between meridional distortion and critical flow angle. This is same conclusion found in section 6.2.5.1. Looking at Figures 203 and 204 one finds that all of the data points are clustered in the 0 – 0.3 range for meridional distortion. This is the range expected by Senoo and Kinoshita in [32]. A few outliers are found in Figures 203 and 204, but it would be expected that these points would show a sharp decrease in critical flow angle [32], but none was found. Overall, it looks like if there is a correlation between meridional velocity distortion and critical flow angle it is not linear as found in [32] and it cannot be found using equation 6.3 to calculate meridional distortion.

7.4 Blade Number Investigation

7.4.1 Blade Number Comparison Investigation Background

It was found that the number of impeller blades has an effect on vaneless diffuser stability in [23]. So, it was decided to use the steady state simulation method employed here to see if changing the number of blades made a difference. Compressor 5 was chosen because the local flow profiles at 15 blades did not cross the Senoo line, but the width ratio of Compressor 5 is 0.056. This width ratio is comparable to that of Compressor 3 (0.055) which did breach the Senoo line, see sections 6.3.3 and 6.3.5 for details.

7.4.2 Blade Number Comparison Results

The results for Compressor 5 at the stall onset point at 13100 RPM, 19240 RPM, and 21870 RPM can be found in Figures 205 – 207. Comparing the local numerical profiles in each example shows that decreasing the blade number from 15 to 13 produced a slight drop in the local flow angle profile. This drop was no greater than 0.4 degrees for any of the three speed lines. So, from the simulations it appears that decreasing the blade number did make the vaneless diffuser less

stable, which was shown by the drop in critical flow angle. This result is in agreement with those seen in [23], but nowhere near the magnitude of the decrease found by Ljevar et al. in [23].

Thus, the best conclusion that can be drawn is that there is merit to the idea that changing impeller blade number will have an effect on stability, but how much that value must change is something that requires a more in-depth investigation. As a note, it was passed along that Compressor 2 (having 13 impeller blades) was tested at 17 impeller blades and the rotating stall phenomenon dissipated [27]. Thus, to see an appreciable change in critical flow angle one must change the number of impeller blades by at least 4 to have an effect. Also, since rotating stall is a natural solution to the physical equations governing the compressor system [15] it stands to reason that to change the solutions to the physical equations one must significantly change the system geometry itself. Therefore, if there is to be an effect caused by changing the number of impeller blades it will need to be large enough to significantly alter the flow path through the compressor stage fundamentally changing the system dynamics. In the case of Compressor 5 a decrease in blade number of 2 is not enough to do this.

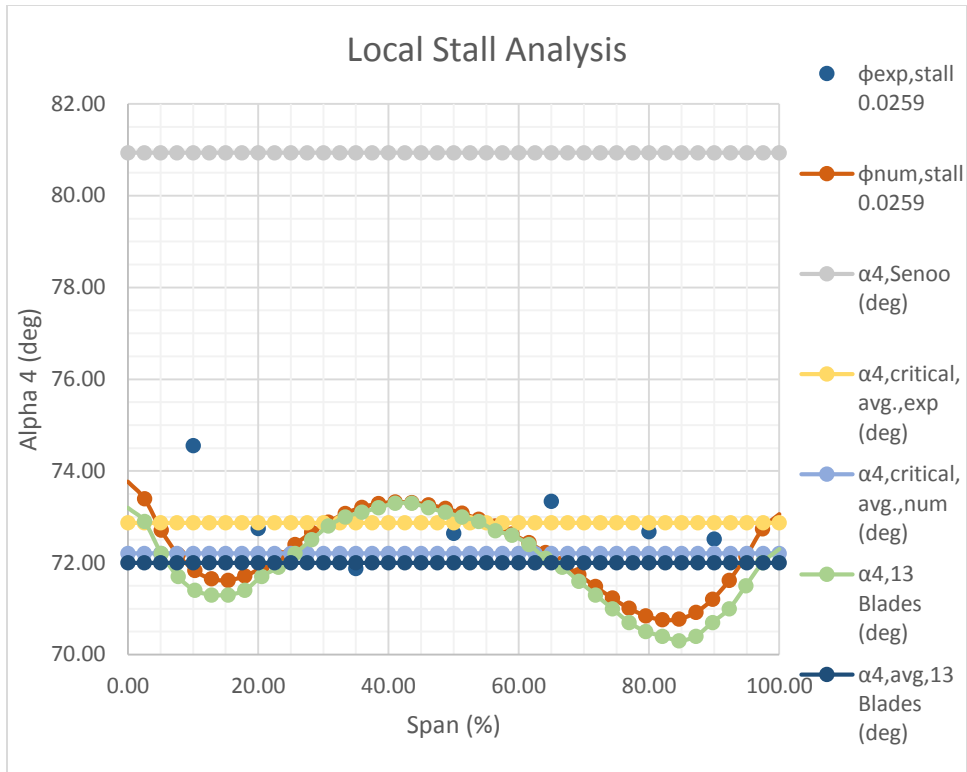


Figure 205: Compressor 5 Local Flow Angle at 13100 RPM Stall Point, 13 Blade Comparison

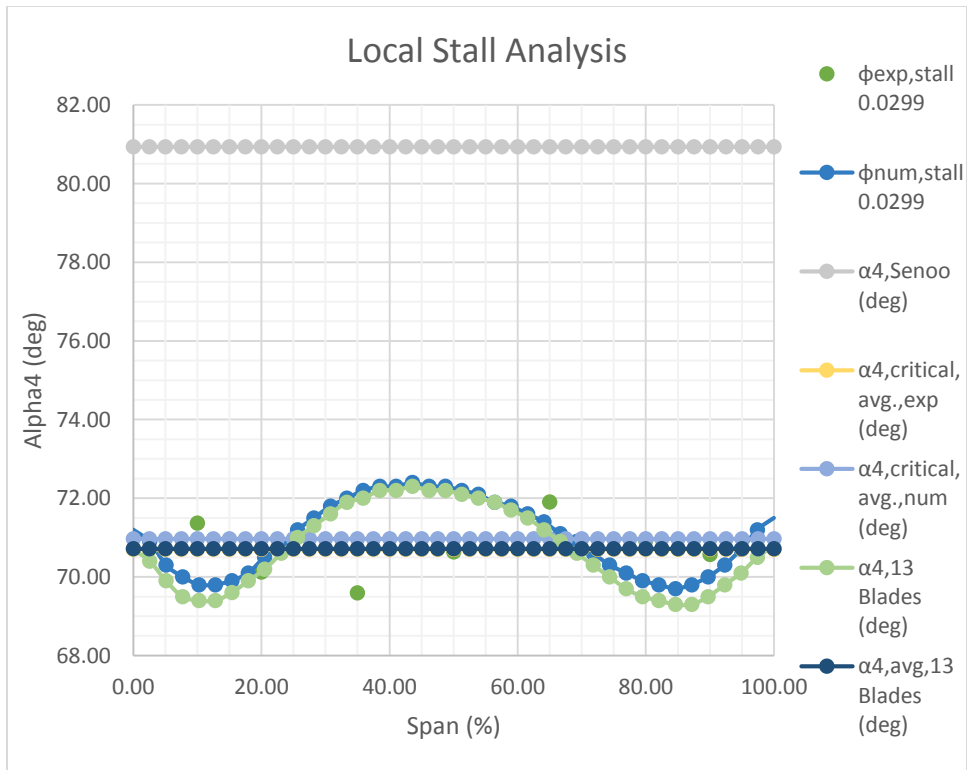


Figure 206: Compressor 5 Local Flow Angle at 19240 RPM Stall Point, 13 Blade Comparison

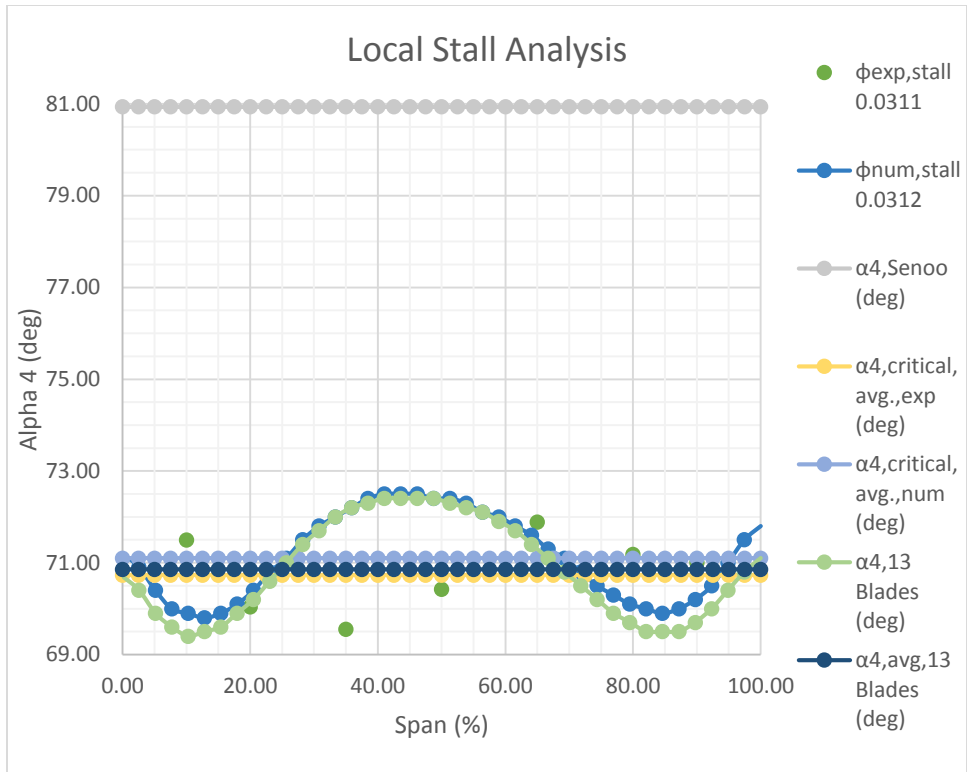


Figure 207: Compressor 5 Local Flow Angle at 21870 RPM Stall Point, 13 Blade Comparison

CHAPTER 8: CONCLUSIONS

8.1 General Conclusions

8.1.1 Conclusions from Average Flow Angle Results

Looking at the average flow angle results presented in section 6.2 one finds a few conclusions. First, the width ratio of the diffuser appears to be the dominant factor in determining stability. This is in agreement with the work of Kinoshita and Senoo in [32]. Second, the radius ratio appears to have a secondary effect on compressor stability which is most often seen in diffusers of comparable width. Third, the Mach number does effect the value of the critical flow angle, but only slightly. Its effects are not nearly as pronounced as those found in [26, 32]. Fourth, the Reynolds number did not affect the results critical flow angle results. This is in agreement with the results found by Kinoshita and Senoo [32] and Wiesner [42]. Fifth, neither the meridional velocity distortion nor tangential velocity distortion, had much effect on the average critical flow angle. This was in direct contradiction to the results expected in [1, 24, and 32].

8.1.2 Conclusions from Local Flow Angle Results

First, the local flow angle analysis works. It was found that for compressors with width ratios of 0.065 and above the local flow angle would cross the Senoo line at the point of rotating stall onset. Second, for compressors with width ratios below 0.045 the local flow angle approach would not cross the Senoo line even at the experimentally determined stall point. Third, for situations where the width ratio was 0.078 and greater localized flow reversal could be captured at the diffuser inlet. This was an unexpected positive result for a steady state simulation procedure. Fourth, for width ratios between 0.045 and 0.065 it was found that the radius ratio and impeller blade number had a secondary effect on the diffuser's stability in agreement with the results of [23 – 25 and 32]. This effect was not manifested so long as the diffuser width ratio was large enough

or small enough for the boundary layer effects to dominate at either suppressing the flow breakdown ($b_4/R_4 \leq 0.045$) or provoking the breakdown ($b_4/R_4 \geq 0.067$).

8.1.3 Conclusions from Diffuser Inlet Flow Reversal Results

Another unexpected positive effect of the local flow angle approach was that one could find regions of localized flow reversal inside of the vaneless diffuser. This was true whether or not the localized flow reversal appeared at the diffuser inlet. This led to a parameter defined in equation 7.2 comparing the diffuser width, b_4 , to the impeller blade pitch distance, d_{pitch} . For regions with $b_4/d_{pitch} \leq 0.152$ it was not possible to capture localized flow reversal inside of the diffuser. However, for diffusers with $b_4/d_{pitch} \geq 0.177$ it was possible to capture localized flow reversal in the vaneless diffuser. This was significant because even if the Senoo angle was not breached one could still show vaneless diffuser instability. Furthermore, this suggests that for wider diffusers the flow breaks down in the span-wise direction, while for narrower diffusers the breakdown is in the circumferential direction. Since the flow is forced to breakdown anyway [15] this would make sense.

Also, this part of the investigation found flow reversal in the “U-Bend” of Compressor 12. Compressor 12, see section 6.3.12, had odd results compared to the other “wide” diffusers. This result showed that with the diffuser experiencing flow reversal outside of the diffuser it was likely that the rotating stall occurred outside of the diffuser as well. This result showed that the local flow angle approach was having trouble with Compressor 12. This is because the flow was breaking down “far” from the diffuser inlet and the local flow angle at the diffuser inlet was not sensitive enough to detect the instability that far downstream from the diffuser inlet.

Lastly, this investigation showed that localized flow reversal was not the trigger mechanism for rotating stall onset. This was in direct contradiction to the work found in [26, 34,

and 41]. However, the results found regions of localized flow reversal that occurred prior to the onset of rotating stall. Therefore, one concludes that localized flow reversal is necessary to provoke rotating stall, but not sufficient.

8.1.4 Conclusions from Digitized Senoo Curve Investigation

The main conclusion from the digitized Senoo curves is that the results were all over the map. There was some consistency when looking at the differences in width of the diffusers. But, using the Senoo curves to find predictive angles still required something to compare against. And while comparisons could be made against the Senoo angle or the local flow angle the point remains that using the digitized Senoo curves forces a designer to look at many different results to determine what is most important. This was the original idea, but after looking at the results it proved to be time consuming and unenlightening. However, using the local flow angle approach gives a designer one reliable set of results to look at broken down by compressor stage width. This would be a better way to approach the determining stage stability than looking through endless values that may not correlate to anything of worth.

8.1.5 Conclusions from Distortion Correlation Results

It was found in section 6.2.5 that the meridional velocity distortion and tangential velocity distortion did not influence in critical flow angle in direct contradiction to the results found by Abdelhamid [1] and Kinoshita and Senoo [32]. In an attempt to determine a correlation between distortion and critical flow angle the results were plotted and displayed in section 7.3. It was found that there was no easy way to correlate distortion values to critical flow angle results. In fact it was found that there was no correlation between distortion and critical flow angle. Even after accounting for diffuser width no correlation was found at all. So, while correlations between

distortion and critical flow angle are often sought the conclusion here is that they are difficult if not impossible to find.

8.1.6 Conclusions from Blade Number Investigation

This investigation simulated Compressor 5 with 13 impeller blades as opposed to the original 15 blades. The hope was to bring the results of Compressor 5 in line with the results for Compressor 3, a stage of comparable geometry. The investigation found that a small change in the number of blades had little to no effect on the model's ability to predict diffuser stability. This made sense in light of the fact that rotating stall is a phenomenon of the geometry one is investigating [15]. Without a fundamental change in the geometry itself a small change in blade number will have no effect on the stages overall stability. However, according to [27] Compressor 2 was tested experimentally with 17 impeller blades instead of the original 13 and vaneless diffuser rotating stall was eliminated. So, it is possible to eliminate diffuser rotating stall by changing blade number, but it takes a large enough change to fundamentally alter the dynamic stability of the compressor itself. This investigation has promise for greater expansion in the future when the geometry of each stage can be more fundamentally altered by larger changes in blade number. It is something of interest that should be pursued since it has been shown that these changes can be used to eliminate rotating stall in a geometry where it once existed [27].

8.2 Next Step of the Project

As with any project this work is not the end of the journey, but the beginning of the journey for other researchers. There are a few potential avenues of work that still need investigation. These avenues will provide a broader picture of the overall problem of vaneless diffuser stability, combined with a more detailed evaluation of the applicability of the local flow investigation.

8.2.1 Different Turbulence Model Investigation

It was suggested by a colleague, Dr. Chris Paul that investigating different turbulence models would be in order [47]. The turbulence model has a direct effect on how refined the mesh needs to be to obtain satisfactory results. At least this is the conventional wisdom. This is especially true of the area directly next to the impeller blade, also known as the O-Grid. The current model SST requires quite a bit of refinement especially near the blade surface. However, other turbulence models ($k-\epsilon$ and $k-\omega$) do not require such refinement. Less refined turbulence models require smaller amounts of computational resources (fewer CPU's and less running time) to simulate geometries as well. However, there is the inevitable tradeoff that comes with a less refined mesh, that being less accurate results for smaller running times. However, it is of interest how detailed the computational mesh needs to be and how powerful the turbulence model needs to be to provide satisfactory results. The purpose of the local flow angle approach is to make the stability determinations quicker, but no less accurate than a transient simulation. Thus, anything to help in this pursuit that does not hinder the accuracy of the results would be a benefit.

8.2.2 Transient Simulation Investigation for Comparison against Steady State Results

It has been found by other researchers that there are distinct differences between the results that a transient simulation provides versus those that a steady state simulation provides [4, 30]. While the results in Chapters 6 and 7 have shown that using a steady state simulation is effective when looking at vaneless diffuser stability in centrifugal compressors, it is still important to make sure that the steady state simulation compares well to transient simulations on the same compressor. This is due to the time dependent nature of the centrifugal compressor itself [8]. An inherently time independent situation should be compared to a transient simulation to make sure

that the results are truly satisfactory between the steady state simulation and the experimental results.

Also, there is much about stall that can be learned from a transient simulation. Using a transient simulation it is possible to determine the size of the stall cell as well as the number of stall cells in the vaneless diffuser. It is also possible to determine the frequency of stall cell rotation using a transient simulation. These factors are of interest from an academic point of view and would serve to provide a better overall understanding of the nature of the rotating stall phenomenon in the centrifugal compressor vaneless diffuser.

8.2.2.1 Single Passage Transient Simulation

The single passage transient simulation is a step between a steady state simulation and a full 360 degree transient simulation. This method allows for a denser mesh in the single passage, similar to the mesh density used in the steady state simulation. However, the periodic boundary conditions will have the effect of washing out some of the unsteadiness in the flow as the simulation is forced to average across the boundary. This simulation type would be a useful first step to see if the transient results are different than the steady state results. It is also less computationally expensive than a full 360 degree transient simulation and would allow for faster running times.

8.2.2.2 Full 360 Degree Transient Simulation

As a matter of completeness it would be wise to complete a full 360 degree transient simulation of at least three geometries near the stall point. This would serve to show whether or not the steady state simulation deviates greatly from the transient simulation. It would also serve to show whether or not the transient simulation provides results that are in satisfactory agreement with the experimental results. Furthermore, the full 360 degree transient simulation would provide details of the flow structure at the point of stall onset. It would also help to determine the type of

stall onset as well as different characteristics about the stall cell(s): such as shape, rotating speed, number of stall cells, type of inception, expansion into the flow path, etc. It would also be of interest to see whether or not the flow breaks down in the circumferential direction for narrower diffusers versus the span-wise direction. This was something that was hinted at in section 7.1, but something that could not be proven conclusively using the steady state simulation method employed for the local flow angle approach.

8.2.3 Experimental Investigation of Prototype Compressor

Finally, there is the gold standard of all numerical simulations, that of testing a prototype compressor. If the local flow angle approach is truly a satisfactory measure of compressor stability then it should be able to determine whether or not a vaneless diffuser will become unstable from a compressor prototype. In fact it should be capable of determining the range of flow coefficients (ϕ) where the diffuser should become unstable. The local flow angle approach combined with the Senoo angle should provide a good estimate as to whether or not the diffuser will experience rotating stall. However, this is predicated on the compressor stage geometry having the appropriate width ratio of 0.055 or greater and a long enough diffuser. Outside of that it will be difficult to determine much about that stability using the local flow angle approach. However, this simulation of a prototype compressor and test is the mark that will determine whether or not the local flow angle approach can be used as a predictive tool. The current results suggest that it will work as a predictive tool, but this is the final mile to traverse in proving the worthiness of the local flow angle approach.

APPENDICES

APPENDIX A: OPERATING ENVELOPE PLOTS

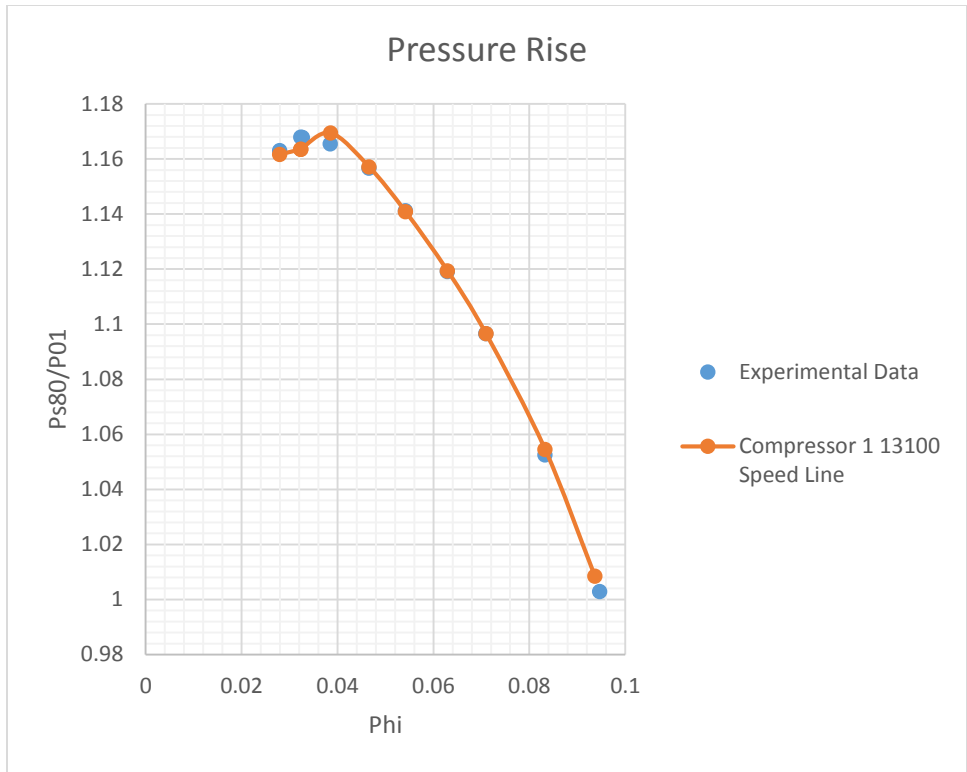


Figure 208: Compressor 1 13100 RPM Operation Envelope

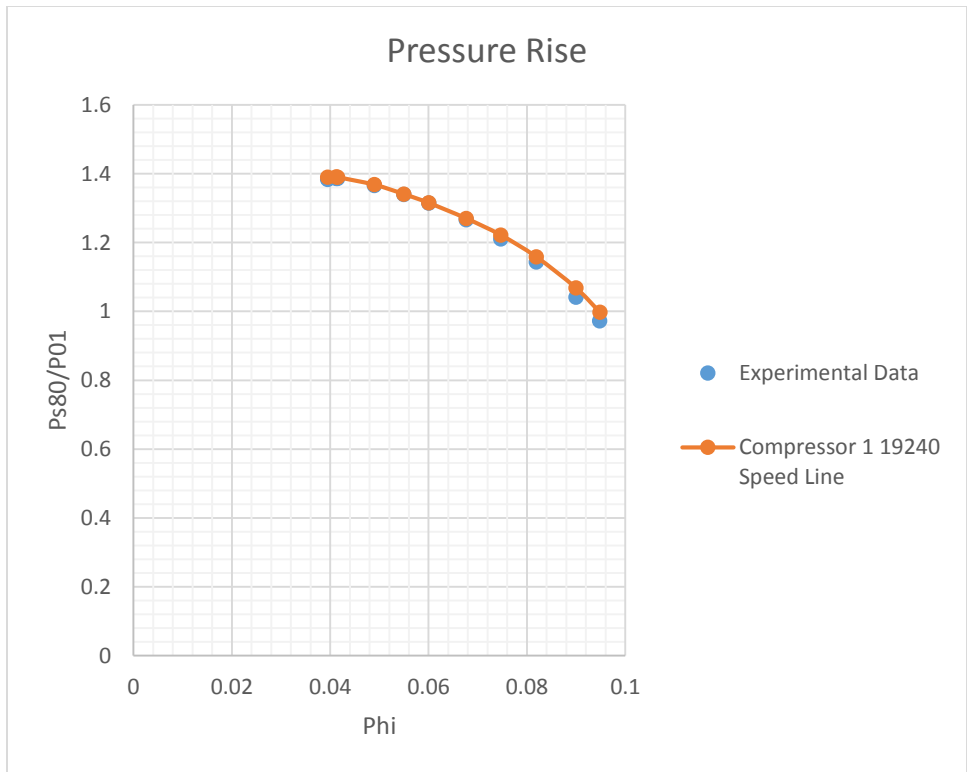


Figure 209: Compressor 1 19240 RPM Operation Envelope

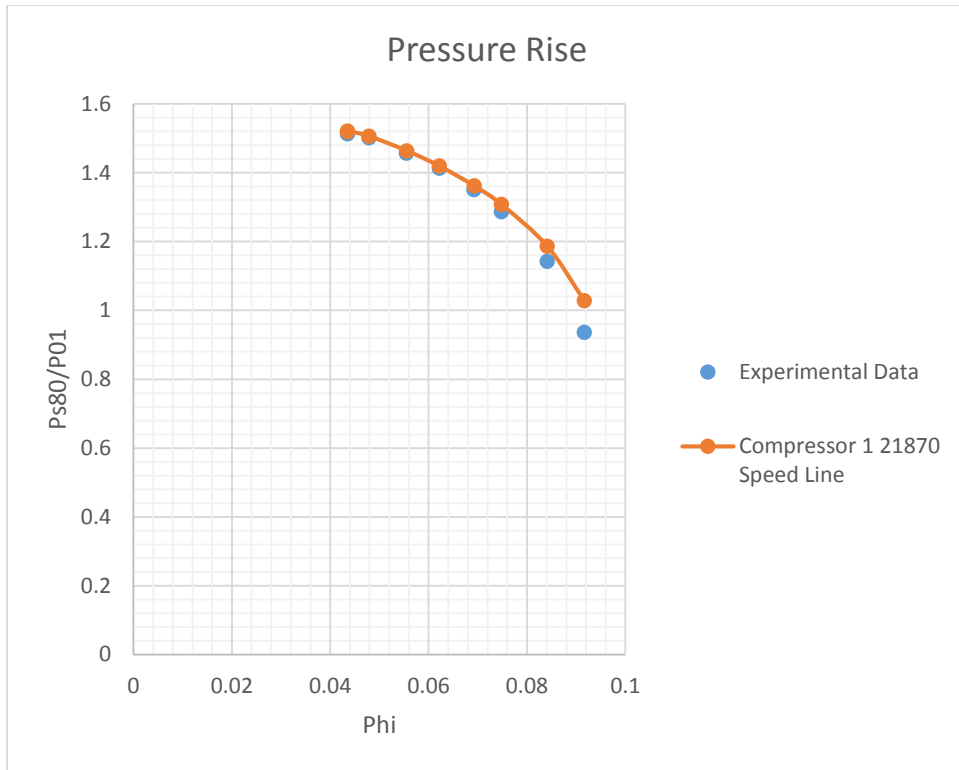


Figure 210: Compressor 1 21870 RPM Operation Envelope

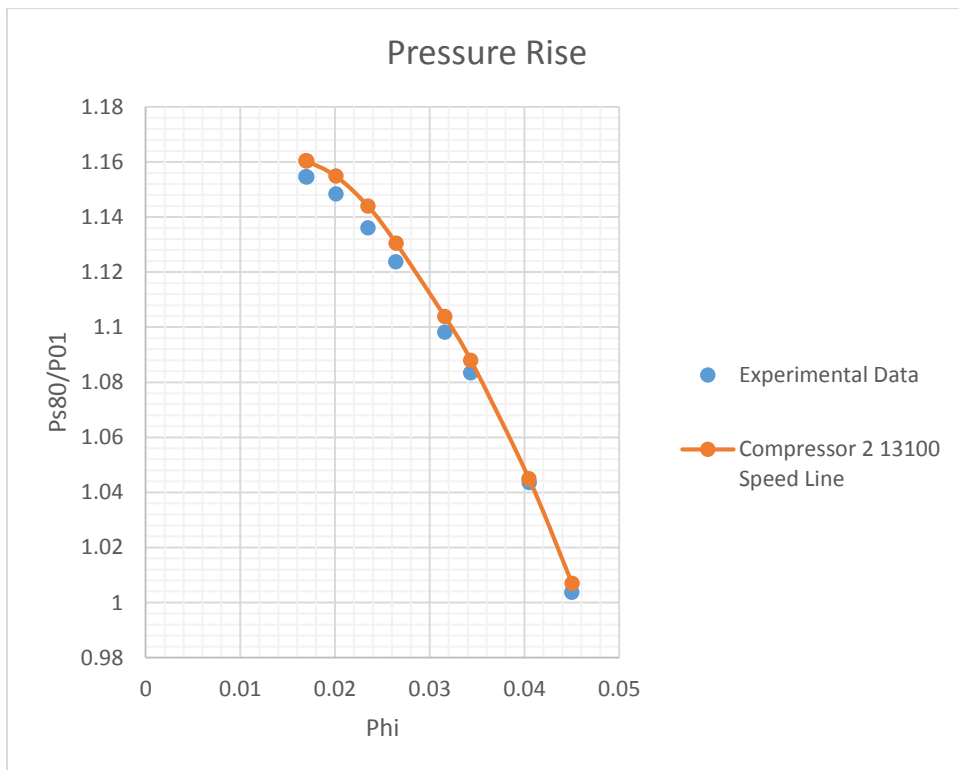


Figure 211: Compressor 2 13100 RPM Operation Envelope

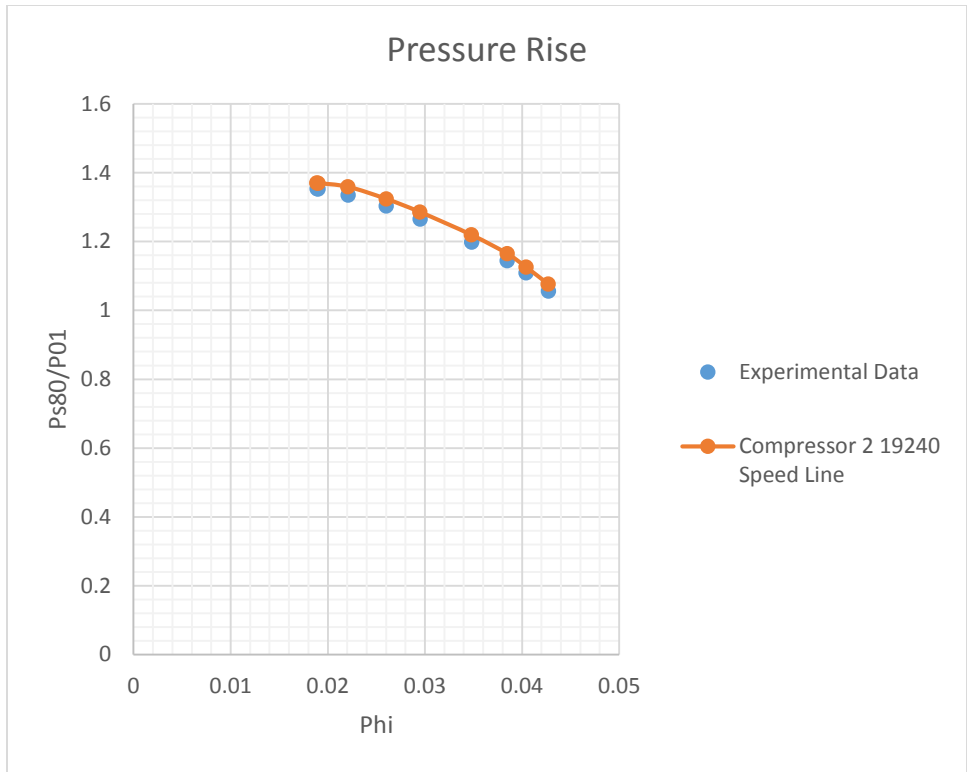


Figure 212: Compressor 2 19240 RPM Operation Envelope

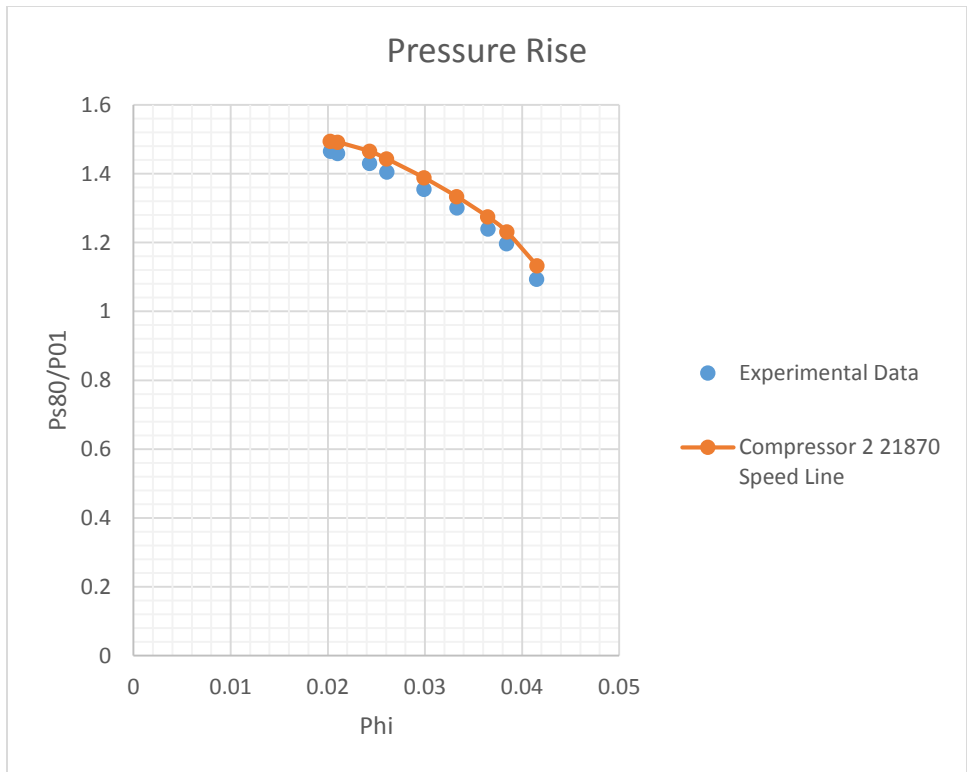


Figure 213: Compressor 2 21870 RPM Operation Envelope

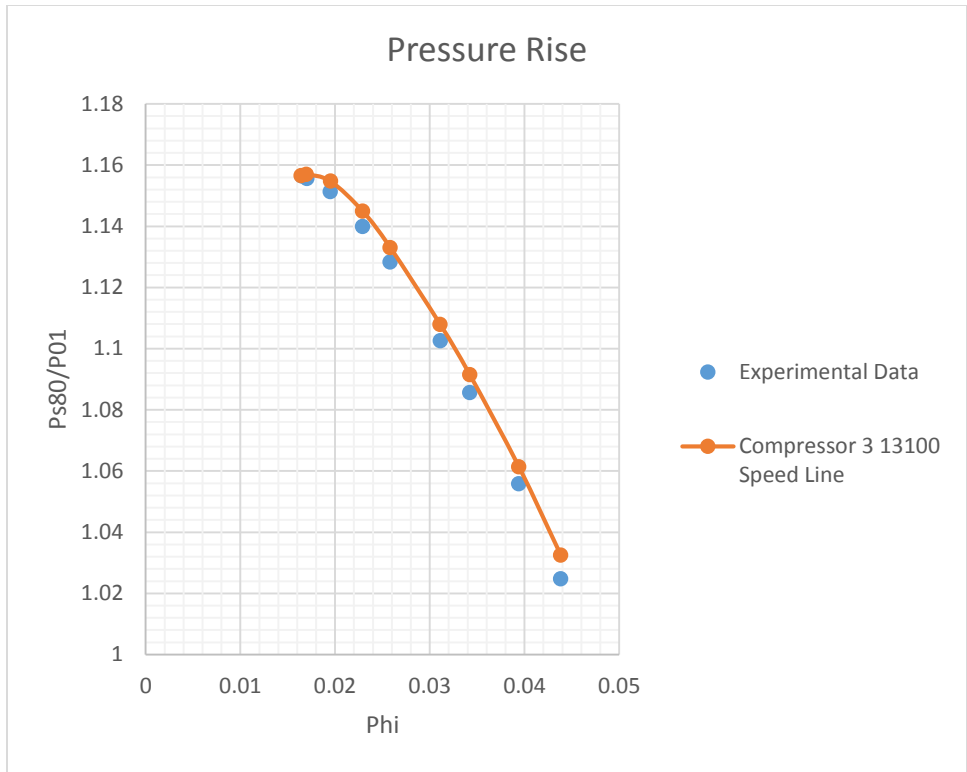


Figure 214: Compressor 3 13100 RPM Operation Envelope

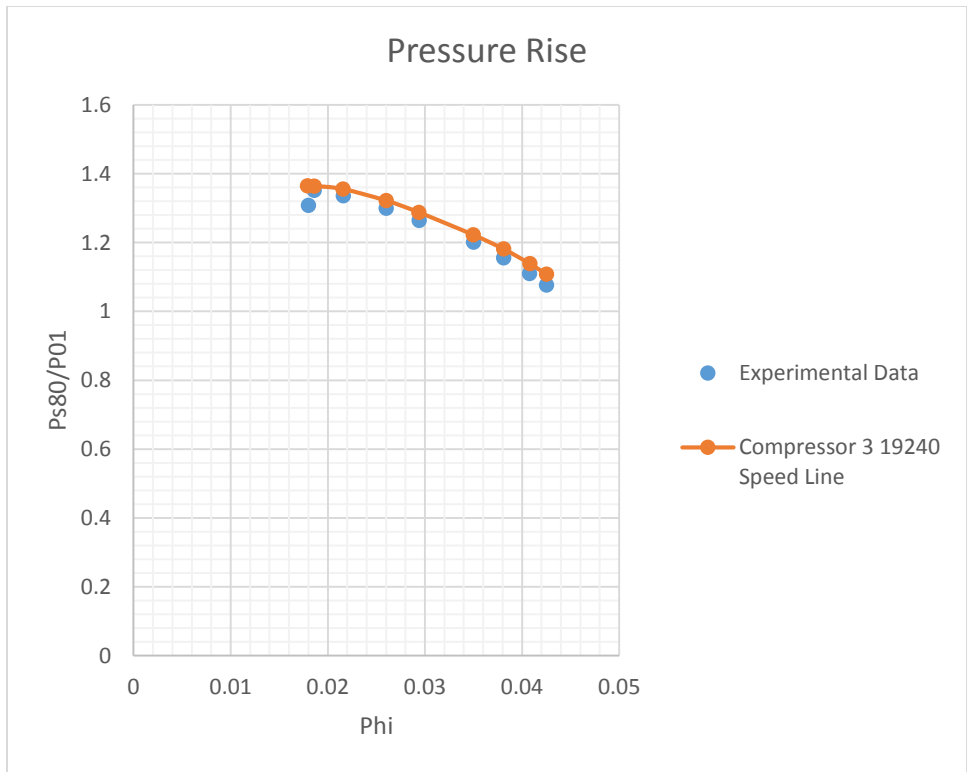


Figure 215: Compressor 3 19240 RPM Operation Envelope

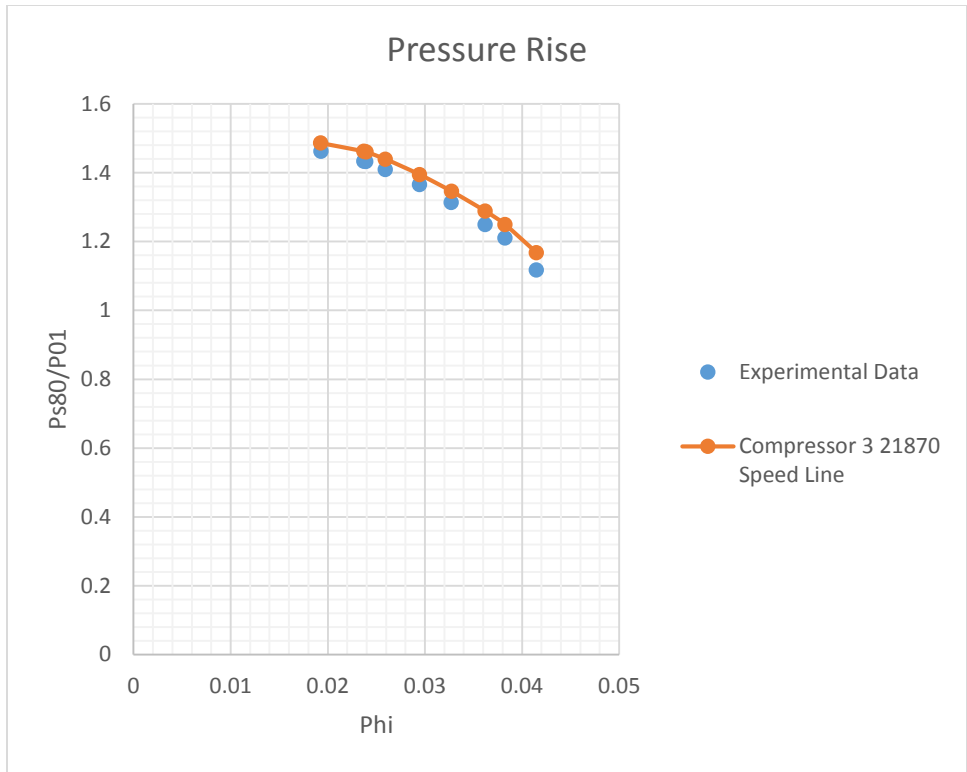


Figure 216: Compressor 3 21870 RPM Operation Envelope

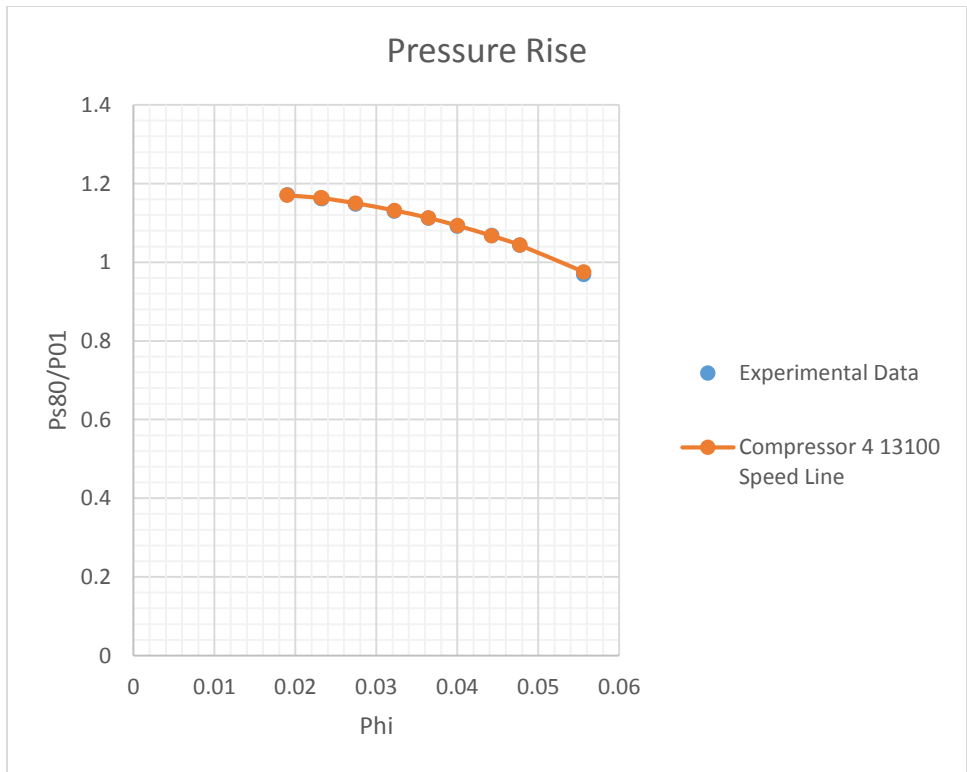


Figure 217: Compressor 4 13100 RPM Operation Envelope

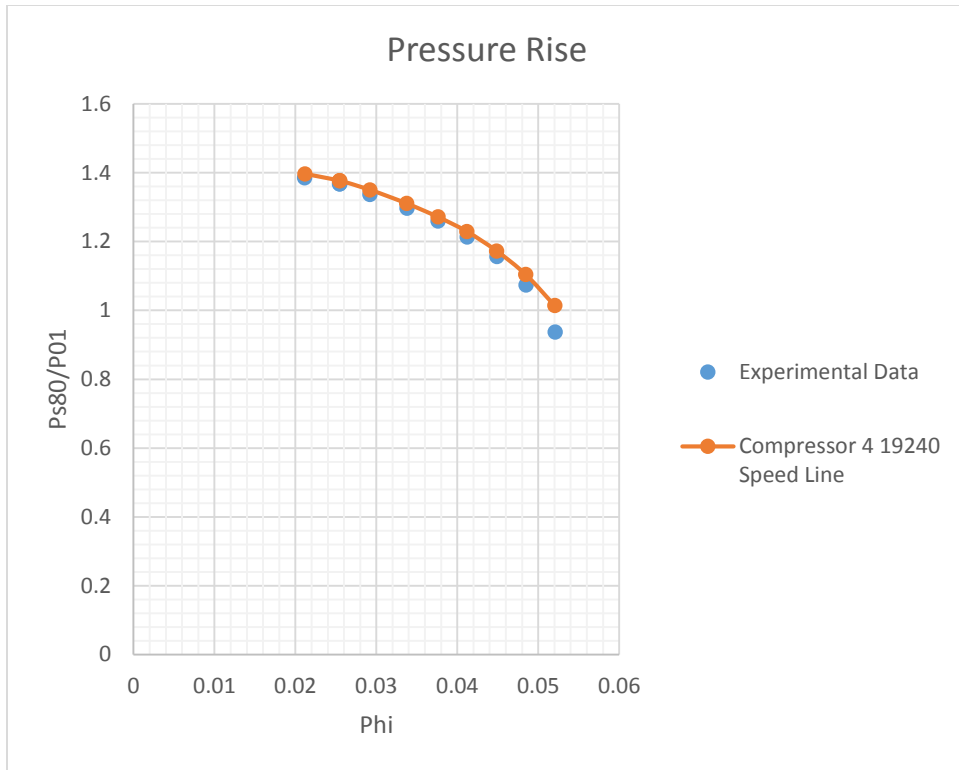


Figure 218: Compressor 4 19240 RPM Operation Envelope

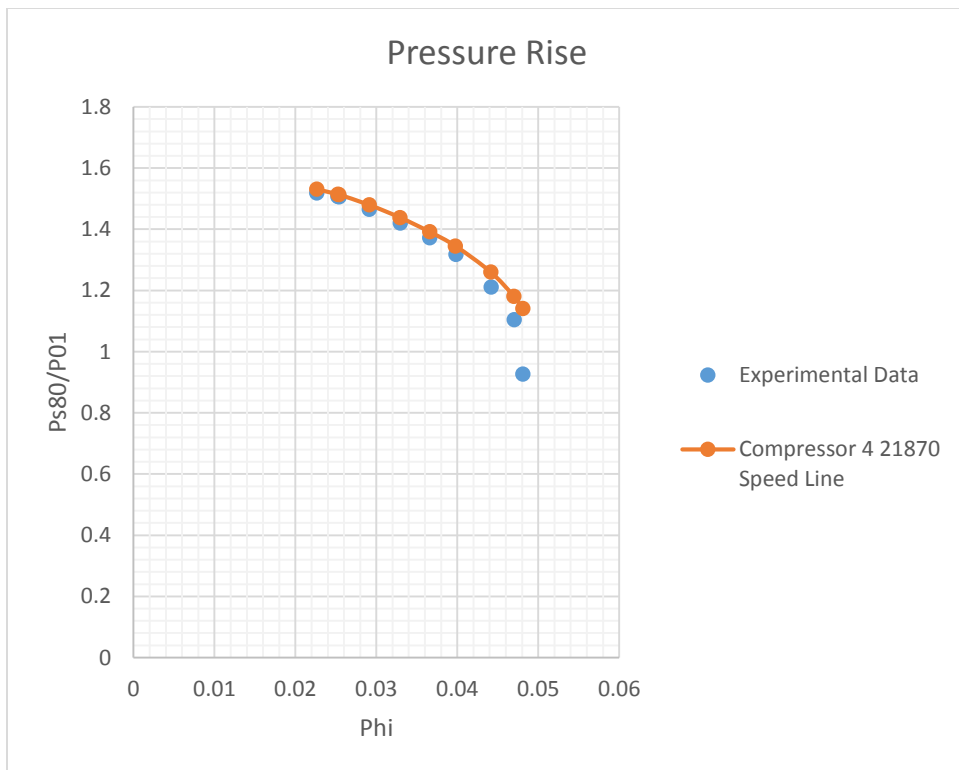


Figure 219: Compressor 4 21870 RPM Operation Envelope

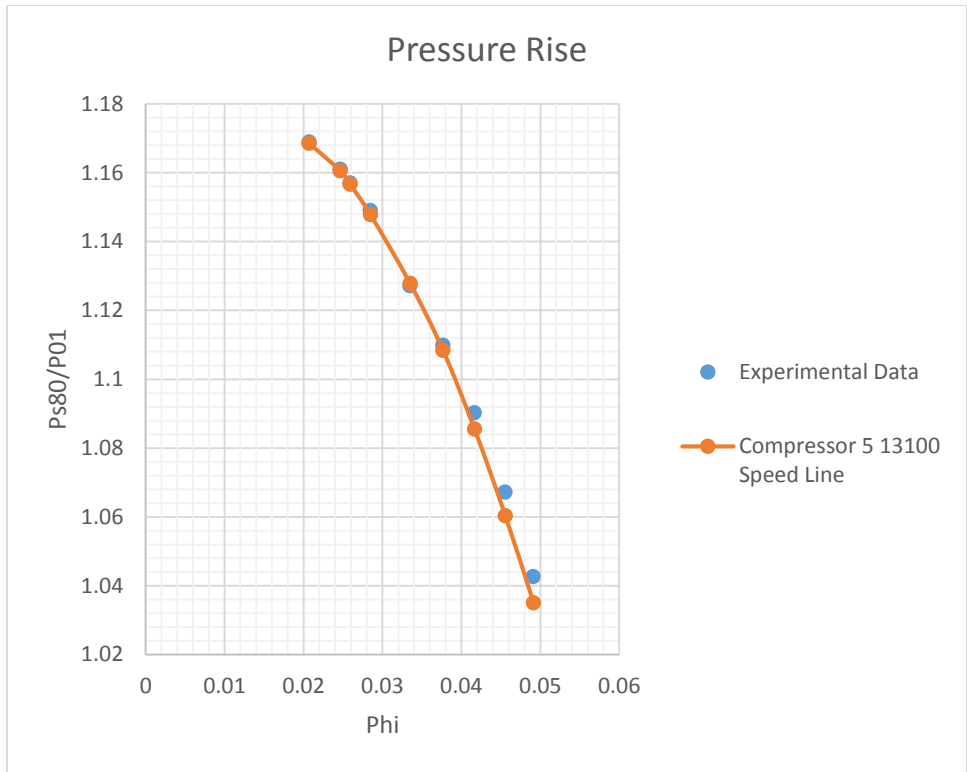


Figure 220: Compressor 5 13100 RPM Operation Envelope

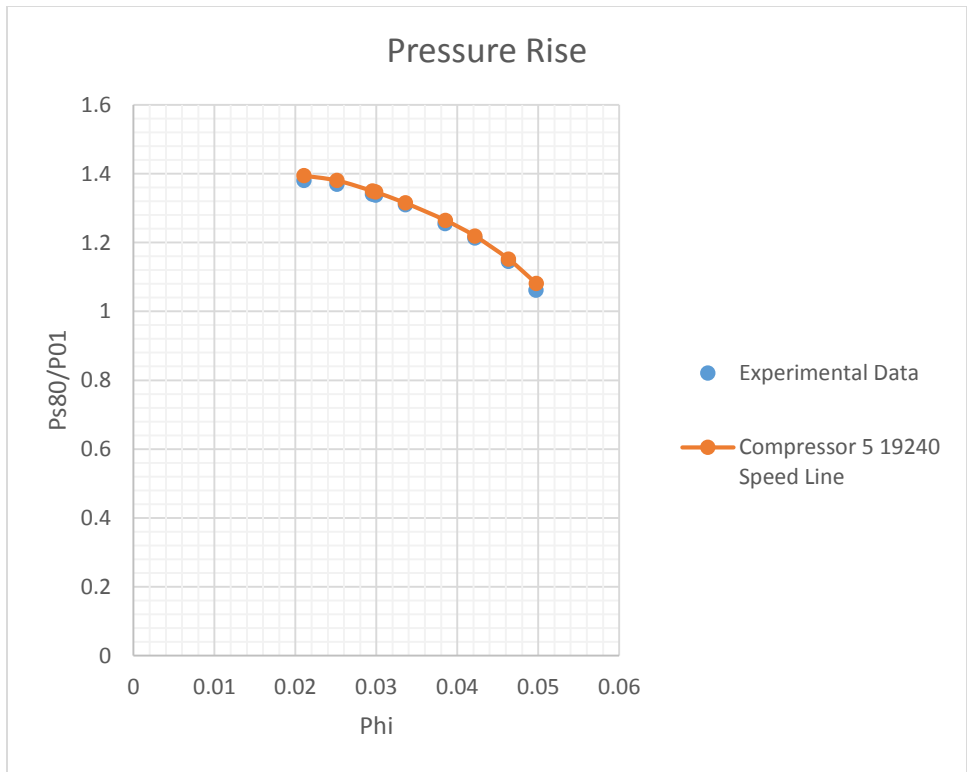


Figure 221: Compressor 5 19240 RPM Operation Envelope

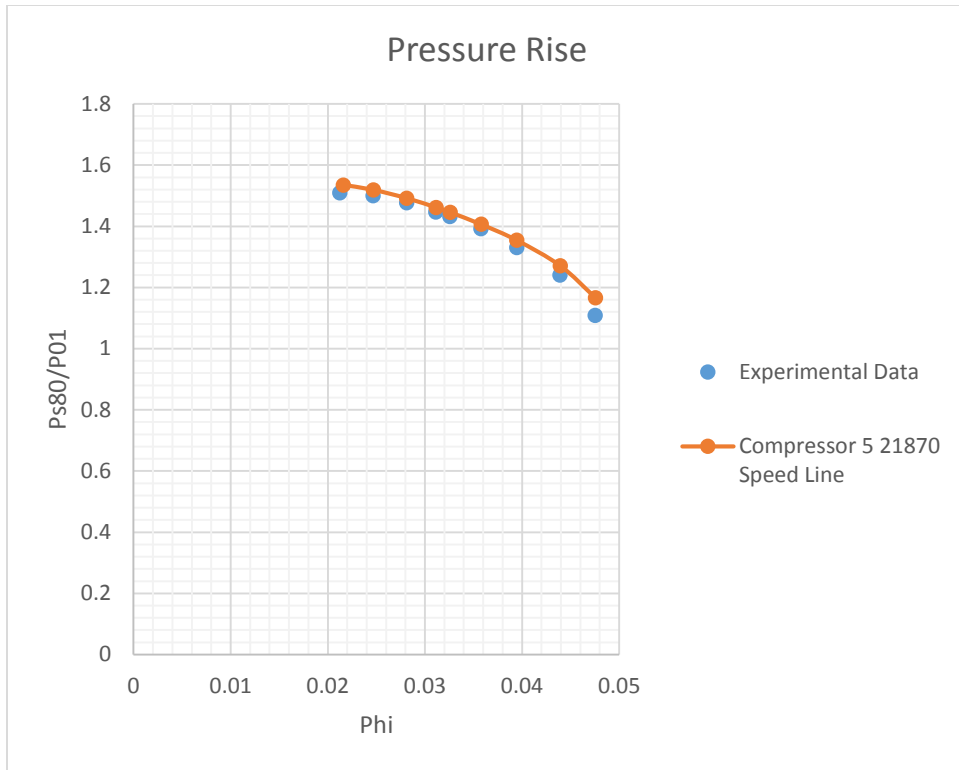


Figure 222: Compressor 5 21870 RPM Operation Envelope

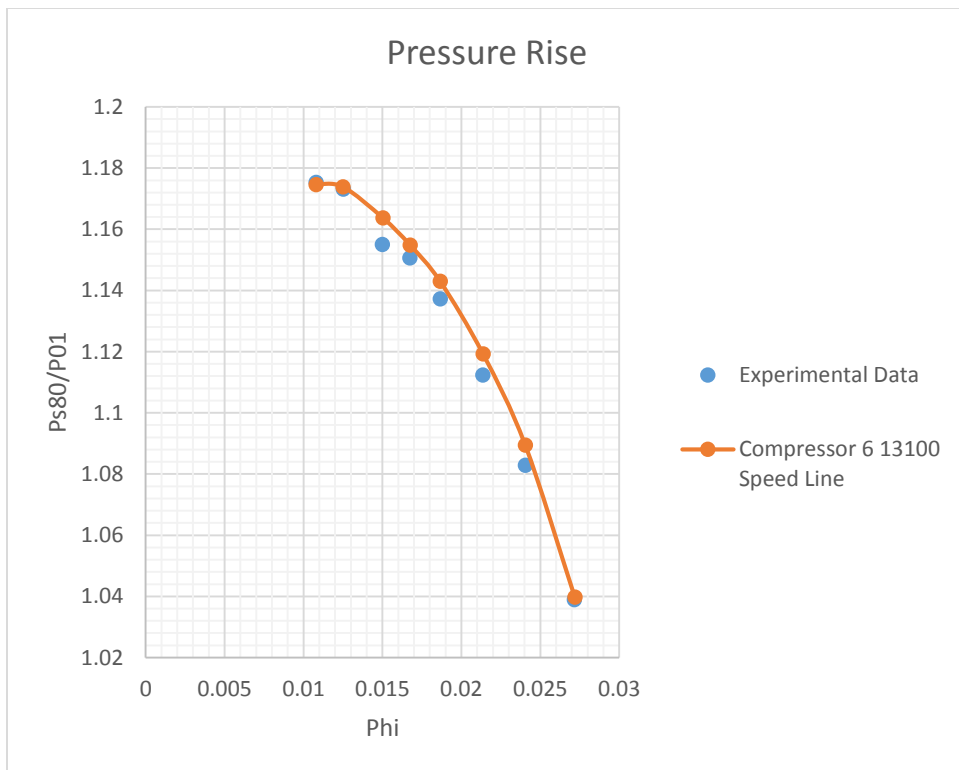


Figure 223: Compressor 6 13100 RPM Operation Envelope

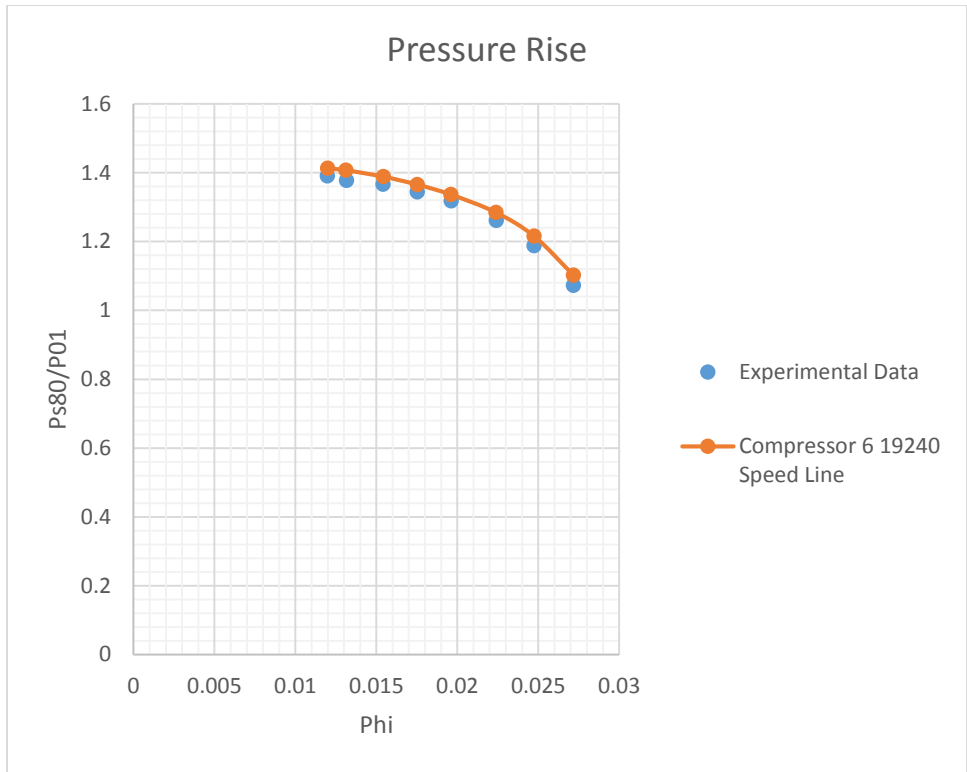


Figure 224: Compressor 6 19240 RPM Operation Envelope

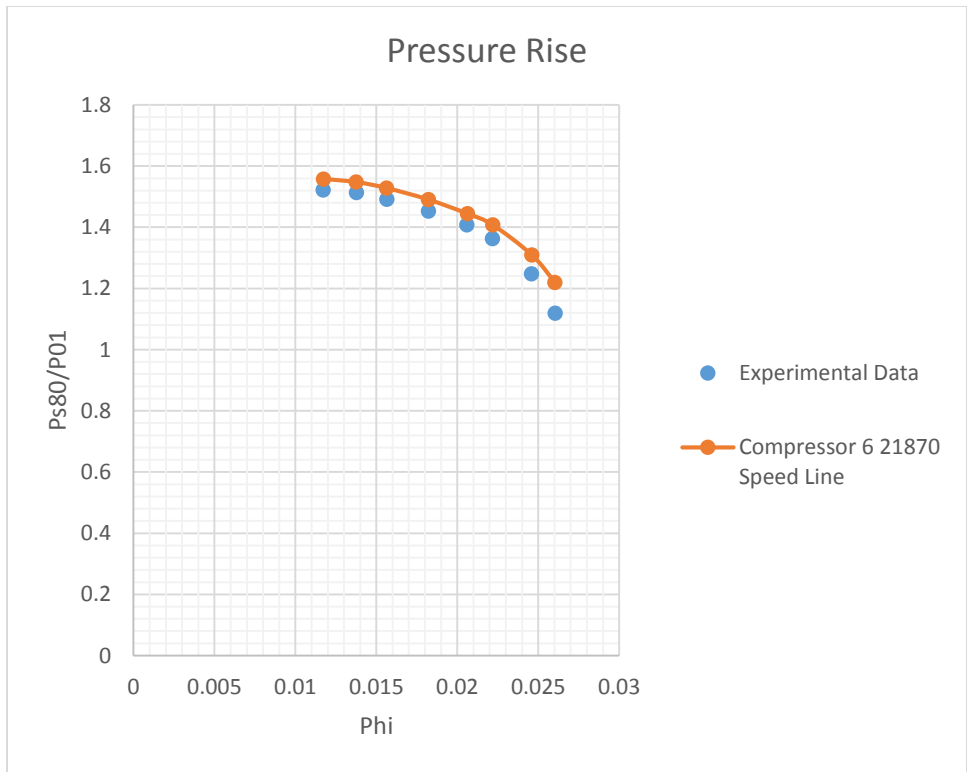


Figure 225: Compressor 6 21870 RPM Operation Envelope

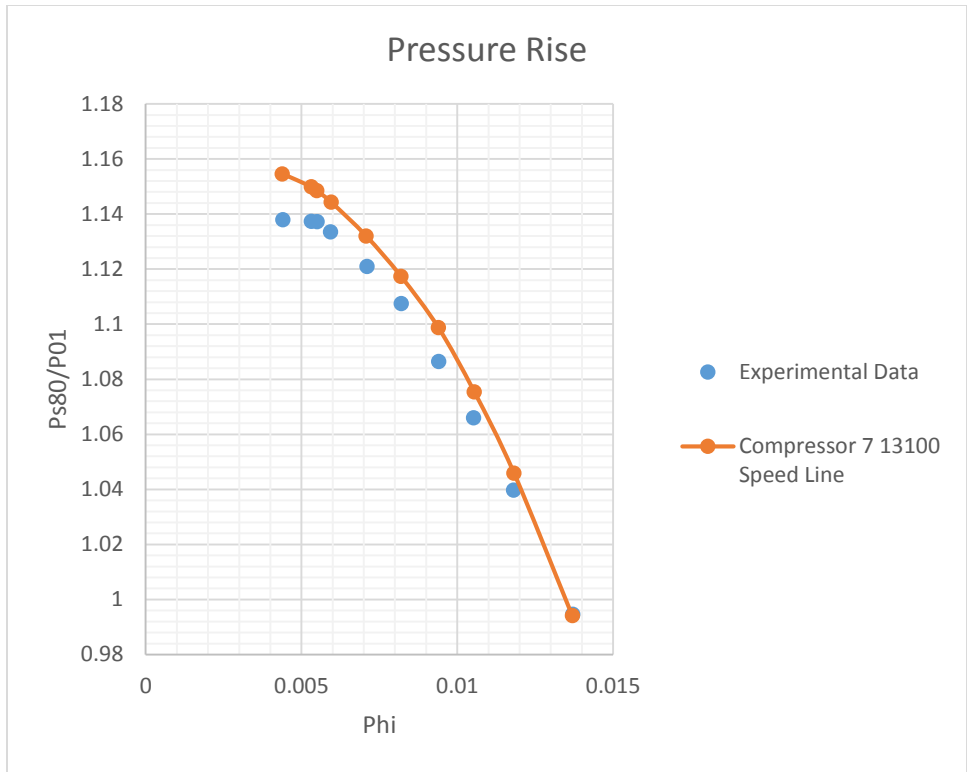


Figure 226: Compressor 7 13100 RPM Operation Envelope

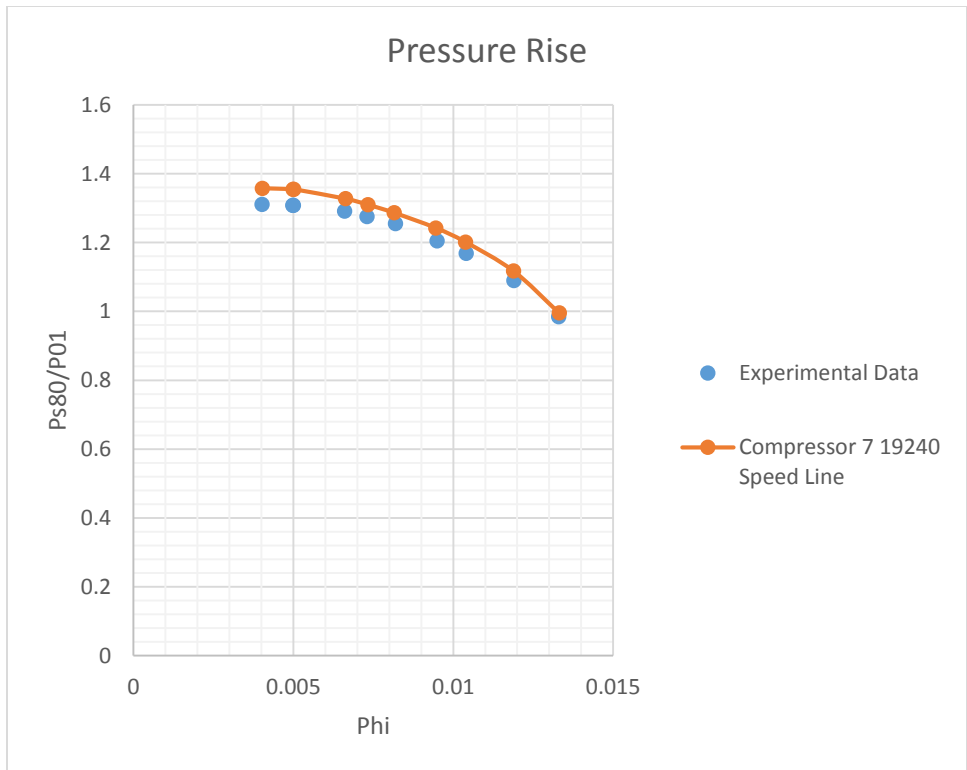


Figure 227: Compressor 7 19240 RPM Operation Envelope

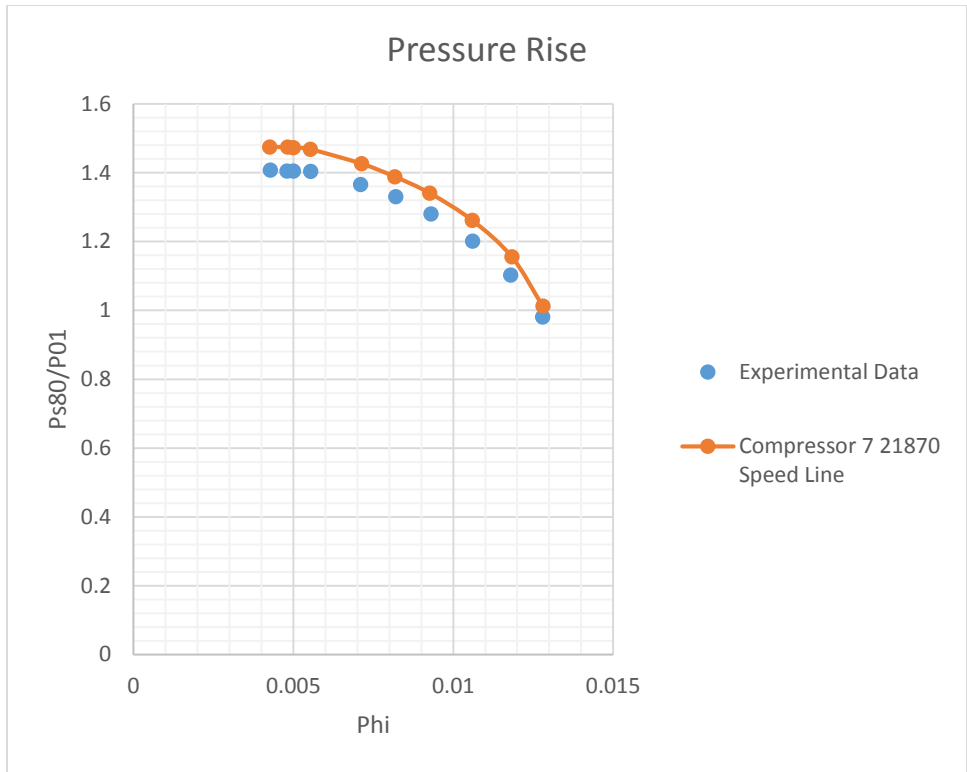


Figure 228: Compressor 7 21870 RPM Operation Envelope

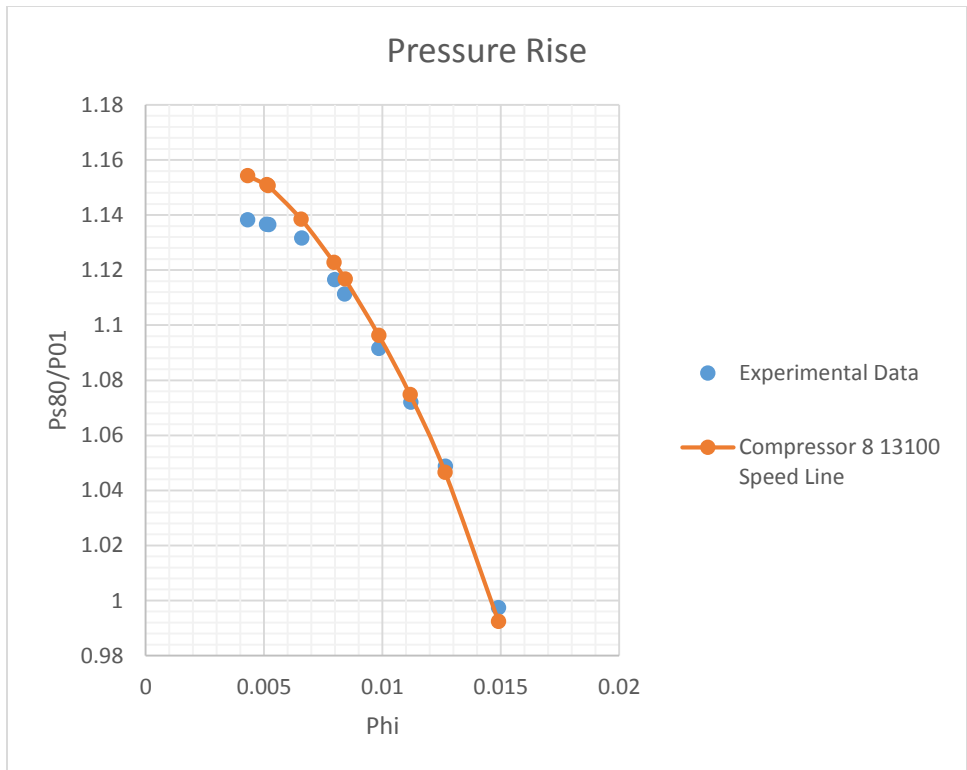


Figure 229: Compressor 8 13100 RPM Operation Envelope

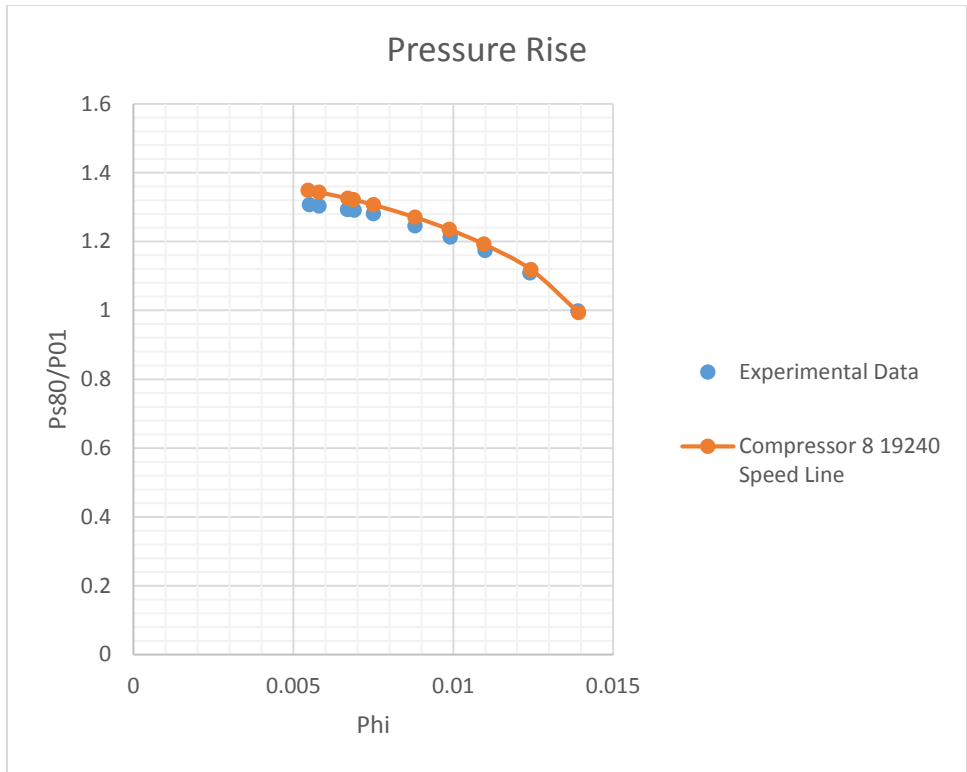


Figure 230: Compressor 8 19240 RPM Operation Envelope

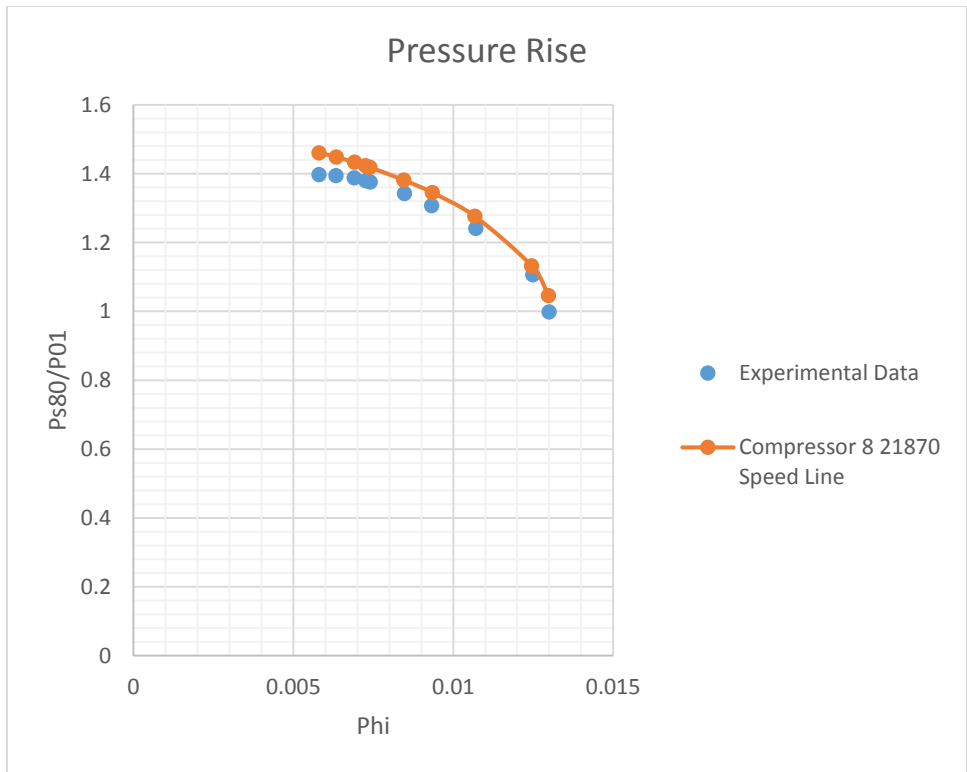


Figure 231: Compressor 8 21870 RPM Operation Envelope

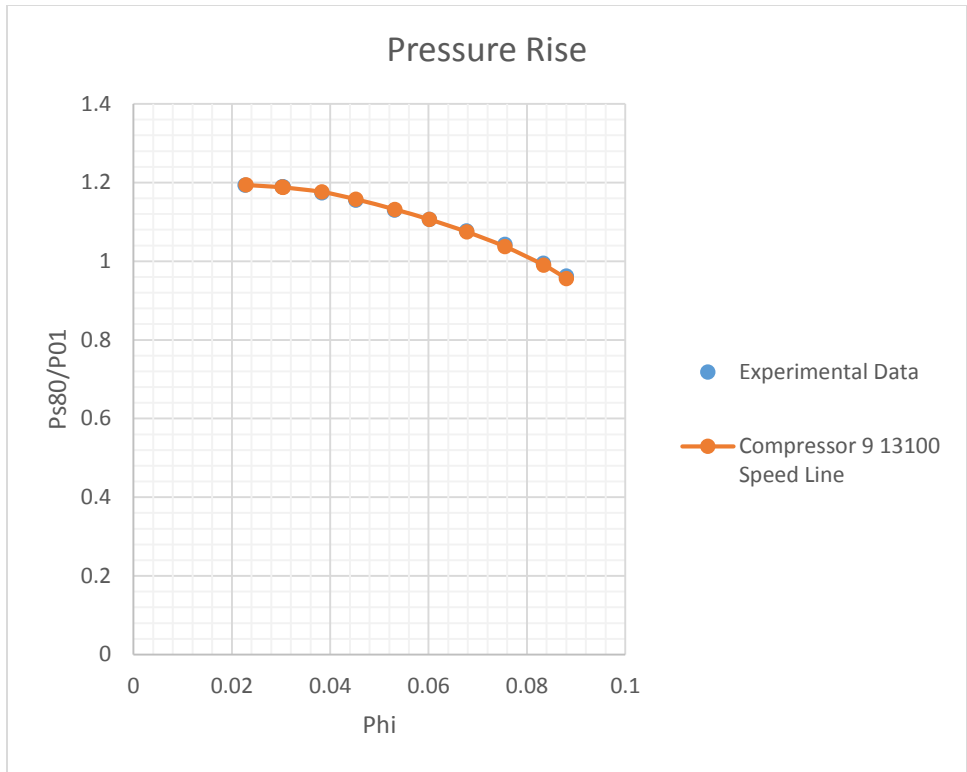


Figure 232: Compressor 9 13100 RPM Operation Envelope

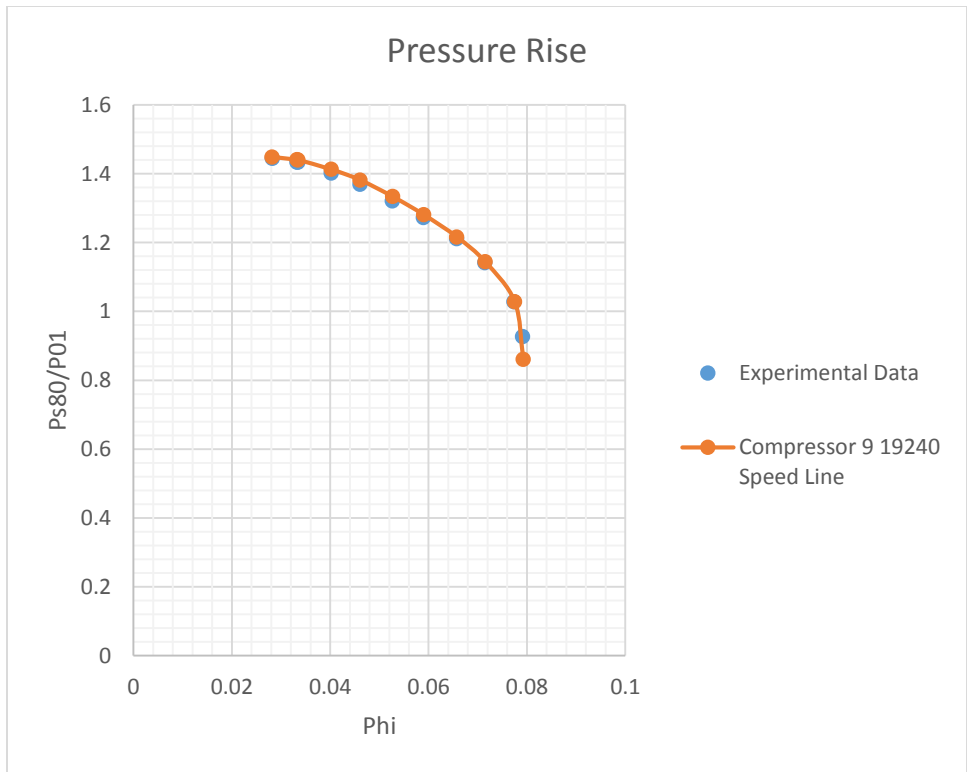


Figure 233: Compressor 9 19240 RPM Operation Envelope

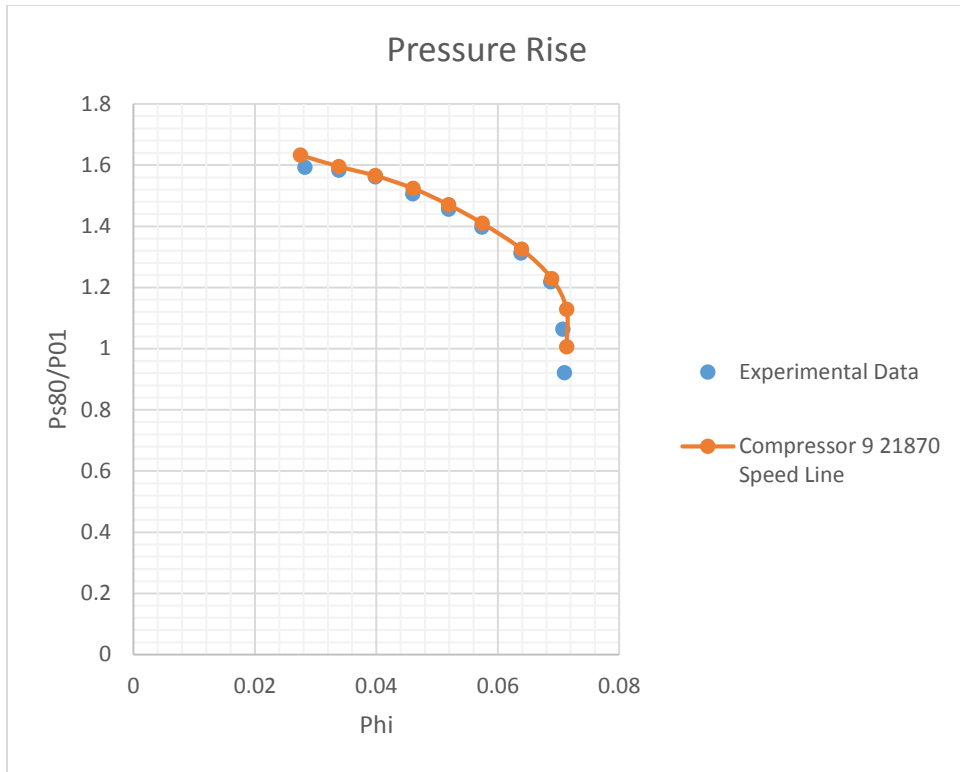


Figure 234: Compressor 9 21870 RPM Operation Envelope

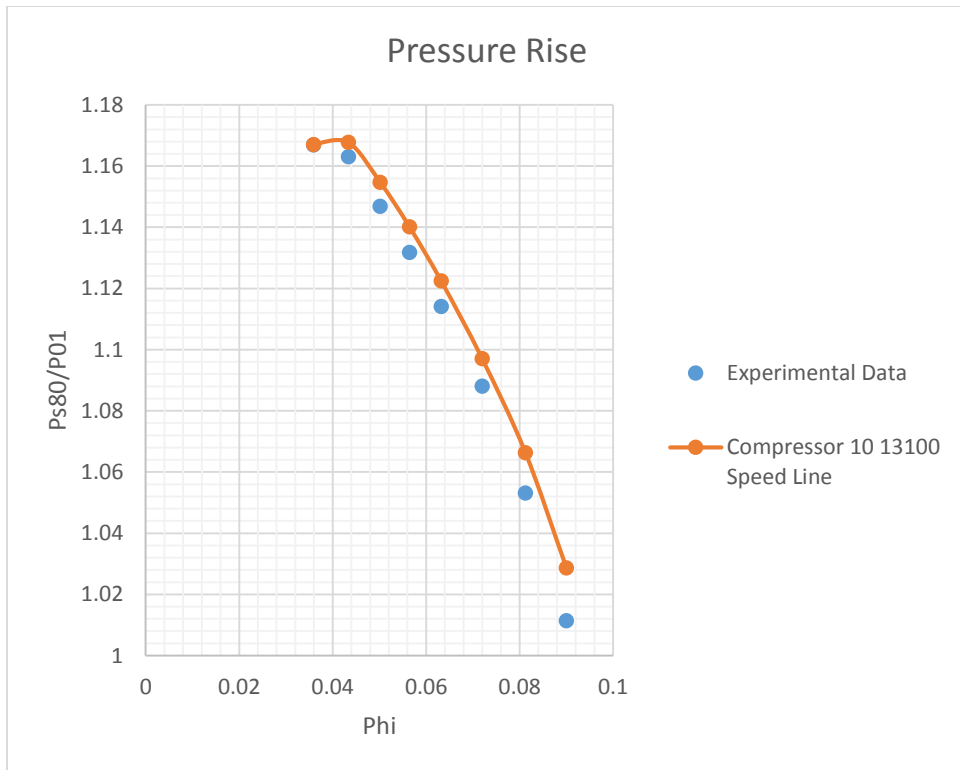


Figure 235: Compressor 10 13100 RPM Operation Envelope

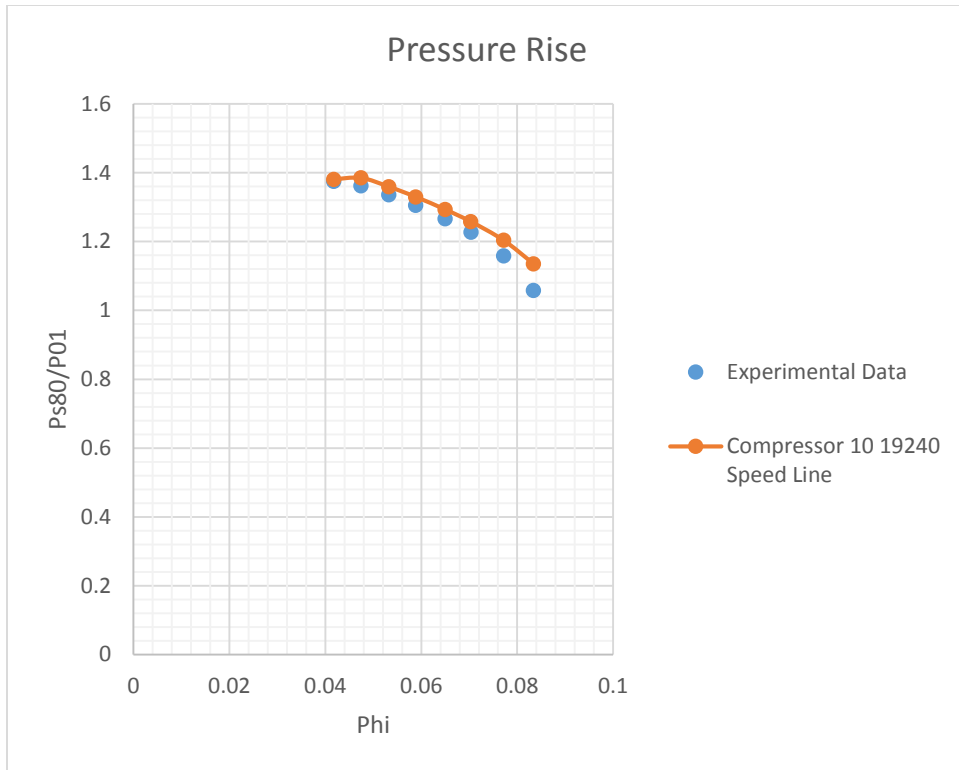


Figure 236: Compressor 10 19240 RPM Operation Envelope

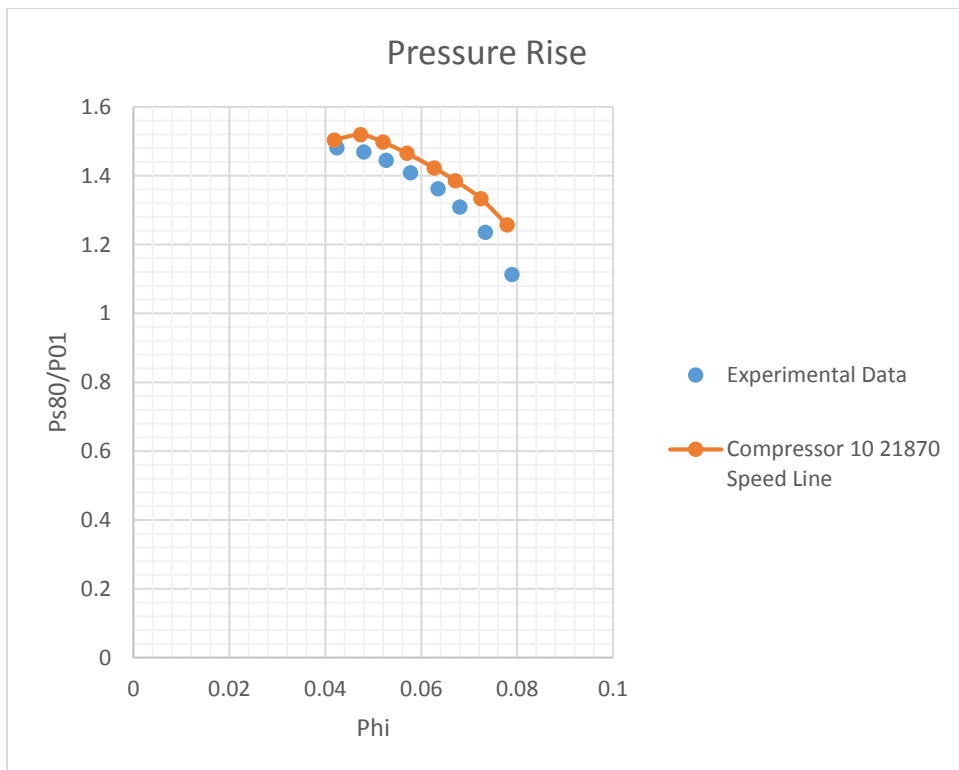


Figure 237: Compressor 10 21870 RPM Operation Envelope

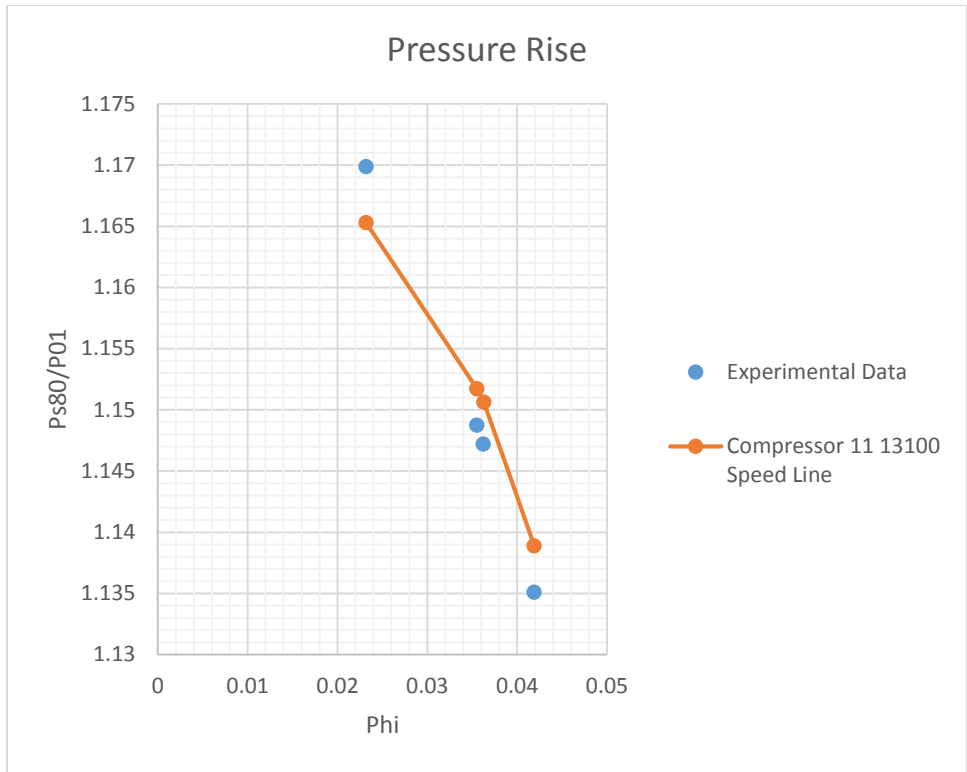


Figure 238: Compressor 11 13100 RPM Operation Envelope

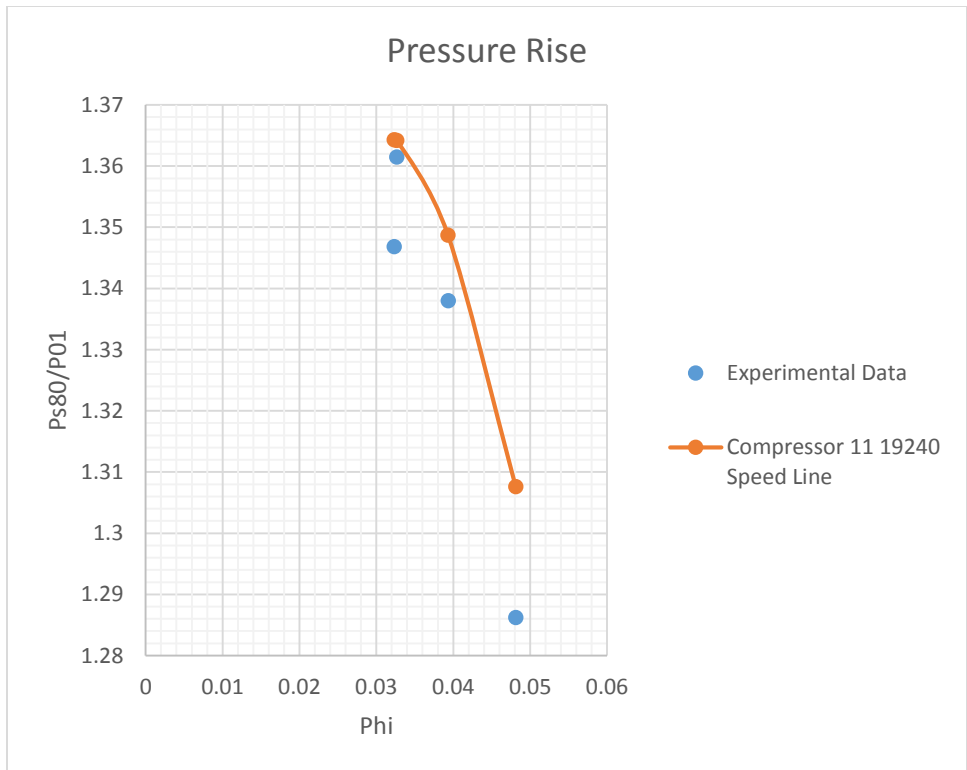


Figure 239: Compressor 11 19240 RPM Operation Envelope

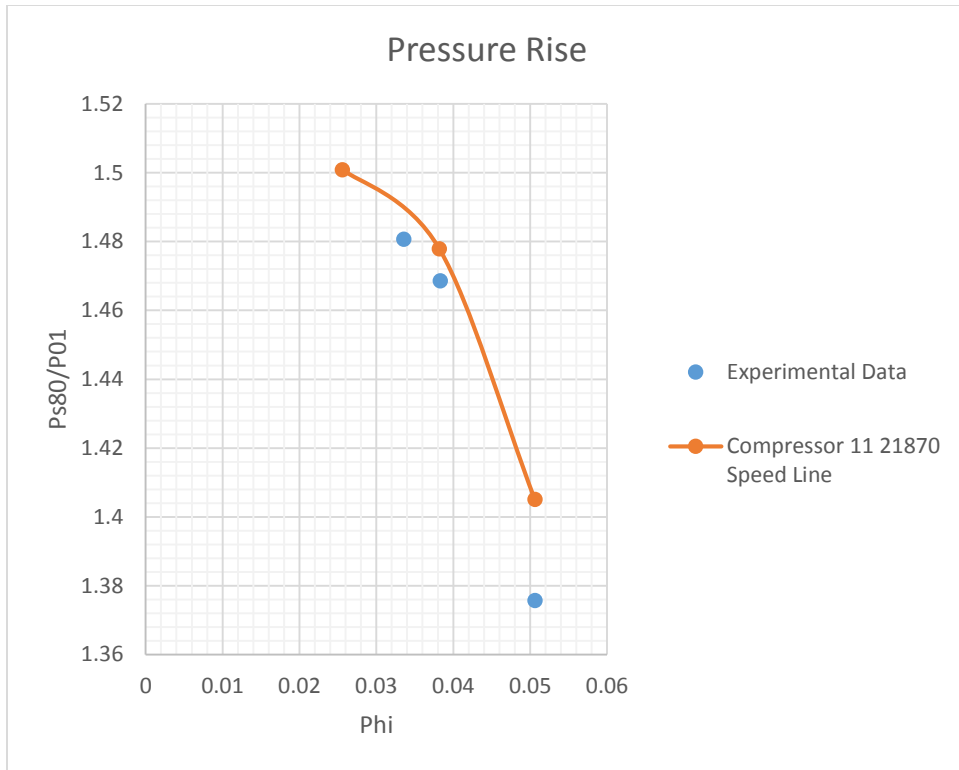


Figure 240: Compressor 11 21870 RPM Operation Envelope

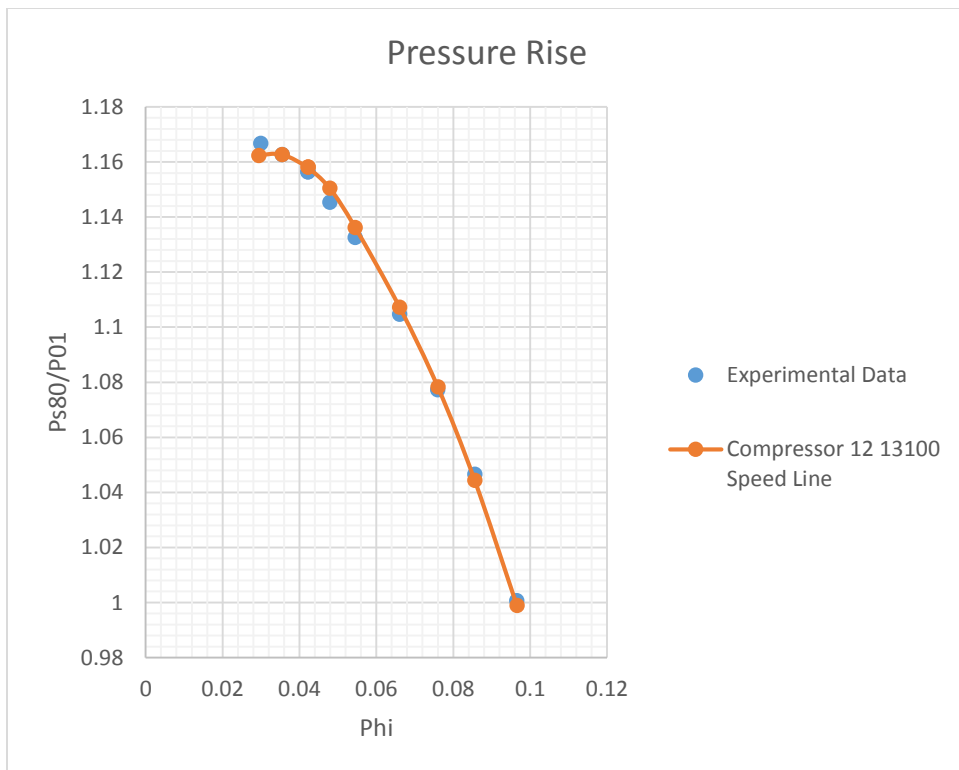


Figure 241: Compressor 12 13100 RPM Operation Envelope

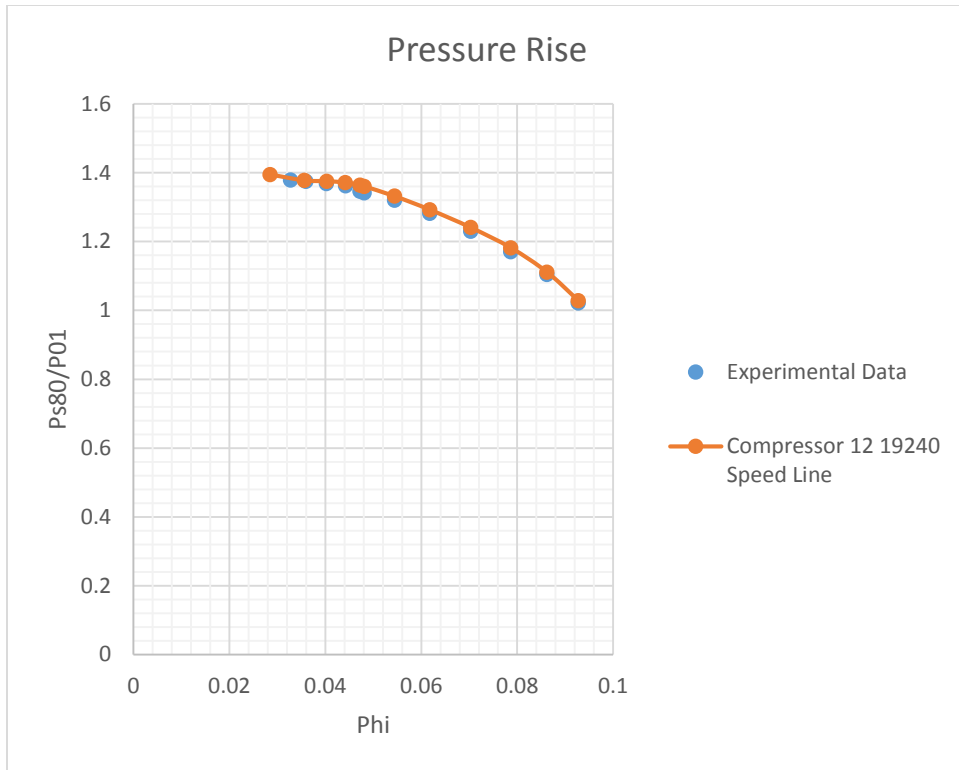


Figure 242: Compressor 12 19240 RPM Operation Envelope

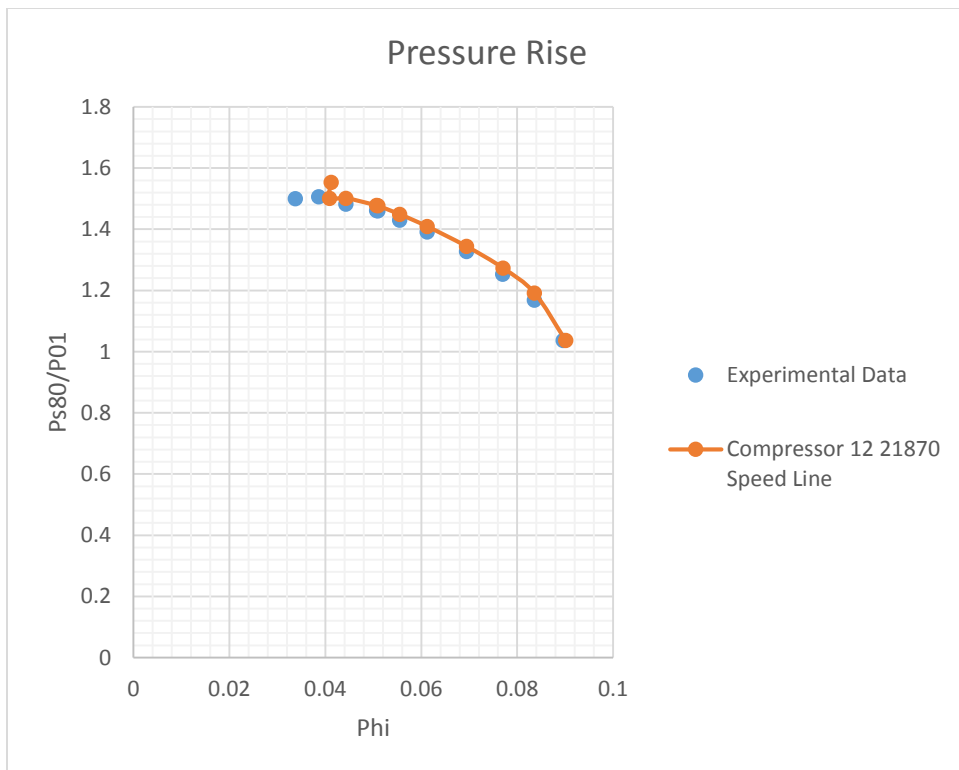


Figure 243: Compressor 12 21870 RPM Operation Envelope

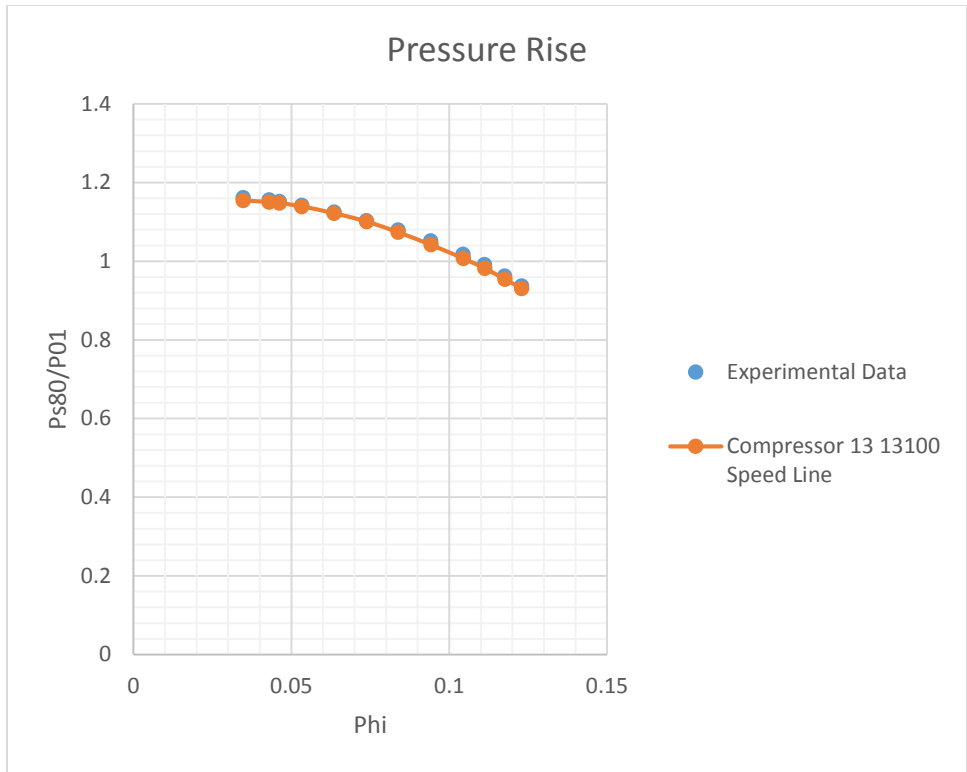


Figure 244: Compressor 13 13100 RPM Operation Envelope

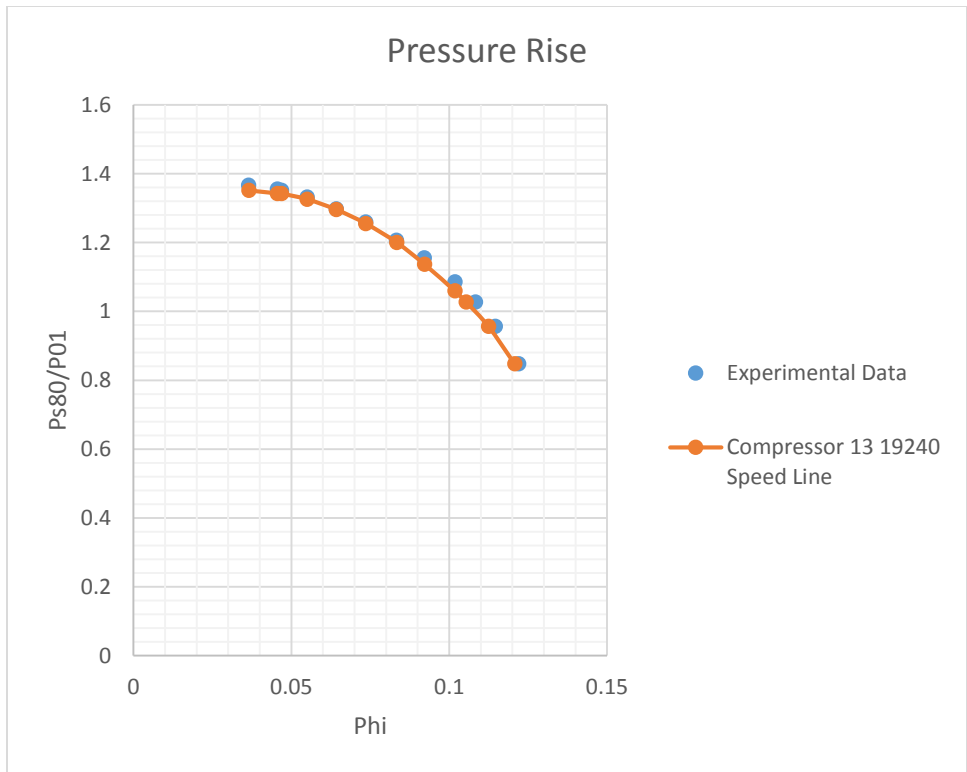


Figure 245: Compressor 13 19240 RPM Operation Envelope

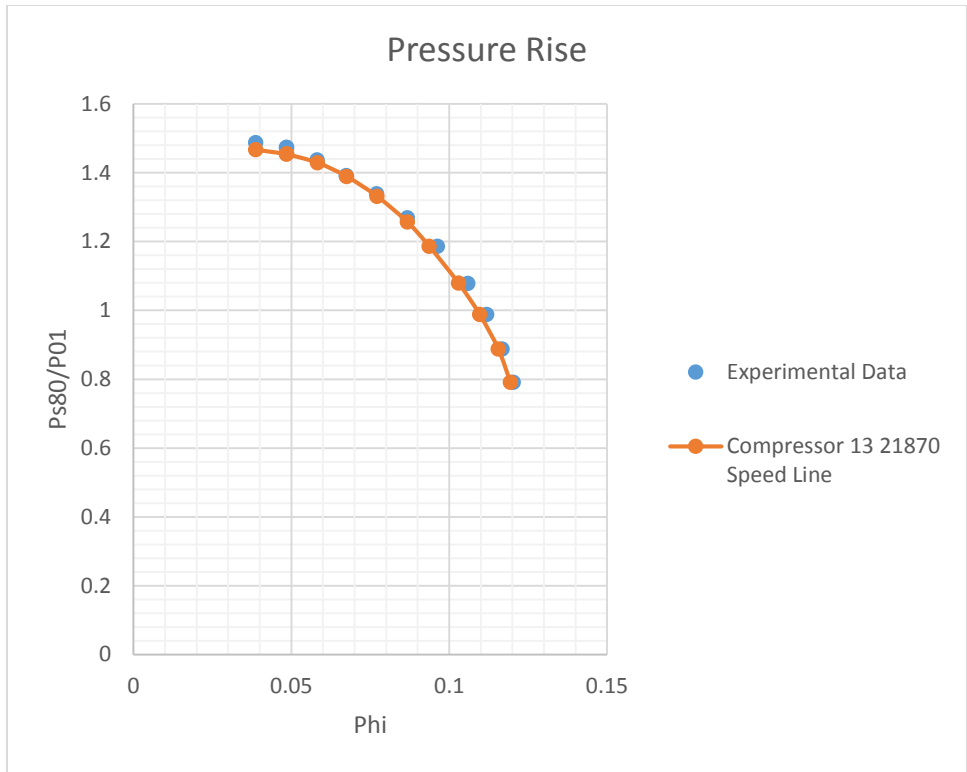


Figure 246: Compressor 13 21870 RPM Operation Envelope

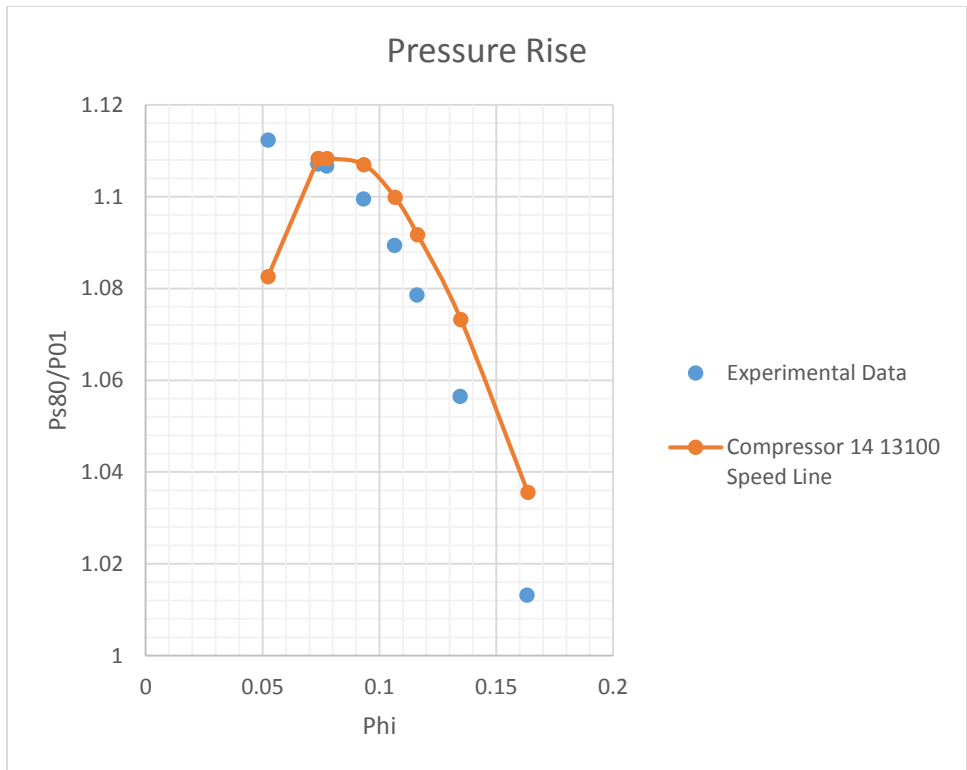


Figure 247: Compressor 14 13100 RPM Operation Envelope

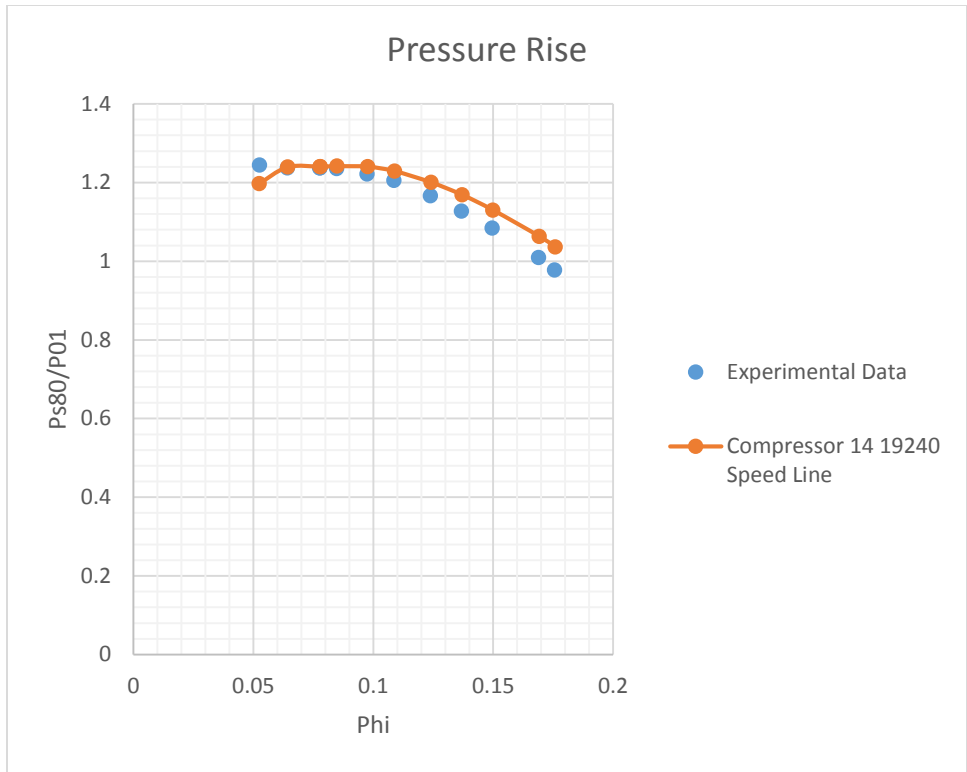


Figure 248: Compressor 14 19240 RPM Operation Envelope

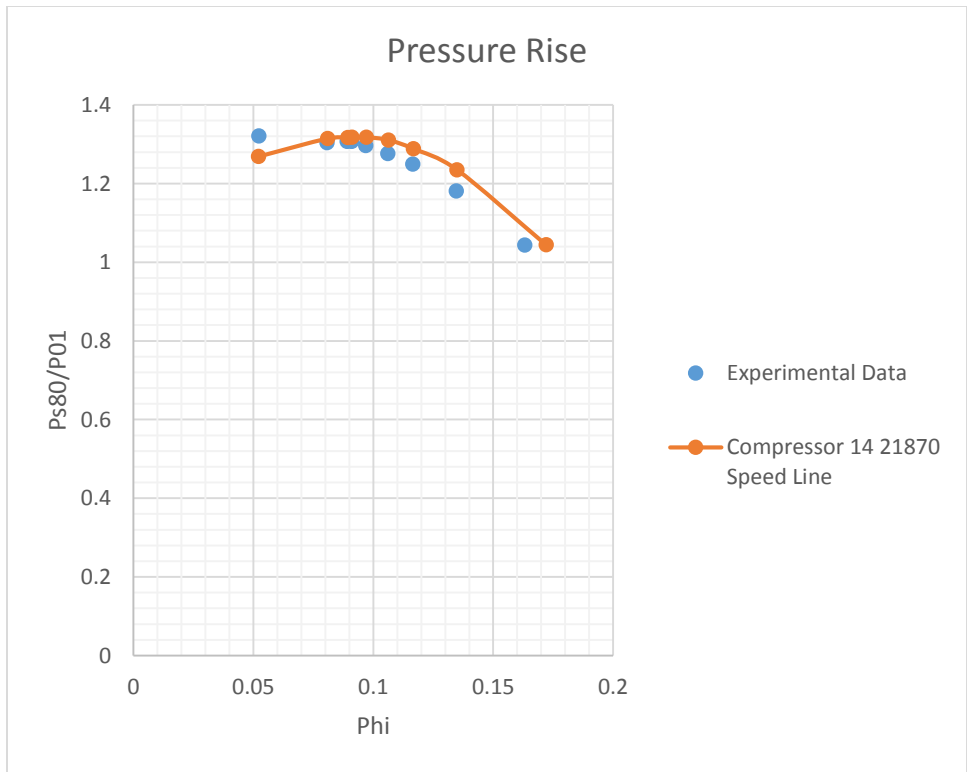


Figure 249: Compressor 14 21870 RPM Operation Envelope

APPENDIX B: TEMPERATURE COMPARISONS

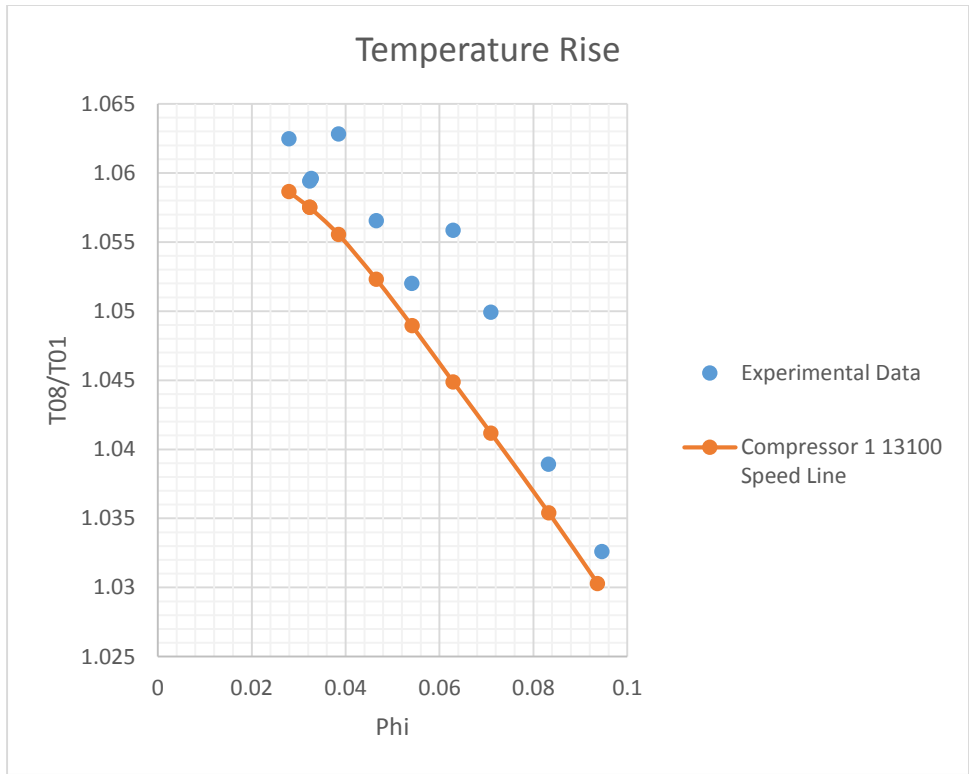


Figure 250: Compressor 1 13100 RPM Temperature Comparison

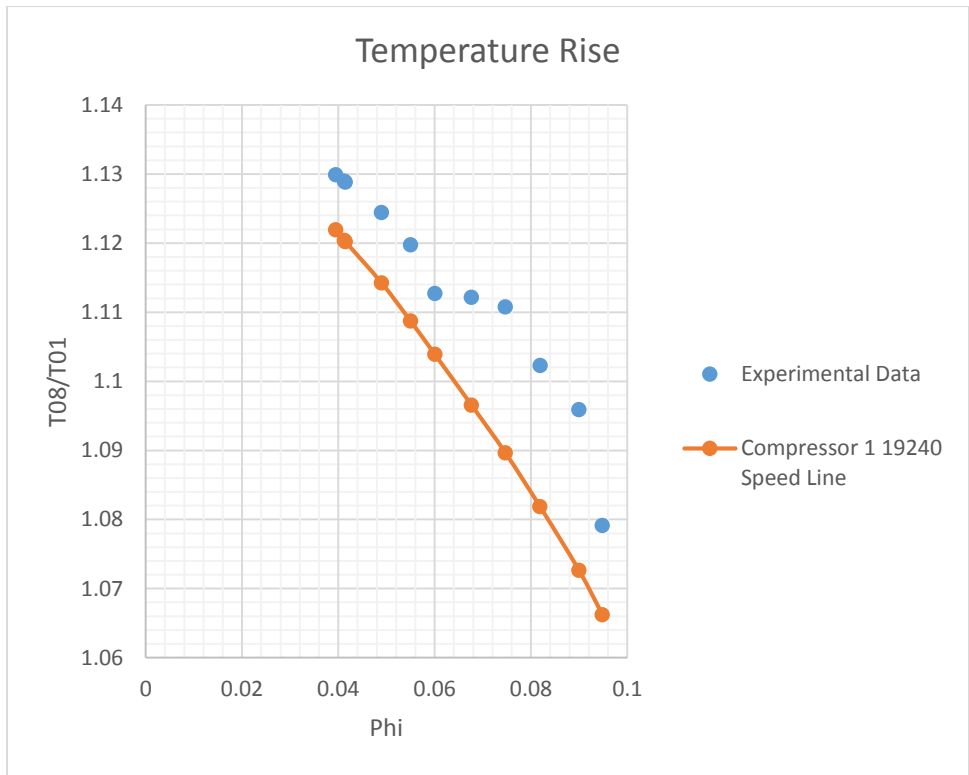


Figure 251: Compressor 1 19240 RPM Temperature Comparison

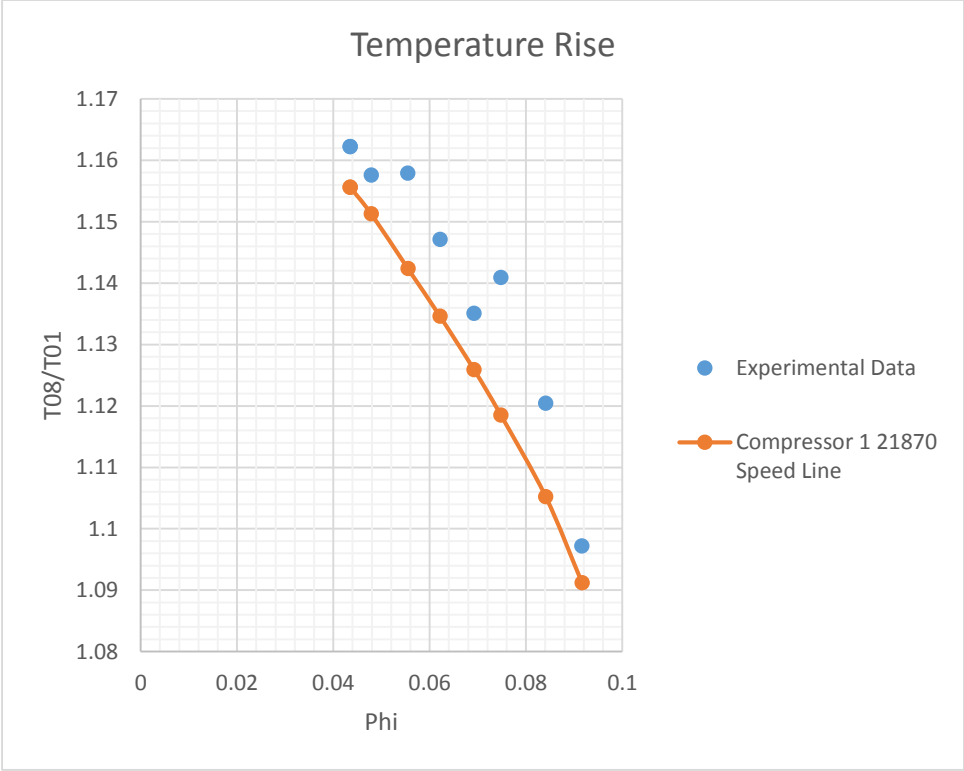


Figure 252: Compressor 1 21870 RPM Temperature Comparison

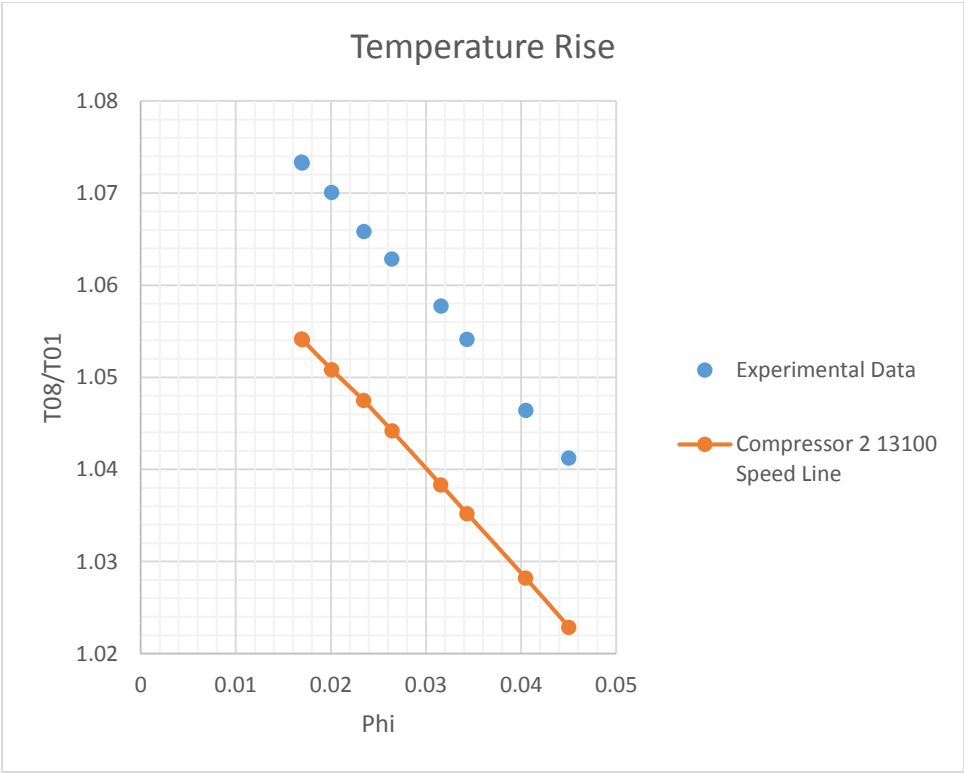


Figure 253: Compressor 2 13100 RPM Temperature Comparison

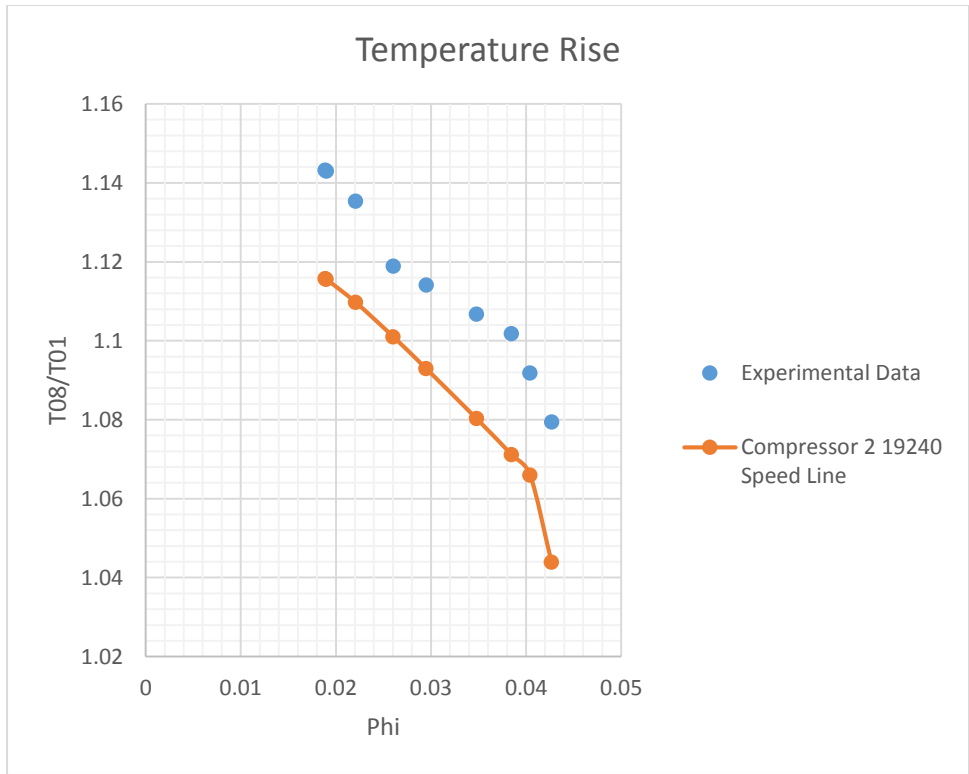


Figure 254: Compressor 2 19240 RPM Temperature Comparison

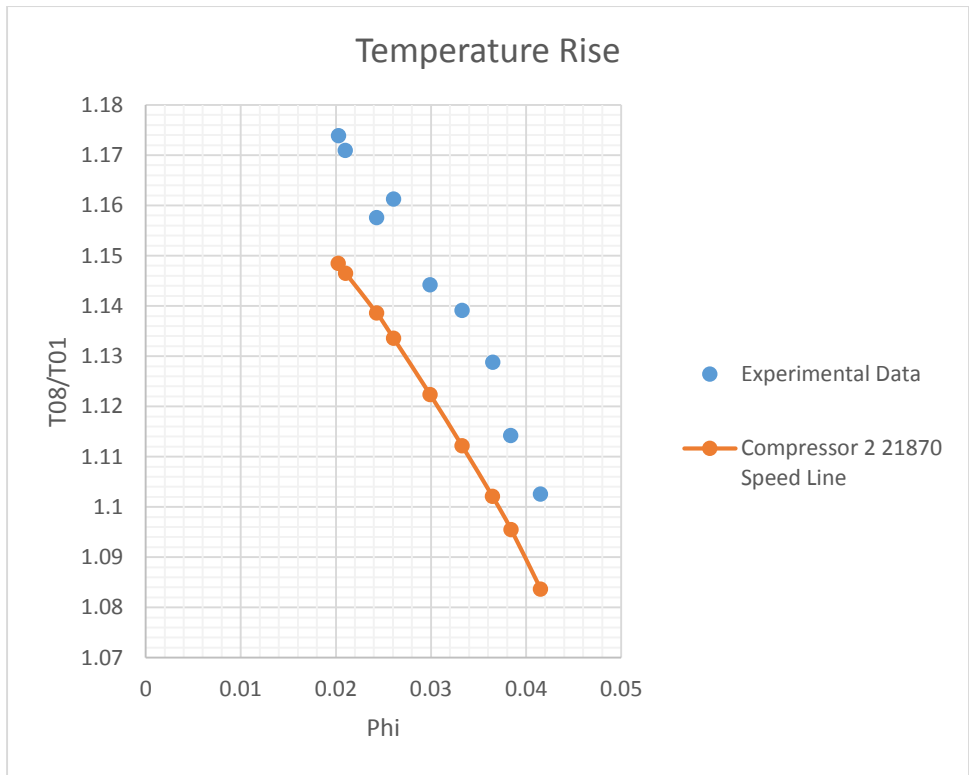


Figure 255: Compressor 2 21870 RPM Temperature Comparison

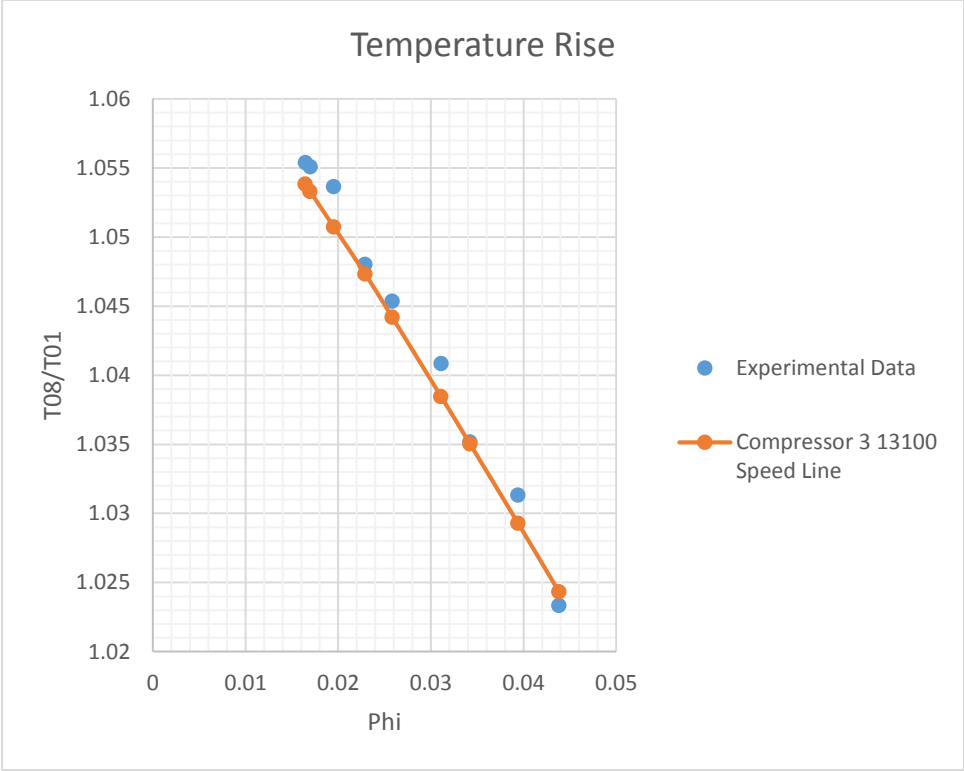


Figure 256: Compressor 3 13100 RPM Temperature Comparison

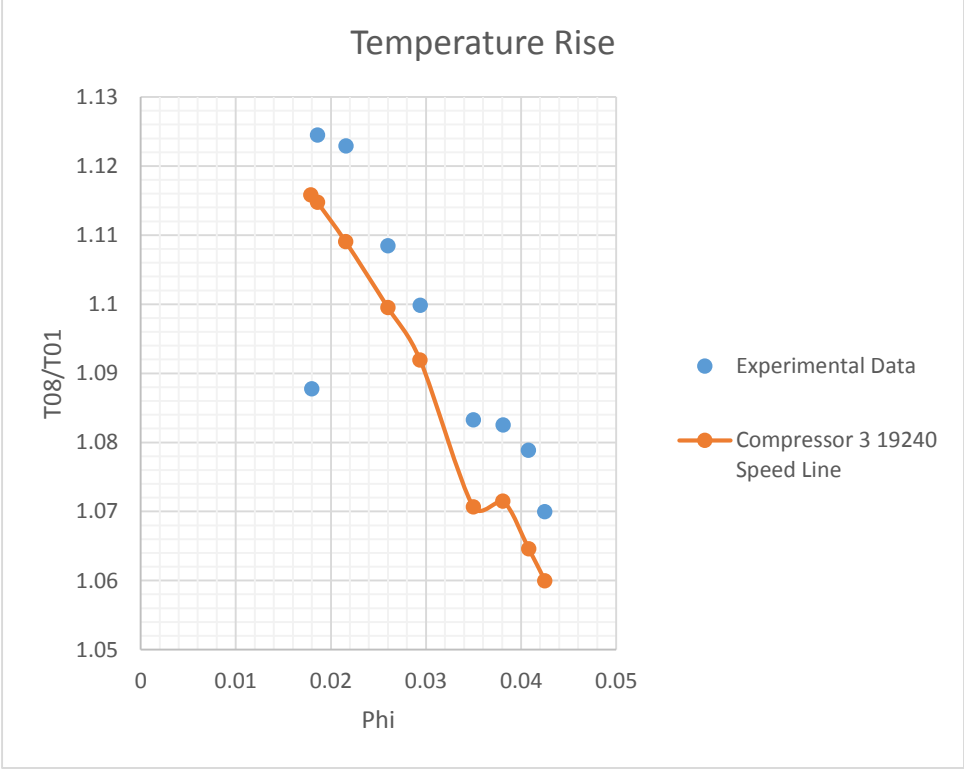


Figure 257: Compressor 3 19240 RPM Temperature Comparison

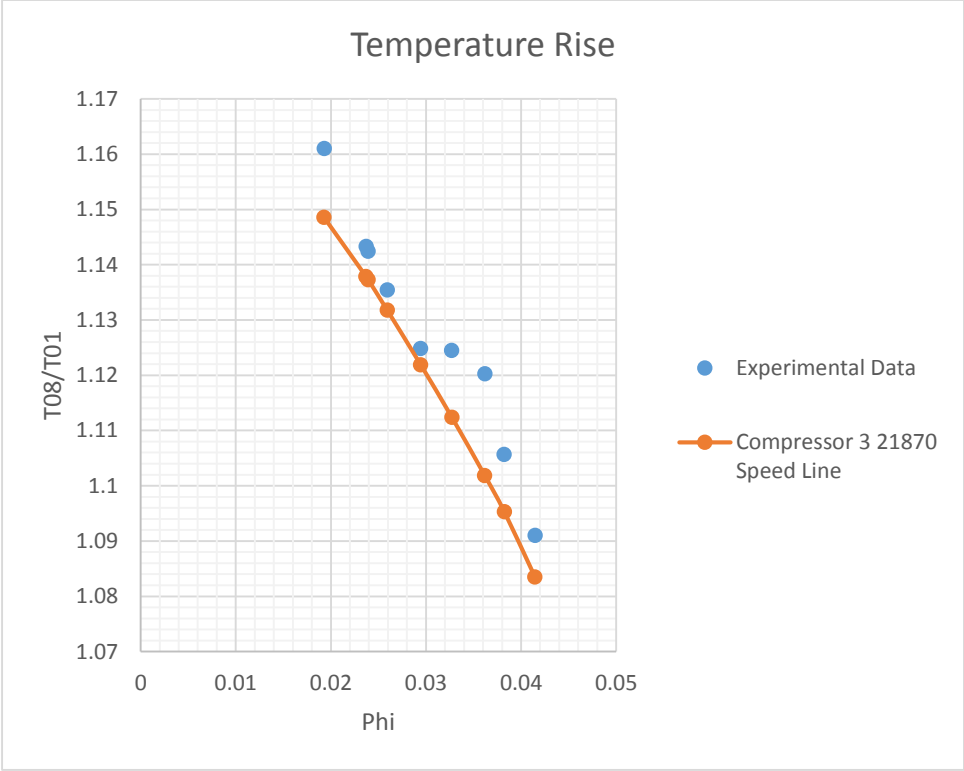


Figure 258: Compressor 3 21870 RPM Temperature Comparison

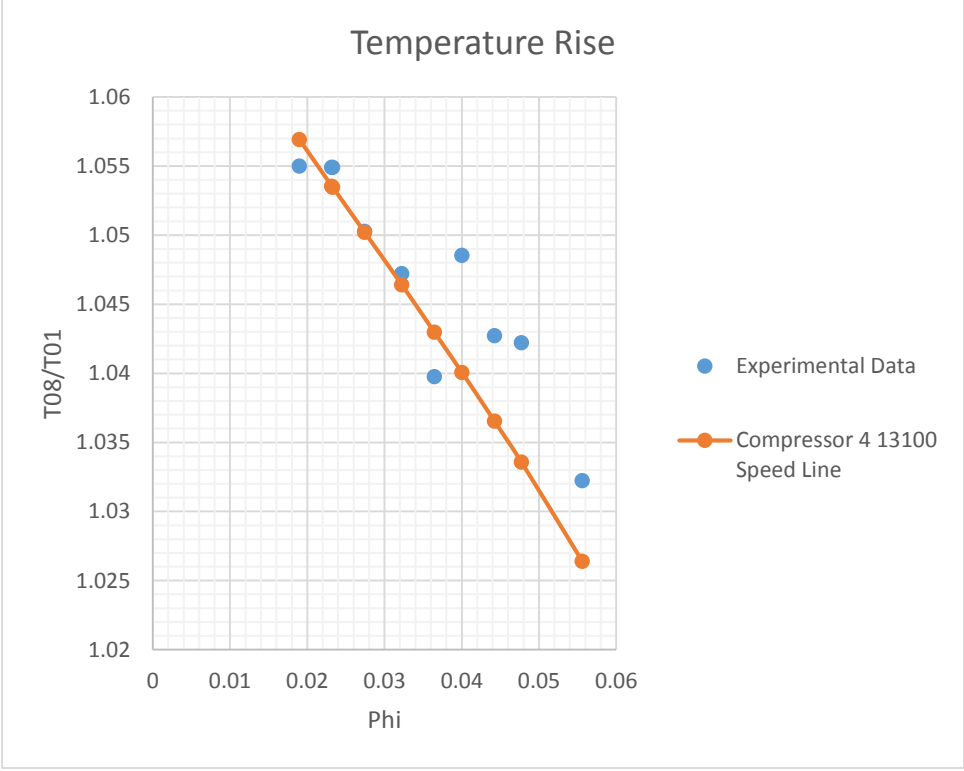


Figure 259: Compressor 4 13100 RPM Temperature Comparison

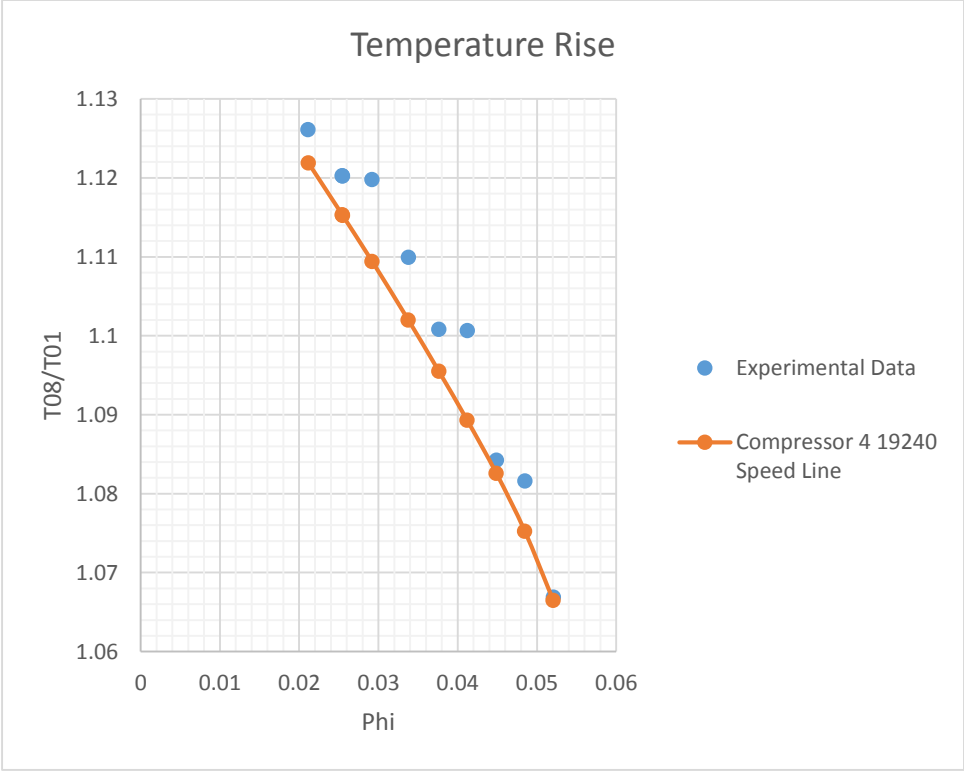


Figure 260: Compressor 4 19240 RPM Temperature Comparison

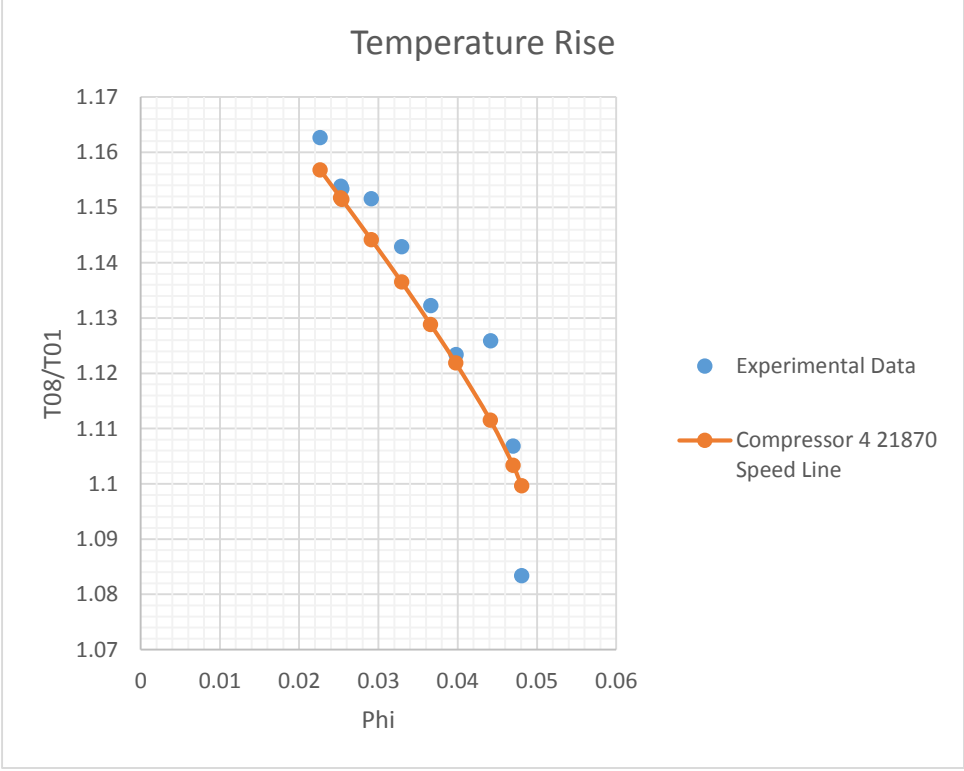


Figure 261: Compressor 4 21870 RPM Temperature Comparison

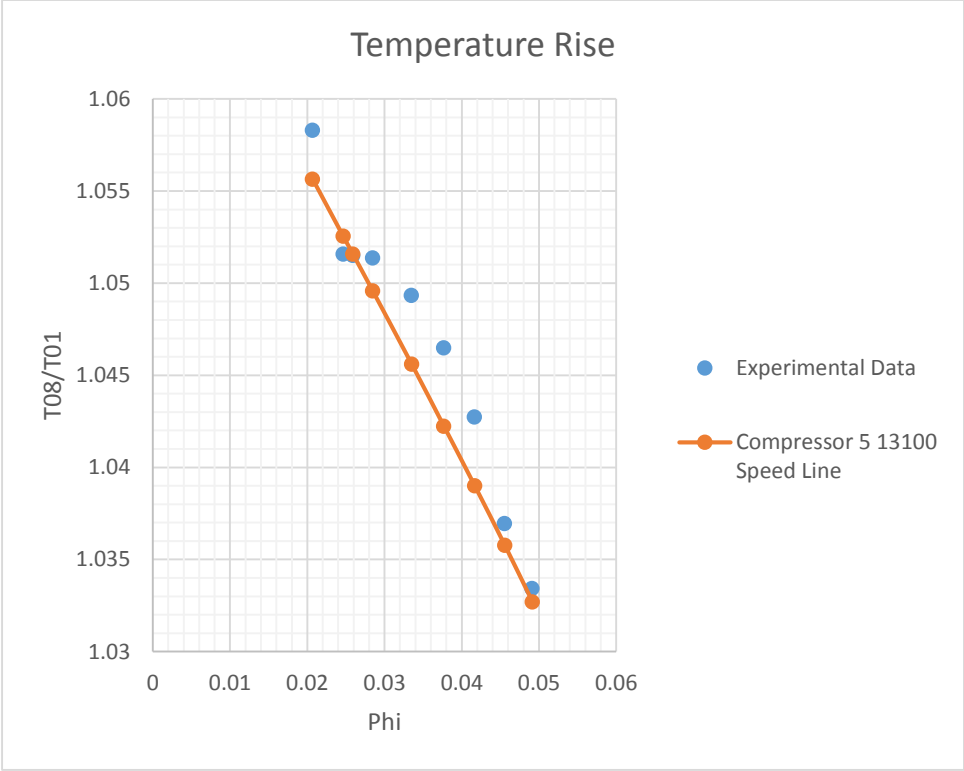


Figure 262: Compressor 5 13100 RPM Temperature Comparison

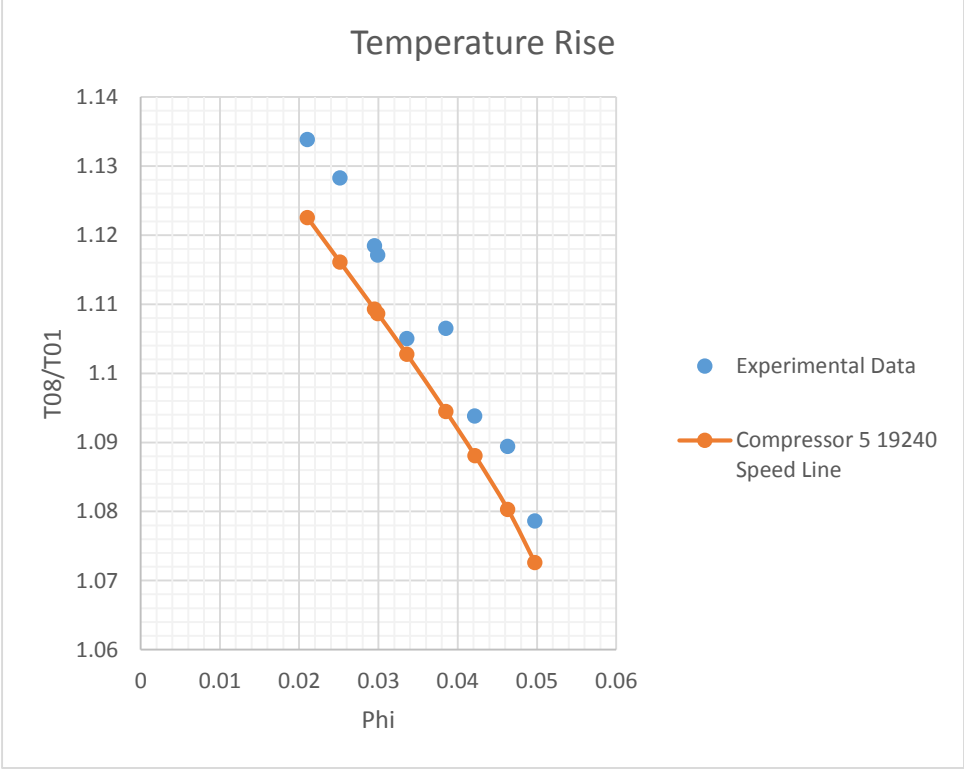


Figure 263: Compressor 5 19240 RPM Temperature Comparison

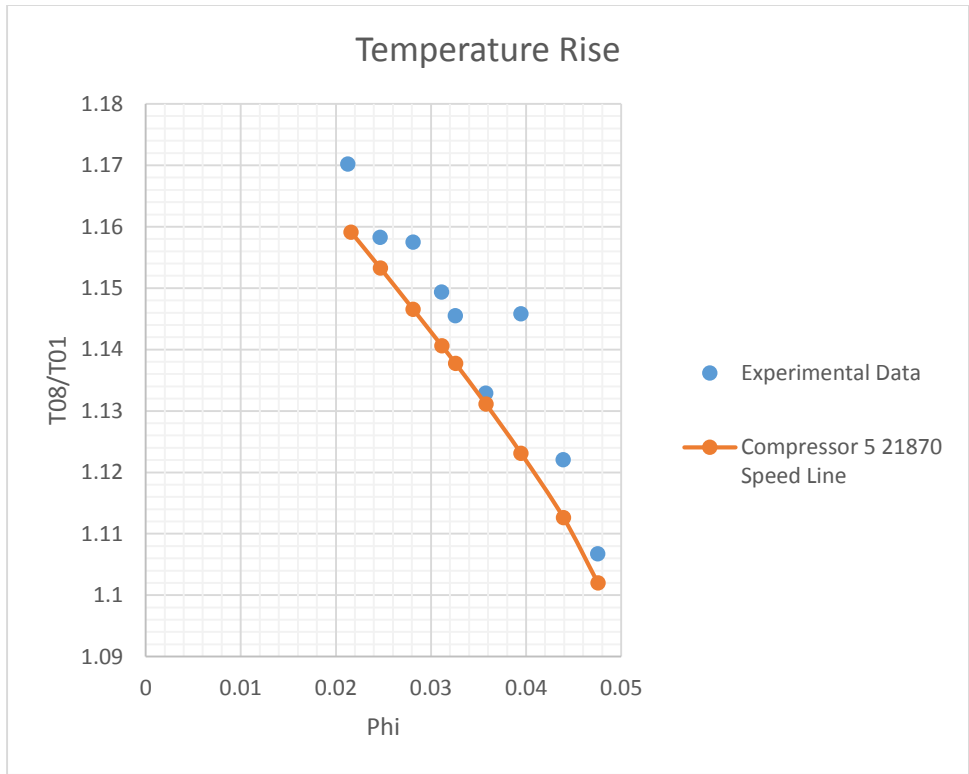


Figure 264: Compressor 5 21870 RPM Temperature Comparison

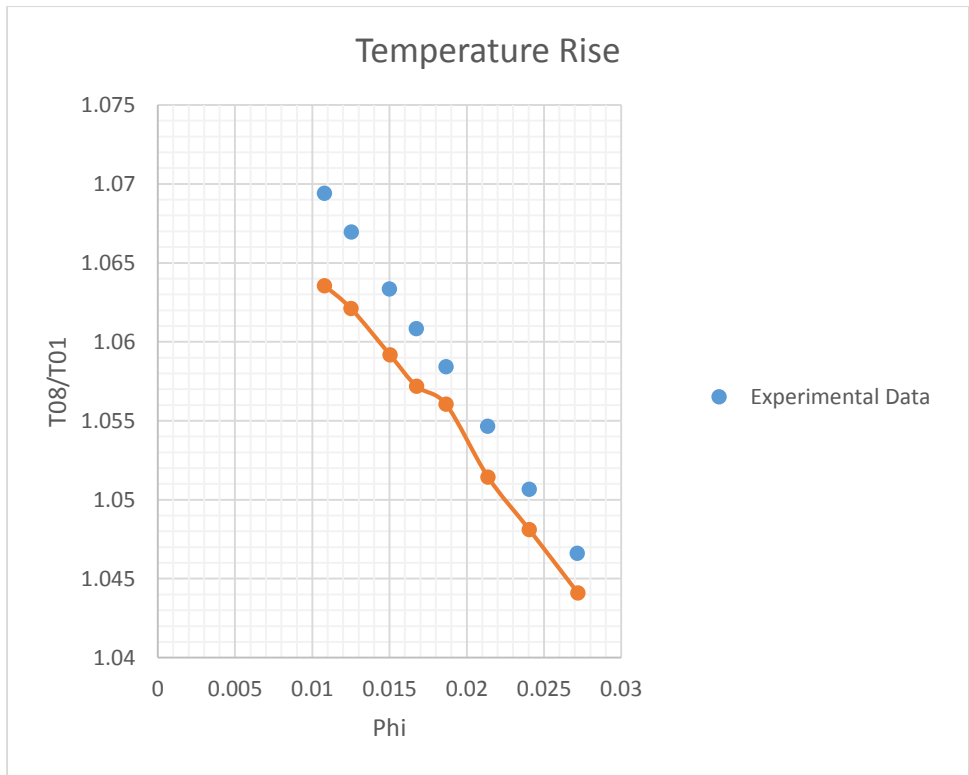


Figure 265: Compressor 6 13100 RPM Temperature Comparison

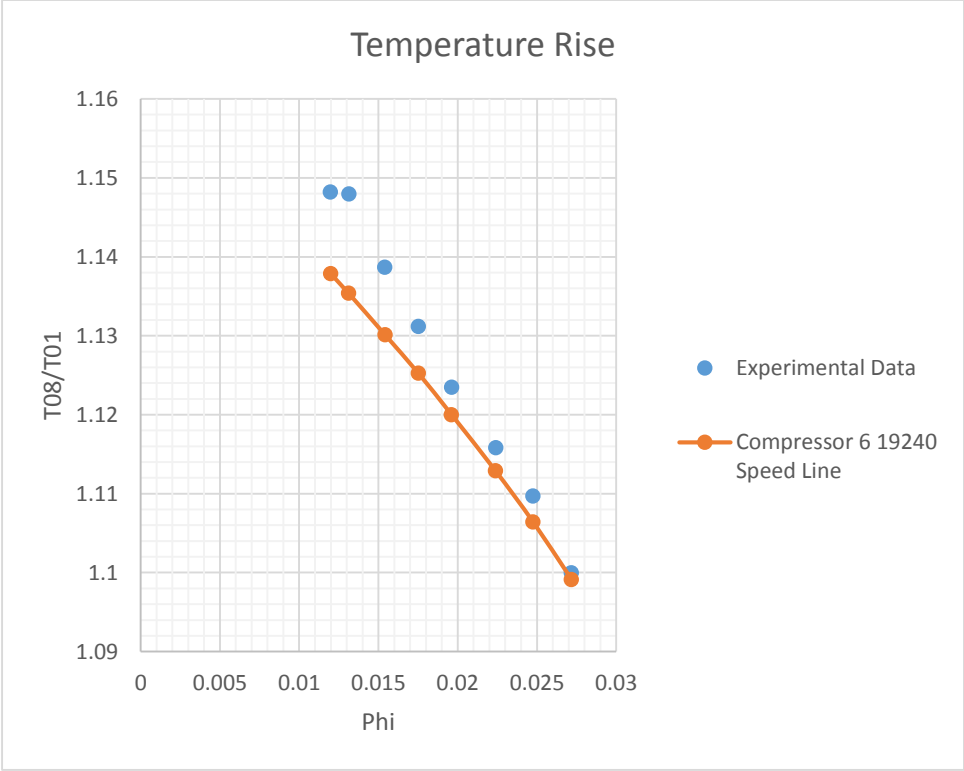


Figure 266: Compressor 6 19240 RPM Temperature Comparison

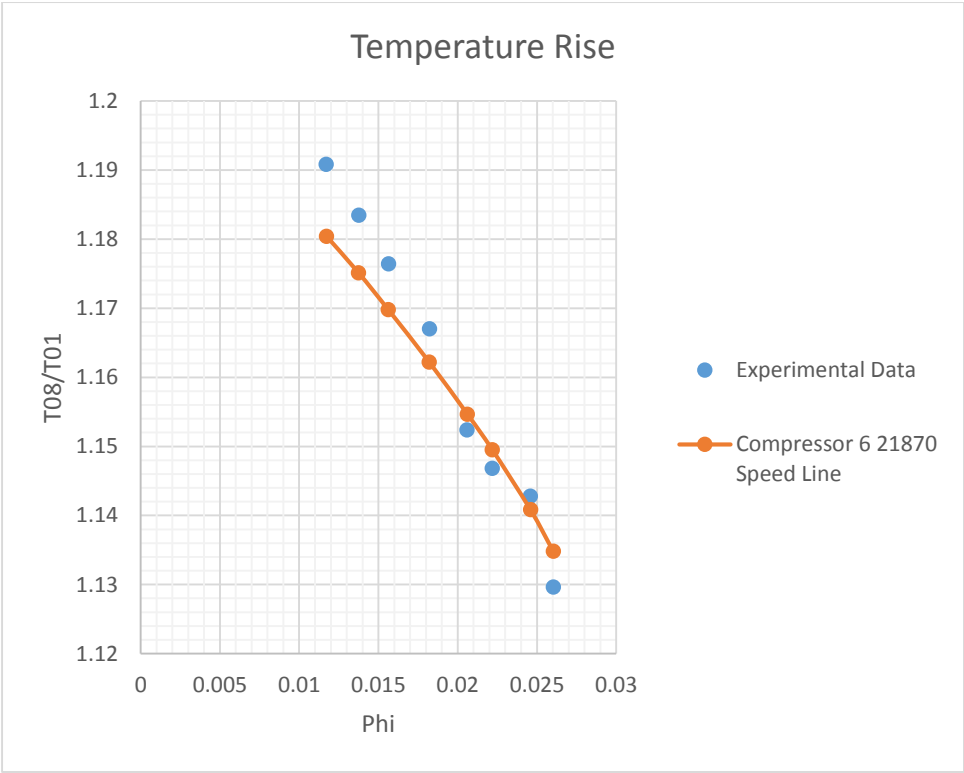


Figure 267: Compressor 6 21870 RPM Temperature Comparison

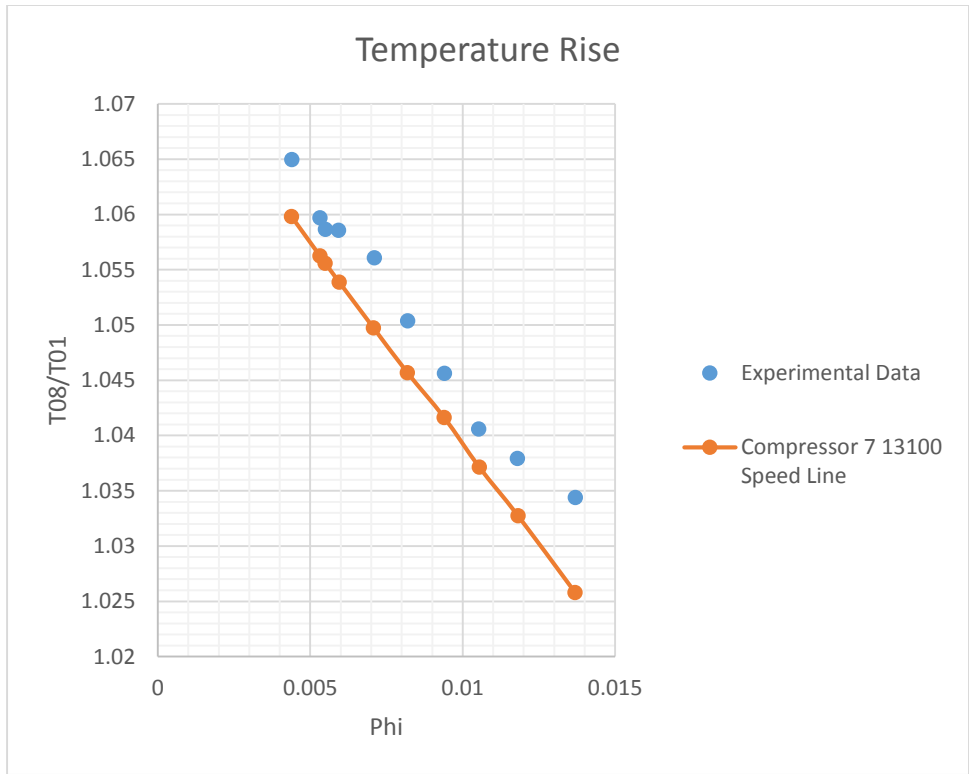


Figure 268: Compressor 7 13100 RPM Temperature Comparison

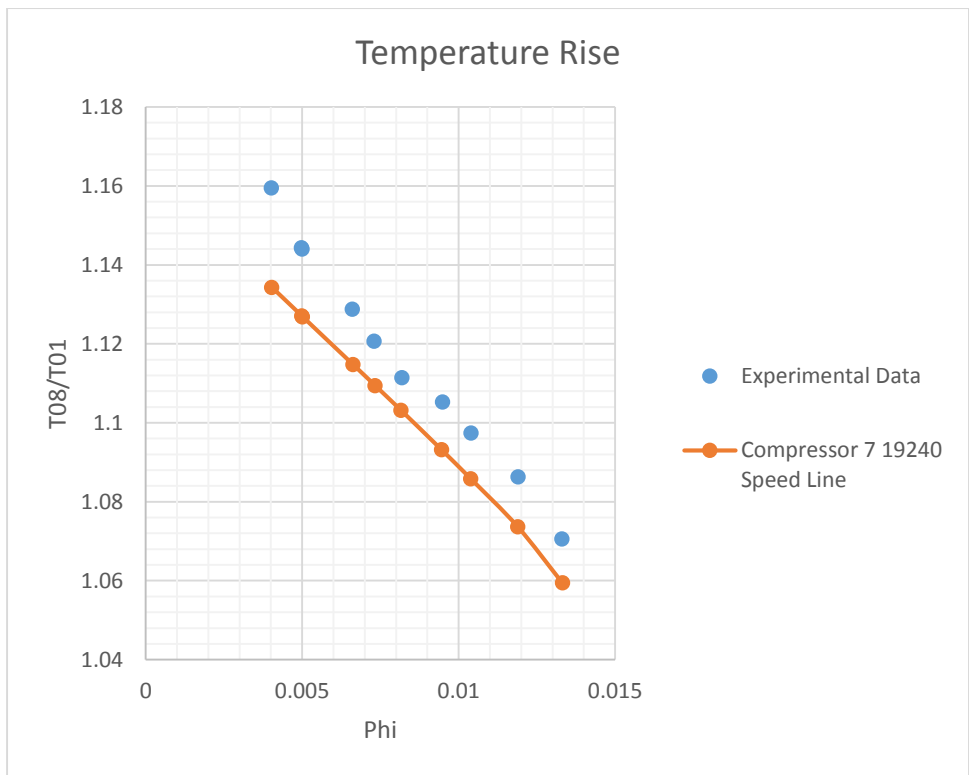


Figure 269: Compressor 7 19240 RPM Temperature Comparison

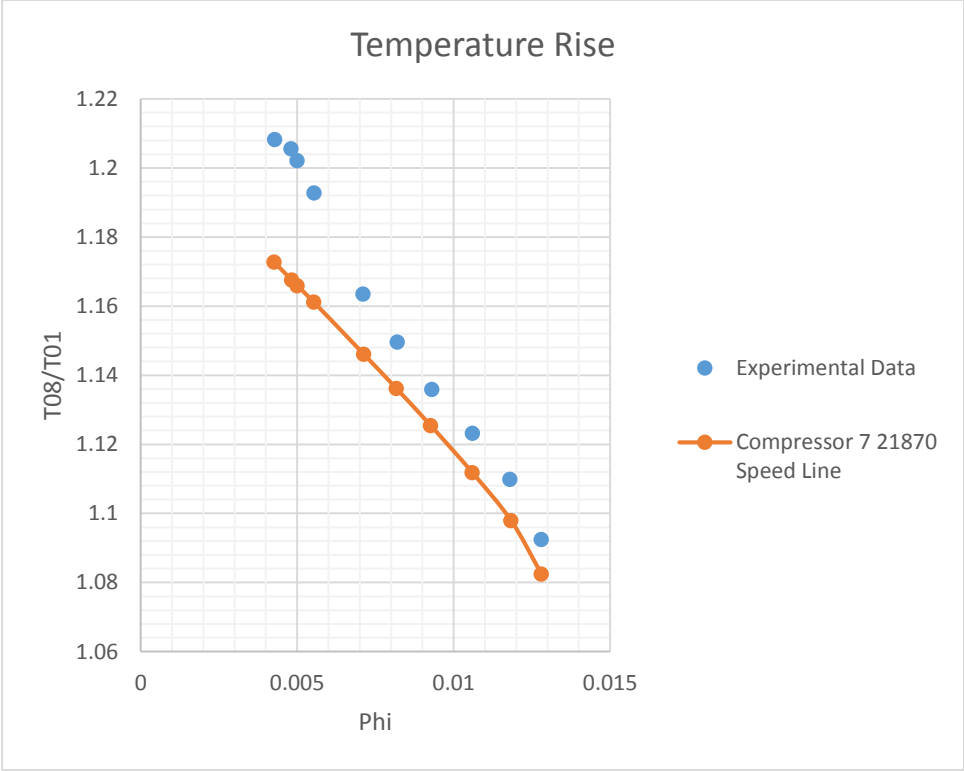


Figure 270: Compressor 7 21870 RPM Temperature Comparison

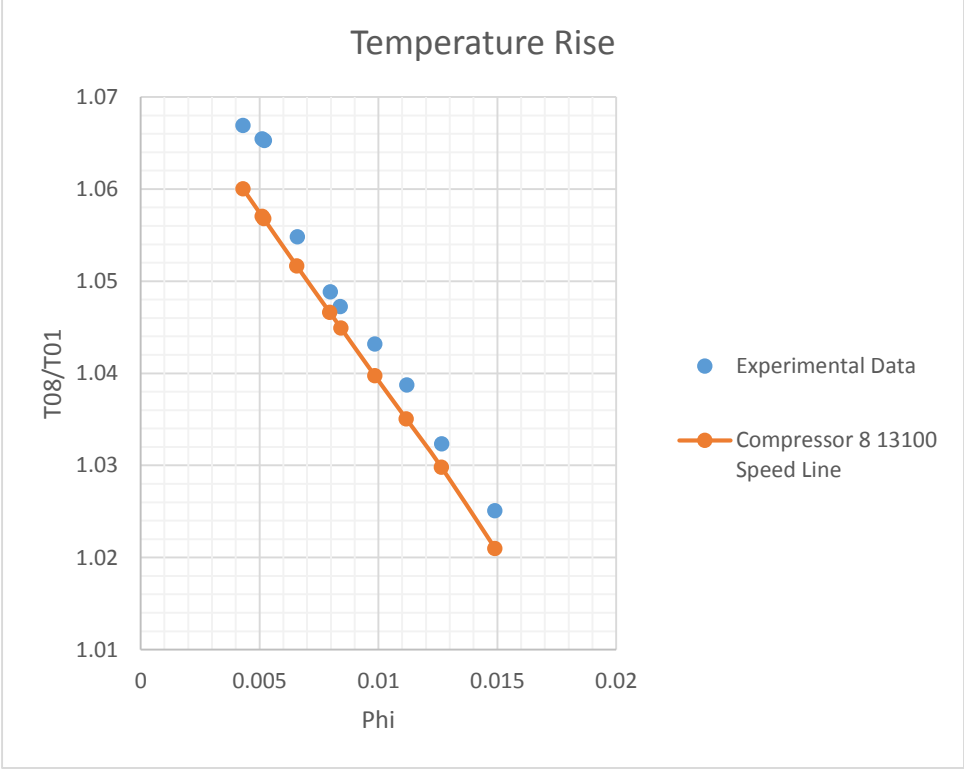


Figure 271: Compressor 8 13100 RPM Temperature Comparison

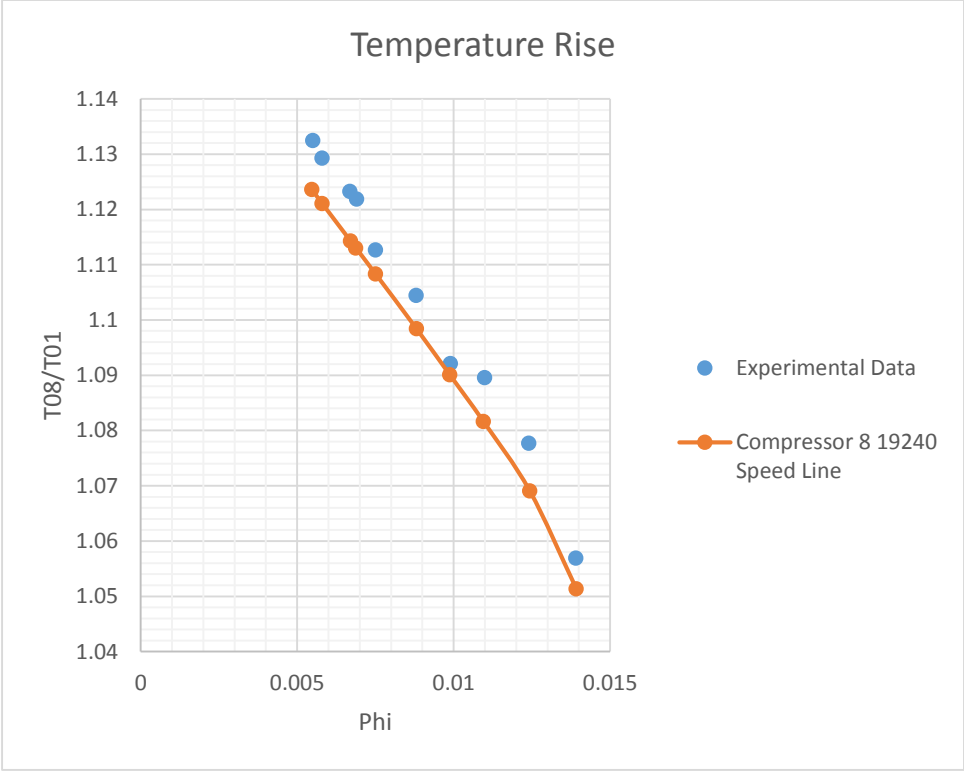


Figure 272: Compressor 8 19240 RPM Temperature Comparison

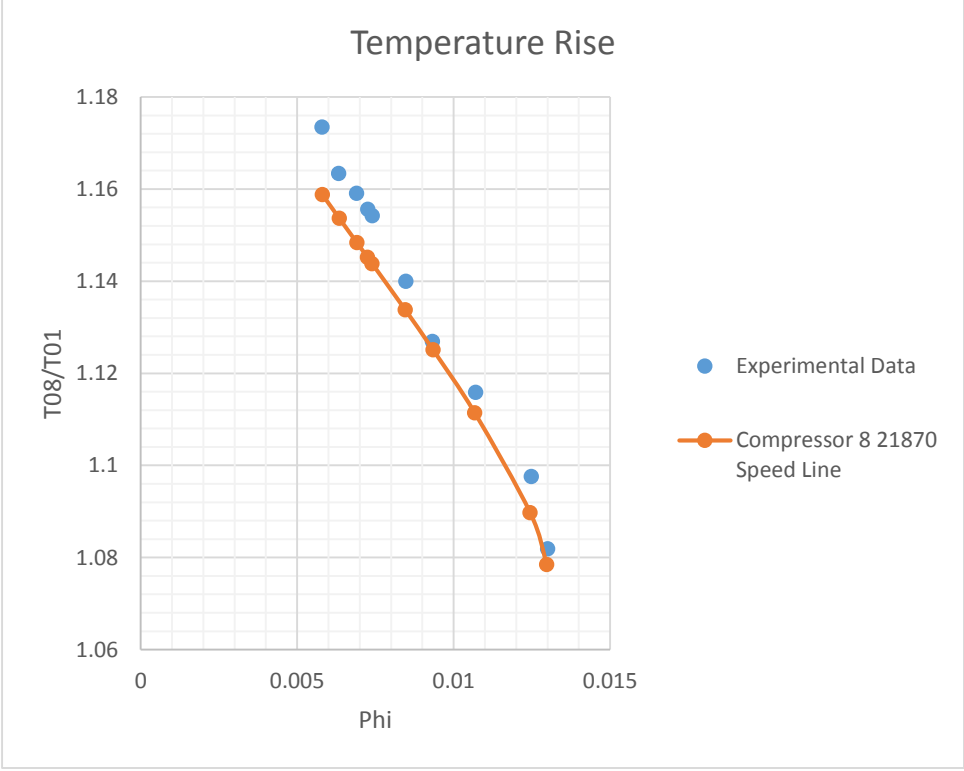


Figure 273: Compressor 8 21870 RPM Temperature Comparison

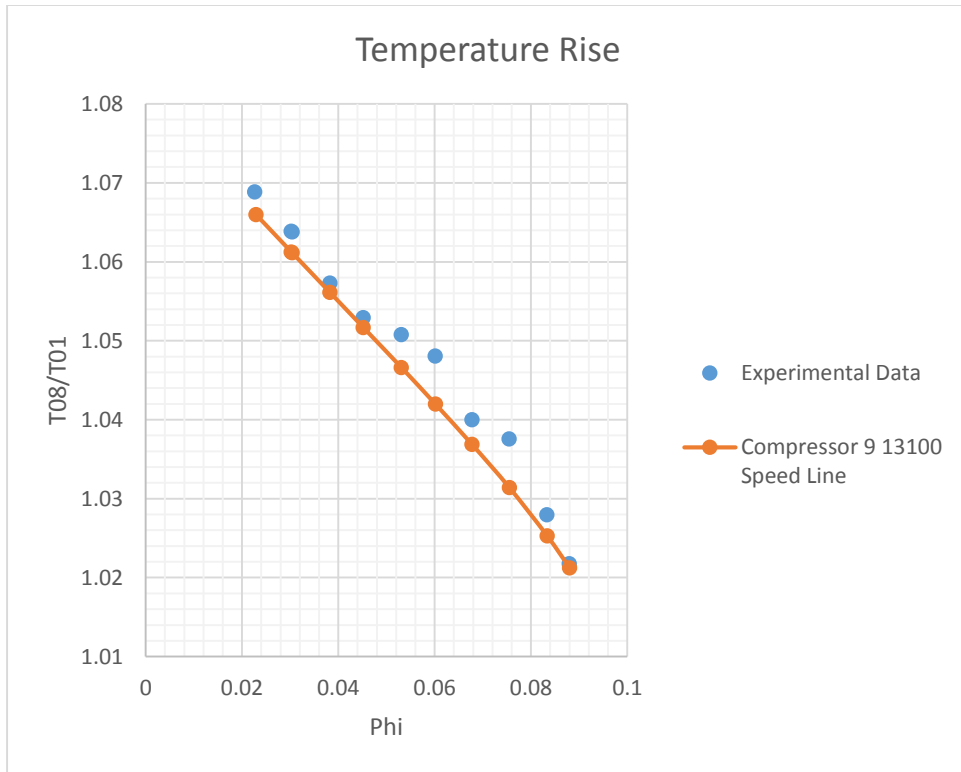


Figure 274: Compressor 9 13100 RPM Temperature Comparison

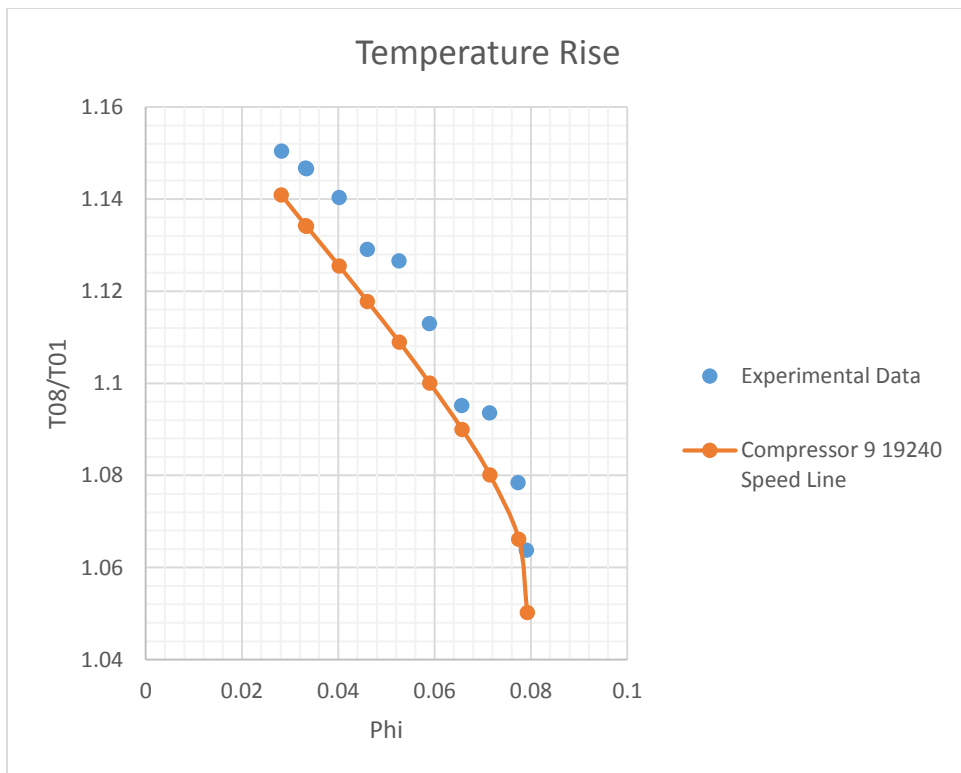


Figure 275: Compressor 9 19240 RPM Temperature Comparison

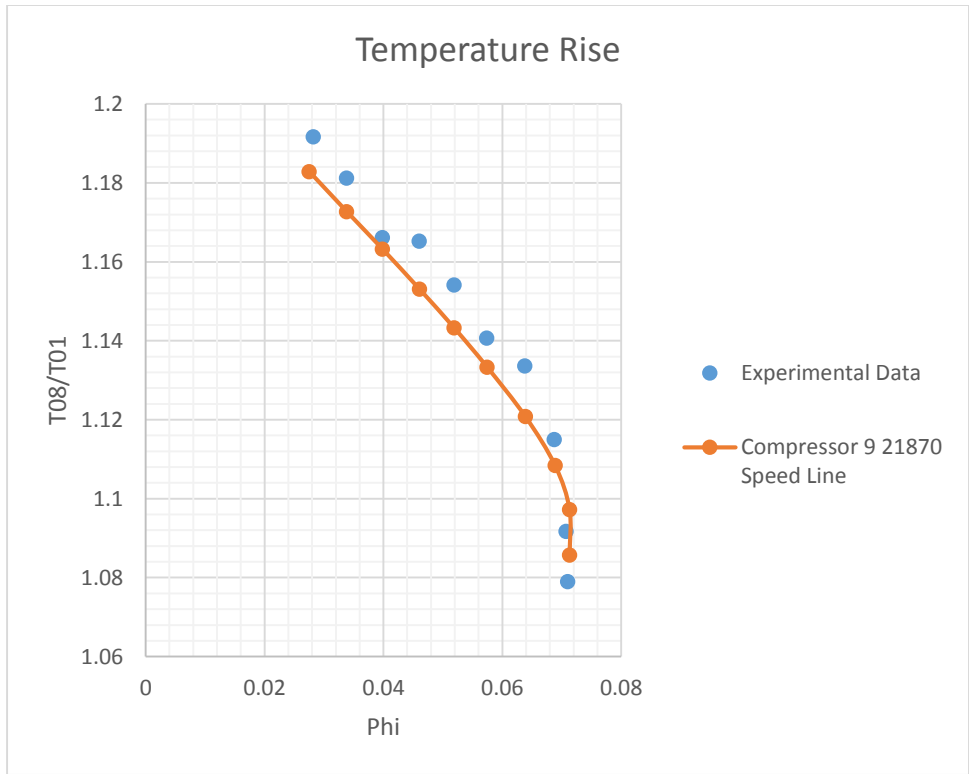


Figure 276: Compressor 9 21870 RPM Temperature Comparison

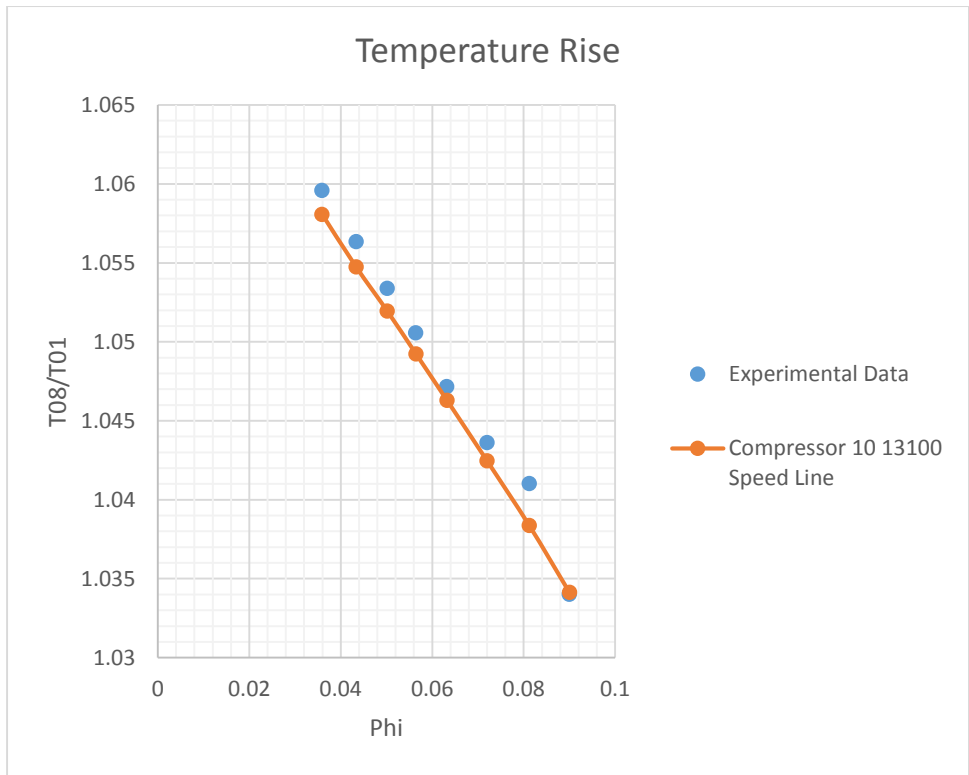


Figure 277: Compressor 10 13100 RPM Temperature Comparison

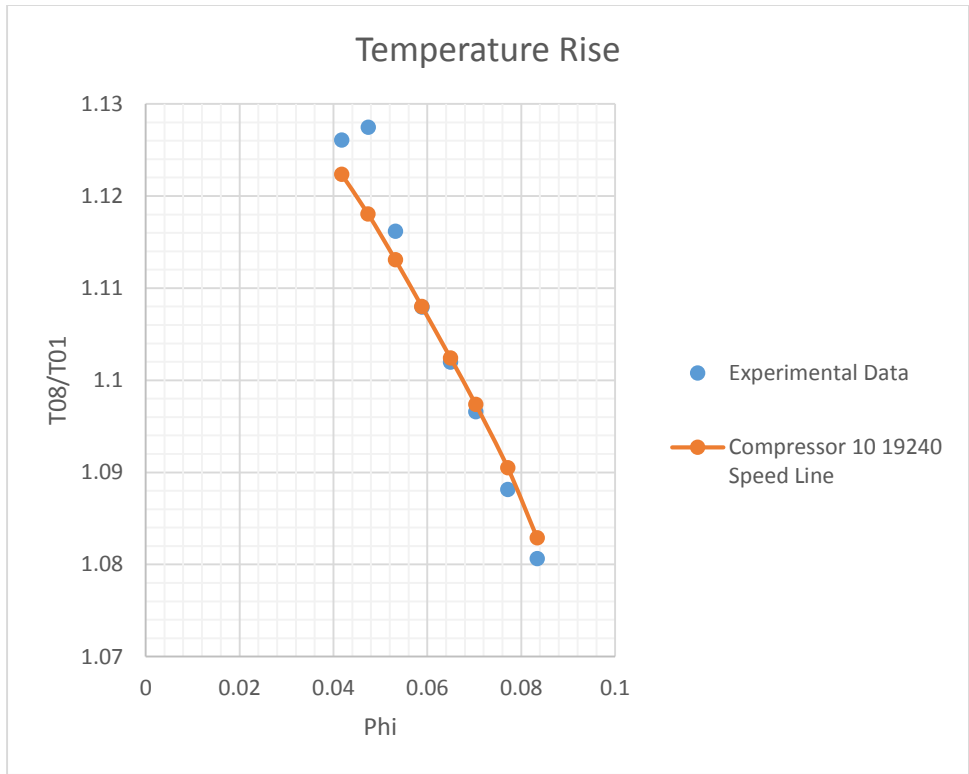


Figure 278: Compressor 10 19240 RPM Temperature Comparison

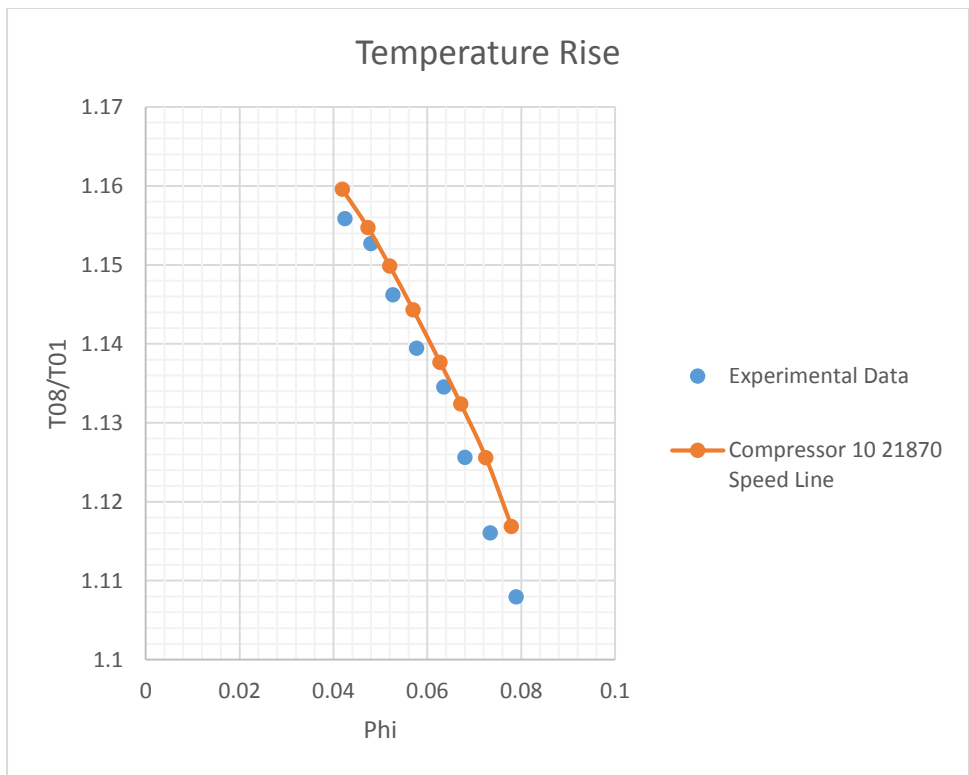


Figure 279: Compressor 10 21870 RPM Temperature Comparison

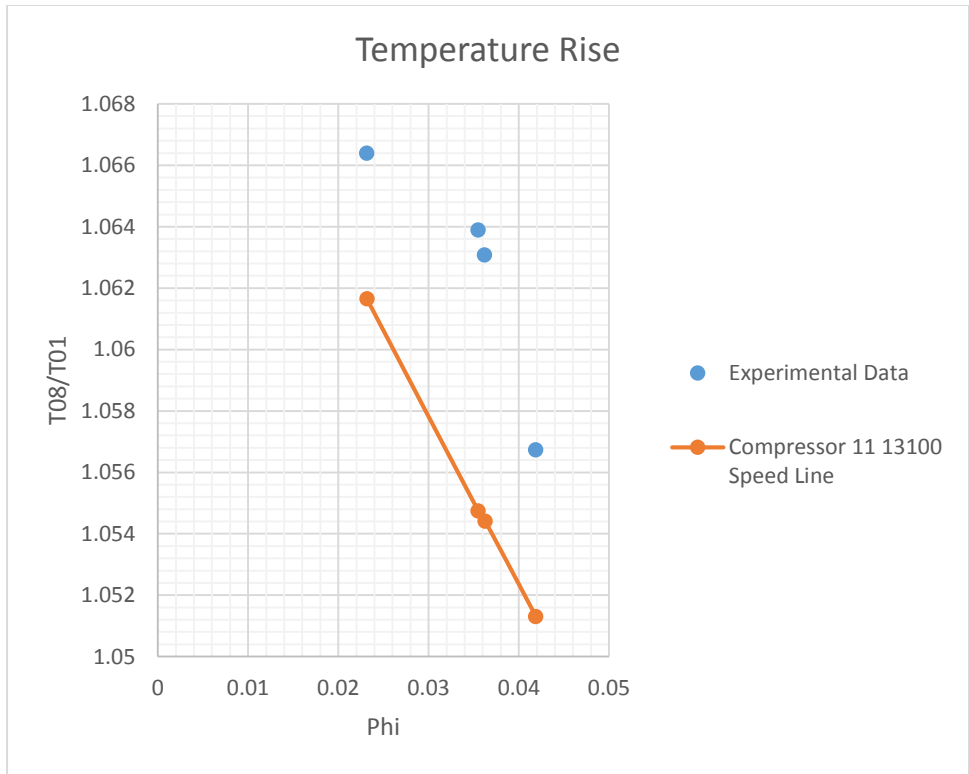


Figure 280: Compressor 11 13100 RPM Temperature Comparison

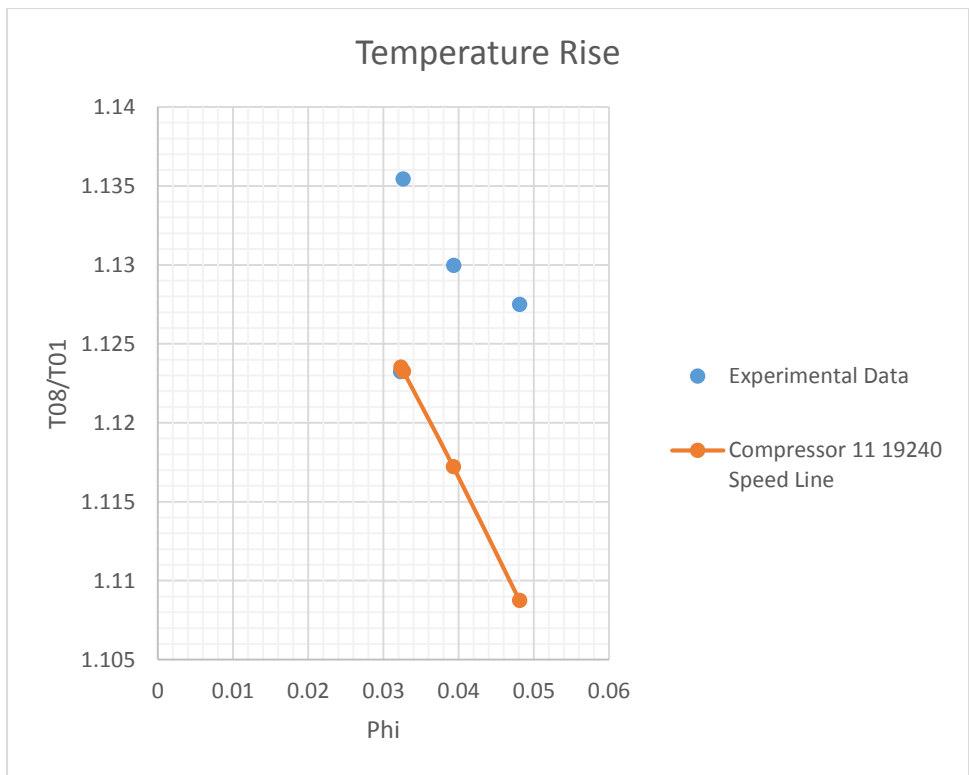


Figure 281: Compressor 11 19240 RPM Temperature Comparison

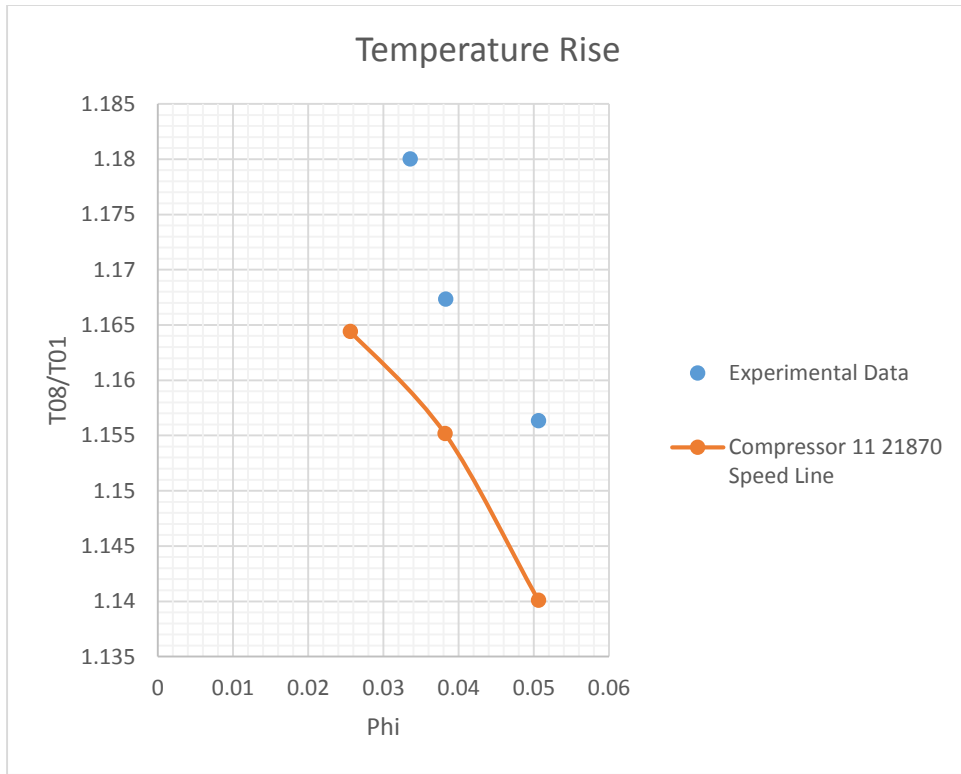


Figure 282: Compressor 11 21870 RPM Temperature Comparison

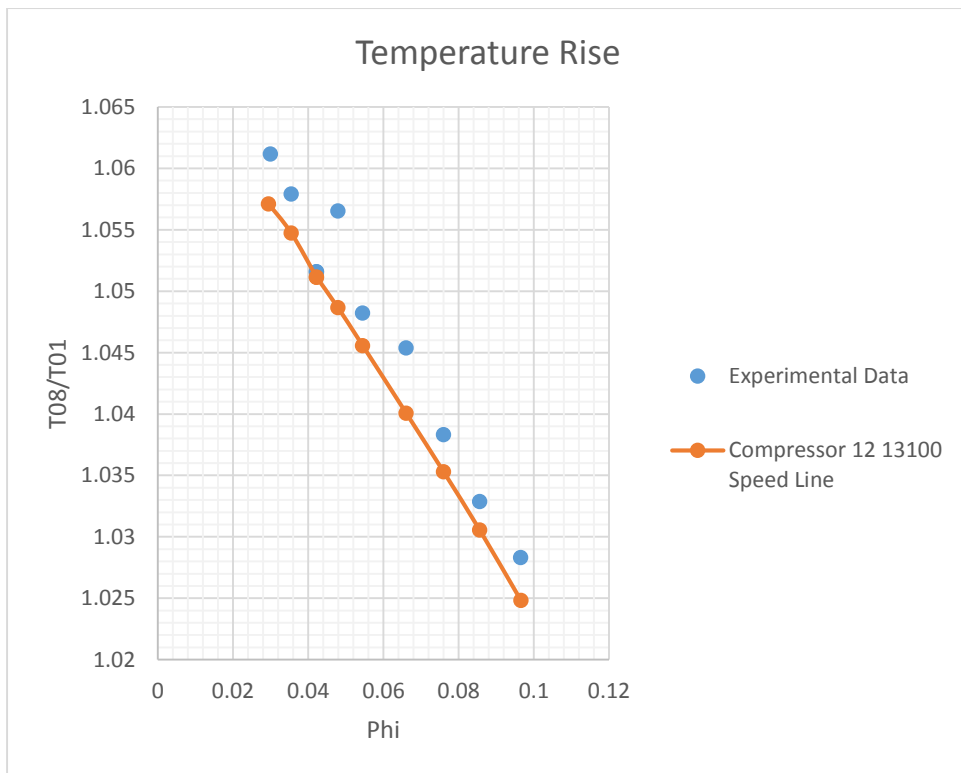


Figure 283: Compressor 12 13100 RPM Temperature Comparison

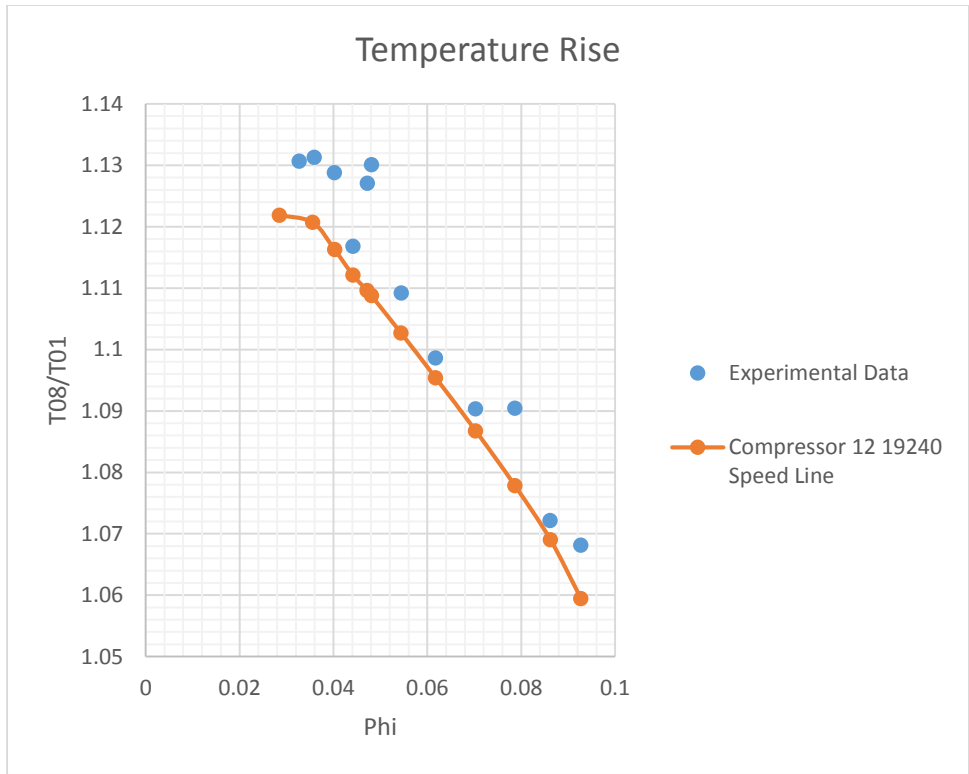


Figure 284: Compressor 12 19240 RPM Temperature Comparison

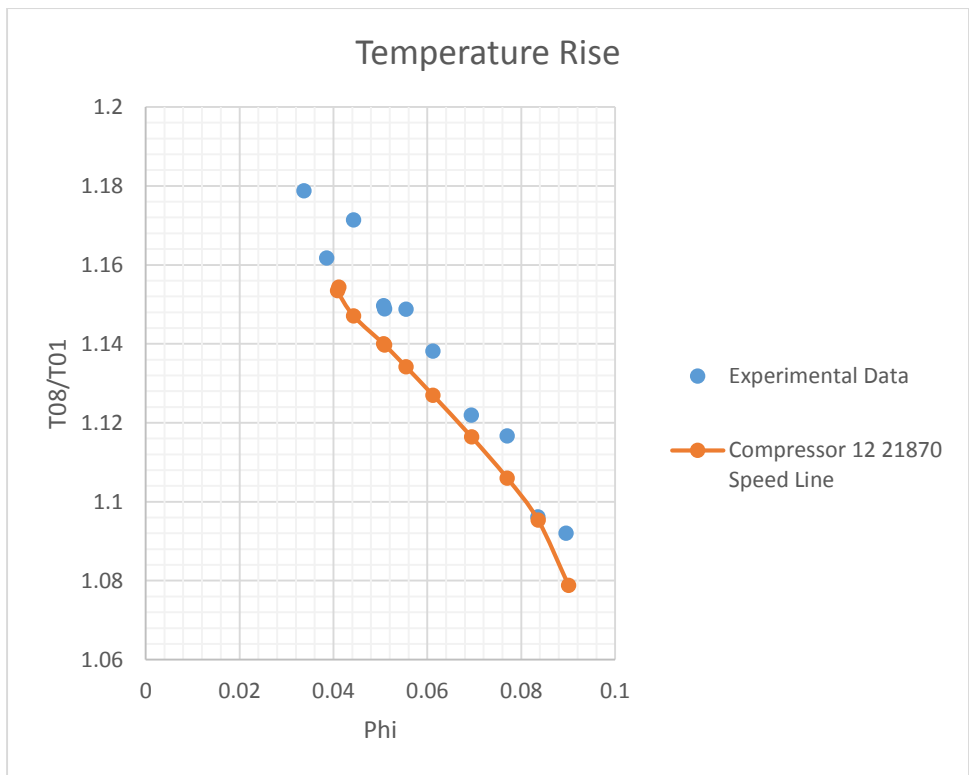


Figure 285: Compressor 12 21870 RPM Temperature Comparison

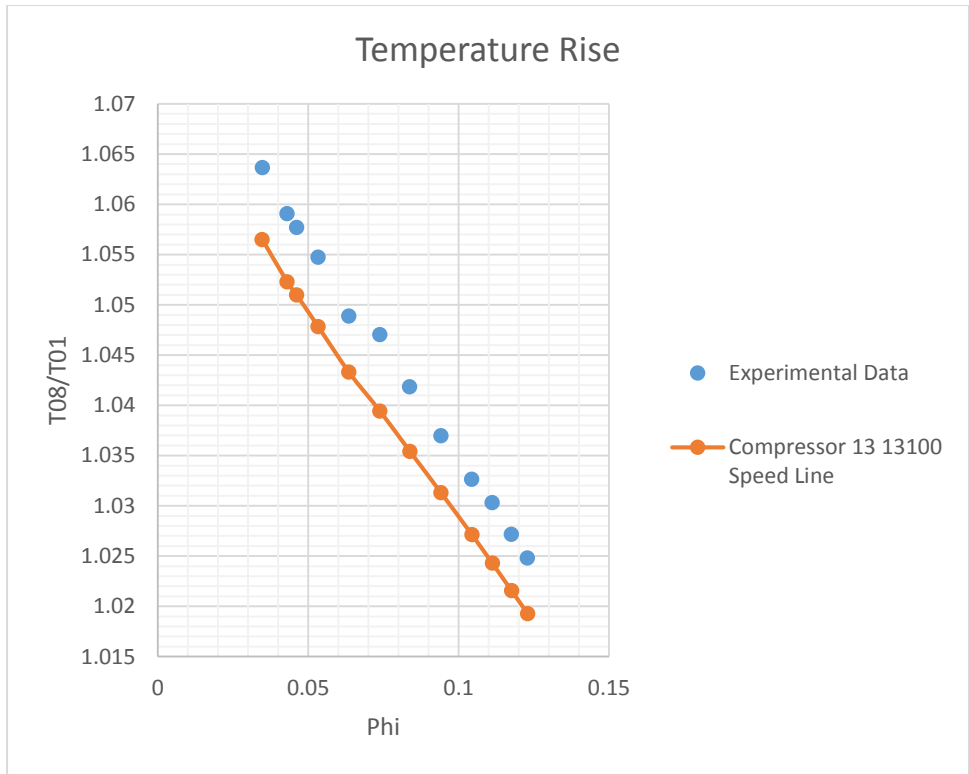


Figure 286: Compressor 13 13100 RPM Temperature Comparison

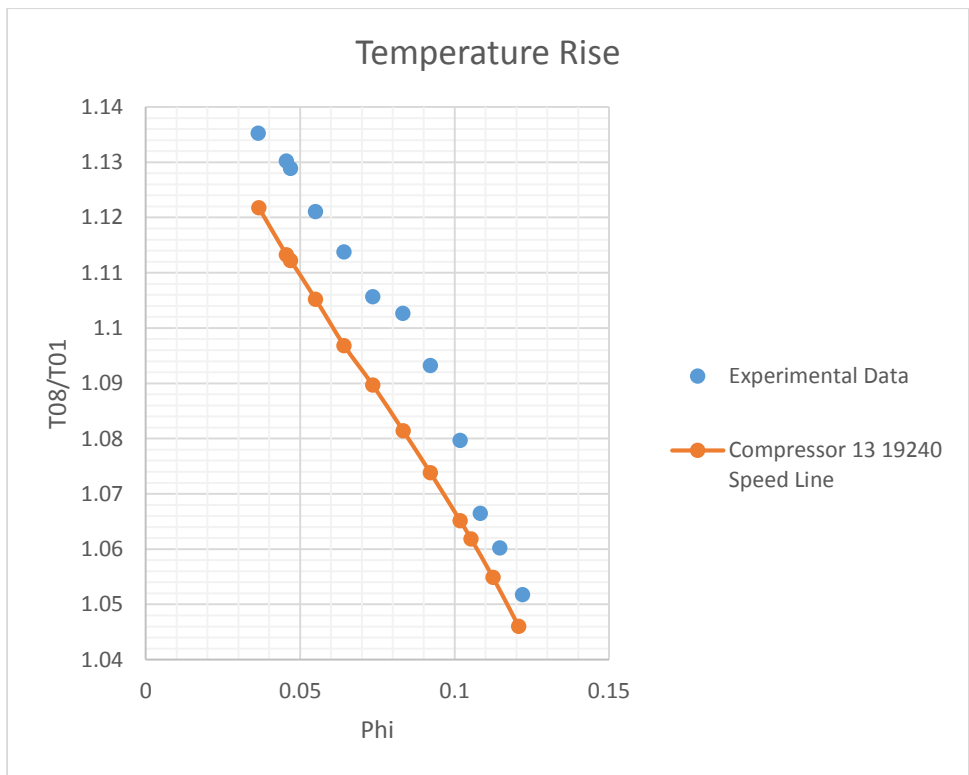


Figure 287: Compressor 13 19240 RPM Temperature Comparison

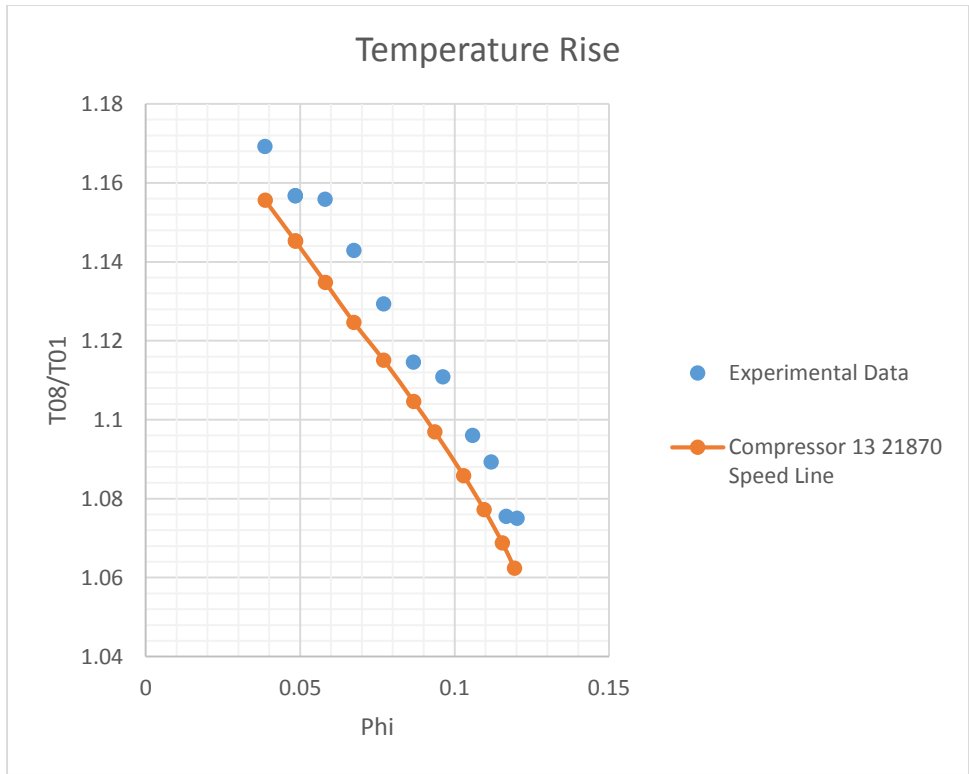


Figure 288: Compressor 13 21870 RPM Temperature Comparison

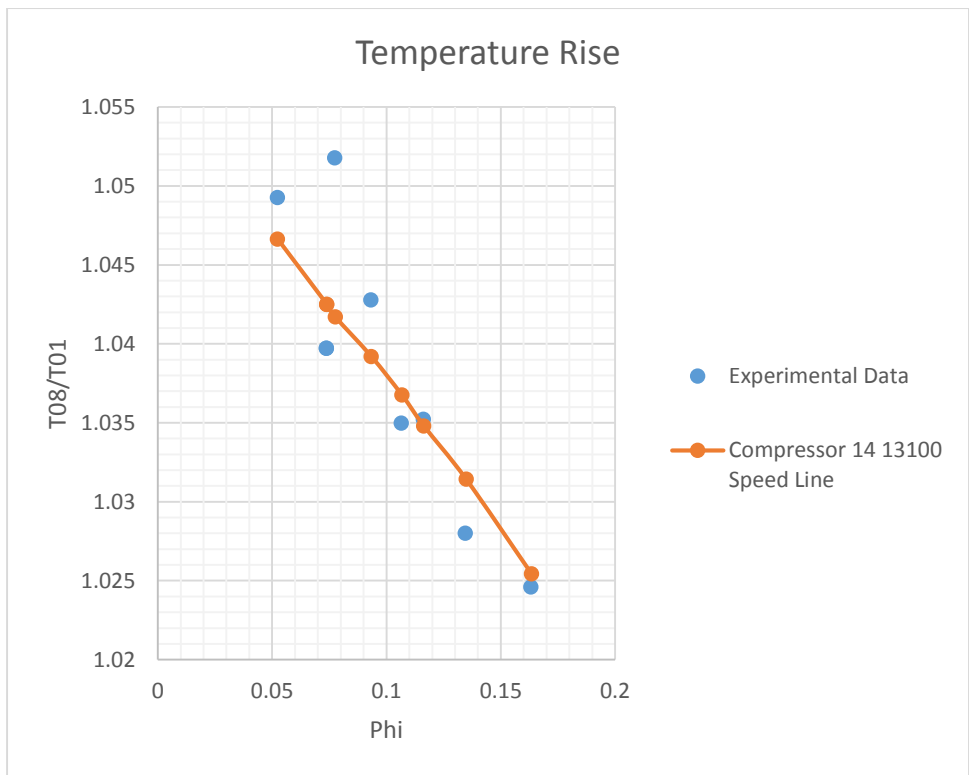


Figure 289: Compressor 14 13100 RPM Temperature Comparison

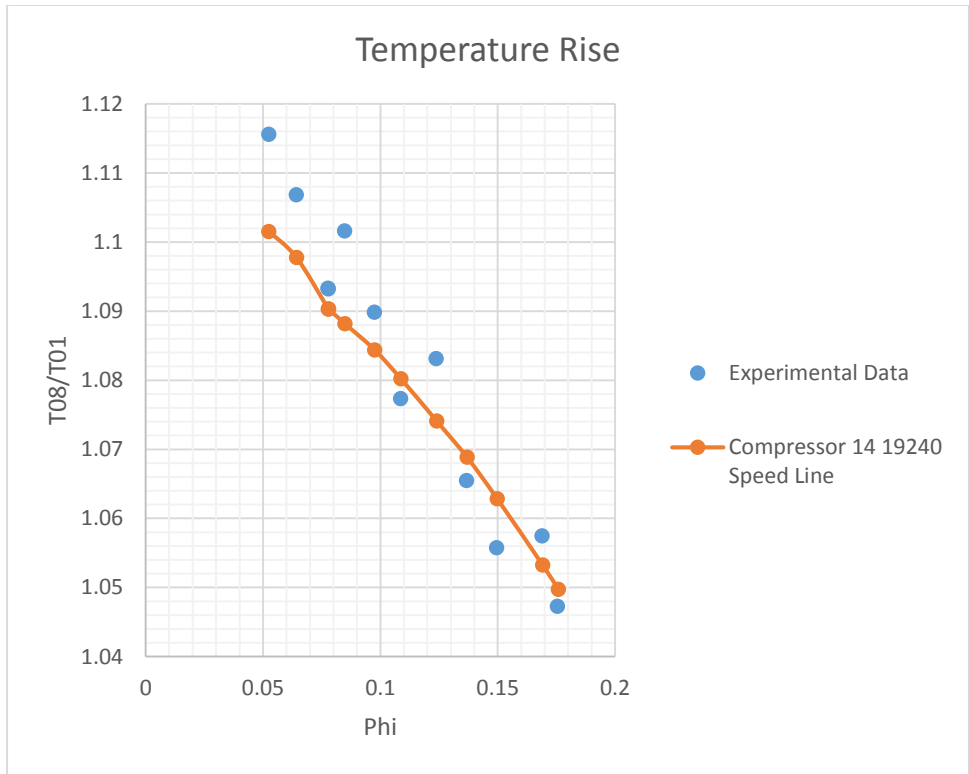


Figure 290: Compressor 14 19240 RPM Temperature Comparison

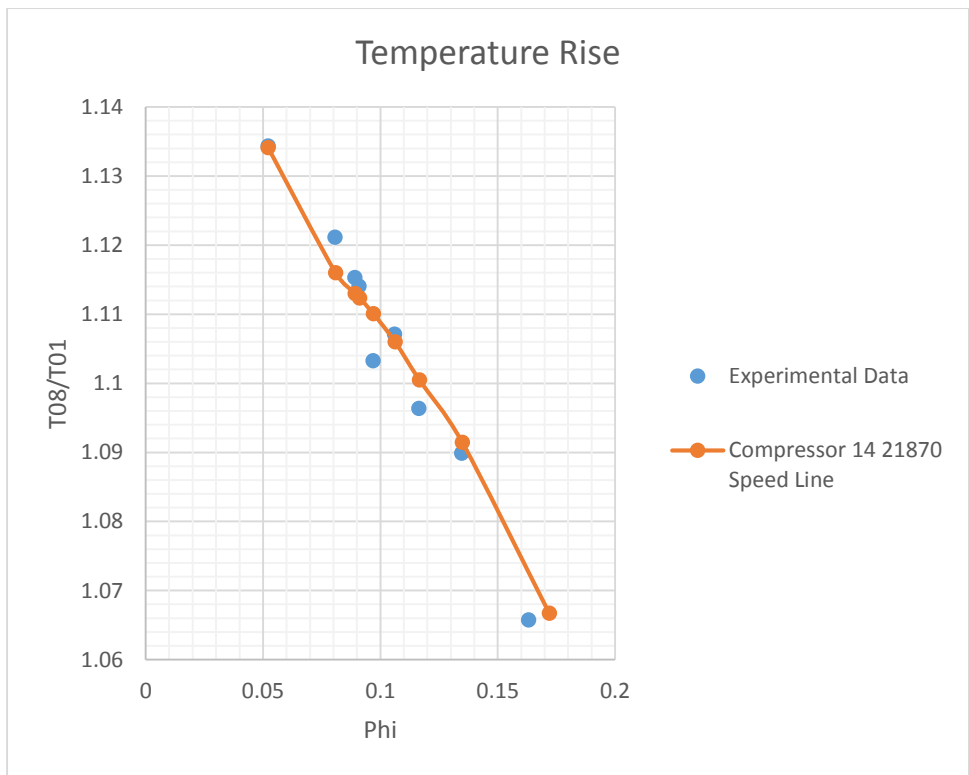


Figure 291: Compressor 14 21870 RPM Temperature Comparison

APPENDIX C: STEADY STATE SIMULATION AND SST INFORMATION

C.1 Steady State Simulation Background and Equations

All fluid flows are governed by the Navier-Stokes equations. The Navier-Stokes equation for momentum is provided below:

$$\frac{\partial(\rho\vec{U})}{\partial t} + \nabla \cdot (\rho\vec{U} \times \vec{U}) = -\nabla p + \nabla \cdot \tau + \rho\vec{g} \quad (\text{C.1})$$

where \vec{U} represents the velocity vector, t is the time, p is the pressure, \vec{g} is made up of the external body forces on the fluid, τ is the shear stress tensor, and ρ is the fluid density. Equation C.1 provides the general Navier Stokes momentum equation. The del operator is shown below:

$$\nabla = \vec{e}_x \frac{\partial}{\partial x} + \vec{e}_y \frac{\partial}{\partial y} + \vec{e}_z \frac{\partial}{\partial z} \quad (\text{C.2})$$

where e_x , e_y , and e_z represent unit vectors in the x , y , and z directions and x , y , and z represent the spacial x , y , and z coordinates.

Now since transient (i.e. time dependent studies) solutions are computationally expensive a steady state simulation is often used. To perform a steady state simulation the transient Navier-Stokes equations (see equation C.1) are time averaged using a Reynolds averaging scheme [48]. The Reynolds averaging scheme states that any variable can be written as

$$U(x, t) = \bar{U}(x) + u(x, t) \quad (\text{C.3})$$

where $u(x,t)$ is a time dependent fluctuation term and \bar{U} is a time independent average term [48]. The fluctuation term is considered to be small such that cross terms (i.e. two fluctuation terms multiplied together) are considered to be zero. It has been found that the time average of the fluctuation term is:

$$\overline{u(x, t)} = 0 \quad (\text{C.4})$$

while the $\bar{U}(x)$ term can be written as:

$$\bar{U}(x) = \frac{1}{\Delta t} \int_t^{t+\Delta t} U(x, t) dt \quad (\text{C.5})$$

where Δt is the time step, t is the time, and $U(x,t)$ is the term that is being time averaged [48].

Applying equations C.3 – C.5 to equation C.1 results in:

$$\frac{\partial(\rho \bar{U}_i)}{\partial t} + \frac{\partial(\rho \bar{U}_j \bar{U}_i)}{\partial x_j} = -\frac{\partial \bar{P}}{\partial x_i} - \frac{\partial(\rho \bar{\tau}_{ij} + \rho \bar{u}_i \bar{u}_j)}{\partial x_j} \quad (C.6)$$

where all of the above terms have been Reynolds averaged and the small cross terms have been removed [48]. Please note that equation C.6 is using tensor notation where i and j represent the numbers 1 – 3 corresponding to the three spacial coordinates used in the system and the Einstein summation convention is used for repeated indices. It has been found that the Reynolds Stress terms can be written as:

$$\rho \bar{u}_i \bar{u}_j = \rho * \begin{pmatrix} \overline{uu} & \overline{uv} & \overline{uw} \\ \overline{uv} & \overline{vv} & \overline{vw} \\ \overline{uw} & \overline{vw} & \overline{ww} \end{pmatrix} \quad (C.7)$$

where u , v , and w represent the fluctuation in the x , y , and z directions respectively [48]. Also note that the viscous stress tensor is given as:

$$\bar{\tau}_{ij} = \nu * \left[\frac{\partial \bar{U}_i}{\partial x_j} + \frac{\partial \bar{U}_j}{\partial x_i} \right] \quad (C.8)$$

where ν represents the kinematic viscosity, and all of the velocity terms have been time averaged [48]. A note about equation C.7 it was stated previously that the cross terms when multiplied would be small enough to be neglected. This is true except when those cross terms are time averaged. In this case the time averaging produces terms that are not small enough to be neglected [50]. Thus, the terms in equation C.7 are important and cannot be neglected. Furthermore, no amount of averaging or manipulation will remove these terms [50]. This represents the basics of the physical equations used in the ANSYS-CFX steady state simulation procedure. For more detail see the presentation by Menter given at ANSYS [48]. This presentation delves into much greater detail in the derivation of the viscous stress tensor.

C.2 SST Background and Equations

As was stated in section C.1 the velocity vector is transformed into a steady term and a smaller time dependent fluctuation term (see equation C.3). As the fluid flows through a geometry there is interaction between the fluid and the walls due to viscosity. This viscous interaction causes eddies to form in the fluid. These eddies will interact forming smaller eddies that are often referred to as turbulence. To account for the effects of turbulence in a steady state simulation a turbulence model is employed. For the purposes of these models the Shear Stress Transport (SST) turbulence model developed by Menter is used.

The boundary layer can be split into four separate regions: the laminar sublayer, the log layer, the wake region, and the boundary layer edge region [48]. The SST model attempts to bridge the gap between two separate turbulence models: k- ϵ and k- ω . The k- ϵ model is good in the boundary layer edge region [48, 49]. However, the k- ϵ model is not very accurate in the laminar sublayer region near the wall [48]. The k- ω model is very good in the region near the wall, and accurate in the log region between the wall and the wake region where mixing takes place [48]. Neither model is terribly accurate in the wake region [48]. So, the SST model seeks to blend the k- ϵ and k- ω models to provide a more accurate reflection of the flow in the boundary layer and its effects on the overall fluid flow through the geometry.

For this model it is found that the turbulent kinetic energy can be expressed as:

$$\frac{\partial(\rho*k)}{\partial t} + \frac{\partial(\rho*U_i*k)}{\partial x_i} = \tilde{P}_k - \beta^* * \rho * k * \omega + \frac{\partial\left(\left(\mu + \sigma_k*\mu_t\right)*\frac{\partial k}{\partial x_i}\right)}{\partial x_i} \quad (C.9)$$

where k is the turbulent kinetic energy, t is the time, x_i represents the spacial derivatives, U_i represents the velocity vector, μ is the viscosity, μ_t is the turbulent eddy viscosity, ω is the dissipation of the turbulent kinetic energy into heat energy, ρ is the fluid density, β^* is a constant,

\tilde{P}_k is a turbulence production limiter to prevent turbulence buildup in stagnation regions (see below), and σ_k is a constant [49]. The dissipation term, ω , is written as:

$$\frac{\partial(\rho^*\omega)}{\partial t} + \frac{\partial(\rho^*U_i^*\omega)}{\partial x_i} = \alpha * \rho * S^2 - \beta * \rho * \omega^2 + \frac{\partial}{\partial x_i} \left[(\mu + \sigma_\omega * \mu_t) * \frac{\partial \omega}{\partial x_i} \right] + 2 * (1 - F_1) * \rho * \sigma_{\omega 2} * \frac{1}{\omega} * \frac{\partial k}{\partial x_i} * \frac{\partial \omega}{x_i} \quad (C.10)$$

where α , β , σ_ω , $\sigma_{\omega 2}$ are constants, μ is the viscosity, μ_t is the turbulent eddy viscosity, x_i represents the spacial derivatives, U_i represents the velocity vector, F_1 is the blending factor, ρ is the fluid density, and S is the invariant measure of the strain rate [49]. Menter showed that F_1 can be written as:

$$F_1 = \tanh \left[\left[\min \left[\max \left(\frac{\sqrt{k}}{\beta^* \omega y}, \frac{500\nu}{y^2 \omega} \right), \frac{4\rho\sigma_{\omega 2}k}{CD_{k\omega}y^2} \right] \right]^4 \right] \quad (C.11)$$

where k is the turbulent kinetic energy, y is the distance to the nearest wall, β^* is a constant, $CD_{k\omega}$ is a constant (defined below), ν is the kinematic viscosity, ω is the dissipation of the turbulent kinetic energy into heat energy, ρ is the fluid density, and $\sigma_{\omega 2}$ is a constant [49]. It was also shown that $CD_{\omega k}$ can be written as:

$$CD_{k\omega} = \max \left(2\rho\sigma_{\omega 2} \frac{1}{\omega} \frac{\partial k}{\partial x_i} \frac{\partial \omega}{\partial x_i}, 10^{-10} \right) \quad (C.12)$$

where ρ is the fluid density, $\sigma_{\omega 2}$ is a constant, k is the turbulent kinetic energy, ω is the dissipation of the turbulent kinetic energy into heat energy, and x_i represents the spacial derivatives [49]. Furthermore, the turbulent eddy viscosity can be written as:

$$\nu_t = \frac{a_1 k}{\max(a_1 \omega, SF_2)} \quad (C.13)$$

where a_1 is a constant, F_2 is a second blending factor (see below), k is the turbulent kinetic energy, ω is the dissipation of the turbulent kinetic energy into heat energy, and S is the invariant measure of the strain rate [49]. The second blending factor, F_2 , is found to be:

$$F_2 = \tanh \left[\left\{ \max \left(\frac{2\sqrt{k}}{\beta^* \omega y}, \frac{500\nu}{y^2 \omega} \right) \right\}^2 \right] \quad (\text{C.14})$$

where k is the turbulent kinetic energy, ω is the dissipation of the turbulent kinetic energy into heat energy, β^* is a constant, ν is the kinematic viscosity, and y is the distance to the nearest wall [49].

Lastly, it was found that \tilde{P}_k is defined as:

$$P_k = \mu_t \frac{\partial U_i}{\partial x_j} \left(\frac{\partial U_i}{\partial x_j} + \frac{\partial U_j}{\partial x_i} \right) \rightarrow \tilde{P}_k = \min(P_k, 10\beta^* \rho k \omega) \quad (\text{C.15})$$

where P_k is the Reynolds Stress term, \tilde{P}_k is a turbulence production limiter to prevent turbulence buildup in stagnation regions, ρ is the fluid density, where k is the turbulent kinetic energy, ω is the dissipation of the turbulent kinetic energy into heat energy, and β^* is a constant [49].

So, equations C.9 – C.15 provide many of the details as to how the SST turbulence model functions and exactly what it is calculating. Please note that to get specific values for each constant refer to Menter et al. in [49]. Also, please note this discussion is meant to serve as a background to the SST model and the underlying equations. For a more in depth discussion see Menter's work in [48, 49].

Also, there is one final point to consider. To use any turbulence model it is best to have a mesh with a y^+ value less than some critical value. The y^+ term is defined as the dimensionless wall distance and is written as:

$$y^+ = \frac{u_* y}{\nu} \quad (\text{C.16})$$

where y is the distance to the nearest wall, ν is the kinematic viscosity, and u_* is the friction velocity. To employ the SST model it is best to have a dense enough grid to have a y^+ of approximately 10 or less [27]. For k - ϵ the y^+ value should be around 300, and the k - ω the y^+ value should be around 30 [27]. It is of note that for this dissertation the y^+ was approximately 150. However, this is not an issue. During the grid sensitivity study the y^+ dependence of the

models was tested. It was found that as the mesh density was increased to decrease the y^+ that significant numerical errors were created. These errors were large enough to create a loss of accuracy between the numerical and experimental results that outweighed any losses caused by the lack of y^+ accuracy. As an interesting note this type of behavior was found by Menter et al. in [49]. This result serves to show that despite the fact that there are guidelines that exist for when a certain turbulence model is applicable those guidelines are just guidelines. The ability to know when to ignore the guidelines and push forward will significantly help a researcher with shortening their simulation time and lessening the computational resources required.

REFERENCES

REFERENCES

1. Abdelhamid, A. N. "Analysis of Rotating Stall in Vaneless Diffusers of Centrifugal Compressors", Canadian Aeronautics and Space Journal, Vol. 26, No. 2, Second Quarter 1980
2. Abdelhamid, A. N. "Effects of Vaneless Diffuser Geometry on Flow Instability in Centrifugal Compression Systems", Canadian Aeronautics and Space Journal, Vol. 29, No. 3, September 1983
3. Abdelhamid, A. N. "Control of Self-Excited Flow Oscillations in Vaneless Diffuser of Centrifugal Compression Systems", Canadian Aeronautics and Space Journal, Vol. 29, No. 4, September 1983
4. Anish, S., and Sitaram, N. "Steady and Transient Computations of Interaction Effects in a Centrifugal Compressor with Different Types of Diffusers", ASME Paper GT 2010-22913, June 14-18, 2010.
5. Aungier, R. "Centrifugal Compressors: A Strategy for Aerodynamic Design and Analysis", ASME Press, February 2000 pgs. 159-166
6. Chen, J., Webster, R., Hathaway, M., Herrick, G., and Skoch, G. "High Performance Computing of Compressor Rotating Stall and Stall Control", DOI 10.3233/ICA-2009-0305, 2009
7. Day, I.J. "Active Suppression of Rotating Stall and Surge in Axial Compressors", Transactions of the ASME, Journal of Turbomachinery, Vol. 115, January 1993
8. Dean, R. C. "On the Necessity of Unsteady Flow in Fluid Machines", Transactions of the ASME, Journal of Basic Engineering, March, 1959
9. Dean, R. C., and Senoo, Y. "Rotating Wakes in Vaneless Diffusers", Transactions of the ASME, Journal of Basic Engineering, September 1960
10. De Jager, B. "Rotating Stall and Surge Control: A Survey", Proceedings of the 34th Conference on Decision and Control, December, 1995
11. Engeda, A. "ME 442: Turbomachinery Notes", Spring 2013, Michigan State University, 2013
12. Engeda, A. Professor, Department of Mechanical Engineering, Michigan State University, Personal Communication, 2015
13. Frigne, P., and Van den Braembussche, R. A. "Distinction Between Different Types of Impeller and Diffuser Rotating Stall in a Centrifugal Compressor With Vaneless Diffuser", Transactions of the ASME, Journal of Engineering for Gas Turbines and Power, Vol 106, April 1984

14. Hildebrandt, A., and Genrup, M. "Numerical Investigation of the Effect of Different Back Sweep Angle and Exducer Width on the Impeller Outlet Flow Pattern of a Centrifugal Compressor with Vaneless Diffuser", ASME Paper GT2006-90622, May 8-11, 2006
15. Jansen, W. "Rotating Stall in a Radial Vaneless Diffuser", Transactions of the ASME, Journal of Basic Engineering, June 22, 1964
16. Jansen, W. "Steady Fluid Flow in a Radial Vaneless Diffuser", Transactions of the ASME, Journal of Basic Engineering, September 1964
17. Kinoshita, Y., Senoo, Y. "Rotating Stall Induced in Vaneless Diffusers of Very Low Specific Speed Centrifugal Blowers", Transactions of the ASME, Journal of Engineering for Gas Turbines and Power, Vol. 107, April 1985
18. Kline, S. J., Moore, C. A., and Cochran, D. L. "Wide-Angle Diffusers of High Performance and Diffuser Flow Mechanisms", Reader's Forum, Journal of the Aeronautical Sciences, Vol. 24, No. 3, pgs. 469-470, June, 1957
19. Kline, S. J., and Runstadler, P. W. "Some Preliminary Results of Visual Studies of the Flow Model of the Wall Layers of the Turbulent Boundary Layer", Transactions of the ASME, Journal of Applied Mechanics, June 1959
20. Kline, S. J. "On the Nature of Stall", Transactions of the ASME, Journal of Basic Engineering, September 1959
21. Krain, H. "Review of Centrifugal Compressor's Application and Development", ASME Paper GT2003-38971, June 16-19, 2003
22. Lennemann, E., and Howard, J. H. G. "Unsteady Flow Phenomena in Rotating Centrifugal Impeller Passages", Transactions of the ASME, Journal of Engineering for Power, January 1970
23. Ljevar, S., De Lange, H. C., and Van Steenhoven, A. A. "Rotating Stall Characteristics in a Wide Vaneless Diffuser", ASME Paper GT2005-68445, June 6-9, 2005
24. Ljevar, S., De Lange, H. C., and Van Steenhoven, A. A. "Two-Dimensional Rotating Stall Analysis in a Wide Vaneless Diffuser", DOI 10.1155/IJRM/2006/56420
25. Ljevar, S., De Lange, H. C., and Van Steenhoven, A. A. "Comparison of a Two-Dimensional Viscid and Inviscid Model for Rotating Stall Analysis", 4th WSEAS International Conference on Fluid Mechanics and Aerodynamics, August 21-23, 2006
26. Ludtke, K.H. "Process Centrifugal Compressors: Basics, Function, Operation, Design, Application", 2004 Edition, pgs. 140-147, Springer, Verlag Berlin Heidelberg, Print
27. Marechale, R. Senior Engineer at Solar Turbines, Personal Communication, 2014

28. Marshall, D.F., and Sorokes, J.M. "A Review of Aerodynamically Induced Forces Acting on Centrifugal Compressors, and Resulting Vibration Characteristics of Rotors", Dresser-Rand Company, Proceedings of the 29th Turbomachinery Symposium
29. Niazi, S., Stein, A., and Sankar, L. "Development and Application of a CFD Solver to the Simulation of Centrifugal Compressors", AIAA Paper 98-0934, January, 1998
30. Peeters, M., and Sleiman, M. "A Numerical Investigation of the Unsteady Flow in Centrifugal Stages", ASME Paper 2000-GT-426, 2000
31. Sankar, L., Prasad, J., Neumeier, Y., Haddad, W., Markopoulos, N., Stein, A., Niazi, S., and Leonessa, A. "Recent Progress in Compressor Stall and Surge Control", AIAA Paper (No paper reference given in article), 1999
32. Senoo, Y., and Kinoshita, Y. "Influence of Inlet Flow Conditions and Geometries of Centrifugal Vaneless Diffusers on Critical Flow Angle for Reverse Flow", Transactions of the ASME, Journal of Fluids Engineering, March 1977
33. Senoo, Y., Kinoshita, Y., and Ishida, M. "Asymmetric Flow in Vaneless Diffusers of Centrifugal Blowers", Transactions of the ASME, Journal of Fluids Engineering, March 1977
34. Senoo, Y., and Kinoshita, Y. "Limits of Rotating Stall and Stall in Vaneless Diffuser of Centrifugal Compressors", ASME Paper 78, 1978
35. Sheard, A., and Corsini, A. "The Impact of an Anti-Stall Stabilization Ring on Industrial Fan Performance: Implications for Fan Selection", ASME Paper GT2011-45187, 2011
36. Spakovszky, Z. "Backward Traveling Rotating Stall Waves in Centrifugal Compressors", Transactions of the ASME, Journal of Turbomachinery, Vol. 126, January, 2004
37. Tamaki, H. "Effect of Recirculation Device with Counter Swirl Vane on Performance of High Pressure Ratio Centrifugal Compressor", ASME Paper GT2011-45360, 2011
38. Torres, R. "ATF C40P C2-1 Vaneless RTV Part I: Insulated Test", Solar Turbines GCER-8210, Issued 8/13/13
39. Vagani, M. "Numerical Simulation and Modeling of Compressor Stage Instability of a Rotating Stall Nature", PhD. Dissertation, Michigan State University, East Lansing, MI, 2012
40. Van den Braembussche, R. A., Frigne, P., and Roustan, M. "Rotating Non Uniform Flow in Radial Compressors", AGARD CP282, 1980
41. Van Den Braembussche, R. "Rotating Stall in Vaneless Diffusers of Centrifugal Compressors", VKI Technical Note 145, 1982

42. Wiesner, F. J. “A New Appraisal of Reynolds Number Effects on Centrifugal Compressor Performance”, Transactions of the ASME, Journal of Engineering for Power, Vol. 101, July 1979
43. Wolfram, D., and Carolus, T. “Experimental and Numerical Investigation of the Unsteady Flow Field and Tone Generation in an Isolated Centrifugal Fan Impeller”, ASME Paper GT2011-45244, 2011
44. Day, I.J. “Stall Inception in Axial Flow Compressors”, Transactions of the ASME, Journal of Turbomachinery, Vol. 115, January 1993
45. Emmons, H. W., Kronauer, R. E., and Rockett, J. A. “A Survey of Stall Propagation – Experiment and Theory”, Transactions of the ASME, Journal of Basic Engineering, September 1959
46. Freeman, B. “ATF Test Procedure: Insulated and Traverse Tests”, Solar Turbines GCER-7964, Issued 8/31/12
47. Paul, C. Academic Teaching Specialist, Department of Mechanical Engineering, Michigan State University, Personal Communication, 2015
48. Menter, F., “RANS Modelling in ANSYS CFD”, PowerPoint Presentation, ANSYS, 2007
49. Menter, F. R., Kuntz, M., Langtry, R. “Ten Years of Industrial Experience with the SST Turbulence Model”, Turbulence, Heat, and Mass Transfer, Begell House, Inc., 2003
50. Naguib, A. “ME 832: Compressible Fluid Mechanics Notes”, Spring 2012, Michigan State University, 2012